# UNIVERSITÉ DE STRASBOURG

*ÉCOLE DOCTORALE DE SCIENCES CHIMIQUES (ED222)*

**[Institut de chimie - UMR 7177]**

# THÈSE

présentée par :

**Fule WU**

soutenue le : **26 November 2021**

pour obtenir le grade de : **Docteur de l'université de Strasbourg**

Discipline/ Spécialité : CHIMIE

# Cobaltacycles du Cp*Co(III): Synthèse rationnelle et implication en catalyse homogène

**THÈSE dirigée par :**

| | |
|---|---|
| **Dr. DJUKIC Jean-Pierre** | Directeur de recherche, Université de Strasbourg |

**RAPPORTEURS :**

| | |
|---|---|
| **Pr. MARTIN-VACA Blanca** | Professeur d'université, Université Paul Sabatier |
| **Dr. AUFFRANT Audrey** | Directrice de recherche CNRS, École Polytechnique, CNRS |

---

**AUTRE MEMBRE DU JURY :**

| | |
|---|---|
| **Pr. RITLENG Vincent** | Professeur d'université, Université de Strasbourg |

**MEMBRE INVITE DU JURY :**

| | |
|---|---|
| **Dr. DERAEDT Christophe** | Chargé de recherche CNRS, Université de Strasbourg |

Chemistry is

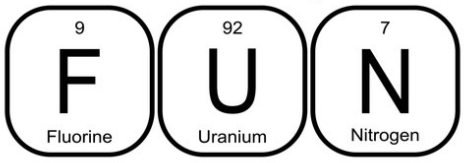

# Acknowledgement

My study at the LCSOM (Laboratoire de Chimie et Systémique Organo-Métalliques) will soon come to an end, and to the completion of my graduation thesis, I wish to express my sincere appreciation to all those who have offered me invaluable help during the three years of my PhD at university of Strasbourg.

Firstly, I would like to express my heartfelt gratitude to my supervisor, Dr. Jean-Pierre DJUKIC, for his constant encouragement and guidance though out my study. Moreover, he provided insightful comments on all the revisions of the thesis and provided me with many inspiring ideas, which encouraged me to a great extent. Without his patient guidance, the completion of this thesis would have been impossible.

Secondly, I should give my hearty thanks to all the members of our group, Dr. Michel PFEFFER, Geneviève STOLL, Mélanie BOUCHER, Christophe DERAEDT, Yann CORNATON, Dang Binh HO for all the help you have given me during my three years. Thanks to Christophe DERAEDT for the experimental support and kinds of suggestions ; thanks to Yann CORNATON for the excellent computational studies ; thanks to Lydia KARMAZIN, Corinne BAILLY, Nathalie GRUBER for the help of X-ray characterization ; thanks to Maurice COPPE and Bruno VINCENT for the help of NMR ; thanks to Laurent Ruhlmann for his help with cyclic voltammetry ; thanks to Sylvie CHOUA and Nolwenn LE BRETON for our EPR experiments; thanks to all the members of the Elemental Analysis and Mass Spectroscopy services for their contribution and assistance.

I would also like to thank Pr. Blanca MARTIN-VACA (Université Paul Sabatier), Dr. Audrey AUFFRANT (École Polytechnique) and Pr. Vincent RITLENG (Université de Strasbourg) for accepting to take part to this thesis jury and to evaluate this work.

My thanks would go to my beloved family for their loving considerations and great confidence in me all through these years. I also owe my sincere gratitude to my friends who have made my life in Strasbourg so enriching.

Finally, I deeply appreciate the financial support provided by the China Scholarship Council (CSC), which gave me an opportunity to study abroad and gain insight.

# Remerciements

Mes études au LCSOM (Laboratoire de Chimie et Systémique Organo-Métalliques) arrivent bientôt à leur terme, et à l'issue de ma thèse de fin d'études, je souhaite exprimer ma sincère reconnaissance à tous ceux qui m'ont apporté une aide précieuse pendant les trois années de mon doctorat à l'université de Strasbourg.

Tout d'abord, je tiens à exprimer ma sincère gratitude à mon directeur de thèse, le Dr Jean-Pierre DJUKIC, pour ses encouragements et ses conseils constants tout au long de mon étude. De plus, il fait des commentaires perspicaces sur toutes les révisions de la thèse et m'a fourni de nombreuses idées inspirantes, ce qui m'a encouragé dans une large mesure. Sans ses conseils patients, l'achèvement de cette thèse aurait été impossible.

Ensuite, je tiens à remercier chaleureusement tous les membres de notre groupe, le Dr Michel PFEFFER, Geneviève STOLL, Mélanie BOUCHER, Christophe DERAEDT, Yann CORNATON, Dang Binh HO pour toute l'aide que vous m'avez apportée durant ces trois années. Merci à Christophe DERAEDT pour le support expérimental et les nombreuses suggestions ; merci à Yann CORNATON pour les excellentes études computationnelles; merci à Lydia KARMAZIN, Corinne BAILLY, Nathalie GRUBER pour la caractérisation aux rayons X; merci à Maurice COPPE et Bruno VINCENT pour la RMN; merci à Laurent Ruhlmann pour la voltammétrie cyclique; merci à Sylvie CHOUA et Nolwenn LE BRETON pour la RPE; merci à tous les membres des services d'analyse élémentaire et de spectroscopie de masse pour leur contribution et leur assistance.

Je remercie également très vivement Pr. Blanca MARTIN-VACA (Université Paul Sabatier), Dr. Audrey AUFFRANT (École Polytechnique) et Pr. Vincent RITLENG (Université de Strasbourg) de m'avoir fait l'honneur accepte de prendre part à ce jury de thèses et d'évaluer ce travail.

Mes remerciements vont à ma famille bien-aimée pour leurs considérations affectueuses et leur grande confiance en moi tout au long de ces années. Je dois également ma sincère gratitude à mes amis qui ont rendu ma vie en Strasbourg si enrichissante.

Enfin, j'apprécie profondément le soutien financier apporté par le China Scholarship Council (CSC), qui m'a donné l'occasion d'étudier à l'étranger et d'acquérir des connaissances.

# Table of Contents

# List of tables

# List of figures

# List of annexes

# Aabbreviations

| | |
|---|---|
| Dichloromethane | DCM |
| 1,2-Dichloroethane | DCE |
| 2-Phenylpyridine | 2-*phpy*H |
| Benzo[*h*]quinoline | *bzq*H |
| Dibenzo[*f,h*]quinoline | *bzbzq*H |
| 2-(*o*-tolyl)pyridine | 2-*tolpy*H |
| 2-(*p*-tolyl)pyridine | 4-*tolpy*H |
| 2-[4-(trifluoromethyl)phenyl]pyridine | 4-*tfmphpy*H |
| 1,2,3,4,5-Pentamethylcyclopentadiene | Cp* |
| Cyclopentadiene | Cp |
| Tetrakis[3,5-bis(trifluoromethyl)phenyl]borate | $NaBArF_{24}$ |
| Anhydrous sodium acetate | NaOAc |
| 4-tertiobutyl,2-(4-*N,N*-dimethylaminophenylene)pyridine | 2-*anpy*H |
| 2-(4-bromophenyl)pyridine | Br-*phpy*H |
| 2-[4-(trifluoromethyl)phenyl]pyridine | $CF_3$-*phpy*H |
| Lithium Acetamidate | LiNHAc |
| (2,2,6,6- tetramethylpiperidin-1-yl)oxy | TEMPO |
| Density functional theory | DFT |
| Noncovalent interactions | NCIs |
| Noncovalent interactions plots | NCI plots |
| Interacting quantum atoms | IQA |
| Local energy decomposition | LED |
| Quantum Theory of Atoms in Molecules | QTAIM |
| Domain-based local pair natural orbital coupled cluster method | DLPNO-CCSD(T) |
| Concerted Metalation-Deprotonation | CMD |
| Ambiphilic Metal Ligand Activation | AMLA |
| Electrophilic aromatic substitution | $S_EAr$ |
| Interacting Quantum Atoms | IQA |
| Oak Ridge Thermal Ellipsoid Plot | ORTEP |

| | |
|---|---|
| Intrinsic bond strength index | IBSI |
| Isothermal Titration Calorimetry | ITC |
| Electron Paramagnetic Resonance | EPR |
| Tetraethylammonium iodide | TEAI |

# Résumé

## Introduction

Au cours des dernières décennies, l'activation de la liaison C-H a connu des avancées majeures grâce aux catalyseurs à base de métaux de transition et cette approche catalytique moderne s'est progressivement imposée comme un outil précieux pour la synthèse organique. Au stade initial de l'activation C-H, la plupart des réalisations dans ce domaine ont été accomplies avec les métaux de transition de deuxième et troisième rangées tels que Pd, Pt, Rh, Ru et Ir. Cependant, le clivage des liaisons C-H à l'aide des métaux de transition de la troisième rangée, peu coûteux et abondants dans le monde, a pris un essor considérable récemment, car il s'agit d'une alternative beaucoup plus respectueuse de l'environnement et économiquement attrayante, qui permet en outre une sélectivité et des schémas de réactivité uniques, en raison de leurs propriétés électroniques. À cet égard, les complexes de cobalt sont apparus comme des catalyseurs efficaces et polyvalents pour l'activation C-H, comme en témoigne le nombre croissant de publications sur l'activation C-H catalysée par le cobalt qui ont été récemment divulguées. Malgré d'excellents travaux réalisés avec des complexes de cobalt à basse valence, qui ont permis d'améliorer le statut du cobalt dans le domaine de l'activation C-H, et d'étendre considérablement l'application de l'activation C-H en synthèse organique, certains défis restent à relever. Contrairement à la prévalence de l'activation C-H catalysée par le cobalt de basse valence, l'activation C-H catalysée par le cobalt de haute valence a progressivement attiré l'attention ces dernières années. Malheureusement, la compréhension mécanistique du fonctionnement de ces nouveaux protocoles catalysés par le cobalt de haute valence est très peu développée. Ceci est probablement une conséquence de l'instabilité des intermédiaires clés, bien qu'il y ait un intérêt croissant pour leur détection et leur isolement. Ainsi, l'objectif principal de cette thèse de doctorat est la synthèse et la caractérisation de métallacycles de cobalt, et nous nous concentrerons sur l'étape d'activation C-H pour élucider le mécanisme de fonctionnement dans le clivage des liaisons C-H médié par le cobalt de haute valence.

## Résultats et discussions

Dans ce travail, une cyclométallation de la 2-phénylpyridine (2-*phpy*H) par Cp*Co(III) a été abordée suivant la procédure communément utilisée pour la cycloiridation et la cyclorhodation, favorisée par le mécanisme CMD (Métallation-Déprotonation Concertée) assisté par une base( Schéma R. 1). Le cobaltacycle [Cp*Co(2-*phpy*-*κ*C,*κ*N)I] peut être efficacement synthétisé à partir du $[Cp^*CoI_2]_2$ stable à l'air et de la 2-phénylpyridine 2- *phpy*H, en présence de LiNHAc comme base, avec un rendement de 83%, alors qu'avec le NaOAc anhydre comme base, seul un rendement de 12% a été obtenu dans des conditions similaires. Parallèlement, une étude théorique systématique de ces réactions de cyclocobaltation assistées par une base a été menée. A l'aide de l'étude des profils d'énergie DFT et du rôle des interactions non covalentes, nous avons décrit les profils d'enthalpie de Gibbs pour la formation de l'intermédiaire agostique transitoire (Figure R. 1) et nous avons analysé également les contributions attractives et répulsives à la coupure de la liaison C-H (Figure R. 1). Les résultats montrent que la cyclométallation avec $AcO^-$ comme base auxiliaire est moins efficace que celle avec $AcNH^-$ sur la base de la thermochimie, ceci est principalement dû au fait que l'acétamidate réduit efficacement l'intéraction de chélation résiduelle avec le métal et par conséquent augmente la polarisation de la liaison C-H qui est déjà engagée dans une interaction agostique partiellement covalente partiellement non covalente avec le centre métallique chargé positivement. Différents cobaltacycles ont ensuite été synthétisés par cyclométallation favorisée par la $[NHAc]^-$, caractérisés analytiquement et leurs structures ont été résolues par l'analyse structurale de diffraction des rayons X, confirmant l'importance de l'acétamidate dans la cyclométallation assistée par une base. En outre, l'effet de la base auxiliaire sur une réaction modèle de condensation alcyne-arène qui met en scène le $[Cp^*CoI_2]_2$ comme catalyseur a été étudié.

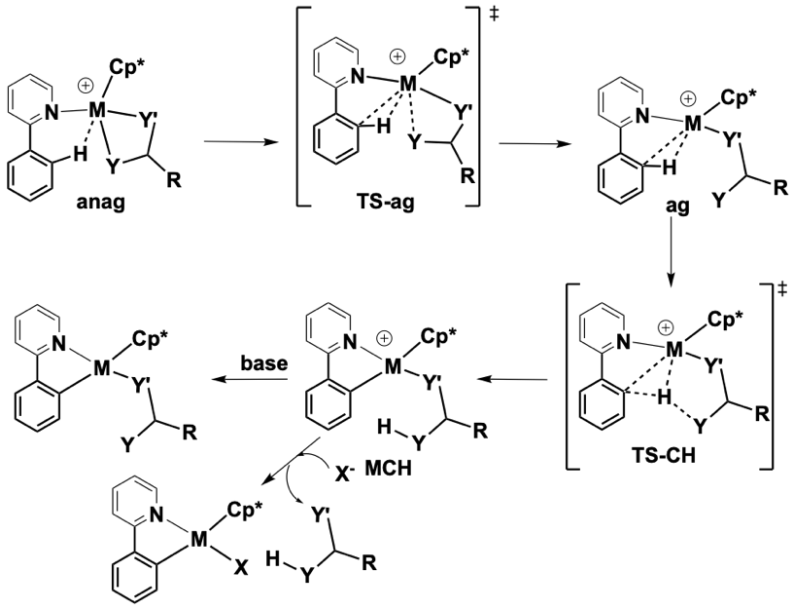


**Schéma R. 1.** Le mécanisme de CMD appliqué aux complexes Cp*M(III) de métaux de transition du groupe 9 : **anag**, le complexe réactif précurseur de l'intermédiaire agostique **ag** via **TS-ag** ; **MCH**, le produit de cyclométallation immédiat issu de la réaction de transfert de protons se produisant via **TS-CH** à partir de **ag**.

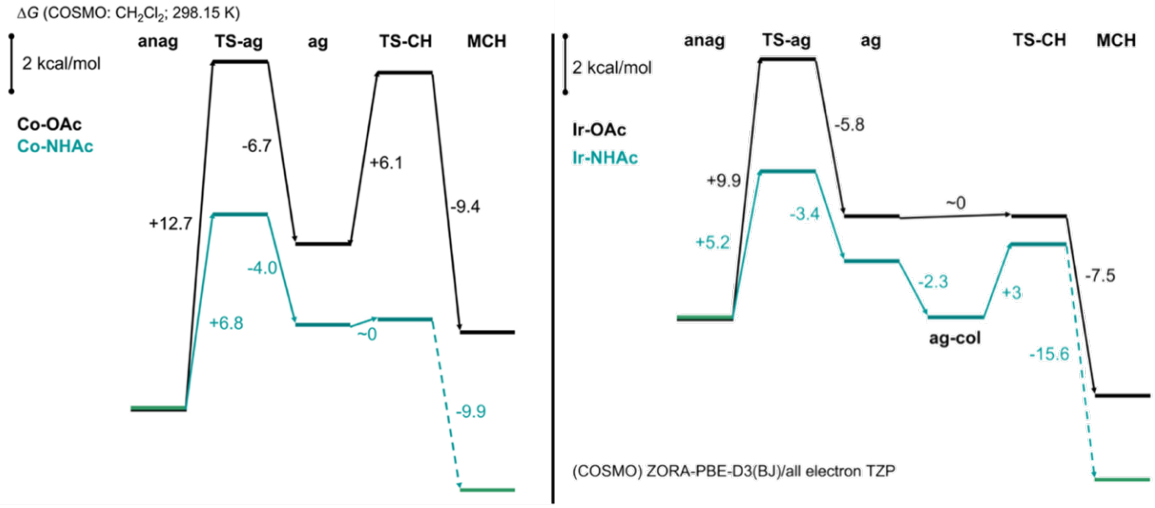


**Figure R. 2.** Profils d'énergie GGA-DFT-D pour les cyclométallations de 2-phpyH assistées par des bases acétate (lignes noires) ou acétamidate (lignes cyan); (gauche : Système Cp*Co(III) ; droite : système Cp*Ir(III)

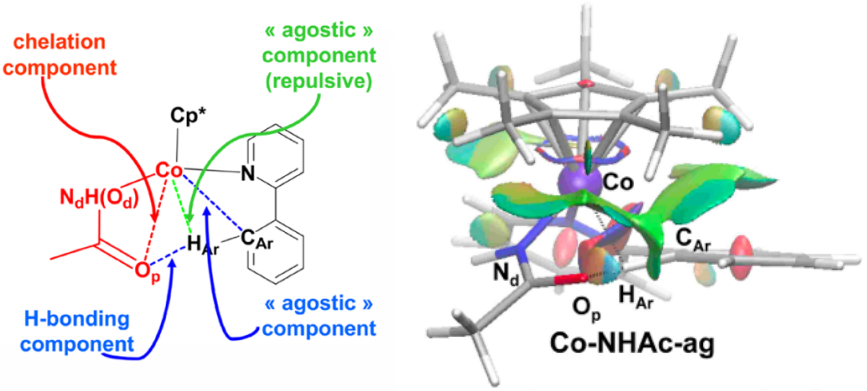


**Figure R. 3.** Gauche). Schéma du site réactif pendant la cyclocobaltation de 2-*phpy*H via le mécanisme CMD; Droite) surfaces NCI (s=0.3, -0.03<sign(l2)r<0.03) pour le complexe **ag** (code couleur des atomes : gris clair, C ; bleu foncé, N ; blanc, H ; rouge, O ; violet, Co ; les interactions fortes et directionnelles sont révélées par des pastilles bleues, les interactions faibles délocalisées apparaissent comme de longues surfaces vertes, et les régions répulsives sont révélées en rouge).

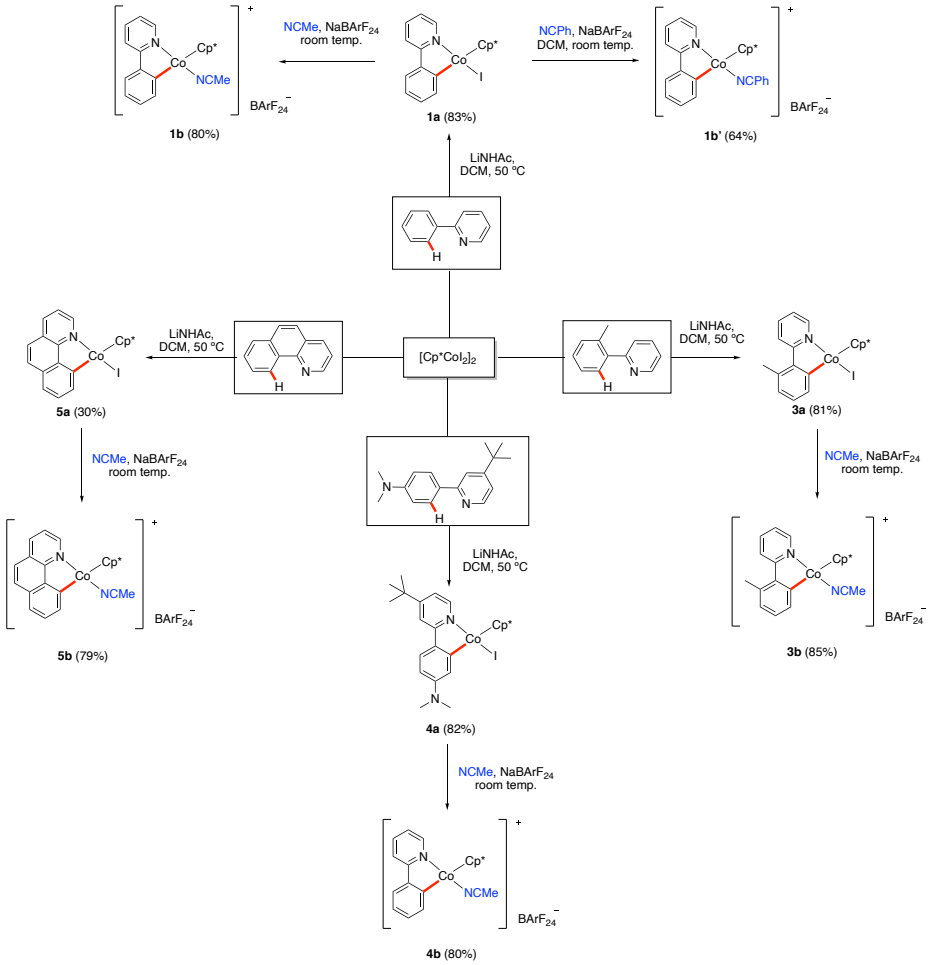


**Schéma R. 2.** Cyclocobaltation de 2-*tolpy*H, 2-*anpy*H et *bzq*H et conversion des cobaltacycles iodo résultants en complexes solvato acétonitrile.

Ensuite, la cyclocobaltisation assistée par LiNHAc a également été étudiée en utilisant les conditions optimisées de 2-*phpy*H mentionnées ci-dessus, et une série de cobaltacycles a été synthétisée (Schéma R. 2). Tous les complexes ont été entièrement caractérisés par RMN $^{1}H$ et $^{13}C$, spectroscopie de masse ESI et analyse élémentaire. Et les structures ont été déterminées par analyse de diffraction des rayons X à partir de monocristaux appropriés (Figure R. 4-7).

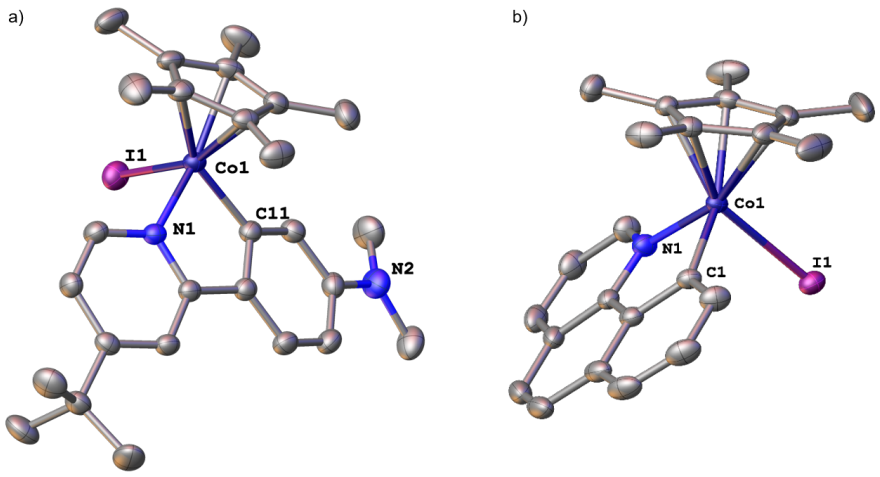


**Figure R. 4.** Diagramme ORTEP des structures de **4a** (a), **5a** (b) dessinées au niveau de probabilité de 50% avec numérotation partielle des atomes. Les atomes H et les molécules de solvant ont été omis pour des raisons de clarté.

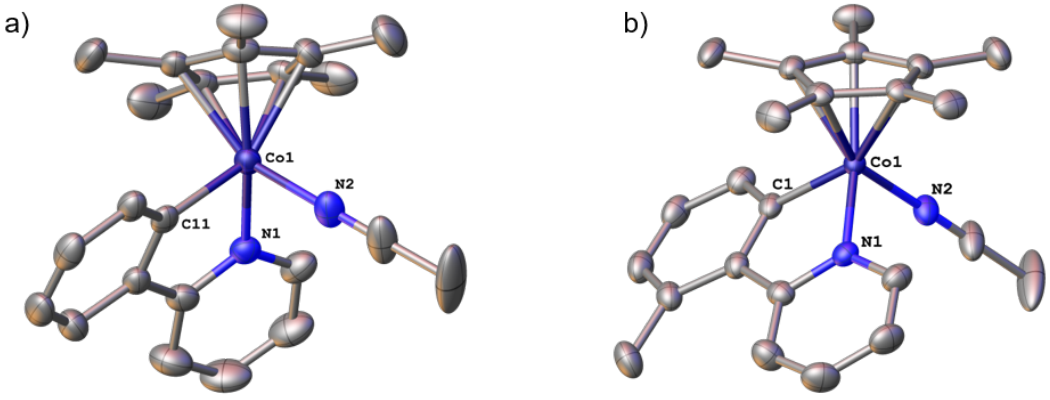


**Figure R. 5.** Diagramme ORTEP des structures de **1b** (a), **3b** (b) dessinées au niveau de probabilité de 50% avec numérotation partielle des atomes. Les atomes H et les molécules de solvant ont été omis pour des raisons de clarté.

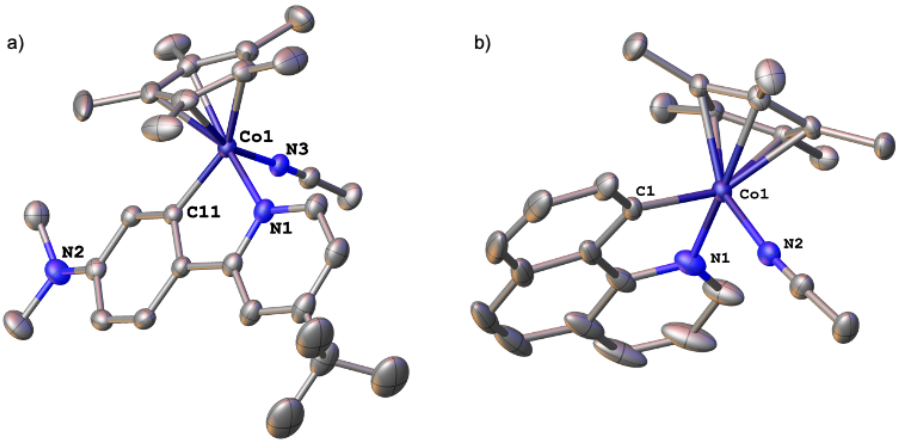


**Figure R. 6.** Diagramme ORTEP des structures de **4b** (a), **5b** (b) dessinées au niveau de probabilité de 50% avec numérotation partielle des atomes. Les atomes H et les molécules de solvant ont été omis pour des raisons de clarté.

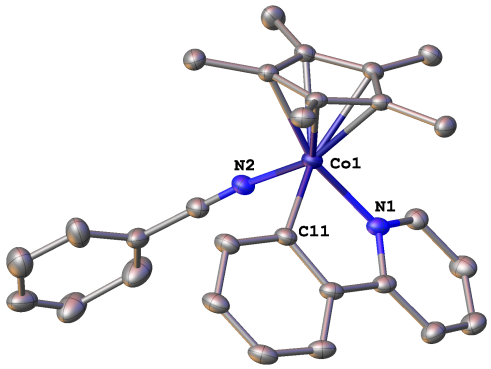


**Figure R. 7.** Diagramme ORTEP des structures de **1b'** dessinées au niveau de probabilité de 50% avec numérotation partielle des atomes. Les atomes H et les molécules de solvant ont été omis pour des raisons de clarté.

Il est intéressant de noter que par accident, un cristal du produit formel de l'insertion de Cp* dans le cobaltacycle a été obtenu, c'est un exemple sans précédent d'un produit d'une réaction du ligand de Cp*, qui est généralement considéré comme un ligand spectateur robuste, avec le ligand 2-*phpy* hétérochélateur (Figure R. 8). Bien que le mécanisme de cette transformation ne soit pas complètement élucidé et qu'aucune auture occurrence similarire n'ait été soit rapportée dans la bibliographie, sa structure cristalline unique a suscité notre intérêt. Nous avons donc mené une étude sur le mécanisme de cette cyclocondensation à la fois théoriquement et expérimentalement. Les résultats montrent que les intermédiaires clés, c'est-à-dire les

métallacycles Cp*Co(III) peuvent réagir rapidement en solution avec des oxydants à un électron pour produire de nouveaux alcaloïdes cationiques par une cyclocondensation des ligands organiques (Schéma R. 3).

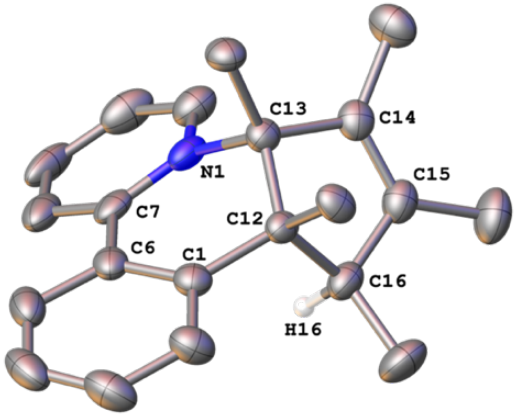


**Figure R. 8**. Diagramme ORTEP de la structure de [**1c**][$I_3$] (condensation de Cp* sur *phpy*) dessiné avec une probabilité de 50%. Les atomes H et les molécules de solvant ont été omis pour des raisons de clarté.

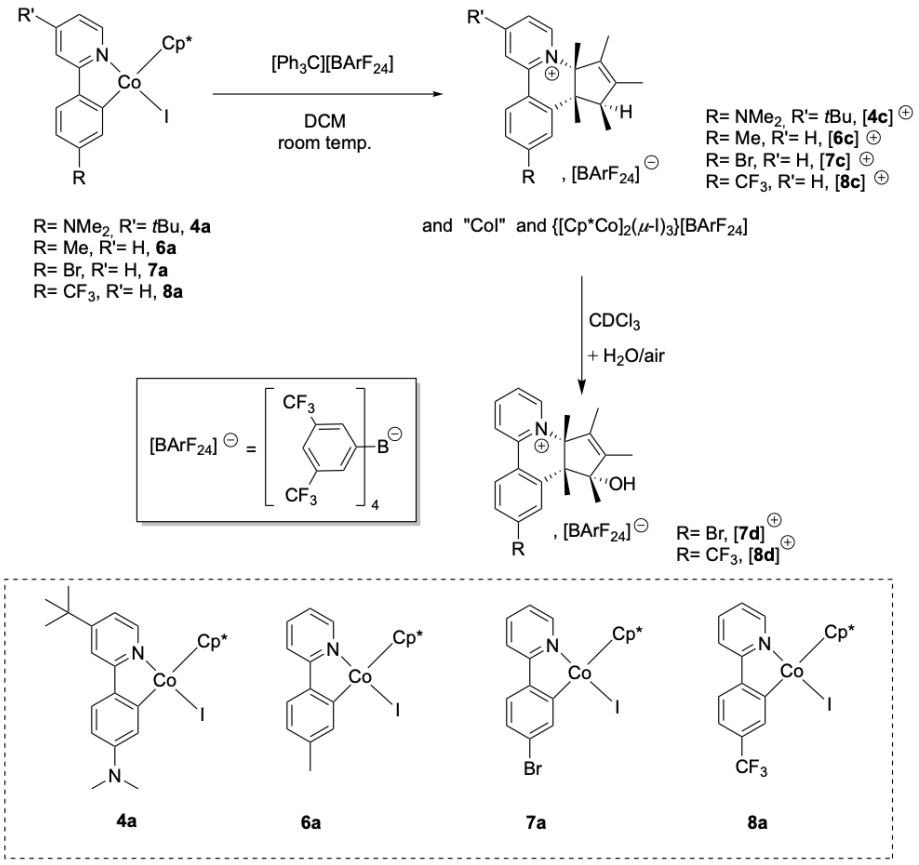


**Schéma R. 3**. Cyclocondensation oxydative de différents cobaltacycles liés à Cp*.

Lors de l'analyse EPR à basse température d'un mélange du cobaltacycle à base de *phpy* avec le cation tritylium, nous avons détecté les signaux des radicaux centrés sur le trityle et sur un centre Co(IV) (Figure R. 9). Les analyses électrochimiques ont également montré que l'oxydation des cobaltacycles considérés est irréversible, produisant une multitude d'espèces électroactives (Figure R. 10).

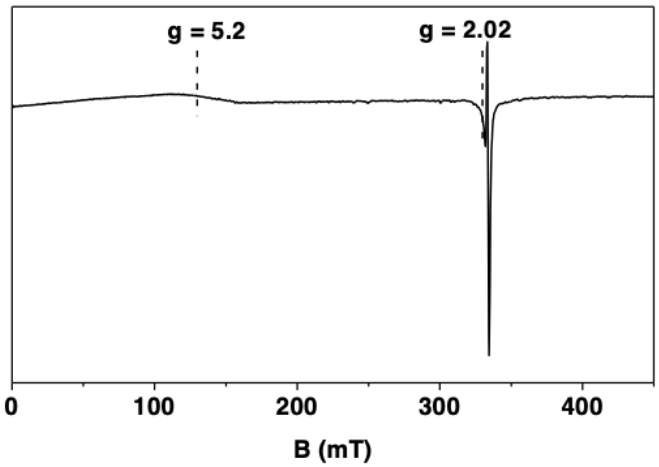


**Figure R. 9.** Spectre RPE en bande X enregistré à 4,3 K après 5 min de réaction entre des solutions 40 mM de [Cp*Co(2-*phpy*-κC,κN)I] et [$Ph_3C$][$BArF_{24}$] dans DCM . Le spectre a été enregistré à une fréquence de 9,345 GHz;

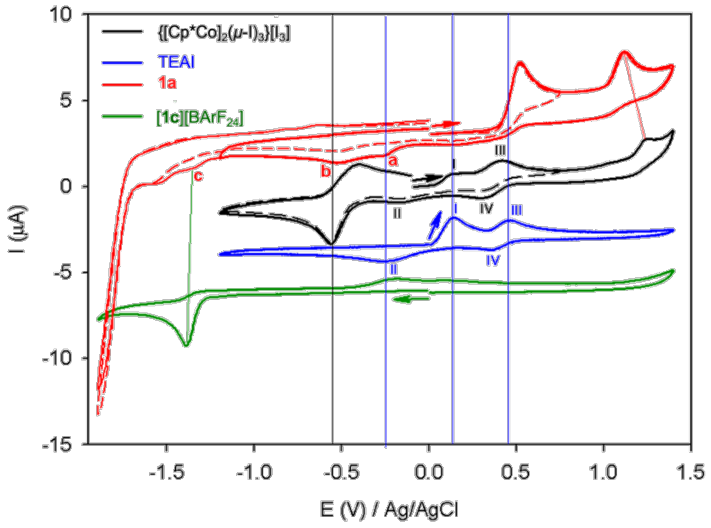


**Figure R. 10.** Voltammogrammes cycliques de {[Cp*Co]$_2$($\mu$-I)$_3$}[$I_3$], TEAI, **1a** and [**1c**][$BArF_{24}$] (0.4 mmol $L^{-1}$) sur une électrode de Pt dans une solution de 1,2-$C_2H_4Cl_2$ en présence de [N(*n*Bu)$_4$][$PF_6$] (0,1 mol L-1). v = 100 mV s-1.

Des études DFT des interactions non covalentes ont révélé une prédisposition des cobaltacycles à la cyclocondensation intramoléculaire induite par le Co(IV) (Figure R. 12), dont l'exploration du profil énergétique de la réaction soutient les rôles clés 1) de l'oxydation du cobaltacycle Co(III) en une espèce Co(IV) à courte durée de vie et 2) des intermédiaires organocobaltés à l'état triplet. Trois voies ont été proposées par la suite (Figure R. 11), mais l'origine d'un atome d'hydrogène capturé lors de la cyclocondensation n'a pas encore été complètement établie.

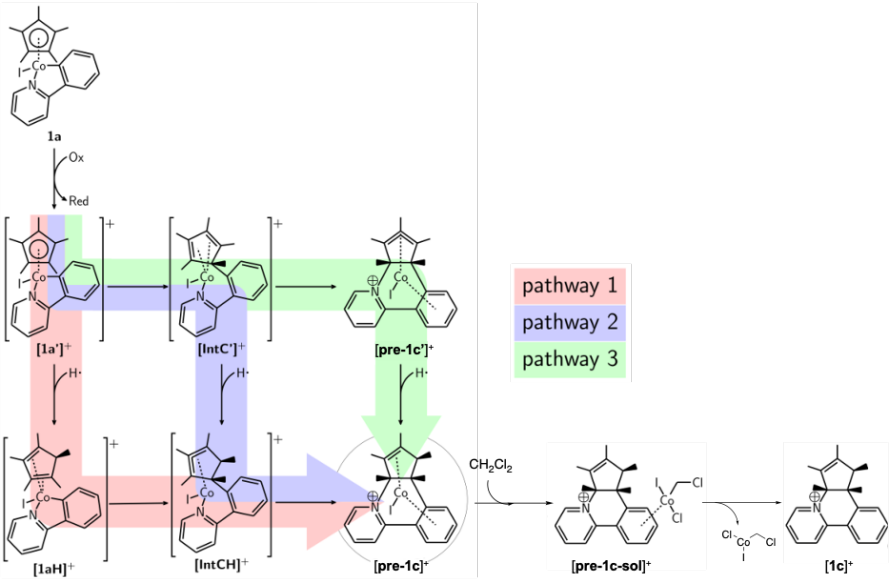


**Figure R. 11.** Schéma des voies proposées pour la condensation de Cp* sur *phpy.*

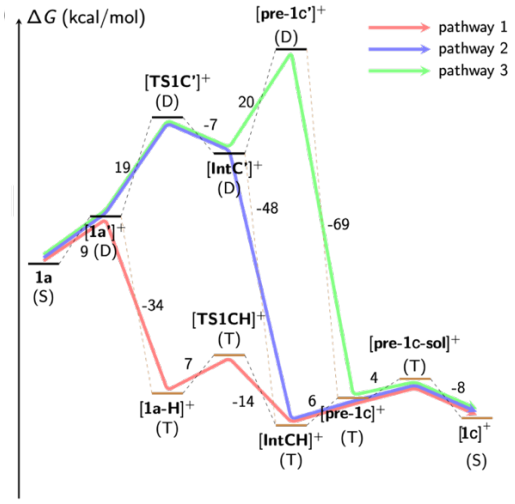


**Figure R. 12.** Profils d'énergie libre de Gibbs calculés proposés. Les trois voies possibles sont matérialisées par des lignes de couleur solide (vert, bleu, rose). Profil d'énergie de Gibbs intrinsèque exergonique en considérant un H· fictif.

## Conclusion générale

Les cobaltacycles en tant qu'intermédiaires clé peuvent être facilement préparés avec de bons rendements via le mécanisme CMD (Métallation-Déprotonation Concertée) assisté par une base, et les avantages déduits de la théorie du sel d'acétamidate en tant que base ont été démontrés. La pertinence des intéractions non covalentes dans la cyclocobaltation promue par CMD (Métallation-Déprotonation Concertée) est évidente d'après l'évolution de ce qu'on dénomme le «site de réaction»: la contribution remarquable des interactions électrostatiques locales et donc de l'environnement multipolaire à la polarisation de la liaison $C_{Ar}$-$H_{Ar}$ avant son activation par la carbométallation et le transfert de proton à la base voisine donne une raison valable pour l'optimisation non seulement de la cyclocobaltation et de la cyclonickelation mais aussi des cyclométallations utilisant d'autres métaux 3d. En outre, la cyclocondensation induite par l'oxydation des métallacycles Cp*Co(III) est un processus assez rapide induit par la formation d'un intermédiaire transitoire Co(IV), qui constitue un nouvel exemple de synthèse par effet " métal-template " centré sur le Co(IV) déclenché par oxydation mono- électronique, qui fournit également une nouvelle direction pour étudier de manière plus systématique et prédictive le mécanisme de fonctionnalisation des liaisonsC-H promues par les précatalyseurs à base d'entité « Cp*Co(III) ».D'une manière plus générale ces travaux fournissent des bases conceptuelles essentielles à la mise en œuvre d'une nouvelle approche prédictive de l'ingénierie de la catalyse de fonctionnalisation des liaisons C-H par les complexes de métaux du bloc 3d des métaux de transition.

# Chapter 1. General introduction

## 1.1. Advantages and challenges of C–H activation

In the last few decades, unprecedented developments have been made in the research of C-H bond activation, providing new disconnection tactics for the formation of C–C and C–X (heteroatom) bonds, and also providing a new approach to the synthesis of natural products and various organic molecules, which became a powerful tool in organic synthesis[1-4]. In the general case, the traditional cross-coupling reaction is one of the most useful synthetic methods for the formation of C-C bonds. However, this reaction needs extra procedures to prepare organohalides or triflate compounds, as well as organoboron compounds or metal-compounds[5, 6]. In contrast, the C–H activation approach does not require pre-functionalization of the starting materials (halogenation or borylation), simplifying the synthesis process and reducing undesired by-products, which is more economical and environmentally friendly in terms of atoms and steps (Scheme 1.1).

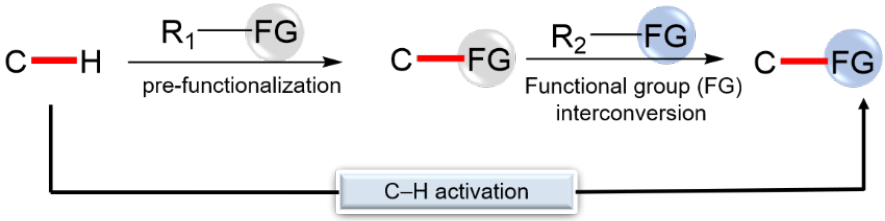


**Scheme 1. 1.** Comparison between traditional cross-coupling approach and C–H activation approach.

Although the activation and functionalization of C-H bond have attracted widespread attention and have become the basis of modern chemistry, it is still limited by two significant challenges[5, 7-11]:

### 1) Reactivity of C–H bond.

It is well known that the C–H bond is usually considered to be an inert chemical bond due to its high bond energy and low polarity. Therefore, the cleavage of the C-H bond and the formation of new carbon-containing chemical bonds under mild conditions is a significant challenge, and a large kinetic barrier needs to be overcome, so that high reaction temperature is required for most reactions associated with C-H activation, which would undoubtedly impose a detrimental effect. Subsequently, various transition metals were found to promote the cleavage of C-H bonds, and have been successfully applied for C–H activation and functionalization, such as Pd, Rh, Fe, Co, Ni, Cu[12-14]. The main reason is that the M–C bond formed via transition metals-catalyzed C-H bond activation is more reactive than C–H bond and can be further converted under mild conditions. In addition, transition metals-catalyzed C–H activation has redefined the organic synthesis and this approach was widely used in the synthesis of natural products, pharmaceutical molecules, and other organic compounds[1, 7, 15-18].

### 2) Selectivity of C-H bond

Despite these advances in the reactivity of the C–H bond, site-selective control remains a principal challenge for C–H activation as most of C–H bonds in the complex organic molecules have similar bond dissociation energies (the BDE of C-H bonds are typically 90-110 kcal·mol$^{-1}$)[19, 20], making it difficult to selectively target and activate the desired C-H bond while retaining all other C-H bonds intact[21, 22]. To solve this problem, three strategies are commonly employed: 1) electronic effect[11]; 2) steric effect[11]; 3) directing group[23] (Scheme 1.2). The first two strategies are mainly relying on the use of either electronically or sterically biased substrates. But they are still severely limited by their substrate scope and general applicability, even though they can effectively promote the activation of C-H bonds.

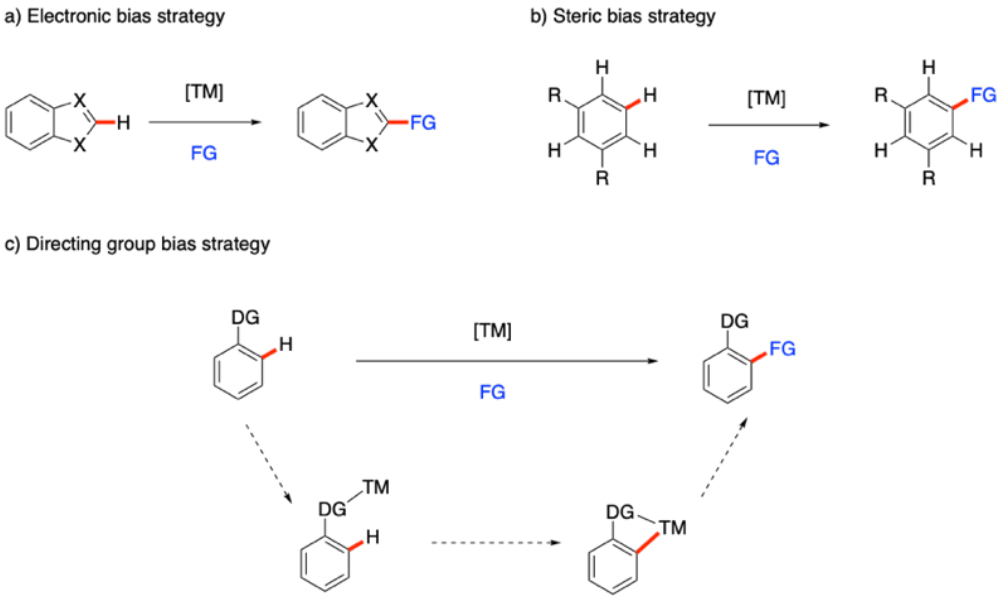


**Scheme 1. 2.** Strategies of the selective for C-H functionalization (TM = transition metal; DG = directing group).

In contrast, the directing group-based approach is more broadly applicable and has considerable potential[12, 21]. This approach typically proceeds by the formation of a [C-H···M] σ-complex (Scheme 1.3). The directing group is usually a Lewis basic functional group and contains non-bonded lone pair electrons (such as amides, imines, amines, oximes and *N*-heterocycles) which can act as a ligand and chelate in terms of coordination chemistry, and subsequently facilitates the cleavage of C–H bond by inducing pre-coordination between the substrate and transition metal, even if it is not the most reactive at the molecule. Then the directing group set up the transition metal close to a desired C-H bond of the substrate, promoting the formation of intermediate *via* cyclometallation, thus acting to control the site-selectivity of the C-H bond.

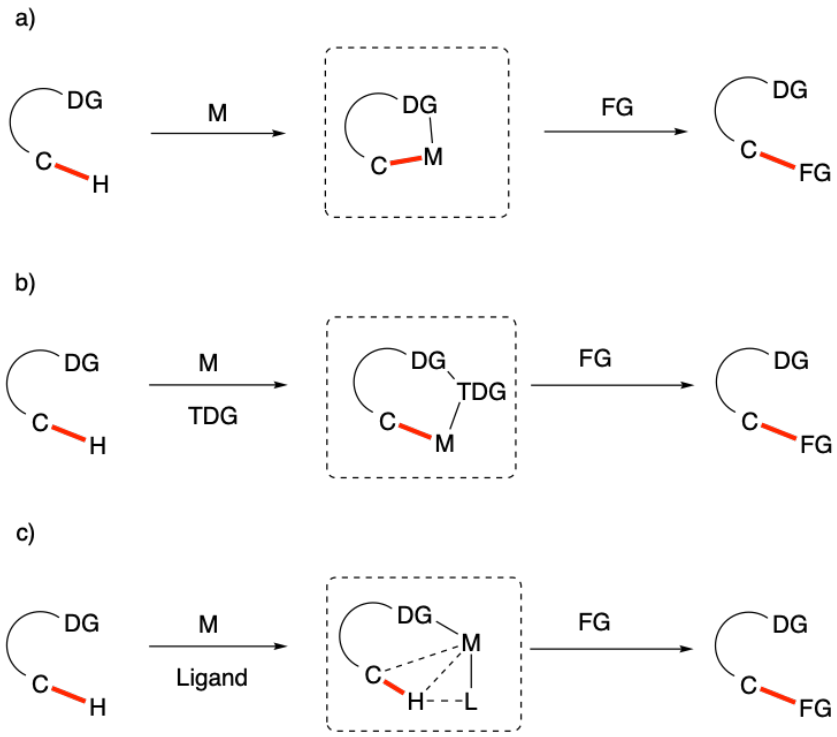


**Scheme 1. 3.** The approaches of transition metal-catalyzed C-H activation. (a) C-H functionalization assisted by DG; (b) C-H functionalization assisted by TDG; (c) C-H functionalization via noncovalent interaction strategy; (M = transition metal; DG = directing group; TDG = transient directing group; L = ligand).

Although great progress has been made by this approach in the last few decades, there are some limitations in the process of construction of the directing groups in the substrate and also the removal at the end, and can also reduce the efficiency and compatibility of the reaction. More recently, these limitations can be overcome by introducing covalent or noncovalent interactions between the substrate and transition-metal center. For the covalent interaction, the desired C-H bond is activated by introducing a designed transient directing group that binds to the substrate as well as the metal center, and then this directing group can be easily removed without changing the substrate (Scheme 1.3b). On the other hand, noncovalent interactions are introduced to direct the selective activation of C-H bond, such as hydrogen, halogen, and also ion-π, agostic, anagostic, mainly involves weak inter- or intra-molecular attractions (Scheme 1.3c)[24, 25]. For the present, the strategy of utilizing noncovalent interactions is potentially powerful and relatively unexplored.

## 1.2. Development of cobalt in C-H activation

In the preliminary stage of C-H activation, the 4d and 5d transition metals dominate this field, such as rhodium, ruthenium, iridium, palladium and platinum, benefiting from the variable valence and strong coordination. Regrettably, these transition metals are not only costly but also toxic. Hence, more environmentally and economically alternatives are increasingly attracting attention. Accordingly, the less toxic, inexpensive, and earth-abundant 3d transition metals have gained enormous interest and became a hot topic recently[26].

Among these 3d transition metals, cobalt complexes have emerged as efficient and versatile catalysts for C-H activation, which is evidenced by the increasing number of papers on cobalt-catalyzed C-H activation that are recently disclosed (Figure 1.1 blue). Notably, the Co(III) catalysts have been developed extremely rapidly in the last few years (Figure 1.1 orange). Compared to the homologous rhodium and iridium, the cobalt is less electronegative, and Co-C bonds are usually more polarized than the corresponding Ir/Rh-C bonds, which permits conversion to organometallic cobalt complexes that are more nucleophilic, allowing for new reactivities and improving chemo- and regioselectivities. Therefore, this has led to increase the attention focused on this area, allowing researchers to develop novel, highly reactive cobalt complexes for the C-H bond activation.

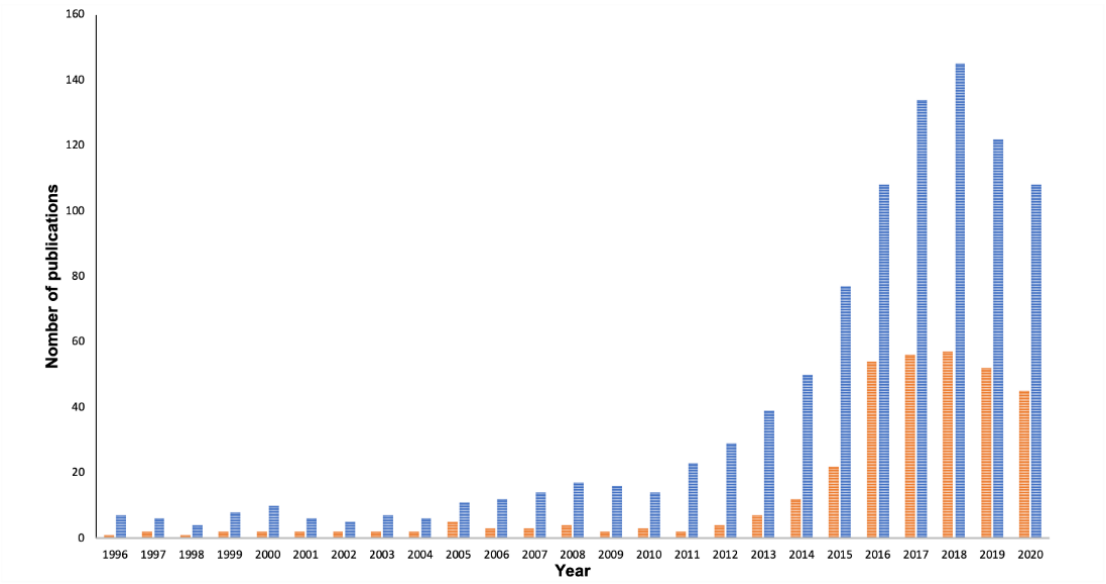


**Figure 1. 1.** Number of papers published per year on cobalt-catalyzed C-H activation. (In blue, cobalt-catalyst; in orange, Co(III) catalyst. Datas obtained from ISI Wos).

The active cobalt complexes used in C-H bond activation have two different oxidation states, low-valent and high-valent. The so-called low-valent cobalt-catalyzed C-H activation involves the addition of Grignard's reagent as a base and reductants to produce an active cobalt species from pre-catalysts. The low-valent cobalt catalysts most commonly used in C-H activation are $[CoH(PMe_3)_4]$, $[CoMe(PMe_3)_4]$, $[CoH(H_2)(PPh_3)_3]$, $[CoH(N_2)(PPh_3)_3]$, and some Cp*Co(I) complexes. Whereas the high-valent cobalt complexes normally are Co(III) complexes that can switch between Co(II) and Co(III) oxidation states during C-H activation, such as Cp*Co(III)-complexes.

### 1.2.1. Low-valent cobalt-catalyzed C-H activation

The use of low-valent cobalt in C-H activation arguably dates back to 1955. Murahashi first reported the use of $Co_2(CO)_8$ to catalyze the *ortho*-carbonylation reaction of aromatic imine under harsh CO pressure to afford an isoindolinone derivative in yield of 80%, which involves cobalt-mediated activation (cyclometallation) of the *ortho* C-H bond (Scheme 1.4a)[27]. Since then, the development of low-valent cobalt catalyzed C–H activation has been dormant. It was only in 1994 that the low-valent cobalt catalyst was further developed by Kisch and co-workers, using the cobalt(I) complex ($[CoH(N_2)(PPh_3)_3]$) to catalyze hydroarylations of alkynes (Scheme 1.4b)[28]. In this reaction, diphenylacetylene reacts with azobenzenes via *anti*-addition to afford the desired product in 70-80% yields. In addition, $[CoH(H_2)(PPh_3)_3]$ was successfully used as a catalyst. Those low-valent cobalt catalysts have high reactivity, but the C-H activation required harsh reaction conditions and was limited by the range of substrates.

Later, Brookhart and coworkers reported a low-valent Cp*Co(I) complex catalyzed hydroacylation in 1997 (Scheme 1.4c)[29, 30]. The $Cp^*Co(VTMS)_2$ (VTMS=Vinyltrimethylsilane) can be used as a pre-catalyst for both *intra*- and *inter*-molecular hydroacylation of aromatic aldehydes with olefins under mild conditions.

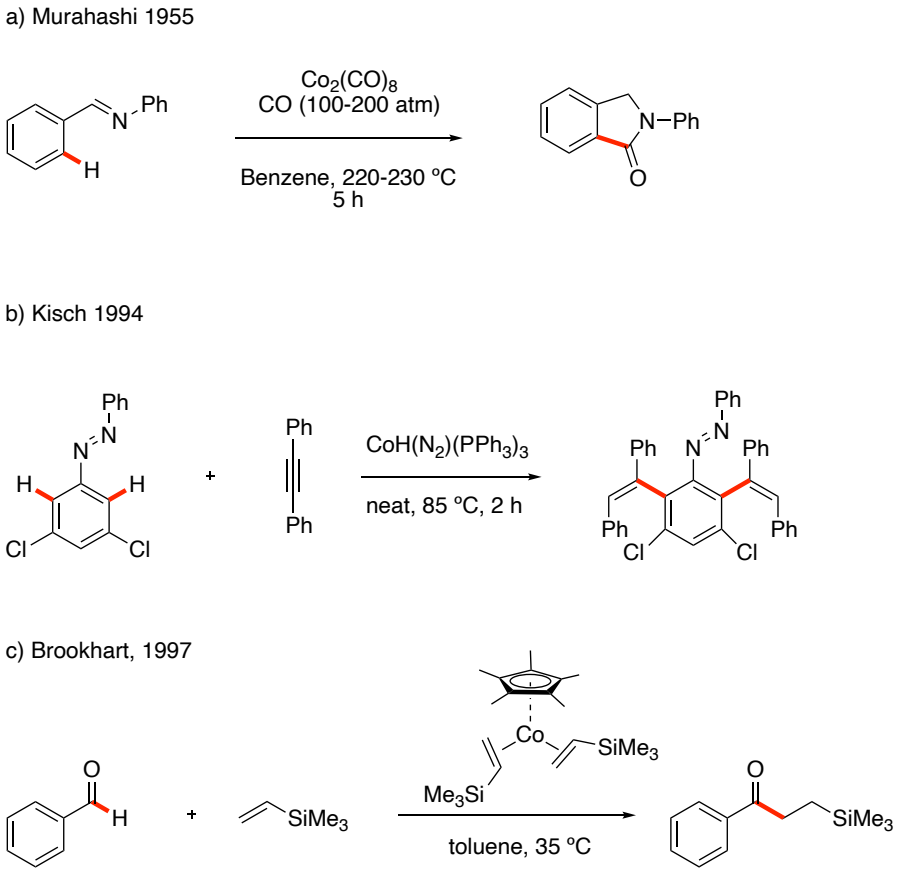


**Scheme 1. 4.** Pioneering examples of cobalt-catalyzed C-H activation.

In these pioneering examples of cobalt-catalyzed C-H activation, where the catalysts used are what we call well-defined low-valent cobalt complexes. Another low-valent cobalt complex used in C-H bond activation is typically a complex generated *in situ* by reaction of simple cobalt(II) salt with Grignard reagents, such as $CoBr_2$ salt.

Based on Kisch's seminal work, the cobalt catalyzed C-H bond hydroarylation regained interest. In 2010, an efficient hydroarylation reaction of alkynes *via* directed C-H activation was reported by Yoshikai and co-workers, by using a ternary catalytic system, which consists of $CoBr_2$, a phosphine ligand ($PMePh_2$ or $P(pMeOC_6H_4)_3$), and a Grignard reagent (MeMgCl or $t$BuCH$_2$MgBr) as reductant (Scheme 1.5)[31]. After this work, the application of Co(II) salt to catalyze C-H functionalization has witnessed a strong development.

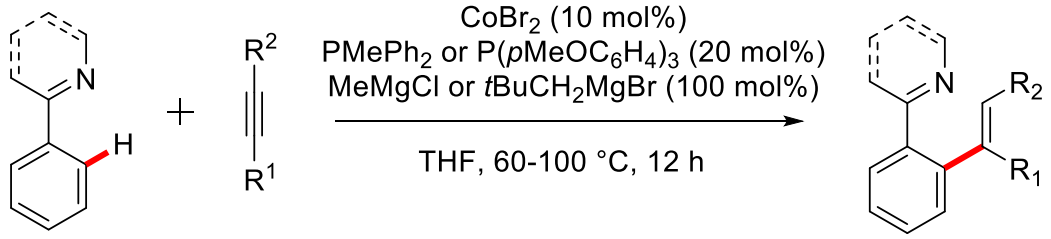


**Scheme 1. 5.** Hydroarylation by low-valent cobalt complex.

Thereafter, this type of low-valent cobalt catalyzed C-H bond activation has been rapidly developed by Yoshikai[32], Ackermann[33, 34], Matsunaga[35], etc.. Despite these excellent works which have improved the status of cobalt in C-H activation and have greatly expanded the application of C-H activation in organic synthesis, it is still subject to some limitations. In the vast majority of low-valent cobalt-catalyzed C-H activation, relatively large amounts of Grignard reagents are required, mainly because the active cobalt species are difficult to form *in situ*. In addition, the Grignard reagents also lead to low functional group compatibility[32, 33, 36-38]. Therefore, it is essential to develop new cobalt catalysts for C-H activation under mild conditions without the use of Grignard reagents.

### 1.2.2. High-valent cobalt-catalyzed C-H activation

The low-valent cobalt-catalyzed C-H activation and functionalization have been widely utilized in organic synthesis, in contrast, the high-valent cobalt-catalysts for CH activation has been gradually attracting attention more recently[37]. Therefore, in this section, the discussion will mainly focus on the development of high-valent cobalt in C-H activation, especially the Cp*Co(III)-complexes. Figure 1.2 summarizes the Cp*Co(III)-complexes and their synthetic routes that have been very common in C-H bond activation in recent years.

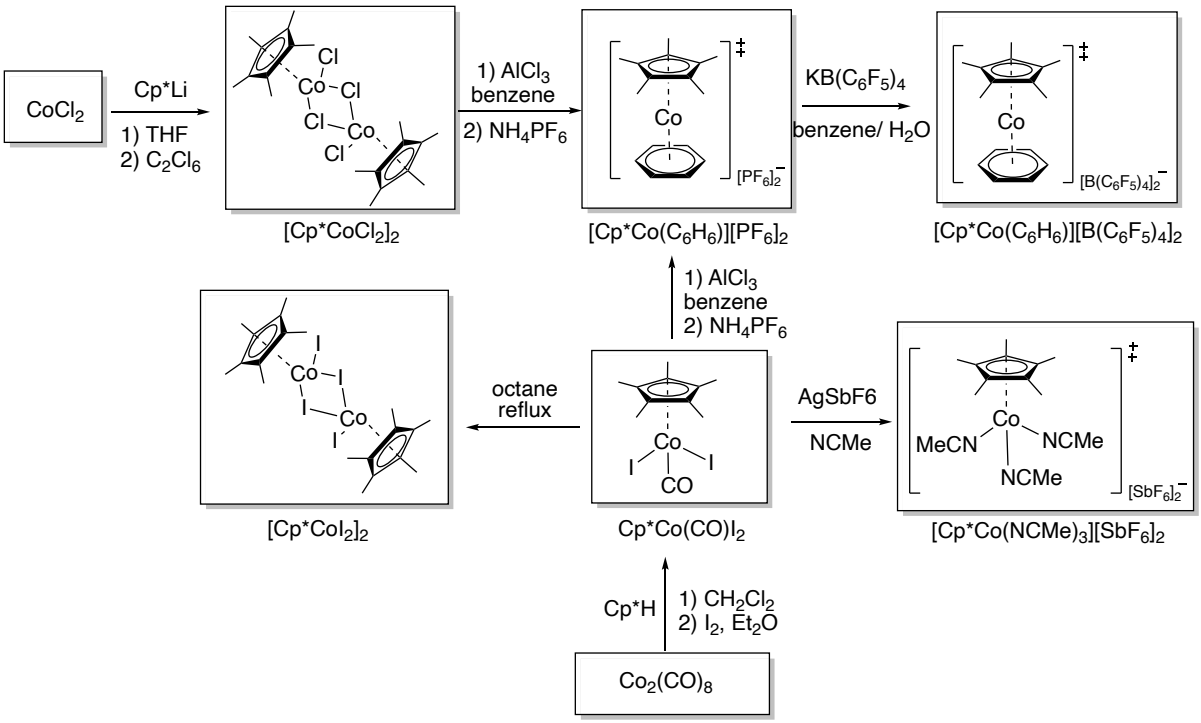


**Figure 1. 2.** The Cp*Co(III)-catalyst precursors and their synthetic routes.

In 1973, Kochi first proposed the use of high-valent cobalt catalysts to functionalize aromatic substrates to synthesize phenyl trifluoroacetate (Scheme 1.6)[39]. In this work, benzene was readily oxidized by the powerful one-electron oxidant ($Co(OTf)_3$) *via* single-electron transfer (SET) in a solution of trifluoroacetic acid, to ring-substituted aryl esters.

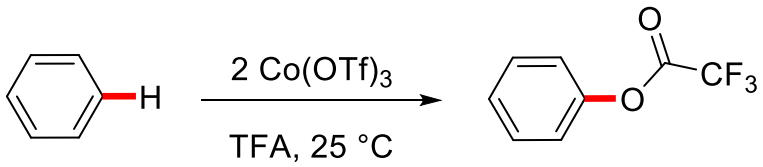


**Scheme 1. 6.** The first example of C-H activation via high-valent cobalt

Since then, the application of high-valent cobalt in C-H activation has been stagnant for a long time. It was finally in 2013 that Matsunaga and Kanai made a significant breakthrough in high-valent cobalt-catalyzed C-H activation, using the cationic Co (III) complex $[Cp^*Co(C_6H_6)](PF_6)_2$ as a catalyst to catalyze C2-selective addition of indoles to imines (Scheme 1.7)[40]. In this reaction, the use of KOAc as the additive can improve the reaction efficiency. The plausible catalytic cycle in the presence of KOAc was

shown in Figure 1.3. Initially, the benzene of $[Cp^*Co(C_6H_6)](PF_6)_2$ is dissociated and then exchanged with the acetate (or substrate) to give the reactive species (**I**). Then coordinate with the pyrimidyl group of indoles (**II**) promotes regioselective C-H metalation at the C2-position via $S_EAr$ or CMD mechanism to afford intermediate **III**. After the coordination of imine with intermediate **III**, the intermediate **IV** is formed followed by addition to the C–N double bond to afford **V**. To finish, the **V** is protonated with AcOH to gives the final product and regenerates active species **I**.

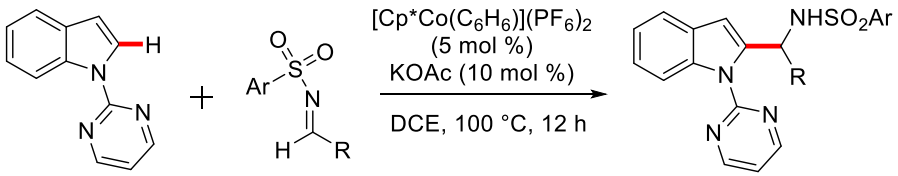


**Scheme 1. 7.** Cp*Co(III)-catalyzed C2-selective C-H bond addition of indoles to imines.

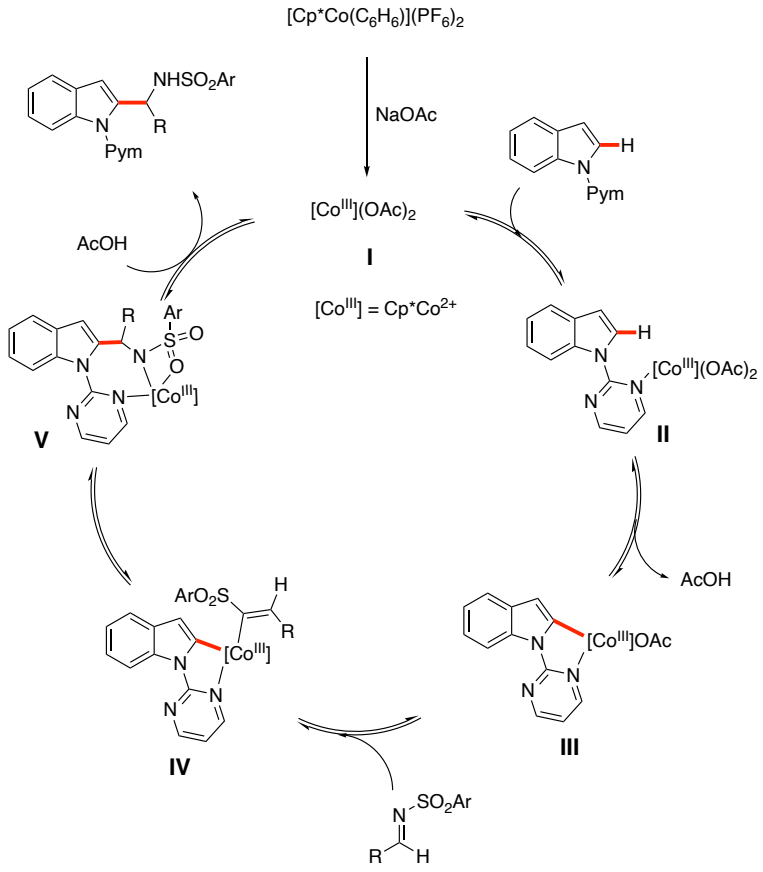


**Figure 1. 3.** Proposed catalytic cycle for C2-selective C-H addition of indoles to imines.

Subsequently, the group of Matsunaga and Kanai conducted further studies on $[Cp^*Co(C_6H_6)](PF_6)_2$ and used it to catalyze the addition reaction of 2-aryl pyridines with imines and *α,β*-unsaturated *N*-acyl pyrroles (Scheme 1.8)[41]. The catalytic cycle is very similar to the C-H addition of indoles, but it is noteworthy that in this addition reaction, the Cp*Co(III) complex catalytically generates the nucleophilic species in situ without any additional reagents and then enables the directed C-H bond addition of 2-aryl pyridines.

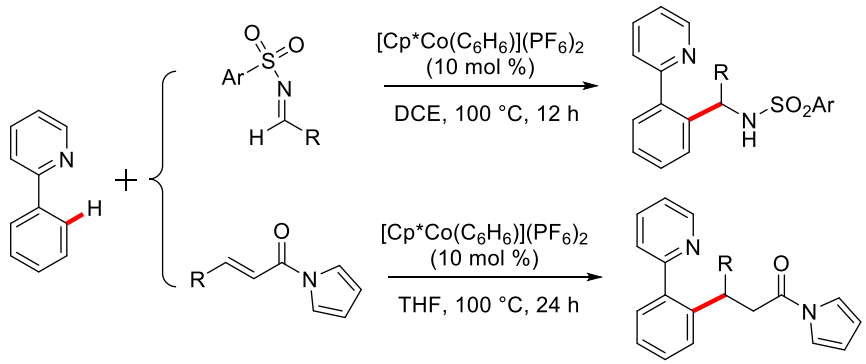


**Scheme 1. 8**. Addition reaction of 2-phenylpyridine.

Thereafter, the Cp*Co(III)-catalysts have attracted an increasing amount of attention in synthetic organic chemistry, and a range of C-H functionalization has been further extended, mainly involving reactions such as terminal coupling reactions as well as the formation of heterocycle.

#### 1.2.2.1. Terminal coupling using Cp*Co(III) catalysts

Terminal coupling via transition metal-catalyzed C-H bond activation has developed into a diverse field of research. The applicable catalysts are multifaceted and the products obtained are diverse, ranging from basic chemicals to complex molecules. As a consequence, a significant number of examples of this type of coupling reaction catalyzed by Cp*Co(III)-catalysts will be discussed in this section. And these examples will be classified according to the type of bond that is formed in the coupling reaction, which can divide into C-C bond formation and C-X bond formation.

#### 1.2.2.1.1. C-C bond formation

As stated previously, the formation of C-C bond is one of the most fundamental reactions in synthetic organic chemistry. The development and improvement of current approaches for the efficient construction of C-C bonds have been emphasized with C-H activation, both from an academic and industrial application perspective. In terms of the number of articles published currently, the construction of C-C bonds via high-valent cobalt-catalyzed C-H activation is now the most widely studied. For better discussion, these examples of C-C bond formation are grouped by substrate type, mainly because in many cases this reaction is found to be substrate type-specific, such as indoles-based substrates, 2-aryl-*N*-containing heterocyclic substrates and other type substrates.

As mentioned previously, Matsunaga and Kanai first reported the use of $[Cp^*Co(C_6H_6)](PF_6)_2$ as a catalyst to catalyze C2-selective addition of indoles in 2013[40]. Further, they also found that the use of $[Cp^*Co(CO)I_2]$ can promote direct dehydrative C-H allylation of non-activated allyl alcohols, thus giving C2-allylated indoles, phenyl-pyrazole, and pyrrole in good yields, whereas analogous Cp*Rh(III) catalyst was ineffective (Scheme 1.9a)[42]. Shortly afterward, the scope of this allylation protocol was extended by Glorius and co-workers, the allyl carbonates can be used as coupling partners (Scheme 1.9b)[43].

Furthermore, an example of alkylation was published by Wang and co-workers, Cp*Co(III)-catalyzed C-H coupling reaction of indoles with *α*-diazomalonates (Scheme 1.9c)[44], which proceeds under relatively mild reaction conditions. In this protocol, *α*-diazomalonates, the most commonly used carbene precursor, can be reacted with metal to give a highly reactive metal-carbene intermediate and promote the alkylation of indoles. With an optimized catalytic system based on previous work, the group of Ackermann reported the C-H alkynylation of indoles by using 1-bromoalkynes and cyclopropanes as coupling partner (Scheme 1.9 d and f)[45,46]. Subsequently, the use of alkynes as coupling partners was further developed by Chen and Yu in 2016 (Scheme 1.9 e and k)[47], in the case of use phenylacetylene, the C-H alkenylation could also be achieved efficiently.

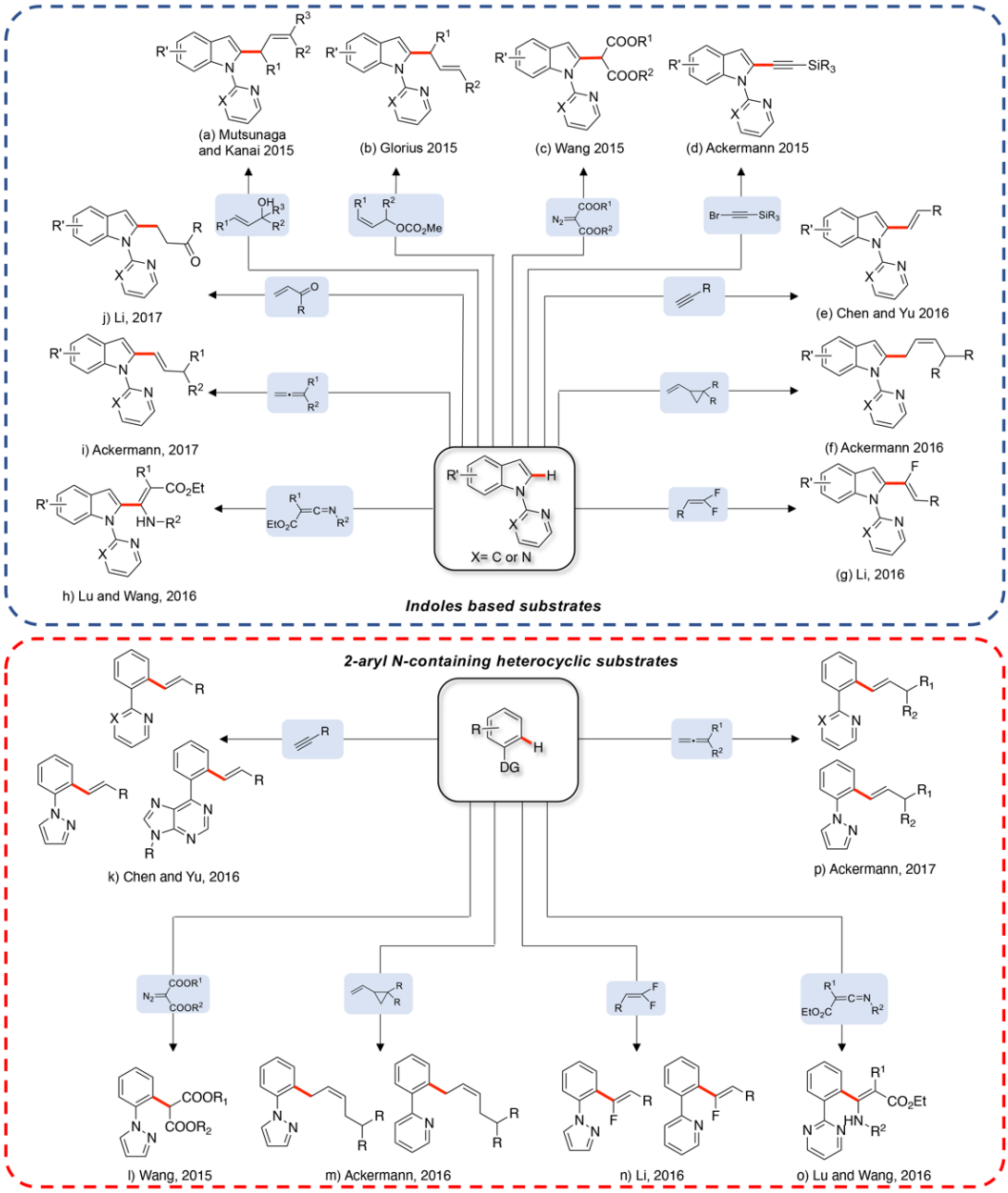


**Scheme 1. 9.** Selected Cp*Co(III)-complex catalyzed C-H activation of Indoles based substrates (top) and 2-aryl *N*-containing heterocyclic substrates (bottom).

Li and co-workers reported the *α*-fluoroalkenylation of indoles via C-H activation and C-F cleavage (Scheme 1.9g)[48]. Under mild reaction conditions, the Cp*Co(CO)$I_2$ has high catalytic activity, but its efficiency and stereoselectivity can be improved by replacing with [Cp*Co(MeCN)$_3$][$SbF_6$]$_2$. Moreover, the optimized catalytic protocol can also successfully convert 2-arylpyridines/related compounds with *N*-containing heterocyclic directing groups (Scheme 1.9n)[48].

In 2016, Cp*Co(CO)$I_2$ catalyzed C-H enaminylation of 1-(pyrimidin-2-yl)-1*H*-indoles was reported by Wang/Lu and co-workers (Scheme 1.9h)[49]. The ketenimines were successfully used as the coupling partner. In addition, this protocol is also suitable for phenyl substrates containing the pyrimidine directing group, whilst the yield of the conversion is comparatively low (Scheme 1.9o)[49].

Recently, the first use of allenes as coupling partners in Cp*Co(III)-complexes catalyzed C-H hydroarylation was reported by Ackermann and co-workers (Scheme 1.9i)[50]. And the use of [Cp*Co(CO)$I_2$] can access alkylated heteroarenes provided with a highly chemo- and regioselective. Moreover, this protocol was also demonstrated to be possible to convert 2-arylpyridines substrates (Scheme 1.9p)[50]. Beyond that, by using *α,β*-unsaturated ketones and glyoxylate as coupling partners with high efficacity, which was demonstrated by Li and co-workers (Scheme 1.9j)[51].

While indole-based substrates and 2-aryl *N*-containing heterocyclic substrates have achieved excellent results with the Cp*Co(III)-catalysts, the application of other substrates have also made good progress (Scheme 1.10).

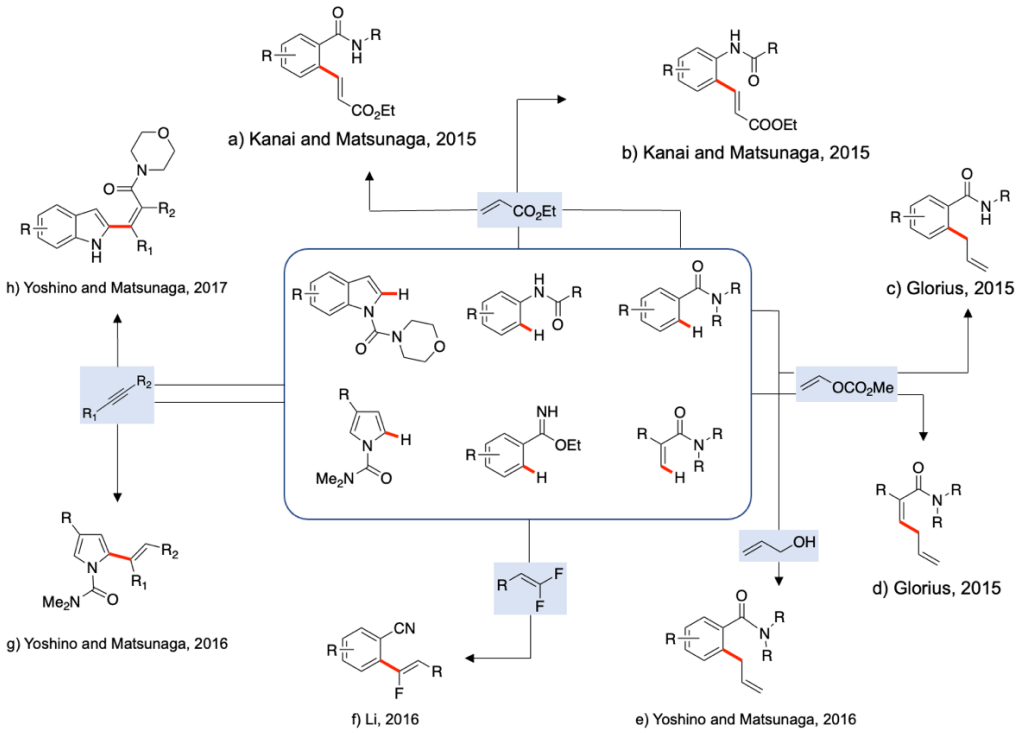


**Scheme 1. 10.** Selected Cp*Co(III)-complex catalyzed C-H activation of other types of substrates.

The C-H functionalization of benzamides is relatively well established by using low-valent cobalt as a catalyst, whereas there are few examples of the use of Cp*Co(III)-complexes. In 2015, Kanai/Matsunaga and co-workers have presented an example about oxidative C–H alkenylation of benzamides using ethyl acrylate as coupling partner (Scheme 1.10a)[52], but this present protocol was limited by stoichiometric oxidant and by the substrate scope. Later, they also found that this coupling reaction could be successfully applied to acetanilide substrates (Scheme 1.10b)[52]. Meanwhile, allyl carbonate can also use as a coupling partner for C–H alkenylation of aryl- and alkenylamides benzamides, which was reported by Glorius and co-workers (Scheme 1.10c,d)[43]. But the yield was significantly lower when compared to the previously mentioned C-H alkenylation of indoles (Scheme 1.9b)[43]. In addition, Yoshino and Matsunaga have also described a method for the allylation of benzamide substrates, by replacing the allyl carbonate with allyl alcohol (Scheme 1.10e)[53].

In 2016, Li and co-workers have explored the potential of cobalt(III)-catalyzed *α*-fluoroalkenylation (Scheme 1.10f)[48]. Notably, an unusual product observed when using ethyl benzimidates as arene substrate, which was also demonstrating the potential of Cp*Co(III) catalyzed *α*-fluoroalkenylation. Later, selective alkenylation reactions were developed by Yoshino/Matsunaga and co-workers, where dimethylcarbamoyl-protected pyrroles can react with alkynes by $[Cp^*Co(CH_3CN)_3](SbF_6)_2$ (Scheme 1.10g)[54]. Furthermore, a new coupling protocol of carbamoyl-protected indoles/pyrrole with alkynes was also provided (Scheme 1.10h)[55], where the carbamoyl group acts not only as a directing group but also as an internal acylating agent, removed and migrated to the alkene moiety of the product.

Currently, C-H bond activation using Cp*Co(III) catalysts has been mainly concentrated on the functionalization of $C(sp^2)$-H bond, but protocols for the $C(sp^3)$-H functionalization are scarce, which might be attributed to the poor stability of the resulting organometallic intermediate. Hence, $C(sp^3)$-H functionalization is also one of the major challenges in the field of C-H activation. In 2016, Cp*Co(III)-catalyzed $C(sp^3)$-H bond alkenylation of 8-methylquinoline with alkynes was demonstrated for the first time under mild conditions by Sundararaju and co-workers (Scheme 1.11a)[56]. Moreover, oxazolone can act as an efficient amidating agent (Scheme 1.11b)[57]. Additionally, another example disclosing the alkylation of 8-methylquinoline with diazo compounds has been reported by Shi and co-workers (Scheme 1.11c)[58].

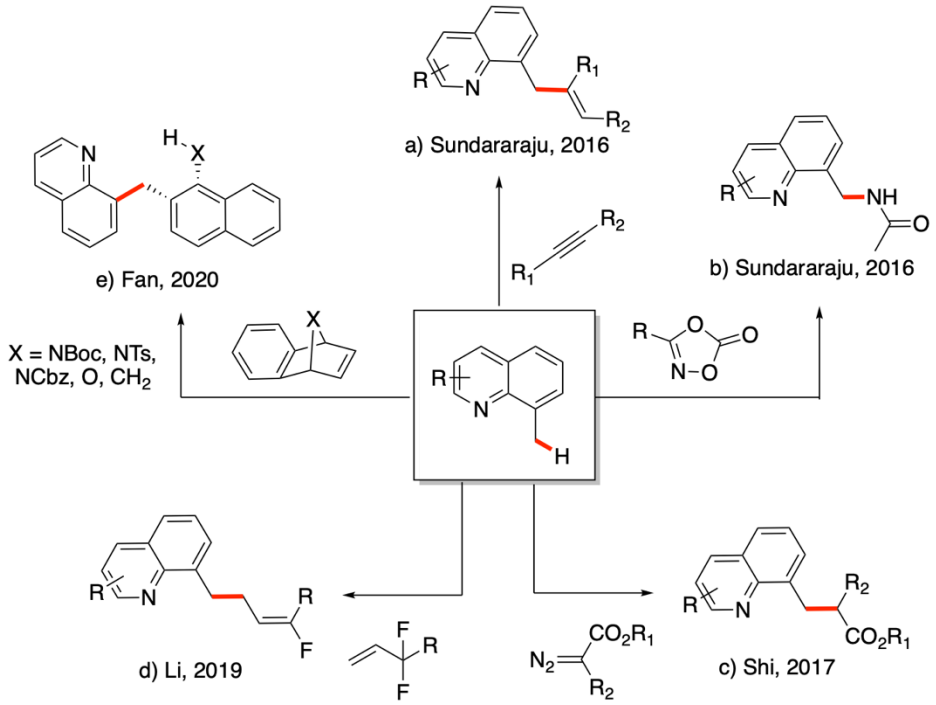


**Scheme 1. 11.** Selected Cp*Co(III)-catalyzed C($sp^3$)-H activation of 8-methylquinoline.

In 2019, C($sp^3$)-H fluorallylation of 8-methylquinolines with fluoroalkyl olefins have been developed by Li and co-workers under mild and redox-neutral conditions (Scheme 1.11d)[59]. In this reaction, either cobalt(III) or rhodium(III) catalysts can achieve this conversion with good efficiency as well as high regio- and stereo-selectivity, but seem to be more reactive and selective under Rh(III)-catalyzed conditions. In 2020, an efficient and economical cobalt-catalyzed C($sp^3$)-H method was first proposed by Fan and co-workers for the addition of 8-methylquinolines with azabenzonorbornadienes (Scheme 1.11e)[60], which exhibited a wide range of substrate scope as well as good functional group tolerance.

#### 1.2.2.1.2. C-X bond formation

In the context of Cp*Co(III)-catalyzed C-H activations, the C-C bond formation has always been a major focus of research, but there are relatively few examples of C-X bond formation, such as C-N bond formation and C-S bond formation, as shown in the Scheme 1.12.

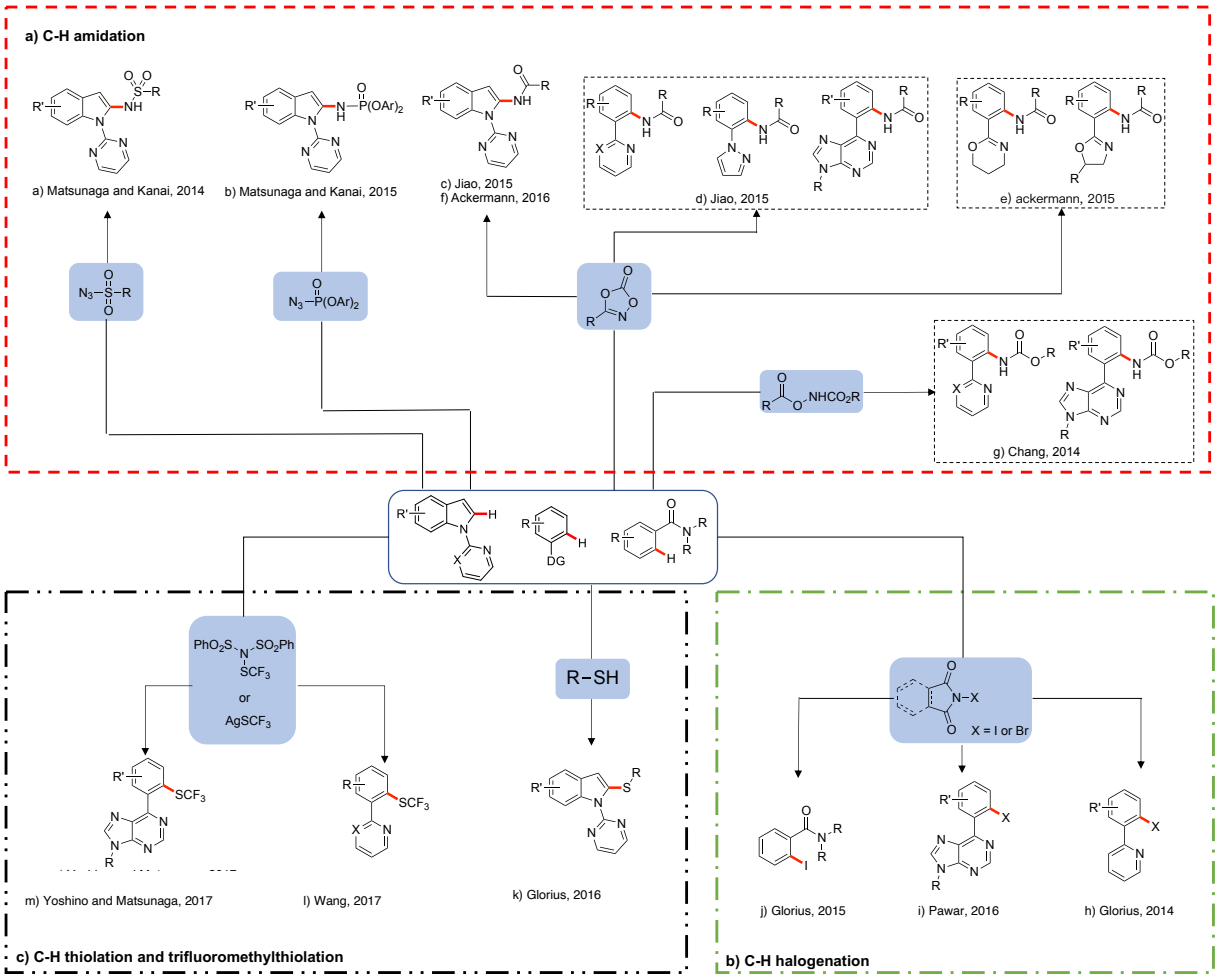


**Scheme 1. 12.** Selected Cp*Co(III)-catalyzed C-X bond formations.

### 1) C-H amidation

Due to the specificity of the amide functional group in organic synthesis, the formation of C-N bond with an economical approach via C-H amidation has attracted much attention[61]. In this reaction, azides, 1,4,2-dioxazol-5-ones and acetoxy carbamates are generally used as the reaction source of amide.

In 2014, the formation of C-N bond by using the Cp*Co(III) complex as a catalyst was first time demonstrated by Matsunaga and Kanai (Scheme 1.12a)[62]. Replacement of $[Cp^*Co(benzene)](PF_6)_2$ by $[Cp^*Co(CO)I_2]$ as a catalyst can increase the efficiency of the amidation of indoles-base substrate with aryl/alkyl sulfonyl azides. Moreover, various substituted indoles can be successfully coupled with aryl/alkyl sulfonyl azides in high yields under optimized conditions. Subsequently, they found that the use of

phosphoryl azides could be also as coupling partners for amidation of indoles base substrate (Scheme 1.12b)[63].

Afterward, 1,4,2-dioxazol-5-ones can also act as amidating agents, the group of Jiao and Ackermann further developed amidation protocols (Scheme 1.12 c-f)[64, 65]. A wide range of substrates was found to be able to convert via this optimized amidation procedure, such as indoles-base substrate (Scheme 1.12c and f) [64, 65], 6-arylpurines, 2-phenylpyridines (Scheme 1.12d)[64, 65], phenyloxazolines as well as phenyloxazines (Scheme 1.12e)[64, 65]. The general mechanism of the present cobalt-catalyzed C-H amidation was proposed currently in Scheme 1.13. The C-H bond was firstly activated and cleaved by Cp*Co(III)-catalyst to produce a five-membered metalacyclic intermediate, then it was coordinated with 3-phenyl-1,4,2-dioxazol-5-one to form a new intermediate containing Co=N bond. Subsequently, the six-membered intermediate is produced by migratory insertion. Finally, the desired product and active species were obtained by protodemetalation.

Later, Chang and co-workers proposed the amidation of 2-aryl *N*-containing heterocyclic substrates via Cp*Co(III)-complex, using acetoxy carbamates as a reactive source of amide (Scheme 1.12g)[66]. In contrast, the formation of C-N bond cannot be achieved with sulfonyl azides (N3-Ts) with the optimized conditions.

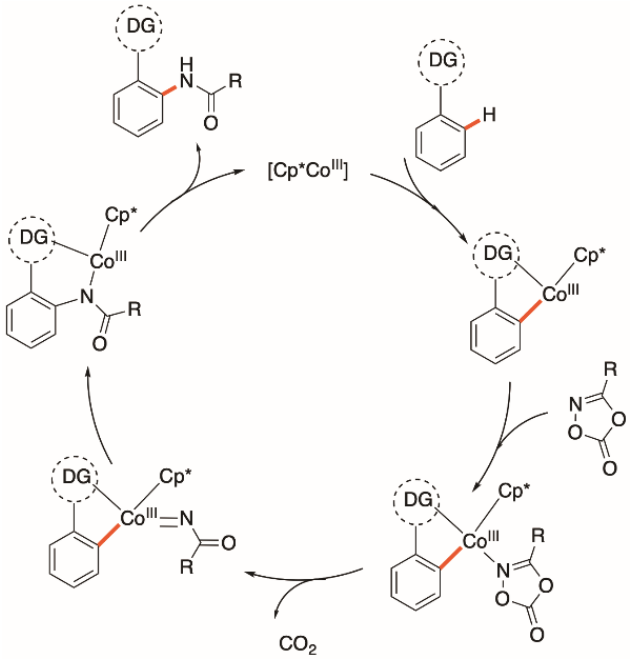


**Scheme 1. 13.** A general mechanism of C-H amidation with 1,4,2-dioxazol-5-ones.

### 2) C-H halogenation

Halogenation is one of the most fundamental transformations in organic chemistry and has a wide range of applications in agrochemicals, pharmaceuticals and material sciences[67]. Although many methods have been developed for introducing halogen atoms into organic molecules, direct C-H halogenation has remained the most effective tool for the synthesis of halogenated molecules.

In 2014, a new example of C-H bromination and iodination of 2-aryl pyridines was described by Glorius and co-workers (Scheme 1.12h)[68]. In those reactions, *N*-bromophthalimide (NBP) and *N*-iodosuccinimide (NIS) were used as brominating and iodinating agents respectively. The brominated products were found to be in low yields. Other substrates were subsequently investigated and provided modest conversions. Later, the halogenation protocols has been further developed and applied by Pawar and co-worker (Scheme 1.12i)[69]. In addition, Glorius and co-workers expanded the range of substrate scope for their iodination protocol to include benzamide substrates (Scheme 1.12j)[68]. An unusual example for the C-H iodination of *N*-alkenylbenzamides was presented, and the potential applicability was further demonstrated.

### 3) C-H thiolation and trifluoromethylthiolation

The thioether groups are common in biologically active compounds and intermediates in organic material synthesis and the direct C-H thiolation provides an attractive strategy. Despite recent progress in this direction, there were few investigations on Cp*Co(III)-catalyzed C-H thiolation.

Most recently, Glorius and co-workers reported a thiolation protocol via cross-dehydrogenative coupling of thiols with indoles (Scheme 1.12k)[70], which is a novel mode of the formation of C-X bonds by Cp*Co(III) catalyst. Under optimized reaction conditions, a variety of indoles with protecting groups can be directly thiolated.

Given the wide range of biological activities of $SCF_3$-substituted (hetero)aromatic compounds, many efforts have been expanded to explore an efficient synthetic method for these compounds. Recently, the first trifluoromethylthiolation via $[Cp^*Co(CO)I_2]$ was proposed by Wang and co-workers (Scheme 1.12l)[71]. However, this reaction was limited by the range of substrates, only in the case of 2-arylpyridine and 2-

arylpyrimidine substrates. In a recent report, the substrate scope has further expended by Yoshino/Matsunaga and co-workers, and also included 6-arylpurines, with the use of *N*-trifluoromethylthiodibenzenesulfonimide as a trifluoromethyl source (Scheme 1.12m)[72].

#### 1.2.2.2. Heterocycle formation using Cp*Co(III) catalysis

In the past decade, transition metals-catalyzed C-H bond activation to form C-C and C-X bonds has emerged as a promising for the formation of heterocycles, which is more atom- and step-economy than the traditional methods. Despite the significant efforts made in the past few years, these approaches are still in their infancy.

##### 1.2.2.2.1. Heterocycles formation by alkynes

One of the effective and powerful methods to form heterocycle is the annulation reaction using alkynes as a coupling partner.

In 2016, the first examples of using alkynes as coupling partner to form indole-substrates via Cp*Co(III)-catalyzed C-H functionalization was provided by Ackermann and co-workers (Scheme 1.14a)[73]. And the $Cp^*Co(CO)I_2$ is widely applicable to the annulation of nitrones with alkynes via C-H/N-O functionalization and has good functional group tolerance and unique regioselectivity. Interestingly, indoles could also be synthesized efficiently with the help of $[Cp^*Co(MeCN)_3](SbF_6)_2$, thereby avoided using additional silver salt. Following on from this work, Zhang and co-workers described a novel method for the formation of quinoline-*N*-oxides via the annulation of aryl nitrones with alkynes (Scheme 1.14i)[74].

*N*-nitrosoanilines, arylhydrazines and Boc-protected hydrazines can be equally used as substrates for the preparation of indoles via Cp*Co(III)-catalyzed C-H functionalization, which was further developed by Jiao, Zhu, Glorius and their co-workers (Scheme 1.14b-d)[75,76,77].

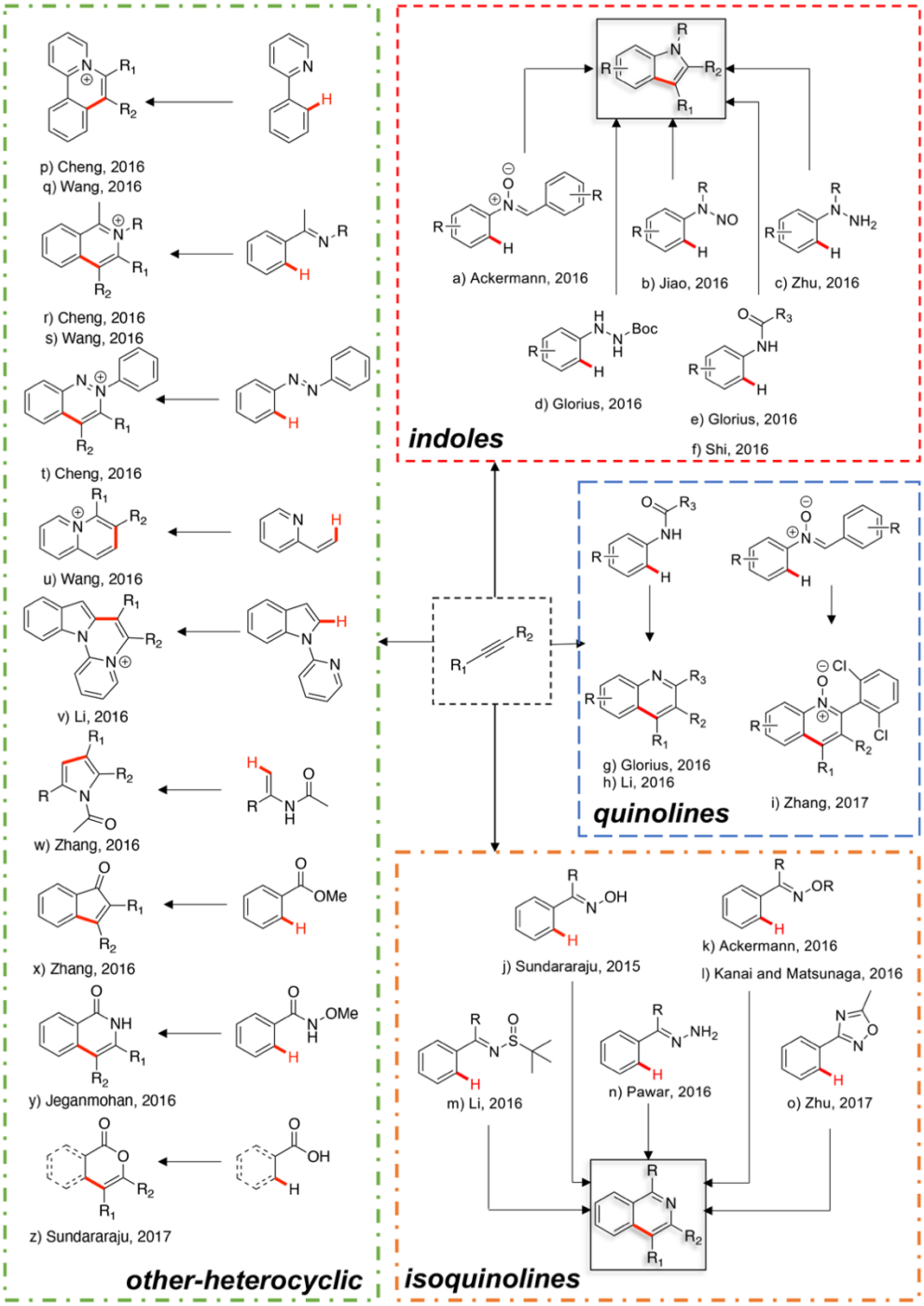


**Scheme 1. 14.** Selected examples for the formation of heterocycles with alkynes via Cp*Co(III)-catalysts.

In 2016, both the groups of Glorius and Shi reported a protocol for the formation of indoles by using of *N*-arylureas as substrates (Scheme 1.14e, f)[78, 79]. Additionally, Glorius and co-workers found that the dehydrative cyclization was greatly accelerated when Lewis acid was introduced, thus allowing for the selective formation of quinolines

(Scheme 1.14g) [81], and Scheme 1.15 shows the proposed pathway for the synthesis of indoles and quinolines. The electrophilicity of the carbonyl group can be improved by the coordination of Cp*Co(III) and Lewis acids, and the nucleophilic addition process was further promoted (Scheme 1.15, cycle A). In contrast, changing the steric and electronic properties of the directing group will inhibit nucleophilic attack, allow the dehydrogenation process (Scheme 1.15, cycle B), which leads to the generation of two different heterocycles. Prior to this work, the analogous quinolines could be synthesized by using unsymmetrical alkynes, which was reported by Li and coworkers (Scheme 1.14h)[80], with good functional group tolerance and relatively high regioselectivity.

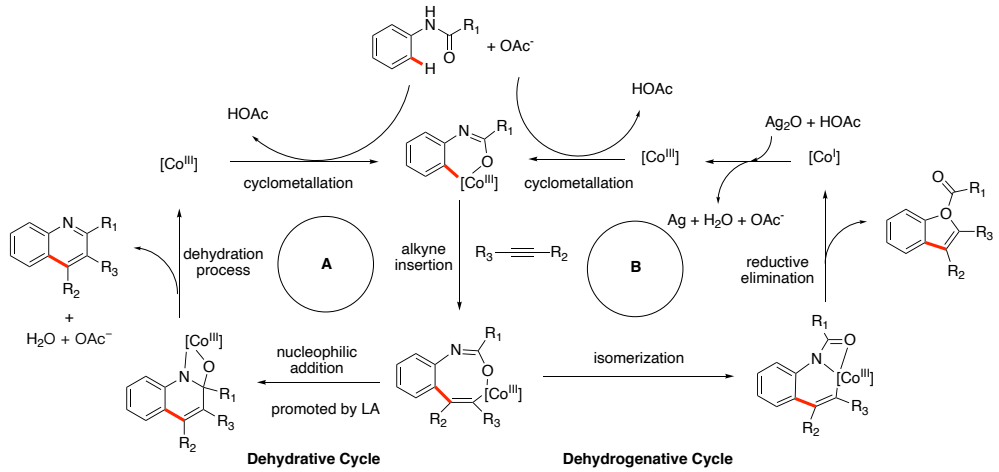


**Scheme 1. 15.** Two pathways for the synthesis of quinolines (cycle A) and indoles (cycle B).

In 2015, Sundararaju and co-workers successfully synthesized isoquinolines for the first time via Cp*Co(III)-catalyzed C-H functionalization (Scheme 1.14j)[81], [Cp*Co(CO)$I_2$] was used to catalyze the dehydrative annulation of oximes with different alkynes without the involvement of any external oxidants. In this protocol, the presence of -OH groups are important in the catalytic cycle as the substitution of -OH groups by -OMe and -OAc groups leads to a dramatic decrease in product yield. However, further studies demonstrated that the high yield of isoquinolines could also be obtained by replacing the -OH group from oximes with -OAc group, which was reported by the group of Ackermann and Kanai/Matsunaga (Scheme 1.14k, l)[82, 83]. Li and co-workers found that when the *N*-sulfinyl group is used instead of -OAc group, it can also be used to synthesize isoquinolines (Scheme 18m)[84].

Another example of isoquinoline derivatives was investigated by Pawar and co-workers (Scheme 1.14n)[85], annulation of arylhydrazones with internal alkynes catalyzed by Cp*Co(CO)$I_2$ via C-H/N-N bond functionalization with good yield, and the N-N bond also acted as an internal oxidant to facilitate this procedure. Most recently, Zhu and co-workers developed a novel method for the formation of 1-aminoisoquinolines via directed C-H activation of oxadiazole with alkynes (Scheme 1.14o)[86].

To synthesize quaternary ammonium salts, there are many methods by using Cp*Co(III) catalysts with different kinds of substrates were reported by Cheng's[87] and Wang's groups[88] in 2016. In these work, 2-arylpyridines (Scheme 1.14 p, q), arylketimines (Scheme 1.14 r, s), azobenzenes (Scheme 1.14t) and 2-vinylpyridines (Scheme 1.14u) were successfully annulated with alkyne to affords the corresponding quaternary heteroaromatic ammonium salts, but the use of unsymmetrical alkynes leads to low regioselectivity. Furthermore, a comparable approach was followed by Li and co-workers, using indole-based substrates containing pyridyl directing group, which yielded a wide range of annulated ammonium salts (Scheme 1.14v)[89]. Later, Zhang and co-workers developed an approach Cp*Co(III)-catalyzed annulation of enamides and benzoic to facilitate the preparation of multi-substituted pyrroles and indenones (Scheme 1.14w,x)[90, 91]. After, the annulation of *N*-methoxybenzamides with alkynes was developed by Jegamohan and co-workers (Scheme 1.14y)[92]. More recently, a simple method to synthesize isocoumarins was described Sundararaju and co-workers, using [Cp*Co(CO)$I_2$] to catalyzed the annulation of carboxylic acids with alkynes (Scheme 1.14z)[93].

In the vast majority of protocols for Cp*Co(III) catalyzed annulation reactions, alkynes are usually employed as coupling partners, with only a few examples using dioxazolones and diazo compounds (Scheme 1.16). In 2016, Li and coworkers described a method for quinazolines via C-H functionalization of *N*-sulfinylimines or benzimidates, in which dioxazolones were used as amidating agents (Scheme 1.16a, b)[94]. Moreover, a novel procedure for C-H activation/double C-N bond formation reaction was developed by Chen and co-workers (Scheme 1.16c)[95], various thiadiazine-1-oxides were produced in good yields from *NH*-sulfoximines and dioxazolones with microwave-assisted.

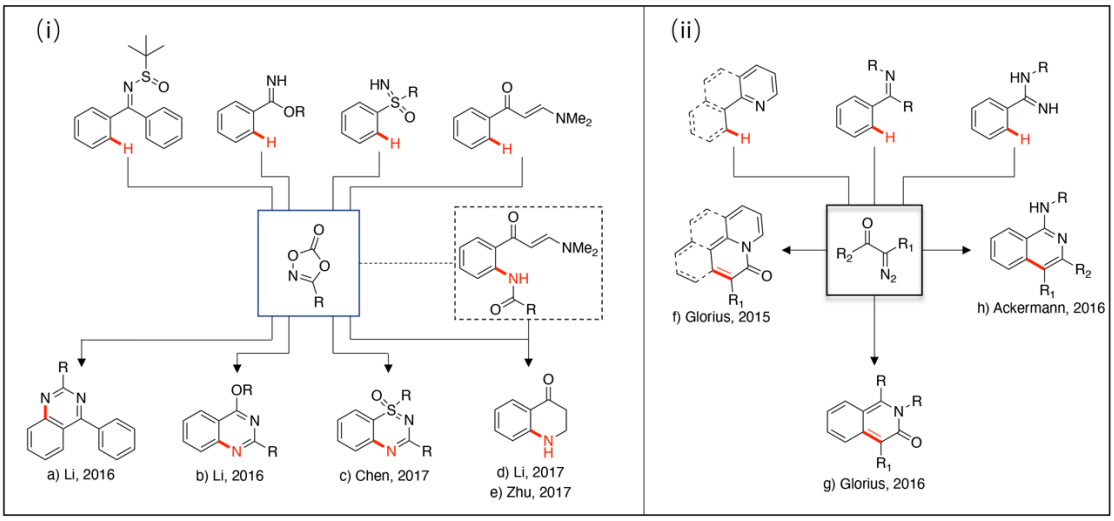


**Scheme 1. 16.** Selected examples of Cp*Co(III)-catalyzed annulation of ioxazolones and diazo compounds.

In 2017, a highly efficient method to synthesize NH-isoquinolones via a “one-pot reaction” was described by both the groups of Li and Zhu (Scheme 1.16 d, e)[96, 97]. The reaction is generally divided into two steps: the C-H amidation of enaminones with dioxazolones was catalyzed by Cp*Co(CO)$I_2$ to form the amidated intermediates firstly, and the electrophilicity of the enaminone group then further utilized in subsequent hydrolysis-cyclization reactions to obtain quinolones in telescoping reactions.

Two different and highly efficient methods for the preparation of isoquinolin-3-ones were presented by Glorius and coworkers (Scheme 1.16 f, g)[98, 99]. Both of them use diazo esters as coupling partners. Noteworthy, in Scheme 1.16 f, the Co species have a dual role, not only as catalysts but also as Lewis acids.

A novel approach for the formation of 1-aminoisoquinoline by cobalt(III)-catalyzed C-H/N-H bond functionalization was proposed by Ackermann and co-workers (Scheme 1.16h)[100]. With this approach, the diazo compounds act as coupling partners with various easily accessible aryl amidines to synthesize the target quinolines efficiently.

In addition to the alkynes, dioxazolones and diazo compounds mentioned above, some other compounds can also be used as coupling partners for the synthesis of heterocyclics, such as CO, aldehydes, anthranils, and vinylene carbonate (Scheme

1.17). In 2015, an approach to synthesis coumarins via direct cyclocarbonylation of 2-vinylphenols with CO was proposed by Wang and co-workers (Scheme 1.17a)[101]. Interestingly, this cyclocarbonylation can occur easily and reactively under a fairly mild reaction condition, and only required balloon pressure of CO. The range of substrates is generally good, with good functional groups tolerance.

The synthesis of indolizines via Cp*Co(III)-catalyzed cycloaddition of 2-arylpyridines with aldehydes was developed by Zeng and co-workers (Scheme 1.17b)[102], providing a simple approach to synthesize the indolizines indolizine derivatives with structural diversity (including benzoindolizines), and with a wide tolerance of functional group. However, it is limited in scope for aldehydes, such as acetaldehyde and benzaldehyde which were not allowed to be used for this reaction.

1*H*-indazoles are commonly regarded as an important skeleton, because of their pharmacological activities, such as antimicrobial, antiviral, anti-inflammatory and anticancer activities. Therefore, there was a great need to develop cheap and efficient methods to synthesize 1*H*-indazole in a green and step-economical manner. In 2016, Li and co-workers have developed a synergistic Cp*Co(III)/Cu(OAc) catalytic system for the formation of substituted 1*H*-indazoles using readily available aryl imidate and anthranils (Scheme 1.17c)[103], where the anthranils also perform as an organic oxidant. Meanwhile, the formation of N-N bond may involve a nitrogen radical intermediate species via the SET step by the copper, which was suggested by mechanistic studies.

Recently, the domino C-H/N-H allylation of aryl imidate to deliver the desired vinyl-substituted heterocycles was first proposed by Ackermann and co-workers (Scheme 1.17d)[104]. In this protocol, 4-vinyl-1,3-dioxolan-2-ones was used as coupling partners and the $[Cp^*Co(CH_3CN)_3](PF_6)_2$ was used as a single-component catalyst, which can effectively catalyze domino allylation including C-H functionalization and N-N allylation, with unique chemo-selectivity. Moreover, the 4-vinyl-1,3-dioxolan-2-ones can also be used as coupling partners in several synthetic protocols and shows great potential.

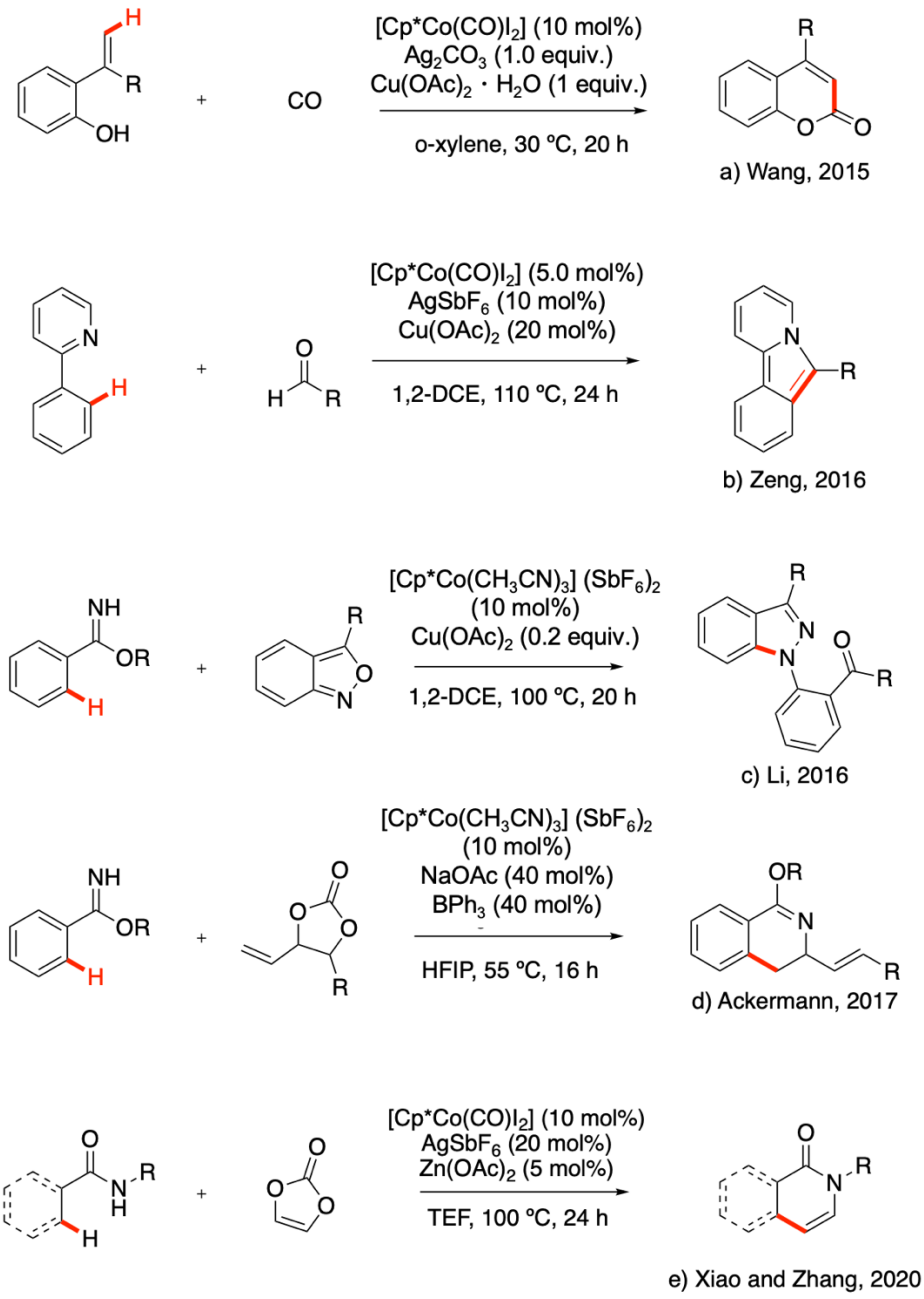


**Scheme 1. 17.** Selected examples of the synthesis of heterocyclics use other compounds as coupling partners.

Another efficient approach to synthesize isoquinolinones and pyridinones use vinylene carbonate as coupling partner via Co(III)-catalyzed C−H activation/annulation vinylenetransfer reaction of benzamides with acrylamides have been developed by Xiao and Zhang in 2020 (Scheme 1.17e)[105], in this reaction, both aryl ring and nitrogen atom bearing a wide range of functional groups, affording the target products with high yields.

## 1.3. Cyclometallation via Cp*M-catalyzed C-H activation (M= Co, Rh, Ir)

As described in the previous two sections, Cp*Co(III)-base catalysts have been considered as a most attractive alternative to the 4d and 5d transition-metals, and widely used for the C-H bond functionalization. However, the understanding of these transformations was still extremely limited, which was related to the high reactivity of the transient cobalt species in these transformations. Normally, these transformations can be divided into two parts: the activation of C-H bond and the functionalization of C-H bond (Scheme 1.18). In the first step, the transition metals-mediated activation of a C-H bond to form a metallacycle consisting of a new C-M bond, which is called a cyclometallation. In addition, this cyclometallation also be divided into two consecutive steps: (**I**) the donor group coordinate to the metal center; (**II**) the intramolecular activation of the C-H bond to direct the coordinated species.

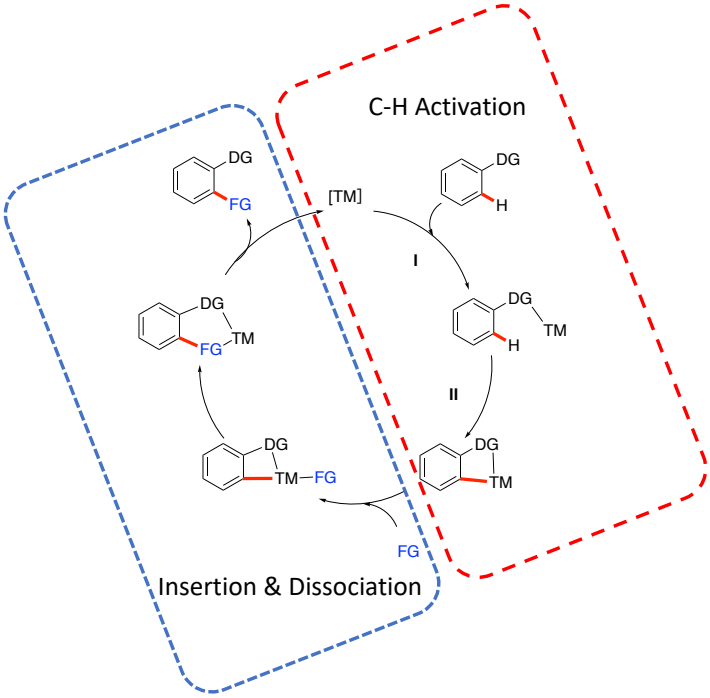


**Scheme 1. 18.** Transition-metal-catalyzed C–H bond functionalization (TM = Transition-metals; DG = Directing Group; FG = Functional Group).

In this section, we mainly focus on the study of cyclometalated [Cp*M(C^N)] complexes for group 9, such as cobalt, rhodium and iridium, which can be readily obtained by using $[Cp^*MCl_2]_2$ (M = Ir, Rh) as a precursor and the activation of C-H promoted with

the help of sodium-acetate. In addition, the successful isolation of metallacycles can provide direct evidence for the mechanism of C-H bond activation.

### 1.3.1. Mechanisms of cyclometallation reactions

The mechanism of cyclometallation is mainly determined by the electronic configuration of the metal center, as well as the nature of the C-H bond. Until now, the widely accepted mechanisms of cyclometallation are divided into three main pathways: (1) electrophilic bond activation[106, 107], (2) oxidative addition[108], and (3) σ-bond metathesis[107]. However, for most cyclometallation processes, the exact mechanism is not yet completely understood, the theoretical and experimental studies just provide a most likely pathway.

#### 1) electrophilic bond activation

In this mechanism pathway, cyclometallation is usually assisted by the coordinated leaving groups or free base in the reaction, which is more common in electron-poor late transition metals, such as palladium(II) and platinum(II) [106]. At any stage of this mechanism, the generation of metal hydride complex is not observed, so there is no change in the oxidation number of the metal center.

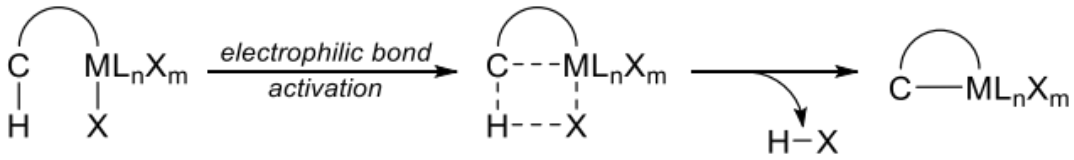


**Scheme 1. 19**. General electrophilic bond activation mechanism of cyclometallation.

According to the intermolecular interactions between the C-H bond and metal-center in this mechanism, it can also be classified into electrophilic aromatic substitution and agostic C-H activation.

**Electrophilic aromatic substitution**: This type of mechanism is mainly related to the formation of a new $C_{aryl}$-M bond by the electronic interaction between the π-electronic cloud of the substrate and the electrophilic metal center, whilst not changing the oxidation state of metal (Scheme 1.20, top). In this mechanism, the σ-complex (also

known as a Wheland intermediate) is first formed, while the carbon bound to the metal becomes tetravalent so that the cyclic conjugation of the aromatic system is thus broken, and then the proton of the tetravalent carbon is eliminated and the aromaticity is regained to form the metallacycle with M-C bond.

**Agostic C-H bond activation:** In this mechanism, the C-H σ-bond will be elongated when the metal center approaches the C-H bond. At the same time, the X-ligand (anionic ligand or radical) interacts with the proton of the extended C-H bond via agostic interaction, which is subsequently removed by deprotonation, leading to the metallacycle (Scheme 1.20, bottom).

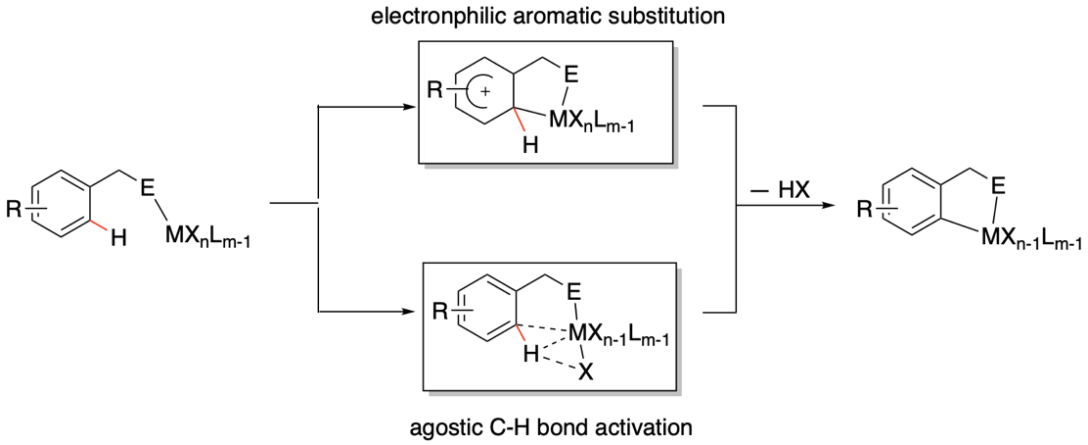


**Scheme 1. 20.** Bond activation by electrophilic aromatic substitution and agostic C-H bond activation (E= donor atom, M=transition metal).

### 2) oxidative addition

This oxidative addition is occurring most commonly in cyclometallations when using iridium(I) and rhodium(I), and also seems to be prevalent in most $C_{alkyl}$-H bond activations when using late-transition metals[108]. This is mainly because the activation of C-H bonds requires an electron-rich metal center. Within this mechanism, the metal-hydride bond will be formed, and the oxidation state of the metal center will be increased by 2, which is rapidly restored to its original valence by the subsequent reductive elimination stage.

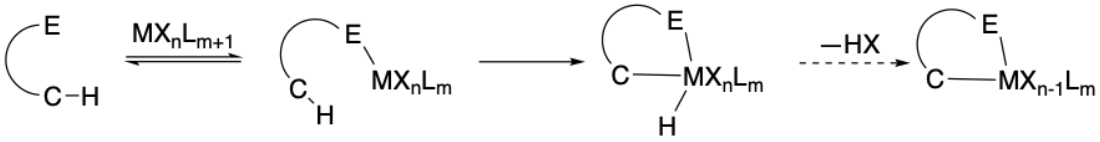


**Scheme 1. 21.** Oxidative addition mechanism for cyclometallation (E= donor atom, M=transition metal).

#### 3) σ-bond metathesis

Most of this activation mechanism occurs in transition metals with a $d^0$ electronic configuration (group III, lanthanides and actinides), but there are also few examples of transition metals of group IV and V.[107] In a basic sense, σ-bond metathesis is the concerted exchange of the σ-bond of metal center with the substrate where the reaction conducted via a four-membered metallacycle transition state instead of an intermediate, so the oxidation state of the metal does not change either. Moreover, the formation of new bond does not involve any metal-hydride species.

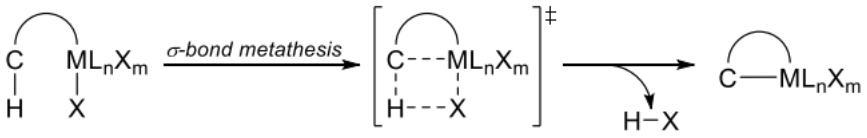


**Scheme 1. 22.** σ-bond metathesis for cyclometallation.

## 1.3.2. Cyclometalated [Cp*M(C^N)] complexes (M= Ir, Rh, Co)

Back to 1998, a preliminary invetigation of the cyclometallation of iridium(III) in the presence of sodium acetate was reported by Beck and co-workers. In this work, the chloro-bridged iridium(III) complex $[Cp^*IrCl_2]_2$ can be cyclometallated with substituted 2-phenyl-4-*R*-5(*4H*)-oxazolidinones to form the Cp*Ir(III)-complexes **1** (Scheme 1.23)[109]. In addition, the substituted oxazoline ligands 4,4'-dimethyl-2-oxazolinylbenzene[110] and 4(S)-isopropyl-2-oxazolinylbenzene[111] could also be readily cyclometalated to form complexes **2** and **3** (Scheme 1.23), which was reported by Davies and co-workers[110, 111].

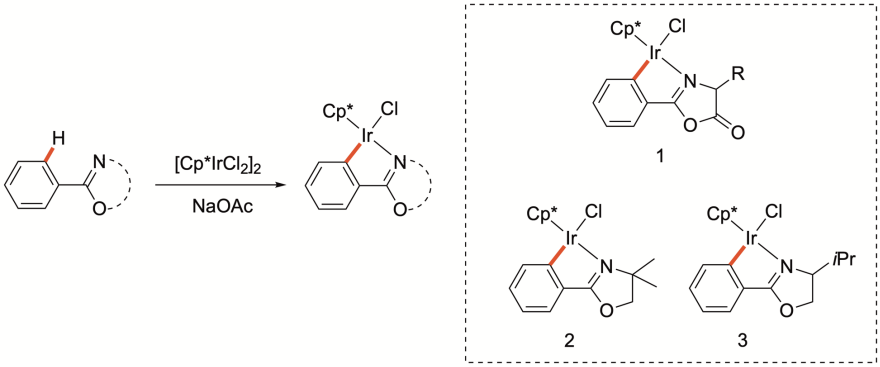


**Scheme 1. 23.** Preliminary examples of the cyclometallation of iridium(III).

Subsquently, in 2013, the cyclometallation of aldimine ligands with $[Cp^*MCl_2]_2$ promoted by acetate was first investigated by Davies and coworkers[110], which was further studied by Jones and others (Scheme 1.24)[112-114]. The results showed that under the same conditions, the cyclometallation of substrate bearing an electron donating group (EDG, such as *p*-OMe) was more efficient than bearing an electron-withdrawing group (EWG, such as *p*-$CF_3$). Moreover, $[Cp^*IrCl_2]_2$ was more efficient than $[Cp^*RhCl_2]_2$ in the cyclometallation reaction with the same substituents.

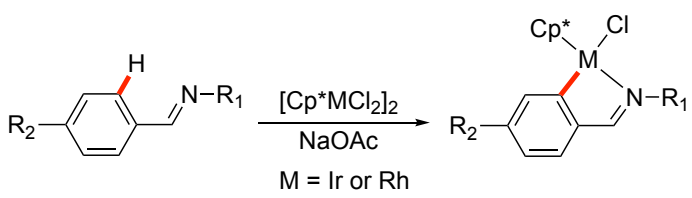


**4a - 8a:** M = Ir
**4b - 8b:** M = Rh
**4a,b:** $R_1 = (CH_2)_2OMe$; $R_2$ = H
**5a,b:** $R_1 = (CH_2)_3OMe$; $R_2$ = H
**6a,b:** $R_1$ = Me; $R_2$ = H
**7a,b:** $R_1$ = Ph; $R_2$ = OMe
**8a,b:** $R_1$ = Ph; $R_2 = CF_3$

**Scheme 1. 24.** Cyclometallation of aldimine ligands with $[Cp^*MCl_2]_2$ (M = Ir, Rh).

In addition, the reactivity of these five-membered iridacycles and rhodacycles with the various of unsaturated molecules has been further investigated by Jones and co-workers (Scheme 1.25)[115]. The reactions with carbon monoxide, they both formed 6-membered metallacycles **9a** and **9b**, while ethylene producing two different products, which depends on the metal center. The reactions of ethylene with iridacycle afforded the coordinated product **10a**, while that with rhodacycle yielded the inserted and rearranged product **10b**, which suggested that reactibity might be affected by both steric and electronic factors.

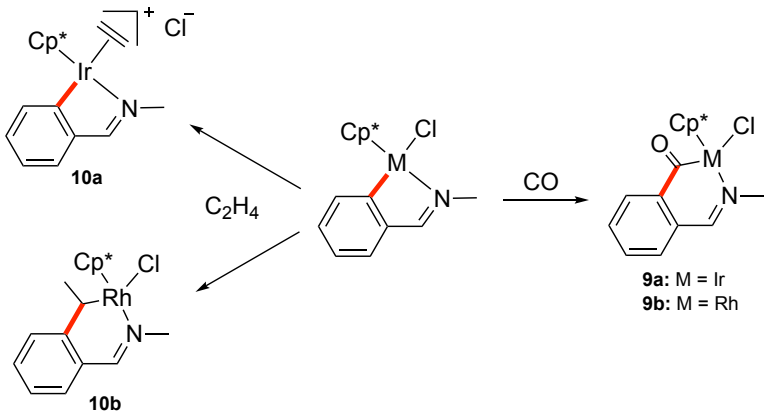


**Scheme 1. 25.** The reactivity of metallacycles with the various of unsaturated molecules.

Similar to aldimine ligands, ketimine ligands can also be use for the cyclometallation of $[Cp^*IrCl_2]_2$, and it reacted equally well as aldimines, which was reported by Xiao and co-workers[116-118]. In this work, the mixture of ketimine and $[Cp^*IrCl_2]_2$ (2.2 : 1) in DCM for 24h afforded the cyclometalated Cp*Ir-complexes with high yields in the present of NaOAc (Scheme 1.26). Interestingly, this reaction also proceeded successfully in MeOH without the addition of any base. Moreover, this type of cyclometalated Cp*Ir complex **11** was an excellent catalyst to catalyze the hydrogen transfer reaction efficiently.

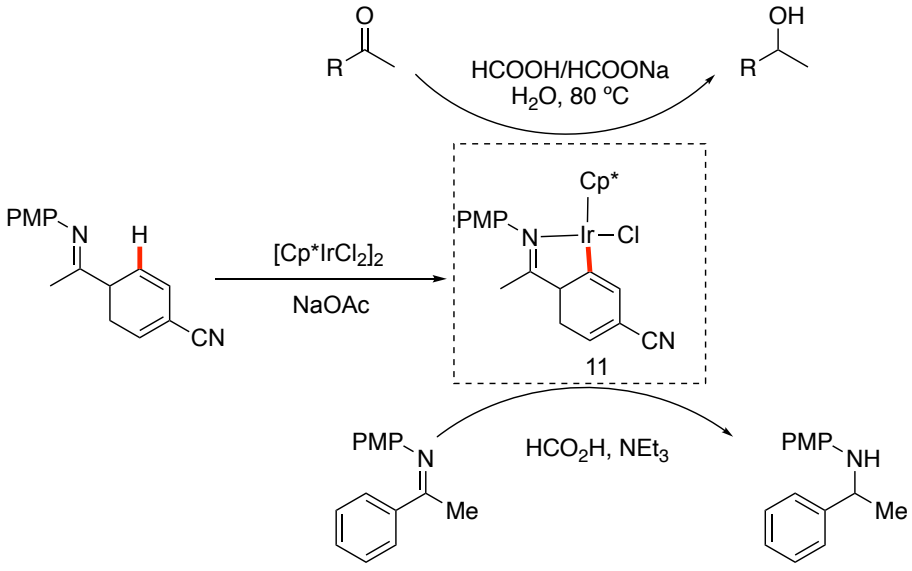


**Scheme 1. 26.** The cyclometallation of $[Cp^*IrCl_2]_2$ with ketimine and application for hydrogen transfer reaction.

The reaction of imines instead of amines with $[Cp^*MCl_2]_2$ (M=Ir, Rh) also produces metallacycles containing M-C bonds (Scheme 1.27). In the present of NaOAc, the cyclometalated complex **12** was readily obtained via cyclometallation of *N,N*-dimethylbenzylamine with $[Cp^*IrCl_2]_2$ at room temperature. Moreover, Barloy/Pfeffer and co-workers also found that the cyclometallation of *N,N*-dimethylbenzylamine with $[Cp^*MCl_2]_2$ can undergo in MeCN solvent to afford the cationic metallacycles **13** in the present of $NaOH/KPF_6$[119, 120].

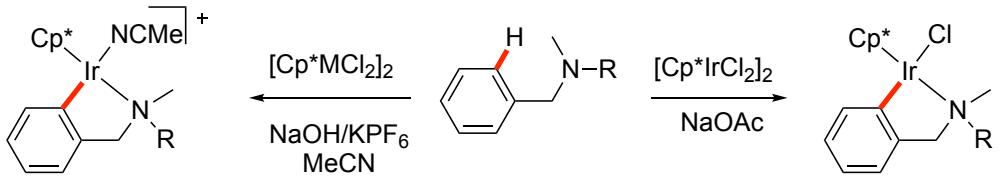


**13a:** M = Ir, R = Me
**13b:** M = Rh, R = Me
**13c:** M = Ir, R = H

**12:** R = Me

**Scheme 1. 27.** The cyclometallation of $[Cp^*MCl_2]_2$ with imines.

More recently, cyclometalated Cp*M-complexes **14** by treating *N*-methoxy-4-nitro-benzamide with $[Cp^*MCl_2]_2]$ (M=Ir, Rh) were further developed by Wang and co-workers (Scheme 1.28).[121] The cyclometalated rhodium and iridium complexes can react with diphenylacetylene afforded the corresponding seven-membered metallacycles **14a'** and **14b'** in 24% and 6% yields, respectively, through the tandem reaction with insertion of two molecules of diphenylacetylene. Subsequently, metallacycles **14a** and **14b** were used as the catalysts for verifying the cyclometalated complexes to be the intermediates of the reaction. These results proved that the five-membered metallacycles **14a** and **14b** probably was the key catalytic intermediates in these reactions.

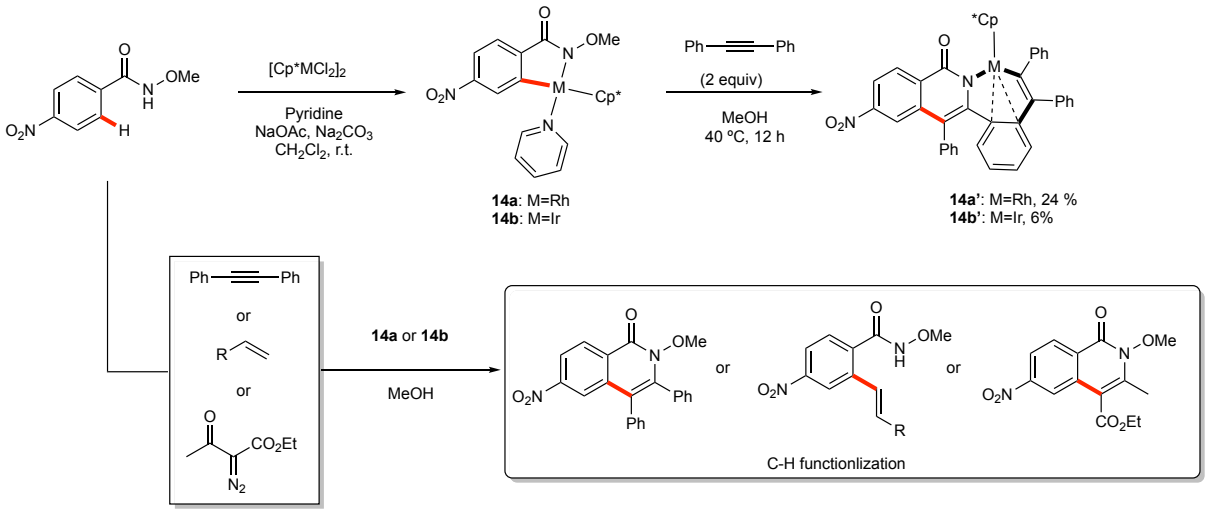


**Scheme 1. 28.** The cyclometallation of *N*-methoxy-4-nitro-benzamide and the coupling reaction catalyzed by cyclometalated complexes.

In addition to the amines and imines we mentioned above, the *N*-Heterocycles are also used in organometallic chemistry frequently, such as pyridines, which can easily undergo cyclometallation with transition metals, such as rhodium and iridium. Similar to the work of Davies[110], the desired cyclometalated complex **15** was readily obtained by the cyclometallation of phenylpyridine or benzo[h]quinoline (Scheme 1.29)[112, 115, 122-124]. In addition, the corresponding hydride complexes **16** can be easily synthsized via the reaction of these metalacycles containing M-Cl bond with the group 13 hydrides to form, which was reported by Norton and co-workers[123].

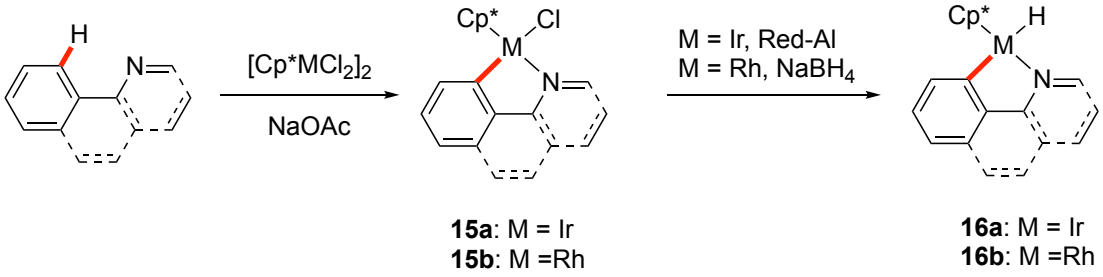


**Scheme 1. 29.** The cyclometallation of *N*-heterocycles and the synthesis of metal-hydride metallacycles.

In 2018, Jones and co-workers have developed an efficient method to synthesize the polycyclic isoquinoline salt via $[Cp^*MCl_2]_2$ (M=Ir, Rh) catalyzed C–H activation at low-temperature (Scheme 1.30)[112]. However, the reaction with 2-phenylpyridine was not

as well as that with the methyl-substituted phenylimine under similar reaction conditions. Notably, in this catalytic system, the key intermediate five-membered metalacycle **15** was first formed by cyclometallization, then the unsaturated DMAD ( dimethyl acetylenedicarboxylate ) molecules were inserted into the C-M bond of the metalacycle **15** to obtain the seven-membered metalacycle **16**, and finally the oxidative cleavage in the presence of anhydrous $CuCl_2$ gave the expected isoquinoline salt in high yield.

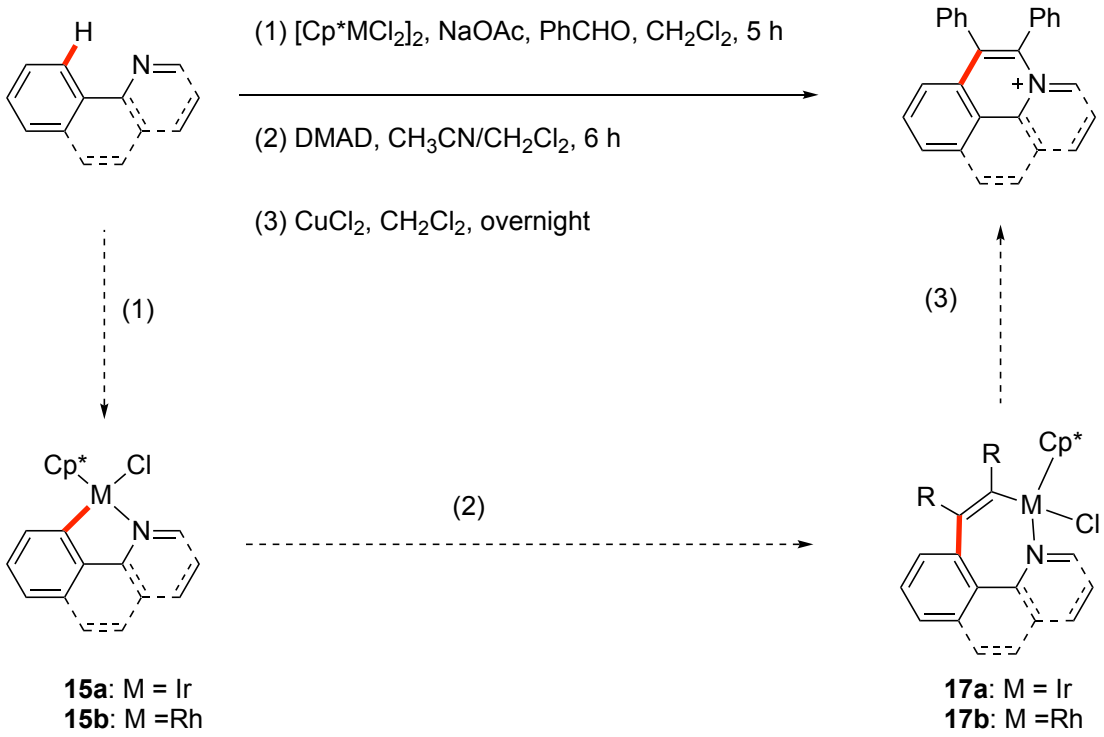


**15a**: M = Ir
**15b**: M =Rh

**17a**: M = Ir
**17b**: M =Rh

**Scheme 1. 30.** The approach for synthesis of polycyclic isoquinoline salt.

A novel catalytic method for the *N*-chelator-directed *ortho*-C-H bond amidation via Cp*Rh(III)-complexes was first developed by Su and co-workers, by using sulfonamides as the amidating reagents under mild reaction conditions (Scheme 1.31)[125]. In this work, the pre-synthesized cyclometalated Cp*Rh(III) complex **18** could not only react with sulfonamide to produce the amidated product in 50% yield, but also acted as a catalyst to catalyze the C-H amidation and provided the desired product in 74% yield, which suggest that cyclometalated complex **18** could be a highly reactive intermediate in the C-H amidation reaction.

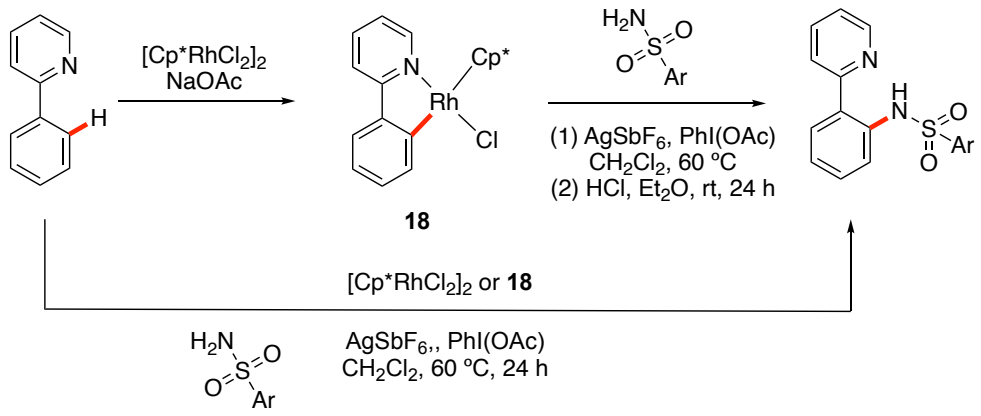


**Scheme 1. 31.** Cp*Rh(III)-catalyzed *ortho*-C-H bond amidation.

More recently, the Cp*Ir-metalcyles catalyzed hydrosilylations has been developed by the group of Agbossou-Niedercorn, Michon and Djukic[126-134]. The Cp*-iridacycle **19** was synthesised and used as a precatalyst for the hydrosilylation of amides (Scheme 1.32)[128]. The activity of this reaction could be improved by ligand modification when 1-phenylisoquinoline ligand was used instead of 2-phenylpyridine, so that the related amines can be obtained in less time under the same conditions, using iridacycle **20** as catalyst.

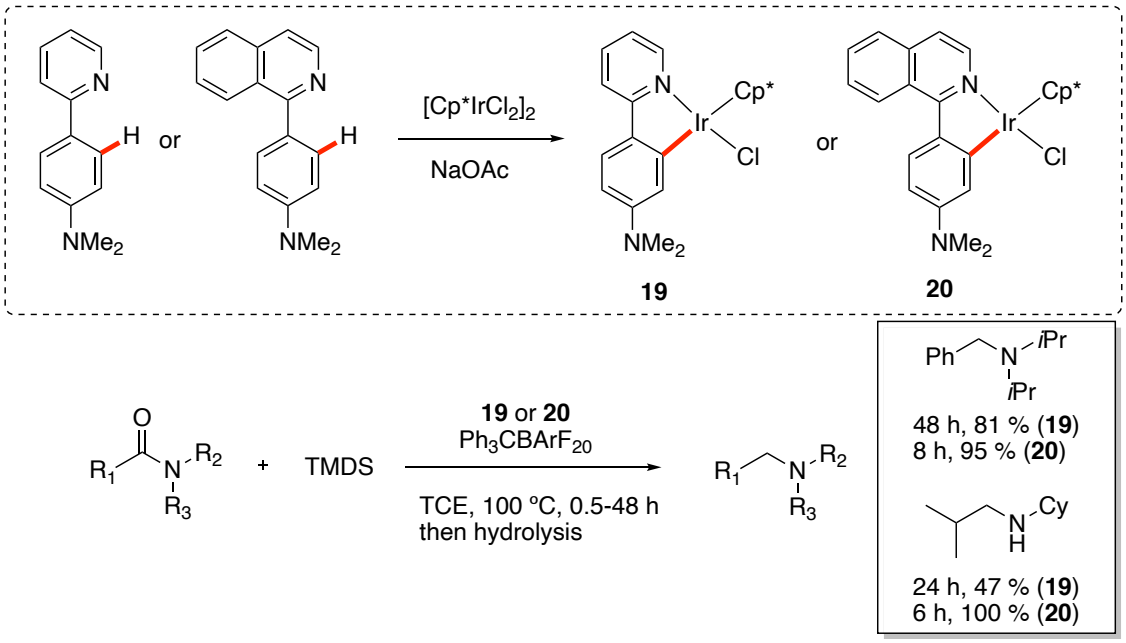


**Scheme 1. 32.** The synthesis of iridacycles and catalyzed hydrosilylation of amides.

The reactivity of a set of prototypical ($\eta^6$-arene)tricarbonylchromium complexes with $[Cp^*MCl_2]_2$ (M=Ir, Rh) has been further investigated by Djukic and co-workers (Scheme 1.33)[126, 135, 136]. This excellent work demonstrated that the cycloirdated 2-phenylpyridine was able to π-coordinate with cationic metal moieties containing one or two positive charges. The complexes **22**, which contain $Cr(CO)_3$, can be readily synthesized not only via cyclometallation of **21'**, but also via ligand-exchange reactions of iridacycle **19** or **21** with tricarbonyl($\eta^6$-naphthalene)chromium. In addition, iridacycles **19** or **21** can also reacted with $[Cp^*Ir(acetone)_3][PF_6]_2$ and $[Cp^*Ru(MeCN)_3]PF_6$ at room temperature for more than 24 h to obtain the corresponding product **22** or **23**, respectively. In comparison, under the same conditions, 2-phenylpyridine was unreacted, suggesting that the presence of positive substituents (e.g. $-NMe_2$ group) is necessary for the formation of these complexes. The theoretical studies suggested that the electron-donating amino groups can transfer electron density from their lone pairs to the aromatic ligands via two channels, thus contributing to the stability of the complexes. Moreover, the iridacycle **19** can also reacted with the terminal alkyne in MeOH and formed the complexes **24** via double insertion, while a new iridium-acyl complex **25** was generated in the reaction of complex **21**. Subsequently, the tandem promote a "one-pot" transformation of terminal alkynes into *N*-phenylamines via hydroamination and hydrosilation–protodesilation can also promoted by the $Cr(CO)_3$-boundiridacycle **22a** (Scheme 1.34)[137].

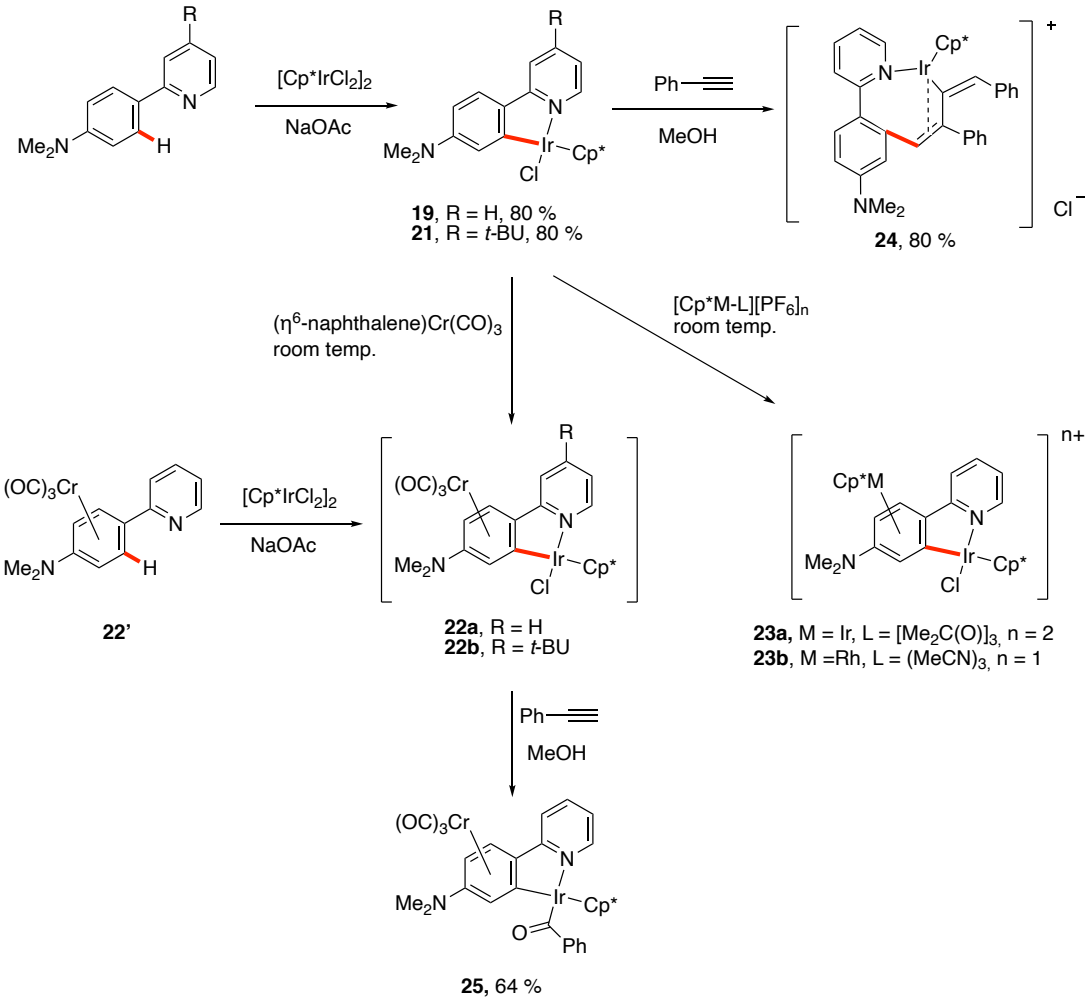


**Scheme 1. 33.** The synthesis of $Cr(CO)_3$-containing metallacycles.

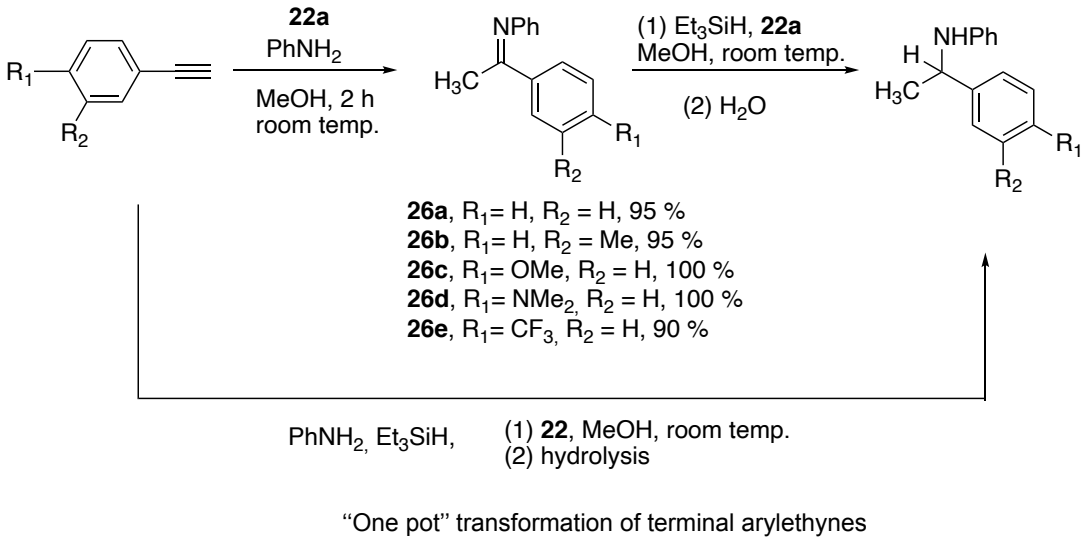


**Scheme 1. 34.** "one-pot" transformation of terminal alkynes promoted by the $Cr(CO)_3$-boundiridacycle

More recently, Djukic and co-workers also reported three different cationic iridacycles **26-28** (Scheme 1.35), which can catalyze hydrosilylation of nitriles and carbonyls with high efficiency. It is noteworthy that the complex **26** (with the counter anion $BArF_{24}^-$) can be use to active the H-Si bond of $HSiEt_3$ and formed a highly reactive hydrido-Ir(III)-silylium intermediate **29**, demonstrated by X-ray crystal structure(Scheme 1.35), which could be the result of hydride transfer from the silane to the iridium center and without any change of the oxidation state of the iridium center.

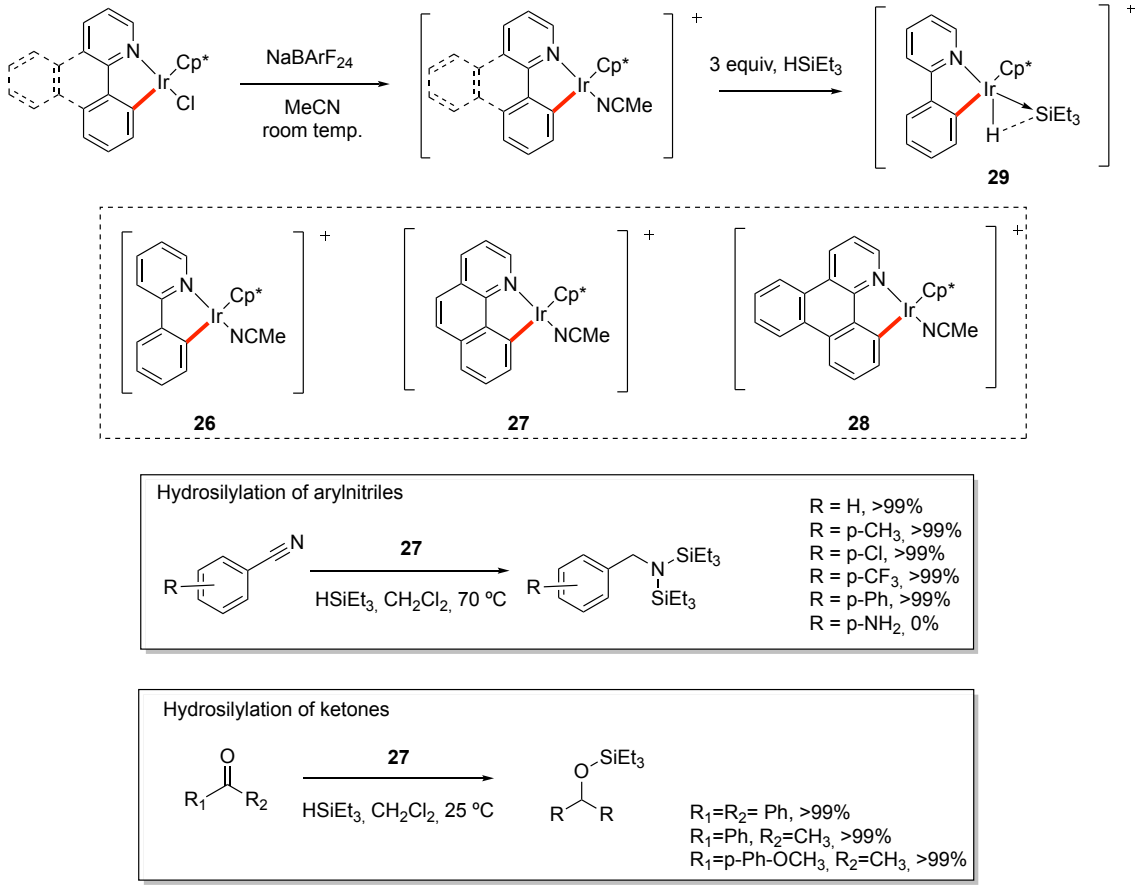


**Scheme 1. 35.** The synthesis of cationic cyclometallated complex and catalyzed hydrosilylation of arylinitriles and ketones.

In contrast to the rapid development of Cp*M-metallacycles (M=Ir, rh), there are few examples of Cp*Co-metallacycles. The first example for the synthesis of the Cp*Co(III) metallacycle **30** via $[Cp^*CoCl_2]_2$ was reported by Matsunaga/Kanai and co-workers in 2014 (Scheme 1.36)[138], for better understanding of Cp*Co(III)-catalyzed C-H functionalization. During this work, the $[Cp^*Co(C_6H_6)](PF_6)_2$ not only present good reactivity in C−H alkenylation/annulation, but also better than the

$Cp^*Rh(CH_3CN)_3](SbF_6)_2$. To evaluate the difference between the cobalt and rhodium, the Cp*Co(III) cyclometalated complex **30** was synthesized and compared with the analogous Cp*Rh(III)-metallacycle, which were subsequently estimated by natural population analysis, revealing that the Co-C bond is more polarized in comparison with the Rh-C bond. Therefore, the source of the difference in reactivity in the Cp*Co(III)-catalyzed C-H functionalization reaction might be attributed to the higher nucleophilicity of the carbon linked to the cobalt center.

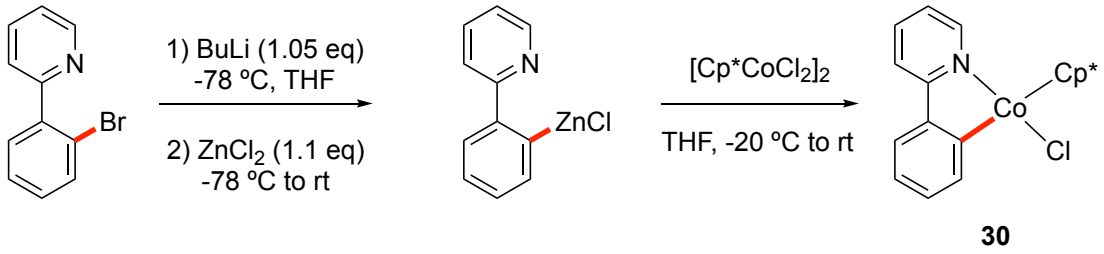


**30**

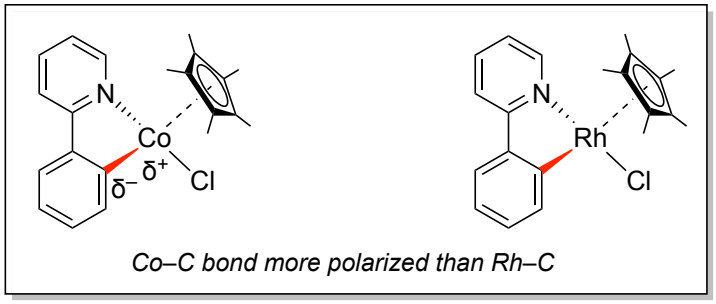


**Scheme 1. 36.** The first example for the synthesis of the Cp*Co(III)-metallacycle.

More recently, the direct synthesis of cobaltacycles via C-H activation were achieved by Zhu and co-workers (Scheme 1.37)[139], providing elusive mechanistic insight into cobalt-catalyzed C−H functionalization reactions. The C-H bond of *N*-chlorobenzamides was activated and cyclometalated by $Cp^*Co(CO)I_2$ afforded a five-membered cobaltacycles **25**. More interestingly, these cobaltacycles not only can react as a stoichiometric reagent with alkynes formed the heterocycles but also can serve as an effective catalyst for the annulation of *N*-chlorobenzamides with alkynes.

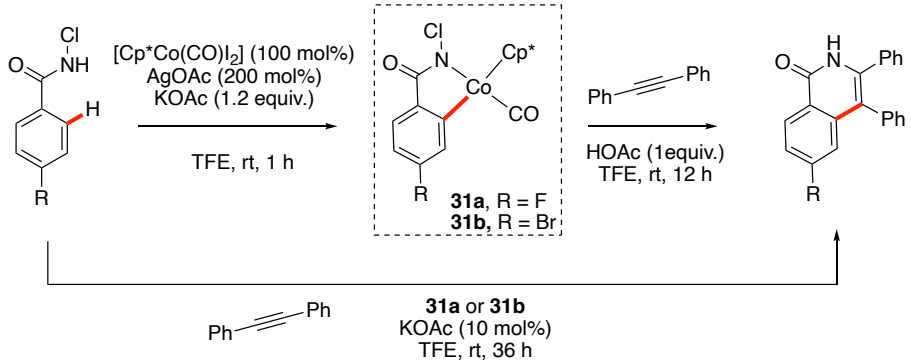


**Scheme 1. 37.** Direct synthesis of cobaltacycles via C-H activation.

In 2018, a new synthetic approach for cationic cobaltacycles via Cp*Co(III)-catalyzed C-H functionalization reactions was described by Perez-Temprano and co-workers (Scheme 1.38)[140-144]. In this reaction, they chose [Cp*Co(III)-$(MeCN)_3$]$X_2$ (X = $BF_4^-$) as the cobalt source to react with 2-arylpyridine or *N*-pyrimidinylindole and formed the Cp*Co(III)-metallacycle (**II**) via C-H activation. Moreover, these Cp*Co(III)-intermediates not only can react as a stoichiometric reagent with alkynes but also can serve as an effective catalyst for the coupling between alkynes and 2-arylpyridine or *N*-pyrimidinylindole, via seven-membered cationic cobaltacycles.

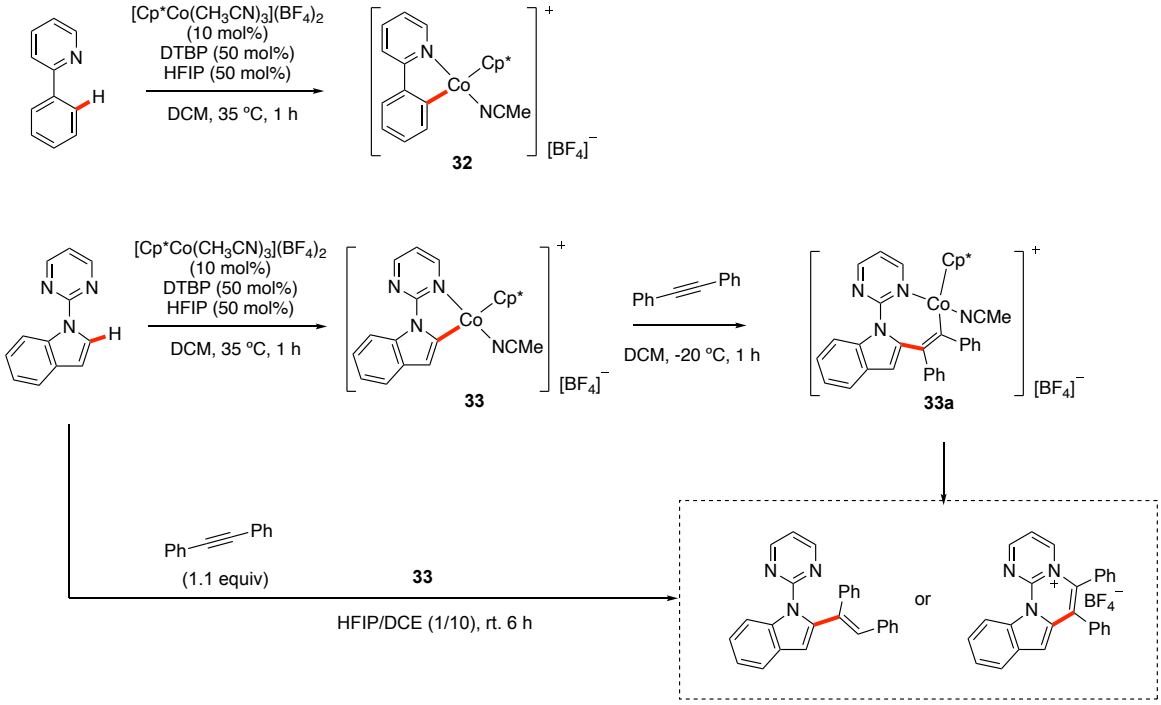


**Scheme 1. 38.** The synthesis of cationic cobaltacycles via Cp*Co(III)-catalyzed C-H functionalization (HFIP: 1,1,1,3,3,3-hexafluoroisopropanol; DTBP: 2,6-Di-tert-butylpyridine)

In summary, as we discussed in this chapter, the Cp*Co(III)-complexes catalyzed C-H activation reaction have been developing rapidly in just few years and have been successfully applied to a variety of C-H functionalization, which were considered to be the future of catalysts for C-H activation. But for now, the understanding of the mechanism for these Cp*Co(III)-catalyzed C-H functionalization was limited, the most of mechanistic proposals remain base on the comparison with other analogous transition metals, such as rhodium, iridium and palladium. Although theoretical studies such as DFT calculations can help us better understand the mechanism, there are still a lack of appropriate strategies to capture the key intermediates (e.g., iridacycles and rhodacycles) to validate the theory.

# Research objectives of this thesis

Despite the rapid development of approaches for the cobalt-catalyzed C-H bond functionalization, the attention seemed to be directed to the application of cobalt-catalysts in various reactions, e.g., the range of reactions, catalyst activity, selectivity and reaction efficiency, as in the various examples mentioned previously. One of most important stages in transition metal-catalyzed C-H activation is constantly overlooked. Therefore, one of the main objectives of this thesis was to get a better understanding of the mechanism of the cobalt-base catalytic system and the role of noncovalent interactions. On the other hand, considering the huge potential application of cyclometalated Cp*Co(III)-complexes, as well as the uncertainty remaining on the mechanistic details, a thorough study of this reactivity by combined experimental and theoretical approaches was systematically undertaken.

# Chapter 2. Noncovalent interaction insights into the cyclometallation of Cp*Co(III)-complex assisted by acetamidate

The most relevant results of this chapter have been already published [reprinted with permission from J.P. DJUKIC et al. Making Base-Assisted C–H Bond Activation by Cp*Co(III) Effective: A Noncovalent Interaction-Inclusive Theoretical Insight and Experimental Validation. *Organometallics* **2020**, 39, 14, 2609–2629. Copyright © 2020 American Chemical Society]. The theoretical aspects were done with the help of Yann CORNATON and Jean-Pierre DJUKIC.

## 2.1. Introduction

As introduced in the Chapter 1, a wide range of applications of Cp*Co(III)-catalysts for C-H bond functionalization have been reported by Kanai and Matsunaga[145-161] and by Ackerman et al.[162-173] and followed by a number of other reports[174, 175]. In many reported cases this powerful class of cobalt catalysts[176] presents reactivity profiles that differ from their rhodium and iridium analogues. It has been argued that this difference is likely due to the lower electronegativity and increased Lewis acidity of cobalt compared to rhodium and iridium.[177] However, there has been seldom[171] attempts to construct a rational around the key problem of how to activate C-H bonds using 3d metals[178, 179] that would connect all the dimensions of chemical bonding, including the role of noncovalent interactions, which play a crucial role in transition metal catalytic systems in reducing the kinetic barriers of reactions by stabilizing transition states. Moreover, prior to or in this transition state, the orchestrated action of various NCIs can also affect the selectivity of catalytic transformation.

In a recent report by our group[179], we attempted to rationalize the differences existing between the well-established Pd(II)-acetate and the less documented Ni(II)-acetate cyclometallation by focusing mainly on the role of noncovalent interactions in CMD

mechanism also assimilated to the AMLA mechanism[180-182], which is now widely applied for the Pd(II) systems catalyzed C-H bond functionalization[178, 183, 184].

In this study, the formation of an agostic intermediate (Figure 2.1), which is the key kinetic determining step in this mechanism, was analyzed systematically, by using state-of-the-art *ab initio* as well as DFT-based QTAIM analysis. It was also points out the crucial role played by electrostatic interactions, which control the whole process to some extent and are very sensitive to the charge carried by the metal center, and the electrostatic repulsion induced activation barriers for the formation of the pivotal Ni-**ag** is about twofold higher than in the case of Pd[179]. When acetamidate was used instead of acetate as an auxiliary base, the repulsive electrostatic interaction between the C-H bond and the metal was found to be abated[179], thus significantly reducing the barrier to the formation of the key agostic intermediate.

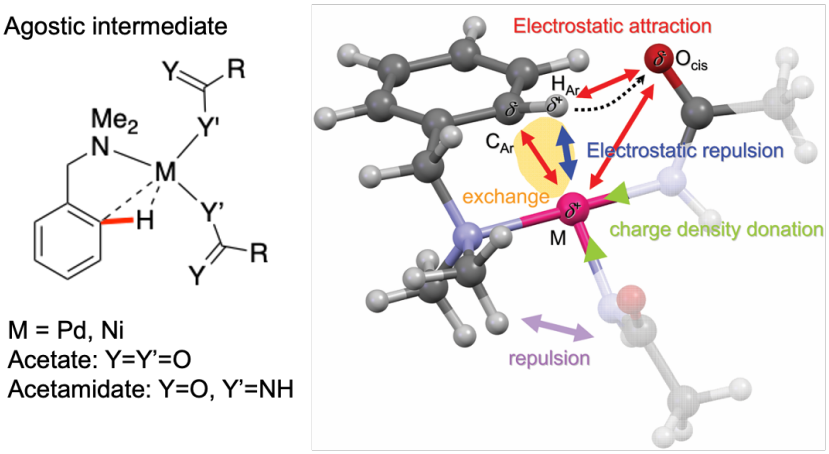


**Figure 2. 1.** Agostic intermediate in the CMD mechanism and summary of the effects governing the reactivity of this intermediate. (N : blue; C : dark grey; H : light grey; O : red; Metals : magenta; Red arrows : electrostatic attraction; Blue arrows : electrostatic repulsive; Green arrows : charge density donation; Purple arrows : repulsion; The egg-shaped orange-yellow area : the weak exchange $C_{Ar}$–$H_{Ar}$–metal interaction.)

In this chapter, we applied the methodology of this theoretical study of the Ni(II)/Pd(II) model dyad to the CMD mechanism-promoted cyclometallation reaction by focusing our interest on the Cp*Co(III) system, having in scope that a good part of the recent applications of Cp*Co(III) catalysts[141, 145, 185] to C-H bond functionalization apparently

proceed also by a different mechanism, i.e via the electrophilic activation[186] of the C-H bond.

## 2.2. Results and discussion

### 2.2.1. Theoretical aspects

#### 2.2.1.1. DFT-D reaction energy profile

Most theoretical studies on the Cp*Co(III)-catalyzed C-H activation have not thoroughly investigate the mechanism of cyclometallation, simplifying this step and focusing on the influence of different substitutions on the reactive species[187-193]. Moreover, there are few DFT study of the cyclometallation via NCI-inclusive approach, so the cyclometallation via CMD mechanism will be investigated here in combination with noncovalent interactions and DFT study.

The CMD (or AMLA) mechanism is a simplified scenario that implies the formation of a reactive complex **anag** , i.e. [Cp*M($\kappa^N$-2-*phpyH*)( $\kappa^2$-YAc)]$^+$, established between the ligand to be metalated and a coordinatively unsaturated metal complex that undergoes a series of intramolecular transformations (Scheme 2.1): the formation of the C-H…metal agostic[194-198] intermediate **ag** via transition state **TS-ag**, which is a rate limiting step in this mechanism, and then the C-H bond breaking by metalation and concerted proton abstraction by an intramolecular base via transition state **TS-CH** to form intermediate **MCH**, *i.e.* [Cp*M($\kappa^2$-2-phpy)(AcYH)]$^+$, the release of the protonated base and eventually the coordination of any anionic ligand (halogen, or anionic base) to the metal center, which was not considered here. It is worth mentioning that a variant[186] to this mechanism considers the external capture of the proton $H_{Ar}^+$ in the bond-breaking step. In the case studied here, implicit solvation was accounted for by a continuum screening model (COSMO[199-201]) assuming a fully intramolecular process. Another variant was also put forward by Jones et al.[122] for cycloiridation and cyclorhodation based on the determination of kinetic isotopic effects which suggested by their rather high value of KIE ~3 a base (namely acetate)-assisted electrophilic C-H bond activation, the proposed formulation of which resembles that of the CMD

mechanism, though. The anionic base-devoid electrophilic activation option is also addressed further.

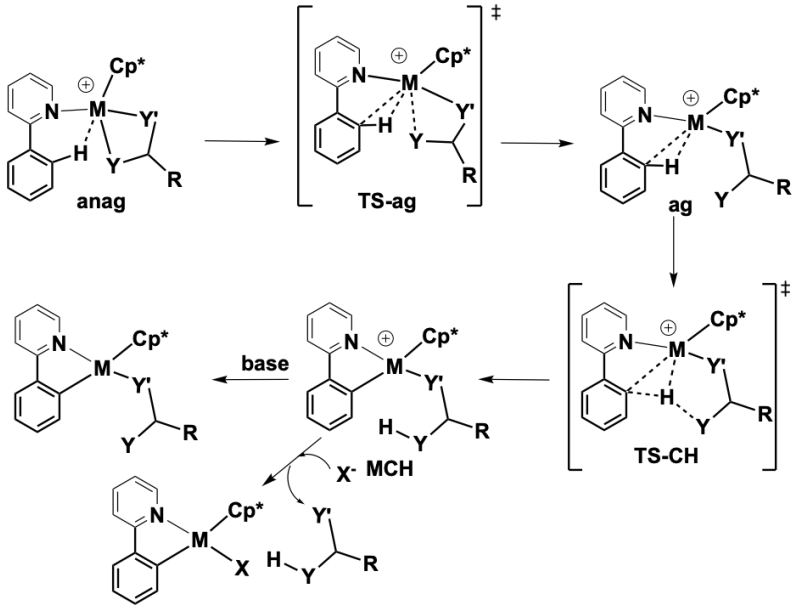


**Scheme 2. 1.** The CMD mechanism applied to group 9 transition metal Cp*M(III) complexes[179]: **anag**, the reactive complex precursor of the agostic intermediate **ag**, via **TS-ag**; **MCH**, the immediate cyclometallation product arising from the proton transfer reaction occurring via **TS-CH** from **ag**.

In order to validate our theoretical study, comparative studies on Cp*Ir(III) were also conducted. The Gibbs enthalpy profiles for the cyclocobaltation (**Co-OAc**, **Co-NHAc**) and cycloiridation (**Ir-OAc**, **Ir-NHAc**) of 2-*phpyH* assisted by acetate and acetamidate are depicted in Figure 2.2.

The singlet ground state intermediates and transition states, which were built based on existing structures of metallacycles, were all optimized at the COSMO[199-201]-ZORA-PBE[202]-D3(BJ)[203-205]/all electron TZP level. It is important to stress that the choice of the DFT functional was guided by repeated failure to localize **TS-CH** by using the dispersion corrected[203, 205] version of the functional that was initially used by Macgregor et al.[181, 182, 206] in their early investigations of the cycloiridation of *N*,*N*-dimethylbenzylamine. The dispersion-inclusive hybrid functional PBE0[207]-ddsc[208], which performed well in localizing all stationary points, was nonetheless found too costly and of low benefit in terms of computational time and accuracy owing to the

calculation of statistical thermodynamic data from vibrational data accessible only by numerical differentiation, which presented a risk of inaccuracy arising from the COSMO[199-201] solvation treatment. We therefore used the dispersion corrected generalized gradient approximation (GGA) PBE[202]-D3(BJ)[203-205] functional and applied analytical frequency calculations throughout the study. Worthy to note, in terms of geometry convergence PBE-D3(BJ) and PBE0-ddsc were rather equivalent for all stationary points. However, even though the localization of **TS-CH** succeeded in all four systems, i.e **Co-OAc**, **Co-NHAc**, **Ir-OAc**, **Ir-NHAc**, it was noticed with both functionals that the potential surface between **ag** and **TS-CH** was relatively shallow with a clear functional dependency emerging for the geometry of **ag**. In most cases at the GGA level **ag** was localized at a local minimum with the carboxy base plane almost parallel with that of the phenyl moiety of the 2-*phpyH* ligand. In the case of **Ir-NHAc** only, was the rotamer with the carboxy oxygen atom aligned with the C-H bond axis, i.e **ag-col**, isolated around 2.5-3 kcal/mol below both **ag** and **TS-CH** in a local shallow potential well. Intermediate **ag-col** is the actual reactive complex leading to **TS-CH**. Test linear transit computations considering the rotation of the metal-bound base following the excursion of dihedral angle $C_{Ar}$-M(Co or Ir)-$O_d$(or $N_d$ in **Co-NHAc**)-$C_{sp2\text{-}base}$ suggest that geometries similar to **ag-col** in **Co-Ac** and **Ir-OAc** systems are of high energy, offering no chance of being localized at this level of theory. Like shown farther in this study, extending the investigation of the reaction energy profile with the ab initio DLPNO-CCSD(T)[209-215] method provided a qualitative estimate of the reliability of the DFT method used here particularly for the kinetic determining step and for the critical proton transfer step.

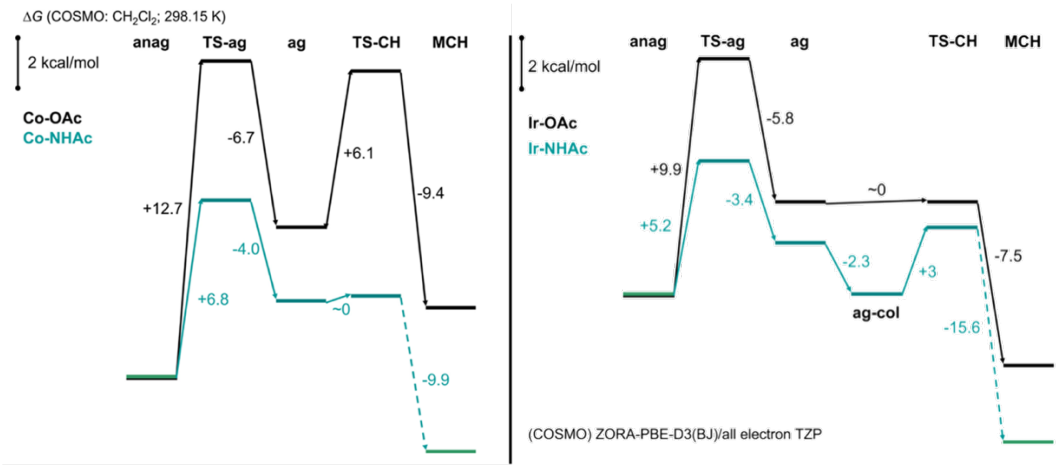


**Figure 2. 2.** GGA-DFT-D energy profiles for the cyclometallation of 2-*phpyH* assisted by acetate (black lines) or by acetamidate (cyan lines) bases: Left) Cp*Co(III) system; Right) Cp*Ir(III) system.

The Ir and Co systems display analogous energy profiles (Figure 2.2). The common feature shared by the two metal systems is the activation barrier for the formation of **ag**, which is about two-fold higher when the auxiliary base is the acetate instead of the acetamidate. Similarly to the Ni/Pd case,[179] the kinetic determining step is the formation of **ag** and the overall exothermicity of the **anag**-to-**MCH** process is higher with the acetamidate as a base. Quite interestingly **anag**-to-**ag** activation barriers with the same base ($AcO^-$ or $AcNH^-$) are only slightly lower for the Ir system as compared to the Co one by ca. 1.5 and 3 kcal/mol.

In the case of **Co-OAc**, **ag** is localized in a significant energy well at almost equal energy distance from **TS-ag** and **TS-CH**, whereas in **Co-NHAc** the **ag**-to-**MCH** barrier is virtually inexistent at the GGA level. If one considers the endothermicity of the **anag**-**MCH** process of about $\Delta G$~+3 kcal/mol in **Co-OAc** at 298.15 K it can be inferred that on the grounds of thermochemistry alone the cyclometallation with $AcO^-$ as auxiliary base is to be less efficient than that with $AcNH^-$, which was verified experimentally later.

#### 2.2.1.2. Noncovalent Interactions (NCIs)

Noncovalent interaction plot (NCIplot)[216, 217], a Quantum Theory of Atoms in Molecule (QTAIM)-based treatment of the electron density topology provides an intuitive spatial

map of local repulsive, non-bonding and attractive NCI materialized by isosurfaces of the signed reduced density gradient. The QTAIM-Interacting Quantum Atoms (QTAIM-IQA) method computes and decomposes in a basis-set independent way interatomic interaction energies into covalent and ionic contributions.[179, 218-220] Also relevant are the so-called QTAIM -or Bader- charges that have proven reliable in expressing the local charge density distribution.[221]

In this method, the analysis of NCI was essentially focused on the "reactive site" of the molecule where the C-H bond disruption occurs during the **anag→TS-ag→ag→TS-CH→MCH** sequence. This reactive site is the group of atoms comprising Co or Ir, $C_{Ar}$, $H_{Ar}$, $O_p$ (proximal to $H_{Ar}$), $O_d$ or $N_d$ (distal to $H_{Ar}$), which undergoes various phenomena that are illustrated by Figure 2.3 and were already outlined with the Ni/Pd dyad previously. Restricting our reasoning to this reactive site does not discard the role of the ligand retinue, i.e here the pentamethylcyclopentadienyl and the pyridyl fragment of 2-*phpyH* that respond in benign ways as the reactive site evolves (*vide infra* the DLPNO-CCSD(T)/LED analysis).

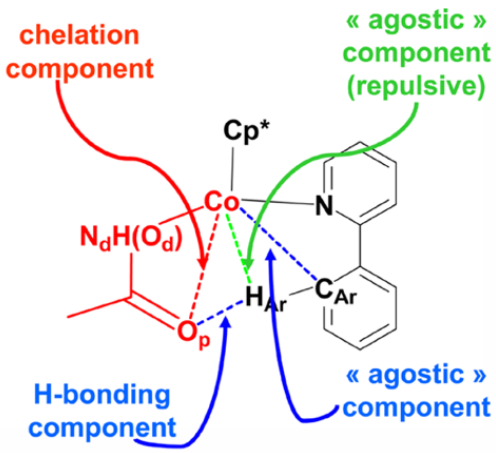


**Figure 2. 3.** Scheme of the reactive site during the cyclocobaltation of 2-*phpyH* via the CMD mechanism.

As a chemical event, the $C_{Ar}$-$H_{Ar}$ bond cleavage can be considered as an evolution of the precarious balance between the agostic interaction of the $C_{Ar}$-$H_{Ar}$ bond in question with the metal center and the buildup of H-bonds mainly with $O_p$ and to a lesser extent with $O_d$ or $N_d$ (Figure 2.3). Within the term "agostic interaction" that we use here we

include the attractive and repulsive components that are constitutive of the $C_{Ar}$-$H_{Ar}$…metal interaction.

#### 2.2.1.3. Interacting Quantum Atoms (IQA)

IQA-data show clearly that in all **ag** intermediates the $C_{Ar}$-metal interaction is attractive with a dominating covalent character. The $H_{Ar}$-metal interactions are more contrasted. In both **Ir-OAc** and **Ir-NHAc** systems the interaction is always repulsive and climbs to a maximum of repulsion at **TS-CH**. In **Co-OAc** and **Co-NHAc** the $H_{Ar}$-metal interaction is significantly attractive only in **ag** ($E_{int}$ ~-9 kcal/mol) and becomes repulsive at **TS-CH**. In such a reduced space around the metal, the existence of a residual $\kappa^2$ chelation of the metal center by the base is evident from the values of the $E_{int}$ for the $O_p$-metal interaction that vary approximately from ~-220 kcal/mol in **anag** to ~-100 kcal/mol in **TS-CH**. For reference, the $E_{int}$ value of the interaction of the distal heteroatom with the metal center, i.e. $O_d$-M and $N_d$-M (where M= Co or Ir) is ~-200 kcal/mol throughout the **anag** –to- **TS-CH** process in all four systems, **Co-OAc/NHAc** and **Ir-OAc/NHAc**. The value of $E_{int}$ ($O_p$-metal) is higher than that of the H-bonding interaction $O_p$-$H_{Ar}$ (~-30 kcal/mol) in all stages of the reaction except **TS-CH** where $E_{int}$ ($O_p$-$H_{Ar}$) equals or slightly supersedes $E_{int}$ ($O_p$-metal) with values of ~100-120 kcal/mol. This residual chelation therefore contributes to the **anag** –to- **ag** barrier of activation. It is a challenger of the concerted carbometallation deprotonation when the strength of the chelation interaction prohibits the establishment of the $O_p$-$H_{Ar}$ interaction and a tighter interaction of $C_{Ar}$ with the metal center. In all the four systems considered here the evolution of the $O_p$-metal interaction shows that the covalent component of the interaction recedes to the ionic character to become residual at **TS-CH** (Figure 2.4).

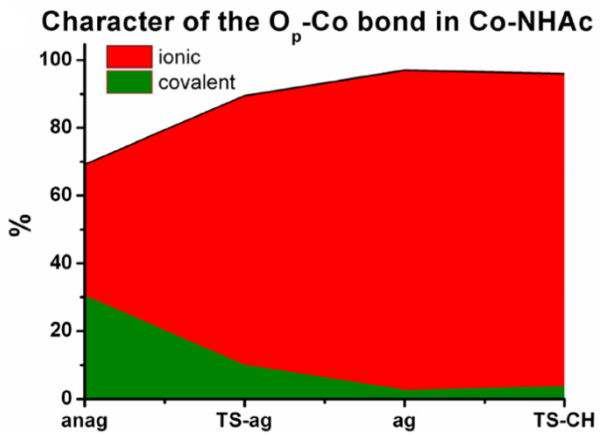


**Figure 2. 4.** Evolution of the ionic and covalent character of the $O_p$−Co interaction in the course of the CMD process expressed as a percentage of the associated interatomic QTAIM-IQA energy of interaction $E_{int}$.

To rationalize the effect of the base on the reaction energy profiles the difference of interaction energy $E_{int}$ for the $O_p$-metal bond in the acetamidate and acetate systems, i.e $\Delta E_{int}(O_p\text{-}M)^{NHAc\text{-}OAc} = E_{int}(O_p\text{-}M)^{NHAc} - E_{int}(O_p\text{-}M)^{OAc}$, was calculated and is plotted in Figure 2.5. It shows that the effect of the replacement of $AcO^-$ by $AcNH^-$ at each stage of the CMD mechanism is in fact the highest at the agostic intermediate **ag** were $\Delta E_{int}(O_p\text{-}M)^{NHAc\text{-}OAc}$ amounts ~-11 kcal/mol, which in other terms means that the substitution of $AcO^-$ for $AcNH^-$ favors the access to **ag** by reducing significantly the residual chelation. Worthy to note the $E_{int}$ value for the H-bonding interaction in the $O_p$-$H_{Ar}$ interactions displays a low sensitivity to the change of base in both Co and Ir systems.

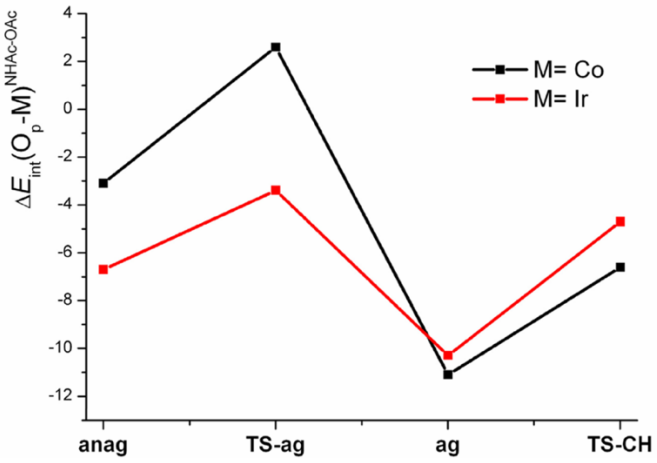


**Figure 2. 5.** Evolution of the QTAIM/IQA $\Delta E_{int}(O_p{-}M)^{NHAc\text{-}OAc}$ value (in kcal/mol) in the course of the CMD process where $\Delta E_{int}(O_p{-}M)^{NHAc\text{-}OAc} = E_{int}(O_p{-}M)^{NHAc} - E_{int}(O_p{-}M)^{OAc}$.

#### 2.2.1.4. NCI Indexes

In order to analyze both the attractive and the repulsive contributions to the C-H bond cleavage we have resorted with the collaboration Dr. Julia Contreras-Garcia (Sorbonne Université) of to the NCI index[216, 217] in **ag** and the **Ir-NHAc-ag-col** geometries. NCI provides intuitive surfaces that identify local non covalent interactions in a system. Strong and directional interactions are revealed as blue pellets, delocalized weak interactions appear as long green surfaces, and repulsive regions are revealed in red.

Figure 2.6 shows the results for the **ag** and **Ir-NHAc-ag-col** complexes in order to analyze the cleavage of the $C_{Ar}$-$H_{Ar}$ bond. If one first looks at the interactions with the metal (M), one can easily see that **Ir-NHAc-ag** and **Ir-NHAc-ag-col** stand aside from the rest. **Co-NHAc-ag**, **Co-OAc-ag** and **Ir-OAc-ag** show strong interactions between the metal and the $C_{Ar}$-$H_{Ar}$ bond which are the deep blue surfaces in Figure 2.6. Slight differences are observed though within the group. One interesting thing to note here is that whereas QTAIM would have identified M-$H_{Ar}$ or M-$C_{Ar}$ interactions, NCI clearly highlights the interaction with the full $C_{Ar}$-$H_{Ar}$ fragment. This is specially so for the **Ir-OAc-ag** complex, where the blue region extends over a greater region of space (see that it is formed by two deep blue regions that have been highlighted by a discontinuous trace).

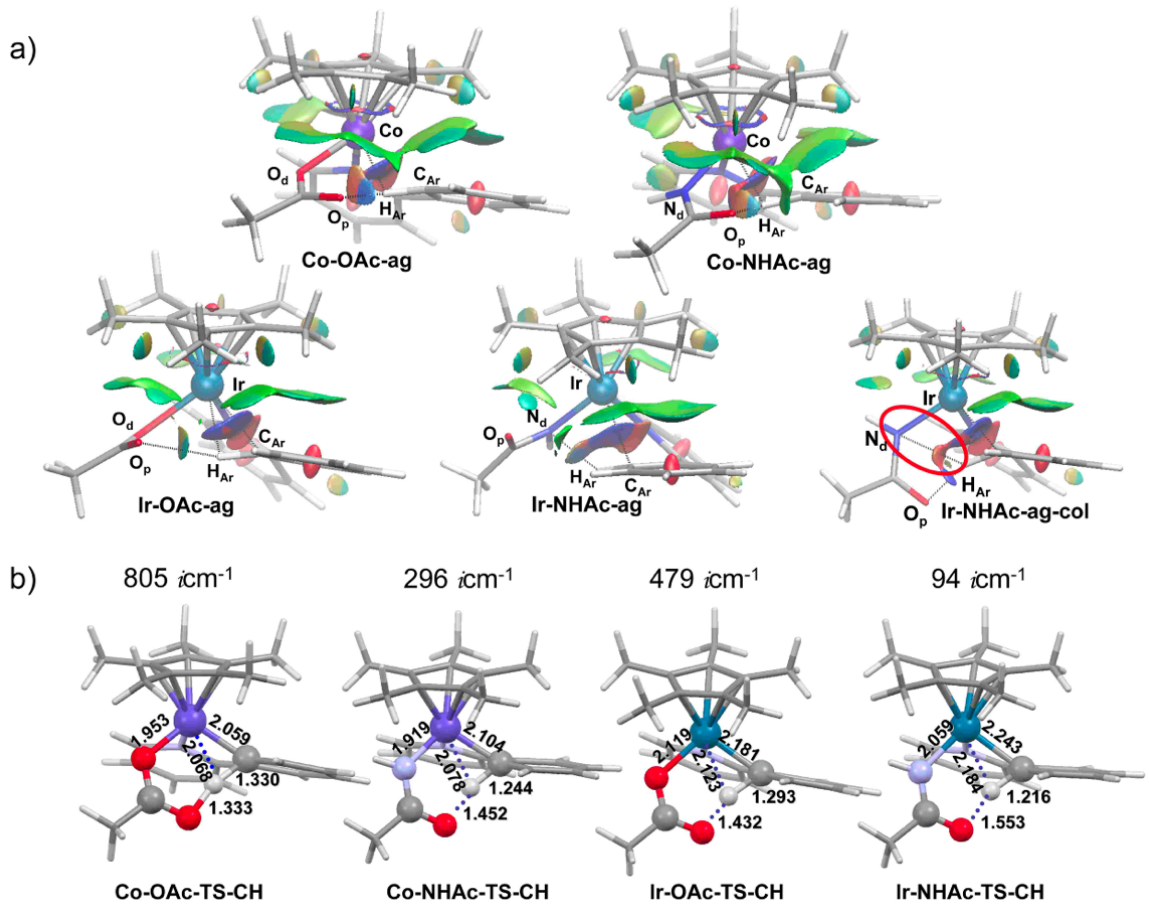


**Figure 2. 6.** a) NCI surfaces ($s$=0.3, -0.03<sign($\lambda_2$)$\rho$<0.03) for the **ag** and **Ir-NHAc-ag-col** complexes (atom color code: light grey, C; dark blue, N; white, H; red, O; violet, Co; cyan, Ir): the circled NCI isosurface in **Ir-NHAc-ag-col** outlines a rather strong repulsive $N_d$-$H_{Ar}$ interaction. b) geometries of **TS-CH** in the Co and Ir- based systems with the associated imaginary vibrational mode frequency as optimized in their singlet state at the COSMO($CH_2Cl_2$)-ZORA-PBE-D3(BJ)/all electron TZP level.

Taking these compounds as reference, we can see that **Ir-NHAc-ag** shows in general weaker interactions, whereas **Ir-NHAc-ag-col** shows stronger ones. Focusing now on the $O_p$-$H_{Ar}$ interaction, one sees that it is very weak both in **Co-OAc-ag** and in **Ir-NHAc-ag**. From this information, we can analyze the density at which these interactions are appearing from the $s(\rho)$ plots (Figure 2.7) in order to quantify the effects of these two intermolecular interactions on the $C_{Ar}$-$H_{Ar}$ strength.

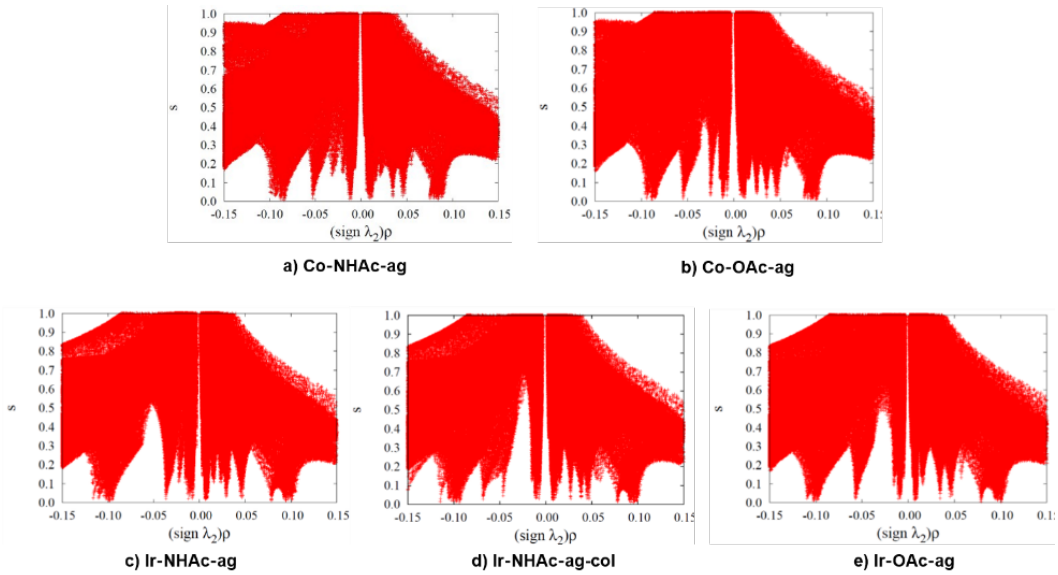


**Figure 2. 7.** s(ρ) diagrams for **ag** and **Ir-NHAc-ag-col** compounds.

It is easy to see in Figure 2.8 that as the interactions of $C_{Ar}$ and $H_{Ar}$ with other atoms are strengthened, the intra-bond $C_{Ar}$-$H_{Ar}$ strength diminishes. Co complexes present intermediate M-($C_{Ar}H_{Ar}$) and $O_p$-$H_{Ar}$ interactions, which weaken the $C_{Ar}$-$H_{Ar}$ bond. **Ir-NHAc-ag** and **Ir-NHAc-ag-col** complexes show the effect of taking these interactions to the extreme: in **Ir-NHAc-ag** both interactions are negligible, so that the $C_{Ar}$-$H_{Ar}$ bond is very strong. The conformational change to arrive to **Ir-NHAc-ag-col** leads to the simultaneous strengthening of M-($C_{Ar}H_{Ar}$) and $O_p$-$H_{Ar}$, so that $C_{Ar}$-$H_{Ar}$ becomes much weaker.

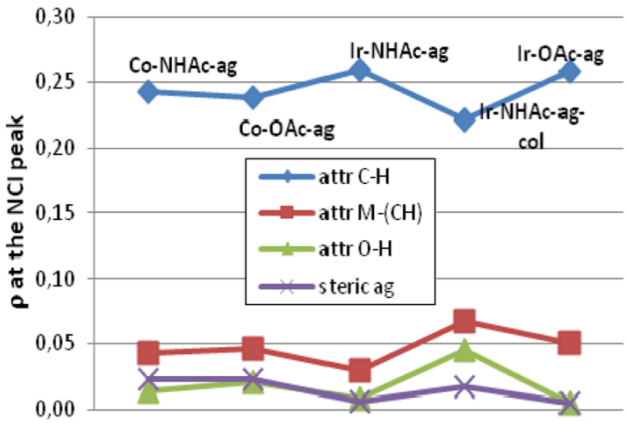


**Figure 2. 8.** NCI peak densities for ag and Ir-NHAc-**ag-col** complexes.

Moreover, in **Ir-NHAc-ag-col** the M-($C_{Ar}H_{Ar}$) interaction is mainly with $C_{Ar}$: this leads to opposite forces pulling the $C_{Ar}$-$H_{Ar}$ atoms away from each other. M pulling from $C_{Ar}$, and simultaneously, $O_p$ pulling from $H_{Ar}$.

In line with previous observations, we have also analyzed the overall evolution of attraction and repulsion in the non-covalent region by means of integrals on the NCI region (Figure 2.9)[222, 223]. An overall increase in steric repulsion is observed in **Ir-NHAc-ag-col** with respect to the other **ag** complexes. Indeed, the atoms becoming closer together, the repulsion between non bonded atoms increases, which also favors atom migration.

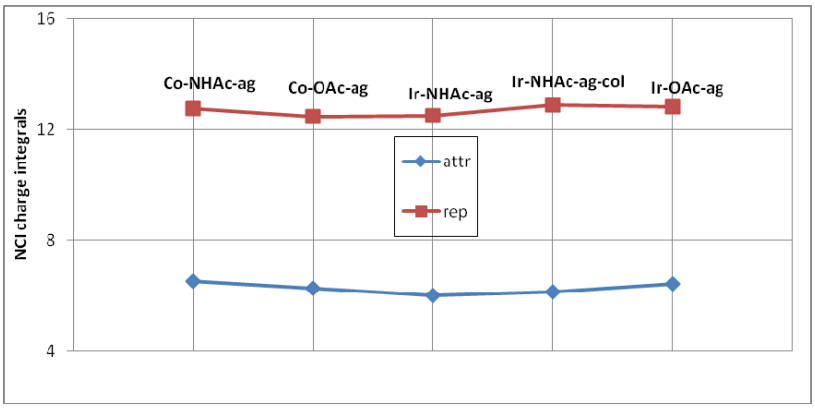


**Figure 2. 9.** NCI integrals for **ag** and Ir-NHAc-**ag-col** compounds.

This is easily seen in Figure 2.6, where an important $H_{Ar}$-$N_d$ repulsion is observed. This further reinforces the weakening of the $C_{Ar}$-$H_{Ar}$ bond, which also leads to a visible deformation. Figure 2.10 shows the $H_{Ar}$-$C_{Ar}$-$C_\beta$-$H_\beta$ dihedral, where the weakening is reflected in the $H_{Ar}$ going out of the planarity of the ring to approach $O_p$. The most representative case being **Ir-NHAc-ag-col**, where $H_{Ar}$ adopts the proper angle to form a strong hydrogen bond. Indeed, in this case, a very localized hydrogen bond (deep blue and round isofurface in Figure 2.6) is observed.

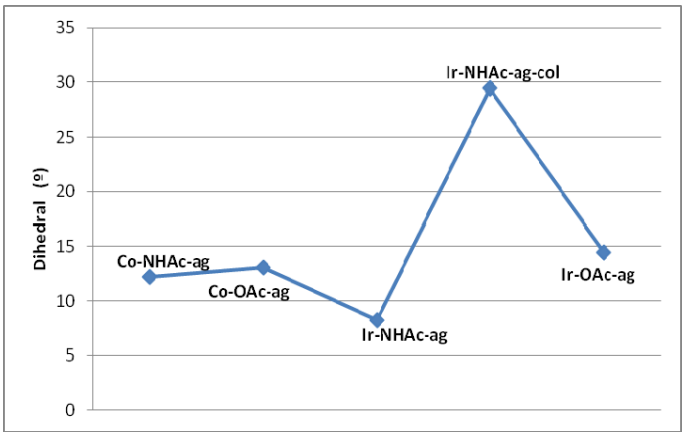


**Figure 2. 10.** $H_{ag}$-$C_{ag}$-$C_{\beta}$-$H_{\beta}$ dihedral for **ag** and **ag-col** compounds.

In the case of **Ir-NHAc-ag-col**, the attractive isosurfaces feature a trend that was already observed in a previous report dealing with the Ni/Pd dyad. The agostic $C_{Ar}$-$H_{Ar}$…metal interaction is characterized by an attractive ring and associated with an attractive domain materializing the C=$O_p$…$H_{Ar}$ interaction that plays a central role in **TS-CH**. It was already stated previously[179, 224] that this NCI pattern– or configuration- was the *sine qua non* condition for the "internal" CMD mechanism to be effective. Analysis of Bader charges (a.k.a. QTAIM charges) and IQA energies support the existence of attractive $O_d$…$H_{Ar}$ and $N_d$…$H_{Ar}$ interactions of dominant ionic character in all **ag** intermediates as well as in **Ir-NHAc-ag-col.**

Figure 2.11 depicts **Ir-NHAc-ag** and **Ir-NHAc-ag-col** rotamers that differ by the orientation of the acetamidate ligand: in **ag** the carbonyl lies further away from the $C_{Ar}$-

$H_{Ar}$ bond than in other agostic intermediates, i.e **Co-Ac-ag**, **Co-NHAc-ag** and **Ir-OAc-ag**.

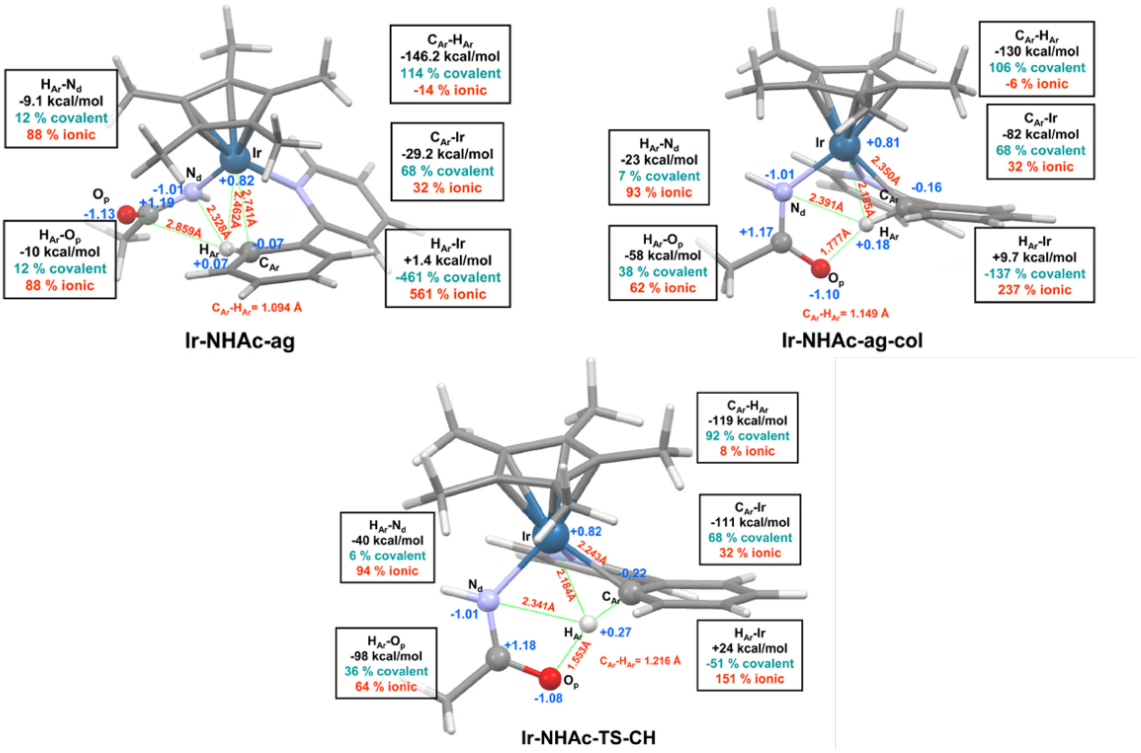


**Figure 2. 11.** Singlet geometries of **Ir-NHAc-ag**, **Ir-NHAc-ag-col** and **Ir-NHAc-TS-CH** with atom numbering, atomic QTAIM charges (blue colored numbers) main interatomic distances and the main QTAIM-IQA interatomic interaction energies $E_{int}$ decomposed into covalent (green colored) and ionic (red colored) percentage of contribution. Positive and negative values of $E_{int}$ indicate repulsive and attractive interactions respectively.

Compared to **Ir-NHAc-ag-col**, **Ir-NHAc-ag** has longer $C_{Ar}$-$H_{Ar}$…Ir distances, the $C_{Ar}$-$H_{Ar}$ bond is surrounded by closely located N (noted $N_d$ for distal to the $C_{Ar}$-$H_{Ar}$ bond) and O atoms (noted $O_p$ for proximal) and by positively charged Ir and $sp^2$ carboxy carbon atoms.

The environment around the $C_{Ar}$-$H_{Ar}$ bond is multipolar and characterized by delocalized electrostatic interactions of the $C_{Ar}$-$H_{Ar}$ bond with the carboxy base and the metal. The rotation of the acetamidate ligand around the Co-$N_d$ axis, which places $O_p$ nearly collinear with the $C_{Ar}$-$H_{Ar}$ axis, enhances the electrostatic interaction with $H_{Ar}$

leading to an enhanced polarization[206] and slight elongation of the $C_{Ar}$-$H_{Ar}$ bond. A collateral effect is the increase of about all the values of interatomic interaction energies and of the repulsion between $H_{Ar}$ and the Ir center that reaches a maximum in **TS-CH**. Strikingly in **Co-NHAc-ag** (Figure 2.6) the $H_{Ar}$-Co interaction is slightly attractive with a dominant covalent contribution. In **Co-NHAc-TS-CH** (Figure 2.6) this situation reverses and the $H_{Ar}$-Co interaction becomes rather strongly electrostatically repulsive, that is by 10 kcal/mol more than in **Ir-NHAc-TS-CH** (Figure 2.5).

Worthy to note, all the computed vibrational spectra of agostic structures, that is **ag** and **Ir-NHAc-ag-col**, show a specific and relatively intense stretching mode of the carboxy base ligand in the 2300-2900 $cm^{-1}$ region, the lowest wavenumber in this range being found for the C=O stretching mode of the amidato ligand of **Ir-NHAc-ag-col**. This information may be useful for tracing down agostic intermediates experimentally by IR techniques, which is not addressed here.

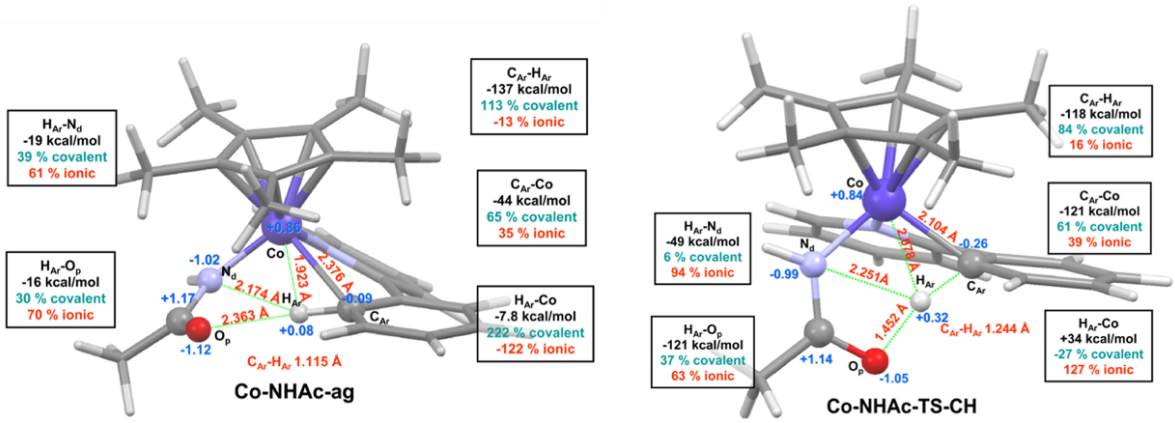


**Figure 2. 12.** Singlet geometries of **Co-NHAc-ag** and **Co-NHAc-TS-CH** with atom numbering, atomic QTAIM charges (blue colored numbers) main interatomic distances (red colored numbers) and the main QTAIM-IQA interatomic interaction energies $E_{int}$ decomposed into covalent (green colored) and ionic (red colored) percentage of contribution. Positive and negative values of $E_{int}$ indicate repulsive and attractive interactions respectively.

#### 2.2.1.5. DLPNO-CCSD(T) Computations and Local Energy Decomposition Analysis

Recent reports have depicted DLPNO-CCSD(T) as a computationally time-effective *ab initio* method suited to the study of agostic interactions in organometallic

compounds.[225-228] The DLPNO-CCSD(T) method combines the high accuracy of the coupled-cluster theory with a computational cost similar to DFT[212, 228, 229] arising from the localization of Hartree-Fock orbitals and the dichotomy between "strong" and "weak" pairs with respect to the inter-orbital distance. The DLPNO-CCSD(T) method, when associated with the Local Energy Decomposition[214] (LED) analysis, provides a sound access to the role of NCI (including dispersion) by assigning localized orbitals to user-defined fragments, thus allowing the differentiation between intra- and inter-fragment contributions to the interaction energies. The localized orbitals being assigned based on Mulliken charges analysis, an orbital expanding on more than one fragment will always be assigned to the fragment with the most electronegative involved atom. By construction, no counterpoise correction for the BSSE is needed for the calculation of interaction energies within the LED framework. In the Ni/Pd dyad case reported recently,[179] this method proved useful in outlining the weight of electrostatics particularly in the critical process of formation of the agostic transient **ag**.

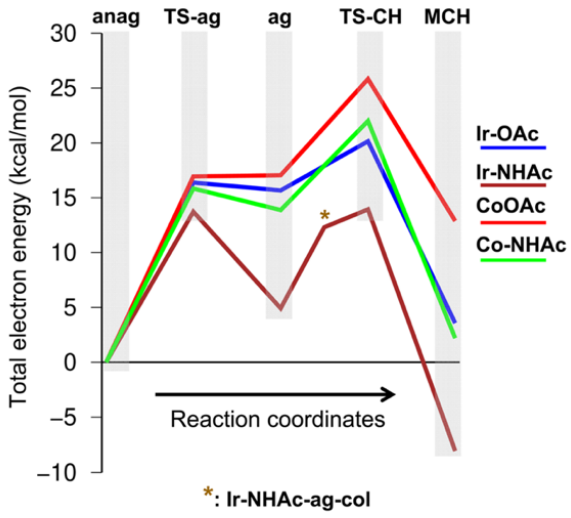


**Figure 2. 13.** Total electron energy profile for **Co** & **Ir** / **-OAc** and **–NHAc** systems computed in the gas phase at the DLPNO-CCSD(T)/def2-TZVPP level from geometries computed at the COSMO($CH_2Cl_2$)-ZORA-PBE-D3(BJ)/all electron TZP level.

Figure 2.13 displays the gas phase DLPNO-CCSD(T) total electron energy profiles for the four systems, from the DFT-optimized structures, which illustrates in a qualitative

fashion the difficulty in accounting for the proton-transfer step **ag**-to-**TS-CH**, in which lies the main and somewhat expected discrepancy with the GGA-DFT investigation. In almost all cases shown in Figure 2.13, the **ag**-to-**TS-CH** activation energy amounts about 4-10 kcal/mol, whereas in the GGA-DFT study the span of values from ca. 0 up to ~6 kcal/mol suggests a symptomatic underestimation. Even more critical is the substantial change of individual reaction energy profiles, which is rather diverse at the GGA-DFT level and more homogenous in feature in the DLPNO-CCSD(T) computations. Quite consistently with the DFT study though, the **anag**-to-**ag** step still requires the highest activation energy barrier, spanning 14-17 kcal/mol; it remains the kinetic determining step at the DLPNO-CCSD(T) level. The agostic transient **ag** is at a local minimum in three out of four systems: **Co-OAc-ag** is slightly destabilized with respect to **Co-OAc-TS-ag**. With both Co and Ir, the replacement of the acetate ligand by the acetamidate results in a lowering of the **anag**-to-**TS-ag** energy barrier and in an energetic stabilization of **ag** stronger in the Ir system than in the Co one. Quite interestingly also the **Ir-NHAc-ag-col** transient is no more localized in a local minimum like suggested by DFT but on an ascending path towards **TS-CH**.

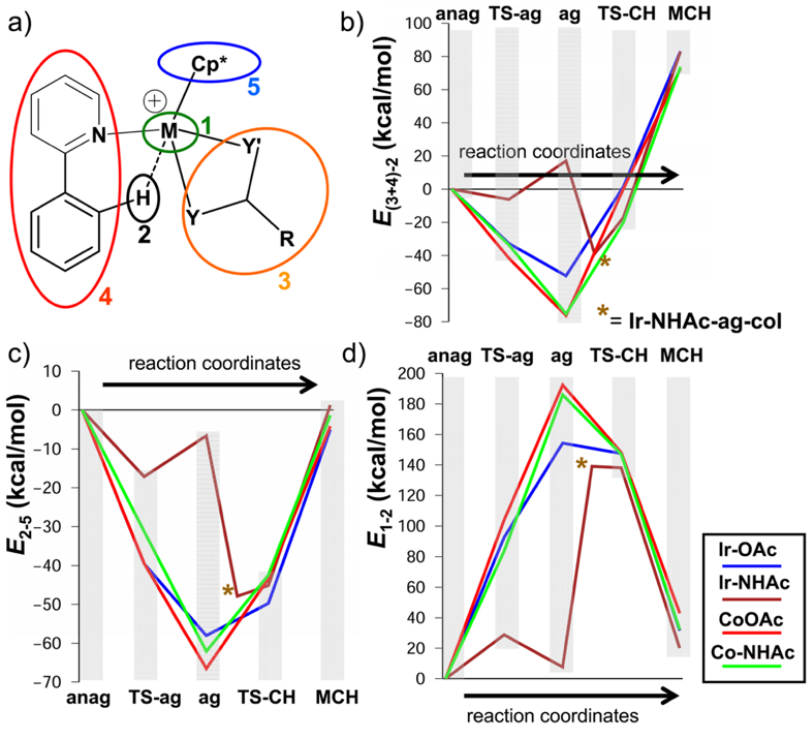


**Figure 2. 14.** Local Energy Decomposition (LED) analysis for the Ir and Co systems along the reaction coordinates of the CMD mechanism with plots of the inter fragment interaction energies $E_{i\text{-}j}$, where *i* and *j* are the considered molecular fragment numbers:

a) fragmentation scheme and numbering for the LED analysis, b) interaction energy between fragment 2 ($H^+$) and the sum of fragments 3 and 4, c) interaction energy between fragments 2 and 5 (Cp* ligand), d) interaction energy between fragments 1 and 2.

For the LED analysis, the studied systems have been subdivided into five chemically meaningful fragments, as shown in Figure 2.14a. Fragment 1 has been defined as the metal center, fragment 2 as $H_{Ar}^+$, fragment 3 as the auxiliary base, fragment 4 as the [2-*phpy*]$^-$ ligand and fragment 5 as the Cp* ligand. As in the Ni/Pd dyad case, the interaction energy between all these fragments is mainly electrostatic in nature, except for the interactions involving fragment 2 that are purely electrostatic. Indeed, the hydrogen constituting fragment 2 being covalently bonded to either $C_{Ar}$ of fragment 4 or the $O_p$ of fragment 5 throughout the reaction path, no orbital has been assigned to this fragment, thus being considered as a proton.

Here, we mainly focus on the interaction energies between the transferred $H^+$ and the four other fragments.

The interaction between the transferred $H^+$, i.e fragment 2 (Figure 2.14a), and [2-*phpy*]$^-$, i.e fragment 4, decreases by 20 to 45 kcal/mol for all four systems from **anag** to **ag** before increasing by ~500 kcal/mol from **ag** to **MCH**, while the interaction between fragment 2 and the auxiliary basis, fragment 3, decreases by ~30-40 kcal/mol during the formation of the agostic intermediate before decreasing again by ~400 kcal/mol along the proton abstraction, except for **Ir-NHAc** for which the interfragment 2-3 interaction energy increases by ~40 kcal/mol during the first step. The interaction between the fragment 2 and the superfragment "3+4", i.e. the sum of interactions between fragments 2 and 3 and between fragments 2 and 4, is shown in Figure 2.8b. For both cobalt analogues and for **Ir-OAc**, this contribution stabilizes the system when forming the agostic intermediate, the stabilization being greater by ~30 kcal/mol in the cobalt cases, before becoming repulsive when the proton is transferred from fragment 3 to fragment 4. For **Ir-NHAc**, the contribution becomes repulsive when forming **ag** and attractive when forming **ag-col**. In both the cobalt and the iridium cases, concerning the (3+4)-2 interaction, no significant difference in stabilization of the agostic intermediate is observed when changing the auxiliary base. This difference in behavior enlightens the importance of the orientation of the base in the stabilization of the

agostic intermediate. The total interaction around the reactive center, i.e. the sum of interaction energies between fragments 2, 3 and 4, still presents its minimum at **ag**, located ~20 kcal/mol lower for the cobalt analogues than for the iridium ones, thus defining the agostic intermediate as the optimal interaction situation within the reactive site.

The interaction between fragment 2 and the "spectator" Cp* ligand, i.e fragment 5, is shown in Figure 2.14c. This interaction energy decreases up to the **ag** stage and then increases towards an almost null final gain in energy (< 5 kcal/mol). The only variation to this trend happens for **Ir-NHAc** for which the interaction energy decreases from **anag** to **TS-ag** then increases to **ag**, decreases to **ag-col** before increasing again to **MCH**. When the auxiliary base is acetamidate instead of acetate, the stabilization of the agostic intermediate is lower in both the cobalt (~7 kcal/mol) and the iridium (~13 kcal/mol compared to the **Ir-NHAc-ag-col**) cases.

The interaction between fragment 2 and the metal center, i.e fragment 1, is shown in Figure 2.14d. In the case of the cobalt analogues, in **Ir-OAc**, and in **Ir-NHAc** if considering only **ag-col** instead of **ag**, this repulsive interaction increases up to **ag** to decline subsequently, the interaction at the **MCH** stage being 20-40 kcal/mol more repulsive than the one at **anag**. The main reason for this behavior is the shortening of the metal-$H_{Ar}$ distance at the **ag** step. In the case of **Ir-NHAc**, the repulsion at **ag** is not greater than the one at **anag**, due to a relatively similar metal-$H_{Ar}$ distance which contrasts with **Ir-NH-ag-col** ($\Delta d_{\mathbf{ag\text{-}anag}}$= 0.05 Å vs. $\Delta d_{\mathbf{ag\text{-}col\text{-}anag}}$= 0.84 Å). Due to shorter metal-$H_{Ar}$ distances for the cobalt analogues the maximum of repulsion is greater in the cobalt systems than in the iridium ones by more than 40 kcal/mol. In both cobalt and iridium systems, the metal-$H_{Ar}$ repulsion is lower in the acetamidate case than in the acetate case by ~14 kcal/mol for Ir (compared to IrNH-ag-col) and by ~7 kcal/mol for Co, mainly due to a shorter distance in the acetate case than in the acetamidate one ($\Delta d_{AcO\text{-}AcNH}$(Co)=0.04 Å and $\Delta d_{AcO\text{-}AcNH}$(Ir)=0.21 Å). Overall, agostic intermediates can be described in the LED analysis as an optimum in interaction between the "transferred $H^+$" and other fragments. In accord with the QTAIM-IQA analysis, the LED analysis shows that stabilizing interactions with the ligands of the polarized C-H bond dominate over the destabilizing contribution of the $H_{Ar}$-metal interaction.

## 2.2.2. Experimental aspects

### 2.2.2.1. Synthesis and characterization of cobaltacycles

As mentioned earlier in Chapter 1, the synthesis of Cp*Ir-metalacycles[107] (Scheme 2.2) typically uses a mixture of the stable dimeric complex $[Cp^*IrCl_2]_2$ and sodium acetate as auxiliary base,[122, 230] which is known to operate cycloiridation via the CMD mechanism according to the work of Davies, Macgregor et al.[111, 181] and to a based assisted electrophilic C-H bond activation by Jones et al[112, 122].

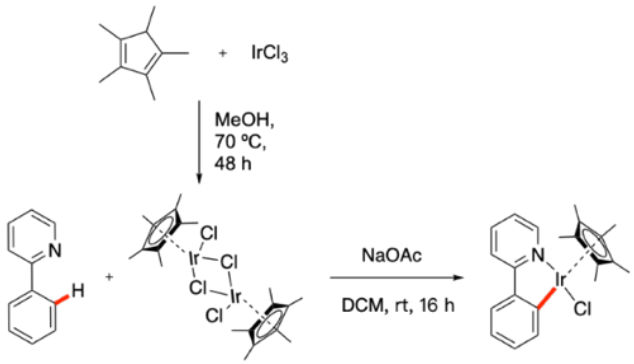


**Scheme 2. 2.** Example of the synthesis of iridacycle with $[Cp^*IrCl_2]_2$.

To synthesize homologous cobaltacycles, we also use the more stable dimeric cobalt(III) complex $[Cp^*CoI_2]_2$, which showed superior performance in comparison to previously reported Co(III) complexes in C-H activation. Moreover, this dimeric complex is air- and temperature-tolerant, and can readily be synthesized in two steps from commercial $Co_2(CO)_8$ (Scheme 2.3).

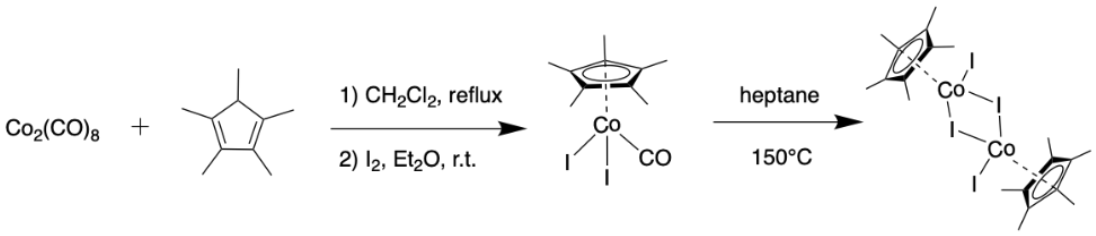


**Scheme 2. 3.** Preparation of $[Cp^*CoI_2]_2$.

Therefore, the initial study of the optimal conditions for cyclocobaltation of 2-*phpy*H was carried out based on the optimal conditions for synthesis of Ir analogues, and $[Cp^*CoI_2]_2$ as the metal source. The performance of the cyclocobaltation of 2-*phpy*H with $[Cp^*CoI_2]_2$ assisted by various carboxy bases (3:1 base/Co ratio) is shown in table 2.1.

**Table 2. 1.** Performance of the cyclocobaltation of 2-*phpy*H by $[Cp^*CoI_2]_2$ under various conditions

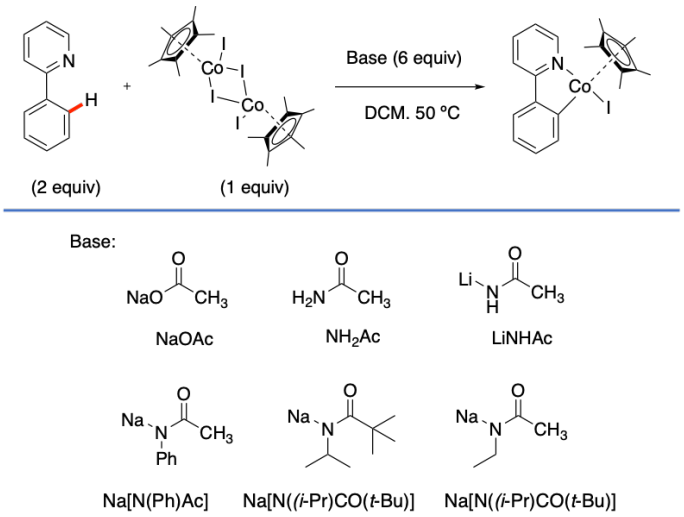


| Entry | Base | Time | Yield |
|---|---|---|---|
| 1 | No base | 17 h | 0% |
| 2 | NaOAc | 48 h | 12% |
| 3 | $NH_2Ac$ | 17 h | 3% |
| 4 | LiNHAc | 17 h | 68% |
| 5 | LiNHAc | 48 h | 83% |
| 6 | Na[N(Ph)Ac] | 17 h | 0% |
| 7 | Na[N((*i*-Pr)CO(*t*-Bu)] | 17 h | 0% |
| 8 | Na[N((*i*-Pr)CO(*t*-Bu)] | 48 h | 39% |
| 9[a] | LiNHAc | 17 h | 60% |
| 10[a] | LiNHAc | 48 h | 65% |
| 11[b] | $NH_2Ac$ | 17 h | 18% |
| 12[c] | $NH_2Ac$ | 17 h | 18% |
| 13[d] | $NH_2Ac$ | 17 h | 29% |

General conditions: 2-*phpyH* (0.2 mmol, 2 eq), $[Cp^*CoI_2]_2$ (0.1 mmol, 1 eq), base (0.6 mmol, 6 eq), DCM (5 mL), 50°C. [a] at room temperature. [b] with 4 eq of 2-*phpyH*. [c] with 8 eq of 2-*phpy*. [d] at room temperature and 2 eq of $Na_2CO_3$. 1,3,5-Trimethoxybenzene was used as internal $^1$H NMR reference.

As shown in table 2.1, in the absence of base no trace of the desired complex **1a** was observed in $^{1}H$ NMR after 17 h (Table 2.1, entry 1). The first base probed for the cyclocobaltation was NaOAc, which performed well in the iridium case, affording **2a** in ~93 % yield for an overnight reaction (17 h).[230] In the case of cobalt, a maximum yield of 12 % in the brown-red-colored **1a** complex was achieved after 2 days of reaction (Table 2.1, entry 2) in the presence of dry NaOAc. Like suggested by theory (Figure 2.2), the C-H activation in the presence of NaOAc with $[Cp^*CoI_2]_2$ is much less favorable than with the $[Cp^*IrCl_2]_2$.

Then, various lithium and sodium acetamidates were probed instead of auxiliary base. The use of the neutral acetamide (Table 2.1, entry 3) surprisingly led to 3 % yield in **1a** after an overnight reaction, whereas the use of its conjugate base produced by deprotonation of the $NH_2$ group, i.e. LiNHAc, yielded **1a** in 68 % yield (Table 2.1, entry 4). By extending the reaction time to 2 days, **1a** was isolated in 83% yield (Table 2.1, entry 5). Worthy to note, the latter yield was readily reproduced when the amounts of reactants and solvent were scaled up 10 times.

Three other amidate salts were also probed to evaluate the impact of steric on the performance of the cyclometallation, that is sodium *N*-ethylacetamidate, sodium *N*-isopropylacetamidate and sodium *N*-phenylacetamidate: all resulted in lower yields in **1a** (Table 2.1, entries 6-8) suggesting that substitution at the N atom was strongly detrimental either on steric or electronic grounds.

Lowering the reaction temperature from 50 °C to room temperature (~20 °C), while keeping reactants' proportions identical resulted into a slight drop of the yield in **1a** when $LiNHCOCH_3$ was the base: 60 % yield were achieved when the reaction was conducted at room temperature over 17 h (Table 2.1, entry 9). A longer reaction time of 48 h was not significantly beneficial (65% yield in **1a**, Table 2.1, entry 10).

From the above comparative experiments, we found that acetamide could also promote cyclocobaltation with the yield of 3% (Table 2.1, entry 3), leading us to investigate the influence of the effect of higher amounts of 2-*phpy*H on the yield in **1a**, because there must be a Brønstedt base in the medium to ensure the irreversibility of the CMD mechanism. When we increased the excess of 2-*phpy*H from 2- to 4- and 8-fold in the presence of acetamide, the yield of **1a** increased significantly that reached

the threshold value of 18% (Table 2.1, entries 11 and 12). Moreover, the addition of the poorly soluble $Na_2CO_3$ (2 equiv) pushed the yield in **1a** further to 30% (Table 2.1, entry 13). These observations of great importance for further applications, suggesting that amidate salts are not absolutely required to achieve the cyclocobaltation as long as an amide and a coordinatively noninterfering base are present in solution, the latter having putatively the role of deprotonating a transient Co-bound amide and generating in situ the amidate-Co species required for the metalation of the ligand via the CMD mechanism.

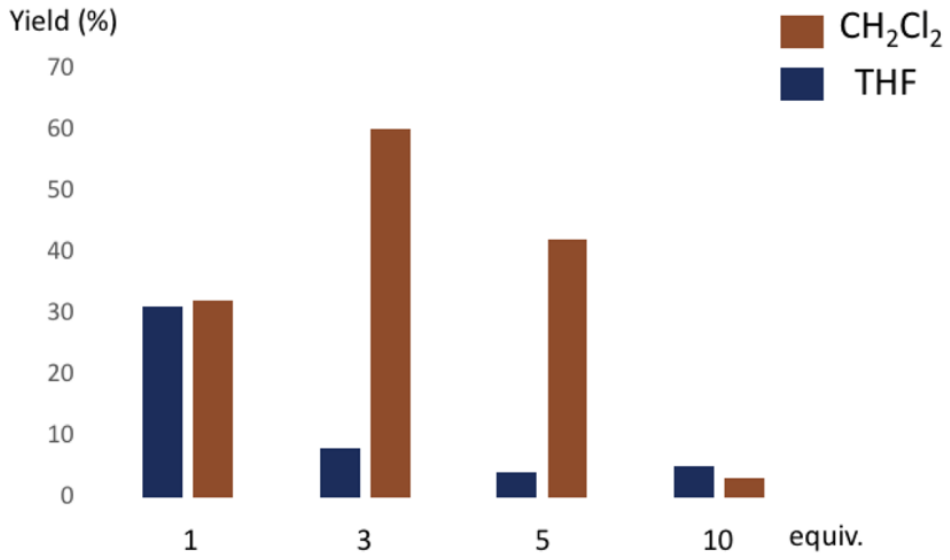


**Figure 2. 15.** Effect of the solvent (THF vs DCM) on the yield in **1a** upon cyclocobaltation of 2-*phpy*H by $[Cp^*CoI_2]_2$ in the presence of various amounts of LiNHAc per Co atom (1, 3, 5, and 10 equiv)

Afterwards, we attempt to perform the cyclocobaltation reaction in DCM or THF with various amounts of LiNHAc (1, 3, 5, and 10 ratios per Co) (Figure 2.15). Increasing the amount of LiNHAc decreased the yield of cobaltacycles from ~30% to ~10% in THF, but in DCM, the yield increased to 68% and then decreased. Meanwhile, a lot of purple precipitate was occurred. The cyclometallation reaction in THF was significantly shut off when use the best proportions of reactants equivalent in DCM, resulting in an 8% yield in **1a**. This result confirmed that the amount of dissolved LiNHAc in a given solvent during the cyclocobaltation was crucial in conditioning the yield in **1a**, and the presence of the purple precipitate inhibits this reaction. The optimal cyclometallation can only be

achieved if competing coordinative saturation of the metal center and the formation of unproductive Co dimers are minimized not only by incomplete dissolution of the base salt but also by its steady dissolution as the reaction proceeds. DCM obviously meets this condition of heterogeneity of the reaction solution that prevents side reactions from overwhelmingly diverting the fate of the cobaltation agent $[Cp^*CoI_2]_2$.

More interestingly, in all experiments performed in DCM, both at room temperature and at 50 °C, the formation of a purple product was noticed at the beginning of the experiment. Later, the reaction of $[Cp^*CoI_2]_2$ (1 equiv) and LiNHAc (6 equiv) was carried out in the $d_2$-DCM in the J-young tube, and the structure was determined by crystallization and analyzed by X-ray diffraction, as shown in Figure 2.16a, which contains one bridging acetamidate and two bridging hydroxo ligands. However, the second time a different structure was obtained containing one bridging acetamidate, one bridging hydroxo ligand and one bridging iodine ligand (Figure 2.16b), probably resulting from a reaction between $[Cp^*CoI_2]_2$, LiNHAc, and adventitious water during crystallization at -20 °C, while oxidation of iodide into $I_3^-$. Both compounds are *triclinic* crystalline system with the space group *P*-1. In comparison with the two structures, it is easy to see that the distances between the two Co-atoms are not the same, the distance of [**1e**][$I_3$] (*d*(Co1-Co2)= 2.8926(5) Å ) is shorter then [**1e'**][$I_3$] (*d*(Co1-Co2)=3.1277(6) Å). From these results, suggest that in the early stage of reaction, $[Cp^*CoI_2]_2$ first reacts with LiNHAc to form Cp*Co-species with high catalytic activity. However, the involvement of adventitious water during the crystallization process led to the production of these two complexes.

A similar dinuclear structure containing two acetate bridging ligands was already pointed out by Perez-Temprano *et al.* for a cyclocobaltation reaction carried out with $[Cp^*Co(MeCN)_3]^+$ in the presence of acetate[185]. [**1e**][$I_3$] is the only indirect but firm structural proof that the displacement of an iodide from $[Cp^*CoI_2]_2$ by the acetamidato ligand may occur in solution. Although the $^1$H NMR monitoring of reactions of $[Cp^*CoI_2]_2$ with LiNHAc did result in the observation of a few new signals, it was not possible to confirm that those putative new species were related to anything close proposed in the CMD-type acetate promoted cyclometallation,[111, 112, 122] such as $Cp^*Co(\kappa^2\text{-NHAc})_2$ species, or $Cp^*Co(\kappa^2\text{-NHAc})^+$.

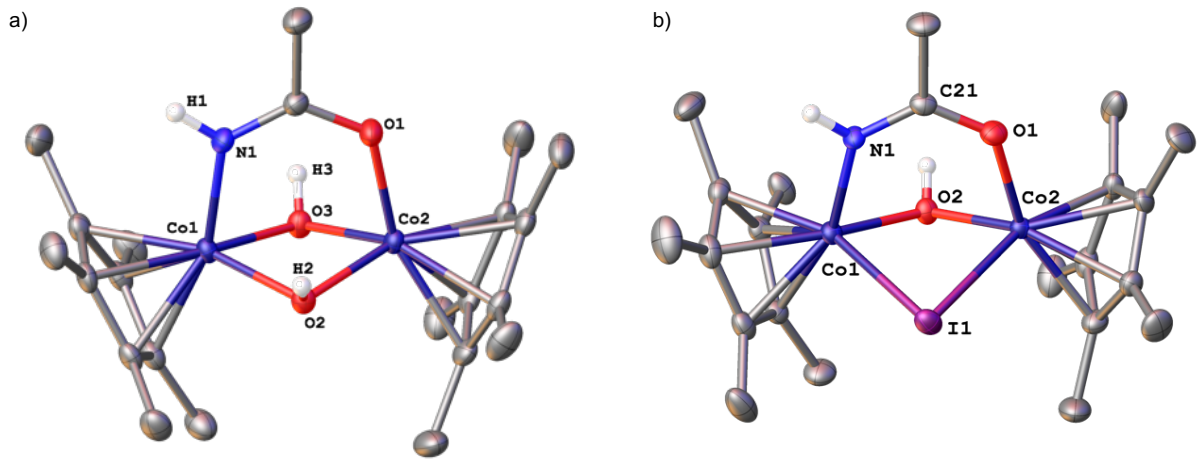


**Figure 2. 16.** ORTEP diagram of the structure of (a) [**1e**][$I_3$] and (b) [**1e'**][$I_3$], ellipsoids displayed at 50% probability. The hydrogen-atoms on the carbon, $[I_3]^-$ and solvent molecules were omitted for clarity. (a) Selected bond distances [Å] and angles [°]: O1-Co2 1.9307(18), O2-Co1 1.9459(17), O2-Co2 1.9443(18), O3-Co1 1.9435(18), O3-Co2 1.9412(17), Co1-Co2 2.8926(5), N1-Co1 1.937(2), C21-O1 1.286(3), C21-N1 1.300(3); O2-Co2-Co1 41.98(5), O1-C21-N1 124.9(2), C21-N1-Co1 126.82(17), C21-O1-Co2 126.05(16), Co2-O2-Co1 96.07(8), Co2-O3-Co1 96.25(8). (b) Selected bond distances [Å] and angles [°]: N1-Co1 1.937(2), O1-Co2 1.935(2), O2-Co2 1.930(2), O2-Co1 1.940(2), Co1-I1 2.6415(4), Co2-I1 2.6384(4); Co2-O2-Co1 107.83(10), N1-Co1-O2 90.04(10), N1-Co1-I1 91.15(7), O2-Co1-I1 86.21(6), O2-Co2-O1 90.11(9), Co2-I1-Co1 72.650(13).

Although the X-ray diffraction structure of **1a** was already reported by Perez-Temprano et al., two very interesting crystals were obtained serendipitously during the crystallization process, and determined their structures by single crystal diffraction, as shown in Figure 2.17. One of them is the insertion of Cp*H into the cobaltacycle of **1a** formed [**1c**][$I_3$] (Figure 2.17a), is one rare if not an unprecedented example of a product of a reaction of the Cp* ligand with the heterochelating 2-*phpy* ligand, as Cp* is generally considered as a spectator ligand and not directly involved in the reaction. Another one is the hydrogen on Cp* was replaced by -OH group, followed by the insertion of an oxygen atom into the Cp* ring and obtained the compound [**1c'**][$I_3$] shown in the Figure 2.17b. Fortunately, we have succeeded in finding the proper

conditions to reproduce the synthesis of [**1c**][$I_3$] at a preparative scale, which will be discussed in detail later.

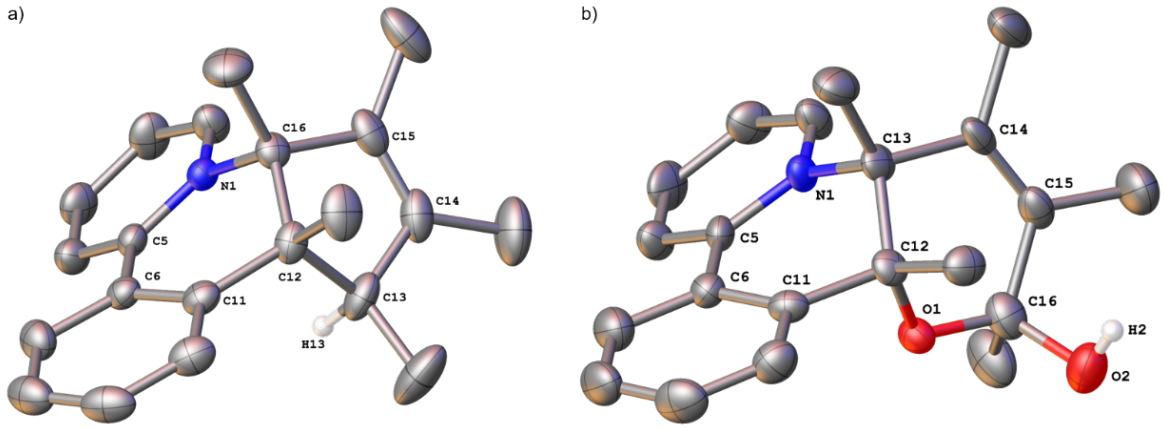


**Figure 2. 17.** ORTEP diagram of the structure of (a) [**1c**][$I_3$] and (b) [**1c'**][$I_3$], ellipsoids displayed at 50% probability. The hydrogen-atoms on the carbon, $[I_3]^-$ and solvent molecules were omitted for clarity. (a) Selected bond distances [Å] and angles [°]: C5-N1 1.359(5), C16-N1 1.544(5), C5-C6 1.470(6), C6-C11 1.399(6), C11-C12 1.513(6), C12-C16 1.557(6); N1-C16-C12 109.0(3), C5-N1-C16 122.0(3), C6-C11-C12 119.8(4), C11-C6-C5 120.0(4). (b) Selected bond distances [Å] and angles [°]: C12-C13 1.557(8), C13-C14 1.536(8), C13-N1 1.539(7), C14-C15 1.322(9), C15-C16 1.507(8), C16-O1 1.417(7), C16-O2 1.446(8), C5-N1 1.371(7), C11-C12 1.521(8), C12-O1 1.441(7); C11-C12-C13 109.9(5), O1-C12-C13 106.8(5), O1-C12-C11 102.6(4), C6-C11-C12 118.2(5), C6-C11-C12 118.2(5), C16-O11-C12 117.2(4), N1-C5-C6 119.1(5), O1-C16-C15 114.0(5), O1-C16-O2 108.9(5).

To further demonstrate that acetamidate can effectively facilitate the cyclometallation reaction, the cycloiridation in the presence of LiNHAc was also attempted, under the identical conditions as cyclocobaltation (50 °C, DCM, 17 h, 3 equiv per Ir). Incredibly, the overall yield of iridacycle (the yield of 20%) was significantly lower than the yield of the standard reaction performed in the presence of NaOAc (the yield of 93%). However, after comparison of the $^1$H NMR spectra, another iridacycle was found to be generated during the cycloiridation, which is the acetamidate derivative **2b** in a 29% yield (Scheme 2.4). The overall yield in iridacycles have actually reached 49%. If the amount of LiNHAc was reduced to 1 equiv during this cycloiridation, the formation of complex

**2b** was no longer observed and only the desired complex **2a** was produced in 92% yield. Therefore, we venture to speculate that the possible reason for this situation is the reaction of **2a** with unreacted excess LiNHAc during the cyclometallation to form compound **2b**, which leads to a low yield of the targeted product.

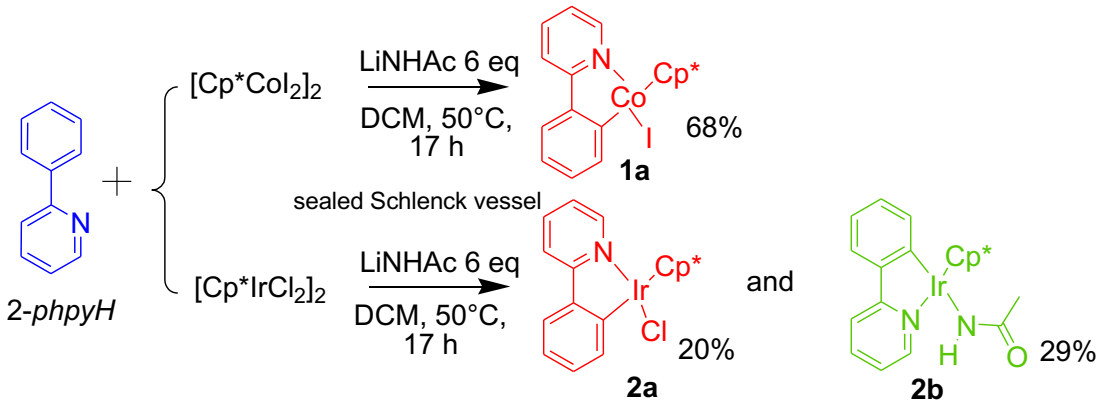


**Scheme 2. 4.** Cyclocobalation and cycloiridation of 2-*phpyH*.

Our speculation was subsequently proved experimentally that **2a** could be easily converted to **2b** (52% NMR yield) by an overnight reaction of the **2a** with excess of LiNHAc in DCM at 50 °C (Scheme 2.5, top). Importantly, compound **2b**, which is rather stable, was found to react quantitatively with aqueous hydrochloric acid to afford **2a**.

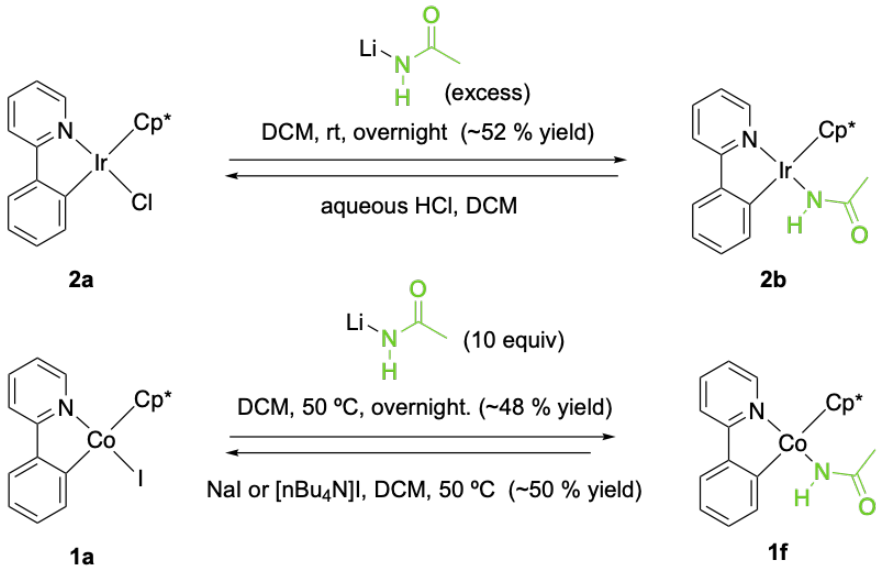


**Scheme 2. 5.** The synthesis of new metallacycles (top: iridacycle; bottom: cobaltacycle).

Notably, while no trace of a similar Co acetamidate complex, i.e. **1f**, was ever detected at the end of the cyclocobaltation reaction, this complex could be easily synthesized in ca. 48% yield (NMR yield) from **1a** by reaction with a large excess (>10-fold) of LiNHAc (Scheme 2.5 bottom). Reaction of **1f** with excess amounts of either NaI or [*n*Bu$_4$N]I in $CH_2Cl_2$ at 50°C in a sealed Schlenk vessel for over 17 h produced complex **1a** in ~50% yield, thus suggesting that the formation of **1f** under the conditions of cyclocobaltation is most probably precluded by amidate ligand's lability and by the higher affinity of the Co center for the iodo ligand. DFT modeling of acetamidate ligand displacement by $I^-$ and $Cl^-$ in **1f** and **2b** respectively, produced slightly endergonic processes, by only 1 kcal/mol more favorable to the Co system. Subsequently both compounds **2b** and **1f** were successfully isolated and fully characterized by spectroscopic and analytical methods, and their structures were established by X-ray diffraction analysis (Figure 2.18).

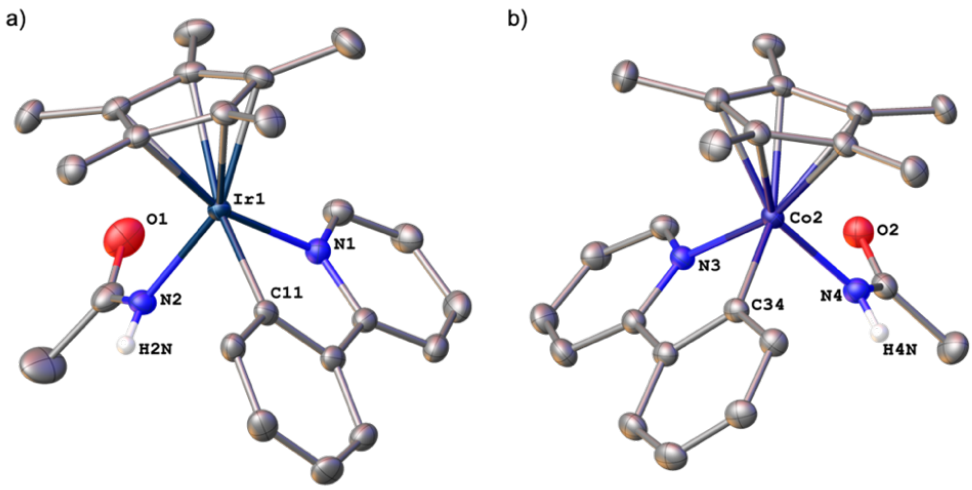


**Figure 2. 18.** ORTEP diagram of the structure of **2b** and **1f**, ellipsoids displayed at 50% probability. The hydrogen-atoms on the carbon were omitted for clarity. (a) Selected bond distances [Å] and angles [°]: C11-Ir1 2.033(2), C22-O1 1.255(3), C22-N2 1.314(3), N1-Ir1 2.0868(17), N2-Ir1 2.0656(18); C5-N1-Ir1 117.08(14), C11-Ir1-N2 82.72(8), C11-Ir1-N1 78.22(8), N2-Ir1-N1 87.45(7), C22-N2-Ir1 125.66(16). (b) Selected bond distances [Å] and angles [°]: N3-Co2 1.9673(15), N4-Co2 1.9286(16), C34-Co2 1.9215(17); C34-Co2-N3 83.11(7), N4-Co2-N3 92.85(7), C34-Co2-N4 88.64(7).

In addition, a large excess of base could promote the formation of a dinuclear Ir(III) amidate identified as complex **2c**, resulting a significant decrease in the yield of **2a**. The structure of **2c** was solved by X-ray diffraction analysis (Figure 2.19). This compound contains, apart from the Cp* ligand, one hydroxo and two acetamidate ligands all $\mu$-bridging the two Ir(III) centers.

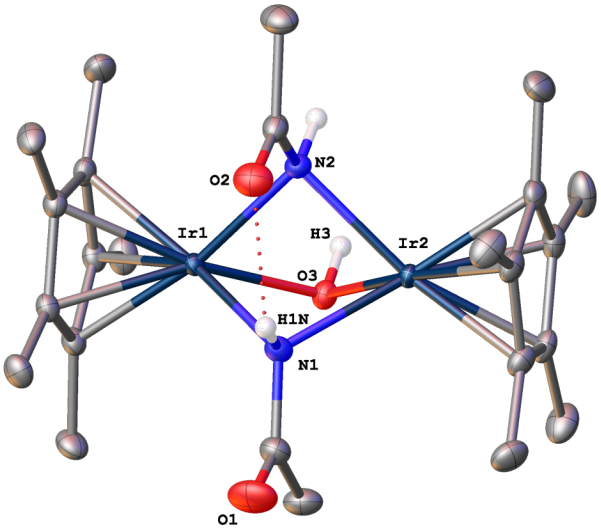


**Figure 2. 19.** ORTEP diagram of the structure of **2c**, ellipsoids displayed at 50% probability. The hydrogen-atoms on the carbon, $[I_3]^-$ and solvent molecules were omitted for clarity. Selected bond distances [Å] and angles [°]: N1-Ir2 2.1508(16), N1-Ir1 2.1525(16), N2-Ir1 2.1530(16), N2-Ir2 2.1536(15), O3-Ir1 2.0856(13), O3-Ir2 2.1035(13), Ir1-Ir2 3.05985(13); N2-Ir2-Ir1 44.72(4), Ir2-N1-Ir1 90.64(6), Ir1-N2-Ir2 90.55(6), Ir1-O3-Ir2 93.84(5), O3-Ir2-Ir1 42.85(4), N1-Ir2-Ir1 44.70(4).

#### 2.2.2.2. Kinetic Isotope Effect

In order to gain insight into the mechanism of this cyclocobaltation, one of the most effective ways to address this problem is the kinetic isotope effects (KIE). In particular, KIEs can give useful information regarding which bond was formed or cleavage in the rate-determining step of the reaction. Traditionally, KIEs are either obtained through parallel reactions or intermolecular competitions of isotopically substituted substrates.

Here, the KIE of the cyclocobaltation of 2-*phpyH* (Scheme 2.6) was determined by those two independent experimental methods.

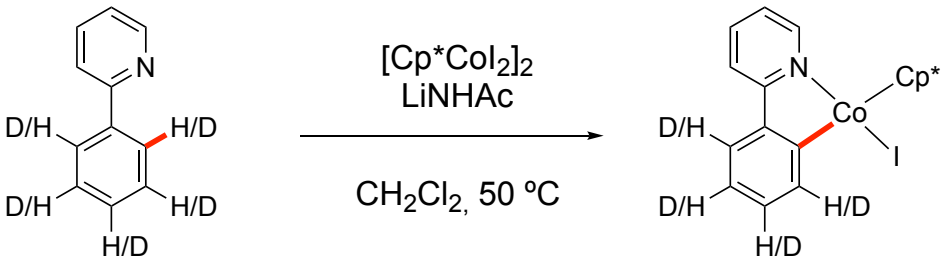


2-*phpy*H/ 2-(d$_5$-*ph*)*py*D

Parallel experiments: apparent KIE = 1.4
Competitive metallation: apparent KIE ~ 1.8 ($^{13}$C NMR estimate)

**Scheme 2. 6.** The KIE of the cyclocobaltation of 2-*phpy*H.

### 1) Parallel experiments

The first one consisted of two independent time-monitored cyclocobaltation experiments carried out with 2-*phpyH* and 2-(*d*$_5$.*ph*)*pyD* with identical amounts of [Cp*CoI$_2$]$_2$ and lithium acetamidate in a sealed vessel at 50°C in the presence of an inert internal reference. Aliquots extracted every hour during a 6 h long monitoring were analyzed by $^1$H NMR spectroscopy to determine the yield in metallacycle and infer the value of the KIE at time *t* as KIE$_t$= (yield in **1a**)/(yield in *d*$_4$-**1a**) (Figure 2.20). Time monitoring of KIE was deemed important to trace down any significant variation of KIE that could be the symptom of competing mechanisms of metalation or to the raise of a partial equilibration of the cyclometallation process that could occur due to the accumulation in the solution of the acetamide released by the reaction.[231-233]

In this method, an average value of KIE was calculated, KIE$_{average}$= 1.4 ± 0.1 with no significant variations of KIE$_t$ over time within the experimental error, suggesting no interference of a competing mechanism over time, and also indicative that C-H bond cleavage was not occurs at the rate-determining step, could occurs somewhere after the rate-determining step.

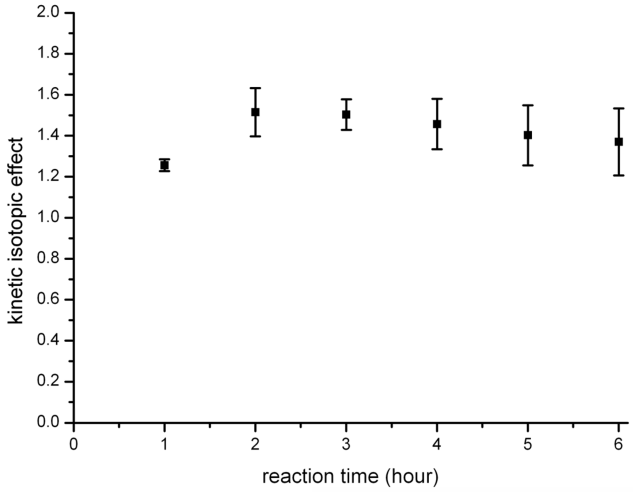


**Figure 2. 20.** Evolution of the KIE with error bars over 6 hours for independent cyclocobaltation reactions carried out under identical conditions in a sealed vessel in $CH_2Cl_2$ at 50°C with 2-*phpyH* and 2-(*d*$_5$.*ph*)*pyD*.

### 2) Intermolecular competition experiment

The second method consisted of the room temperature cyclocobaltation of a 1:1 molar mixture of 2-*phpyH* and 2-(*d*$_5$.*ph*)*pyD* with $[Cp^*CoI_2]_2$ and lithium acetamidate followed by a $^1$H-coupled $^{13}$C NMR spectroscopy analysis and integration of the $^{13}$C signals typical of **1a** and *d*$_4$-**1a** that are readily discriminated by isotope shifts.[234, 235] The KIE was determined by comparing the integrations of $^{13}$C signals of the Co-bound aromatic carbon of **1a** and *d*$_4$-**1a** as well as those of the vicinal H/D-bound ortho carbon.

The second method based on the analysis of a $^1$H –coupled $^{13}$C NMR noise corrected spectrum of a raw reaction mixture gave a larger span or primary KIE values comprised between 1.7 and 2.0 that are most probably biased by different spin-lattice relaxation times $T_1$ in **1a** and *d*$_4$-**1a** for the considered carbon nuclei (Figure 2.21) showing up at $\delta$ ~ 180.6 and 141.4 ppm.

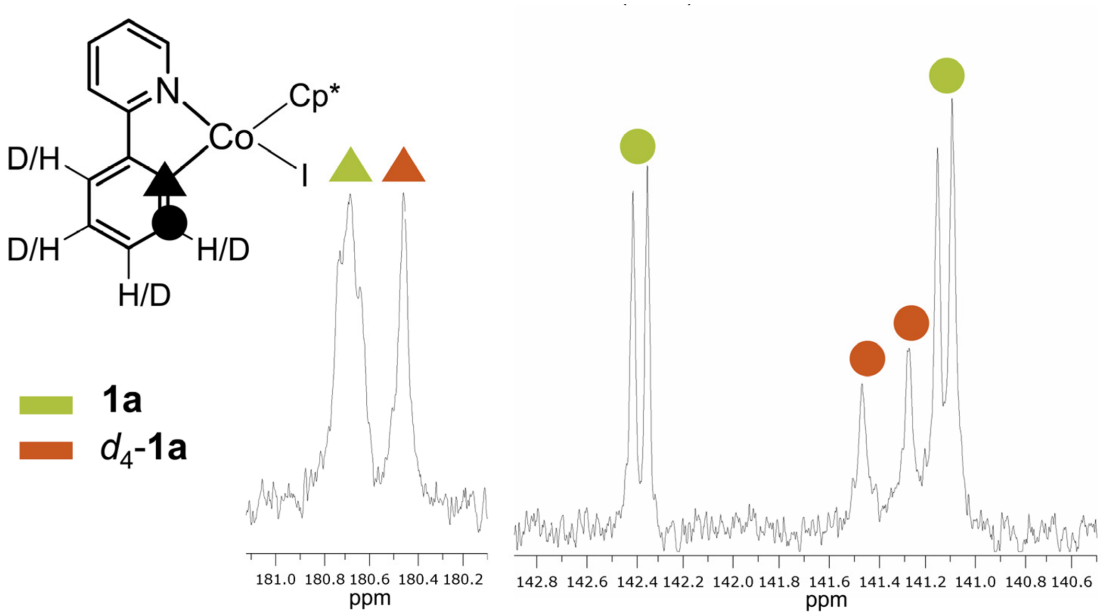


**Figure 2. 21.** Excerpts of the $^{1}H$ coupled $^{13}C$ NMR spectrum of the raw product displaying isotope shifts of resonances for the characteristic signals used for the estimation of the KIE from their integration.

A recent review by Hartwig et al.[236] is particularly informative of the pitfalls in drawing conclusions from experimental KIEs without the complementary knowledge of reaction energy profiles that theoretical support can provide. To probe the CMD mechanism and its consistency with the experimental apparent KIE we applied the simplified Bigeleisen equation[237-242] to compute KIEs of the key steps of the CMD mechanism. Quite interestingly this equation has been seldom used in investigations of the CMD mechanism. Most information available from literature that pertain to the KIE in C-H bond activation are extracted from investigations of catalyzed C-H bond functionalization or have been inferred from DFT using the Eyring equation[180] with the approximation that the ratio between the transmission coefficients is unity, which can be an erroneous approximation.[237]

The simplified Bigeleisen equation[243] offers ready access to KIEs of every single step in the CMD mechanism, it is deemed “semi-classical” as it neglects tunneling effects that may be relevant in the proton transfer step.[244, 245] In cases where the rate determining step coincides with the bond breaking step computed values of KIE are

known to be systematically underestimated.[240] Nevertheless, this approach has proven efficient in determining KIE for different proton-transfer reactions.[240, 241]

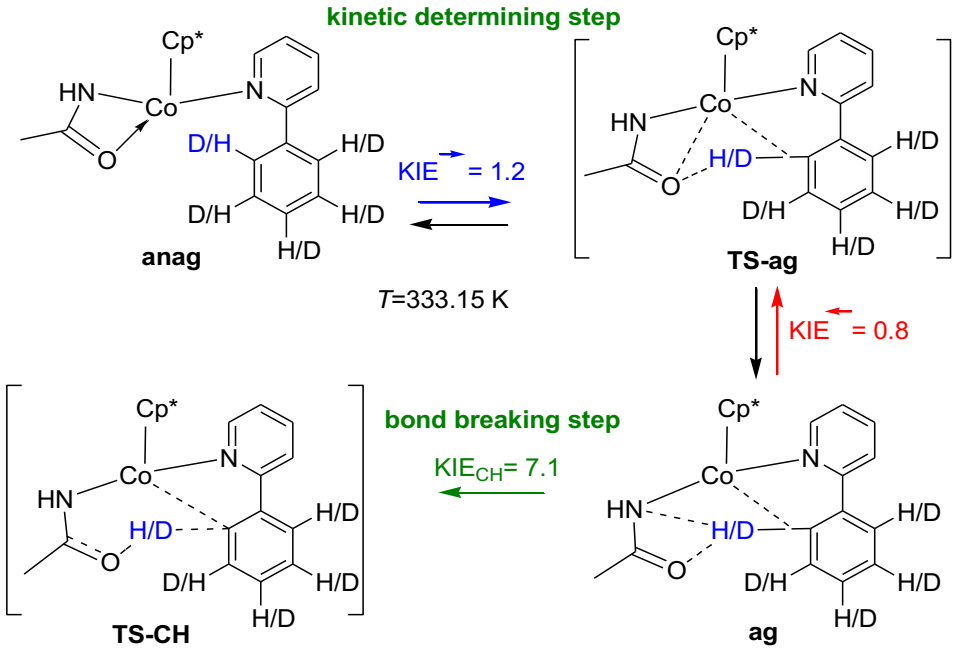


**Scheme 2. 7.** Kinetic isotope effect computed from DFT-computed vibrational frequencies with the Bigeleisen equation for key steps in the cyclocobaltation of 2-*phpyH* and 2-($d_5$.*ph*)*pyD* according to the CMD mechanism.

In this study, KIEs were determined using solely harmonic vibrational frequencies that were readily calculated by DFT routines assuming the Born-Oppenheimer approximation.[243] Forward $KIE^{\rightarrow}$ and backward $KIE^{\leftarrow}$ for the **anag**-**ag** step and $KIE^{CH}$ for the forward **ag**-to-**TS-CH** step were determined with the vibrational frequencies analytically computed for the considered stationary points at the COSMO ($CH_2Cl_2$)-ZORA-PBE-D3(BJ)/ all electron TZP level. This provided values of $KIE^{\rightarrow}$and $KIE^{\leftarrow}$ of 1.2 and 0.8 respectively, and 8.9 for $KIE^{CH}$ at *T*= 298.15 K. The values slightly changed at *T*= 333.15 K (Scheme 2.7) to $KIE^{\rightarrow}$= 1.2, $KIE^{\leftarrow}$= 0.8 and $KIE^{CH}$= 7.1. In spite of the physical limitations of the Bigeleisen equation, those values of KIE are consistent with the experimental primary KIE of the cyclocobaltation reaction if one considers the formation of the agostic intermediate as being the kinetic determining step. Quite interestingly the computed $KIE^{\rightarrow}$ values indicate that the formation of **ag** is not marked with an “inverse” KIE value typical of formally non-bond-breaking steps (i.e KIE < 1).[233]

Furthermore the $KIE^{\leftarrow}$ value is consistent with a strengthening of the C-H(D) bond more favorable to the deuterated isomer in the backward **ag**-to-**TS-ag** path corresponding to the dismantlement of the agostic C-H…Co interaction. Also important is the fact that $KIE^{CH}$ holds the highest value, which is consistent with the quasi-linearity of the key bonds being disrupted and formed in **TS-CH** according to Westheimer's model.[246]

### 2.2.3. The synthesis of cobaltacycles assisted by acetamidate

Afterwards, the cyclocobaltation of other ligands assisted by LiNHAc was also investigated, by using the optimization conditions for the 2-*phpy*H descried above (Scheme 2.8). 7,8-benzo[*h*]quinoline (abbr. *bzqH*), 4-[4-(*t*-butyl)pyridin-2-yl]-*N*,*N*-dimethylaniline[132] (abbr. 2-*anpyH*) and the 2-(2-methylphenyl)pyridine (abbr. 2-*tolpyH*) were successfully used allowing the formation of the corresponding complexes **3a, 4a** and **5a** in 81%, 82% and 30% isolated yield respectively. But all attempts to cyclometallation of 1,2-diphenylquinoxaline or *N*,*N*-dimethylbenzylamine failed to produce any traceable organometallic complex. Moreover, the unique stabilizing ability of MeCN is also utilized to synthesize cationic Cp*Co(III)-complexes (**1b**, **3b**, **4b**, and **5b**) by displacing the iodo ligand by acetonitrile in the presence of 1 equiv of $NaBArF_{24}$ at room temperature over 1 h. Similarly, benzonitrile can also use to synthesize the corresponding cationic compound **1b'**.

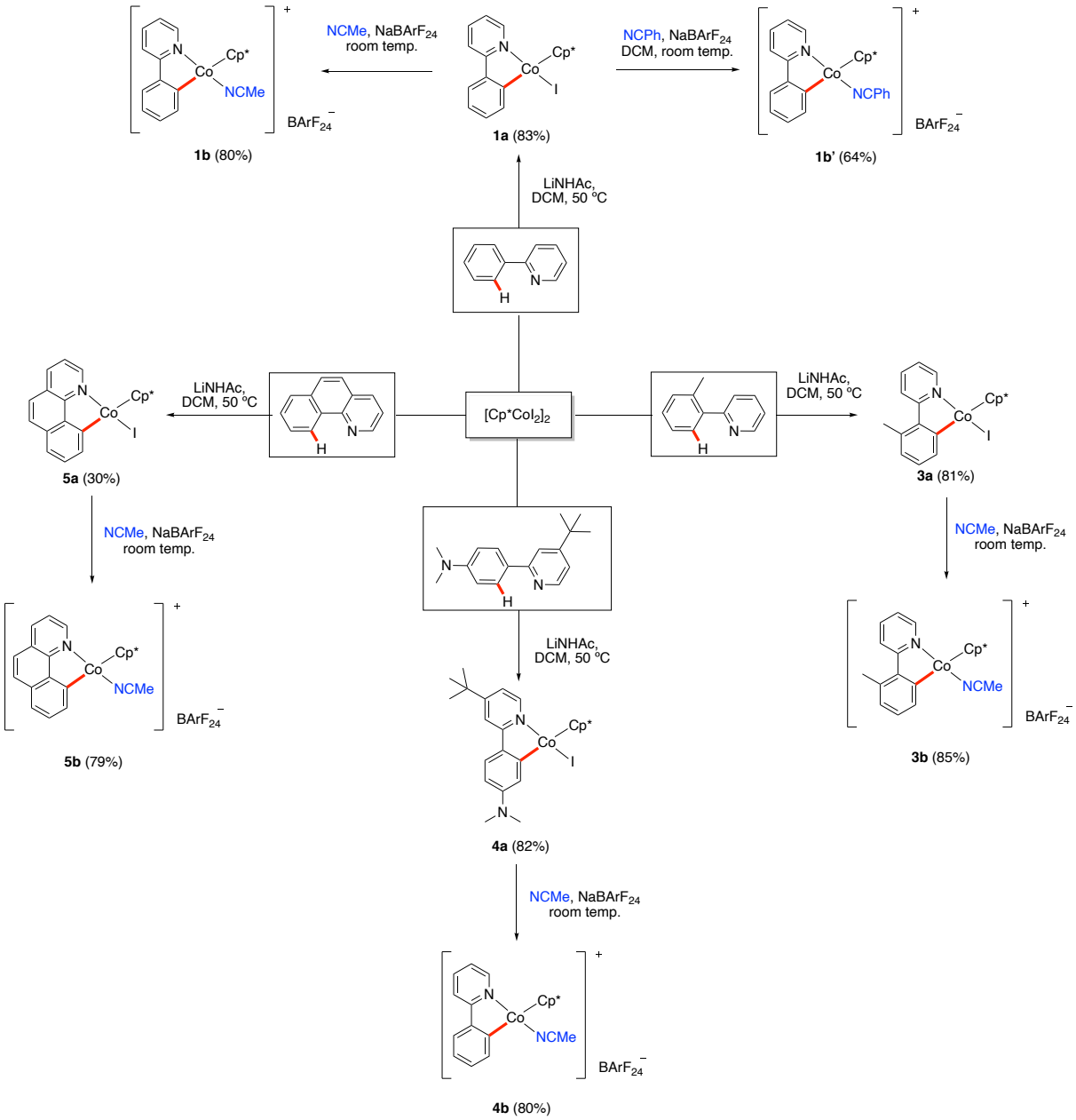


**Scheme 2. 8.** Cyclocobaltation of 2-*tolpy*H, 2-*anpy*H, and *bzq*H and the conversion of the resulting iodo cobaltacycles into the ionic cobaltacyles.

All complexes were fully characterized by $^{1}H$ and $^{13}C$ NMR, ESI mass spectroscopy, and elemental analysis. And the structures of **4a**, **5a**, **1b**, **1b'**, **3b**, **4b**, and **5b** were determined by X-ray diffraction analysis from suitable single crystals (Figures 2.22-2.25).

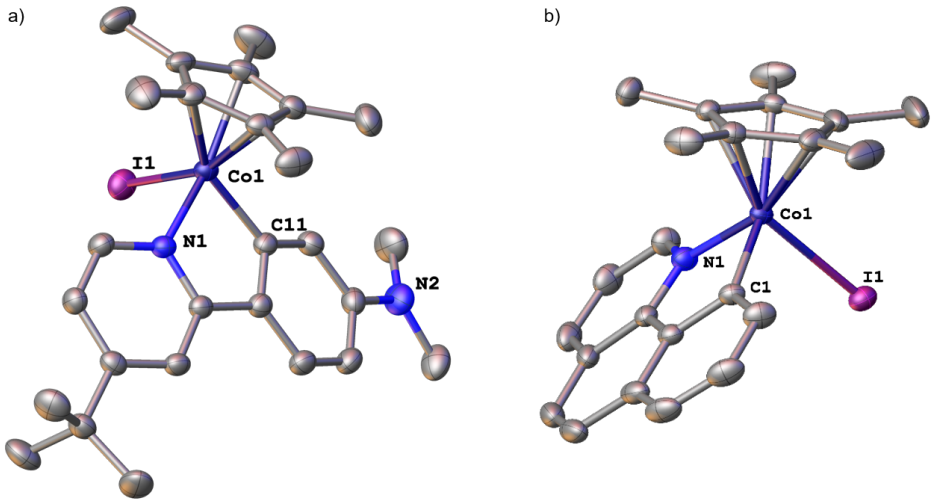


**Figure 2. 22.** ORTEP diagram of the structure of (a) **4a** and (b) **5a**, ellipsoids displayed at 50% probability. The hydrogen-atoms on the carbon were omitted for clarity. (a) Selected bond distances [Å] and angles [°]: N1-Co1 1.9439(16), Co1-I1 2.5738(3), C11-Co1 1.9313(19); C11-Co1-N1 82.44(7), C11-Co1-I1 91.70(6), N1-Co1-I1 92.98(5). (b) Selected bond distances [Å] and angles [°]: N1-Co1 1.9703(17), Co1-I1 2.5730(3), C1-Co1 1.9631(18), C1-Co1-N1 83.65(7), C1-Co1-I1 90.66(5), N1-Co1-I1 90.79(5).

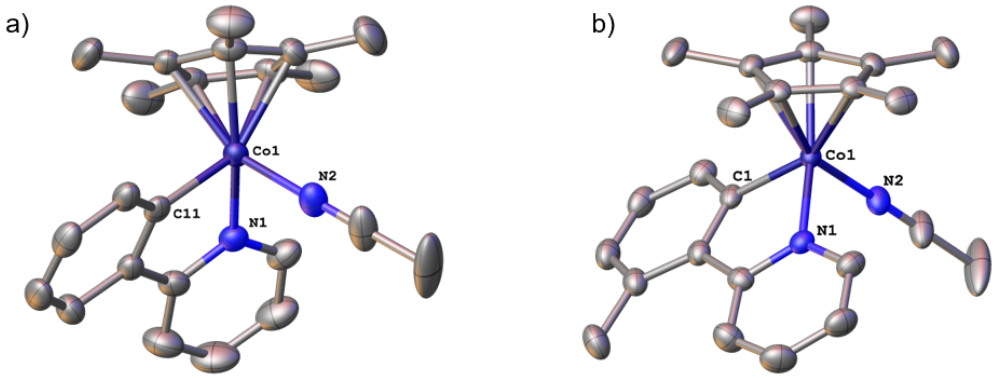


**Figure 2. 23.** ORTEP diagram of the structure of (a) **1b** and (b) **3b**, ellipsoids displayed at 50% probability. The hydrogen-atoms on the carbon and $BArF_{24}^{-}$ were omitted for clarity. (a) Selected bond distances [Å] and angles [°]: N1-Co1 1.964(3), N2-Co1 1.905(4), C11-Co1 1.949(4), N2-Co1-N1 90.11(16), N2-Co1-C11 94.82(16), C11-Co1-N1 82.48(16). (b) Selected bond distances [Å] and angles [°]: C1-Co1 1.927(3), N1-Co1 1.942(2), N2-Co1 1.906(3), C1-Co1-N1 82.06(12), N2-Co1-C1 94.30(11), N2-Co1-N1 90.85(11).

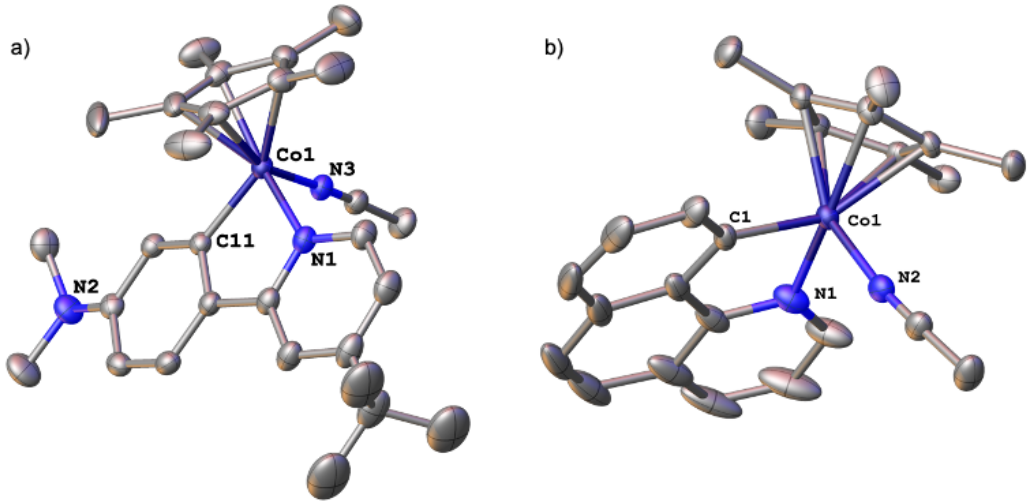


**Figure 2. 24.** ORTEP diagram of the structure of (a) **4b** and (b) **5b**, ellipsoids displayed at 50% probability. The hydrogen-atoms on the carbon and $BArF_{24}^{-}$ were omitted for clarity. (a) Selected bond distances [Å] and angles [°]: N1-Co1 1.974(2), N3-Co1 1.907(2), C11-Co1 1.944(2), N3-Co1-C11 90.03(10), N3-Co1-N1 93.72(9), C11-Co1-N1 82.94(10). (b) Selected bond distances [Å] and angles [°]: N1-Co1 1.977(3), N2-Co1 1.910(3), C1-Co1 1.958(3), N2-Co1-C1 91.92(11), N2-Co1-N1 95.47(12), C1-Co1-N1 83.89(13).

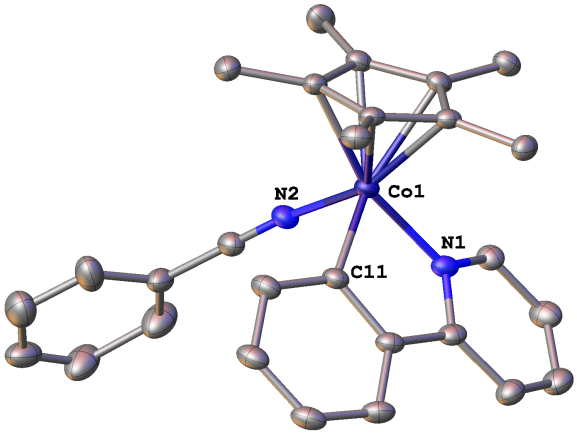


**Figure 2. 25.** ORTEP diagram of the structure of **1b'**, ellipsoids displayed at 50% probability. The hydrogen-atoms on the carbon and $BArF_{24}^{-}$ were omitted for clarity. (a) Selected bond distances [Å] and angles [°]: N1-Co1 1.966(5), N2-Co1 1.895(5), C11-Co1 1.943(6); C11-Co1-N1 82.2(2), N2-Co1-C11 89.0(2), N2-Co1-N1 94.1(2).

Worthy to note, compounds **3-5b** were also probed as potential hydrosilylation catalysts[133, 134, 247] but showed no activity in benchmark catalytic test runs of the dehydro-O-silylation of benzyl alcohol (see the chapter 4).[134] Therefore, we attempted to investigated the application of the acetamidate assisted C-H functionalization, and the role of base in the C-H functionalization.

### 2.2.4. Catalytic application of the acetamidate assisted C-H bond activation to the condensation of diphenylacetylene with aromatic substrates

The condensation of alkyne with metallacycles[248-252] is a well-established process that has recently been ported to Cp*Co(III) catalysis by the groups of Zhu,[253] Cheng[176] and Perez-Temprano[141, 143, 144, 185]. In the latter's reports particularly, the outlying feature of this catalytic process is the putative electrophilic activation of the C-H bond of the main heterocyclic substrate by $[Cp^*Co(MeCN)_3]^+$.

Given the accessibility of $[Cp^*CoI_2]_2$ and its great temperature and air stability, several attempts to achieve the condensation of diphenylacetylene with 2-*phpyH* (Scheme 2.9) were undertaken in this study so as to figure out whether an auxiliary base could be beneficial.

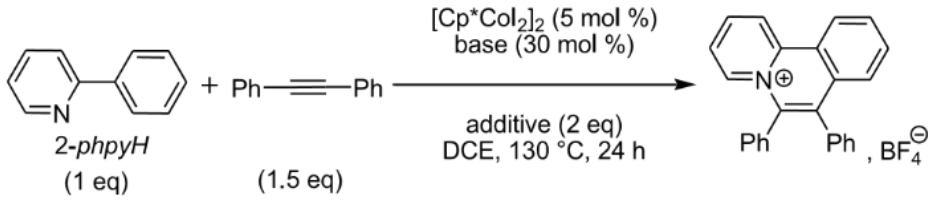


**Scheme 2. 9.** The condensation of diphenylacetylene with 2-*phpyH*

Table 2.2 summarizes the methodology used therein, which was mostly inspired by that used by Perez-Temprano *et al.*[12,16,47] for the purpose of comparison. Quite expectedly blank experiments in the presence of the sole $AgBF_4$ and excluding $[Cp^*CoI_2]_2$ led to no conversion (Table 2.2, entry 9). The contribution of the electrophilic activation pathway was confirmed by performing the condensation reaction with 2 eq. of $AgBF_4$ relative to 2-*phpyH* and no base, which provided a yield in the condensation product of 49 % (Table 2.2, entry 1). Under identical conditions the addition of molar

30 % of NaOAc (Table 2, entry 7) did not improve the yield in condensation product. However, the use of molar 30 % of LiNHAc raised the yield up to 71 % (Table 2.2, entry 8).

**Table 2. 2.** Performance of the catalyzed condensation 1,2-diphenylacetylene with 2-*phpy*H

| Entry | Base | Additive | Yield |
|---|---|---|---|
| 1 | no base | $AgBF_4$ (2 equiv) | 49% |
| 2 | LiNHAc | $NaBF_4$ (2 equiv) | 8% |
| 3 | LiNHAc | $NaBF_4$ (2 equiv) + $Cu(OAc)_2$ (2 equiv) | 0% |
| 4 | LiNHAc | $NaBF_4$ (2 equiv) + $CuCl_2$ (2 equiv) | 0% |
| 5 | LiNHAc | $AgBF_4$ (10 mol %) + $NaBF_4$ (1.9 equiv) | 10% |
| 6 | no base | $AgBF_4$ (10 mol %) + $NaBF_4$ (1.9 equiv) | 9% |
| 7 | NaOAc | $AgBF_4$ (2 equiv) | 48% |
| 8 | LiNHAc | $AgBF_4$ (2 equiv) | 71% |
| 9 | no base | $AgBF_4$ (2 equiv) no $[Cp^*CoI_2]_2$ | 0% |

General conditions: 2-*phpy*H (0.1 mmol, 1 equiv), diphenylacetylene (0.15 mmol, 1.5 equiv), $[Cp^*CoI_2]_2$ (0.005 mmol, 5 mol %), with or without LiNHAc (0.03 mmol, 30 mol %), DCE (5 mL), and additive, at 130 °C for 24 h. Trimethoxy benzene was used as internal $^1$H NMR reference.

Other variants entail the use of a preformed cobalt(III) solvato-metallacycle of 2-*phpy* as the catalyst. In almost all cases reported to date with Cp*Co catalysts the effective assistance of an auxiliary base was either not considered or not established.[253]

The role of the silver salt is particularly important, for it contributes to halide abstraction and to the necessary oxidation of transient Cp*Co(I) species produced in the reductive coupling step: reducing its amount to molar 10 % and replacing it by $NaBF_4$ for the purpose of ionic balance, expectedly cuts the yield in condensation product down to ~10 % (Table 2.2, entry 5). Worthy to note, its replacement by a copper(II) acetate in the presence of LiNHAc does not produce any annulation product (Table 2.2, entry 3).

Further condensation reactions (Table 2.3) were undertaken with other aromatic substrates using the conditions that afforded the best yields with 2-*phpyH* (Table 2.2, entry 8). All the considered substituted 2-arylpyridines provided the condensation

products with yields higher than 60% after 3 h of reaction at 130°C in DCE in a sealed Schlenk tube. Worthy to note, 1,2-diphenylquinoxaline and *N*,*N*-dimethylbenzylamine, which already showed no propensity to afford a cobaltacycle were left unchanged. Furthermore, *bzqH*, which showed moderate ability to form cobaltacycle **5a** provided the condensation product in 75 % yield after 24 h of reaction under the conditions of catalysis. Its parent dibenzo[*f,h*]quinoline, i.e *bzbzq*H, reacted more sluggishly affording the annulation product in 34 % yield after 24 h.

If this information plead in favor of a dominant electrophilic C-H bond activation pathway where an auxiliary base such as the heterocyclic substrate itself or any other base could act unbonded to the metal center for instance, the contribution of a concurrent CMD mechanism cannot be ruled out when LiNHAc is present. Worthy to note, in the case of a domino catalysis promoted by Cp*Co(III), Ackermann et al.[254] have indeed recently privileged the so-called base assisted intramolecular electrophilic-type substitution (BIES) mechanism rather than the CMD one even though the formulation of their mechanism is again very similar to that of the CMD where the formation of an agostic intermediate remains crucial.

However, this contribution might be minor if one considers that in the absence of $AgBF_4$ the conversion in the conditions required for the CMD mechanism to operate corresponds to the maximum achievable value in the absence of any oxidizing agent with 10 mol% catalyst (Table 2.2, entry 2).

Situations where two mechanisms might coexist are not specific to Co though and have been considered earlier by Davies, Macgregor et al. for the condensation of alkynes with 3-arylpyrazoles catalyzed by either $[Cp^*Rh(MeCN)_3][PF_6]_2$ or $[(p\text{-cymene})RuCl_2]_2$.[250] Another example addressed by Qu and Cramer[190] for the C-H bond functionalization with diazo compounds catalyzed by Cp*Co(III)/Rh(III) complexes tends to suggest the possible coexistence of two mechanisms of C-H bond activation. On the basis of the data collected in the present study the KIE might be a good indication of the nature of the dominating mechanism : an electrophilic activation (abbr. EA) of a C-H bond being expected to produce a much higher KIE than that of a reaction governed by the CMD mechanism[122] for which the kinetic determining step is the formation of the agostic intermediate **ag**. This assumption is supported by the data published by Cheng et al.[174] for the annulation reaction of *2-phpyH* with 1,2-

diphenylacetylene promoted by the $[Cp^*RhCl_2]_2/Cu[BF_4]_2/O_2$ mixture in 1,2-dimethoxyethane, which showed KIE values spanning 2.03 - 2.84.

**Table 2. 3.** Catalyzed condensation of various aromatic substrates with 1,2-diphenylacetylenea.

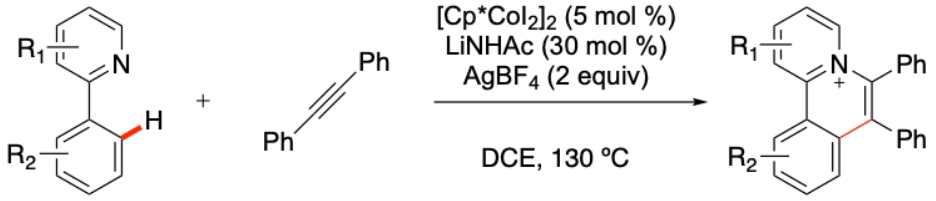


(1 equiv) (1.5 equiv)

| Entry | Substrates | Reaction time | Isolated yield |
|---|---|---|---|
| 1 | 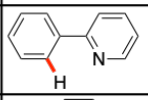 (2-*phpy*H) | 3 h | 61 % |
| | | 24 h | 71 % |
| 2 | 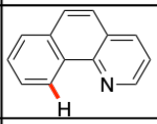 (*bzq*H) | 24 h | 75 % |
| 3 | 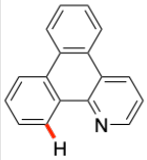 (*bzbzq*H) | 24 h | 38 % |
| 4 | 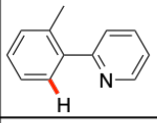 (2-*tolpy*H) | 3 h | 27 % |
| | | 24 h | 45 % |
| 5 | 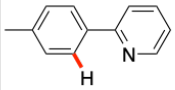 (4-*tolpy*H) | 24 h | 45 % |
| 6 | 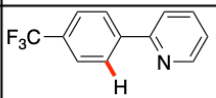 (4-*tfmphpy*H) | 24 h | 50 % |
| 7 | 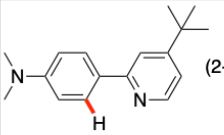 (2-*anpy*H) | 24 h | 0 % |
| 8 | 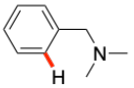 (*N,N*-dimethyl benzylamine) | 3 h | 0 % |
| | | 17 h | 0 % |
| 9 | 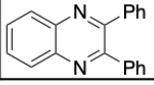 (2,3-diphenylquinoxaline) | 3 h | 0 % |
| | | 17 h | 0 % |

General conditions: substrates (0.1 mmol, 1 equiv), diphenylacetylene (0.15 mmol, 1.5 equiv), $[Cp^*CoI_2]_2$ (0.005 mmol, 5 mol %), LiNHAc (0.03 mmol, 30 mol %), $AgBF_4$ (0.2 mmol, 2 equiv), DCE (5 mL), at 130 °C for 24 h. Trimethoxy benzene was used as internal $^1H$ NMR reference.

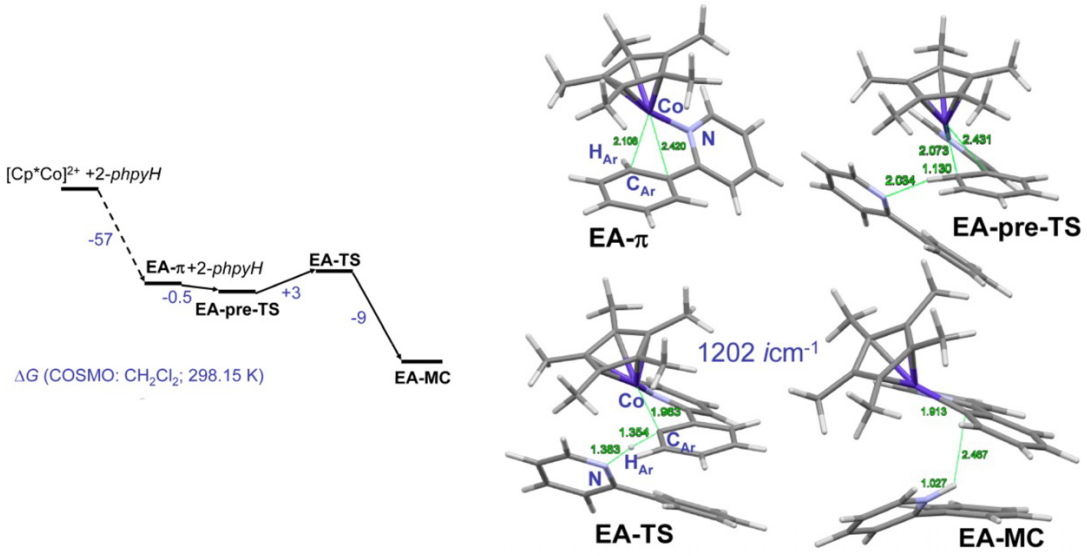


**Figure 2. 26.** Left: Gibbs enthalpy profile (in kcal/mol at *T*= 298.15 K) computed at the COSMO($CH_2Cl_2$)-ZORA-PBE-D3(BJ)/all electron TZP level for a model of the electrophilic activation of the $C_{Ar}$-$H_{Ar}$ bond of 2-*phpyH* with the exogenous intervention of external 2-*phpyH* acting as proton acceptor in the **EA-π-**to-**EA-MC** process via dicationic reactive complex **EA-pre-TS** and transition state **EA-TS**. Right: CSD-Mercury drawings of geometries and selected interatomic distances (green colored fonts) are given in Å.

We evaluated the KIE of the cyclocobaltation of a modeled EA mechanism that most likely occurs in reactions wherein excess Ag(I) salt is used: this hypothesis entails the formation of a 14-electron dicationic π-complex, i.e **EA-π** from the fictitious $[Cp^*Co]^{2+}$ species and 2-*phpyH*. In this mechanism a second exogenous molecule of 2-*phpyH* intervenes as a base to form reactive complex **EA-pre-TS** and abstract the $H_{Ar}$ proton via **EA-TS** to afford a dicationic molecular complex between the cobaltacycle and the protonated 2-phenylpyridine, i.e $[H(2\text{-}phpyH)]^+$. This scenario is slightly different from the one privileged by Qu and Cramer[190] for a Cp*Rh(III) electrophilic C-H bond activation mechanism which considered the preliminary Rh binding of the second 2-*phpy*H ligand prior to its migration to abstract the proton of the C-H bond, resulting in a large activation barrier of ca. 16 kcal/mol. The theoretical $KIE^{\rightarrow}$(4.6) and $KIE^{\leftarrow}$(6.3) values (Scheme 2.10) were computed by applying the simplified Bigeleisen method,[243]

considering the Born-Oppenheimer approximation on the pentadeuterophenyl fragment that undergoes metalation in **EA-pre-TS** and **EA-TS** and on the non-bonded *N*-deuterio,2-phenylpyridinium and the tetra deuterated phenylene of the metallacycle in molecular complex **EA-MC**. In such a scenario the proton abstraction step is the kinetic determining step and requires a rather low Gibbs enthalpy of activation (+3 kcal/mol) as compared to that required to the acetamidate-promoted CMD mechanism (ca. +7 kcal/mol, Figure 2.2), which demonstrates clearly that the EA mechanism is indeed a serious challenger to the CMD mechanism discussed previously.

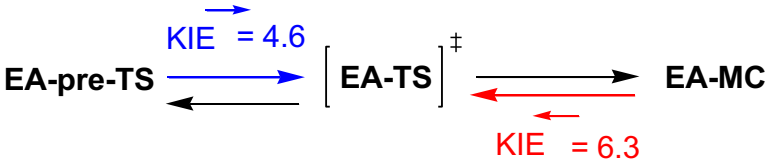


**Scheme 2. 10.** Kinetic isotope effects as determined by the Bigeleisen method from the Born-Oppenheimer treatment of the vibrational frequencies of protio and deuterio stationary points in Figure 2.26.

## 2.3. Conclusion

This chapter shows that cobaltacycles are not elusive and can be readily prepared in good yields via the base assisted CMD mechanism provided that the proper base is chosen to optimize the formation of the transient agostic intermediate. This choice of base can be greatly enlightened by theory like shown in this study, which considered necessary to approach the C-H bond activation mechanism by focusing attention on the role of the noncovalent interactions. The relevance of noncovalent interactions in the CMD-promoted cyclocobaltation is evident from the evolution of the so-called reaction site along reaction coordinates: the remarkable contribution of local electrostatic interactions and of the multipolar environment to the polarization of the $C_{Ar}$-$H_{Ar}$ bond prior to its activation by carbometallation and proton transfer to the neighboring base gives a valid rationale for the optimization not only of cyclocobaltation but also of cyclometallations using other 3d metals. This account of NCI constitutes in our view the cornerstone to the effective use of 3d metal complexes in C-H bond activation be it via the CMD or the EA mechanism. In this study, like in the previous

one dealing with cyclonickelation[179] wherein experimental validation was not sought, the benefit of using an acetamidate salt as base inferred from theory has now been confirmed experimentally. This study shows that the use of an acetamidate base/ligand reduces the residual chelation interaction with metal and consequently enhances the polarization of the C-H bond that is already engaged in a partly covalent partly noncovalent agostic interaction with the positively charged metal center. This is a promising basis for the further development of enantioselective C-H bond functionalization[255, 256] Cp*Co(III) catalysis[257] since it has been recently reported that amide-based enantiopure ligands[224, 258, 259] may not only assist C-H bond activation via the CMD mechanism but also induce stereo-discrimination at the level of the agostic transient in Pd(II)-promoted catalysis. By extension to Co(III) stereocenters the same concept could lead to effective stereo-differentiation in the proton transfer-carbometallation step and consequently initiate chiral induction in further steps, a feature that the herein merely addressed EA mechanism is less prone to achieve.

# Chapter 3. The oxidative collapse of cobaltacycles

The most relevant results of this chapter have been already published [reprinted with permission from J.P. DJUKIC et al. Fate of Cobaltacycles in Cp*Co-Mediated C–H Bond Functionalization Catalysis: Cobaltacycles May Collapse upon Oxidation via Co(IV) Species. *Organometallics* **2021**, 40, 15, 2624–2642. Copyright © 2021 American Chemical Society]. The theoretical aspects were done with the help of Yann CORNATON and Jean-Pierre DJUKIC.

## 3.1. Introduction

Cyclopentadienyl ligands have always played an important role in organometallic chemistry, mainly because they can stabilize metals with a variety of binding modes (Scheme 3.1). The $\eta^5$-pentamethylcyclopentadienyl[260], one widely used cyclopentadienyl ligand, generally shows more stability, solubility and crystallized easier when compared to its cyclopentadienyl analogues, so, it has received a lot of attention. In addition, Cp* has traditionally being considered an innocent ligand[260, 261] in an abundant literature[262-270], which means that it only provides electronic support for a metal and it is not involved in chemical reactions[271].

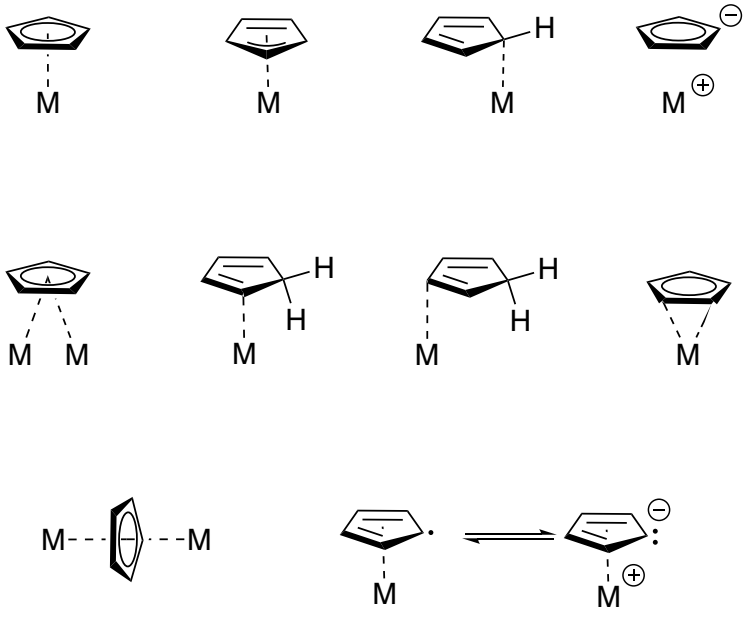


**Scheme 3. 1.** Distinct bonding modes for the cyclopentadienyl ligand.

However, in specific cases, the hydrogen atom can endo migrated to the carbon atom of the Cp* ligand[272-274]. For example, protonation of Cp*Rh(bpy) (bpy = 2,2′-bipyridyl), a catalyst for $H_2$ generation, yields a new rhodium(I) species bearing an $\eta^4$-Cp*H ligand with H positioned endo with respect to the rhodium center(Scheme 3.2). Moreover, we disclosed the crystal structure of an intriguing $I_3^-$ salt of a cationic Cp*-2-phenylpyridine condensation product in chapter 2, i.e [**1c**]$^+$ (Scheme 3.3), serendipitously discovered whilst attempting to grow crystals of **1a**. It was obvious that [**1c**]$^+$ resulted from the collapse of cobaltacycle **1a** by the cyclocondensation of the Cp* and 2-*phpy* ligands with the capture of an exogenous H atom. But this issue being overlooked in most reports dealing with the use of Cp*Co-based catalysts in aromatic C-H bond functionalization employing redox co-catalysts where cobaltacycles are central intermediates.[178, 271, 275, 276]

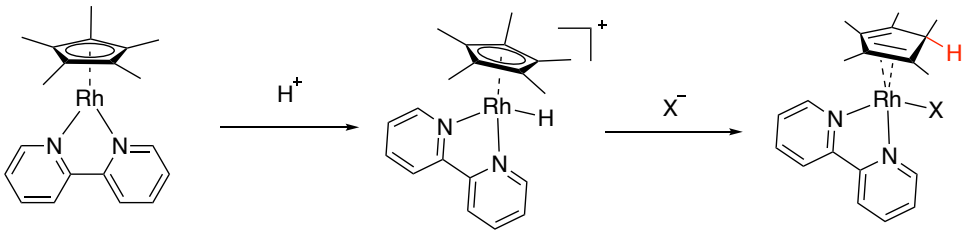


**Scheme 3. 2.** The example of Cp* ligand protonation.

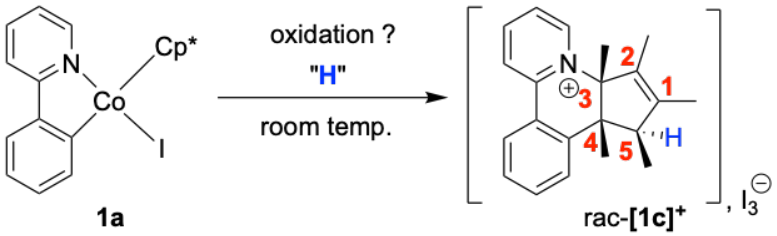


**Scheme 3. 3.** The example of collapse of cobaltacycle.

One can find a rare report on the metal-templated collapse of a metallacycle of a CpNi (II) complex reported by Ustinyuk et al.[277] where an azobenzene-based nickelacycle undergoes interligand condensation and metal decoordination under oxidative conditions, affording a new organic extended aromatic product (Scheme 3.4). It is probably because of the scarcity of similar reports that Cp* bound metallacycles of group 9 metals at the +I and +III formal oxidation states are usually considered as structurally viable[278] candidate catalysts.[178, 183, 279, 280] In the majority of reports dealing

with group 9 metallacycles bearing an heterochelating carbanionic ligand $^{281-}$ with Cp* bound metals, the latter ligand was, if not never, at least rarely shown to interfere explicitly with other ligands bound to the metal by other means but steric repulsion and synergetic “through bonds” electronic effects.

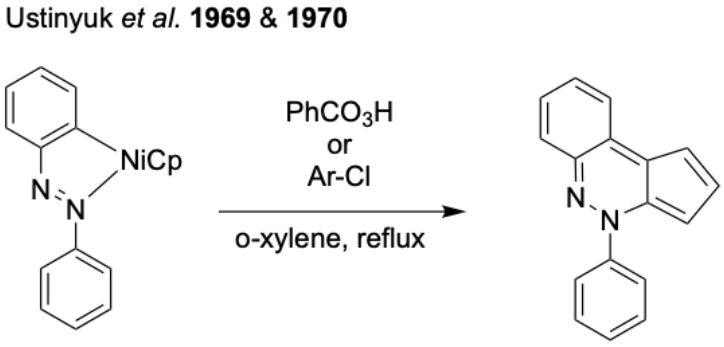


**Scheme 3. 4.** The example of collapse of a metallacycle of a CpNi (II) complex.

Hence, in this chapter, we will undertake to investigate the cyclocondensation reaction in cobaltacycles[144, 185, 282] of 2-phenylpyridine derivatives, and gain insight into their possible reaction mechanisms. Moreover, the introduced quantum theory of atom molecule-based $\Delta g^{inter}$ interaction score[283, 284]and IBSI index[285] is used to reveal the effect of oxidation of Co(III) cobaltacycles on the attractive noncovalent Cp*-*phpy* interactions and their possible role in this unexpected cyclocondensative collapse of cobaltacycles. Because such a demetallative cyclocondensation reaction, if relevant in its extent, could limit (if not compromise) further developments of Cp*Co(III) catalysts[271] at the industrial scale where recycling of metal catalysts might be crucial both for economic and environmental reasons.[286-290]

## 3.2. Results and discussion

### 3.2.1. Synthetic outlook

In chapter 2, the compound [**1c**][$I_3$][281] was crystallized from a solution that originally contained **1a**. The presence of $I_3^-$ as counter anion suggested that the initial solution of **1a** might have been contaminated by either $I_2$ or some $I_3^-$ salts introduced or formed

in the course of the synthesis of $[Cp^*CoI_2]_2$,[281] i.e the precursor of **1a**. Suspecting an oxidoreductive process responsible for the formation of the condensation product $[\mathbf{1c}]^+$, **1a** was hence reacted with two equiv. of $I_2$ in DCM for 16 h at 20°C (Scheme 3.5). The $^1H$ NMR analysis of the reaction mixture revealed the full conversion of **1a** into a mixture of various products among which a few could be identified readily from their specific signature: 2-(2'-iodophenyl)pyridine, tris-$\mu$-iodo dimeric Cp*cobalt (III) cation $\{[Cp^*Co]_2(\mu\text{-}I)_3\}^+$ and compound $[\mathbf{1c}]^+$ were formed in 40%, 66% and 33% yield according to $^1H$ NMR analysis.

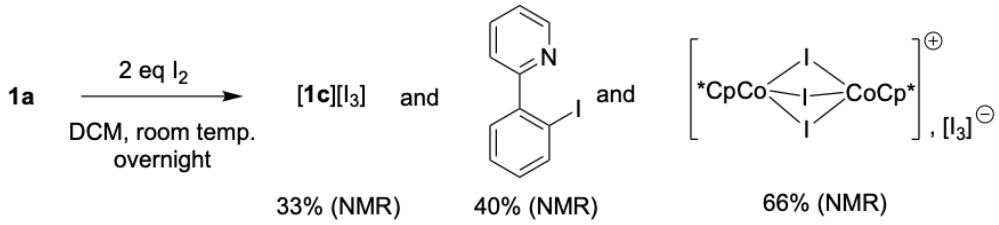


**Scheme 3. 5.** The reaction of **1a** with $I_2$.

From the $^1H$ NMR spectrum, compound $\{[Cp^*Co]_2(\mu\text{-}I)_3\}[I_3]$ produces one signal for the Cp* ligand at $\delta$ 1.80 ppm in $CDCl_3$. For $[\mathbf{1c}][I_3]$, the expected magnetic inequivalence of the five methyl groups of the cyclopentenyl fragment were observed at $\delta$ 0.96 (d), 1.31 (s), 1.56 (s), 1.75 (s) and 2.33(s) ppm, and the proton $H_5$ appears at $\delta$ 2.49 ppm as a broad multiplet integrating for 1 proton. Additional ES-MS analysis of the raw reaction mixture confirmed the presence of the latter three compounds alongside a strong signal of a $[Cp^*CoI]^+$ moiety at *m/z* 321, stemming from the dimer $\{[Cp^*Co]_2(\mu\text{-}I)_3\}^+$ showing up with lower intensity at *m/z* 769. Worthy to note, compound $\{[Cp^*Co]_2(\mu\text{-}I)_3\}[I_3]$ was successfully partly isolated and subsequently recrystallized to afford stable dark green crystals suitable for X-ray diffraction analysis. The structure of $\{[Cp^*Co]_2(\mu\text{-}I)_3\}[I_3]$ shows three symmetrically bridging iodo ligands between the two Co(III) centers that are distant from each other by 3.177(5) Å (Figure 3.1).

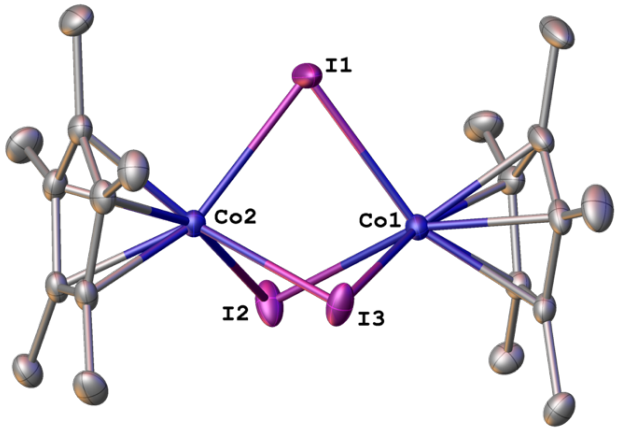


**Figure 3.1.** ORTEP diagram of the structure of {[Cp*Co]$_2$($\mu$-I)$_3$}[I$_3$], ellipsoids displayed at 50% probability. The hydrogen-atoms, $[I_3]^-$ and solvent molecules were omitted for clarity. Selected bond distances [Å] and angles [°]: Co1-I1 2.5873(5), Co1-I2 2.6123(5), Co1-I3 2.6320(5), Co2-I1 2.5847(5), Co2-I2 2.6300(5), Co2-I3 2.6242(5), I1-Co1-I2 86.677(15), I1-Co1-I3 87.706(15), I2-Co1-I3 86.301(15), I1-Co2-I2 86.363(15), I1-Co2-I3 87.927(15), I3-Co2-I2 86.099(14), Co2-I1-Co1 75.791(14), Co1-I2-Co2 74.599(14), Co2-I3-Co1 74.370(14).

This first test reaction clearly revealed that at least two pathways are involved in the observed oxidative decomposition of **1a**: 1) the reductive elimination of 2-(2'-iodophenyl)pyridine and 2) Cp*-*phpy* cyclocondensation, both triggered by the formal oxidation of the Co(III) center to either the open shell Co(IV) or the diamagnetic Co(V) state. The major question remaining to be answered being that of the origin of the "$H_5$" atom in [**1c**]$^+$ (Scheme 3.3).

Given the intricate mixture produced by the reaction of **1a** with $I_2$, as an alternative to the latter, we decided to probe the oxidizing property of the one-electron oxidant [$Ph_3C$][$BArF_{24}$].[291] The tritylium $[Ph_3C]^+$, which undergoes a swift decomposition[292] in the gas phase, is in solution a well-known stable multi-facetted Lewis acidic cation[293-297] that may act as a hydride[298] and/or a halide[299] abstraction agent but also as a one-electron oxidant[300-306] ($Ph_3C$• / $Ph_3C^+$ couple[307]) in the ground as well as in the excited state[308, 309] that may be involved also in the hydride abstraction process as reported by Mandon, Astruc et al.[310] Quite interestingly, to the best of our knowledge there has been no mention of any major drawbacks related to the oxidative properties of the

tritylium as “activator”, i.e as a halido ligand “remover”, in transition metal-mediated homogeneous catalysis. For instance hydrosilylation catalysis otherwise ineffective with Cp*-bound chloridoiridacycles[133, 134] can be triggered if a [$Ph_3C$][$BArF_{24}$] salt is added to the reaction mixture seemingly acting as a chloride scavenger.[128-131]

Subsequently, the reaction between **1a** and [$Ph_3C$][$BArF_{24}$] carried out at 25°C in DCM for 16 h produced [**1c**][$BArF_{24}$] with an NMR yield of 72% (Table 3.1, entry 1). In fact, $^1$H NMR spectroscopy monitoring showed that the reaction reached 100% conversion after only 30 min. It is also noteworthy that same experiment carried out with the chloridoiridacycle analog left the substrate unchanged. In addition, this reaction was also performed in DCE and $d_5$-PhCl to obtain the target product in 40% and 51% yields, respectively (Table 3.1, entries 5 and 6). The same reaction carried out using 2 equiv. of $AgPF_6$ as oxidant instead of [$Ph_3C$][$BArF_{24}$] was completed with 100% conversion of **1a** into a mixture of [**1c**][$PF_6$] in 70% NMR yield (Table 3.1, entry 2) and other aromatic products. Despite the fact that $Ag^+$ was also efficient in this reaction, the significant content in side organic products and the overall higher heterogeneity of the reaction mixture led us to privilege [$Ph_3C$][$BArF_{24}$] as a standard oxidant for further physical investigations.

Noteworthy, in order to check the radical mechanism, 1 or 4 equiv. of (2,2,6,6-tetramethylpiperidin-1-yl)oxy (TEMPO) was added into the reaction mixture, which resulted in a significant inhibition (Table 3.1, entries 3 and 4) of the reaction perceptible from an NMR yield decrease to 35% after 17 h, suggesting that open shell species and radicals essential to the formation of [**1c**]$^+$ are partly trapped by the rather bulky nitroxyl radical.

**Table 3.1.** Reaction of **1a** with $[Ph_3C][BArF_{24}]$ in various conditions.

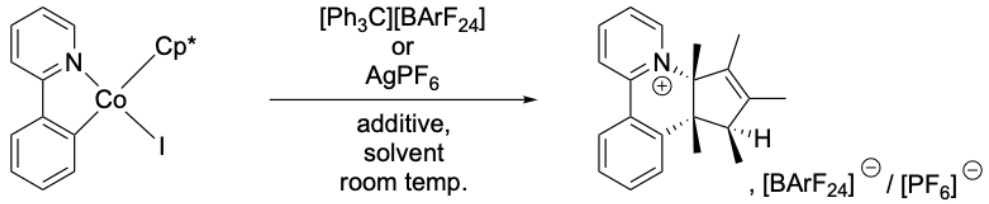


| Entry | Oxidant | Solvent | Additive | Product(s) (yield) |
|---|---|---|---|---|
| 1 | $[Ph_3C][BArF_{24}]$ | DCM | no additive | [**1c**][$BArF_{24}$] (72%[a], 29%[b]) |
| 2 | $AgPF_6$ | DCM | no additive | [**1c**][$PF_6$] (70%[a]) |
| 3 | $[Ph_3C][BArF_{24}]$ | DCM | TEMPO (1 equiv) | [**1c**][$BArF_{24}$] (35%[a]) |
| 4 | $[Ph_3C][BArF_{24}]$ | DCM | TEMPO (4 equiv) | [**1c**][$BArF_{24}$] (17%[a]) |
| 5 | $[Ph_3C][BArF_{24}]$ | DCE | no additive | [**1c**][$BArF_{24}$] (40%[a]) |
| 6 | $[Ph_3C][BArF_{24}]$ | [$D_5$].PhCl | no additive | [**1c**][$BArF_{24}$] (51%[a]) |

General conditions: under argon atmosphere, **1a** (0.1 mmol, 1 eq), $[Ph_3C][BArF_{24}]$ (0.1 mmol, 1 eq) or $AgPF_6$ (0.2 mmol, 2 eq), DCM (5 mL), 25°C, 16 h. [a] $^1H$ NMR yield in the presence of 1,3,5-trimethoxybenzene as an internal standard. [b] isolated yield.

Compound [**1c**][$BArF_{24}$] was isolated pure by repeated recrystallization with a major loss of material due to the difficulty that arose in the separation of this salt from other polar Co-containing residues (isolated yield: 29 %). The structure of the cation of [**1c**][$BArF_{24}$] obtained by X-ray diffraction analysis is in all aspects identical (Figure 3.2) to that already published[281] for [**1c**][$I_3$]. Alongside this organic salt, amounts of $Ph_3C$-I and $\{[Cp^*Co]_2(\mu\text{-}I)_3\}^+$ were also identified by ES-MS analysis. More interesting was the formation of small amounts of *N*-protio,2-phenylpyridinium indicating that even with $[Ph_3C][BArF_{24}]$ the hydrodechelation of the *phpy* ligand jointly with the release of $\{[Cp^*Co]_2(\mu\text{-}I)_3\}[BArF_{24}]$ is a competing process.

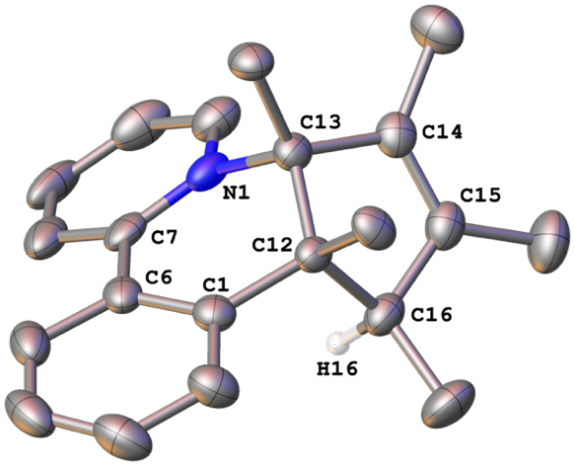


**Figure 3. 2**. ORTEP-type drawings of the structures of [**1c**][$BArF_{24}$] at 50% probability with partial atom numbering. The [$BArF_{24}$] anion and lattice solvent were omitted for clarity. Selected bond distances [Å] and angles [°]: C1-C12 1.528(3), C13-N1 1.552(3), C12-C13 1.545(3), C13-C14 1.521(3), C14-C15 1.335(4), C15-C16 1.513(4), C12-C16 1.556(3), C1-C12-C13 113.23(19), C14-C13-N1 108.51(19), C12-C13-N1 108.84(18), C15-C14-C13 110.0(2), C15-C16-C12 101.1(2).

Next, the scope of the tritylium-triggered condensation reaction was examined with other Cp*-bound cobaltacycles (Scheme 3.6), i.e **4a, 6a, 7a** and **8a**, which were synthesized via cyclometallation of Cp*Co(III)-complex assisted by acetamidate mentioned in Chapter 2. All new cobaltacycles (**6a, 7a** and **8a)** were fully characterized by $^{1}H$ and $^{13}C$ NMR, ESI mass spectroscopy, and elemental analysis. And the structures of **7a** and **8a** were determined by X-ray diffraction analysis from suitable single crystals (Figure 3.3). All reactive towards [$Ph_3C$][$BArF_{24}$], although showing distinct outcomes depending on the presence (**4a**, **6a**)[281] or absence (**7a**, **8a**) of methyl hydrogens substractable by $[Ph_3C]^+$ (Table 3.2). The data listed in Table 3.2 were all acquired under standard conditions of reaction time of 17h at room temperature.

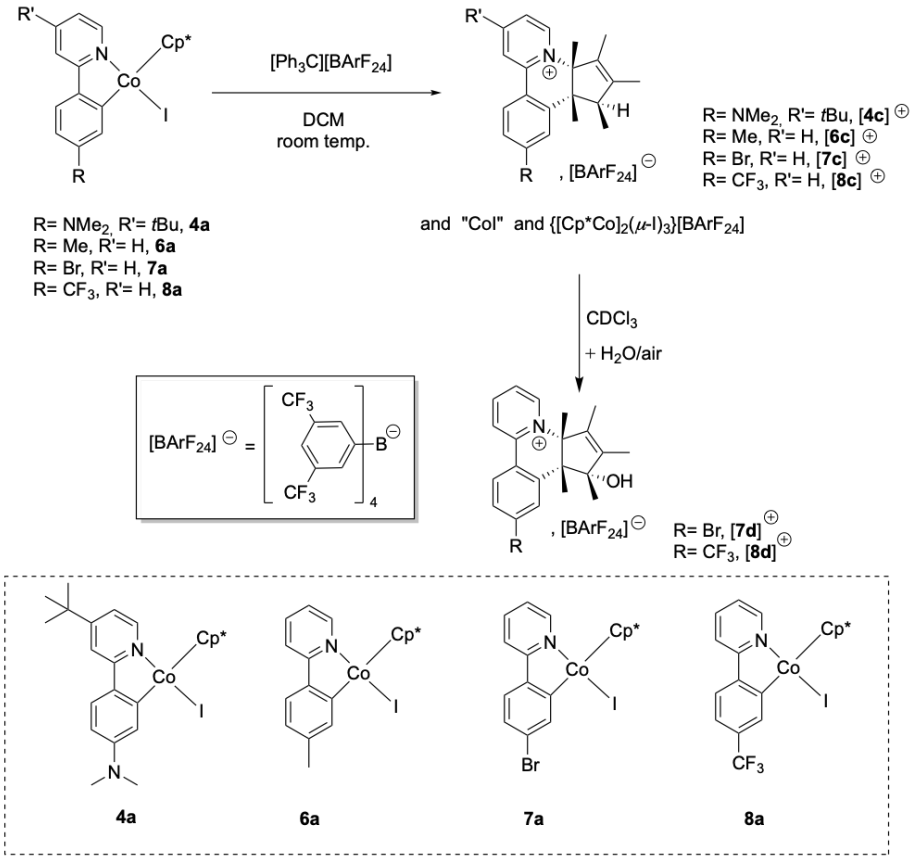


**Scheme 3. 6.** The Co-templated oxidative cyclocondensation of different Cp*-bound cobaltacycles.

**Table 3. 2.** Reaction of Co(III) cobaltacycles with $[Ph_3C][BArF_{24}]$ in DCM

| Entry | Complex | Solvent (atm.) | Product(s) (yield) |
|---|---|---|---|
| 1 | **4a** | DCM (Ar) | [**4c**][$BArF_{24}$] (0%) |
| 2 | **6a** | DCM (Ar) | [**6c**][$BArF_{24}$] (0%) |
| 3 | **7a** | DCM (Ar) | [**7c**][$BArF_{24}$] (57%[a]) |
| 4 | **7a** | DCM (ambient air) | [**7c**][$BArF_{24}$] (84%[a], 37%[b]) |
| 5 | **7a** | DCM (Ar) and $CDCl_3$ (air) | [**7d**][$BArF_{24}$] (21%[b]) |
| 6 | **8a** | DCM (Ar) | [**8c**][$BArF_{24}$] (63%[a]) |
| 7 | **8a** | DCM (ambient air) | [**8c**][$BArF_{24}$] (88%[a], 35%[b]) |
| 8 | **8a** | DCM (Ar) and $CDCl_3$ (air) | [**8d**][$BArF_{24}$] (17%[b]) |

General conditions: under argon atmosphere, cobaltacycles (0.1 mmol, 1 eq), $[Ph_3C][BArF_{24}]$ (0.1 mmol, 1 eq), DCM (5 mL), 25°C, 16 h. a $^1H$ NMR yield in the presence of 1,3,5-trimethoxybenzene as an internal standard. [b] isolated yield.

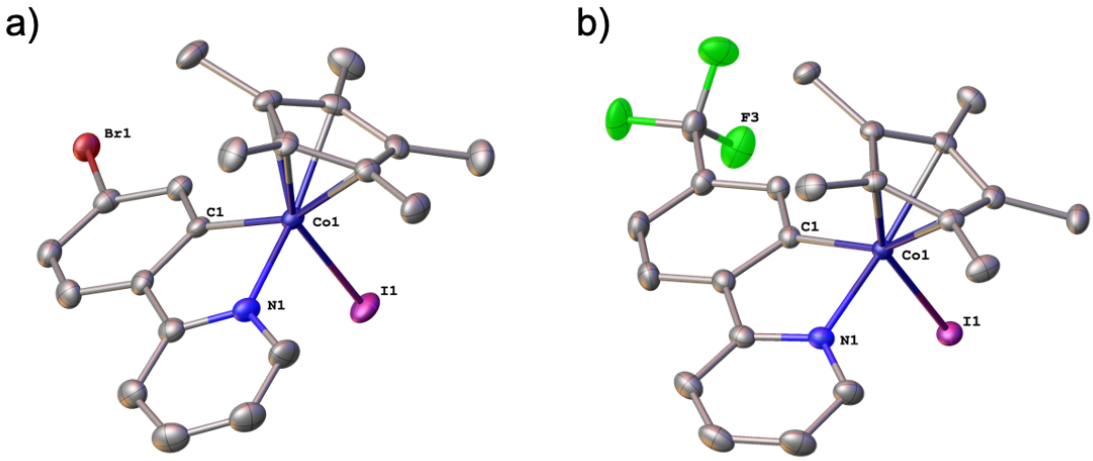


**Figure 3.3.** ORTEP-type drawings of the structures of (a) **7a** and (b) **8a** at 50% probability with partial atom numbering. The hydrogen-atoms on the carbon were omitted for clarity. (a) Selected bond distances [Å] and angles [°]: C1-Co1 1.917(5), N1-Co1 1.957(4), I1-Co1 2.5633(7), C1-Co1-I1 88.76(14), N1-Co1-I1 92.37(13), C1-Co1-N1 82.63(18). (b) Selected bond distances [Å] and angles [°]: N1-Co1 1.9546(14), Co1-I1 2.5625(2), C1-Co1 1.9204(15), C1-Co1-N1 82.77(6), C1-Co1-I1 90.54(4), N1-Co1-I1 94.78(4).

Only the substrates bearing –Br and $–CF_3$ substituents, i.e **7a** and **8a** (Table 3.2, entries 3 and 6), afforded cyclic pyridiniums [**7c**]$^+$ and [**8c**]$^+$, the $^1$H NMR signature of which could be recognized readily in the spectrum of the raw mixture from the specific pattern of methyl groups showing in the $\delta$ 0.9-2.5 ppm range. But, the reaction with compounds **4a** and **6a** yielded untraceable mixtures of soluble and insoluble residues with no distinguishable main product (Table 3.2, entries 1 and 2). The structures of [**7c**]$^+$ and [**8c**]$^+$were both established by X-ray diffraction analysis (Figure 3.4), which revealed features akin to those of [**1c**]$^+$.

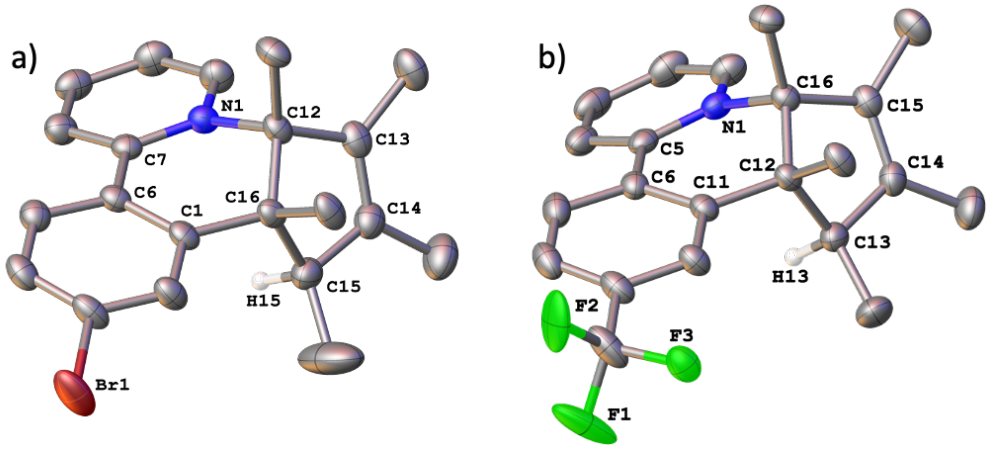


**Figure 3. 4.** ORTEP-type drawings of the structures of (a) [**7c**]$^{+}$ and (b) [**8c**]$^{+}$ at 50% probability with partial atom numbering. The [$BArF_{24}$] anion and lattice solvent were omitted for clarity. (a) Selected bond distances [Å] and angles [°]: C1-C16 1.516(3), C12-N1 1.546(3), C12-C13 1.521(4), C13-C14 1.345(4), C14-C15 1.499(4), C15-C16 1.556(4), N1-C12-C16 109.33(19), C14-C13-C12 109.7(2), C13-C14-C15 111.5(2), C14-C15-C16 102.5(2), C1-C16-C15 113.2(2), C12-C16-C15 101.5(2), N1-C12-C16 109.33(19). (b) Selected bond distances [Å] and angles [°]: C16-N1 1.550(2), C11-C12 1.512(3), C12-C13 1.562(3), C13-C14 1.519(3), C14-C15 1.329(3), C15-C16 1.525(3), C12-C16 1.555(2), C11-C12-C16 113.19(15), C11-C12-C13 113.44(15), N1-C16-C12 108.87(14), C14-C13-C12 101.51(15), C14-C15-C16 110.12(17), C15-C16-N1 107.94(14), C15-C14-C13 111.47(17).

Cobaltacycle **5a**[281] also conducted the cyclocondensation reaction, it is noteworthy that there was no observed generation of the target product in the presence of [$Ph_3C$][$BArF_{24}$], but the **5a** was collapsed and fully converted to afford the Cp*Co-dimer complex {[$Cp^*Co$]$_2$($\mu$-I)$_3$}[$BArF_{24}$] and the product of hydrodemetalation (Scheme 3.7), that is namely the *N*-protonated benzo[*h*]quinoline [**5a**'][$BArF_{24}$],[311] the structure of which was ascertained by X-ray diffraction analysis (Figure 3.5).

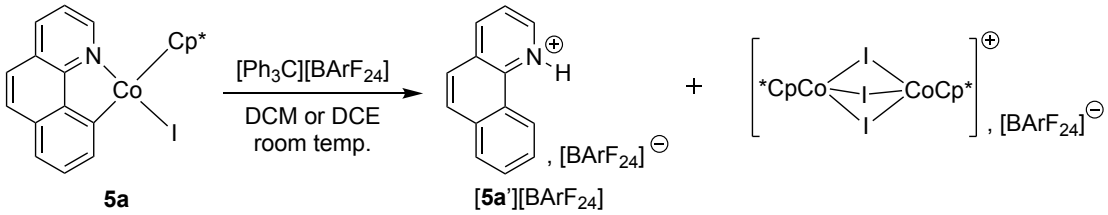


**5a** [**5a**'][$BArF_{24}$]

**Scheme 3. 7.** The cyclocondensation reaction of **5a** with [$Ph_3C$][$BArF_{24}$]

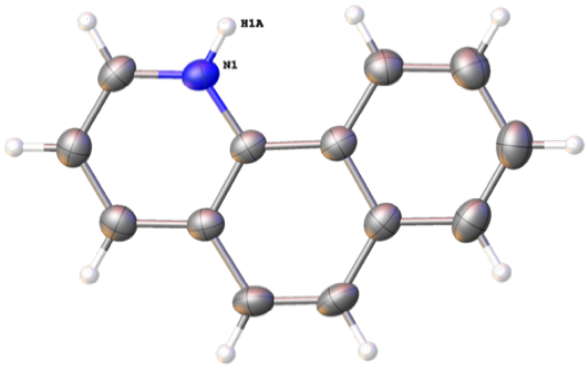


**Figure 3. 5.** ORTEP-type drawings of the structures of [**5a'**][$BArF_{24}$] at 50% probability with partial atom numbering. The [$BArF_{24}$] anion were omitted for clarity.

Quite intriguing is that when the crude products of reactions of **7a** and **8a** with [$Ph_3C$][$BArF_{24}$] were analyzed by NMR using $CDCl_3$, the crystals of [**7d**][$BArF_{24}$] and [**8d**][$BArF_{24}$] were obtained in the NMR tubes, respectively, and their structures were determined by X-ray diffraction analysis (Figure 3.6). And the reason for these results might be the contamination of $CDCl_3$ solvent by the adventitious moisture of air. Then, the related experiments were performed (Scheme 3.3), after the cyclocondensation reaction, undried $CDCl_3$ was added into the raw reaction residue obtained upon DCM evaporation to form the compounds [**7d**][$BArF_{24}$] and [**8d**][$BArF_{24}$] after an overnight reaction (Table 3.2, entries 5 and 8), which were readily isolated as they showed much lower solubility in $CDCl_3$ than their respective precursors.

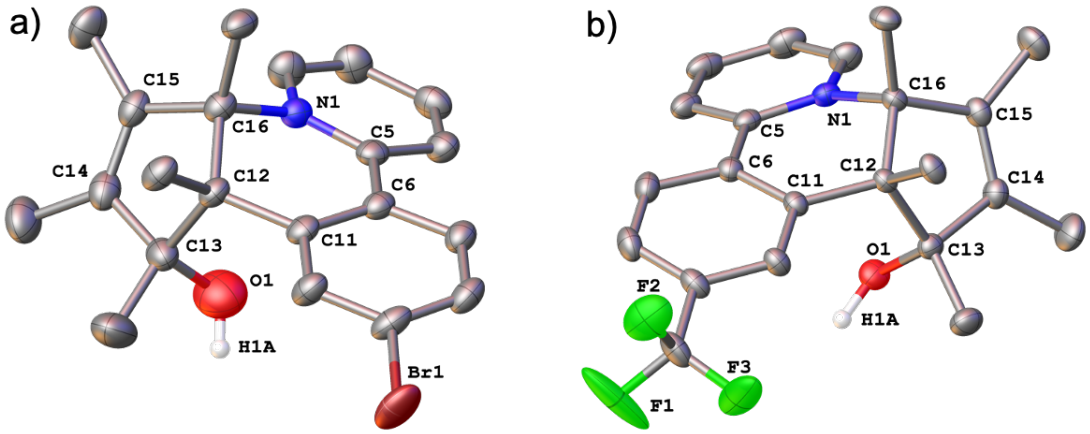


**Figure 3. 6.** ORTEP-type drawings of the structures of (a) [**7d**][$BArF_{24}$], and (b) [**8d**][$BArF_{24}$] at 50% probability with partial atom numbering. The [$BArF_{24}$] anion and lattice solvent were omitted for clarity. (a) Selected bond distances [Å] and angles [°]: C11-C12 1.518(5), C12-C13 1.563(5), C13-O1 1.409(6), C13-C14 1.506(6), C14-C15 1.336(6), C15-C16 1.519(5), C16-N1 1.548(5), C12-C16 1.553(5), C11-C12-C16 113.6(3), C11-C12-C13 112.6(3), O1-C13-C14 108.9(4), O1-C13-C12 110.0(3), C14-C13-C12 102.1(3), C15-C14-C13 111.5(3), C14-C15-C16 110.6(3), C15-C16-N1 108.5(3), C15-C16-C12 101.5(3). (b) Selected bond distances [Å] and angles [°]: C11-C12 1.5109(19), C12-C13 1.572(2), C13-O1 1.4440(18), C13-C14 1.512(2), C14-C15 1.335(2), C15-C6 1.527(2), C16-N1 1.5427(19), C12- C16 1.557(2), C11-C12-C16 113.41(12), C11-C12-C13 112.72(11), C16-C12-C13 102.23(11), O1-C13-C14 106.60(12), O1-C13-C12 109.67(12), C15-C14-C13 112.09(13), C14-C15-C16 110.32(13), C15-C16-N1 108.51(12), C15-C16-C12 101.94(12), N1-C16-C12 110.26(11).

To gain more insights into whether the adventitious moisture of air affects the cyclocondensation reaction of the cobaltacycles bearing –Br and $–CF_3$ substituents, the comparative experiments were also performed (Table 3.2, entries 4 and 7). However, the results were unexpected, whereby the yields of the cyclocondensation were significantly higher in ambient air than under argon protection, in addition, the formation of Cp*Co-dimer complex ({[Cp*Co]$_2$($\mu$-I)$_3$}[$BArF_{24}$]) was not observed at the end of the reaction.

Comparing their structures of [**7d**][$BArF_{24}$], [**8d**][$BArF_{24}$] with [**7c**][$BArF_{24}$], [**8c**][$BArF_{24}$], it was observed that the H atom at the $C_5$ position was replaced by -OH group, which suggests that they may result from the hydroxylation of the $C_5$-H position. The interference of Co species[312] released by the cyclocondensation process with the unreacted tritylium cation capable to interact with $O_2$ and/or water to form possible tritylperoxo species[313] can be suspected in this hydroxylation[140].

Particularly informative is the reaction of the chlorido analogue of **1a**, i.e **9a**, and the cationic cobaltacycle, i.e **1b**, with [$Ph_3C$][$BArF_{24}$] which afforded [**1c**][$BArF_{24}$] in 21 % and 10 % yield (NMR yield) respectively, at room temperature after about 17 h of reaction in DCM (Scheme 3.8 and 3.9). Interestingly, in the case of cationic cobaltacycle, the yield increased to 45 % after 48 h.

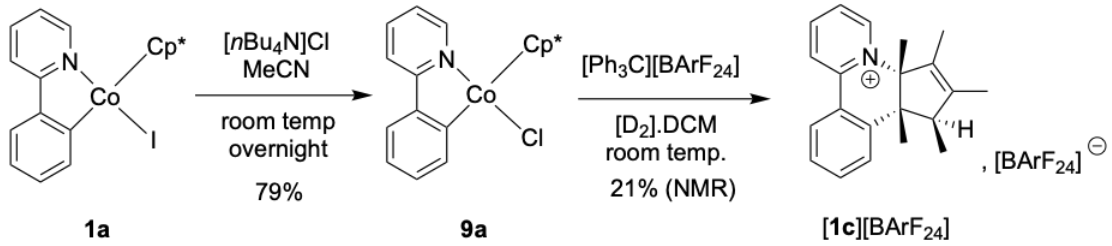


**Scheme 3. 8.** Synthesis of **9a** and its reaction with [$Ph_3C$][$BArF_{24}$].

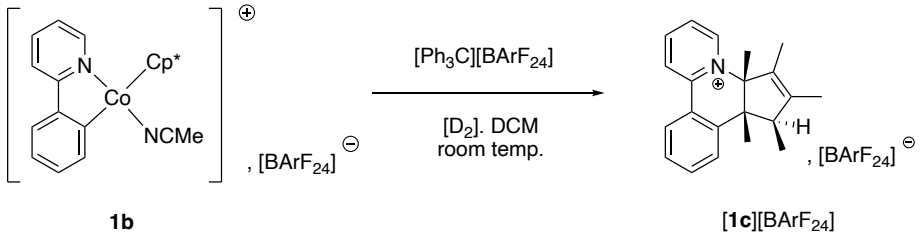


**Scheme 3. 9.** The cyclocondensation reaction of **1b** with [$Ph_3C$][$BArF_{24}$].

In addition to the Cp*containing cobaltcycles, the Cp-containing cobaltcycle **10a** (Figure 3.7a) is also undergoes cyclocondensation reaction. And the result is particularly striking (Scheme 3.10). The complex **10a** was readily synthesized via cyclocobaltation of 2-*phpy*H with $[CpCoI_2]_2$. Then the reaction of **10a** with [$Ph_3C$][$BArF_{24}$] carried out in DCM at room temperature yielded a mixture of mostly untraceable products, among which the condensation product [**10c**]$^+$ (Figure 3.7b) was

isolated in ca. 12% yield and crystallized. Compound [**10c**]$^+$ differs from the previous condensation products by the cationic spiro motif resulting formally from the condensation of the *phpy* ligand to the same carbon atom at the Cp ligand in combination with a prototropy. The incorporation of two 2-phenylenepyridine units in [**10c**]$^+$ obviously entails two distinct processes of intra- and intermolecular nature that, for obvious structural reasons, cannot occur with the Cp* complex **1a**.

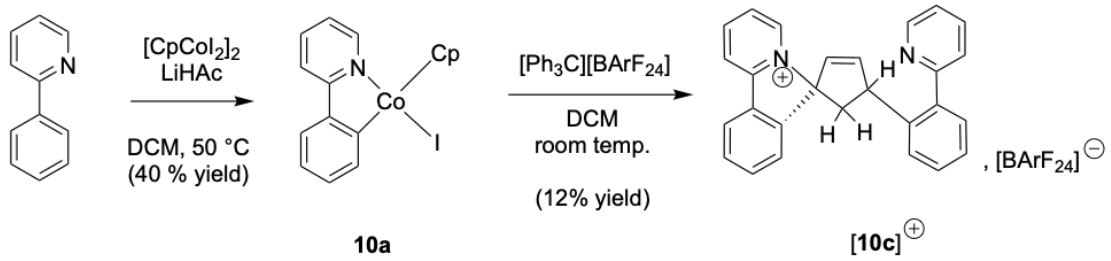


**Scheme 3. 10.** Synthesis of **10**a and its conversion to [**10c**][BArF24] upon treatment with [$Ph_3C$][$BArF_{24}$].

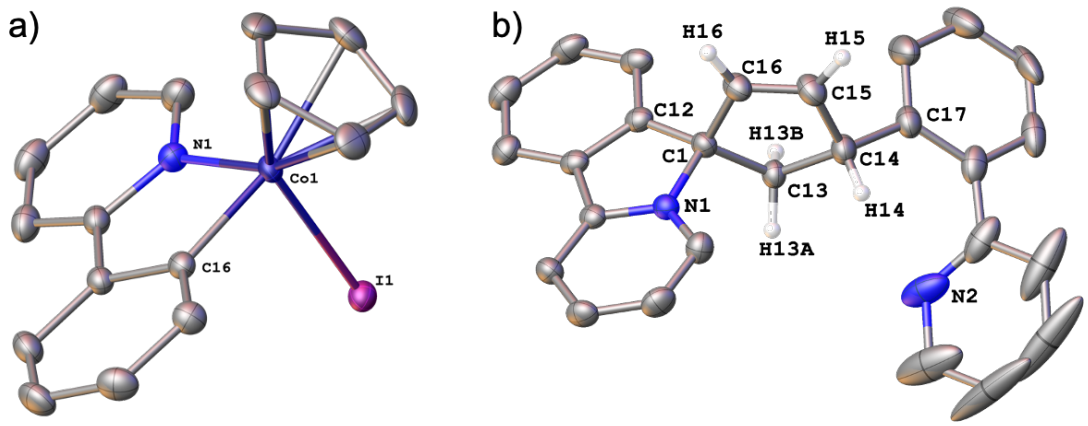


**Figure 3. 7.** ORTEP-type drawing of the structure of (a) **10a** and (b) [**10c**][$BArF_{24}$] at 50% probability with partial atom numbering. The [$BArF_{24}$]$^-$ anion and solvent were omitted for clarity. (a) Selected bond distances [Å] and angles [°]: I1-Co1 2.5767(3), Co1-N1 1.9355(19), Co1-C16 1.934(2), N1-Co1-I1 90.25(6), C16-Co1-I1 92.10(6), C16-Co1-N1 83.13(8). (b) Selected bond distances [Å] and angles [°]: C1-C12 1.494(3), C1-C16 1.510(3), C1-N1 1.523(3), C1-C13 1.554(3), C13-C14 1.548(3), C14-C15 1.507(4), C15-C16 1.318(4), C14-C17 1.519(3), C12-C1-C16 116.6(2), C12-C1-N1 99.79(18), C16-C1-N1 109.58(19), C12-C1-C13 115.43(19), N1-C1-C13 111.97(19), C16-C1-C13 103.60(19), C14-C13-C1 105.63(19), C15-C14-C13 102.8(2), C16-C15-C14 113.5(2), C15-C16-C1 111.5(2).

### 3.2.2. Isothermal titration calorimetry (ITC) experiments

Isothermal titration calorimetry (ITC) is one of the physical techniques that directly measures the heat discharged or consumed all along a bimolecular reaction. It is also the only method capable of determining the enthalpy, entropy, and the Gibbs free energy of a reaction in a single titration experiment. The microcalorimeter has two cells, as shown in Figure 3.8: one contains solvent and acts as a reference cell, the other contains the sample, into which a binding partner is titrated using an injection syringe. Heat sensing devices detect temperature differences between the cells when binding occurs in the sample cell and give feedback to the heaters, which compensate for this difference and return the cells to equal temperature.

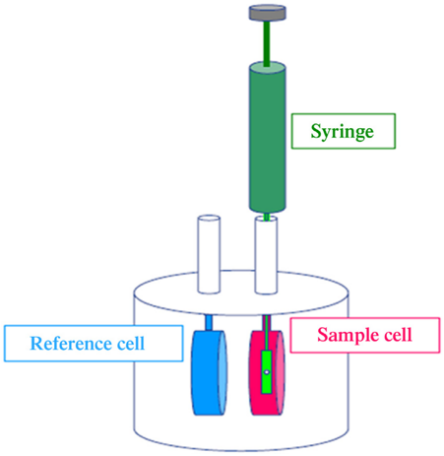


**Figure 3. 8.** Instrumentation of the typical isothermal titration calorimetry.

In this study, the thermochemistry of the reaction of **1a** with $[Ph_3C][BArF_{24}]$ was addressed by isotherm titration calorimetry at +25.00 °C in 1,2-dichloroethane (DCE); the cobalt complex was placed in a 1 mL cell and the tritylium salt in a servo-controlled injection syringe. Quite interestingly the heat flow decreased steadily down to a marked inflexion point at a $[Ph_3C][BArF_{24}]$ /**1a** ratio *n* of ~1:1 (Figure 3.9). The enthalpy of reaction was determined from the raw values of heat flow corrected by subtraction of the residual heat peaks at $n$>1.5:1 as $\Delta H$= -13.7 ± 0.5 kcal/mol (from three independent titrations), which is the total exothermicity of all the chemical processes that take place under those conditions up to the heat inflexion point before athermicity, that is namely: the oxidation of **1a** and the cyclocondensation reaction, dechelation by protonation, possible radical captures and recombination in which it is expected that the solvent or any H-atom donor species might be a player.

A control reaction carried out under identical conditions was checked by $^{1}H$ NMR spectroscopy and showed that a yield of 40% in [**1c**]$^{+}$ could be achieved (Table 3.1, entry 5), suggesting that about 60% of the amount of tritylium cation might be diverted to an oxidative chemical pathway either disconnected from or instrumental to the formation of [**1c**]$^{+}$

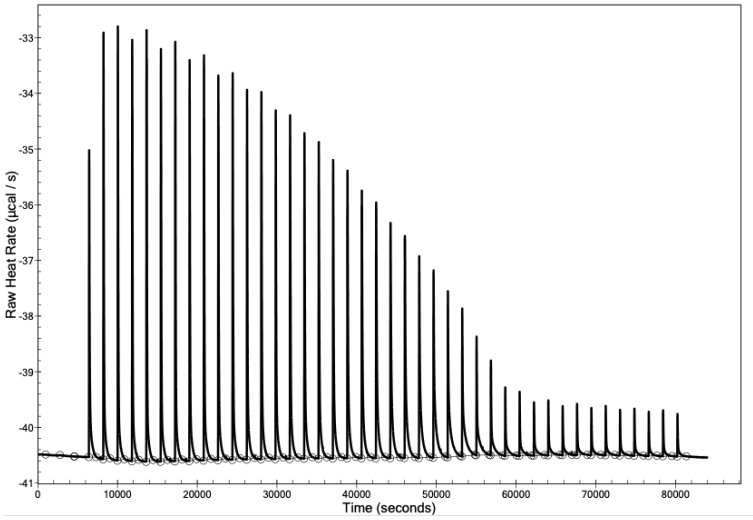


**Figure 3. 9.** Thermographic trace of the isotherm calorimetric titration of a solution of **1a** (0.94 mM) by sequential addition of 2 µL of a solution of [$Ph_3C$][$BArF_{24}$] (19.6 mM) in DCE at 25°C in an argon-filled glovebox. Individual heat flow peaks correspond to the response of the cell containing **1a** after the addition of portions of a solution of [$Ph_3C$][$BArF_{24}$]. The inflexion point considered at the 29$^{th}$ peak (at ca. 55000 s) corresponds to a *n*=1:1 stoichiometry.

### 3.2.3. Attempts to track down the H atom source

To trace the origin of the H atom incorporated in [**1c**]$^{+}$, [**7c**]$^{+}$ and [**8c**]$^{+}$, two sets of experiments were carried out using $^{2}H$-labeled molecules, expecting that a major isotopic effect could allow the identification of the main source of H atom in the reaction of **1a** with [$Ph_3C$][$BArF_{24}$] (Scheme 3.11).

The first set consisted of two parallel reactions in deuterated and non-deuterated solvents, namely $CD_2Cl_2$ and $CH_2Cl_2$, under identical conditions. $^{1}H$ NMR analysis of

the raw reaction mixtures indicated that the yields in [**1c**]$^+$ were the same in both cases with no incorporation of deuterium at the key position $H_5$.

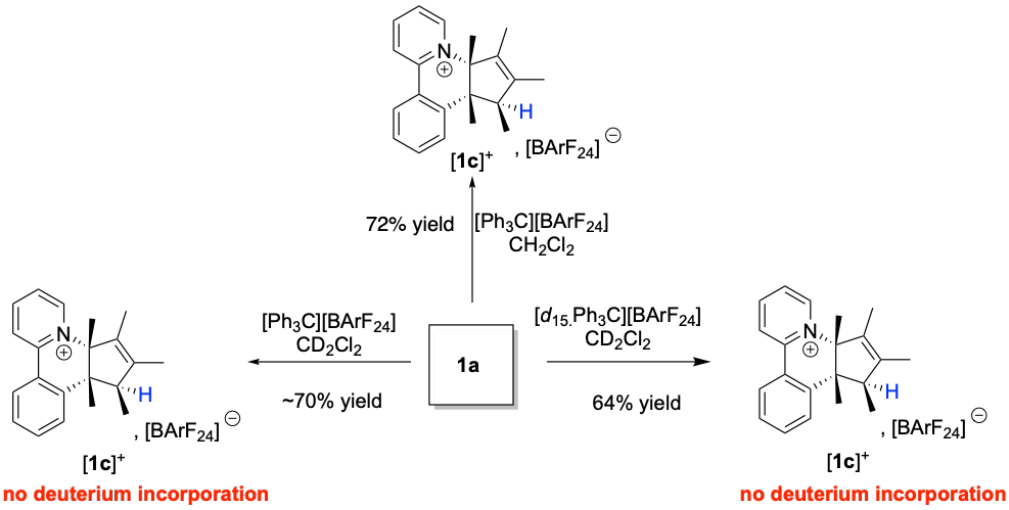


**Scheme 3. 11.** Use of $CD_2Cl_2$ and/or [$d_{15}$-$Ph_3C$][$BArF_{24}$] that does not result in the incorporation of $^2H$ at the $C^5$ position in [**1c**][$BArF_{24}$].

It is well established that the trityl radical recombines to give a polyaromatic species, i.e the so-called the Gomberg-Jacobson-Lankamp-Nauta-MacLean asymmetric quinoid-like structure[313] (Scheme 3.12) that is more favorable than $Ph_3C$-$CPh_3$, which displays a weak reactive C-C bond. This compound could be seen as another rather favorable H atom donor according to the DFT-computed thermochemistry. So, the second experiment, ran in $CD_2Cl_2$, using {[$D_{15}$].$Ph_3C$}[$BArF_{24}$][314, 315] afforded [**1c**][$BArF_{24}$] in 64% yield with no incorporation of deuterium at the $H_5$ position, seemingly rules out this scenario as well.

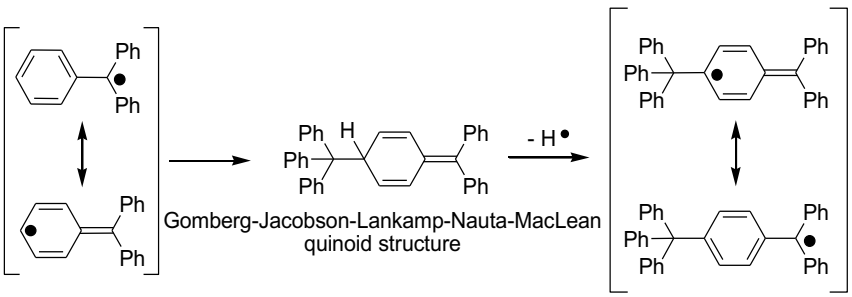


**Scheme 3. 12.** The so-called the Gomberg-Jacobson-Lankamp-Nauta-MacLean asymmetric quinoid-like structure as a source of H•.

The latter result suggests that the most probable source of H atom is either the $BArF_{24}$ anion, **1a** or any of the products of its degradation such as 2-phenylpyridine, $\{[Cp^*Co]_2(\mu\text{-}I)_3\}[BArF_{24}]$. To eventually rule out $[BArF_{24}]^{-}$ anion as a potential source of H atom, the reaction of **1a** with $[Ph_3C][PF_6]$[314, 315] was undertaken, which led to the formation of [**1c**]$^+$ in yields similar to that obtained with the tritylium $BArF_{24}$ salt. Whether the H atom is captured directly from **1a** by an oxidized form of **1a** or from an organic source such as $Ph_3CH$, was not elucidated experimentally. Triphenylmethane could indeed arise from an hydride abstraction from the Cp* ligand of **1a** by $[Ph_3C]^+$ if one refers to the work of Tilley et al.[316] that was originally carried out with a tetraphenyl borate salt. However, the presence of $Ph_3CH$ was not overwhelming in all analyzed reaction media. Furthermore, like shown below in the theoretical investigation, $Ph_3CH$ is a very unlikely source of H radical for thermochemical reasons.

It is worth noting that the treatment of **1a** with 1 equiv. of $CF_3SO_3H$ in $CH_2Cl_2$ (Scheme 3.13) swiftly led to the hydro-decobaltation of the *phpy* ligand with the formation of *N*-protio,2-phenylpyridinium, suggesting that any formation of $H^+$ in the reaction of **1a** with $[Ph_3C]^+$ should result in a significant hydrodemetallation of the *phpy* ligand, which is not the case. Treatment with 1 equiv of a weaker acid, such AcOH, under identical conditions resulted in the hydrodemetalation of **1a** and the formation of 2-phenylpyridine, though in lower yield: 14% after 5h and 34% after 24h.

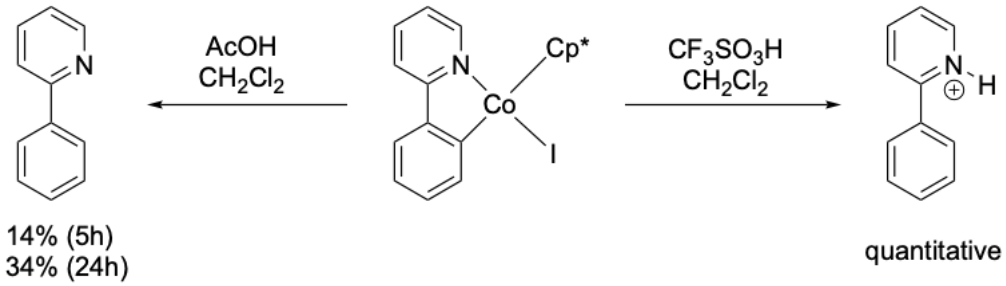


**Scheme 3. 13.** Treatment with acid that results in hydrodemetalation.

Also, the effect on the reaction of **1a** with $[Ph_3C][BArF_{24}]$ in the present of 5 equiv of $H_2O$ or $D_2O$ that was probed under an atmosphere of either argon or air (Table 3.3): when the atmosphere is disregarded, with $D_2O$ an $^1H$ NMR analysis of the reaction mixture revealed no incorporation of deuterium at the $C_5$ position of [**1c**][$BArF_{24}$].The formation of the latter in the presence of water occurred with a lower yield when the

reaction was run under argon(~10%) in comparison to that run under air (~80%). This result suggests that the combination of water contamination with oxidizing conditions (one-electron oxidant + air) favors the formation of [**1c**]$^+$.It is worth noting that [Cp*Co]$_2$($\mu$-I)$_3^+$, i.e. the main side product of the collapse of **1a**, fully decomposes in the reaction carried out in the presence of water under air.

**Table 3. 3**. Treatment with $D_2O$/$H_2O$ that promotes the formation of [**1c**][$BArF_{24}$] under an atmosphere of Air or Argon

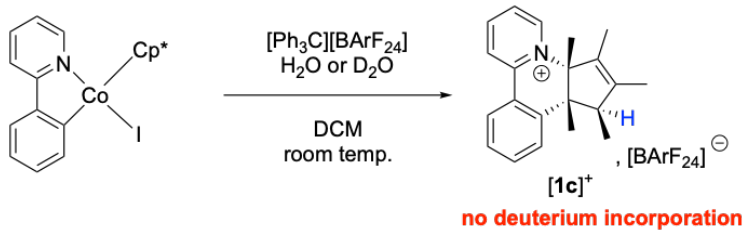


| Entry | $H_2O$ or $D_2O$ | Atmosphere | Yield |
|---|---|---|---|
| 1 | $H_2O$ | Argon | 13% |
| 2 | $D_2O$ | Argon | 8% |
| 3 | $H_2O$ | Air | 87% |
| 4 | $D_2O$ | Air | 77% |

General conditions: **1a** (0.1 mmol, 1 eq), [$Ph_3C$][$BArF_{24}$] (0.1 mmol, 1 eq), DCM (5 mL), $H_2O$ or $D_2O$ (0.5 mmol, 5 eq), 25°C, 16 h. $^1$H NMR yield in the presence of 1,3,5-trimethoxybenzene as an internal standard.

The body of evidence gathered here points at **1a** or some degraded from of it as a probable source of the H atom that incorporates into [**1c**]$^+$. A contribution of the solvent cannot be completely excluded neither at this stage as a major kinetic barrier to deuterium incorporation (not addressed here) may well lead to the consumption of the residual protio-dichloromethane in the experiments ran in deuterated solvent.

### 3.2.4. Electrochemical experiments

The electrolyte consisted of a solution of 0.1 mol $L^{-1}$ of anhydrous tetrabutylammonium hexafluorophosphate ($[NBu_4][PF_6]$) in dry distilled 1,2-$C_2H_4Cl_2$.The reference electrode was the Ag/AgCl electrode, which was electrically connected to the solution by a junction bridge filled with 5 mL of anhydrous $CH_3CN$ + 0.1 M $[NBu_4][PF_6]$. The working electrode was a platinum-disk electrode (d = 3 mm in diameter). All potentials are given vs Ag/AgCl used as an external reference and are uncorrected for Ohmic drop.

The electrochemical behavior of the compounds involved in the cyclocondensation of **1a** was studied by cyclic voltammetry under argon with solutions in the moderately volatile 1,2-dichloroethane using $[N(nBu)_4][PF_6]$ (0.1 mol $L^{-1}$) as background electrolyte (Figure 3.10 and Table 3.4).

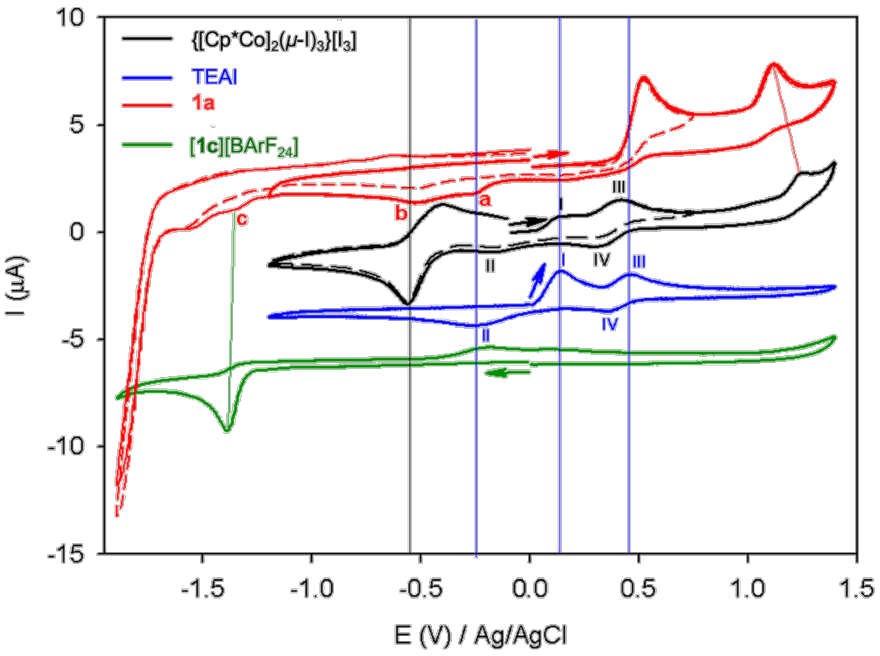


**Figure 3. 10.** Cyclic voltammograms of $\{[Cp^*Co]_2(\mu\text{-}I)_3\}[I_3]$, TEAI, **1a** and [**1c**][$BArF_{24}$] (0.4 mmol $L^{-1}$) on Pt electrode in a DCE solution in the presence of $[N(nBu)_4][PF_6]$ (0.1 mol $L^{-1}$). $v$ = 100 mV $s^{-1}$.

**Table 3.1.** Electrochemical data for **1a**, **7a**, **8a**, **9a**, **10a**, {[Cp*Co]$_2$($\mu$-I)$_3$}[I$_3$], **[1c]$^+$**, and TEAI.

| Compounds | $E_{1/2}$ | | | | |
|---|---|---|---|---|---|
| 1a | | 1.11$^{irr}$ | 0.52$^{irr}$ | | |
| 7a | | 1.19$^{irr}$ | 0.59$^{irr}$ | -1.60 | |
| 8a | | 1.23$^{irr}$ | 0.61$^{irr}$ | | |
| 9a | | | 0.80$^{irr}$ | -1.21$^{irr}$ | -1.76$^{irr}$ |
| 10a | | 1.11$^{irr}$ | 0.49$^{irr}$ | | |
| {[Cp*Co]$_2$($\mu$-I)$_3$}[I$_3$] | 1.25$^{irr}$ | 0.36 (168) | -0.02$^a$ (293) | -0.51 (120) | -1.76$^{irr}$ |
| [**1c**][ BArF$_{24}$] | | | | -1.39$^{irr}$ | |
| TEAI | | 0.40 (116) | -0.08$^a$ (400) | | |
| Fc | | | 0.16 (72) | | |

Potentials (in V) vs. Ag/AgCl were obtained from cyclic voltammetry in DCE with 0.1 mol L$^{-1}$ [N($n$Bu)$_4$][PF$_6$]. Scan rate = 100 mV s$^{-1}$. Working electrode: Pt, $d$= 3 mm in diameter. The given half-wave potentials are equal to $E_{1/2}$ = ($E_{pa}$+ $E_{pc}$)/2. Under bracket: $\triangle E_p$ = |$E_{pa}$-$E_{pc}$|. $^{irr}$: Irreversible peak potential. $^a$ Slow process: couple $I_3^-/I^-$ or $I_2/I_3^-$.

Cyclic voltammogram of {[Cp*Co]$_2$($\mu$-I)$_3$}[I$_3$] (Figure 3.10 black curve and Figure 3.11) shows the presence of three successive oxidation processes at -0.02 V, 0.36 V and 1.25 V *vs.* Ag/AgCl. The last oxidation at 1.25 V is irreversible and may correspond to the oxidation of the cobalt center, while the two first oxidations are similar to the redox behavior of tetraethylammonium iodide (abbr. TEAI) (Figure 3.12). It corresponds to the redox properties of the triiodide $I_3^-$ counter-anion. In fact, at the potential applied

at the start of the sweep; $I_3^-$ is first reduced to $I^-$, redox behavior similar to that of TEAI is observed.

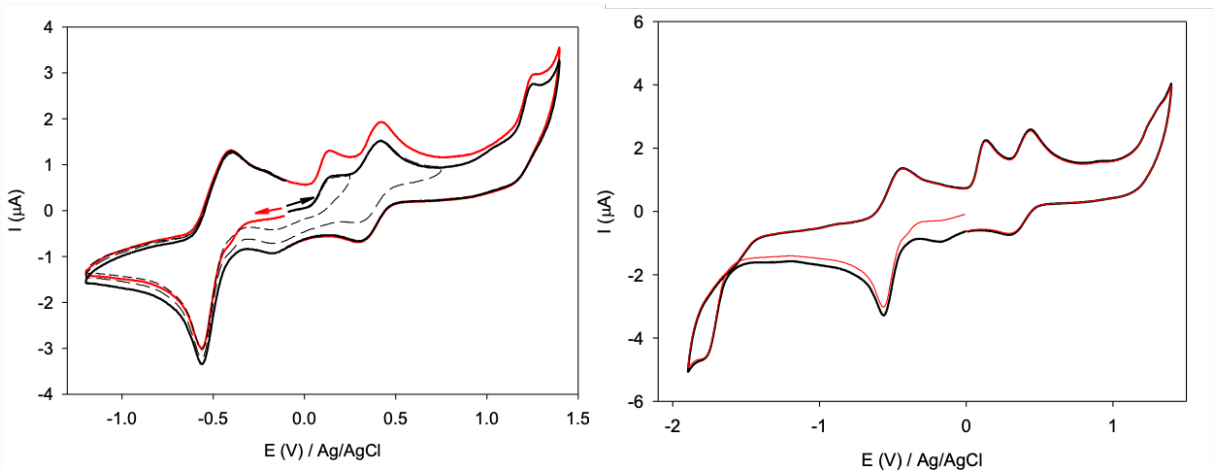


**Figure 3. 11.** Cyclic voltammograms of $\{[Cp^*Co]_2(\mu\text{-}I)_3\}[I_3]$ (0.4 mmol $L^{-1}$) on Pt electrode in a 1,2-$C_2H_4Cl_2$ solution in the presence of $NBu_4PF_6$ (0.1 mol $L^{-1}$). $v$ = 100 mV $s^{-1}$.

Indeed, cyclic voltammogram of 0.4 mmol. $L^{-1}$ solution of TEAI recorded in 0.1 mol $L^{-1}$ [N(*n*Bu)$_4$][$PF_6$]/DCE at a platinum electrode and scan rate of 0.1 V $s^{-1}$ (Figure 3.10, blue curve and Figure 3.12) exhibited also two anodic oxidative peaks at $E_{pa1}$ (I) = -0.08 V *vs.* Ag/AgCl and at $E_{pa2}$(III)= 0.40 V *vs.* Ag/AgCl coupled with an cathodic peaks at $E_{pc1}$(II) = -0.28 V *vs.* Ag/AgCl and $E_{pc2}$(IV) = 0.35 V. The presence of two coupled peaks is well documented in the literature. It indicates the presence of a two chemical processes following the two steps of the quasi-reversible electron transfer ($E_1C_1E_2C_2$ mechanism).[317]

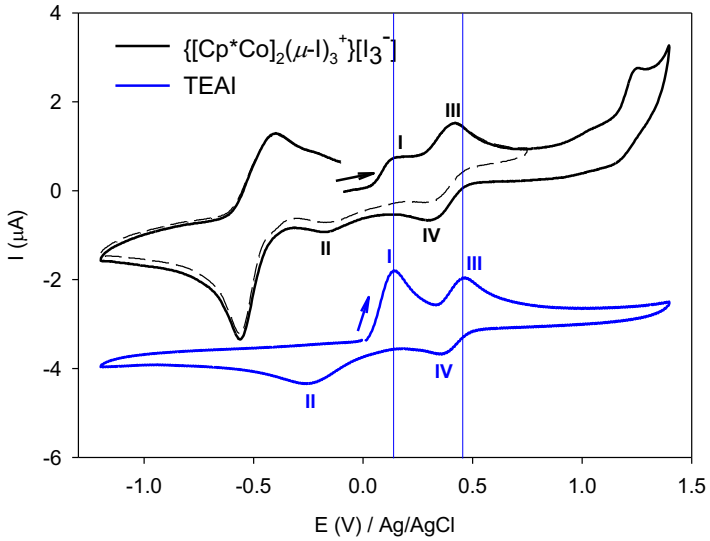


**Figure 3. 12.** Cyclic voltammograms of $\{[Cp^*Co]_2(\mu\text{-}I)_3\}[I_3]$ and of TEAI (0.4 mmol $L^{-1}$) on Pt electrode in a 1,2-$C_2H_4Cl_2$ solution in the presence of $NBu_4PF_6$ (0.1 mol $L^{-1}$). $v$ = 100 mV $s^{-1}$.

According to the literature,[318-320] the peak **I** (Figure 3.10) is attributed to the $E_1C_1$ mechanism: first the oxidation of two iodides to $I_2$ (Eq 1, electrochemical step $E_1$, two electron oxidation wave) followed by the chemical reaction $C_1$ with $I^-$ giving triodide $I_3^-$ (chemical step $C_1$, Eq 2). The peak **II** (Figure 3.10) is attributed to the reduction of $I_3^-$ to regenerate $I^-$. The second anodic peak (**III**, Figure 3.10) yielded from $I_3^-$ is one electron oxidation wave (electrochemical step $E_2$). The peak **III** (Figure 3.10) is attributed to the oxidation of $I_3^-$ obtained after the $E_1C_1$ process to form $I_2$ while peak **IV** (Figure 3.10) is attributed to the reduction of $I_2$ to $I_3^-$ (Eq 3).

$2\ I^- \rightarrow I_2 + 2\ e^-$ (Eq 1, step $E_1$)

$I_2 + I^- \rightarrow I_3^-$ (Eq. 2, step $C_1$, fast addition)

$I_3^- \rightarrow 3/2I_2 + e^-$ (Eq. 3, step $E_2$)

$3/2I_2 + 3/2\ 1,2\text{-}C_2H_4Cl_2 \rightarrow 3/2\ [1,2\text{-}\ C_2H_4Cl_2I]^+[I]^-$ (Eq. 4, step $C_2$)

The second chemical process ($C_2$) arising from the slow interaction of the generated $I_2$ with DCE due to the small dielectric constant where substantial ion association begins to take place. DCE as a donor solvent promotes the ionization of covalent compounds

to form intimate ion – pairs. Ionization is stimulated in a donor solvent by solvation of cations where iodine I2 is ionized in a donor solvent according to the reaction (Eq. 4)[321].

For **1a**, two irreversible oxidation peaks were detected at 0.52 and 1.11 V *vs.* Ag/AgCl (Figure 3.10, red curve). The first oxidation corresponds to the oxidation of Co(III) to Co(IV). Note that the intensity of the peak current of the second irreversible oxidation at 1.11 V is a little less than half of the intensity of the first oxidation. It may corresponds to the oxidation of the intermediate of the reaction giving [**1c**]$^+$ (Figure 3.13) or may be related to the oxidation of {[Cp*Co(III)]$_2$($\mu$-I)$_3$}$^+$ (Figure 3.14).

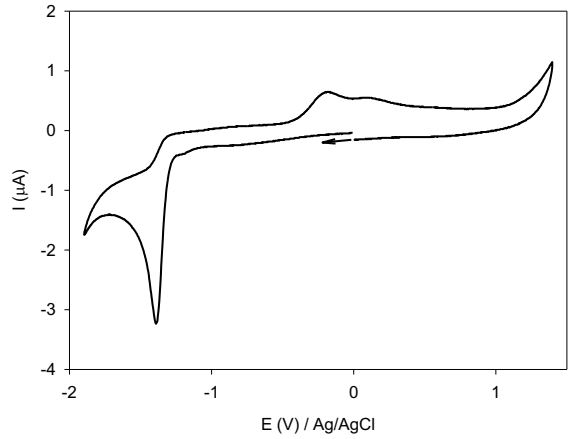


**Figure 3. 13.** Cyclic voltammograms of [**1c**][BArF$_{24}$] (0.4 mmol L$^{-1}$) on Pt electrode in a 1,2-$C_2H_4Cl_2$ solution in the presence of $NBu_4PF_6$ (0.1 mol L$^{-1}$). $v$ = 100 mV s$^{-1}$.

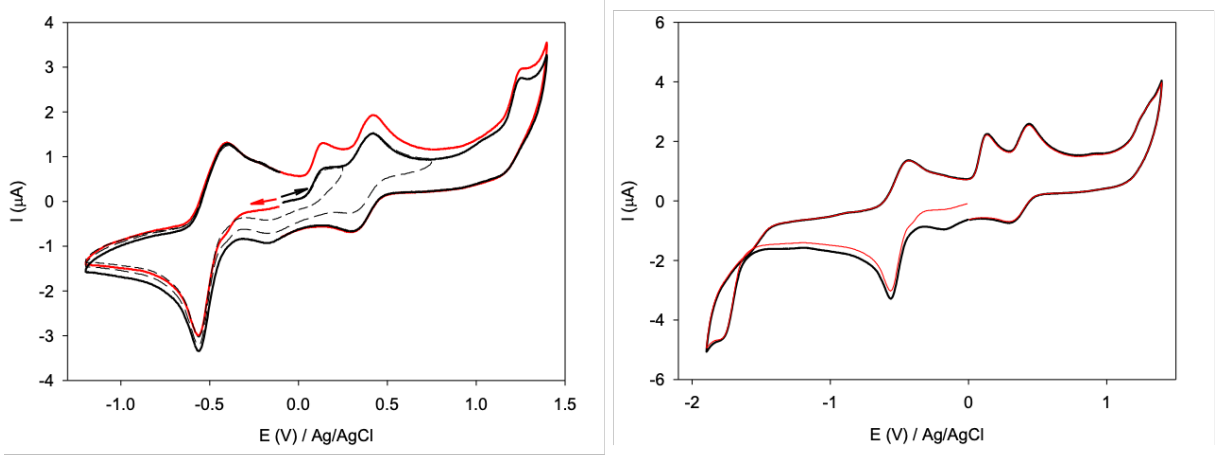


**Figure 3. 14.** Cyclic voltammograms of {[Cp*Co]$_2$($\mu$-I)$_3$}[I$_3$] (0.4 mmol L$^{-1}$) on Pt electrode in a 1,2-$C_2H_4Cl_2$ solution in the presence of $NBu_4PF_6$ (0.1 mol L$^{-1}$). $v$ = 100 mV s$^{-1}$.

The irreversibility of the oxidation **1a** is fully in agreement with the reactivity of **1a** with $[Ph_3C][BArF_{24}]$ leading to the formation of $[\mathbf{1c}]^+$, "CoI" and $\{[Cp^*Co]_2(\mu\text{-}I)_3\}^+$. During the reverse sweep after the oxidation **1a**, three new irreversible peaks are detected at -0.25 V (peak a), -0.57 V (peak b) and -1.37 V (peak c). The three signals should correspond to the detection of the compounds formed during the irreversible oxidation.

The first irreversible cathodic peak at -0.25 V has a redox potential similar to that of TEAI and may correspond to the reduction of $I_3^-$ to $I^-$ indicating probably the release of $I^-$ during the oxidation of **1a**.

The second signal at -0.57 V (peak b) can be attributed to the reduction of the $\{[Cp^*Co]_2(\mu\text{-}I)_3\}$ species which gives similar redox potential reduction wave at -0.51 V. The potential is a little different, which can be explained by the nature of the counter-anion ($PF_6^-$ *vs.* $I_3^-$) for $\{[Cp^*Co]_2(\mu\text{-}I)_3\}[I_3]$.

The last reduction at -1.37 V (peak c) may be due to the irreversible reduction of the pyridinium group of $[\mathbf{1c}]^+$. Indeed, the cyclic voltammogram of $[\mathbf{1c}][BArF_{24}]$ shows similar irreversible reduction at -1.39 V (Figure 3.10, green curve and Figure 3.13). This irreversible reduction is attributed to the formation of a reactive pyridyl radical which may undergo homocoupling through C-C bond formation[322].

Finally, compounds **7a**, **8a** and the new "CpCo" complex **10a** give a redox behavior similar to that of **1a** (Table 3.4 and Figures 3.13-3.19) showing that the potential of oxidation of the Co(III) is little affected by the nature of substituent R (R = H, Br or $CF_3$) or by substitution of Cp* by Cp in cobaltacycles. However, the redox behavior is dissimilar in the case of **9a** by changing I by Cl substituent where only one irreversible oxidation and two irreversible reductions are detected at 0.80 V, -1.21 V and -1.76 V respectively.

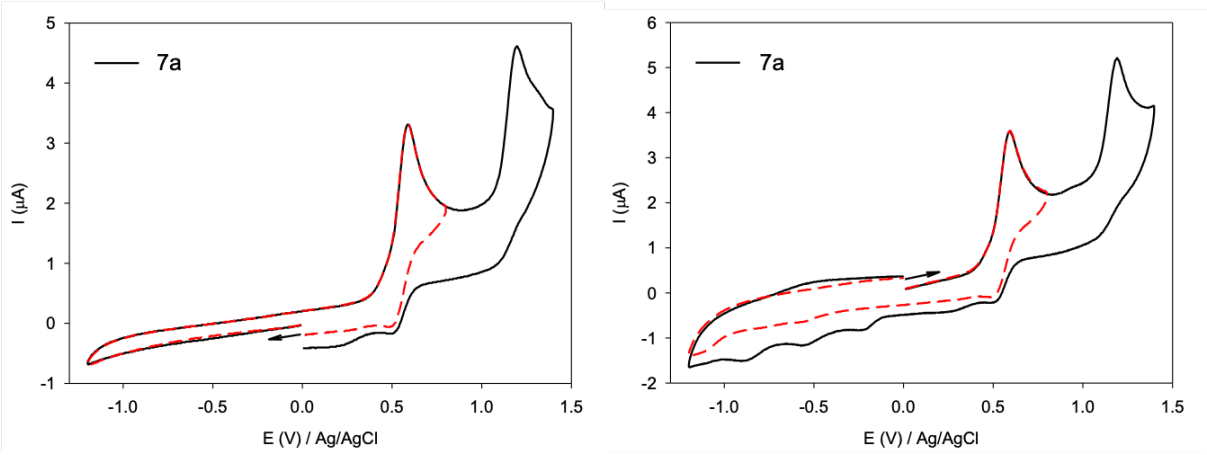


**Figure 3. 15.** Cyclic voltammograms of **7a** (0.4 mmol $L^{-1}$) on Pt electrode in a 1,2-$C_2H_4Cl_2$ solution in the presence of $NBu_4PF_6$ (0.1 mol $L^{-1}$). $v$ = 100 mV $s^{-1}$.

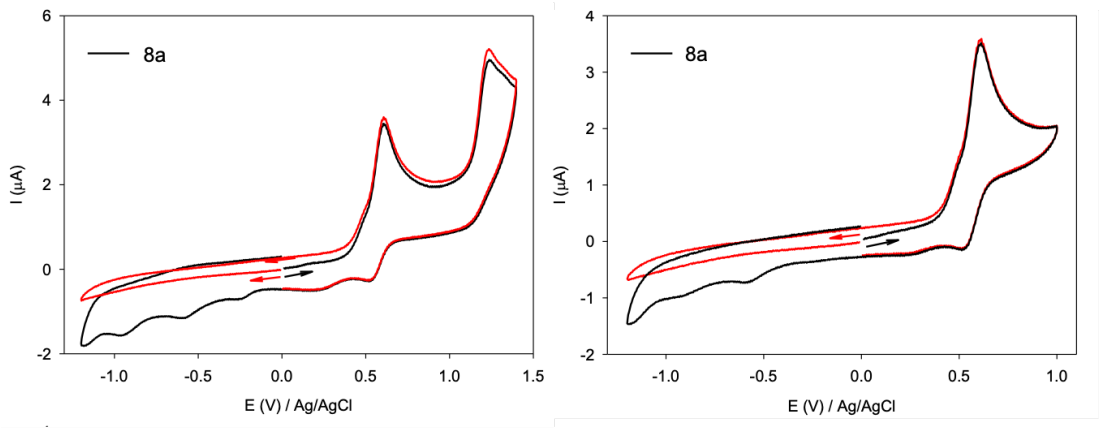


**Figure 3. 16.** Cyclic voltammograms of **8a** (0.4 mmol $L^{-1}$) on Pt electrode in a 1,2-$C_2H_4Cl_2$ solution in the presence of $NBu_4PF_6$ (0.1 mol $L^{-1}$). $v$ = 100 mV $s^{-1}$.

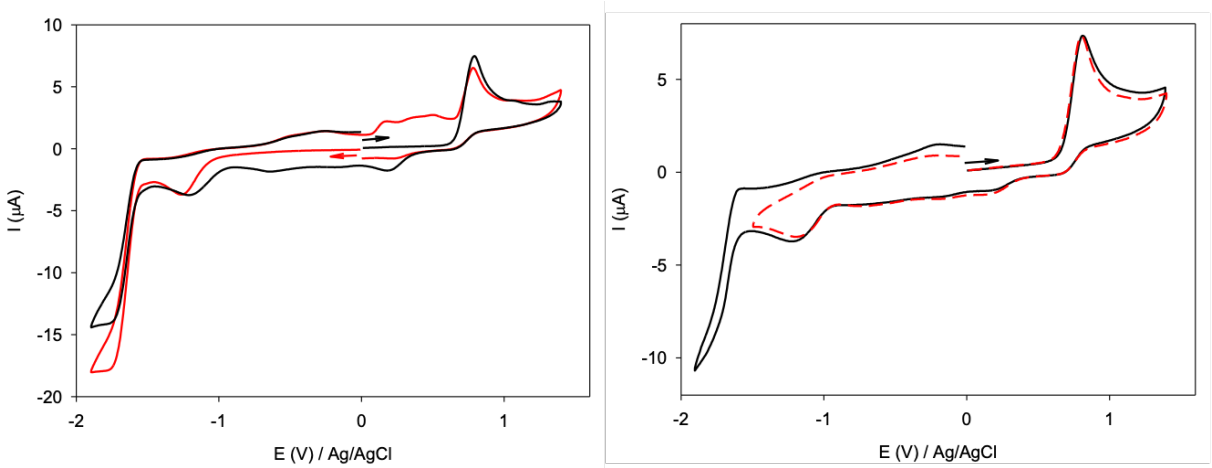


**Figure 3. 17.** Cyclic voltammograms of **9a** (0.4 mmol $L^{-1}$) on Pt electrode in a 1,2-$C_2H_4Cl_2$ solution in the presence of $NBu_4PF_6$ (0.1 mol $L^{-1}$). $v$ = 100 mV $s^{-1}$.

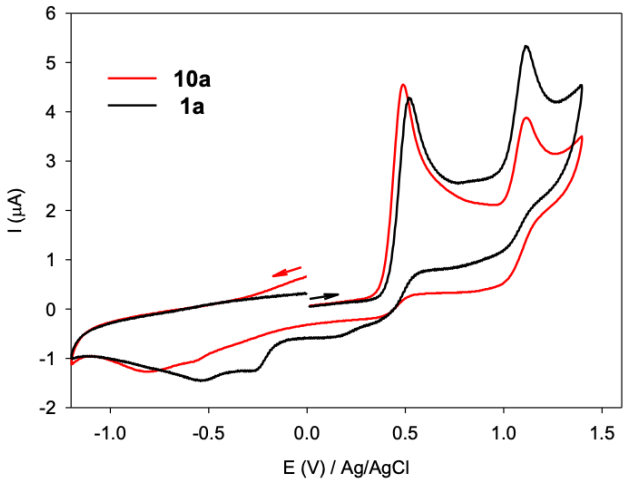


**Figure 3. 18.** Cyclic voltammograms of **1a** and **10a** (0.4 mmol $L^{-1}$) on Pt electrode in a 1,2-$C_2H_4Cl_2$ solution in the presence of $NBu_4PF_6$ (0.1 mol $L^{-1}$). $v$ = 100 mV $s^{-1}$.

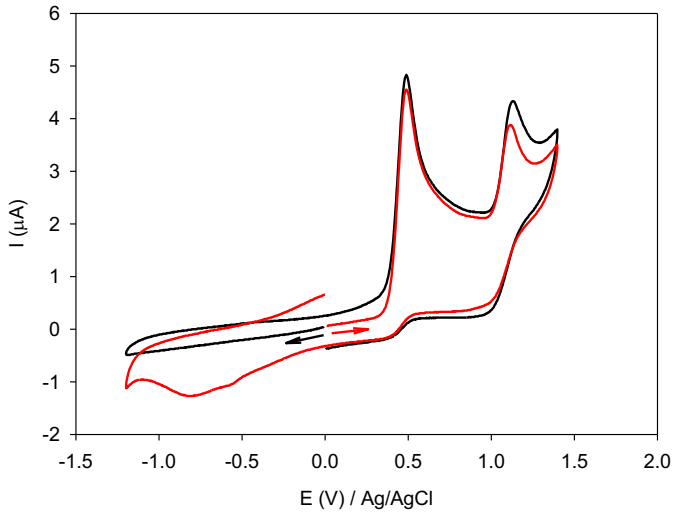


**Figure 3. 19.** Cyclic voltammograms of **10a** (0.4 mmol $L^{-1}$) on Pt electrode in a 1,2-$C_2H_4Cl_2$ solution in the presence of $NBu_4PF_6$ (0.1 mol $L^{-1}$). $v$ = 100 mV $s^{-1}$.

### 3.2.5. Electron paramagnetic resonance (EPR) experiments

EPR spectra were recorded on a continuous wave X-band EMX-plus instrument equipped with a TE102 rectangular cavity (ER 4102ST, Bruker) and an ESR900 continuous flow cryostat controlled with an Oxford ITC503S apparatus. EPR spectra were recorded with the following parameters: a microwave power of 1 mW, a modulation frequency and amplitude of respectively 100 kHz and 0.4 mT, a conversion time of 300 ms, and a time constant of 20.48 ms. A second-order polynomial baseline was subtracted from the spectra recorded between 0 and 450 mT. The simulation was done using the Easyspin 63 toolbox working under MatLab (MathWorks).

The mixture produced by the reaction of 40 mM **1a** and $[Ph_3C][BArF_{24}]$ was analyzed by EPR spectroscopy at low temperature in frozen DCM. The EPR spectrum (Figure 3.20) recorded after 5 minutes of reaction at 4 K shows the superposition of the signatures of two species. One intense is centered at $g$~2.003 ($\Delta H_{pp}$=1.25 mT) and supports the presence of an organic radical[323-330] in frozen solution. The second signal of lower intensity displays a distorted axial pattern with broad resonances and effective $g$ values at $g$~ 4.80 and $g$~ 2.02 similar to that already reported by Wang et al.[331] These main peaks point to high-spin Co(IV) species[331, 332] ($S$= 3/2 or $S$= 5/2) as a result of the

oxidation of **1a** and in agreement with their disappearance at higher temperature in frozen solution, i.e from 30 K.[332] After 1 hour of reaction of the molten mixture, both signals disappeared when the sample was frozen back to 4 K and analyzed.

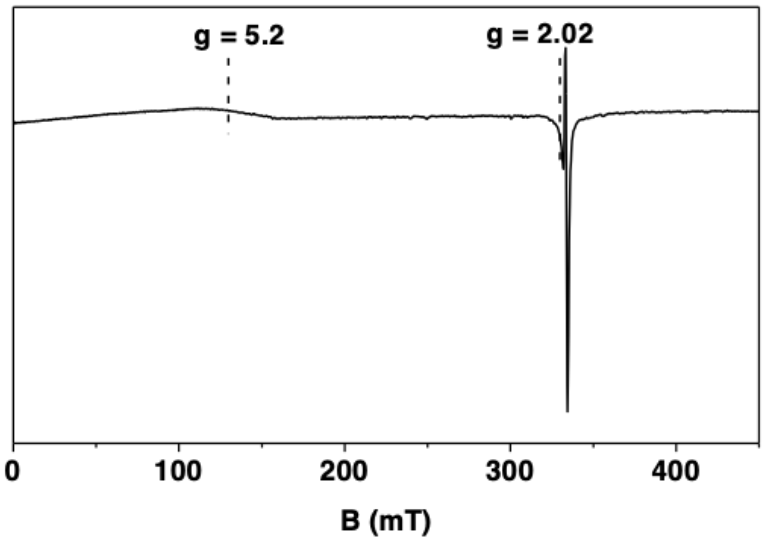


**Figure 3. 20.** X-band EPR spectrum recorded at 4.3 K after 5 min of reaction between 40 mM solutions of **1a** and $[Ph_3C][BArF_{24}]$ in DCM . The spectrum was recorded at a frequency of 9.345 GHz.

From the above experimental section, our conjecture has been verified that the irreversible oxidation of Co(III) center into the Co(IV) state leads to the collapse of the cobaltacycle. In contrast, Perez-Temprano and co-workers have recently proposed that transient Co(IV) species[140] may play a central role in oxidative C-H bond thiolation,[333] but the collapse of the cobaltacycle was not observed in this report. Indeed, in an effort to clarify the mechanism of the catalysis reported by Glorius et al.,[333] showed that the treatment of a trifluoromethylthiolato complex of a 2-phenyl,pyridine Cp*-bound cobaltacycle with excess Ag(I) salts may lead to the oxidation of the Co(III) center into a Co(IV) complex purportedly responsible for the formation of the expected ortho-substituted product of C-S coupling (Scheme 3.14) in various yields (from ca. 99% to 0%) depending on the amount and nature of oxidant. We speculate that in the context of complex catalytic mixtures containing reagents and co-catalysts endowed with oxidoreductive mediation roles where similar metallacycles are claimed to be key

intermediates,[159, 178, 276] the occurrence of such an unwanted cyclocondensation pathway depends on the nature of the ligand X coordinated to the metal center.

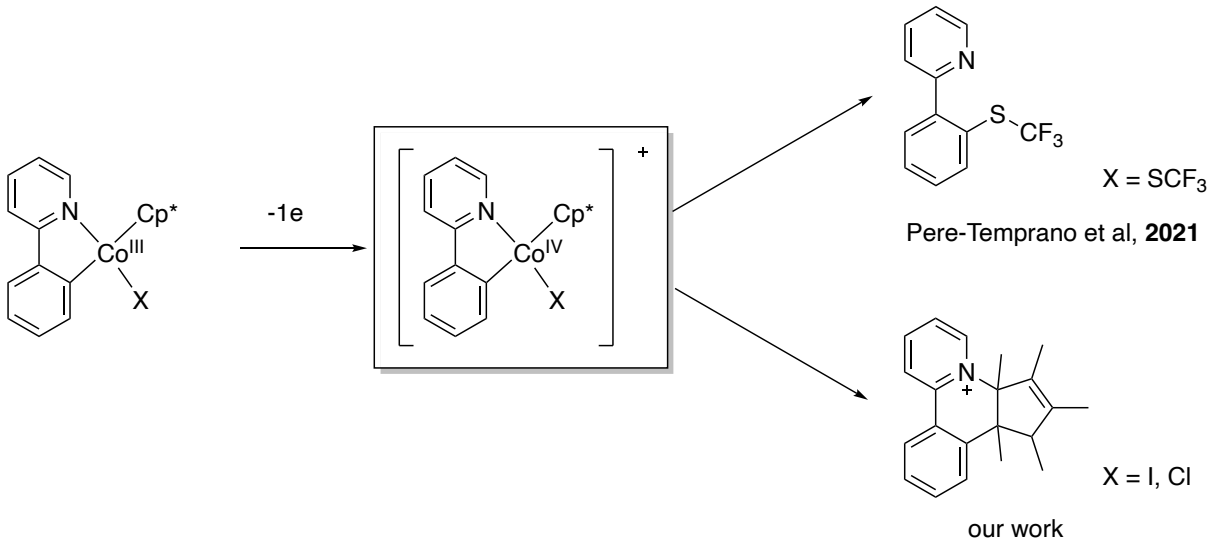


**Scheme 3. 14.** Two possible scenarios result from the oxidation of the Co(III)-X complexes.

## 3.2.6. DFT evaluation of the mechanism of formation of [1c]$^+$

### 3.2.6.1. NCI plots and IBSI suggest a predisposition to cyclocondensation

A preliminary comparative study between the reactive cobalt complex **1a** and the iodoiridium analogue **Ir-1a** was carried out to address the propensity of **1a** to undergo the condensation of Cp* with *phpy* under oxidative conditions while its Ir analogue supposedly remains unchanged. The computed difference in the Gibbs free energy of oxidation for the Co(III) and Ir(III) complexes is negligible and cannot explain the difference of behavior ($\Delta\Delta G$=0.1 kcal/mol). Our attention turned to the possible existence of attractive noncovalent interactions that could predispose **1a** to its collapse by cyclocondensation.

Recent reports[281, 334] have indeed stressed the assisting effect of local attractive NCI interactions in the reactant complexes of base assisted aromatic C-H bond activation by Pd(II), Ni(II), Co(III) and Ir(III) centers. NCI plots are particularly informative of the interactions in reactant complexes that may prefigure new bonds appearing once the transition state is passed.[335] NCI plots[25, 336] were therefore scrutinized for peculiar features related to the uncommon cyclocondensation reported here.

The NCI plots[25, 336] depicted in Figure 3.21 and Figure 3.22 display the isosurfaces of attractive domains (red colored isosurfaces) and repulsive or non-bonding ones (blue colored isosurfaces) in various singlet and doublet state geometries of complexes relevant to this report. NCIs are materialized by reduced density gradient isosurfaces (cut-off value $s$ = 0.5 au, $\rho$ =0.02 au.) colored according to the sign of the signed density i.e. in red for attractive NCI domains and in blue for repulsive (or non-bonding) NCI domains. Specific NCI attraction domains between the Cp* and the *phpy* ligand are circled in green.

The circular attractive domain isosurface located underneath the Cp*ligand in all the cases depicted in Figure 3.21 is quite usually observed in $\eta^5$-cyclopentadienyl and $\eta^6$-arene- metal complexes.[337, 338] One uncommon feature however is when this ring-like isosurface is no more circular like in **Ir-1a** but displays attractive outgrowths like in **1a** that are symptomatic of a peculiar attractive relationship between one carbon atom at the cyclopentadienyl moiety and an atom of a group of atoms at a different vicinal ligand.

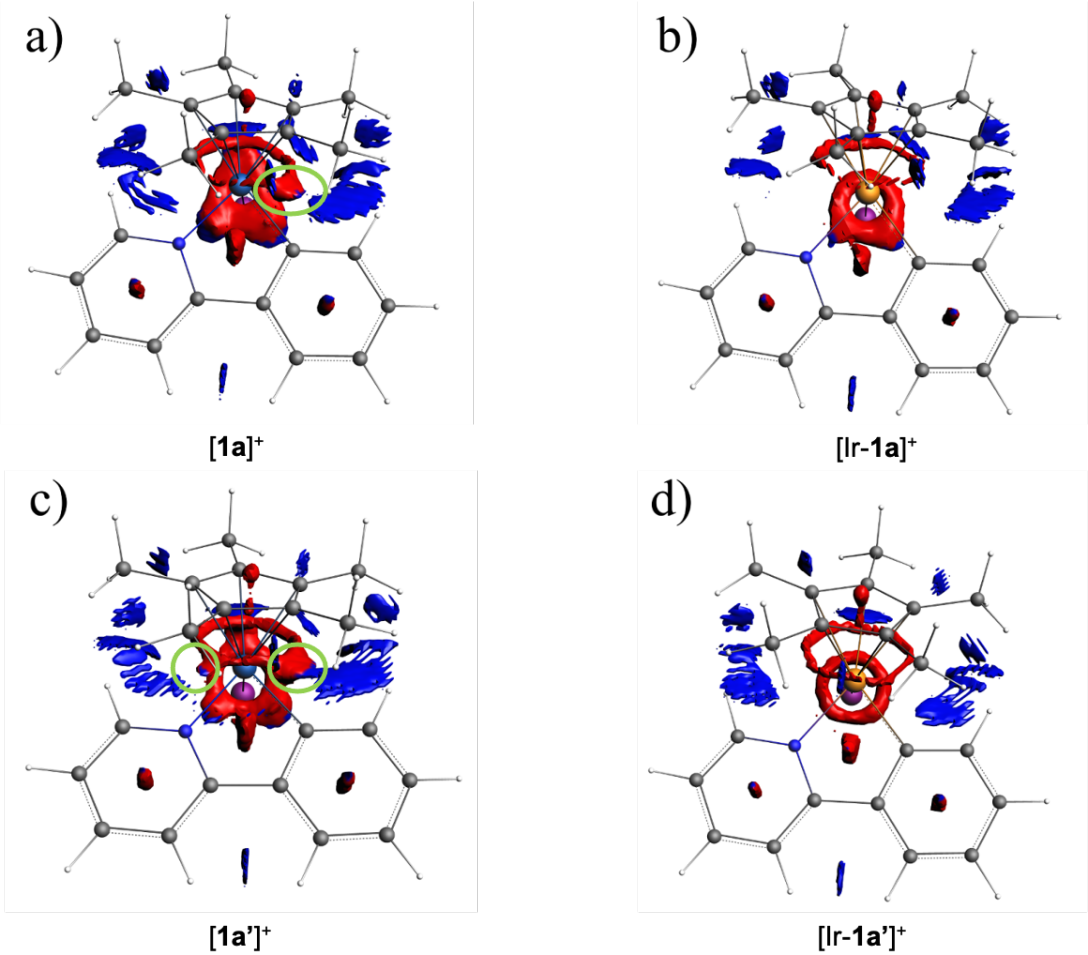


**Figure 3. 21.** NCI plots[25, 336] from ADFview2019 for optimized geometries of a) singlet ground state **1a**, b) its singlet ground state Ir analogue **Ir-1a**, c) doublet ground state [**1a'**]$^+$, d) doublet ground state [**Ir-1a'**]$^+$ (SCM-ADF2019[339] ZORA[340]-PBE[202]-D4(EEQ)[341] / all electron TZP / COSMO[342]($CH_2Cl_2$) level). Color code for atoms: dark blue, N; gray, C; white, H; organe, Ir; purple, I; indigo, Co. NCIs are materialized by reduced density gradient isosurfaces (cut-off value $s$ = 0.5 au, $\rho$ =0.02 au.) colored according to the sign of the signed density i.e. in red for attractive NCI domains and in blue for repulsive (or non-bonding) NCI domains. Specific NCI attraction domains between the Cp* and the *phpy* ligand are circled in green.

This is the case for the attractive domains between carbon $C_4$ of the Cp* and carbon $C_{2'}$ of the *phpy* ligand that bind during the cyclocondensation and which are present in singlet state **1a** but not in singlet state **Ir-1a**. This difference in attractive NCI is even

more pronounced when the Co(III) center is oxidized to Co(IV) to give [**1a'**]$^+$ (Figure 3.21) .

The doublet state Co(IV) complex [**1a'**]$^+$ not only exhibits a larger attractive domain between $C_4$ of the Cp* and $C_{2'}$ of the *phpy* ligand, but an attractive domain between $C_3$ of the Cp* and N of *phpy* also appears, while none of these attractions appear for the Ir(IV) analogue. It is also worthy to note the slight rapprochement between Cp* and *phpy* induced by oxidation in both cases.

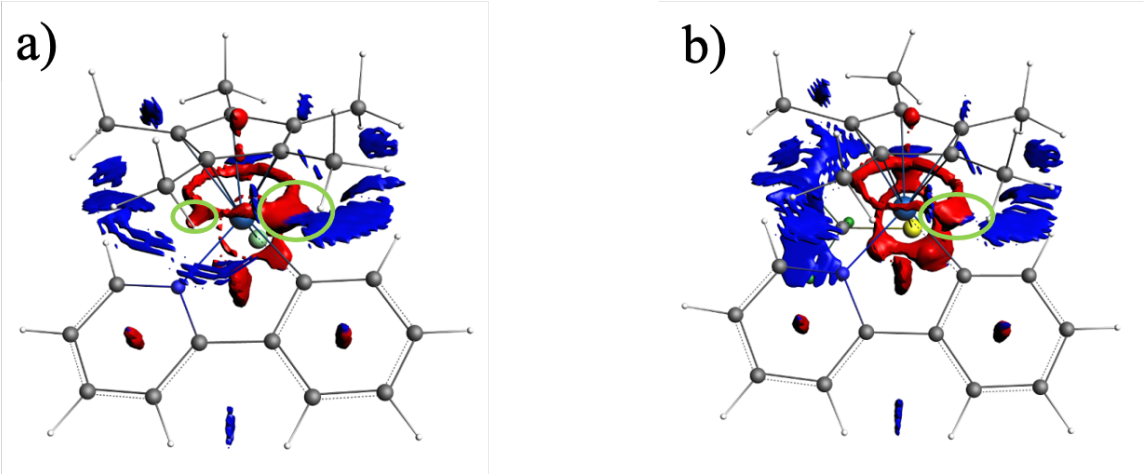


**Figure 3. 22.** NCI plots[25, 336] from ADFview2019 for optimized geometries of a) doublet ground state [**9a'**]$^+$ and b) doublet ground state [Cp*Co($SCF_3$)(*phpy*)]$^+$ (SCM-ADF2019[339] ZORA[340]-PBE[202]-D4(EEQ)[341] / all electron TZP / COSMO[342]($CH_2Cl_2$) level). Color code for atoms: dark blue, N; gray, C; white, H; yellow, S; light green, F; indigo, Co; green, Cl. NCIs are materialized by reduced density gradient isosurfaces (cut-off value $s$ = 0.5 au, $\rho$ =0.02 au.) colored according to the sign of the signed density i.e. in red for attractive NCI domains and in blue for repulsive (or non-bonding) NCI domains. Specific NCI attraction domains between the Cp* and the *phpy* ligand are circled in green.

NCI plots of the doublet states of Co(IV) [Cp*Co($SCF_3$)(*phpy*)]$^+$ [140] and [**9a'**]$^+$, i.e the oxidized form of **9a,** (Figure 3.22) all show a significant Cp*-*phpy* C-C attractive domain while the N-$C_3$ attractive domain develops weakly only for [**9a'**]$^+$ and is absent in Co(IV) [Cp*Co($SCF_3$)(*phpy*)]$^+$. Worthy to note, in the case of [Cp*Co($SCF_3$)(*phpy*)]$^+$ the *phpy*-

related $C_{2'}$-S interaction is strongly attractive whereas in [**1a**]$^+$ the $C_{2'}$-I interaction bears a repulsive/non-bonding character inwards $C_{2'}$.

To get a more quantitative insight on the difference in interaction strength between the Co and and Ir complexes **1a** and **Ir-1a**, at the +III and +IV formal oxidation states and for [Cp*Co($SCF_3$)(*phpy*)] and **9a** at the +III and +IV formal oxidation state, the integrated independent Gradient Model (IGM)-based $\delta g^{inter}$ descriptor[283, 284] (also called $\Delta g^{inter}$ interaction score) was computed to quantify the interaction between *phpy* and each of the two other ligands. The IGM-$\delta g^{inter}$ descriptor compares density gradients of fragments with and without interference. Integrating this descriptor gives rise to the $\Delta g^{inter}$ interaction score that measures the interaction between two user-defined fragments. The recently developed Intrinsic Bond Strength Index[285] (IBSI) was also computed for the key atom pairs involved in the reaction. IBSI is an efficient quantitative index to intra-molecularly probe the "strength" of a given chemical bond or interaction. It is also based on the so-called Independent Gradient Model,[285] which was designed to reveal and quantify molecular interactions from the electron density topology, and was validated by tests on 677 bonds in 235 molecular systems. Both $\Delta g^{inter}$ score and IBSI have previously successfully been applied in mechanistic studies.[343]

Like many QTAIM[221]-based analytical methods it is exempt of issues related to basis set superposition error. In the cases addressed here (*cf.* Table 3.5), $\Delta g^{inter}$ evidences a stronger interaction between the Cp* and *phpy* ligands in the Co case than in the Ir one, being in the +III or +IV formal oxidation state. Oxidation increases the interaction between Cp* and *phpy* in the Co case, while the increase is almost null in the Ir one. Conversely, the interaction between *phpy* and I decrease with the oxidation on both cases and while it is stronger in the Co case than in the Ir one at the +III formal oxidation state, it is the opposite iat the +IV formal oxidation state.

IBSI evidences a stronger interaction between $C_3$ of the Cp* moiety and $C_{2'}$ of the *phpy* ligand, as well as between $C_4$ of the Cp* and N of the *phpy*, in **1a** than in its Ir analogue, while the interaction between the four aforementioned atoms and the metal center is stronger in the Ir analogue. The same observation stands when the complex is oxidized. Moreover, oxidation increases, in the Co case, the strength of the interaction between the Cp* and the *phpy*, while decreasing the strength of the interaction

between the ligands and the metal center. This analysis suggests that the condensation of the *phpy* ligand with the Cp* moiety could be somewhat encoded in the favorable IBSI and NCI signatures observed in **1a** and its oxidized Co(IV) form [**1a'**]$^{+}$.

The general qualitative behavior of the $\Delta g^{inter}$ interaction score and of the IBSI remains the same when replacing the iodo ligand by a chloro one in the Co complex (Table 3.5). The main difference lies in the $\Delta g^{inter}$ between *phpy* and the halido ligand which is lower in the chloro analogue than in the iodo at the +III formal oxidation state, while it is higher at the +IV formal oxidation state.

When comparing **1a** to [Cp*Co($SCF_3$)(*phpy*)],[140, 333] the general quantitative behavior of the $\Delta g^{inter}$ interaction score between Cp* and *phpy*, and of the IBSI remain the same (Table 3.5). However, the $\Delta g^{inter}$ interaction score between *phpy* and the X ligand is higher when X= $SCF_3$ than when X= I : while it decreased in the latter case, it increases in the former, seemingly explaining the possibility of the C-S bond formation.[140]. More important is the fact the the $\Delta g^{inter}$ for the Cp*-*phpy* interaction in almost identical in **1a**/[**1a'**]$^{+}$ and [Cp*Co($SCF_3$)(*phpy*)]/[Cp*Co($SCF_3$)(*phpy*)]$^{+}$ whereas in the latter case no metallacycle collapse was mentioned.[140]

**Table 3.2.** Interatomic "Intrinsic Bond Strength Indexes" (IBSI)[285] and the integrated difference between the density gradients with and without interference IGM[283, 284]: $\Delta g^{inter}$ computed for **1a** and [**1a'**]$^+$, **Ir-1a** [**Ir-1a**]$^+$, **9a**, [**9a'**]$^+$, [Cp*Co($SCF_3$)(*phpy*)] and [Cp*Co($SCF_3$)(*phpy*)]$^+$.

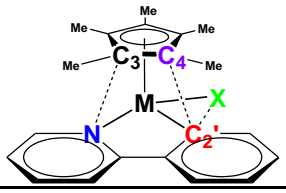


| | **1a** | **Ir-1a** | [**1a'**]$^+$ | [**Ir-1a'**]$^+$ | **9a** | [**9a'**]$^+$ | [Cp*Co($SCF_3$)(*phpy*)] | [Cp*Co($SCF_3$)(*phpy*)]$^+$ |
|---|---|---|---|---|---|---|---|---|
| IBSI Atom-Pair Interactions (au) | | | | | | | | |
| $C_4$-$C_{2'}$ | 0.047 | 0.038 | 0.052 | 0.020 | 0.044 | 0.053 | 0.038 | 0.048 |
| $C_3$-N | 0.026 | 0.012 | 0.048 | 0.009 | 0.026 | 0.027 | 0.021 | 0.029 |
| $C_4$-Co/Ir | 0.253 | 0.274 | 0.232 | 0.248 | 0.244 | 0.203 | 0.242 | 0.192 |
| $C_3$-Co/Ir | 0.259 | 0.301 | 0.213 | 0.247 | 0.250 | 0.223 | 0.235 | 0.204 |
| $C_{2'}$-Co/Ir | 0.479 | 0.488 | 0.469 | 0.498 | 0.497 | 0.460 | 0.485 | 0.459 |
| N-Co/Ir | 0.385 | 0.402 | 0.376 | 0.410 | 0.385 | 0.378 | 0.392 | 0.391 |
| $C_{2'}$-X | 0.026[a] | 0.024[a] | 0.024[a] | 0.020[a] | 0.030[b] | 0.027[b] | 0.046[c] | 0.032[c] |
| *Interacting Fragments* $\Delta g^{inter}$ (au) | | | | | | | | |
| Cp*-*phpy* | 0.865 | 0.630 | 0.935 | 0.633 | 0.857 | 0.920 | 0.859 | 0.917 |
| *phpy*-X | 0.292[a] | 0.343[a] | 0.220[a] | 0.216[a] | 0.288[b] | 0.270[b] | 0.458[d] | 0.513[d] |

Noncovalent interactions (NCIs) are evidenced[285] by 0 < IBSI < 0.15, transition-metal coordination bond by 0.15 < IBSI < 0.60, and covalent bonding by 0.15 < IBSI < 4.0 values. [a] X= I. [b] X= Cl. [c] X=S. [d] X=$SCF_3$

### 3.2.6.2. The DFT exploration of the formation of [1c]$^+$

Several scenarios were considered for the mechanism of formation of [**1c**]$^+$. In this study, only intramolecular mechanisms of condensation were considered, but from the experimental investigations, there are still two major issues that remain unresolved:

a) where does the hydrogen $H_5$ originate from?

b) what is the fate of the Co after the release of [**1c**]$^+$?

We considered that the formulation of a plausible reaction energy profile should be based on the following crucial three steps starting from **1a**:

i) attack of the carbanionic carbon of the *phpy* ligand, on carbon $C_4$ at Cp*

ii) attack of the nitrogen of the *phpy* on carbon $C_3$ at Cp*

iii) capture of hydrogen $H_5$ (likely as a H•).[≠]

#### 3.2.6.2.1. Intrinsic Mechanism of Cyclocondensation

Like strongly suggested by EPR spectroscopy, cyclic voltammetry and experimental evidence of the ready oxidation of **1a**, the first step of the condensation reaction conspicuously involves the oxidation of singlet-state **1a** into Co(IV) complex [**1a'**]$^+$ which was considered therein in its doublet-state (by about 20 kcal/mol more stable than the quartet 3/2 spin state) in a way similar to the treatment operated by Pérez-Temprano et al.[140] for [Cp*Co($SCF_3$)(*phpy*)]. The computed Gibbs free energies of the single electron oxidation of **1a** by $Ph_3C^+$ and by $I_2$ amount to + 9 kcal/mol and + 19 kcal/mol respectively. The Gibbs enthalpy value for $Ph_3C^+$ is a rather low endergonic value for an equilibrated oxidation, given that the irreversible consumption of [**1a'**]$^+$ draws this oxidation step to completion by virtue of the mass action law. An additional single-electron oxidation of [**1a'**]$^+$ into singlet or triplet state [**1a'**]$^+$ was eventually discarded, for its Gibbs free energy exceeded +40 kcal/mol. Note that the spin density of [**1a'**]$^+$ is essentially located at the Co center.

The doublet-state Co(IV) species [**1a'**]$^+$ was therefore considered as pivotal in the mechanism of formation of [**1c**]$^+$. Three pathways appeared to be realistic with respect to the crucial H atom capture step (Scheme 3.15), all three pathways start with the

oxidation of **1a** into doublet [**1a'**]$^+$ and subsequently diverge. From [**pre-1c**]$^+$ the three pathways converge. The Co(I) center undergoes an oxidative addition by a solvent molecule and [**1c**]$^+$ is finally released.

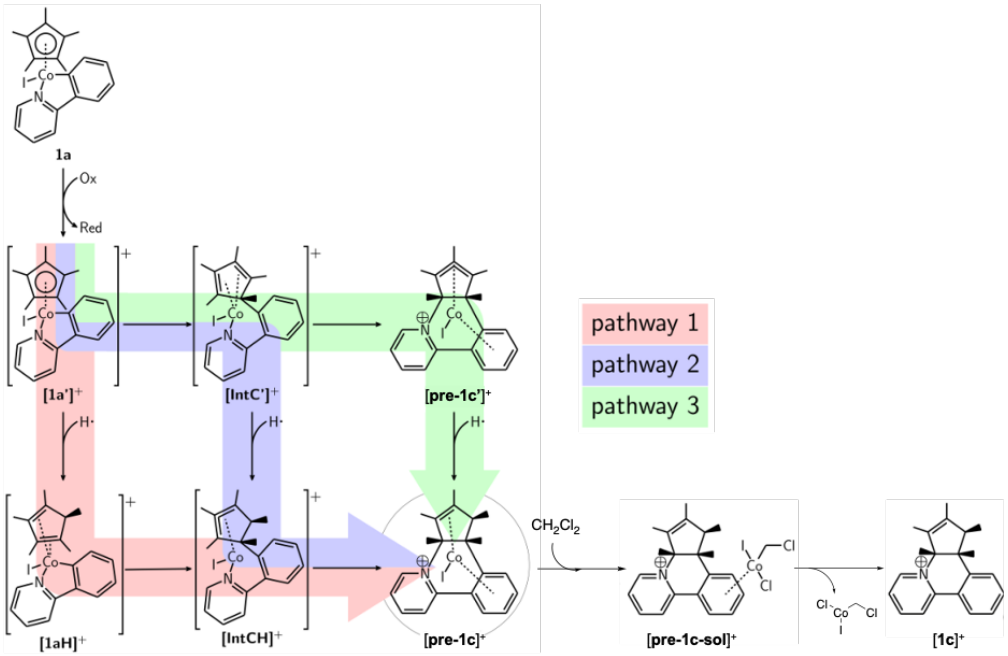


**Scheme 3. 15.** Proposed pathways for the condensation of Cp* on *phpy*. Pathway1 (light pink): **1a** → [**1a'**]$^+$ → [**IntC'**]$^+$ → [**IntCH**] → [**pre-1c**]$^+$ → [**pre-1c-sol**]$^+$ → [**1c**]$^+$. Pathway 2 (light blue): **1a** → [**1a'**]$^+$ → [**IntC'**]$^+$ → [**pre-1c'**]$^+$→ [**pre-1c**]$^+$ → [**pre-1c-sol**]$^+$ → [**1c**]$^+$. Pathway 3 (light green): **1a** → [**1a'**]$^+$ → [**1aH**]$^+$ → [**IntCH**] → [**pre-1c**]$^+$ → [**pre-1c-sol**]$^+$ → [**1c**]$^+$.

**Pathway 1:** The capture of a formal H• by [**1a'**]$^+$ occurs before the condensation reaction, H$^•$ is first captured by the Co(IV) radical and migrates spontaneously to $C_5$, then $C_4$ of the Cp* first attacks on $C_{2'}$ of the *phpy* and finally rearrangement occurs around the Co position leading to the formation of the $C_3$-N bond.

**Pathway 2:** The capture of a formal H• occurs after the migration of *phpy*'s C to the Cp* ligand and before the migration of the N center, $C_4$ of the Cp* first attacks on $C_{2'}$ of the *phpy*, then H$^•$ is captured by the radical Co(IV) and migrates spontaneously to

$C_5$ of the Cp*, and finally rearrangement occurs around the Co position leading to the formation of the $C_3$-N bond;

**Pathway 3:** The condensation of the Cp* with the *phpy* ligand occurs prior to the capture of a formal H•, $C_4$ of the Cp* first attacks on $C_{2'}$ of the *phpy*, then $C_3$ of the former Cp* attacks on N and finally H• is captured;

#### 3.2.6.2.2. The "H" Atom Capture Question

Discrimination between these three pathways for which Figure 3.23 a materializes the intrinsic energy profile considering the intervention of fictitious H• depends on the source of the latter, which remains still to be identified. Figure 3.23 b and c shows how two different H• sources, namely $Ph_3CH$ and $Ph_3C$-$C_6H_5C(Ph_2)$, may affect the overall energy reaction profile changing the energy precedence of pathways 1, 2 and 3 by raising activation barriers at different stages.

Due to the uncertainty existing around the origin of $H_5$ all calculations were carried out considering the intervention of a fictitious H• as a starting model to compute reaction "intrinsic" energy profiles (Figure 3.23a). This hypothesis has the advantage of providing a lower-bound reference value of the H• capture energy to which actual sources of H atom can be confronted. For instance, considering intuitively that $Ph_3CH$ could be the source of H• in either oxidative mechanism entailed a prohibitive surge in the overall reaction Gibbs enthalpy of $\Delta\Delta G$ = +71 kcal/mol, which discards $Ph_3CH$ as a reasonable H• atom source (Figure 3.23b).

The so-called Gomberg−Jacobson−Lankamp−Nauta−MacLean asymmetric quinoid-like structure $Ph_3C-C_6H_5C(Ph_2)$ arising from the reaction of two units of $Ph_3C$• ($\Delta G$ = +9 kcal/mol) was also considered as a potential source of H•, as shown in Scheme 3.8. This hypothesis proved to be unfavorable, as it would result in a surge in the overall reaction Gibbs enthalpy of $\Delta\Delta G$ = +46 kcal/mol in comparison to the reference reaction Gibbs enthalpy with H• (Figure 3.23c). The same observation could be made when the Cp* ligand from external **1a** or [**1a'**]$^+$ is considered to be the source of H• ($\Delta\Delta G$ = +82 and +68 kcal/mol, respectively).

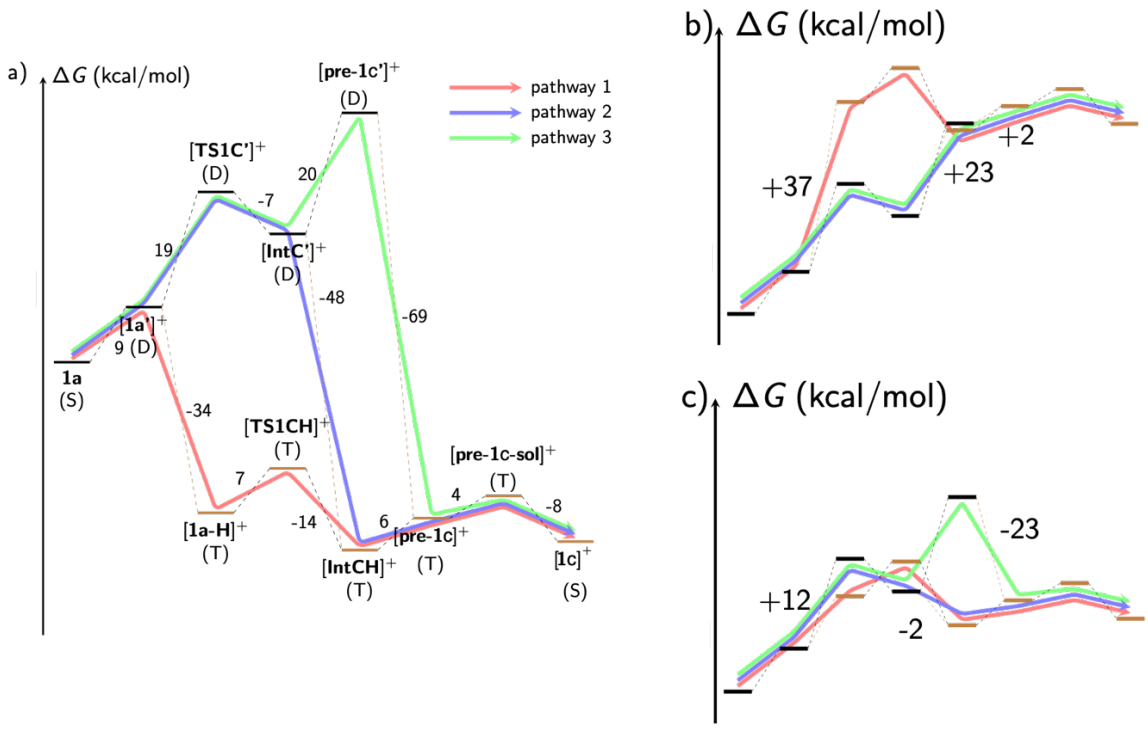


**Figure 3. 23.** Proposed computed Gibbs free energy profiles of the formation of [**1c**]$^+$. The three possible pathways are materialized by solid-colored lines (green, blue, pink). a) Exergonic intrinsic Gibbs energy profile considering a fictitious H•. b) Endergonic intrinsic Gibbs energy profile considering $Ph_3CH$ as the source of H•. c) Endergonic intrinsic Gibbs energy profile considering $Ph_3C$-$C_6H_5C(Ph_2)$ as the source of H•.

#### 3.2.6.2.3. Early capture of H• and spin state in pathway 1

The formation of a hydrido cobalt(V) species by capture of H• was considered to account for the exclusive endo positioning of $H_5$. The oxidation of singlet state **1a** into doublet state [**1a'**]$^+$ followed by the capture of H• to yield a putative cationic hydrido cobalt(V) species corresponds formally to the capture of $H^+$ by **1a**, which has already been ruled out experimentally, for it leads exclusively to the demetallation of the *phpy* ligand.

Moreover, all attempted optimizations of the hydrido Co(V) species in the singlet state, which is the intermediate arising from the capture of H• by [**1a'**]$^+$ (or of $H^+$ by **1a**) evolved into "agostic"[196, 281] C−H···Co complexes (Figure 3.24), where the hydrogen is

bound either to the $C_{2'}$ of the *phpy* ([**ag-*phpy***]$^+$ ) or to the $C_5$ of the Cp* ([**ag-Cp*-H**]$^+$ ), [**ag-*phpy***]$^+$ being more stable than [**ag-Cp*-H**]$^+$ by 20 kcal/mol (ΔΔG).

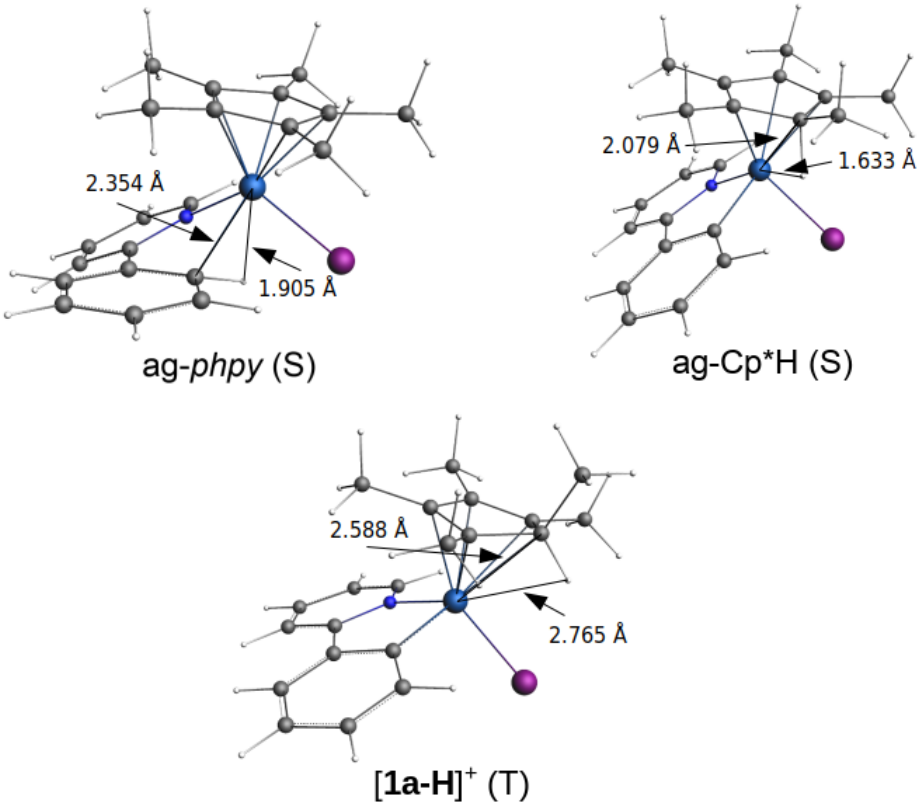


**Figure 3. 24.** Singlet and triplet state C−H···Co agostic transient geometries computed at the (COSMO)-ZORA-PBE-D4(EEQ)/all- electron TZP level with selected interatomic distances. Color code for atoms: gray, C; blue, N; indigo, Co; white, H; purple, I.

Triplet spin states have also been considered for the different intermediates after capture of the hydrogen as spin transitions between triplet and singlet states cannot be fully[275] ruled out in chemical reactions implying Co(III)[344].

Tentative optimization of the hydrido-intermediate Co(V) [H-**1a**]$^+$ in the triplet state evolved unavoidably either into a non-agostic ($\eta^4$-Cp*H)Co(III)complex that might undergo the condensation of Cp* with the *phpy* ligand or by the insertion of H in the Co-I bond leading to the release of HI, the former being the most favorable by 6 kcal/mol (ΔΔ*G*). Both products in the triplet state are less stable than other products formed along a singlet state path.

#### 3.2.6.2.4. Cyclocondensation in pathway 1

Considering the attack of the Cp* on the *phpy* from the ($\eta^4$-Cp*H)Co complex in the triplet state, three possible paths can be followed, as for **1a**, that is namely : i) attack of $C_3$ of Cp* on the nitrogen of the *phpy* ligand first, then of $C_4$ of the Cp* on the carbanionic $C_{2'}$ of *phpy*, ii) attack of $C_4$ of Cp* on $C_{2'}$ of *phpy*, then of $C_3$ of Cp* on N of *phpy*, iii) concerted attack of $C_3$ and $C_4$ of Cp* on N and $C_{2'}$ of *phpy* respectively.

Out of these possible paths, the attack of $C_4$ of Cp* by $C_{2'}$ (*phpy*) displays the lowest activation barrier ($\Delta G$= + 7 kcal/mol, while $\Delta G$=+ 48 kcal/mol for the concerted attack and $\Delta G$= + 42 kcal/mol for the attack on N). Considering these three paths from the agostic ($\eta^4$-Cp*H) complex in the singlet state, each of these display an activation barrier higher than + 30 kcal/mol, causing all of these possible transition states to be higher in energy than the one for the attack on $C_{2'}$ (*phpy*) in the triplet state.

Following this path, the formation of the intermediate where the C-C bond has been formed, i.e [**IntCH**]$^+$, is exergonic ($\Delta G$= - 14 kcal/mol). This intermediate is more stable in the triplet state than in the singlet by a $\Delta\Delta G$ of +15 kcal/mol. In the triplet state the formation of the final complex [**pre-1c**]$^+$, i.e when the final condensation product [**1c**]$^+$ is still bound to the "CoI" moiety, from [**IntCH**]$^+$ is then endergonic ($\Delta G$= + 6 kcal/mol). Computations suggest this reaction as barrierless, the shift of the Co from a *κN* position to a $\eta^2$ position on the aryl fragment combined with the search for planarity of the *phpy* moiety leading to a proximity between $C_3$ of the former Cp* and the N, which favors the formation of the C-N bond. Intermediate [**pre-1c**]$^+$ is more likely to stay in the triplet state, as its singlet equivalent lies 7 kcal/mol above.

#### 3.2.6.2.5. Early C-C coupling in pathway 2 and 3:

Also considered was the attack of the Cp* by the *phpy* ligand in [**1a'**]$^+$ before the capture of the hydrogen atom occurs later in the process. Again, three possible paths can be considered. The prior attack of $C_4$ at Cp* by $C_{2'}$ at the *phpy* ligand shows the lowest activation barrier ($\Delta G$= + 19 kcal/mol, while $\Delta G$= + 48 kcal/mol for the concerted attack and $\Delta G$= + 42 for the prior attack on N). In these conditions, the formation of the C-C bond in intermediate [**IntC'**]$^+$ from [**1a'**]$^+$ is endergonic with a $\Delta G$ of + 12 kcal/mol.

#### 3.2.6.2.6. Capture of H• in pathway 2

The deferred capture of H• by intermediate [**IntC'**]$^+$ was considered by attempting the optimization of a hydrido Co(III) species, which eventually ended up in the migration of H to $C_5$, thus yielding the triplet state intermediate [**IntCH**]$^+$, which undergoes the N-C coupling as mentioned for the pathway 1.

#### 3.2.6.2.7. N-C coupling followed by H• capture in pathway 3

From [**IntC'**]$^+$, the formation of the C-N bond is also endergonic ($\Delta G$= + 20 kcal/mol) and barrierless. Tentative optimization of a Co(III) hydride species accounting for the capture of H• eventually ended up in the migration of H to $C_5$, yielding [**pre-1c**]$^+$.

#### 3.2.6.2.8. Fate of "CoI"

The question of the fate of the "CoI" moiety when [**1c**]$^+$ is released has been addressed heuristically. Calculation reveals that the release of "naked" CoI as such from triplet-state [**pre-1c**]$^+$ is highly unfavorable whatever the spin multiplicity of CoI may eventually be ($\Delta G$= + 81 kcal/mol for the singlet, $\Delta G$= + 48.8 kcal/mol for the triplet, and $\Delta G$= + 69 kcal/mol for the quintet). It was therefore inferred that the "CoI" moiety might undergo the oxidative-addition of a solvent molecule. Insertion of the Co(I) of CoI in the C-Cl bond of a solvent molecule after the release of [**1c**]$^+$ was found highly stabilizing ($\Delta G$= - 48 kcal/mol). The addition of a solvent molecule before the release of [**1c**]$^+$ was also considered. The insertion of the Co in the C-Cl bond is endergonic ($\Delta G$= + 4 kcal/mol) in the triplet state (lowest spin state). From there, the release of [**1c**]$^+$, generating a [Co(Cl)(I)($CH_2Cl$)] complex, becomes exergonic ($\Delta G$= - 8 kcal/mol).

## 3.3. Conclusion

In this chapter, we described the method for the synthesis of cyclocondensation complex obtained in Chapter 2. Halogeno-Cp*Co(III) metallacycles derived from 2-phenylpyridine (*phpy*-H) react in solution with one-electron oxidants to irreversibly structurally collapse by a cyclocondensation of the organic ligands with the capture of a H atom from the medium to afford new cationic alkaloids. Low temperature EPR

analysis of a mixture of the *phpy*-based cobaltacycle with the tritylium cation reveals the signatures of trityl and Co(IV)-centred radicals. Electrochemical analyses showed that the oxidation of the considered cobaltacycles is irreversible, producing a host of electroactive species. DFT investigations of noncovalent interactions suggest a predisposition of cobaltacycles to intramolecular Co(IV)-templated cyclocondensation, of which the exploration of the reaction energy profile supports the key roles 1) of the Co(III) cobaltacycle oxidation into a short lived Co(IV) species and 2) of triplet state organocobalt intermediates.

Overall, this unexpected result draws some light on the widely accepted catalytic systems, thus questioning its robustness.

# Chapter 4. Attempted catalytic reactions with Cp*Co(III)-metallacycles

## 4.1. Introduction

As we mentioned in the chapter 1, the Cp*metallacycles are not only intermediates in the C-H functionalization, but also can act as efficient catalysts for organic transformations. In this chapter, we will discuss about our different attempts to apply these cobaltacycles in various catalytic reactions.

Hydrosilylation, the addition of Si−H bond across unsaturated bonds, which is a very powerful reaction for the generation of organosilicon compounds, has been widely used in the polymer chemistry, material science and inorganic synthesis[345]. In the recent years, our group has developed a series of iridium-base metallacycles and successfully applied to the hydrosilylation of alcohols, ketones, esters, nitrile, amides and imines showing very high activity[133, 134, 247]. These metallacycles derived from 2-phenypyridine or benzo(h)quinoline with $[Cp^*IrCl_2]_2$ (Scheme 4.1). In our previous work, there cationic Cp*Ir(III)-complexes, e.g., $[Cp^*Ir(\kappa^2\text{-}(C,N)\text{-}(L)(NCMe))][BArF_{24}]$ (L= ligands) can react with silanes $HSiR_3$ to form a key $(R_3Si)(H)Ir$ reactive intermediates[346], corresponding to the activation of the Si-H bond, ready to hydrosilylate.

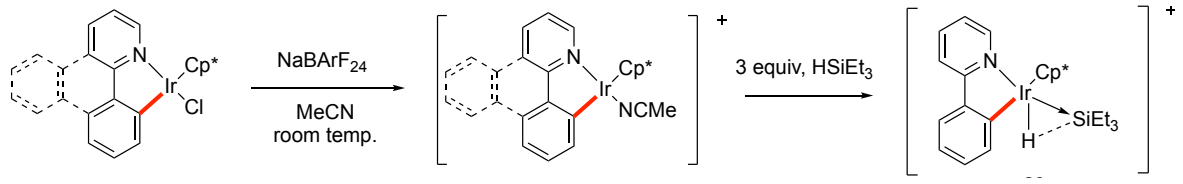


Scheme 4. 1. The synthesis of iridacycles and the reaction of iridacycles with $HSiEt_3$.

Since the discovery of $Co_2(CO)_8$ catalyzed hydrosilylation of terminal alkenes by Chalk and Harrod in 1960s (Scheme 4.2)[347], there has been long-standing research interest in cobalt-catalyzed hydrosilylation reaction. In this pioneering study, no efficient cobalt-based catalyst was obtained, however, the two most important mechanisms for

transition metal-catalyzed hydrosilylation of alkenes were proposed, namely the Chalk-Harrod mechanism and the modified Chalk-Harrod mechanism [348, 349] (Scheme 4.3). Until now, a series of well-defined cobalt-based catalysts have been developed for hydrosilylation with high catalytic efficiency and selectivity, by introducing new ligand groups and changing the oxidation state of the metal center [345]. However, there are no examples of Cp*Co(III)-metallacycles catalyzing hydrosilylation. In our case, these Cp*Co(III)-metallacycles might be a promising catalyst for hydrosilylation, so here, we attempted to investigate their activity.

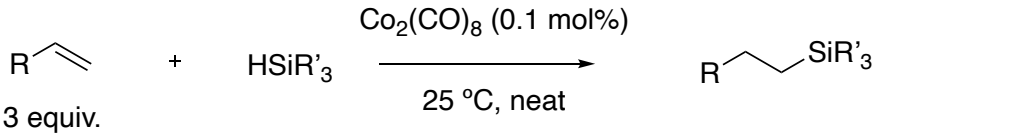


R = *n*-$C_3H_7$, *n*-$C_4H_9$, *n*-$C_6H_{13}$
$HSiR'_3$ = $HSiEt_3$, $HSi(OMe)_3$, $HSiPhCl_2$

**Scheme 4. 2.** The pioneering example of $Co_2(CO)_8$ catalyzed hydrosilylation of terminal alkenes

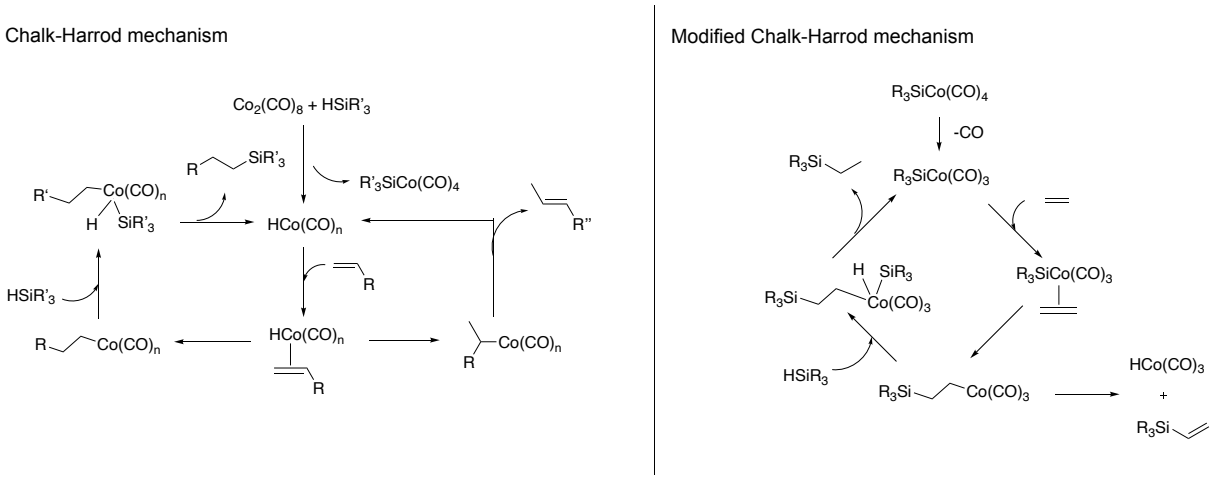


**Scheme 4. 3.** The two mechanisms for $Co_2(CO)_8$ catalyzed hydrosilylation of alkenes.

## 4.2. Results and discussion

Considering the hydrosilylation results obtained with the cationic iridacycles, the main idea was to reproduce the same chemistry but in the presence of homologous cobaltacycles. So, we started by checking the catalytic efficiency of complex **1b** under the similar reaction conditions used for the Cp*Ir(III)-metallacycles catalyzed hydrosilylation of ketones and nitriles (room temperature in DCM using $HSiEt_3$ silane

as reducing agent and 0.1 mol% of catalyst) as reported by our group[133]. Unfortunately, the hydrosilylation of ketones catalyzed by cobaltacycles **1b** and **5b** did not produce the desired product, as shown in table 4.1.

**Table 4. 1.** Hydrosilylation of ketone via cobaltacycles **1b** and **5b**

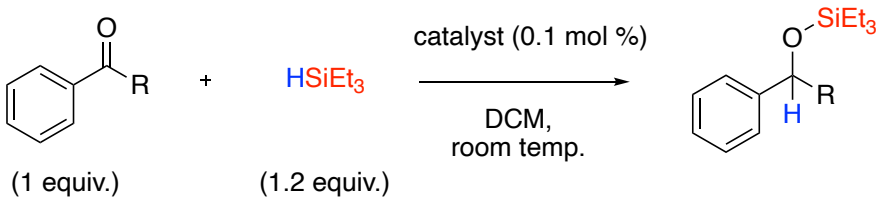


| Entry | Ketone | Catalyst | Yield |
|---|---|---|---|
| 1 | Acetophenone | **1b** | 0% |
| 2 | Benzophenone | **1b** | 0% |
| 3 | Acetophenone | **5b** | 0% |
| 4 | Benzophenone | **5b** | 0% |

Reaction conditions: Ketone (1 mmol), catalyst (0.1 mol%), silane (1.2 mmol), DCM (0.5 mL), 1,3,5-trimethoxybenzene as internal reference.

Nevertheless, in order to further evaluate the activity of the Cp*Co(III)-metallacycles and also to gain insight into the catalytic reactions, we investigated the stoichiometric reaction of **1b** with silane. The cationic cobaltacycle **1b** was mixed with $HSiEt_3$ (1 equiv.) in J. Young valve NMR tube in DCM-$d_2$ at 298 K or 247 K, and the reaction was monitored by $^1H$ NMR spectroscopy. Unfortunately, no reaction occurred as no Si-H activation, or Co-H complex were observed in the $^1H$ NMR spectrum. Noteworthy, the Si-H activation is instantaneous with the iridacyles. (Figure 4.1), which is consistent with the result of the catalytic experiment we first performed with cobaltacycles.

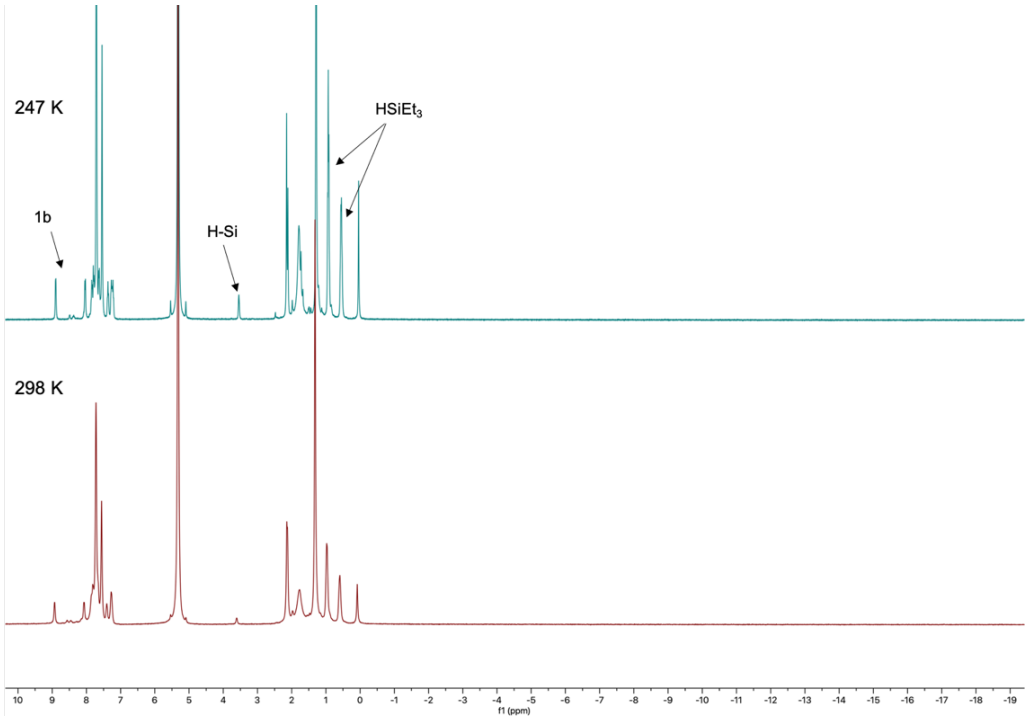


**Figure 4. 1.** Standard stoichiometric reaction of **1b** with $HSiEt_3$ monitored by $^1H$ NMR. (top: at 247 K ; bottom : 298K)

Based on our theoretical studies of the Cp*Ir(III)-metallacycles catalyzed hydrosilylation of ketones, the crucial elements of this reaction were the activation of Si-H bond and the formation of Co-H bond. So, we attempted to add a hydride source to promote this reaction, such as $NaHBEt_3$[350, 351] and Red-Al. Subsequently, the hydrosilylations of benzophenone were carried out with different set of cobalt-complexes, replacing the DCM with toluene. As shown in the table 4.2, when complex **1b** is used (5% mol) for the catalysis of benzophenone and $HSiEt_3$ in toluene at 40°C during 5 hours, no any conversion was detected in toluene (Table 4.2, entry 1) and only 5.5% of silylated product **A** was observed when the reaction was performed in $CH_2Cl_2$ (Table 4.2, entry 2), showing the different reactivity of Ir and Co. When the neutral **1a** was used as catalyst alone also no conversion of the starting benzophenone was detected by $^1H$ NMR after 5 hours of reaction (Table 4.2, entry 3). The addition of $NaBHEt_3$ (10% mol) to **1a** allows an interesting reactivity, transforming quite completely the benzophenone (Table 4.2, entry 4). Red-Al as source of hydride did not bring such result.

**Table 4. 2.** Hydrosilylation of benzophenone with $HSiEt_3$.

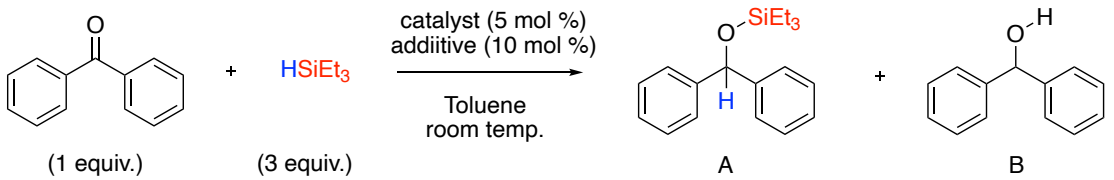


| Entry | Catatalyst | Additive | Conv. to **A** (**B**) (%) | Total Conv. (%) | NMR* Yield (%) |
|---|---|---|---|---|---|
| 1 | **1b** | - | 0 | 0 | 0 |
| 2[a] | **1b** | - | 5.5 (1.6) | 7.1 | 7 |
| 3 | **1a** | - | 0 (0) | 0 | 0 |
| 4 | **1a** | $NaBHEt_3$ | 78.6 (18.1) | 96.7 | 83 |
| 5 | **1a** | Red-Al | 9 (33.9) | 42.8 | 9 |
| 6 | **5a** | $NaBHEt_3$ | 55.9 (17.3) | 73.3 | 58 |
| 7 | **9a** | $NaBHEt_3$ | 75.6 (21.7) | 97.3 | 74 |
| 8 | **10a** | $NaBHEt_3$ | 3.4 (11.9) | 15.2 | 6 |
| 9 | $[Cp^*CoI_2]_2$ | $NaBHEt_3$ | 61 (-) | 61 | 70 |
| 10 | $[Co_2(CO)_8]$ | $NaBHEt_3$ | 0 (17) | 17 | 0 |
| 11 | $[CoCp^*(CO)I_2]$ | $NaBHEt_3$ | 18 (18) | 36 | 19 |
| 12 | $[CoCl_2]$ | $NaBHEt_3$ | 0 (21) | 21 | 0 |
| 13 | $[Co(acac)_2]$ | $NaBHEt_3$ | 3 (16) | 19 | 3 |
| 14 | - | $NaBHEt_3$ | 0 (23) | 23 | 0 |
| 15 | - | - | 0 (0) | 0 | 0 |

Reaction conditions: benzophenone (1 mmol), catalyst (5 mol%), $HSiEt_3$(3 mmol), toluene (2 mL); [a] same condition in DCM. 1,3,5-trimethoxybenzene as internal reference.

None of the simple starting Co complexes such as $[Co_2(CO)_8]$, $[Cp^*CoI_2]_2$, $[CoCp^*(CO)I_2]$, $[CoCl_2]$, $[Co(acac)_2]$ presented similar activity (Table 4.2, entries 9-13). Moreover, the cobaltacyle **9a** with chloride instead of iodine, shown a lower activity as contrary to the previous results with the homologous Ir complexes. The cobaltacycle **10a**, with Cp instead of Cp*, gave us no hope as new catalyst (Table 4.2, entry 8) proving again the importance of the Cp* ligand in catalysis. None of the blank reactions

(without cobalt or without $NaBHEt_3$) have shown any tiny activity towards this reaction (Table 4.2, entry 15) nevertheless $NaBHEt_3$ (10% mol) alone, allows the reduction to benzophenol (23%) (Table 4.2, entry 14).

These results were obtained a week before the writing of my thesis. The scope of the reaction (change of carbonyl) and hydroslilyation of Nitrile are studying by another researcher of our research group now. Over all, the use of $NaBHEt_3$ as an activator can improve the hydrosilylation of ketones, which provides a basis for our consequential study of hydrosilylation.

Moreover, before using $NaBHEt_3$, we also attempted with different activators, such as $[Ph_3C][BArF_{24}]$, the idea was to add $[Ph_3C][BArF_{24}]$ as a remover of the halido ligand in order to form a new "unsaturated" cobaltacycle more reactive than **1a** or **1b**. Unfortunately, we observed the decomposition of the complex as discussed in detail in chapter 3.

## 4.3. Other attempted reactions with cobaltacycles

In addition to the hydrosilylation, we also attempted other catalytic reactions to further investigate the reactivity of the Cp*Co(III)-metallacycles, the hydroboration reaction, and the cycloaddition reaction of alkyne or ethyl diazoacetate were considered.

### 4.3.1. Hydroboration

In recent years, the hydroboration of alkenes catalyzed by cobalt-complexes have also recceived a significant attention, which provide a convenient route to aklylboronic acid derivative that can acts as versatile intermediates for a wide range of application in various bond-forming reactions[351-354]. While the cobalt-catalysts used in the vast majority of protocols were well-defined cobalt(II) complexes, a significant need remains for the development of new cobalt catalysts for hydroboration reactions, such as Cp*Co(III)-complexes.

Before starting the catalytic reaction, we also investigated the stoichiometric reaction of cobaltcycles with boranes, such as pinacolborane (HBPin), catecholborane (HBCat). Complexes **1b** or **5b** were reacted with boranes (10 equiv) in NMR tube in DCM-$d_2$ at

room temperature, then this reaction was monitored by $^{1}H$ NMR spectroscopy. Unfortunately, we did not observe the formation of the expected product similar to the [Ir-H-Si] complex, which is consistent with the reaction of **1b** and $HSiEt_3$.

It is worth noting that we obtained a crystal structure in the reaction of **1b** and HBPin, which is shown in Figure 4.2. This structure is similar to that of **1b**, where the NCMe coordinated to cobalt center was replaced by the -$SMe_2$ ligand. Then the question arises, where does the -$SMe_2$ group comes from? The only explanation is that the -$SMe_2$ group could be arising from the pinacolborane, which can be synthesized from $BH_3{\cdot}SMe_2$[355], so tiny amount of $SMe_2$ impurities were present in the commercial pinacolborane. However, this is only our hypothesis and has not been further investigated. We also attempted to activate $HBR_2$ several times, with different temperature, changing the solvent and so on, but nothing happened positively.

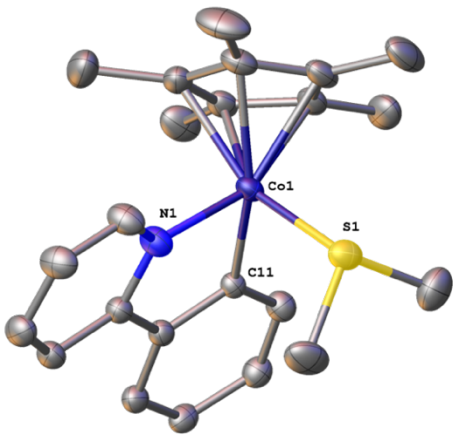


**Figure 4. 2.** ORTEP diagram of the structure of **1g**, ellipsoids displayed at 50% probability. The hydrogen-atoms on the carbon and $BArF_{24}^{-}$ were omitted for clarity. Selected bond distances [Å] and angles [°]: Co1-S1 2.2309(8), N1-Co1 1.944(2), C11-Co1 1.955(2); C11-Co1-S1 94.99(7), N1-Co1-S1 90.98(7), N1-Co1-C11 82.99(10).

### 4.3.2. Cycloaddition reaction of alkynes or diazo compounds

As introduced in the chapter 1, the alkenes and diazo compounds are usually employed as coupling partners in the vast majority of Cp*Co(III)-catalyzed annulation reaction[2, 74]. The idea was to evaluate the reactivity of these neutral and cationic

Cp*Co(III)-metallacycles in this kind of annulation reaction. Therefore, a series of stoichiometric reactions between cobaltacyles and alkene (or diazo compound) were performed.

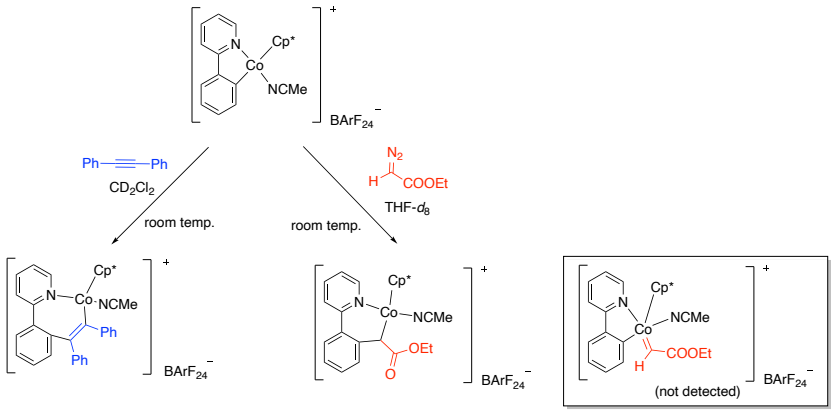


**Scheme 4. 4.** Reaction of cobaltacyle with diphenylacetylene and ethyl diazoacetate.

The reaction of the **1b** with diphenylacetylene and ethyl diazoacetate were monitored by $^1$H NMR spectroscopy at room temperature in $CD_2Cl_2$ and THF-$d_8$, respectively. In the reaction with diphenylacetylene, we observed the conversion of **1b** to the seven-membered cationic cobaltacycle, which is consistent with the results reported by Perez-Temprano and co-workers[282]. Meanwhile, the six-membered cationic cobaltacycle was observed in the reaction with ethyl diazoacetate, which was evidenced by X-ray structure (Figure 4.3), however, the metal carbene complex was not observed. To further capture the metal carbene complex, the variable-temperature $^1$H NMR study was carried out (Figure 4.4). At 213 K, a distinct NMR peak at $\delta$ 11.5 ppm was observed, but we are not quite sure what it is, when the temperature increased from 213 K to 263 K, this signal was decreased and shifted, and subsequently disappeared at 273 K, giving rise to a new set of signals that can be tentatively attributed to the six-membered cationic cobaltacycle, and the metal-carbene complex was still not observed.

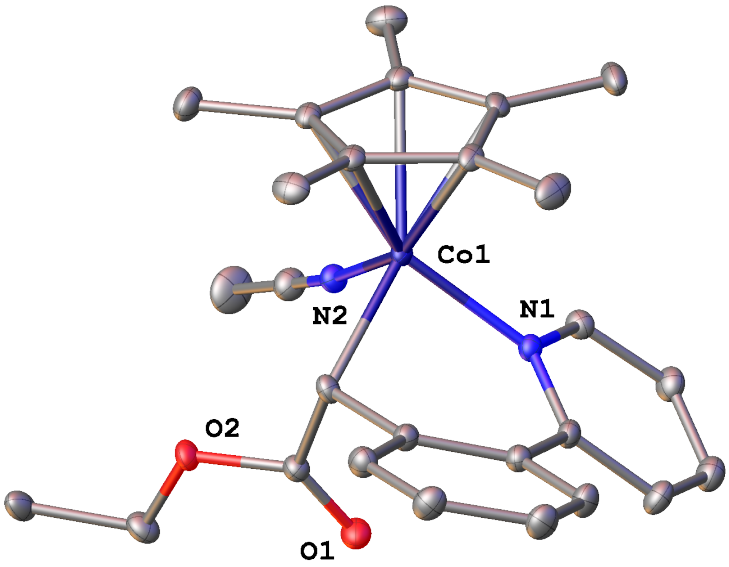


**Figure 4. 3.** ORTEP diagram of the preliminary structure of **1h**, ellipsoids displayed at 50% probability. The hydrogen-atoms on the carbon and $BArF_{24}^-$ were omitted for clarity.

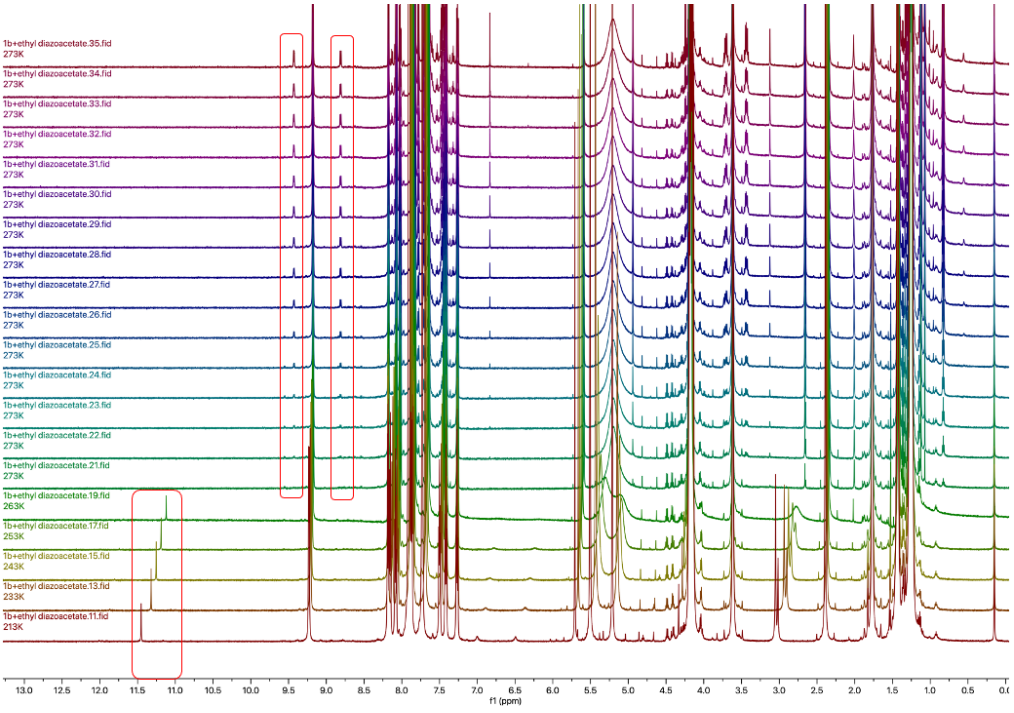


**Figure 4. 4.** Variable-temperature $^1$H NMR spectra of the reaction of **1b** with ethyl diazoacetate (600 MHz, THF-$d_8$).

After, the cycloaddition reactions of ethyl diazoacetate were tried with different temperature and solvent, but we only observed that the homocoupling of ethyl diazoacetate.

## 4.4. Conclusion

As discussed in this section, we have attempted a variety of catalytic reactions with Cp*Co(III)-metallacycles, such as hydrosilylation, hydroboration, and the cycloaddition reaction of alkynes or diazo compounds. For the hydrosilylation, although Cp*Co(III)-metallacycles do not exhibit catalytic properties under the same conditions used for analogs Ir complexes, we found in subsequently studies that it can also effective to catalyzed the hydrosilylation of ketones in the presence of $NaBHEt_3$. Despite the results, the study was still in the initial stage. The unexpected crystal structure obtained by hydroboration, providing a new idea to develop new Cp*Co(III)-metallacycles. Undoubtedly, the Cp*Co(III)-metallacycle as a promising catalyst that still has many applications to be developed.

# Chapter 5. Experimental Part

## 5.1. General information

### 5.1.1. Materials and methods

All experiments were conducted under a dry argon atmosphere using standard Schlenk lines and dry glovebox techniques. All glassware was cleaned and oven-dried prior to use. All organic chemicals were purchased from Sigma Aldrich, TCI Chemicals and Alfa Aesar. $Co_2(CO)_8$ was purchased from Pressure Chemical Co. The compound 4-tertiobutyl,2-(4-*N*,*N*-dimethylaminophenylene)-pyridine (abbr. 2-*anpyH*), 2,3-Diphenylquinoxaline, chloro(2-phenylpyridine-$k^2$-*C,N*)(pentamethylcyclopentadienyl)-iridium(III) (**2a**) and the cobalt(III) complexes $[Cp^*Co(\mu\text{-}I)I]_2$ were prepared as reported in the literature.[147, 356, 357] All solvents were distilled over sodium or $CaH_2$ under argon before use. Deuterated solvents were dried over sodium or $CaH_2$, filtered over activated neutral alumina, and stored under argon before use. $^1H$ (300, 400, 500, and 600 MHz), $^{11}B$ (128 MHz), $^{13}C$ (75 and 126 MHz), and $^{19}F$ (282 MHz) NMR spectra were measured on Bruker DPX 300 and 400, Avance I 500, and Avance III 600 spectrometers. Chemical shifts (expressed in parts per million) were referenced against solvent peaks or external reference standards ($CF_3C_6H_5$ in $CDCl_3$ for $^{19}F$, and $NaBH_4$ in $D_2O$ for $^{11}B$). Mass spectra were run on a MicroTOF Bruker Daltonics spectrometer, using a TOF-ESI coupling analysis system. Elemental analyses were achieved with Thermo Scientific FLASH 2000 CHNS/O analyzers.

### 5.1.2. Structural X-ray diffraction analyses

The crystals were placed in oil, and a single crystal was selected, mounted on a glass fibre and placed in a low-temperature $N_2$ stream. For complexes [**1b**][$I_3$], [**1b'**][$I_3$], [**1c**][$I_3$], [**1c'**][$I_3$], **4a** and **5a**, X-Ray diffraction data collection was carried out on a Bruker APEX II DUO Kappa-CCD diffractometer equipped with an Oxford Cryosystem liquid $N_2$ device, using Mo-Kα radiation ($\lambda$ = 0.71073 Å). The crystal-detector distance was 38 mm. The cell parameters were determined (APEX3 software)[358] from reflections

taken from three sets of 12 frames, each at 10 s exposure. The structures were solved using the program SHELXT-2014.[359] The refinement and all further calculations were carried out using SHELXL-2014[360] or SHELXL-2018.[360] The H-atoms were included in calculated positions and treated as riding atoms using SHELXL default parameters. The non-H atoms were refined anisotropically, using weighted full-matrix least-squares on $F^2$. A semi-empirical absorption correction was applied using SADABS in APEX3[358]. For complexes **1f**, **2b, 2c, 3b, 4b**, **5b**, **1a, 7a, 8a,** [**1c**][$BArF_{24}$]**,** [**7c**][$BArF_{24}$]**,** [**8c**][$BArF_{24}$]**,** [**7d**][$BArF_{24}$] and [**8d**][$BArF_{24}$]**,** X-ray diffraction data collection was carried out on a Bruker PHOTON III DUO CPAD diffractometer equipped with an Oxford Cryosystem liquid $N_2$ device, using Mo-K$\alpha$ radiation ($\lambda$= 0.71073 Å). The crystal-detector distance was 37 mm. The cell parameters were determined (APEX3 software)[358] from reflections taken from 1 set of 180 frames at 1 s exposure. The structures were solved using the program SHELXT-2014.[359] The refinement and all further calculations were carried out using SHELXL-2014 or SHELXL-2018.[360] For complexes **1f**, **2b** and **2c** the hydrogen atoms of the NH groups, OH groups and of the water molecules were located from Fourier difference. For complexes **4b** and **5b**, the SQUEEZE instruction in PLATON[361] was applied. A semi-empirical absorption correction was applied using SADABS in APEX3[358]. For compound [**8c**][$BArF_{24}$], the hydrogen atom of the OH group was located from Fourier difference. The other H-atoms were included in calculated positions and treated as riding atoms using SHELXL default parameters. The non-H atoms were refined anisotropically, using weighted full-matrix least-squares on $F^2$. A semi-empirical absorption correction was applied using SADABS in APEX3[362].

### 5.1.3. Cyclic voltammetry

Cyclic Voltammetry was conducted under the supervision of Prof. Laurent RUHLMANN (Laboratoire d'Electrochimie et Chimie Physique du Corps Solide, Institut de Chimie de Strasbourg). All glassware was dried for 24 hours at 90°C prior to use. Voltammetric data were recorded using an Autolab PGSTAT30 potentiostat (Eco Chemie, Holland) driven by the GPSE software with a standard three-electrode system flushed with a gentle stream of argon. The electrolyte was a solution of 0.1 mol $L^{-1}$ of anhydrous tetrabutylammonium hexafluorophosphate ([$NBu_4$][$PF_6$]) in dry distilled 1,2-$C_2H_4Cl_2$. The reference electrode was the Ag/AgCl electrode, which was electrically connected to the solution by a junction bridge filled with 5 mL of anhydrous $CH_3CN$ + 0.1 M

[$NBu_4$][$PF_6$]. The working electrode was a platinum disk electrode (*d* = 3 mm in diameter). All potentials are given *vs.* Ag/AgCl used as external reference and are uncorrected from ohmic drop.

### 5.1.4. EPR spectroscopy

EPR spectra were recorded by Sylvie CHOUA and Nolwenn LE BRETON (Laboratoire Propriétés Optiques et Magnétiques des Architectures Moléculaires, Institut de Chimie de Strasbourg) on a continuous-wave X-band EMX-plus equipped with TE102 rectangular cavity (ER 4102ST, Bruker) and an ESR900 continuous flow cryostat controlled with an Oxford ITC503S. EPR spectra were recorded with the following parameters: microwave power of 1 mW, a modulation frequency and amplitude of respectively 100 kHz and 0.4 mT, a conversion time of 300 ms and a time constant of 20.48 ms.

### 5.1.5. ITC experiments

Isothermal titration calorimetry (ITC) experiments were carried out on a Waters-SAS nano-ITC device (TA Instruments®) equipped with two stainless steel Hastelloy cells of 1 mL volume each) and housed in an argon-filled glovebox. Auto equilibration of the ITC was performed before every experiment to reach an acceptable baseline. The solutions of reactants were prepared in the same glovebox by dissolving a mass of substrate placed in a volumetric flask in pure, freshly distilled and degassed 1,2-dichloroethane. The ITC experiments were performed by sequential injection at 25.00ºC with a stirring rate of 300 rpm. The solution of tritylium salt was placed in the injection syringe and the solution of compound **1a** in the measure cell. Three thermograms were acquired by sequential injection of 2-3 µL with a delay between two injections not exceeding 900 s, and the raw enthalpy of the reaction was inferred by summing up the heat flow released from which was deduced the residual heat flow after the thermal inflexion point.

## 5.1.6. Computational details for chapter 2

### 5.1.6.1. DFT-D computations

Geometry optimizations of reactants, intermediates, transitions states and products were performed with the methods of density functional theory using the SCM-ADF2019.01 package,[363] considering the molecules in the gas phase at the singlet state. The PBE[202] functional augmented with Grimme's DFT-D3(BJ) implementation of dispersion[364, 365] with a Becke−Johnson (BJ) damping function[203-205] was used in all geometry optimizations. All geometry computations were carried out using scalar relativistic corrections within the zeroth order regular approximation for relativistic effects with ad hoc all-electron (abbr. ae) single polarization function triple-ζ Slater type basis sets (TZP).[366-368] Solvation was treated by the COSMO[199-201] procedure assuming $CH_2Cl_2$ ($\varepsilon$= 8.93) as the solvent. Geometry optimizations by energy gradient minimization were carried out in all cases with integration grid accuracy comprised between 4.5 and 6.5, an energy gradient convergence criterion of $10^{-3}$ au, and tight to very tight SCF convergence criteria. All transition states were submitted to the Intrinsic Reaction Coordinate (IRC) procedure to verify the connection to their reactive complexes and products. Counterpoise correction for basis set superposition error (BSSE) was neglected throughout this study. Vibrational modes were analytically computed to verify that the optimized geometries were related to energy minima or to transition states. Bader (QTAIM) charges[221] and Interacting Quantum Atoms[218, 220] analyses (IQA) were carried out using the embedded QTAIM functionalities of the ADF package. For technical reasons regular all electron TZP Slater type basis sets for all elements except for Ir, for which a basis set with a frozen core up to 3*d* was used for IQA. Drawings of molecular structures were produced with ADFview2019 and with CSD-Mercury.[369]

### 5.1.6.2. DLPNO-CCSD(T) computations

For each of the four studied system, DLPNO-CCSD(T)[209-215] calculations with the TightPNO threshold on the PBE-D3(BJ) optimized geometries for **anag**, **TS-ag**, **ag**, **TS-CH** and **MCH** were performed using the ORCA[209] program system version 4.1.1. The balanced Karlsruhe 2nd generation default triple-ζ valence plus polarization (def2-TZVP[370]) basis set was used in these calculations, as well as automatically generated

auxiliary basis set. The LED[214] analysis has been performed to quantify the different intra- and inter-fragment contributions to the energy.

#### 5.1.6.3. NCI plots

The NCI index is based on the analysis of the reduced density gradient[216, 217]:

$$s(r) = \frac{1}{2(3\pi^2)^{\frac{1}{3}}} \times \frac{|\nabla\rho|}{\rho^{\frac{4}{3}}}$$

which depends on the electron density and its gradient. It is based on two simple considerations to define all possible NCIs: *i*) given the fact that the density decays exponentially with distance from the nuclear position, the regions of space involved in NCIs have low density, and *ii*) in the NCI regions the reduced density gradient approaches zero, leading to a local minimum. Combining these two criteria, one can detect NCIs over a three-dimensional grid looking for the low $\rho(r)$ and low $s(r)$ regions of space of a given system. Three-dimensional visualization of NCIs can be obtained by representing isosurfaces of $s(r)$ surrounding the local minimum of $s(r)$. Qualitative information on the strength and sign of the NCI can be obtained from the electron density and the sign of the second eigenvalue of its Hessian matrix, sign($\lambda_2$), which is negative for attractive interactions and positive for repulsive ones. NCIs are normally associated to density values between 0.00 and 0.1, the weakest interactions, e.g. dispersion, being close to zero and the strongest interactions, e.g. hydrogen bonds, shifted towards larger density values. When sign($\lambda_2$) is taken into account, the range of sign($\lambda_2$) $\rho(r)$ spanned by NCIs extends from -0.1 to 0.1 a.u. It is known that different types of weak interactions decay differently with distance, with the electrostatic terms decaying slower than van der Waals. To mirror this behavior, the volume and $\rho(r)$ were integrated over the volume of NCIs according to two ranges: *i*) -0.05<sign($\lambda_2$)<0.00 corresponding to attractive interactions (attr), *ii*) 0.00< sign($\lambda_2$)<0.05, corresponding to repulsive interactions (rep).[222, 223] These values have been chosen to include the interactions around the hydrogen atom. As can be seen in Figure S56, H interactions cover up to $\rho$=0.05 a.u.

## 5.1.7. Computational details for chapter 3

### 5.1.7.1. DFD-D computations

Geometry optimization of the reactants, intermediates, transition states, and products were performed using the SCM-ADF2019.01 package[371], at the Density Functional Theory (DFT) level in the gas phase. The Perdew-Burke-Ernzerhof (PBE)[372] functional augmented with Grimme's dispersion corrections with the electronegativity equilibrium model (DFT-D4(EEQ))[373] was used in all geometry optimizations. All geometry computations were carried out using scalar relativistic effects with *ad hoc* all-electron (abbr. ae) single polarization functions triple-ζ Slater-type basis set (TZP)[374-376]. Solvation was treated by the Conductor-like Screening Model (COSMO)[377-379] procedure assuming $CH_2Cl_2$ ($\varepsilon$=8.9, $r$=2.94 Å) as a solvent. Geometry optimization by energy gradient minimization were carried out in all cases with integration grid accuracy "Normal"[380]. All transition states were found using the Nudged Elastic Band (NEB)[381] procedure and submitted to the Intrinsic Reaction Coordinate (IRC)[382, 383] procedure to verify the connection to their reactive complexes and products. Vibrational modes were analytically computed to verify that the optimized geometries were related to energy minima or to transition states. For the monoatomic systems that were considered ($H^-$ and $I^-$), as the enthalpy and entropy corrections to the energy are usually computed from the vibrational energies, these contributions were neglected and the Gibbs free energy was approximated as the bond energy.

### 5.1.7.2. IBSI computations

Intrinsic Bond Strength Index (IBSI) of the key atom pairs were computed using the IGMPLOT program[384, 385] using gaussian-type wavefunctions obtained from single-point calculations with the PBE functional[372] augmented with Grimme's correction to the dispersion with a Becke-Johnson damping function[386, 387](PBE-D3(BJ)), scalar relativistic effects with the balanced Karlsruhe 2nd generation default triple-ζ valence plus polarization (def2-TZVP) basis set[370] and Conductor-like Polarizable Continuum Model (CPCM)[388] simulating dichloromethane ($\varepsilon$=8.9, $r$=2.94 Å) as a solvent on the previously optimized geometry using the ORCA program system[389] version 4.1.1.

## 5.2. Synthesis

### 5.2.1. Preparation of LiNHAc

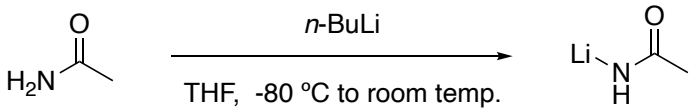


Acetamide (945 mg, 15.9 mmol) was dissolved in ~20 mL of THF in a sealed Schlenk vessel under an Ar atmosphere and the resulting solution was cooled to -80°C. The resulting solution was vigorously stirred and added with a solution of *n*-BuLi in hexanes (1.6 M, 1 eq, 10 mL) and the resulting suspension left to react overnight while the vessel was slowly warmed to room temperature. The resulting suspension was filtrated and the collected solid was washed with dry *n*-pentane and dried under reduced pressure (77% yield). IR (ATR, neat): δ 1588 (m, C=O stretching) $cm^{-1}$. $^1H$ NMR (400 MHz, $CDCl_3$) δ 7.27 (d, J = 1.6 Hz, 1H), 2.02 (d, J = 2.9 Hz, 3H).

### 5.2.2. Preparation of the tritylium tetrakis[3,5-bis(trifluoromethyl)-phenyl]borate ([$Ph_3C$][$BArF_{24}$])

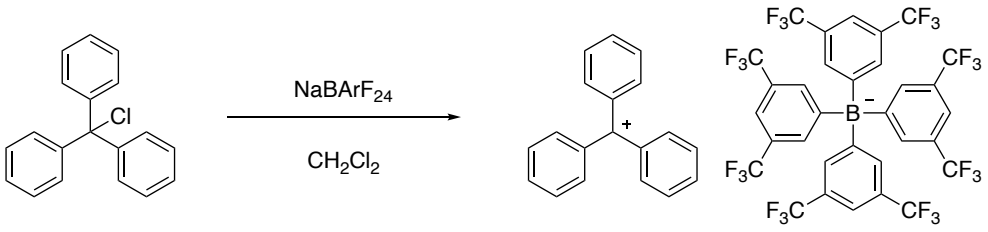


[$Ph_3C$][$BArF_{24}$] was prepared according to a literature procedure with minor modification.[390] Under argon atmosphere, a mixture $NaBArF_{24}$ (886.2 mg, 1 mmol) and tritylium chloride (278.1 mg, 1 mmol) was stirred overnight in ~20 mL of $CH_2Cl_2$ at room temperature in a sealed Schlenk vessel. The reaction mixture was then filtrated through Celite, the filtrate was evaporated under reduced pressure. The resulting solid was first washed with *n*-pentane and then purified by recrystallization with $CH_2Cl_2$/*n*-pentane to afford bright yellow microcrystals (973 mg, 88% yield). $^1H$ NMR (300 MHz, $CDCl_3$) δ 8.15 (ddt, *J* = 8.8, 7.3, 1.3 Hz, 3H), 7.80 – 7.73 (m, 6H), 7.68 (p, *J* = 2.1 Hz, 8H), 7.59 – 7.54 (m, 6H), 7.48 (s, 4H).

### 5.2.3. Preparation of the $d_{15}$-trityl chloride

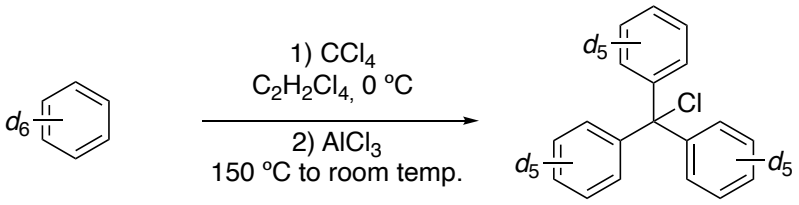


$d_{15}$-Tritylium chloride was prepared according to a literature procedure with minor modification[391]. Under argon atmosphere, a mixture of $d_6$-benzene (5.0 mL, 0.05 mmol) and carbon tetrachloride (1.0 mL, 0.01 mmol) was dissolved in 20 mL of 1,1,2,2-tetrachloroethane in a sealed Schlenk vessel, and cooled down to 0 °C. Aluminium trichloride (1.6 g, 0.01 mmol) was then added slowly during stirring. After 15 min of stirring, the solution was refluxed for 90 min and then cooled down to room temperature. The solution was quenched with 1 M HCl, and the organic phase was extracted with DCM and dried over $Mg_2SO_4$. After removal of the solvent under vaccum, the crude solid was purified by column chromatography (hexanes/ethyl acetate = 9:1) to afford $d_{15}$-tritylium chloride (1.2 g, 37%).

### 5.2.4. Synthesis of $CpCo(CO)I_2$ and $[CpCoI_2]_2$

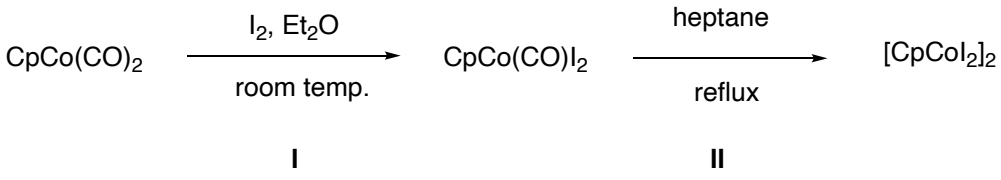


**Procedure I:** In a Schlenk tube, $CpCo(CO)_2$ (1 mL, 7.5 mmol) and 20 mL of distilled $Et_2O$ were introduced under argon atmosphere. $I_2$ (2 g, 7.9 mmol) dissolved in distilled $Et_2O$ was added to the Schlenk tube with a cannula. The reaction was stirred overnight at room temperature. At the end of the reaction, the solvent was removed under reduced pressure and the residual solid washed 4 times with distilled pentane. $^1H$ NMR analysis in $CDCl_3$ revealed the disappearance of the signal of the starting compound at 5.06 ppm that was replaced by a new Cp singlet at 5.68 ppm. Analytical data were in accord with those reported in the literature.[392, 393]

**Procedure II:** The synthesis of the $[CpCoI_2]_2$ was carried out by applying the methodology reported for $[Cp^*CoI_2]_2$.[281] In a round bottom flask, 1 g of $[CpCo(CO)I_2]$

were introduced with 50 mL of distilled heptane. The solution was stirred and refluxed during 2 days. After reaction, the solid was filtrated and washed 3 times with distilled pentane. [$CpCoI_2$] was insoluble in most solvents, but slightly soluble in coordinating solvents such as $CH_3CN$ and THF giving rise to quite air and light sensitive solutions. All analytical data were in accord with data published in literature.[393-396]

### 5.2.5. General procedure for the synthesis of iodocobaltacycles

Under the argon atmosphere, a mixture of $[Cp^*CoI_2]_2$ (1 equiv), LiNHAc (6 equiv.), and 2-arylpyridine ligand (2 equiv.) were stirred in ~10−15 mL of $CH_2Cl_2$ at 50 °C for 48 h in a sealed Schlenk vessel. The reaction mixture was filtrated over Celite and followed by the removal of the solvent. The resulting residue was then purified by column chromatography (DCM/*n*-pentane= 4/1) and recrystallization with $CH_2Cl_2$/*n*-pentane and/or washing with *n*-pentane.

### 5.2.6. General procedure for the synthesis of acetonitrilo-cobalt with $BArF_{24}^-$ salts.

Under the argon atmosphere, in a Schlenk flask an equimolar mixture of [$\kappa^2$-(*C,N*)-(**L**)CoI] and Na[$BArF_{24}$] was dissolved in acetonitrile (~7-10mL). The resulting mixture was vigorously stirred at room temperature within a period not exceeding 6h, unless otherwise stated. The solution was subsequently filtrated through a pad of celite, and the solvent was removed from the filtrate under reduced pressure. The solid was either recrystallized in a mixture of $CH_2Cl_2$ and *n*-pentane or washed with *n*-pentane, to afford an analytically pure compound.

### 5.2.7. Synthesis of chloro(2-phenylpyridine-*k*$^2$-*C,N*)(pentamethyl-cyclopentadienyl)cobalt(III) (9a)

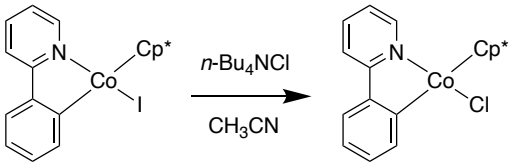


Under argon atmosphere, a mixture of **1a** (95 mg, 0.2 mmol) and dry tetrabutylammonium chloride (100 mg, 0.35 mmol) was stirred overnight in ~10−15 mL

of acetonitrile at room temperature in a sealed Schlenk vessel. After reaction, washed and filtrated with $H_2O$, the resulting residue was purified by recrystallization with $CH_2Cl_2$/*n*-pentane and/or washing with *n*-pentane, to afford the pure compound the analytical data which matched published data[138] (60 mg, 79 %). $^1$H NMR (400 MHz, $CDCl_3$) δ 9.24 (dt, *J* = 5.6, 1.2 Hz, 1H), 8.28 (dd, *J* = 7.7, 1.1 Hz, 1H), 7.70 – 7.63 (m, 2H), 7.53 (dd, *J* = 7.6, 1.5 Hz, 1H), 7.32 (td, *J* = 7.4, 1.5 Hz, 1H), 7.15 – 7.07 (m, 2H), 1.29 (s, 15H).

### 5.2.8. General procedure for the oxidative cyclocondensation of 1c, 7c, 8c.

Under argon atmosphere, a mixture of Iodocobaltacycles (1 equiv) and $[Ph_3C][BArF_{24}]$ (1 equiv) was stirred overnight in ∼10−15 mL of $CH_2Cl_2$ at room temperature in a sealed Schlenk vessel. The reaction mixture was filtrated through Celite followed by removal of the solvent. The resulting residue was purified by column chromatography and then recrystallized with $CH_2Cl_2$/*n*-pentane and/or washed with n-pentane to obtain the white powder.

## 5.3. Characterization

### 5.3.1. Iodo(pentamethylcyclopentadienyl)(2-phenylenepyridine-$\kappa^2$-*C,N*) cobalt (III) (1a)

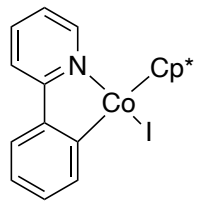


$[Cp^*CoI_2]_2$ (448 mg, 0.5 mmol), LiNHAc (195.1 mg, 3 mmol), and 2-phenylpyridine (155.2 mg, 1mmol) in 10 mL of $CH_2Cl_2$, yield is 78 % (370 mg). Anal. calcd for $C_{21}H_{23}NICo•CH_2Cl_2$: C, 52.72; H, 5.03; N, 2.79. Found: C, 52.51; H, 4.91; N, 3.19. $^1$H NMR (500 MHz, $CDCl_3$) δ 9.20 (dt, *J* = 5.6, 1.2 Hz, 1H), 8.27 (dd, *J* = 7.7, 1.1 Hz, 1H), 7.66 – 7.58 (m, 2H), 7.56 (dd, *J* = 7.6, 1.5 Hz, 1H), 7.30 – 7.26 (m, 1H), 7.04 (td, *J* = 6.2, 2.1 Hz, 2H), 1.49 (s, 15H); $^{13}$C NMR (126 MHz, $CDCl_3$) δ 181.4, 167.2, 155.0, 145.7, 142.5, 136.6, 129.4, 123.3, 122.7, 121.2, 118.5, 93.5, 10.4. MS-ESI (m/z): [M] calcd for $C_{21}H_{23}CoIN$, 475.02; Found, 475.02; $[M–I]^+$ calcd for $C_{21}H_{23}CoN$, 348.12; Found, 348.12.

### 5.3.2. Iodo[2-(2-methylphenylene)pyridine-$\kappa^2$-*C,N*](pentamethylcyclo-pentadienyl)cobalt (III) (3a)

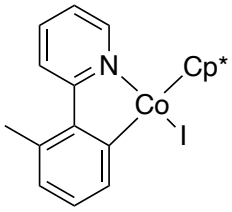


$[Cp^*CoI_2]_2$ (216.5 mg, 0.24 mmol), LiNHAc (97.58 mg, 1.5 mmol), and 2-(2-methylphenyl)pyridine (84.61mg, 0.5 mmol) in 10 mL of $CH_2Cl_2$, yield is 81% (198 mg). Anal. calcd for $C_{22}H_{25}NICo$: C, 54.01; H, 5.15; N, 2.86. Found: C, 53.79; H, 5.20; N, 2.87. $^1H$ NMR (500 MHz, $CD_2Cl_2$) δ 9.38 (dd, *J* = 5.7, 1.7 Hz, 1H), 8.21 – 8.15 (m, 1H), 7.87 (d, *J* = 8.3 Hz, 1H), 7.62 (ddd, *J* = 8.5, 7.3, 1.7 Hz, 1H), 7.26 (s, 2H), 7.12 (t, *J* = 7.5 Hz, 1H), 7.02 (ddd, *J* = 7.2, 5.7, 1.4 Hz, 1H), 6.82 (d, *J* = 7.2 Hz, 1H), 2.64 (s, 3H), 1.45 (s, 15H). $^{13}C$ NMR (126 MHz, $CDCl_3$) δ 184.7, 167.9, 156.2, 144.5, 140.7, 136.4, 135.3, 127.9, 127.1, 122.1, 120.2, 94.0, 23.9, 10.3. MS-ESI (m/z): $[M+Na]^+$ calcd for $C_{22}H_{25}NINaCo$, 512.03; Found, 512.03; $[M-I]^+$ calcd for $C_{22}H_{25}CoN$, 362.13; Found, 362.13.

### 5.3.3. Iodo(pentamethylcyclopentadienyl)[4-tertiobutyl,2-(4-*N,N*-dimethylaminophenylene)pyridine-$\kappa^2$-*C,N*]cobalt (III) (4a)

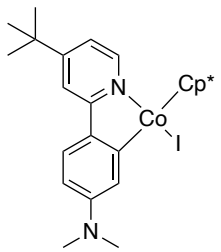


$[Cp^*CoI_2]_2$ (225 mg, 0.25 mmol), LiNHAc (97.58 mg, 1.5 mmol), and 4-(4-(tert-butyl)pyridin-2-yl)-*N*,*N*-dimethyl-aniline (127.18 mg, 0.5 mmol) in 10 mL of $CH_2Cl_2$, yield was 82% (239 mg). Anal. calcd for $C_{27}H_{36}N_2ICo \bullet CH_2Cl_2$: C, 55.72; H, 6.35; N, 4.63. Found: C, 55.54; H, 6.36; N, 4.92. $^1H$ NMR (500 MHz, $CDCl_3$) δ 8.91 (d, J = 6.2 Hz, 1H), 7.62 (d, J = 2.5 Hz, 1H), 7.42 (d, J = 8.5 Hz, 1H), 7.37 (d, J = 2.2 Hz, 1H), 6.89 (dd, J = 6.2, 2.2 Hz, 1H), 6.45 (dd, J = 8.5, 2.4 Hz, 1H), 3.12 (s, 6H), 1.50 (s, 15H), 1.30 (s, 9H). $^{13}C$ NMR (126 MHz, $CDCl_3$) δ 182.2, 166.8, 160.4, 153.7, 150.4, 135.5, 124.9, 123.6, 117.4, 113.8, 108.0, 93.0, 40.7, 34.9, 30.8, 30.6, 10.5. MS-ESI (m/z): [M] calcd for $C_{27}H_{36}N_2ICo$, 574.13; Found, 574.12; $[M+H]^+$ calcd for $(C_{27}H_{36}N_2ICo)H$, 575.13; Found, 575.13.

### 5.3.4. (Benzo[h]quinolynyl-$\kappa^2$-*C,N*)iodo(pentamethylcyclopentadienyl)-cobalt (III) (5a)

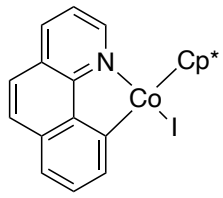


$[Cp^*CoI_2]_2$ (216.25 mg, 0.25 mmol), LiNHAc (130 mg, 2 mmol), and 7,8-benzo[*h*]quinoline (89.61 mg, 0.5 mmol) in 10 mL of $CH_2Cl_2$, yield was 30% (75.3 mg). Anal. calcd for $C_{23}H_{23}NICo•5/4CH_2Cl_2$: C, 53.30; H, 4.70; N, 2.56. Found: C, 53.39; H, 4.66; N, 2.72. $^1$H NMR (500 MHz, $CDCl_3$) $\delta$ 9.43 – 9.38 (m, 1H), 8.49 (d, $J$ = 7.3 Hz, 1H), 8.10 – 8.05 (m, 1H), 7.76 (d, $J$ = 8.7 Hz, 1H), 7.71 (t, $J$ = 7.5 Hz, 1H), 7.51 (dd, $J$ = 8.2, 5.6 Hz, 2H), 7.45 (dd, $J$ = 7.9, 5.3 Hz, 1H), 1.54 (s, 15H). $^{13}$C NMR (126 MHz, $CDCl_3$) δ 176.6, 156.8, 152.6, 142.1, 139.3, 134.9, 133.2, 129.6, 129.4, 126.6, 122.8, 121.1, 120.6, 93.1, 10.6. MS-ESI (m/z): [M] calcd for $C_{23}H_{23}CoIN$, 499.02; Found, 499.02; $[M–I]^+$ calcd for $C_{23}H_{23}NCo$, 372.12; Found, 372.12.

### 5.3.5. Iodo[2-(4-methylphenyl)pyridine-$\kappa^2$-*C,N*](pentamethylcyclopentadienyl)cobalt(III) (6a)

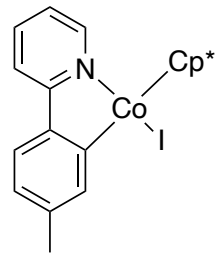


$[Cp^*CoI_2]_2$ (448 mg, 0.5 mmol), LiNHAc (195 mg, 3 mmol), and 2-(4-methylphenyl)pyridine (169 mg, 1 mmol) in 20 mL of $CH_2Cl_2$ afforded **6a** in 60 % yield (145 mg). Anal. calcd for $C_{22}H_{25}CoIN$: C 54.01, H 5.15, N 2.86. Found: C 53.64, H 5.20, N 3.02. $^1$H NMR (500 MHz, $CDCl_3$) δ 9.16 (dt, $J$ = 5.8, 1.3 Hz, 1H), 8.07 (dd, $J$ = 1.6, 0.8 Hz, 1H), 7.62 – 7.53 (m, 2H), 7.44 (d, $J$ = 7.7 Hz, 1H), 7.00 (td, $J$ = 5.9, 2.7 Hz, 1H), 6.84 (ddd, $J$ = 7.8, 1.6, 0.7 Hz, 1H), 2.46 (d, $J$ = 0.7 Hz, 3H), 1.48 (s, 15H). $^{13}$C NMR (126 MHz, $CDCl_3$) δ 167.21, 154.96, 143.24, 143.04, 139.09, 136.54, 124.09, 122.97, 120.75, 118.10, 93.38, 22.12, 10.38, 1.17. $^{13}$C NMR (126 MHz, CDCl3) δ 181.18, 167.16, 154.93, 143.22, 143.01, 139.08, 136.54, 124.08, 122.96, 120.76, 118.11, 93.36, 22.13, 10.38. HRMS (ESI, m/z) calcd. for $C_{22}H_{25}CoN^+$: 362.1319. Found: 362.13.

### 5.3.6. Iodo[2-(4-bromophenyl)pyridine-$\kappa^2$-*C,N*](pentamethylcyclopentadienyl)cobalt(III) (7a)

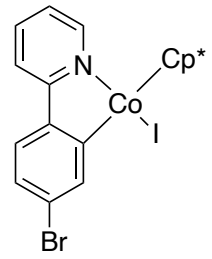


$[Cp^*CoI_2]_2$ (448 mg, 0.5 mmol), LiNHAc (195 mg, 3 mmol), and 2-(4-bromophenyl)pyridine (235 mg, 1 mmol) in 20 mL of $CH_2Cl_2$ afforded a yield of 71% (393 mg). Anal. calcd for $C_{21}H_{22}BrCoIN$: C,45.52, H 4.00, N 2.53. Found: C 45.33, H 4.05, N 2.62. $^1$H NMR (500 MHz, $CDCl_3$) δ 9.16 (ddd, *J* = 5.7, 1.5, 0.8 Hz, 1H), 8.34 (d, *J* = 1.9 Hz, 1H), 7.63 (ddd, *J* = 8.0, 7.1, 1.5 Hz, 1H), 7.59 (ddd, *J* = 8.2, 1.8, 0.8 Hz, 1H), 7.40 (d, *J* = 8.2 Hz, 1H), 7.17 (dd, *J* = 8.2, 1.9 Hz, 1H), 7.08 (ddd, *J* = 7.3, 5.7, 1.7 Hz, 1H), 1.50 (s, 15H). $^{13}$C NMR (126 MHz, $CDCl_3$) δ 184.10, 166.10, 154.92, 144.21, 143.88, 136.78, 125.80, 124.07, 123.94, 121.52, 118.54, 93.58, 10.26. HRMS (ESI, m/z) calcd. for $C_{21}H_{22}BrCoN^+$: 426.0268. Found: 426.0262.

### 5.3.7. Iodo[2-(4-(trifluoromethyl)phenyl)pyridine-$\kappa^2$-*C,N*](pentamethylcyclopentadienyl)cobalt(III) (8a)

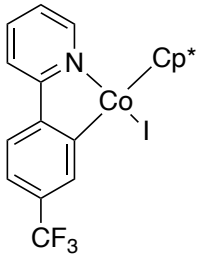


$[Cp^*CoI_2]_2$ (448 mg, 0.5 mmol), LiNHAc (195 mg, 3 mmol), and 2-(4-(trifluoromethyl)phenyl)pyridine (224 mg, 1 mmol) in 10 mL of $CH_2Cl_2$ afforded **8a** in 62% yield (335 mg). Anal. calcd for $C_{53}H_{36}BF_{24}N$: C,48.64; H,4.08; N,2.58. Found: C, 48.55; H, 4.04; N, 2.64. $^1$H NMR (500 MHz, $CDCl_3$) δ 9.25 – 9.20 (m, 1H), 8.50 (dd, *J* = 1.8, 0.9 Hz, 1H), 7.72 – 7.66 (m, 2H), 7.63 (dd, *J* = 8.1, 0.9 Hz, 1H), 7.29 – 7.26 (m, 1H), 7.14 (ddd, *J* = 6.6, 5.7, 2.2 Hz, 1H), 1.50 (s, 15H). $^{13}$C NMR (126 MHz, $CDCl_3$) δ 181.93, 165.71, 155.20, 148.65, 138.28, 137.04, 130.04, 122.49, 122.31, 119.76, 119.35, 93.86, 10.36. $^{19}$F NMR (282 MHz, $CDCl_3$): δ -62.1 ppm. HRMS (ESI, m/z) calcd. for $C_{22}H_{22}CoF_3N^+$: 416.1036. Found: 416.1035.

### 5.3.8. Iodo[2-phenylpyridine-$\kappa^2$-*C,N*](cyclopentadienyl)cobalt(III) (10a).

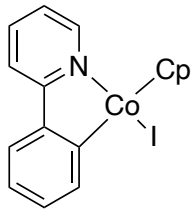


The synthesis of **10a** was performed similarly to the one of **1a** published recently.[2] Under argon atmosphere, $[CpCoI_2]_2$ (40 mg, 0.053 mmol), 2-phenylpridine (15.1 µL, 0.106 mmol) and LiNHAc (20 mg, 0.307 mmol) were introduced in a Schlenk tube. 5 mL of distilled $CH_2Cl_2$ were added. The reaction was stirred two days at 50°C. The reaction was filtrated and the solvent removed under reduced pressure. The resulting solid was washed 3 times with distilled pentane. The solid was then purified by chromatography column. 100% of pentane was first used, and then 100% of $CH_2Cl_2$ allowed the migration of the desired purple compound. The compound was obtained in 40% yield (17 mg). Anal. calcd. for $C_{16}H_{13}CoIN \cdot 1/2\ H_2O$: C 46.40, H 3.41, N 3.38. Found: C 46.26, H 3.24, N 3.29. $^1$H NMR (500 MHz, $CDCl_3$) δ 9.69 – 9.63 (dd, 1H), 8.48 (dd, *J* = 7.7, 1.1 Hz, 1H), 7.70 – 7.60 (m, 3H), 7.31 (td, *J* = 7.4, 1.5 Hz, 1H), 7.14 – 7.02 (2dd, 2H), 5.15 (s, 5H). $^{13}$C NMR (126 MHz, $CDCl_3$) δ 169.83, 167.67, 157.17, 146.86, 144.25, 137.09, 129.44, 124.25, 123.28, 121.62, 119.03, 86.99. HRMS (ESI, m/z) calcd. for $C_{16}H_{13}CoN^+$: 278.0380. Found: 278.0374.

### 5.3.9. Acetamidato[2-phenylenepyridine-$\kappa^2$-*C,N*](pentamethyl-cyclopentadienyl)cobalt (III) (1f)

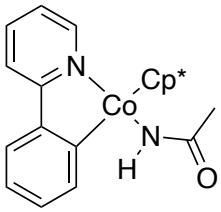


Under an argon atmosphere, **1a** (28.1 mg, 0.059 mmol) and excess of LiNHAc (38.4 mg, 0.59 mmol) were stirred in $CH_2Cl_2$ (~7-10 mL) in a Schlenk flask at 50 °C overnight and the resulting solution subsequently filtrated through celite. The resulting filtrate was stripped of the solvents under reduced pressure and the residue was extracted with pentane and filtrated through Celite. The filtrate was stripped of solvent under reduced pressure to afford the product (5.04 mg, yield: 20.8%). Anal. calcd for $C_{23}H_{27}CoN_2O \bullet 0.55\ CH_2Cl_2 \bullet 0.9\ C_5H_{12}$: C, 65.03; H, 7.57; N, 5.41. Found: C, 65.14; H, 7.17; N, 5.02. $^1$H NMR (500 MHz, $CDCl_3$) δ 9.76 (d, *J* = 5.7 Hz, 1H), 8.20 – 8.15 (m, 1H), 7.64 – 7.59 (m, 1H), 7.59 – 7.52 (m, 2H), 7.35 (td, *J* = 7.4, 1.4 Hz, 1H), 7.19 – 7.12 (m, 1H), 7.08 (td, *J* = 6.1, 2.4 Hz, 1H), 1.76 (s, 3H), 1.34 (s, 15H). $^{13}$C NMR (126 MHz, $CDCl_3$) δ 185.00, 178.86, 166.31, 155.99, 146.77, 137.74, 136.29, 129.28,

122.96, 122.72, 120.87, 117.49, 93.57, 28.40, 9.41. MS-ESI (m/z): $[M–NHAc]^+$ calcd for $C_{21}H_{23}NCo$, 348.12; Found, 348.12.

### 5.3.10. Acetamidato[2-phenylenepyridine-$\kappa^2$-*C,N*](pentamethyl-cyclopentadienyl)iridium (III) (2b)

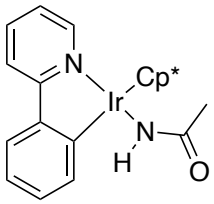


Under an argon atmosphere, **2a** (26.6 mg, 0.0514 mmol) and excess of LiNHAc (33.4 mg, 0.514 mmol) were dissolved in $CH_2Cl_2$ (~7-10 mL) in a Schlenk flask. The resulting suspension was vigorously stirred at room temperature overnight and the reaction mixture filtrated through celite. The filtrate was stripped of solvents under reduced pressure to afford a solid residue that displayed some reactivity with $SiO_2$, which prevented chromatographic separation. The residue was therefore redissolved in $CH_2Cl_2$ and the resulting solution was swiftly filtered through dry $SiO_2$. The filtrate was stripped of solvent and recrystallized from $CH_2Cl_2$ and pentane to afford **2b** slightly contaminated with acetamide (9.05 mg, yield: 32,6%). Anal. calcd for $C_{23}H_{27}IrN_2O$•1/3 $CH_2Cl_2$•4/3 $NH_2COCH_3$: C, 48.46; H, 5.35; N, 7.2. Found: C, 48.09; H, 5.71; N, 6.99. $^1$H NMR (500 MHz, $CDCl_3$) δ 9.14 – 9.11 (m, 1H), 7.79 (dd, J = 7.5, 1.2 Hz, 1H), 7.74 – 7.71 (m, 1H), 7.66 (dd, *J* = 7.7, 1.5 Hz, 1H), 7.57 (td, *J* = 7.7, 1.6 Hz, 1H), 7.19 (td, *J* = 7.3, 1.4 Hz, 1H), 7.09 (td, *J* = 7.4, 1.2 Hz, 1H), 7.01 (ddd, *J* = 7.3, 5.8, 1.5 Hz, 1H), 3.47 (s, 1H), 1.71 (s, 15H), 1.70 (s, 3H). $^{13}$C NMR (126 MHz, $CDCl_3$) δ 175.14, 166.79, 163.96, 153.82, 145.26, 136.39, 134.79, 130.36, 123.75, 121.79, 121.60, 118.08, 88.48, 26.69, 9.10. MS-ESI (m/z): $[M–NHAc]^+$ calcd for $C_{21}H_{23}NIr$, 482.15; Found, 482.15.

### 5.3.11. Acetonitrilo(pentamethylcyclopentadienyl)(2-phenylenepyridine-$\kappa^2$-*C,N*) cobalt (III) tetrakis[3,5-bis(trifluoromethyl)phenyl]borate (1b)

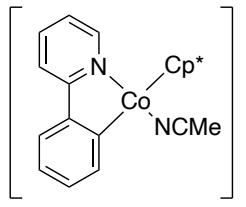


**1a** (47.5 mg, 0.1 mmol) and $NaBArF_{24}$ (88.6 mg, 0.1 mmol) in 10 mL of acetonitrile, yield is 80 % (100.2 mg). Anal. calcd for $C_{55}H_{38}N_2BF_{24}Co$ • 3/2$CH_2Cl_2$: C, 51.25; H, 3.13; N, 2.11. Found: C, 51.34; H, 2.97; N, 2.14. $^1$H NMR (500 MHz, $CD_2Cl_2$) δ 8.92 (d, *J* = 5.7 Hz, 1H), 8.09 – 8.04 (m, 1H), 7.90 – 7.78 (m, 2H), 7.72 (p, *J* = 2.4 Hz, 8H), 7.65 (dd, *J* = 7.6, 1.5 Hz, 1H), 7.56 (s, 4H), 7.40 (td, *J* = 7.4, 1.5 Hz, 1H), 7.31 – 7.22 (m, 2H), 2.14 (s, 3H), 1.31 (s, 15H). $^{13}$C NMR (126 MHz, $CD_2Cl_2$) δ 175.4,

167.6, 162.1 (dd, *J* = 99.7, 49.8 Hz), 153.1, 147.1, 139.3 (d, *J* = 17.5 Hz), 135.2, 131.1, 129.9 – 128.6 (m), 128.2, 126.1, 125.3, 124.7, 123.9, 123.4, 121.7, 120.0, 118.0 – 117.7 (m), 96.9, 9.5, 4.7. $^{19}$F NMR (282 MHz, $CD_2Cl_2$) δ -62.9. $^{11}$B NMR (96 MHz, $CD_2Cl_2$) δ -6.6 (dq, *J* = 5.4, 2.8 Hz). MS-ESI (m/z): $[M\text{-}BArF_{24}]^+$ calcd for $C_{23}H_{26}CoN_2$, 389.14; Found, 389.14; $[BArF_{24}]^-$ calcd for $C_{32}H_{12}F_{24}B$, 863.07; Found, 863.06.

### 5.3.12. Acetonitrilo[2-(2-methylphenylene)pyridine-$\kappa^2$-*C,N*](pentamethyl-cyclopentadienyl)cobalt (III) tetrakis[3,5-bis(trifluoromethyl)phenyl]-borate (3b).

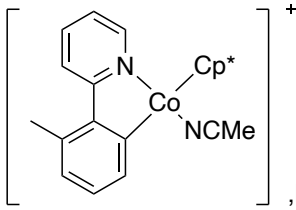


**3a** (49 mg, 0.1 mmol) and $NaBArF_{24}$ (88.6 mg, 0.1 mmol) in 10 mL of acetonitrile, yield is 85 % (108.1 mg). Anal. calcd for $C_{56}H_{40}N_2BF_{24}Co\bullet 4/3CH_2Cl_2$: C, 49.87; H, 3.12; N, 2.03. Found: C, 49.93; H, 3.15; N, 1.95. $^1$H NMR (500 MHz, $CDCl_3$) δ 8.95 (dd, *J* = 5.7, 1.7 Hz, 1H), 8.00 (d, *J* = 8.3 Hz, 1H), 7.84 (d, *J* = 7.6 Hz, 1H), 7.78 (ddd, *J* = 8.6, 7.4, 1.7 Hz, 1H), 7.70 (dt, *J* = 5.0, 2.3 Hz, 8H), 7.52 (s, 4H), 7.24 (t, *J* = 7.5 Hz, 1H), 7.12 (ddd, *J* = 7.2, 5.6, 1.4 Hz, 1H), 7.04 (d, *J* = 7.4 Hz, 1H), 2.66 (s, 3H), 2.06 (s, 3H), 1.22 (s, 15H). $^{13}$C NMR (126 MHz, $CDCl_3$) δ 177.99, 167.99, 161.82 (dd, *J* = 99.6, 49.8 Hz), 153.59, 145.12, 138.96, 137.11, 136.38, 134.93, 129.68 (d, *J* = 11.0 Hz), 129.18 (d, *J* = 3.2 Hz), 128.94, 128.40, 127.92, 125.76, 117.65 (d, *J* = 5.9 Hz), 96.94, 23.63, 9.22, 4.02. $^{19}$F NMR (282 MHz, $CDCl_3$) δ -62.4. $^{11}$B NMR (96 MHz, $CDCl_3$) δ -6.6 (p, *J* = 2.6 Hz). MS-ESI (m/z): $[M\text{-}BArF_{24}]^+$ calcd for $C_{24}H_{28}N_2Co$, 403.16; Found, 403.16; $[BArF_{24}]^-$ calcd for $C_{32}H_{12}F_{24}B$, 863.07; Found, 863.06.

### 5.3.13. Acetonitrilo[4-tertiobutyl,2-(4-*N,N*-dimethylaminophenylene)-pyridine-$\kappa^2$-*C,N*](pentamethyl-cyclopentadienyl)cobalt (III) tetrakis[3,5-bis(trifluoromethyl)phenyl]borate (4b)

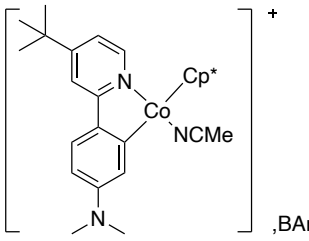


**4a** (58 mg, 0.1 mmol) and $NaBArF_{24}$ (88.6 mg, 0.1 mmol) in 10 mL of acetonitrile, yield was 80% (108.2 mg). Anal. Calcd for $C_{61}H_{51}N_3BF_{24}Co\bullet CH_2Cl_2$: C, 53.68; H, 3.86; N, 3.02. Found: C, 53.53; H, 3.82; N, 3.09. $^1$H NMR (500 MHz, $CDCl_3$) δ 8.57 (d, *J* = 6.2 Hz, 1H), 7.69 (p, *J* = 2.4 Hz, 8H), 7.52 (s, 4H), 7.49 (d, *J* = 2.1 Hz, 1H), 7.47 (d, *J* = 8.6 Hz, 1H), 7.28 (s, 1H), 7.05 (dd,

*J* = 6.1, 2.1 Hz, 1H), 6.56 (dd, *J* = 8.6, 2.4 Hz, 1H), 3.14 (s, 6H), 2.04 (s, 3H), 1.33 (s, 9H), 1.27 (s, 15H). $^{13}$C NMR (126 MHz, $CDCl_3$) δ 176.8, 167.2, 163.4, 162.4, 162.0, 161.6, 161.2, 151.34, 151.3, 134.9, 134.7, 129.4, 128.9, 128.7, 128.3, 127.9, 125.8, 125.0, 123.6, 121.43, 120.4, 118.8, 117.6, 114.8, 109.1, 96.1, 40.4, 35.2, 30.4, 9.4, 4.1. $^{19}$F NMR (282 MHz, $CDCl_3$) δ -62.38. $^{11}$B NMR (96 MHz, $CDCl_3$) δ -6.64 (dq, *J* = 5.4, 2.8 Hz). MS-ESI (m/z): $[M\text{-}BArF_{24}]^+$ calcd for $C_{29}H_{39}N_3Co$, 488.25; Found, 488.25; $[BArF_{24}]^-$ calcd for $C_{32}H_{12}F_{24}B$, 863.07; Found, 863.06.

### 5.3.14. Acetonitrilo(benzo[h]quinolynyl-$\kappa^2$-*C,N*)(pentamethyl-cyclopentadienyl)cobalt (III) tetrakis[3,5-bis(trifluoromethyl)phenyl]-borate (5b).

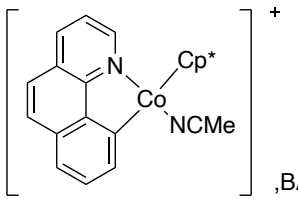


**5a** (50 mg, 0.1 mmol) and $NaBArF_{24}$ (88.6 mg, 0.1 mmol) in 10 mL of acetonitrile, yield was 79 % (100.9 mg). Anal. calcd for $C_{57}H_{38}N_2BF_{24}Co \bullet 7/3CH_2Cl_2$: C, 50.41; H, 3.04; N, 1.98. Found: C, 50.55; H, 2.85; N, 1.81. $^1$H NMR (500 MHz, $CDCl_3$) δ 9.13 (dd, *J* = 5.3, 1.3 Hz, 1H), 8.28 (dd, *J* = 7.2, 0.9 Hz, 1H), 8.23 (dd, *J* = 8.0, 1.3 Hz, 1H), 7.84 (d, *J* = 8.8 Hz, 1H), 7.77 (t, *J* = 7.5 Hz, 1H), 7.73 (d, *J* = 0.9 Hz, 1H), 7.71 (dd, *J* = 5.3, 2.7 Hz, 8H), 7.60 (d, *J* = 8.8 Hz, 1H), 7.52 (d, *J* = 1.8 Hz, 4H), 7.50 (d, *J* = 5.5 Hz, 1H), 1.94 (s, 3H), 1.31 (s, 15H). $^{13}$C NMR (126 MHz, $CDCl_3$) δ 170.6, 162.4, 162.0, 161.6, 161.2, 156.5, 150.9, 142.5, 137.32, 136.3, 134.9, 134.0, 130.5, 130.0, 129.19, 129.17, 129.15, 129.0, 128.94, 128.9, 128.7, 127.9, 127.4, 125.7, 123.62, 123.6, 123.2, 122.5, 121.4, 117.7, 117.65, 117.6, 96.2, 9.5, 4.0. $^{19}$F NMR (282 MHz, $CDCl_3$) δ -62.4. $^{11}$B NMR (96 MHz, $CDCl_3$) δ -6.6 (dq, *J* = 5.6, 2.8 Hz). MS-ESI (m/z): $[M\text{-}BArF_{24}]^+$ calcd for $C_{25}H_{26}N_2Co$, 413.13; Found, 413.13; $[BArF_{24}]^-$ calcd for $C_{32}H_{12}F_{24}B$, 863.07; Found, 863.06.

### 5.3.15. Benzonitrilo(pentamethylcyclopentadienyl)(2-phenylenepyridine-$\kappa^2$-*C,N*) cobalt (III) tetrakis[3,5-bis(trifluoromethyl)phenyl]borate (1b')

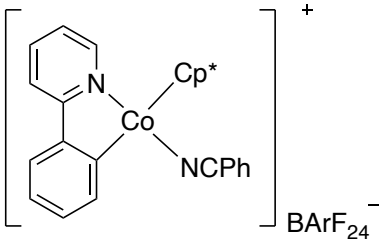


**1a** (50 mg, 0.1 mmol), benzonitrile(1mL) and $NaBArF_{24}$ (88.6 mg, 0.1 mmol) in 10 mL of DCM, yield was 64 % (88.5 mg). Anal. calcd for $C_{60}H_{40}N_2BF_{24}Co \cdot 0.25\ CH_2Cl_2 \cdot 0.1\ C_5H_{12}$: C, 54.33; H, 3.13; N, 2.09. Found: C, 54.35; H, 3.13; N, 2.06. $^1$H NMR (500 MHz, $CD_2Cl_2$) δ 8.98 (d, *J* = 5.8 Hz, 1H), 8.10 (d, *J* = 7.8 Hz, 1H), 7.88 (t, *J* = 7.6 Hz, 1H), 7.84 (d, *J* = 8.1 Hz, 1H), 7.71 (s, 8H), 7.68 (s, 1H), 7.64 (dd, *J* = 9.2, 4.7 Hz, 2H), 7.55 (s, 4H), 7.44 (d, *J* = 4.7 Hz, 4H), 7.29 (dt, *J* = 14.4, 7.1 Hz, 2H). $^{13}$C NMR (126 MHz, $CD_2Cl_2$) δ 153.20, 139.47, 139.05, 135.19, 132.94, 131.32, 129.95, 129.38, 129.14, 126.07, 125.45, 124.84, 123.90, 123.45, 120.22, 117.86, 97.46, 9.64. $^{19}$F NMR (471 MHz, $CD_2Cl_2$) δ -62.87. $^{11}$B NMR (96 MHz, $CD_2Cl_2$) δ -6.6 (dq, *J* = 5.4, 2.8 Hz). MS-ESI (m/z): [M-NCPh-$BArF_{24}$]$^+$ calcd for $C_{21}H_{23}CoN^+$, 348.12; Found, 348.11; [$BArF_{24}$]$^-$ calcd for $C_{32}H_{12}F_{24}B^-$, 863.07; Found, 863.06.

### 5.3.16. [1c][$BArF_{24}$]

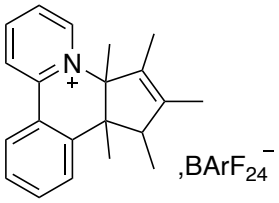


Under argon atmosphere, **1a** (48 mg, 0.1 mmol) and [$Ph_3C$][$BArF_{24}$] (111 mg, 0.1 mmol) in 10 mL of $CH_2Cl_2$, isolated yield: 29% (33 mg). Anal. Calcd for $C_{53}H_{36}BF_{24}N$: C 55.18, H 3.15, N 1.21. Found: C 55.21, H 3.34, N 1.21. $^1$H NMR (500 MHz, $CDCl_3$) δ 8.30 (dd, *J* = 6.5, 1.5 Hz, 1H), 8.06 (dd, *J* = 8.4, 1.6 Hz, 1H), 7.97 (ddd, *J* = 8.5, 7.3, 1.4 Hz, 1H), 7.87 (dd, *J* = 8.0, 1.3 Hz, 1H), 7.73 (td, *J* = 7.7, 1.3 Hz, 1H), 7.70 (dt, *J* = 5.2, 2.3 Hz, 8H), 7.59 – 7.51 (m, 2H), 7.50 (s, 4H), 7.45 (ddd, *J* = 7.8, 6.6, 1.6 Hz, 1H), 2.42 – 2.36 (m, 1H), 2.09 (dq, *J* = 2.7, 1.3 Hz, 3H), 1.70 (p, *J* = 1.3 Hz, 3H), 1.40 (s, 3H), 1.29 (s, 3H), 0.96 (d, *J* = 7.2 Hz, 3H). $^{13}$C NMR (126 MHz, $CDCl_3$) δ 162.43, 162.04, 161.64, 161.25, 150.29, 148.75, 144.57, 141.09, 138.75, 135.37, 130.92, 129.49, 128.76, 127.87, 127.17, 125.94, 125.70, 123.54, 123.41, 122.54, 121.37, 117.65, 85.48, 53.28, 49.20, 19.84, 16.59, 13.52, 13.00, 9.71. HRMS (ESI, m/z) calcd. for $C_{21}H_{24}N^+$: 290.1903. Found: 290.1897.

### 5.3.17. [7c][BArF$_{24}$]

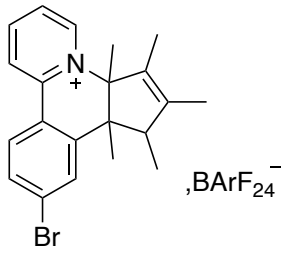

Under argon atmosphere, **7a** (27 mg, 0.05 mmol) and [$Ph_3C$][$BArF_{24}$] (55 mg, 0.1 mmol) in 10 mL of $CH_2Cl_2$, the NMR yield: 57%; under air, NMR yield : 84%, isolated yield : 37% (22 mg). Anal. calcd for $C_{53}H_{35}BBrF_{24}N \cdot 0.15\ CH_2Cl_2$: C 51.26, H 2.86, N 1.12. Found: C 51.24, H 2.95, N 1.26. $^1$H NMR (500 MHz, $CDCl_3$) δ 8.29 (dd, *J* = 6.6, 1.4 Hz, 1H), 7.98 (dd, *J* = 8.5, 1.7 Hz, 1H), 7.90 (ddd, *J* = 8.4, 7.3, 1.4 Hz, 1H), 7.71 (s, 3H), 7.69 (dd, *J* = 5.1, 2.7 Hz, 8H), 7.50 (s, 4H), 7.45 – 7.38 (m, 1H), 2.42 – 2.37 (m, 1H), 2.08 (dd, *J* = 2.8, 1.4 Hz, 3H), 1.72 – 1.68 (m, 3H), 1.40 (s, 3H), 1.30 (s, 3H), 0.98 (d, *J* = 7.2 Hz, 3H). $^{13}$C NMR (126 MHz, $CDCl_3$) δ 162.43, 162.03, 161.64, 161.24, 150.27, 147.88, 144.83, 141.27, 140.61, 134.88, 132.96, 132.11, 131.01, 130.92, 129.24, 128.99, 128.40, 127.85, 126.28, 125.69, 123.52, 123.19, 121.45, 121.35, 117.67, 85.61, 53.15, 49.14, 19.89, 16.65, 13.48, 13.02, 9.81. HRMS (ESI, m/z) calcd. for $C_{21}H_{23}BrN^+$: 368.1008. Found: 368.10.

### 5.3.18. [8c][BArF$_{24}$].

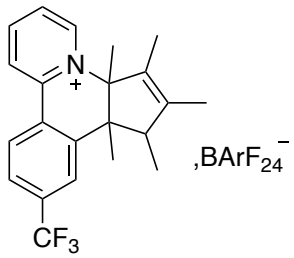

Under argon atmosphere**,** **8a** (16 mg, 0.03 mmol) and [$Ph_3C$][$BArF_{24}$] (33 mg, 0.03 mmol) in 10 mL of $CH_2Cl_2$, the NMR yield: 63%; under air, NMR yield: 88%, isolated yield: 35% (13 mg). Anal. calcd for $C_{54}H_{35}BF_{27}N$: C 53.09, H 2.89, N 1.15. Found: C 52.86, H 3.06, N,1.30. $^1$H NMR (500 MHz, $CDCl_3$) δ 8.36 (dd, *J* = 6.6, 1.4 Hz, 1H), 8.06 – 8.01 (m, 1H), 7.98 (d, *J* = 8.3 Hz, 1H), 7.93 (td, *J* = 7.9, 1.4 Hz, 1H), 7.83 (dd, *J* = 8.2, 1.8 Hz, 1H), 7.80 (s, 1H), 7.72 – 7.67 (m, 8H), 7.51 – 7.48 (m, 4H), 7.47 (d, *J* = 7.7 Hz, 1H), 2.40 (s, 1H), 2.11 (dq, *J* = 2.6, 1.3 Hz, 3H), 1.73 – 1.70 (m, 3H), 1.41 (s, 3H), 1.35 (s, 3H), 0.99 (d, *J* = 7.2 Hz, 3H). $^{13}$C NMR (126 MHz, $CDCl_3$) δ 162.43, 162.04, 161.65, 161.24, 150.54, 147.08, 145.25, 141.70, 139.85, 134.86, 131.00, 129.28, 129.01, 127.81, 127.17, 126.39, 125.67, 123.86, 123.51, 117.71, 85.98, 53.26, 49.14, 20.00, 16.68, 13.49, 13.06, 9.81. $^{19}$F NMR (282 MHz, $CDCl_3$): δ -62.4 ppm. HRMS (ESI, m/z) calcd. for $C_{22}H_{23}F_3N^+$: 358.1777. Found: 358.18.

### 5.3.19. [7d][BArF$_{24}$].

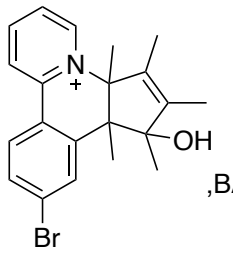

**7a** (16 mg, 0.03 mmol) and [Ph$_3$C][BArF$_{24}$] (30 mg, 0.03 mmol) in 10 mL $CH_2Cl_2$, isolated yield: 21% (8 mg). Anal. Calcd for $C_{53}H_{35}BBrF_{24}NO$: C,50.99; H,2.83; N, 1.12. Found: C 50.69, H 2.76, N 1.18. $^1$H NMR (500 MHz, $CDCl_3$) δ 8.46 (dd, *J* = 6.6, 1.4 Hz, 1H), 8.28 (ddd, *J* = 8.7, 7.4, 1.4 Hz, 1H), 8.18 (dd, *J* = 8.3, 1.6 Hz, 1H), 7.91 (d, *J* = 8.5 Hz, 1H), 7.85 – 7.77 (m, 2H), 7.73 (d, *J* = 6.4 Hz, 1H), 7.73 – 7.70 (m, 8H), 7.56 (s, 4H), 5.34 – 5.30 (m, 7H), 2.21 (q, *J* = 1.3 Hz, 3H), 1.80 (q, *J* = 1.3 Hz, 3H), 1.51 (s, 3H), 1.40 (s, 3H), 1.32 (s, 3H), 1.06 (s, 1H). $^{13}$C NMR (126 MHz, $CDCl_3$) δ 162.90, 162.50, 162.11, 161.71, 149.63, 148.79, 145.21, 141.00, 138.82, 135.36, 134.91, 133.33, 132.47, 130.34, 129.54, 129.30, 128.55, 128.39, 126.57, 126.23, 125.74, 124.24, 124.06, 118.03, 86.18, 82.57, 55.64, 22.27, 21.38, 21.01, 14.22, 11.54. HRMS (ESI, m/z) calcd. for $C_{21}H_{23}BrNO^+$: 384.0958. Found: 384.1006.

### 5.3.20. [8d][BArF$_{24}$].

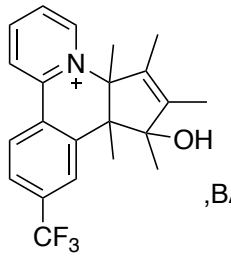

**8a** (15 mg, 0.03 mmol) and [Ph$_3$C][BArF$_{24}$] (30 mg, 0.03 mmol) in 10 mL $CH_2Cl_2$, isolated yield: 17% (6 mg). Anal. calcd for $C_{54}H_{35}BF_{27}NO$: C 52.41, H 2.85, N 1.13. Found: C 52.03, H 2.80, N 1.13. $^1$H NMR (500 MHz, $CD_2Cl_2$) δ 8.53 (dd, *J* = 6.5, 1.4 Hz, 1H), 8.33 (ddd, *J* = 8.7, 7.4, 1.4 Hz, 1H), 8.26 (dd, *J* = 8.4, 1.6 Hz, 1H), 8.18 (d, *J* = 8.2 Hz, 1H), 7.91 (d, *J* = 8.2 Hz, 2H), 7.79 (ddd, *J* = 7.9, 6.5, 1.6 Hz, 1H), 7.72 (p, *J* = 2.3 Hz, 8H), 7.55 (s, 4H), 2.21 (q, *J* = 1.4 Hz, 3H), 1.81 – 1.75 (m, 3H), 1.51 (s, 3H), 1.44 (s, 3H), 1.32 (s, 3H), 1.11 (s, 1H). $^{13}$C NMR (126 MHz, $CD_2Cl_2$) δ 162.69, 162.30, 161.90, 161.50, 149.61, 147.87, 145.42, 141.17, 137.81, 135.14, 134.69, 129.74, 129.59, 129.36, 129.34, 129.32, 129.29, 129.11, 129.09, 129.07, 129.04, 128.18, 127.71, 127.20, 126.58, 126.55, 126.01, 125.82, 125.79, 124.68, 123.85, 121.68, 117.88, 117.85, 117.81, 85.96, 82.60, 55.52, 21.99, 21.23, 20.79, 13.99, 11.34. $^{19}$F NMR (282 MHz, $CDCl_3$): δ -62.8 ppm. HRMS (ESI, m/z) calcd. for $C_{22}H_{23}F_3NO^+$: 374.1726. Found: 374.1700.

### 5.3.21. [10c][BArF$_{24}$].

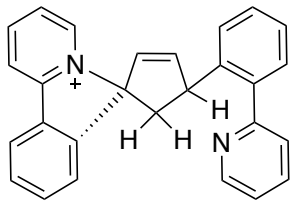

,BArF$_{24}^-$ **10a** (15 mg, 0.03 mmol) and [Ph$_3$C][BArF$_{24}$] (30 mg, 0.03 mmol) in 10 mL $CH_2Cl_2$, isolated yield: 17% (6 mg). Anal. calcd for $C_{59}H_{33}BF_{24}N_2 \cdot 1.1\ CH_2Cl_2$: C 54.27, H 2.67, N 2.11. Found: C 54.15, H 2.80, N 2.04. $^1$H NMR (300 MHz, $CDCl_3$) δ 8.52 (d, *J* = 5.4 Hz, 1H), 8.25 (d, *J* = 6.2 Hz, 1H), 8.01 – 7.89 (m, 2H), 7.89 – 7.75 (m, 3H), 7.69 (d, *J* = 4.2 Hz, 8H), 7.67 – 7.60 (m, 2H), 7.58 – 7.50 (m, 2H), 7.48 (d, *J* = 1.3 Hz, 4H), 7.47 – 7.38 (m, 3H), 7.26 – 7.17 (m, 1H), 6.83 (dd, *J* = 5.4, 2.0 Hz, 1H), 5.75 (dd, *J* = 5.4, 2.7 Hz, 1H), 5.30 (s, 1H), 5.08 (d, *J* = 7.5 Hz, 1H), 3.06 (dd, *J* = 15.9, 8.0 Hz, 1H), 2.80 (dd, *J* = 15.9, 6.7 Hz, 1H). $^{13}$C NMR (126 MHz, $CDCl_3$) δ 162.41, 162.02, 161.62, 161.23, 149.12, 148.74, 146.05, 145.93, 140.15, 139.67, 137.33, 135.62, 134.87, 131.30, 130.89, 130.38, 130.01, 129.70, 129.26, 128.99, 128.17, 127.83, 126.34, 125.66, 125.26, 124.45, 123.80, 123.49, 123.29, 122.53, 120.25, 117.68, 91.44, 85.17, 83.21, 82.47, 53.59, 49.67, 48.10. HRMS (ESI, m/z) calcd. for $C_{27}H_{21}N_2^+$: 373.1699. Found: 373.17.

## 5.4. Experiments related to chapter 2

### 5.4.1. Determination of the KIE of cyclocobalation

#### 5.4.1.1. Parallel experiments

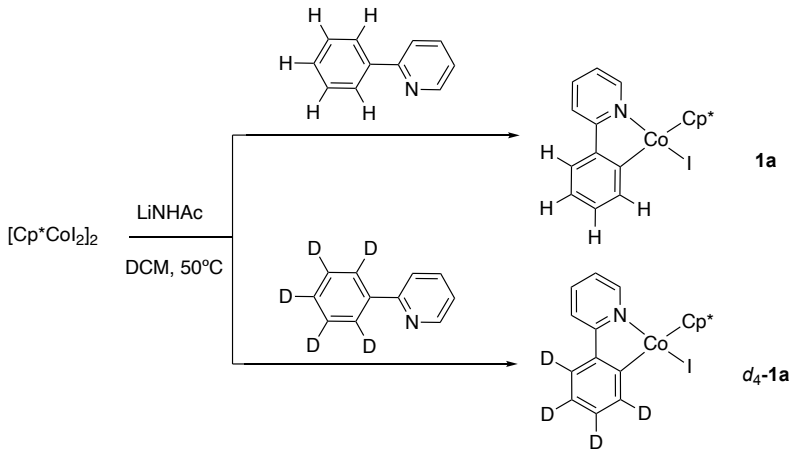


2-*phpyH* and 2-(*d*$_5$.*ph*)*pyD* (0.10 mmol, 2 eq) were placed in two separate Schlenk vessels to which identical amounts of [Cp*CoI$_2$]$_2$ (0.05 mmol, 1 eq), LiNHAc (0.3 mmol,

6 eq), 1,3,5-trimethoxybenzene as internal inert reference and 5 mL of DCM were added. Upon sealing the vessel, the resulting suspension was vigorously stirred at 50 °C for 6 h and aliquots of both vessels were removed every hour, the solvent was evaporated and replaced by $CD_2Cl_2$ (0.3 mL) and the resulting solution analyzed by $^1H$ NMR spectroscopy for the determination of the yield in **1a** and *d*$_4$.**1a**. The isotopic effect at time *t* , i.e $KIE_t$ was determined by the ratio of the yield in **1a** over the yield in *d*$_4$.**1a**.

**Table 5.1.** The yields of **1a** or *d*$_4$-**1a** in 6 hours.

| | Entry | 1h | 2h | 3h | 4h | 5h | 6h |
|---|---|---|---|---|---|---|---|
| **1a** | 1 | 12.65 | 28.92 | 39.31 | 43.37 | 46.09 | 50.16 |
| | 2 | 12.95 | 31.34 | 40.81 | 46.7 | 49.44 | 51.8 |
| | average | 12.8 | 30.13 | 40.06 | 45.035 | 47.765 | 50.98 |
| *d*$_4$-**1a** | 1 | 10.4 | 21.22 | 27.89 | 33.29 | 37.46 | 41.62 |
| | 2 | 9.99 | 18.55 | 25.42 | 28.54 | 30.68 | 32.82 |
| | average | 10.195 | 19.885 | 26.655 | 30.915 | 34.07 | 37.22 |

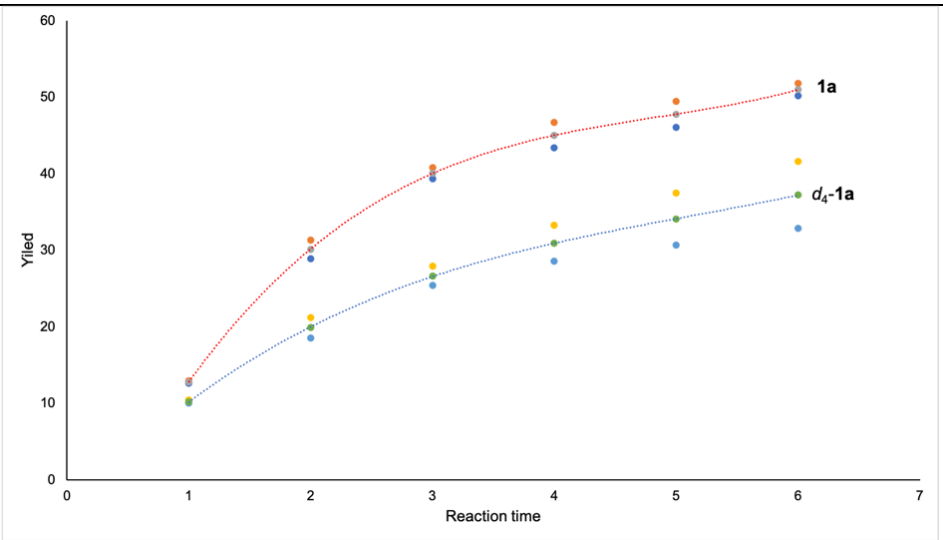


### 5.4.1.2. Intermolecular competitive reaction

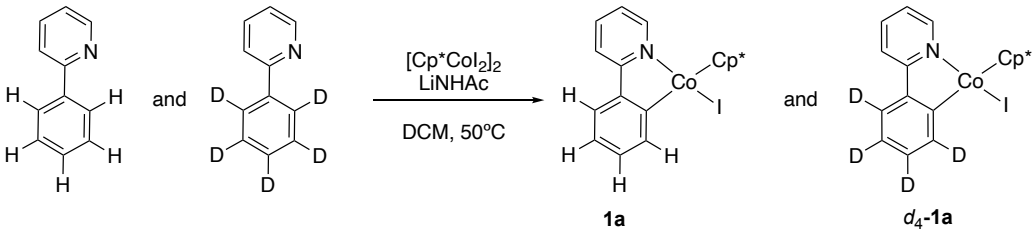


$[Cp^*CoI_2]_2$ (0.05 mmol) and LiNHAc (0.15 mmol) were mixed in 5 mL of distilled DCM. 2-*phpyH* (0.05 mmol) and 2-(*d*$_5$.*ph*)*pyD* (0.05 mmol) were added to the suspension. The reaction was stirred vigorously at 50°C during 17 hours in a sealed Schlenk vessel.

At the end of the reaction, the solution was filtrated through Celite and the solvent was removed under reduced pressure. The resulting solid residue was washed with distilled pentane to remove the soluble components of the mixture to afford a solid composed of a mixture of the desired cobaltacycles **1a** and *d*$_4$-**1a** in proportion estimated by $^1$H-coupled $^{13}$C NMR. Two signals typical of **1a** and *d*$_4$-**1a** were readily discriminated by their isotope shifts. The KIE was determined by comparing the integrations of $^{13}$C signals of the Co-bound aromatic carbon of **1a** and *d*$_4$-**1a** as well as those of the vicinal H/D-bound ortho carbon. Two KIE were obtained, 1.7 and 2.0 that are most probably biased by different spin-lattice relaxation times $T_1$ in **1a** and *d*$_4$-**1a** for the considered carbon nuclei showing up at δ ~ 180.6 and 141.4 ppm.

## 5.4.2. The annulation of 2-aryl pyridines with 1,2-diphenylacetylene

### 5.4.2.1. General procedure

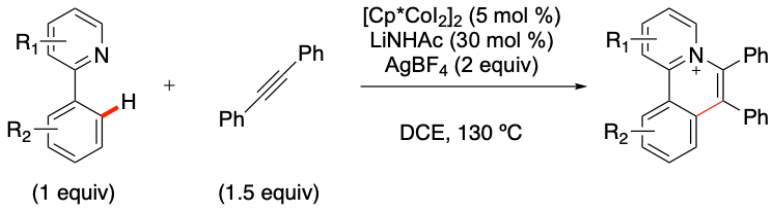


Under an argon atmosphere, 1,2-diphenylacetylene (0.15 mmol), [Cp*CoI$_2$]$_2$ (5 mol %) and LiNHAc (30 mol %) were added to a Schlenk vessel. Then, the tube was moved to an Ar-filled glove box and 2-arylpyridines (0.10 mmol), $AgBF_4$ (0.20 mmol) were added to the load of the vessel. DCE (2 mL) was added to the solid mixture, the Schlenk vessel was sealed and the suspension was stirred at 130 °C for 24 h. The reaction vessel was hence cooled to room temperature and the suspension diluted with DCM (10 mL). The mixture was filtered through a Celite pad and the Celite pad was washed with DCM (30 mL). The filtrate was concentrated and purified by silica gel column chromatography using DCM/MeOH (95:5) as eluent to deliver the desired annulation product.

#### 5.4.2.2. 5,6-diphenylbenzo[de]pyrido[3,2,1-ij]quinolin-4-ium tetrafluoroborate

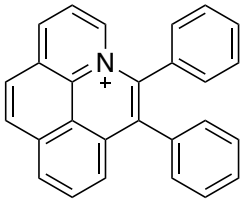

,$BF_4^-$ Yellow solid; 1 H NMR (500 MHz, DMSO-d6) δ 9.47 (d, J = 7.9 Hz, 1H), 9.21 (dd, J = 6.6, 1.0 Hz, 1H), 8.83 (d, J = 7.8 Hz, 1H), 8.77 (d, J = 9.2 Hz, 1H), 8.67 (d, J = 9.2 Hz, 1H), 8.52 (td, J = 7.8, 3.7 Hz, 2H), 7.89 – 7.84 (m, 1H), 7.62 – 7.47 (m, 5H), 7.47 – 7.33 (m, 5H). 13C NMR (126 MHz, DMSO-d6) δ 140.07, 138.85, 136.48, 135.85, 134.40, 133.32, 132.76, 132.65, 131.17, 131.06, 130.69, 130.27, 130.23, 129.98, 129.60, 129.18, 128.85, 128.51, 128.43, 126.72, 125.31, 123.14, 118.42.

#### 5.4.2.3. 5,6-diphenyldibenzo[de,g]pyrido[3,2,1-ij]quinolin-4-ium tetrafluoroborate

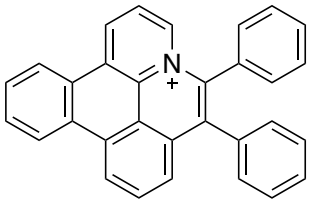

,$BF_4^-$ Yellow solid; 1 H NMR (500 MHz, DMSO-d6) δ 10.20 (d, J = 7.6 Hz, 1H), 9.56 (d, J = 7.6 Hz, 1H), 9.25 (dt, J = 7.8, 1.7 Hz, 2H), 9.19 (d, J = 6.7 Hz, 1H), 8.57 – 8.49 (m, 2H), 8.15 – 8.05 (m, 2H), 7.83 (d, J = 7.9 Hz, 1H), 7.62 – 7.49 (m, 5H), 7.46 – 7.35 (m, 5H). 13C NMR (126 MHz, DMSO-d6) δ 138.72, 136.46, 135.76, 135.43, 134.55, 134.48, 133.19, 131.47, 131.16, 131.12, 131.01, 130.96, 130.26, 130.11, 129.99, 129.60, 128.79, 128.50, 128.42, 128.16, 126.50, 125.69, 125.42, 124.89, 124.74, 123.26, 117.97.

## 5.5. Experiments related to chapter 3

### 5.5.1. Effect of radical scavengers TEMPO

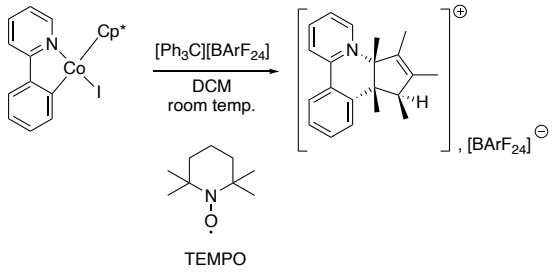


| Entry | Radical Scavenger | Yield |
|---|---|---|
| 1 | - | 70% |
| 2 | TEMPO (1 equiv) | 35% |
| 3 | TEMPO (4 equiv) | 16% |

Under argon atmosphere, a mixture of 1a (4.7 mg, 0.01 mmol) and $[Ph_3C][BArF_{24}]$ (10 mg, 0.01 mmol) was added in three sealed Schlenk vessels, one Schlenk vessel acting as a "blank" reference was exempt of TEMPO. In two of them, TEMPO (1.5 mg, 0.01

mmol; 6.1 mg, 0.04 mmol) was added in different amounts in ~1 mL of deuterated DCM, and the three resulting solutions were stirred at room temperature overnight.

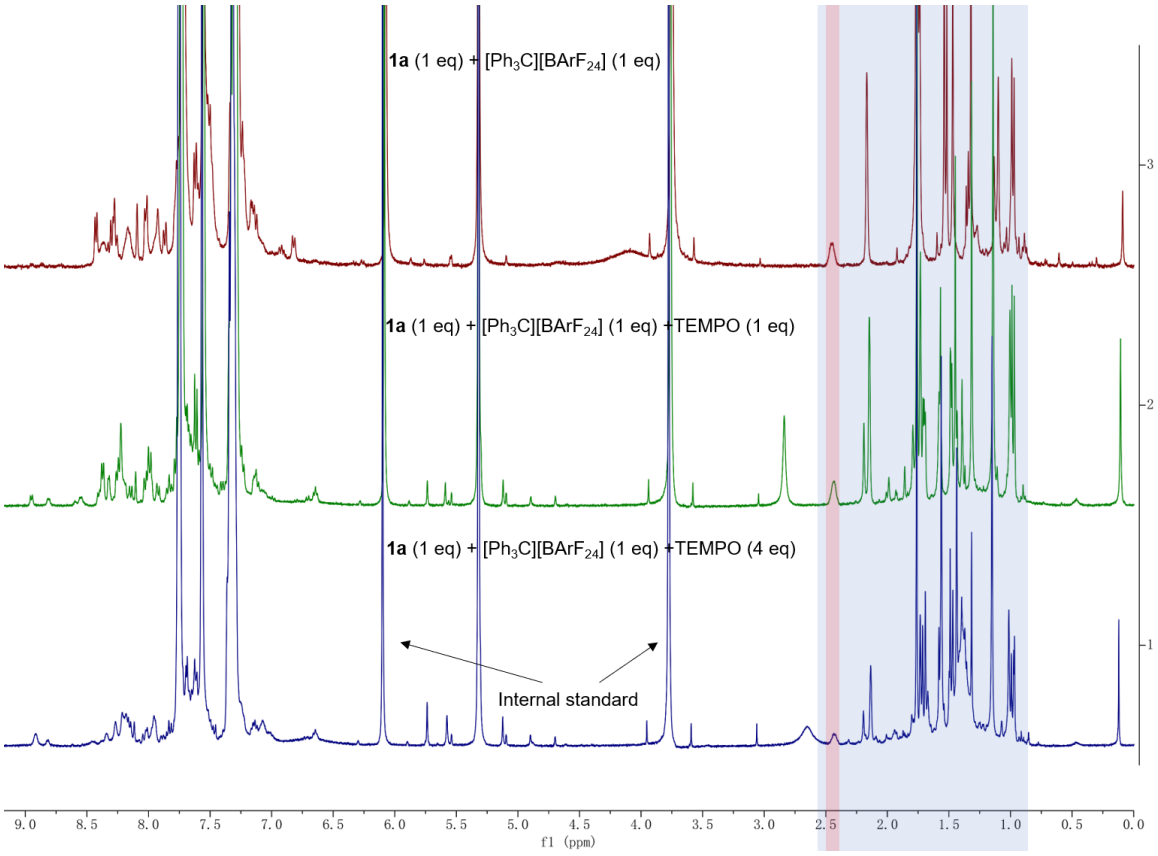


**Figure 5. 1.** Comparison of $^{1}H$ NMR spectra for the reaction of **1a** with $[Ph_3C][BArF_{24}]$ with or without TEMPO.

Noteworthy, during this reaction, without TEMPO, a large precipitate formed while with 1 equiv. TEMPO, only a small amount of precipitate was observed; with 4 equiv. TEMPO, the solution remained homogenous. (The red stripe highlights proton $H_5$.)

### 5.5.2. Experiment of 1a with $AgPF_6$ or $[Ph_3C][PF_6]$

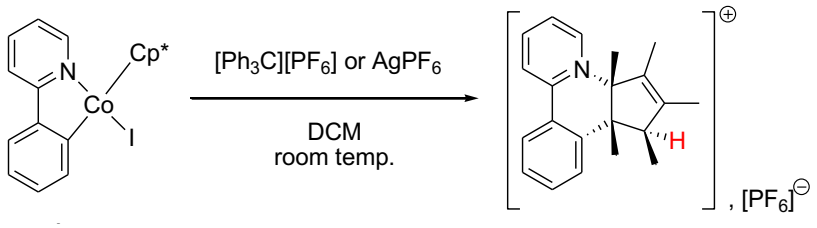


Under argon atmosphere, a mixture of **1a** (1 equiv., 0.02 mmol) and $[Ph_3C][PF_6]$ (1 equiv.) or $AgPF_6$ (2 equiv.) was stirred overnight in ~10−15 mL of $CH_2Cl_2$ at room temperature in a sealed Schlenk vessel. After the reaction, the crude compound was analyzed by $^1H$ NMR.

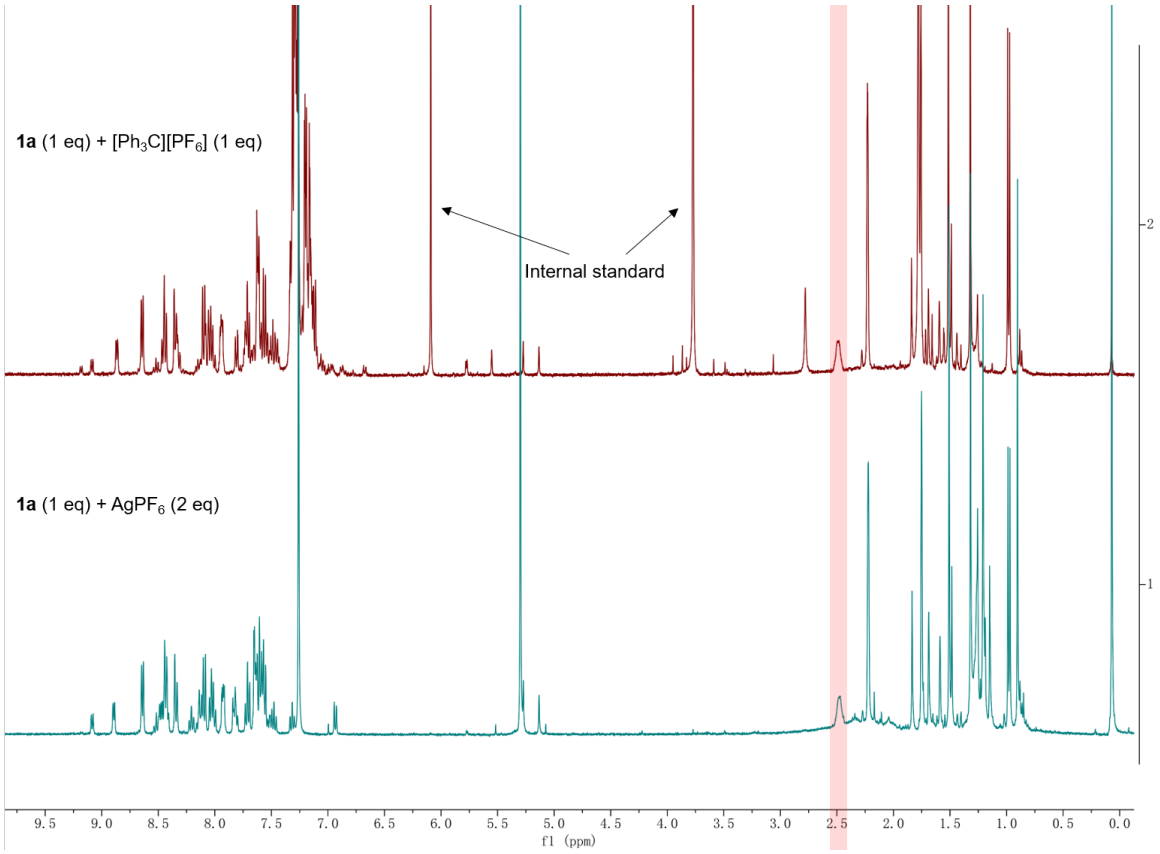


**Figure 5. 2.** $^1H$ NMR spectra of **1a** with $[Ph_3C][PF_6]$ (top) or $AgPF_6$ (bottom). The red stripe highlights the resonance of $H_5$.

## 5.5.3. Reaction of 1a with acid

### 5.5.3.1. Reaction of 1a with triflic acid

Under argon atmosphere, **1a** (9.4 mg, 0.02 mmol) was dissolved in ~1 mL of DCM in a *J*-Young tube, and then triflic acid (1.8 µL, 0.02 mmol) was added. The color changed quickly from brown to green. After 20 min, the NMR was checked, and full conversion of **1a** was observed.

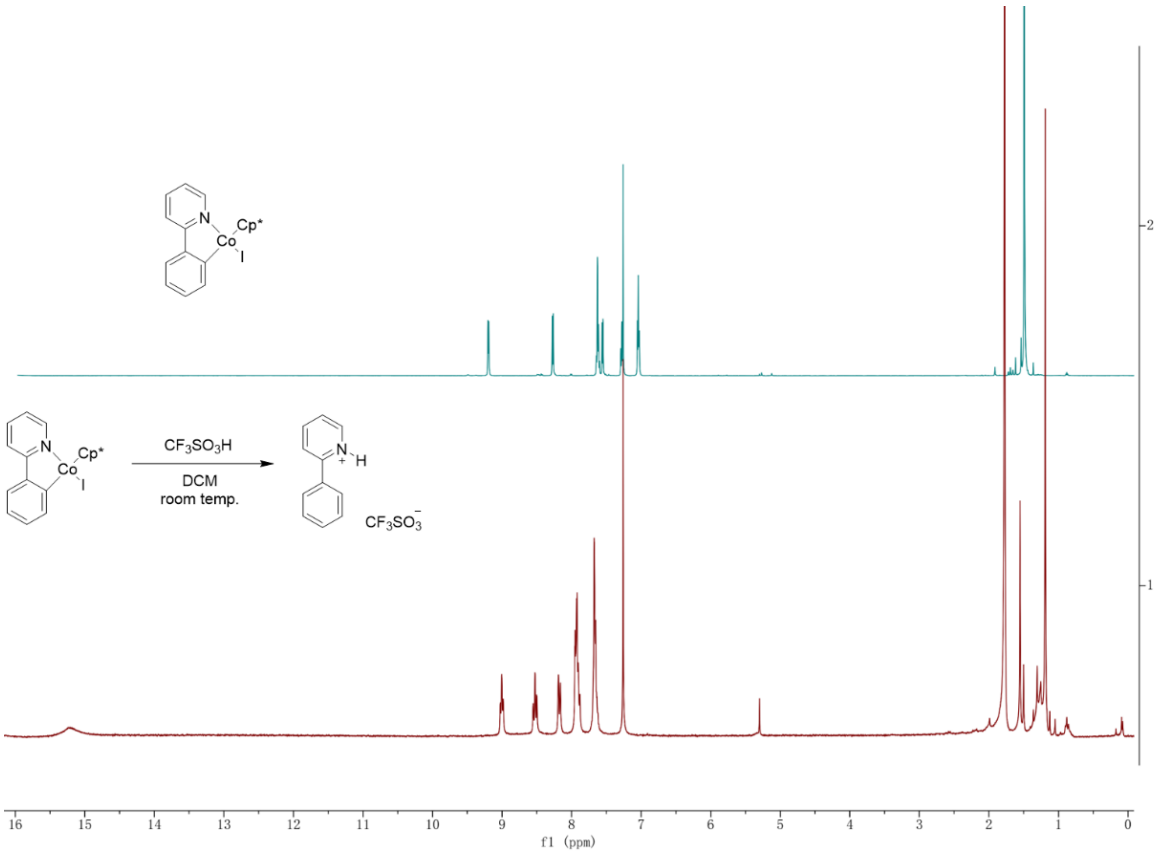


**Figure 5. 3.** NMR spectrum of the experiment of **1a** with triflic acid (J-Young tube). Stacked $^{1}$H NMR spectra of **1a** and of the reaction mixture resulting from the reaction of **1a** with triflic acid.

### 5.5.3.2. Reaction of 1a with AcOH


Under an argon atmosphere, **1a** (12.8 mg, 0.026 mmol) was dissolved in ~3 mL of DCM in a sealed Schlenk vessel, and then acetic acid (1.6 µL, 0.03 mmol) was added. After 5 h and 24 h, the yields were calculated respectively by $^{1}$H NMR with an internal reference.

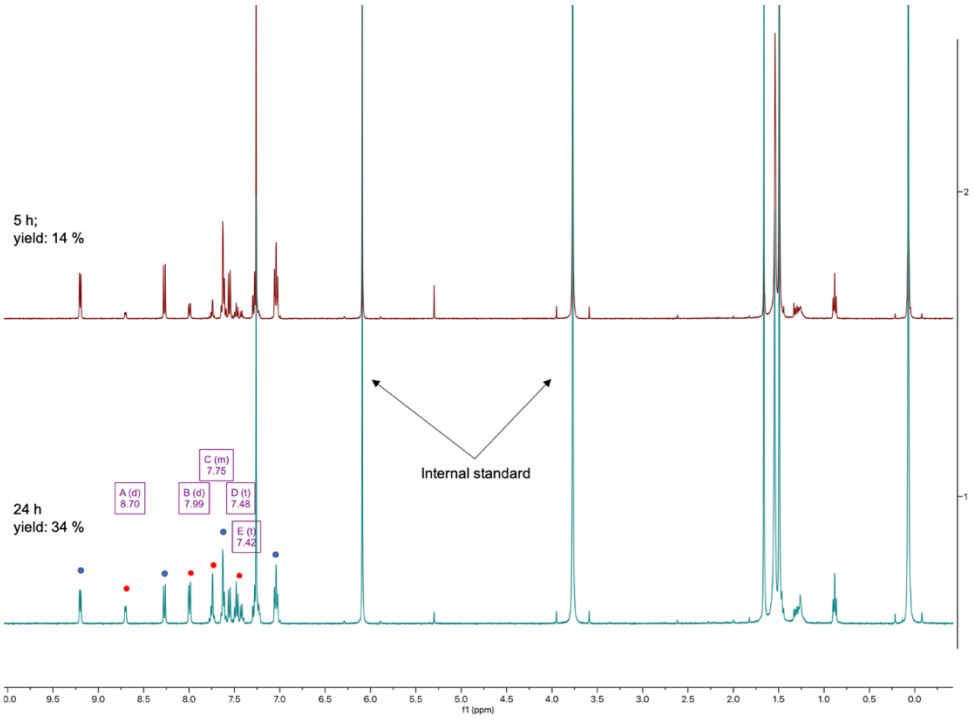


**Figure 5. 4.** $^{1}$H NMR spectra of the reaction of **1a** with acetic acid (top: 5 h; bottom: 24 h; blue point: starting materiel; red point: final product). In this reaction, the color slowly changed from red-brown to green.

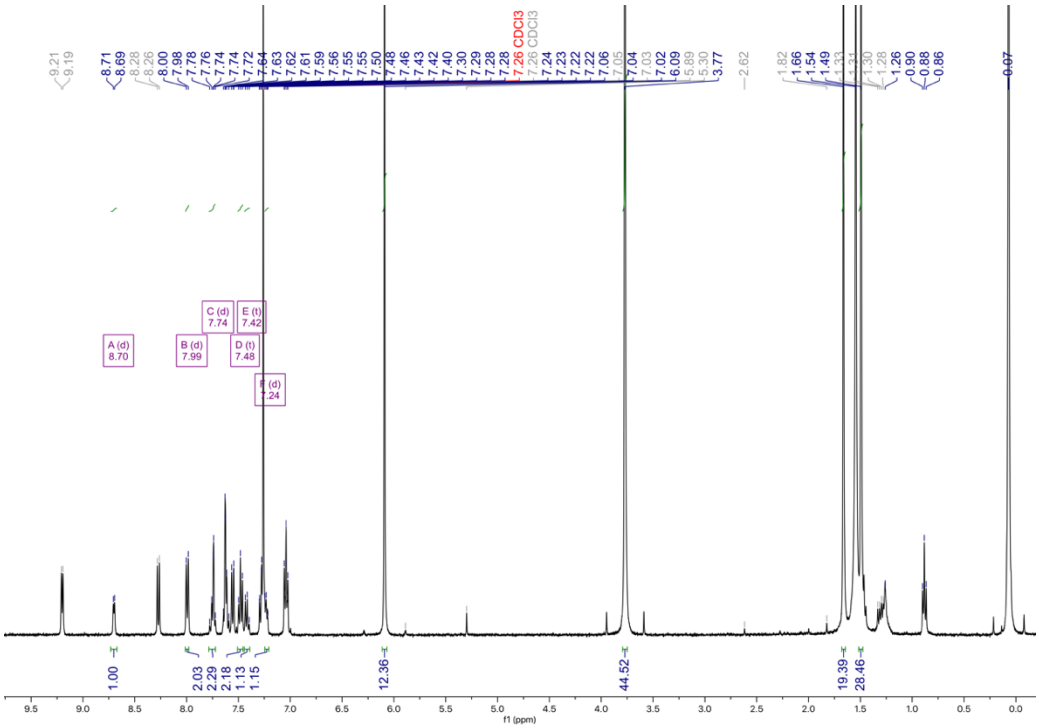

**Figure 5. 5.** $^{1}$H NMR spectrum of the reaction of **1a** with acetic acid after 24 h.

### 5.5.4. Effect of air

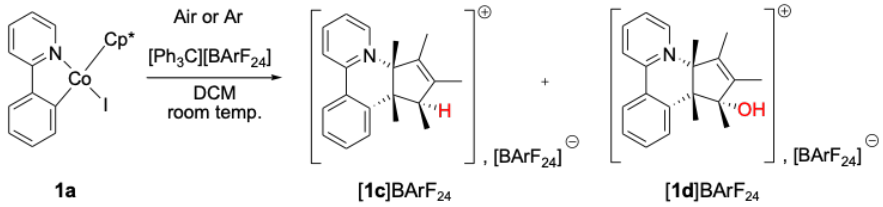


**1a** **[1c]**$BArF_{24}$ **[1d]**$BArF_{24}$

Under argon or air atmosphere, a mixture of **1a** (1 equiv) and $[Ph_3C][BArF_{24}]$ (1 equiv) was stirred overnight in ~10−15 mL of $CH_2Cl_2$ at room temperature in a sealed Schlenk vessel. After 12 h of reaction the $^{1}$H NMR spectrum was acquired with an internal reference.

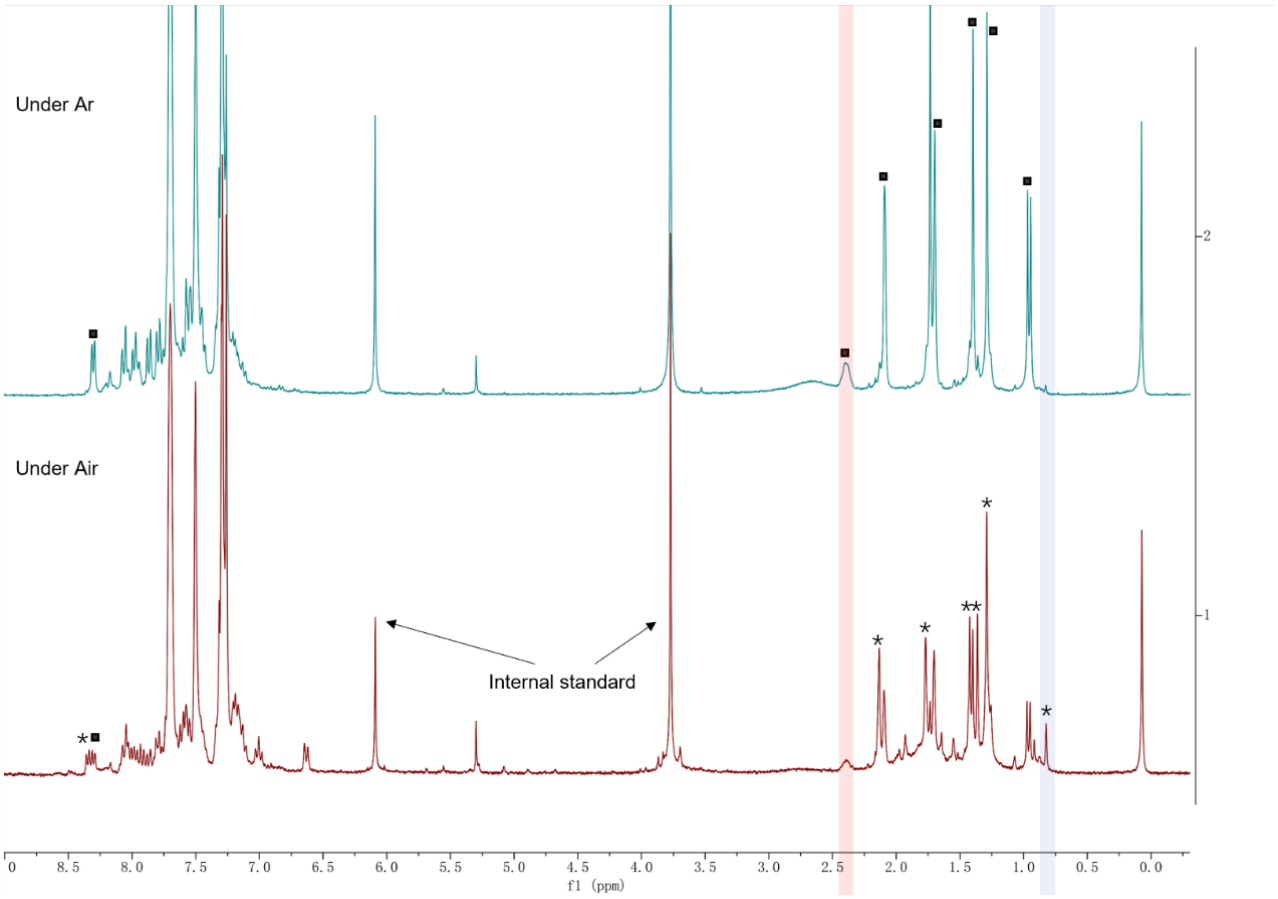


**Figure 5. 6.** $^{1}$H NMR spectra of the reaction of **1a** with [$Ph_3C$][$BArF_{24}$] under argon (top) or air (bottom). After the reaction mixture was filtrated over Celite followed by removal of the solvent. The resulting residue was purified by column chromatography and then recrystallized with $CH_2Cl_2$/*n*-pentane and/or washed with *n*-pentane to obtain a white powder. The red stripe highlights $H_5$ in [**1c**]$^+$ and the blue stripe highlights [**1d**]$^+$. The ■ point the salient signals of [**1c**]$^+$. The * point the signals of [**1d**]$^+$, which was derived by comparing the **7d** and **8d** NMR spectra).

### 5.5.5. Reaction of 5a with [$Ph_3C$][$BArF_{24}$]

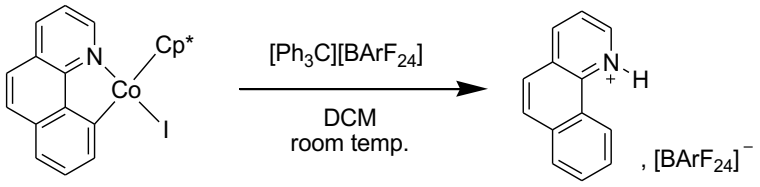


Under argon atmosphere, a mixture of **5a** (1 equiv) and [$Ph_3C$][$BArF_{24}$] (1 equiv) was stirred overnight in ~10−15 mL of $CH_2Cl_2$ at room temperature in a sealed Schlenk vessel. After reaction, the color changed from brown red to green, and the crude compound was analyzed by $^{1}$H NMR with an internal reference.

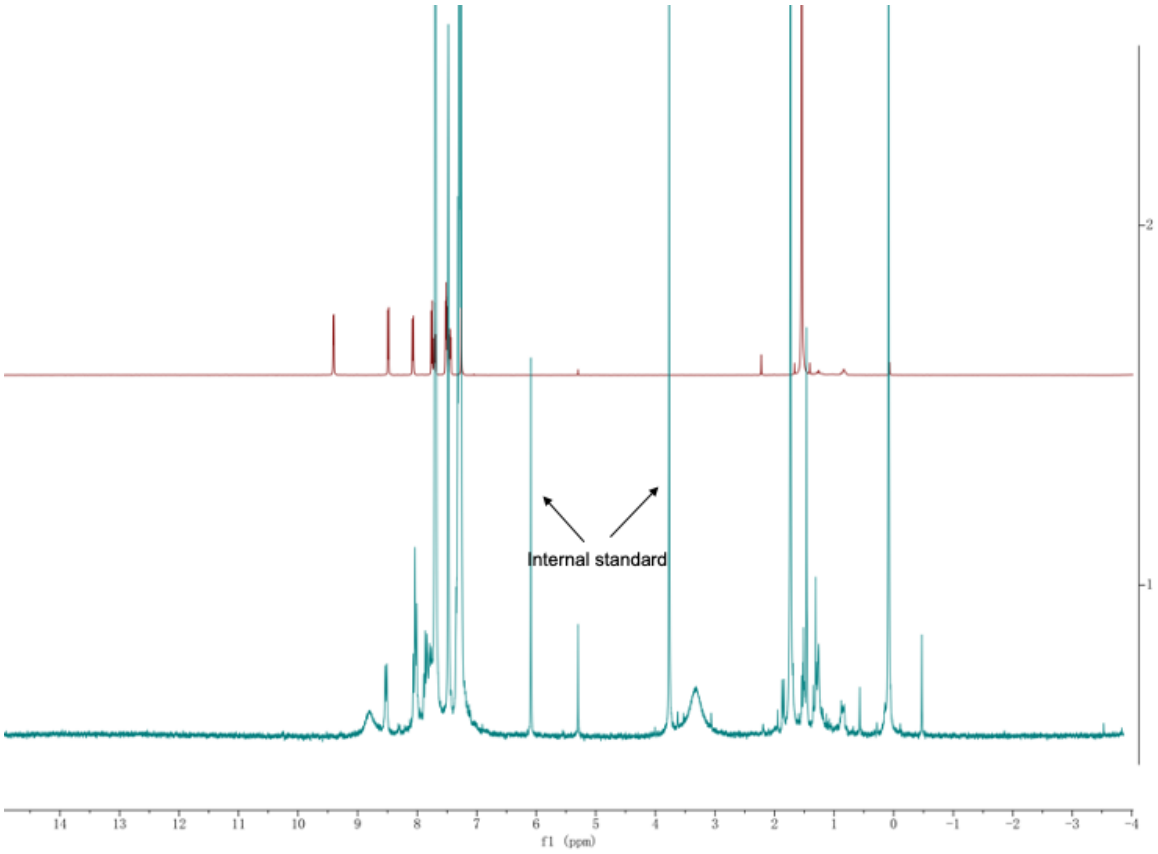


**Figure 5. 7.** $^{1}$H NMR spectrum of the reaction mixture (bottom) resulting from the reaction of **5a** (top) with [$Ph_3C$][$BArF_{24}$]**.**

The $^{1}$H NMR spectrum did not show the presence of the product of oxidative cyclocondensation. Crystallization of the reaction mixture afforded the *N*-protonated benzo[*h*]quinoline $BArF_{24}$ salt.

### 5.5.6. Reaction of 9a with [$Ph_3C$][$BArF_{24}$]

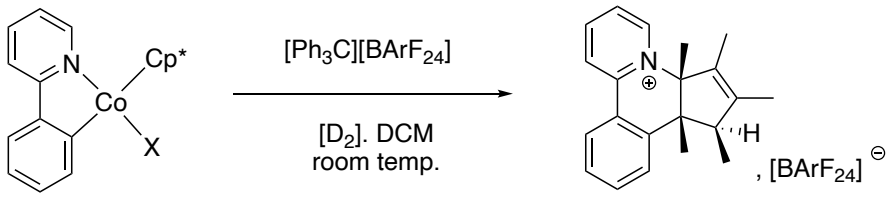


[**1c**][$BArF_{24}$]

X= Cl, **9a** (21 % NMR yield)
X= I, **1a** (72 % NMR yield)

Under argon atmosphere, a mixture of **9a** or **1a** (1 equiv) and [$Ph_3C$][$BArF_{24}$] (1 equiv) was stirred overnight in ~10−15 mL of $CH_2Cl_2$ at room temperature in a sealed Schlenk

vessel. After reaction, the color changed from brown red to green, and the crude compound was analyzed by $^1$H NMR with an internal reference.

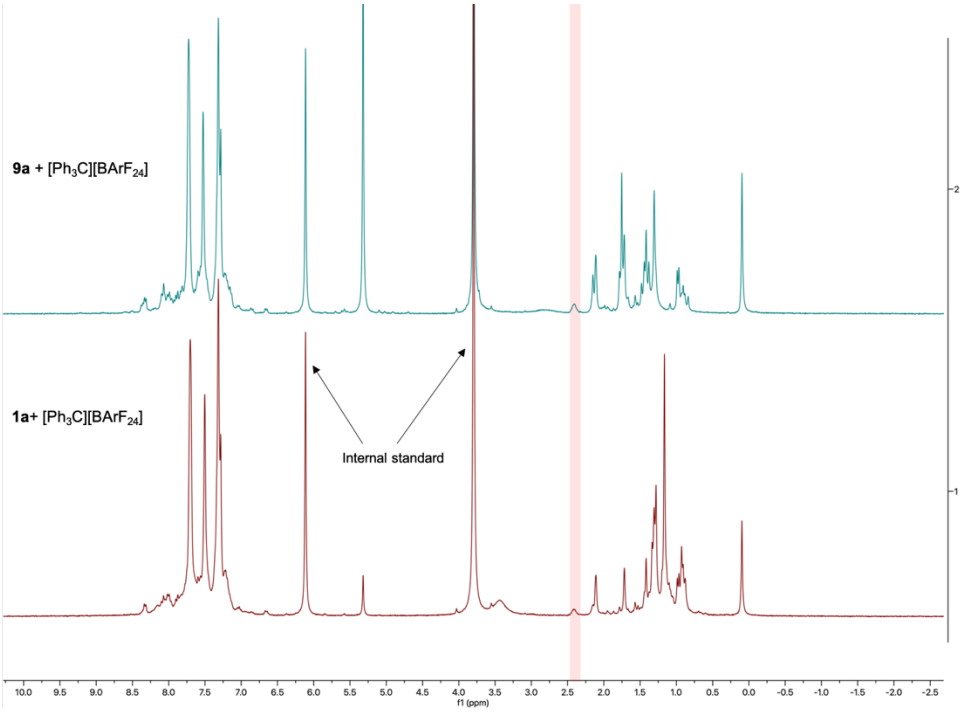


**Figure 5. 8.** $^1$H NMR spectrum of the reaction mixture (bottom) resulting from the reaction of **9a** (top) or **1a** (bottom) with $[Ph_3C][BArF_{24}]$.

## 5.5.7. Reaction of 1b with $[Ph_3C][BArF_{24}]$

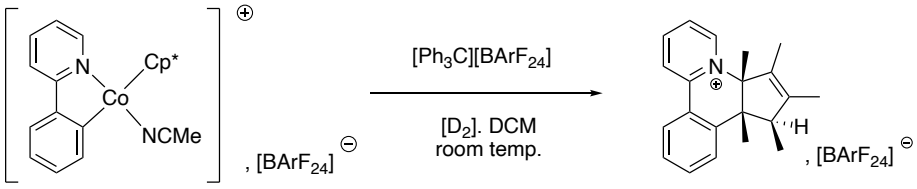


**1b** [**1c**][$BArF_{24}$]

Under argon atmosphere, a mixture of **1b** (1 equiv) and $[Ph_3C][BArF_{24}]$ (1 equiv) was stirred overnight in ~1 mL of $D_2$-DCM at room temperature in a sealed Schlenk vessel. After reaction, the crude compound was analyzed by $^1$H NMR with an internal reference.

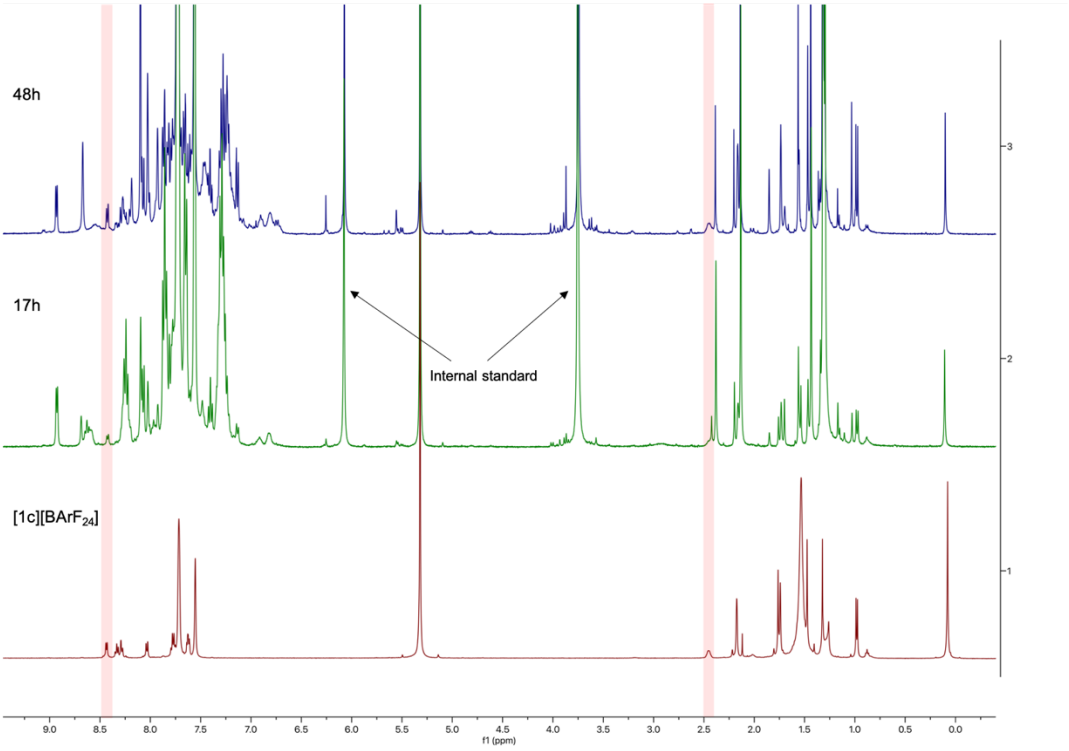


**Figure 5. 9.** $^{1}$H NMR spectrum of the reaction mixture produced by the reaction of **1b** with $[Ph_3C][BArF_{24}]$ after 17 h and 48 h.

## 5.5.8. Reaction of $[Ph_3C][BArF_{24}]$ with another metallacycles

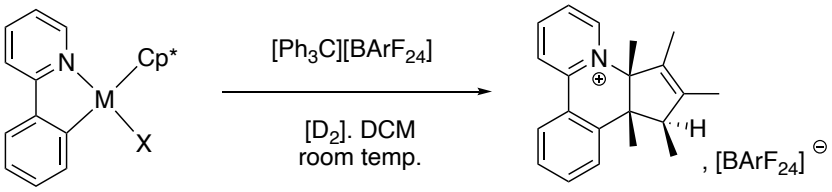


M = Ir, X= Cl , **2a**
M = Co, X = $SCF_3$, **Co-$SCF_3$**
M = Co, X = NCPh, **Co-NCPh**

[**1c**][$BArF_{24}$]

Under argon atmosphere, a mixture of metallacycle (1 equiv) and $[Ph_3C][BArF_{24}]$ (1 equiv) was stirred overnight in ~1 mL of $D_2$-DCM at room temperature in a sealed Schlenk vessel. After reaction, the crude compound was analyzed by $^{1}$H NMR.

| Entry | metallacycles | yields |
|---|---|---|
| 1 | **2a** | 0 % |
| 2 | Co-$SCF_3$ | 0 % |
| 3 | Co-NCPh (**1b''**) | 0 % |

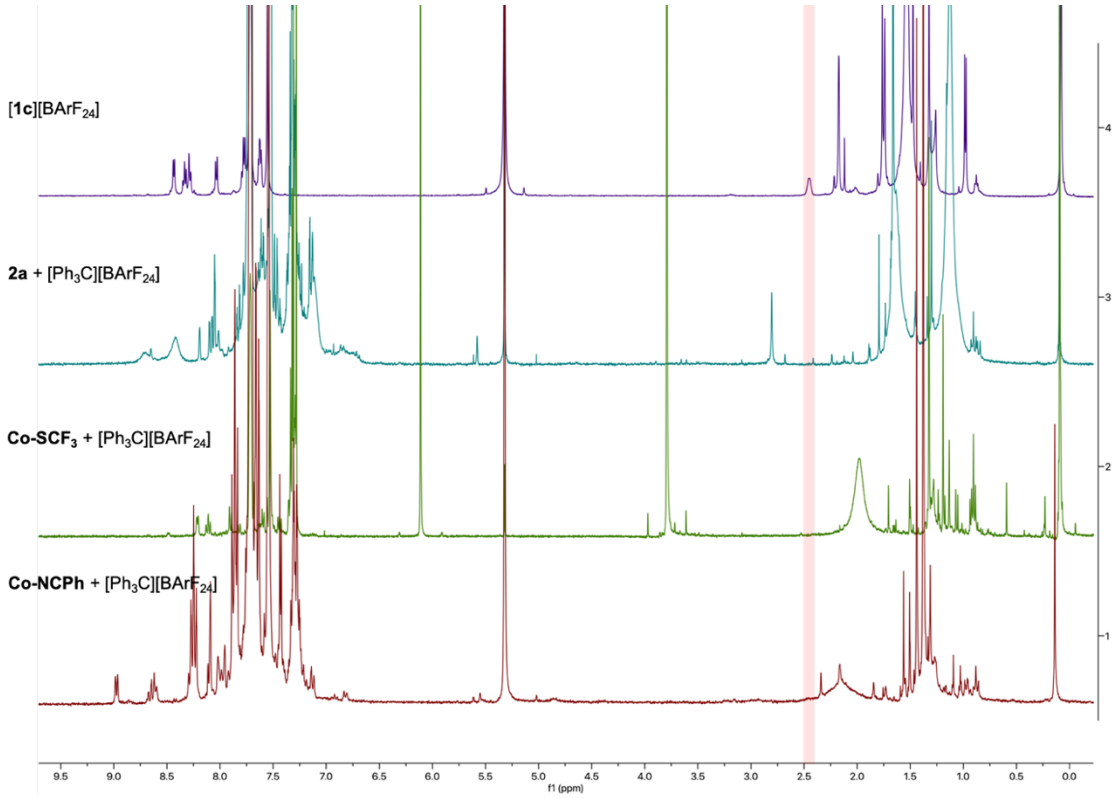


**Figure 5. 10.** $^{1}$H NMR spectrum of the reaction mixture resulting from the reaction of metallacycles with $[Ph_3C][BArF_{24}]$.

## 5.6. Experiments related to chapter 4

### 5.6.1. Hydrosilylation of ketone via cobaltacycles 1b and 5b

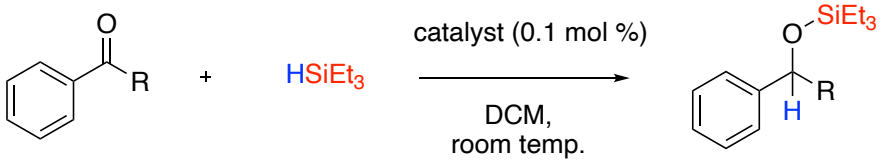


(1 equiv.) (1.2 equiv.)

Under argon atmosphere, to a solution of cobaltacycles (0.1 mol %) and ketone (0.1 mmol, 1 equiv) in ~2 mL of DCM was added $HSiEt_3$ (0.12 mmol, 1.2 equiv). The reaction mixture was stirred overnight at room temperature. After reaction, the crude compound was analyzed by $^{1}$H NMR (1,3,5-trimethoxybenzene as internal reference)

### 5.6.2. The stoichiometric reaction of 1b with $HSiEt_3$

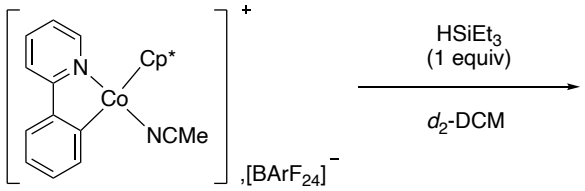


**1b**

Under argon atmosphere, the cationic cobaltacycle **1b** (0.02 mmol) was mixed with $HSiEt_3$ (0.02 mmol) in *J*. Young valve NMR tube in DCM-$d_2$ at 298 K or 247 K, and the reaction was monitored by $^1H$ NMR spectroscopy.

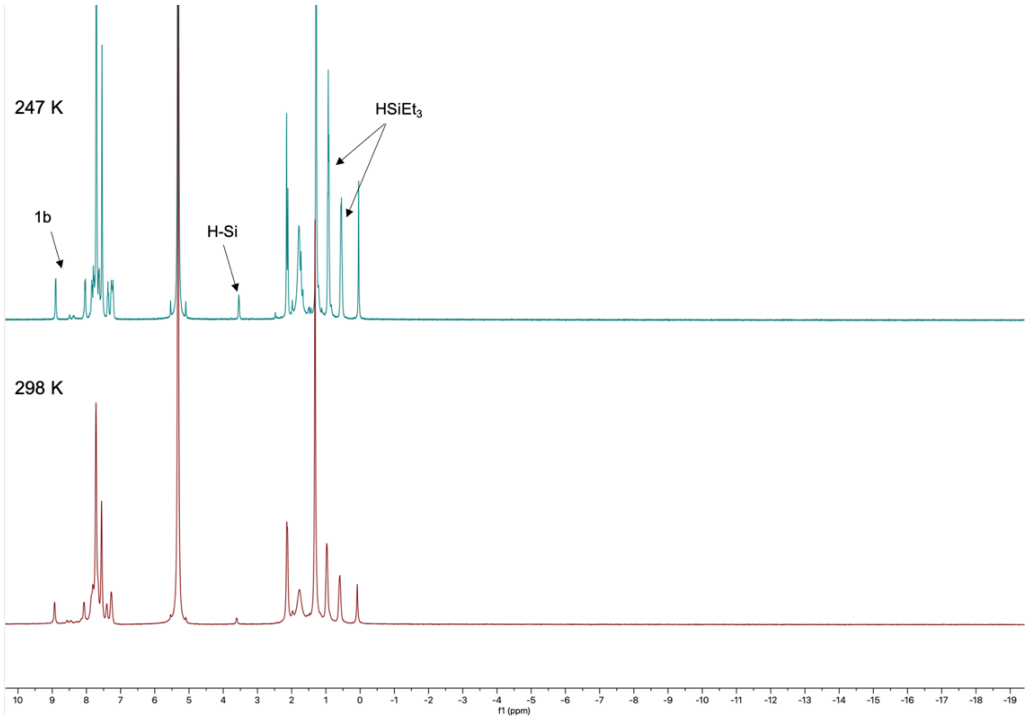


**Figure 5. 11.** Standard stoichiometric reaction of **1b** with $HSiEt_3$ monitored by $^1H$ NMR. (top: at 247 K; bottom: 298K).

### 5.6.3. Attempts for the cobalt hydride with additive

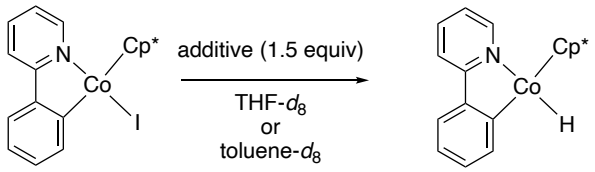


Under argon atmosphere, the compound **1a** (10 mg, 0.021 mmol) was mixed with $NaBHEt_3$ (0.032, mmol, 1.5 equiv) in *J*. Young valve NMR tube in THF-$d_8$ at -40 °C, and the reaction was monitored by $^1H$ NMR spectroscopy.

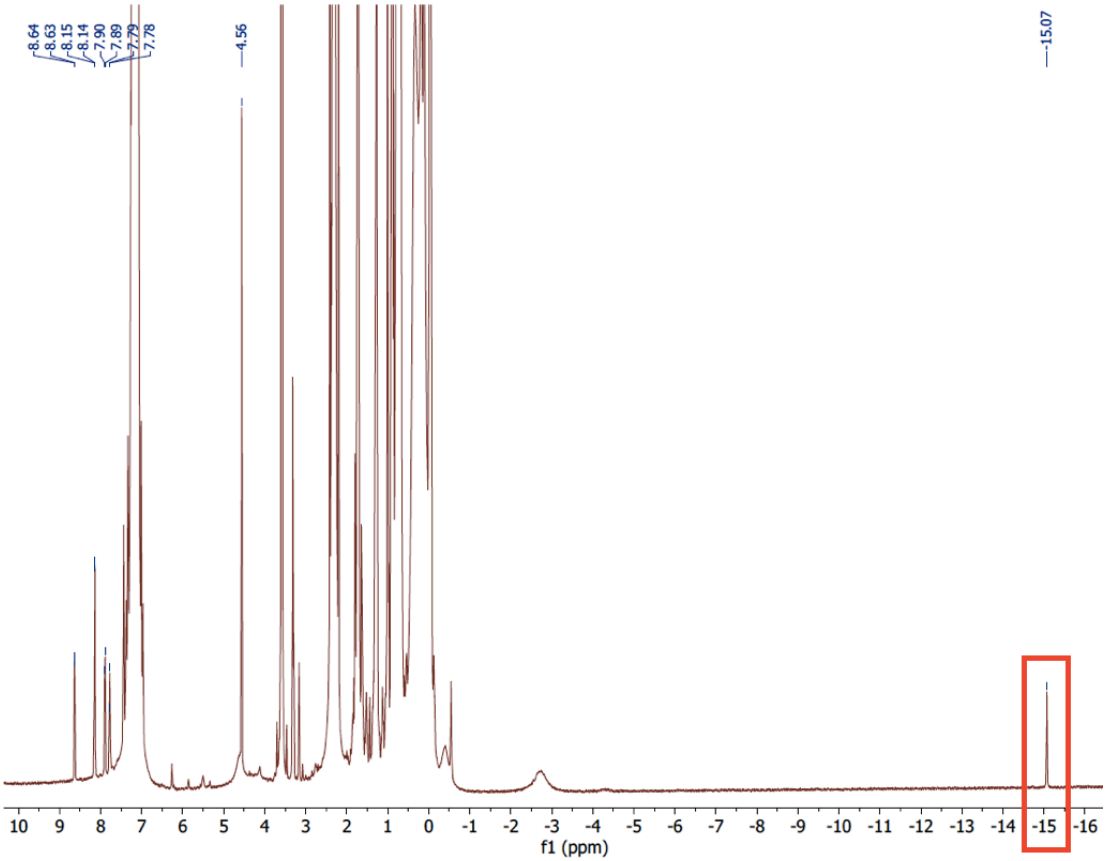


**Figure 5. 12.** Standard stoichiometric reaction of **1a** with $NaBHEt_3$ monitored by $^1H$ NMR. A hydride peak signature was observed at -15.07 ppm, however this signal disappearing progressively.

## 5.6.4. Hydrosilylation of benzophenone with $HSiEt_3$

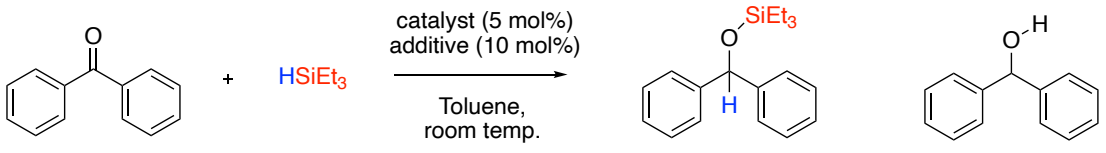


(1 equiv) (3 equiv) A B

Under argon atmosphere, the Benzophenone (30.7 mg, 0.168 mmol) and cobaltacycles (0.008 mmol, 5 mol%) were dissolved in toluene (2 ml), and then, the $HSiEt_3$ (0.08 ml, 0.505 mmol, 3 equiv.) was added, along with $NaBHEt_3$ (10 mol%), and the mixture was stirred for 5 hours at room temperature. the crude compound was analyzed by $^1H$ NMR (1,3,5-trimethoxybenzene as internal reference).

# General conclusions and perspectives

In this thesis, we have synthesized and characterized a serie of cobaltacycles metalated by $[Cp^*CoI_2]_2$, which shows that cobaltacycles are not elusive and can be readily prepared in good yields via the base assisted CMD mechanism if the proper base is chosen to optimize the formation of the transient agostic intermediate.

Furthermore, it was demonstrated that noncovalent interactions play an important role in C-H bond activation via base-assisted CMD mechanism. The relevance of noncovalent interactions in the cyclocobaltation can be evident via the evolution of the reaction: Prior to the activation of $C_{Ar}$-$H_{Ar}$ bond by carbometallation and proton transfer to the neighboring base coordinated to the metal center, the local electrostatic interactions and the multipolar environment make a significant contribution to the polarization of this bond, which provides a reasonable theroretical explanation not only for the cyclocobaltation but also for the cyclometallations of other 3d metals. The use of acetamidate as an auxiliary base can effectively reduces the residual chelation interaction with metal, which enhances the polarization of the C-H bond that is already engaged in a partly covalent partly noncovalent agostic interaction with the positively charged metal centre.

Moreover, we found that the Cp*Co(III)-metallacycles, e.g., Cp*Co($\kappa^2$-(*C,N*)-(2-*phpy*))I] may collapse under oxidative conditions and generate new three-dimensional cationic alkaloids via the cyclocondensation of the 2-*phpy*H and Cp*, which was demonstrated by experimetal methods. The intramolecular cyclocondensation of the {κ*N*,κ*C*}$^-$ heterochelating ligand with the Cp* moiety is a rather fast process induced by the formation of a Co(IV) transient. DFT calculations suggest a pathway where C-C and C-N bond forming steps may occur before the capture of a H atom, the origin of the H atom has not yet been fully settled. The relevance of this unprecedented process of collapse of the Co metallacycle particularly raises the fundamental question of the viability of such organometallic intermediates in C-H bond functionalization catalysis where “redox” co-catalysts are commonly used on a trial-and-error basis.[333, 397]

In the context of the catalysis, the cyclocondensative collapse of cobaltacycles represents an irreversible destructive deactivation pathway, which further confirms that establishing the whereabouts of the Cp(*)Co(III)-based catalysts after catalysis is an imperious need.

From the view point of metal mediated synthesis, the oxidation-induced cyclocondensation of Cp*Co(III) metallacycles in this thesis is a new example of oxidation triggered Co(IV)-centred "metal-templated"[398-401] synthesis of valuable three-dimensional alkaloids of the Berberine[362] class, the hydroxylation reaction of which deserves further investigations. In addition, the application of these new Cp*Co(III)-metallacycles will continued to be investigated, such as in hydrosilylation and hydroboration catalysis mentioned in chapter 4. Overall, the Cp*Co(III)-complexes are promising catalysts and catalysis intermediates.

# Bibliography


1. Basu, D.; Kumar, S.; Sudhir, V. S.; Bandichhor, R., Transition metal catalyzed C-H activation for the synthesis of medicinally relevant molecules: A Review. *J. Chem. Sci.* **2018,** *130* (6).

2. Zhu, C.; Wang, C. Q.; Feng, C., Recent advance in transition-metal-catalyzed oxidant-free 4+1 annulation through C-H bond activation. *Tetrahedron Lett.* **2018,** *59* (5), 430-437.

3. Balcells, D.; Clot, E.; Eisenstein, O., C—H Bond Activation in Transition Metal Species from a Computational Perspective. *Chem. Rev.* **2010,** *110* (2), 749-823.

4. Chavan, L. N.; Gollapelli, K. K.; Chegondi, R.; Pawar, A. B., Cp*Co(III)-Catalyzed C-H Functionalization Cascade of N-Methoxyamides with Alkynedione for the Synthesis of Indolizidines. *Org. Lett.* **2017,** *19* (8), 2186-2189.

5. Rat, C. I.; Soran, A.; Varga, R. A.; Silvestru, C., C-H Bond Activation Mediated by Inorganic and Organometallic Compounds of Main Group Metals. *Adv. Organomet. Chem.* **2018,** *70*, 233-311.

6. Lyons, T. W.; Sanford, M. S., Palladium-Catalyzed Ligand-Directed C-H Functionalization Reactions. *Chem. Rev.* **2010,** *110* (2), 1147-1169.

7. Xu, Z.; Huang, W. S.; Zhang, J.; Xu, L. W., Recent Advances in Transition-Metal-Catalyzed Silylations of Arenes with Hydrosilanes: C-X Bond Cleavage or C-H Bond Activation Synchronized with Si-H Bond Activation. *Synthesis* **2015,** *47* (23), 3645-3668.

8. Luo, J.; Zhang, C.; Su, F.; Zhang, B.; Jia, F., Mechanism and Origins of Regio- and Mono/Di-Selectivity in Rh(III)-Catalyzed meta-C-H Alkenylation with Alkynes. *Eur. J. Org. Chem.* **2020,** *2020* (22), 3294-3302.

9. de Azambuja, F.; Correia, C. R. D., The Challenge of C-H Activation in Organic Synthesis. *Quimica. Nova.* **2011,** *34* (10), 1779-1790.

10. Li, H.; Lia, B. J.; Shi, Z. J., Challenge and progress: palladium-catalyzed sp(3) C-H activation. *Catal. Sci. Technol.* **2011,** *1* (2), 191-206.

11. Schwarz, H.; Shaik, S.; Li, J. L., Electronic Effects on Room-Temperature, Gas-Phase C-H Bond Activations by Cluster Oxides and Metal Carbides: The Methane Challenge. *J. Am. Chem. Soc.* **2017,** *139* (48), 17201-17212.

12. Yang, X. L.; Shan, G.; Wang, L. G.; Rao, Y., Recent advances in transition metal (Pd, Ni)-catalyzed C(sp(3)) H bond activation with bidentate directing groups. *Tetrahedron Lett.* **2016,** *57* (8), 819-836.

13. Ranu, B. C.; Ghosh, T.; Jalal, S., Recent developments in C-H functionalization via C-H bond activation using ball milling and transition-metal catalysts. *Arkivoc* **2019**, 79-92.

14. Landaeta, V. R.; Rodriguez-Lugo, R. E., Insights on the C-H Bond activation by Transition Metal Complexes from Groups 8-10 Bearing (P-N) Chelates. *J. Mol. Catal. A Chem.* **2017,** *426*, 316-325.

15. Yang, S.; Shi, M., Recent Advances in Transition-Metal-Catalyzed/Mediated Transformations of Vinylidenecyclopropanes. *Acc. Chem. Res.* **2018,** *51* (7), 1667-1680.

16. Yin, Z. P.; Wang, Z. C.; Wu, X. F., Transition-Metal-Catalyzed Carbonylative Synthesis and Functionalization of Heterocycles. *Chinese J. Org. Chem.* **2019,** *39* (3), 573-590.

17. Tang, H. M.; Huo, X. H.; Meng, Q. H.; Zhang, W. B., Palladium-Catalyzed Allylic C-H Functionalization: The Development of New Catalytic Systems. *Acta Chim. Sin.* **2016,** *74* (3), 219-233.

18. Yan, G. B.; Wu, X. M.; Yang, M. H., Transition-metal-catalyzed additions of C-H bonds to C-X (X = N, O) multiple bonds via C-H bond activation. *Org. Biomol. Chem.* **2013,** *11* (34), 5558-5578.

19. Shi, S.; Nawaz, K. S.; Zaman, M. K.; Sun, Z. K., Advances in Enantioselective C-H Activation/Mizoroki-Heck Reaction and Suzuki Reaction. *Catalysts* **2018,** *8* (2).

20. Newhouse, T.; Baran, P. S., If C-H Bonds Could Talk: Selective C-H Bond Oxidation. *Angew. Chem. Int. Ed.* **2011,** *50* (15), 3362-3374.

21. Wu, M. J.; Chu, J. H., Directing group assists in transition metal-catalyzed site-selective C-H bond activation/transformations. *J. Chin. Chem. Soc.* **2020,** *67* (3), 399-421.

22. Wencel-Delord, J.; Colobert, F., Diastereoselective Substrate-Controlled Transition-Metal-Catalyzed C-H Activation: An Old Solution to a Modern Synthetic Challenge. *Synlett* **2015,** *26* (19), 2644-2658.

23. Zhang, J.; Zhang, S.; Gogula, T.; Zou, H., Versatile Regioselective Deuteration of Indoles via Transition-Metal-Catalyzed H/D Exchange. *ACS Catal.* **2020,** *10* (14), 7486-7494.

24. Hamdaoui, M.; Djukic, J.-P., CHAPTER 27 Noncovalent Interactions in Key Metal-centred Catalytic Intermediates: Structure–Electronic Relationship. In *Noncovalent Interactions in Catalysis*, The Royal Society of Chemistry: 2019; pp 579-607.

25. Johnson, E.; Keinan, S.; Mori-Sanchez; Contreras-Garcia, J.; Cohen, A. J.; Yang, W., Revealing Noncovalent Interactions. *J. Am. Chem. Soc.* **2010,** *132*, 6498-6506.

26. Gandeepan, P.; Muller, T.; Zell, D.; Cera, G.; Warratz, S.; Ackermann, L., 3d Transition Metals for C-H Activation. *Chem. Rev.* **2019,** *119* (4), 2192-2452.

27. Murahashi, S., SYNTHESIS OF PHTHALIMIDINES FROM SCHIFF BASES AND CARBON MONOXIDE. *J. Am. Chem. Soc.* **1955,** *77* (23), 6403-6404.

28. Halbritter, G.; Knoch, F.; Wolski, A.; Kisch, H., Functionalization of Aromatic Azo Compounds by the Cobalt-Catalyzed, Regioselective Double Addition of Tolane: 2,6-Distilbenylazobenzenes and 2,3-Dihydrocinnolines. *Angew. Chem. Int. Ed. Engl.* **1994,** *33* (1516), 1603-1605.

29. Lenges, C. P.; Brookhart, M., Co(I)-Catalyzed Inter- and Intramolecular Hydroacylation of Olefins with Aromatic Aldehydes. *J. Am. Chem. Soc.* **1997,** *119* (13), 3165-3166.

30. Lenges, C. P.; White, P. S.; Brookhart, M., Mechanistic and Synthetic Studies of the Addition of Alkyl Aldehydes to Vinylsilanes Catalyzed by Co(I) Complexes. *J. Am. Chem. Soc.* **1998,** *120* (28), 6965-6979.

31. Gao, K.; Lee, P.-S.; Fujita, T.; Yoshikai, N., Cobalt-Catalyzed Hydroarylation of Alkynes through Chelation-Assisted C−H Bond Activation. *J. Am. Chem. Soc.* **2010,** *132* (35), 12249-12251.

32. Gao, K.; Yoshikai, N., Low-valent cobalt catalysis: new opportunities for C-H functionalization. *Acc. Chem. Res.* **2014,** *47* (4), 1208-19.

33. Oliveira, J. C. A.; Dhawa, U.; Ackermann, L., Insights into the Mechanism of Low-Valent Cobalt-Catalyzed C–H Activation. *ACS Catal.* **2021,** *11* (3), 1505-1515.

34. Moselage, M.; Li, J.; Ackermann, L., Cobalt-Catalyzed C–H Activation. *ACS Catal.* **2015,** *6* (2), 498-525.

35. Yamamoto, S.; Saga, Y.; Andou, T.; Matsunaga, S.; Kanai, M., Cobalt-Catalyzed C-4 Selective Alkylation of Quinolines. *Adv. Synth. Catal.* **2014,** *356* (2-3), 401-405.

36. Baccalini, A.; Vergura, S.; Dolui, P.; Zanoni, G.; Maiti, D., Recent advances in cobalt-catalysed C-H functionalizations. *Org. Biomol. Chem.* **2019,** *17* (48), 10119-10141.

37. Wang, S.; Chen, S. Y.; Yu, X. Q., C-H functionalization by high-valent Cp*Co(III) catalysis.*ChemComm. (Camb)* **2017,** *53* (22), 3165-3180.

38. Cong, X.; Zhai, S.; Zeng, X., Low-valent cobalt-catalyzed C–H allylation. *Org. Chem. Front.* **2016,** *3* (6), 673-677.

39. Kochi, J. K.; Tang, R. T.; Bernath, T., Mechanisms of aromatic substitution. Role of cation-radicals in the oxidative substitution of arenes by cobalt(III). *J. Am. Chem. Soc.* **1973,** *95* (21), 7114-7123.

40. Yoshino, T.; Ikemoto, H.; Matsunaga, S.; Kanai, M., Cp*Co(III)-catalyzed C2-selective addition of indoles to imines. *Chemistry* **2013,** *19* (28), 9142-6.

41. Yoshino, T.; Ikemoto, H.; Matsunaga, S.; Kanai, M., A cationic high-valent Cp*Co(III) complex for the catalytic generation of nucleophilic organometallic species: directed C-H bond activation. *Angew. Chem. Int. Ed. Engl.* **2013,** *52* (8), 2207-11.

42. Suzuki, Y.; Sun, B.; Sakata, K.; Yoshino, T.; Matsunaga, S.; Kanai, M., Dehydrative Direct C-H Allylation with Allylic Alcohols under [Cp*Co(III)] Catalysis. *Angew. Chem. Int. Ed. Engl.* **2015,** *54* (34), 9944-7.

43. Gensch, T.; Vasquez-Cespedes, S.; Yu, D. G.; Glorius, F., Cobalt(III)-Catalyzed Directed C-H Allylation. *Org. Lett.* **2015,** *17* (15), 3714-7.

44. Liu, X.-G.; Zhang, S.-S.; Wu, J.-Q.; Li, Q.; Wang, H., Cp∗Co(III)-catalyzed direct functionalization of aromatic C–H bonds with α-diazomalonates. *Tetrahedron Lett.* **2015,** *56* (27), 4093-4095.

45. Sauermann, N.; Gonzalez, M. J.; Ackermann, L., Cobalt(III)-Catalyzed C-H Alkynylation with Bromoalkynes under Mild Conditions. *Org. Lett.* **2015,** *17* (21), 5316-9.

46. Zell, D.; Bu, Q.; Feldt, M.; Ackermann, L., Mild C-H/C-C Activation by Z-Selective Cobalt Catalysis. *Angew. Chem. Int. Ed. Engl.* **2016,** *55* (26), 7408-12.

47. Wang, S.; Hou, J. T.; Feng, M. L.; Zhang, X. Z.; Chen, S. Y.; Yu, X. Q., Cobalt(III)-catalyzed alkenylation of arenes and 6-arylpurines with terminal alkynes: efficient access to functional dyes. *ChemComm. (Camb)* **2016,** *52* (13), 2709-12.

48. Kong, L.; Zhou, X.; Li, X., Cobalt(III)-Catalyzed Regio- and Stereoselective alpha-Fluoroalkenylation of Arenes with gem-Difluorostyrenes. *Org. Lett.* **2016,** *18* (24), 6320-6323.

49. Zhou, X.; Fan, Z.; Zhang, Z.; Lu, P.; Wang, Y., Construction of Pyrrolo[1,2-a]indoles via Cobalt(III)-Catalyzed Enaminylation of 1-(Pyrimidin-2-yl)-1H-indoles with Ketenimines and Subsequent Base-Promoted Cyclization. *Org. Lett.* **2016,** *18* (18), 4706-9.

50. Nakanowatari, S.; Mei, R.; Feldt, M.; Ackermann, L., Cobalt(III)-Catalyzed Hydroarylation of Allenes via C–H Activation. *ACS Catal.* **2017,** *7* (4), 2511-2515.

51. Li, J.; Zhang, Z.; Ma, W.; Tang, M.; Wang, D.; Zou, L.-H., Mild Cobalt(III)-Catalyzed C-H Hydroarylation of Conjugated C=C/C=O Bonds. *Adv. Synth. Catal.* **2017,** *359* (10), 1717-1724.

52. Suzuki, Y.; Sun, B.; Yoshino, T.; Kanai, M.; Matsunaga, S., Cp∗Co(III)-catalyzed oxidative C–H alkenylation of benzamides with ethyl acrylate. *Tetrahedron* **2015,** *71* (26-27), 4552-4556.

53. Bunno, Y.; Murakami, N.; Suzuki, Y.; Kanai, M.; Yoshino, T.; Matsunaga, S., Cp*Co(III)-Catalyzed Dehydrative C-H Allylation of 6-Arylpurines and Aromatic Amides Using Allyl Alcohols in Fluorinated Alcohols. *Org. Lett.* **2016,** *18* (9), 2216-9.

54. Tanaka, R.; Ikemoto, H.; Kanai, M.; Yoshino, T.; Matsunaga, S., Site- and Regioselective Monoalkenylation of Pyrroles with Alkynes via Cp*CoIII Catalysis. *Org. Lett.* **2016,** *18* (21), 5732-5735.

55. Ikemoto, H.; Tanaka, R.; Sakata, K.; Kanai, M.; Yoshino, T.; Matsunaga, S., Stereoselective Synthesis of Tetrasubstituted Alkenes via a Cp*Co III -Catalyzed C−H Alkenylation/Directing Group Migration Sequence. *Angew. Chem. Int. Ed.* **2017,** *56* (25), 7156-7160.

56. Sen, M.; Emayavaramban, B.; Barsu, N.; Premkumar, J. R.; Sundararaju, B., Cp*Co(III)-Catalyzed C(sp3)–H Bond Activation: A Highly Stereoselective and Regioselective Alkenylation of 8-Methylquinoline with Alkynes. *ACS Catal.* **2016,** *6* (5), 2792-2796.

57. Barsu, N.; Rahman, M. A.; Sen, M.; Sundararaju, B., Cp*CoIII-Catalyzed C(sp3)−H Bond Amidation of 8-Methylquinoline. *Chem. Eur. J.* **2016,** *22* (27), 9135-9138.

58. Yan, S.-Y.; Ling, P.-X.; Shi, B.-F., Cobalt(III)-Catalyzed Alkylation of Primary C(sp 3 )-H Bonds with Diazo Compounds. *Adv. Synth. Catal.* **2017,** *359* (17), 2912-2917.

59. Li, N.; Wang, Y.; Kong, L.; Chang, J.; Li, X., Cobalt(III)/Rhodium(III)-Catalyzed Regio- and Stereoselective Allylation of 8-Methylquinoline via sp 3 C−H Activation. *Adv. Synth. Catal.* **2019,** *361* (16), 3880-3885.

60. Tan, H.; Khan, R.; Xu, D.; Zhou, Y.; Zhang, X.; Shi, G.; Fan, B., Cobalt-catalyzed ring-opening addition of azabenzonorbornadienes via C(sp3)–H bond activation of 8-methylquinoline. *ChemComm.* **2020,** *56* (83), 12570-12573.

61. Wan, J.-P.; Jing, Y., Recent advances in copper-catalyzed C–H bond amidation. *Beilstein J. Org. Chem.* **2015,** *11*, 2209-2222.

62. Sun, B.; Yoshino, T.; Matsunaga, S.; Kanai, M., Air-Stable Carbonyl(pentamethylcyclopentadienyl)cobalt Diiodide Complex as a Precursor for Cationic (Pentamethylcyclopentadienyl)cobalt(III) Catalysis: Application for Directed C-2 Selective C-H Amidation of Indoles. *Adv. Synth. Catal.* **2014,** *356* (7), 1491-1495.

63. Sun, B.; Yoshino, T.; Matsunaga, S.; Kanai, M., A Cp*CoI2-dimer as a precursor for cationic Co(III)-catalysis: application to C-H phosphoramidation of indoles. *ChemComm. (Camb)* **2015,** *51* (22), 4659-61.

64. Liang, Y.; Liang, Y. F.; Tang, C.; Yuan, Y.; Jiao, N., Cationic Cobalt(III)-Catalyzed Aryl and Alkenyl C-H Amidation: A Mild Protocol for the Modification of Purine Derivatives. *Chemistry* **2015,** *21* (46), 16395-9.

65. Mei, R.; Loup, J.; Ackermann, L., Oxazolinyl-Assisted C–H Amidation by Cobalt(III) Catalysis. *ACS Catal.* **2016,** *6* (2), 793-797.

66. Patel, P.; Chang, S., Cobalt(III)-Catalyzed C–H Amidation of Arenes using Acetoxycarbamates as Convenient Amino Sources under Mild Conditions. *ACS Catal.* **2015,** *5* (2), 853-858.

67. Tu, H.; Zhu, S.; Qing, F.-L.; Chu, L., Visible-light-induced halogenation of aliphatic C H bonds. *Tetrahedron Lett.* **2018,** *59* (3), 173-179.

68. Yu, D. G.; Gensch, T.; de Azambuja, F.; Vasquez-Cespedes, S.; Glorius, F., Co(III)-catalyzed C-H activation/formal SN-type reactions: selective and efficient cyanation, halogenation, and allylation. *J. Am. Chem. Soc.* **2014,** *136* (51), 17722-5.

69. Pawar, A. B.; Lade, D. M., Cobalt(III)-catalyzed C-H halogenation of 6-arylpurines: facile entry into arylated, sulfenylated and alkoxylated 6-arylpurines. *Org. Biomol. Chem.* **2016,** *14* (12), 3275-83.

70. Gensch, T.; Klauck, F. J. R.; Glorius, F., Cobalt-Catalyzed C−H Thiolation through Dehydrogenative Cross-Coupling. *Angew. Chem. Int. Ed.* **2016,** *55* (37), 11287-11291.

71. Liu, X.-G.; Li, Q.; Wang, H., (Pentamethylcyclopentadienyl)cobalt(III)-Catalyzed Direct Trifluoromethylthiolation of Arenes via C−H Activation. *Adv. Synth. Catal.* **2017,** *359* (11), 1942-1946.

72. Yoshida, M.; Kawai, K.; Tanaka, R.; Yoshino, T.; Matsunaga, S., Cp*Co(III)-catalyzed directed C-H trifluoromethylthiolation of 2-phenylpyridines and 6-arylpurines. *ChemComm. (Camb)* **2017,** *53* (44), 5974-5977.

73. Wang, H.; Moselage, M.; González, M. J.; Ackermann, L., Selective Synthesis of Indoles by Cobalt(III)-Catalyzed C–H/N–O Functionalization with Nitrones. *ACS Catal.* **2016,** *6* (4), 2705-2709.

74. Liu, Y.; Wang, C.; Lv, N.; Liu, Z.; Zhang, Y., Synthesis of QuinolineN-Oxides by Cobalt-Catalyzed Annulation of Arylnitrones and Alkynes. *Adv. Synth. Catal.* **2017,** *359* (8), 1351-1358.

75. Liang, Y.; Jiao, N., Cationic Cobalt(III) Catalyzed Indole Synthesis: The Regioselective Intermolecular Cyclization of N-Nitrosoanilines and Alkynes. *Angew. Chem.* **2016,** *128* (12), 4103-4107.

76. Zhou, S.; Wang, J.; Wang, L.; Chen, K.; Song, C.; Zhu, J., Co(III)-Catalyzed, Internal and Terminal Alkyne-Compatible Synthesis of Indoles. *Org. Lett.* **2016,** *18* (15), 3806-3809.

77. Lerchen, A.; Vasquez-Cespedes, S.; Glorius, F., Cobalt(III)-Catalyzed Redox-Neutral Synthesis of Unprotected Indoles Featuring an N-N Bond Cleavage. *Angew. Chem. Int. Ed. Engl.* **2016,** *55* (9), 3208-11.

78. Lu, Q.; Vásquez-Céspedes, S.; Gensch, T.; Glorius, F., Control over Organometallic Intermediate Enables Cp*Co(III) Catalyzed Switchable Cyclization to Quinolines and Indoles. *ACS Catal.* **2016,** *6* (4), 2352-2356.

79. Zhang, Z. Z.; Liu, B.; Xu, J. W.; Yan, S. Y.; Shi, B. F., Indole Synthesis via Cobalt(III)-Catalyzed Oxidative Coupling of N-Arylureas and Internal Alkynes. *Org. Lett.* **2016,** *18* (8), 1776-9.

80. Kong, L.; Yu, S.; Zhou, X.; Li, X., Redox-Neutral Couplings between Amides and Alkynes via Cobalt(III)-Catalyzed C-H Activation. *Org. Lett.* **2016,** *18* (3), 588-91.

81. Sen, M.; Kalsi, D.; Sundararaju, B., Cobalt(III)-Catalyzed Dehydrative [4+2] Annulation of Oxime with Alkyne by C-H and N-OH Activation. *Chemistry* **2015,** *21* (44), 15529-33.

82. Wang, H.; Koeller, J.; Liu, W.; Ackermann, L., Cobalt(III)-Catalyzed C-H/N-O Functionalizations: Isohypsic Access to Isoquinolines. *Chemistry* **2015,** *21* (44), 15525-8.

83. Sun, B.; Yoshino, T.; Kanai, M.; Matsunaga, S., Cp*CoIIICatalyzed Site-Selective C-H Activation of Unsymmetrical O-Acyl Oximes: Synthesis of Multisubstituted Isoquinolines from Terminal and Internal Alkynes. *Angew. Chem.* **2015,** *127* (44), 13160-13164.

84. Wang, F.; Wang, Q.; Bao, M.; Li, X., Cobalt-catalyzed redox-neutral synthesis of isoquinolines: C–H activation assisted by an oxidizing N–S bond. *Chinese J. Catal.* **2016,** *37* (8), 1423-1430.

85. Pawar, A. B.; Agarwal, D.; Lade, D. M., Cp*Co(III)-Catalyzed C-H/N-N Functionalization of Arylhydrazones for the Synthesis of Isoquinolines. *J. Org. Chem.* **2016,** *81* (22), 11409-11415.

86. Yang, F.; Yu, J.; Liu, Y.; Zhu, J., Cobalt(III)-Catalyzed Oxadiazole-Directed C–H Activation for the Synthesis of 1-Aminoisoquinolines. *Org. Lett.* **2017,** *19* (11), 2885-2888.

87. Prakash, S.; Muralirajan, K.; Cheng, C.-H., Cobalt-Catalyzed Oxidative Annulation of Nitrogen-Containing Arenes with Alkynes: An Atom-Economical Route to Heterocyclic Quaternary Ammonium Salts. *Angew. Chem.* **2016,** *128* (5), 1876-1880.

88. Lao, Y.-X.; Zhang, S.-S.; Liu, X.-G.; Jiang, C.-Y.; Wu, J.-Q.; Li, Q.; Huang, Z.-S.; Wang, H., High-Valent Pentamethylcyclopentadienylcobalt(III) or -iridium(III)-Catalyzed C-H Annulation with Alkynes: Synthesis of Heterocyclic Quaternary Ammonium Salts. *Adv. Synth. Catal.* **2016,** *358* (13), 2186-2191.

89. Yang, Y.; Li, B.; Liu, W.; Zhang, R.; Yu, L.; Ma, Q.-G.; Lv, R.; Du, D.; Li, T., Cp*CoIII-Catalyzed Synthesis of Pyrido[2′,1′:2,3]pyrimido[1,6-a]indol-5-iums via Tandem C–H Activation and Subsequent Annulation from 1-(Pyridin-2-yl)-1H-indoles and Internal Alkynes. *J. Org. Chem.* **2016,** *81* (22), 11335-11345.

90. Yu, W.; Zhang, W.; Liu, Y.; Zhou, Y.; Liu, Z.; Zhang, Y., Cobalt(iii)-catalyzed synthesis of pyrroles from enamides and alkynes. *RSC Adv.* **2016,** *6* (29), 24768-24772.

91. Yu, W.; Zhang, W.; Liu, Z.; Zhang, Y., Cobalt(iii)-catalyzed annulation of esters and alkynes: a facile route to indenones. *ChemComm.* **2016,** *52* (41), 6837-6840.

92. Sivakumar, G.; Vijeta, A.; Jeganmohan, M., Cobalt-Catalyzed Cyclization of N-Methoxy Benzamides with Alkynes using an Internal Oxidant through C-H/N-O Bond Activation. *Chemistry* **2016,** *22* (17), 5899-903.

93. Mandal, R.; Sundararaju, B., Cp*Co(III)-Catalyzed Annulation of Carboxylic Acids with Alkynes. *Org. Lett.* **2017,** *19* (10), 2544-2547.

94. Wang, F.; Wang, H.; Wang, Q.; Yu, S.; Li, X., Co(III)-Catalyzed Synthesis of Quinazolines via C-H Activation of N-Sulfinylimines and Benzimidates. *Org. Lett.* **2016,** *18* (6), 1306-9.

95. Huang, J.; Huang, Y.; Wang, T.; Huang, Q.; Wang, Z.; Chen, Z., Microwave-Assisted Cp*CoIII-Catalyzed C–H Activation/Double C–N Bond Formation Reactions to Thiadiazine 1-Oxides. *Org. Lett.* **2017,** *19* (5), 1128-1131.

96. Wang, F.; Jin, L.; Kong, L.; Li, X., Cobalt(III)- and Rhodium(III)-Catalyzed C-H Amidation and Synthesis of 4-Quinolones: C-H Activation Assisted by Weakly Coordinating and Functionalizable Enaminone. *Org. Lett.* **2017,** *19* (7), 1812-1815.

97. Shi, P.; Wang, L.; Chen, K.; Wang, J.; Zhu, J., Co(III)-Catalyzed Enaminone-Directed C-H Amidation for Quinolone Synthesis. *Org. Lett.* **2017,** *19* (9), 2418-2421.

98. Zhao, D.; Kim, J. H.; Stegemann, L.; Strassert, C. A.; Glorius, F., Cobalt(III)-Catalyzed Directed C□H Coupling with Diazo Compounds: Straightforward Access towards Extended π-Systems. *Angew. Chem. Int. Ed.* **2015,** *54* (15), 4508-4511.

99. Kim, J. H.; Greßies, S.; Glorius, F., Cooperative Lewis Acid/Cp*$Co^{III}$Catalyzed C−H Bond Activation for the Synthesis of Isoquinolin-3-ones. *Angew. Chem. Int. Ed.* **2016,** *55* (18), 5577-5581.

100. Li, J.; Tang, M.; Zang, L.; Zhang, X.; Zhang, Z.; Ackermann, L., Amidines for Versatile Cobalt(III)-Catalyzed Synthesis of Isoquinolines through C–H Functionalization with Diazo Compounds. *Org. Lett.* **2016,** *18* (11), 2742-2745.

101. Liu, X.-G.; Zhang, S.-S.; Jiang, C.-Y.; Wu, J.-Q.; Li, Q.; Wang, H., Cp*Co(III)-Catalyzed Annulations of 2-Alkenylphenols with CO: Mild Access to Coumarin Derivatives. *Org. Lett.* **2015,** *17* (21), 5404-5407.

102. Chen, X.; Hu, X.; Deng, Y.; Jiang, H.; Zeng, W., A [4 + 1] Cyclative Capture Access to Indolizines via Cobalt(III)-Catalyzed Csp2–H Bond Functionalization. *Org. Lett.* **2016,** *18* (18), 4742-4745.

103. Li, L.; Wang, H.; Yu, S.; Yang, X.; Li, X., Cooperative Co(III)/Cu(II)-Catalyzed C–N/N–N Coupling of Imidates with Anthranils: Access to 1H-Indazoles via C–H Activation. *Org. Lett.* **2016,** *18* (15), 3662-3665.

104. Wang, H.; Lorion, M. M.; Ackermann, L., Domino C–H/N–H Allylations of Imidates by Cobalt Catalysis. *ACS Catal.* **2017,** *7* (5), 3430-3433.

105. Li, X.; Huang, T.; Song, Y.; Qi, Y.; Li, L.; Li, Y.; Xiao, Q.; Zhang, Y., Co(III)-Catalyzed Annulative Vinylene Transfer via C–H Activation: Three-Step Total Synthesis of 8-Oxopseudopalmatine and Oxopalmatine. *Org. Lett.* **2020,** *22* (15), 5925-5930.

106. Zucca, A.; Pilo, M. I., Rollover Cyclometalation as a Valuable Tool for Regioselective C-H Bond Activation and Functionalization. *Molecules* **2021,** *26* (2).

107. Albrecht, M., Cyclometalation Using d-Block Transition Metals: Fundamental Aspects and Recent Trends. *Chem. Rev.* **2010,** *110* (2), 576-623.

108. Ryabov, A. D., Mechanisms of intramolecular activation of carbon-hydrogen bonds in transition-metal complexes. *Chem. Rev.* **1990,** *90* (2), 403-424.

109. Bauer, W.; Prem, M.; Polborn, K.; Sünkel, K.; Steglich, W.; Beck, W., Organometallic Complexes of Iridium, Palladium, Chromium and Iron from 2-Phenyl-5(4H)-oxazolones − Organometallic Labelled Dipeptides. *Eur. J. Inorg. Chem.* **1998,** *1998* (4), 485-493.

110. Davies, D. L.; Al-Duaij, O.; Fawcett, J.; Giardiello, M.; Hilton, S. T.; Russell, D. R., Room-temperature cyclometallation of amines, imines and oxazolines with $[MCl_2Cp^*]_2$(M = Rh, Ir) and $[RuCl_2(p\text{-cymene})]_2$. *Dalton Trans.* **2003,** (21), 4132-4138.

111. Boutadla, Y.; Davies, D. L.; Jones, R. C.; Singh, K., The Scope of Ambiphilic Acetate-Assisted Cyclometallation with Half-Sandwich Complexes of Iridium, Rhodium and Ruthenium. *Chem. Eur. J.* **2011,** *17*, 3438-3448.

112. Li, L.; Brennessel, W. W.; Jones, W. D., An Efficient Low-Temperature Route to Polycyclic Isoquinoline Salt Synthesis via C-H Activation with $[Cp^*MCl_2]_2$ (M ) Rh, Ir). *J. Am. Chem. Soc.* **2008,** *130*, 12414-12419.

113. Li, L.; Brennessel, W. W.; Jones, W. D., C−H Activation of Phenyl Imines and 2-Phenylpyridines with [Cp*MCl2]2 (M = Ir, Rh): Regioselectivity, Kinetics, and Mechanism. *Organometallics* **2009,** *28* (12), 3492-3500.

114. Watanabe, M.; Kashiwame, Y.; Kuwata, S.; Ikariya, T., Synthesis, Structures, and Transfer Hydrogenation Catalysis of Bifunctional Iridium Complexes Bearing a C–N Chelate Oxime Ligand. *Eur. J. Inorg. Chem.* **2012,** *2012* (3), 504-511.

115. Li, L.; Jiao, Y.; Brennessel, W. W.; Jones, W. D., Reactivity and Regioselectivity of Insertion of Unsaturated Molecules into M−C (M = Ir, Rh) Bonds of Cyclometalated Complexes. *Organometallics* **2010,** *29* (20), 4593-4605.

116. Wei, Y.; Xue, D.; Lei, Q.; Wang, C.; Xiao, J., Cyclometalated iridium complexes for transfer hydrogenation of carbonyl groups in water. *Green Chem.* **2013,** *15* (3), 629.

117. Wang, C.; Chen, H.-Y. T.; Bacsa, J.; Catlow, C. R. A.; Xiao, J., Synthesis and X-ray structures of cyclometalated iridium complexes including the hydrides. *Dalton Trans.* **2013,** *42* (4), 935-940.

118. Wang, C.; Pettman, A.; Basca, J.; Xiao, J., A Versatile Catalyst for Reductive Amination by Transfer Hydrogenation. *Angew. Chem. Int. Ed.* **2010,** *49* (41), 7548-7552.

119. Haak, R. M.; Berthiol, F.; Jerphagnon, T.; Gayet, A. J. A.; Tarabiono, C.; Postema, C. P.; Ritleng, V.; Pfeffer, M.; Janssen, D. B.; Minnaard, A. J.; Feringa, B. L.; De Vries, J. G., Dynamic Kinetic Resolution of Racemic β-Haloalcohols: Direct Access to Enantioenriched Epoxides. *J. Am. Chem. Soc.* **2008,** *130* (41), 13508-13509.

120. Jerphagnon, T.; Gayet, A. J. Â. A.; Berthiol, F.; Ritleng, V.; Mrsić, N. A.; Meetsma, A.; Pfeffer, M.; Minnaard, A. J.; Feringa, B. L.; De Vries, J. G., Fast Racemisation of Chiral Amines and Alcohols by Using Cationic Half-Sandwich Ruthena- and Iridacycle Catalysts. *Chem. Eur. J.* **2009,** *15* (46), 12780-12790.

121. Zhou, T.; Li, L.; Li, B.; Song, H.; Wang, B., Syntheses, Structures, and Reactions of Cyclometalated Rhodium, Iridium, and Ruthenium Complexes of N-Methoxy-4-nitrobenzamide. *Organometallics* **2018,** *37* (3), 476-481.

122. Li, L.; Brennessel, W. W.; Jones, W. D., C-H Activation of phenyl imines and 2-phenylpyridines with $[Cp^*MCl_2]_2$ (M = Ir, Rh): regioselectivity, kinetics, and mechanism. *Organometallics* **2009,** *28*, 3492-3500.

123. Hu, Y.; Li, L.; Shaw, A. P.; Norton, J. R.; Sattler, W.; Rong, Y., Synthesis, Electrochemistry, and Reactivity of New Iridium(III) and Rhodium(III) Hydrides. *Organometallics* **2012,** *31* (14), 5058-5064.

124. Chan, W.-W.; Lo, S.-F.; Zhou, Z.; Yu, W.-Y., Rh-Catalyzed Intermolecular Carbenoid Functionalization of Aromatic C–H Bonds by α-Diazomalonates. *J. Am. Chem. Soc.* **2012,** *134* (33), 13565-13568.

125. Zhao, H.; Shang, Y.; Su, W., Rhodium(III)-Catalyzed Intermolecular N-Chelator-Directed Aromatic C–H Amidation with Amides. *Org. Lett.* **2013,** *15* (19), 5106-5109.

126. Djukic, J.-P.; Iali, W.; Pfeffer, M.; Goff, X.-F. L., Charge-induced facial-selectivity in the formation of new cationic planar chiral iridacycles derived from aniline. *ChemComm.* **2011,** *47* (12), 3631.

127. Corre, Y.; Rysak, V.; Capet, F.; Djukic, J.-P.; Agbossou-Niedercorn, F.; Michon, C., Selective Hydrosilylation of Esters to Aldehydes Catalysed by Iridium(III) Metallacycles through Trapping of Transient Silyl Cations. *Chem. Eur. J.* **2016,** *22* (39), 14036-14041.

128. Corre, Y.; Trivelli, X.; Capet, F.; Djukic, J.-P.; Agbossou-Niedercorn, F.; Michon, C., Efficient and Selective Hydrosilylation of Secondary and Tertiary Amides Catalyzed by an Iridium(III) Metallacycle: Development and Mechanistic Investigation. *ChemCatChem.* **2017,** *9*, 2009-2017.

129. Corre, Y.; Rysak, V.; Trivelli, X.; Agbossou-Niedercorn, F.; Michon, C., A Versatile Iridium(III) Metallacycle Catalyst for the Effective Hydrosilylation of Carbonyl and Carboxylic Acid Derivatives. *Eur. J. Org. Chem.* **2017,** *2017*, 4820-4826.

130. Corre, Y.; Rysak, V.; Nagyhazi, M.; Kalocsai, D.; Trivelli, X.; Djukic, J.-P.; Agbossou-Niedercorn, F.; Michon, C., One-Pot Controlled Reduction of Conjugated Amides by Sequential Double Hydrosilylation Catalyzed by an Iridium(III) Metallacycle. *Eur. J. Org. Chem.* **2020,** *2020*, 6212-6220.

131. Corre, Y.; Werle, C.; Brelot-Karmazin, L.; Djukic, J.-P.; Agbossou-Niedercorn, F.; Michon, C., Regioselective hydrosilylation of terminal alkynes using pentamethylcyclopentadienyl iridium(III) metallacycle catalysts. *J. Mol. Catal. A: Chem.* **2016,** *423*, 256-263.

132. Djukic, J.-P.; Iali, W.; Pfeffer, M.; Le Goff, X.-F., Synthesis of Planar Chiral Iridacycles by Cationic Metal π-Coordination: Facial Selectivity, and Conformational and Stereochemical Consequences. *Chem. - Eur. J.* **2012,** *18*, 6063-6078.

133. Hamdaoui, M.; Desrousseaux, C.; Habbita, H.; Djukic, J.-P., Iridacycles as Catalysts for the Autotandem Conversion of Nitriles into Amines by Hydrosilylation: Experimental Investigation and Scope. *Organometallics* **2017,** *36*, 4864-4882.

134. Hamdaoui, M.; Ney, M.; Sarda, V.; Karmazin, L.; Bailly, C.; Sieffert, N.; Dohm, S.; Hansen, A.; Grimme, S.; Djukic, J.-P., Evidence of a Donor-Acceptor (Ir-H)→$SiR_3$ Interaction in a Trapped Ir(III) Silane Catalytic Intermediate. *Organometallics* **2016,** *35*, 2207-2223.

135. Scheeren, C.; Maasarani, F.; Hijazi, A.; Djukic, J.-P.; Pfeffer, M.; Zarić, S. D.; Le Goff, X.-F.; Ricard, L., Stereoselective "Electrophilic" Cyclometalation of Planar-Prochiral ($\eta^6$-Arene)tricarbonylchromium Complexes with Asymmetric Metal Centers: pseudo-T-4 $[Cp^*RhCl_2]_2$ and $[Cp^*IrCl_2]_2$. *Organometallics* **2007,** *26* (14), 3336-3345.

136. Djukic, J.-P.; Boulho, C.; Sredojevic, D.; Scheeren, C.; Zaric, S.; Ricard, L.; Pfeffer, M., The Stereospecific Ligand Exchange at a Pseudo-BenzylicT-4 Iridium Centre in Planar-Chiral Cycloiridium (η6-Arene)tricarbonylchromium Complexes. *Chem. Eur. J.* **2009,** *15* (41), 10830-10842.

137. Iali, W.; Paglia, F. L.; Goff, X.-F. L.; Sredojević, D.; Pfeffer, M.; Djukic, J.-P., Room temperature tandem hydroamination and hydrosilation/protodesilation catalysis by a tricarbonylchromium-bound iridacycle. *ChemComm.* **2012,** *48* (83), 10310.

138. Ikemoto, H.; Yoshino, T.; Sakata, K.; Matsunaga, S.; Kanai, M., Pyrroloindolone synthesis via a Cp*Co(III)-catalyzed redox-neutral directed C-H alkenylation/annulation sequence. *J. Am. Chem. Soc.* **2014,** *136* (14), 5424-31.

139. Yu, X.; Chen, K.; Guo, S.; Shi, P.; Song, C.; Zhu, J., Direct Access to Cobaltacycles via C-H Activation: N-Chloroamide-Enabled Room-Temperature Synthesis of Heterocycles. *Org. Lett.* **2017,** *19* (19), 5348-5351.

140. López-Resano, S.; Martínez de Salinas, S.; Garcés-Pineda, F. A.; Moneo-Corcuera, A.; Galán-Mascarós, J. R.; Maseras, F.; Pérez-Temprano, M. H., Redefining the Mechanistic Scenario of Carbon−Sulfur Nucleophilic Coupling via High-Valent Cp*CoIV Species. *Angew. Chem. Int. Ed.* **2021**, 60, 11217.

141. Martinez de Salinas, S.; Sanjose-Orduna, J.; Odena, C.; Barranco, S.; Benet-Buchholz, J.; Perez-Temprano, M. H., Weakly Coordinated Cobaltacycles: Trapping Catalytically Competent Intermediates in $Cp^*Co^{III}$ Catalysis. *Angew. Chem. Int. Ed.* **2020**, 59, 6239.

142. Sanjose-Orduna, J.; Sarria Toro, J. M.; Perez-Temprano, M. H., HFIP-Assisted C-H Functionalization by Cp*Co(III) : Access to Key Reactive Cobaltacycles and Implication in Catalysis. *Angew. Chem. Int. Ed. Engl.* **2018,** *57* (35), 11369-11373.

143. Sanjose-Orduna, J.; Benet-Buchholz, J.; Perez-Temprano, M. H., Unravelling Molecular Aspects of the Migratory Insertion Step in Cp*Co(III) Metallacyclic Systems. *Inorg. Chem.* **2019,** *58*, 10569-10577.

144. Sanjose-Orduna, J.; Gallego, D.; Garcia-Roca, A.; Martin, E.; Benet-Buchholz, J.; Perez-Temprano, M. H., Capturing Elusive Cobaltacycle Intermediates: A Real-Time Snapshot of the Cp*CoIII-Catalyzed Oxidative Alkyne Annulation. *Angew. Chem. Int. Ed.* **2017,** *56*, 12016.

145. Yoshino, T.; Ikemoto, H.; Matsunaga, S.; Kanai, M., A Cationic High-Valent Cp*CoIII Complex for the Catalytic Generation of Nucleophilic Organometallic Species: Directed C-H Bond Activation. *Angew. Chem. Int. Ed.* **2013,** *52* (8), 2207-2211.

146. Yoshino, T.; Ikemoto, H.; Matsunaga, S.; Kanai, M., Cp*CoIII-Catalyzed C2-Selective Addition of Indoles to Imines. *Chem. Eur. J.* **2013,** *19* (28), 9142-9146.

147. Sun, B.; Yoshino, T.; Matsunaga, S.; Kanai, M., Air-Stable Carbonyl(pentamethylcyclopentadienyl)cobalt Diiodide Complex as a Precursor for Cationic (Pentamethylcyclopentadienyl)cobalt(III) Catalysis: Application for Directed C-2 Selective C-H Amidation of Indoles. *Adv. Synth. Catal.* **2014,** *356* (7), 1491-1495.

148. Ikemoto, H.; Yoshino, T.; Sakata, K.; Matsunaga, S.; Kanai, M., Pyrroloindolone Synthesis via a $Cp^*Co^{III}$-Catalyzed Redox-Neutral Directed C–H Alkenylation/Annulation Sequence. *J. Am. Chem. Soc.* **2014,** *136* (14), 5424-5431.

149. Sun, B.; Yoshino, T.; Matsunaga, S.; Kanai, M., A $Cp^*CoI_2$-dimer as a precursor for cationic Co(III)-catalysis: application to C–H phosphoramidation of indoles. *Chem. Commun.* **2015,** *51* (22), 4659-4661.

150. Suzuki, Y.; Sun, B.; Sakata, K.; Yoshino, T.; Matsunaga, S.; Kanai, M., Dehydrative Direct C-H Allylation with Allylic Alcohols under [Cp*CoIII] Catalysis. *Angew. Chem. Int. Ed.* **2015,** *54* (34), 9944-9947.

151. Sun, B.; Yoshino, T.; Kanai, M.; Matsunaga, S., Cp*CoIII Catalyzed Site-Selective C-H Activation of Unsymmetrical O-Acyl Oximes: Synthesis of Multisubstituted Isoquinolines from Terminal and Internal Alkynes. *Angew. Chem. Int. Ed.* **2015,** *54* (44), 12968-12972.

152. Bunno, Y.; Murakami, N.; Suzuki, Y.; Kanai, M.; Yoshino, T.; Matsunaga, S., Cp*CoIII-Catalyzed Dehydrative C–H Allylation of 6-Arylpurines and Aromatic Amides Using Allyl Alcohols in Fluorinated Alcohols. *Org. Lett.* **2016,** *18* (9), 2216-2219.

153. Tanaka, R.; Ikemoto, H.; Kanai, M.; Yoshino, T.; Matsunaga, S., Site- and Regioselective Monoalkenylation of Pyrroles with Alkynes via Cp*CoIII Catalysis. *Org. Lett.* **2016,** *18* (21), 5732-5735.

154. Yoshida, M.; Kawai, K.; Tanaka, R.; Yoshino, T.; Matsunaga, S., Cp*CoIII-catalyzed directed C–H trifluoromethylthiolation of 2-phenylpyridines and 6-arylpurines. *ChemComm.* **2017,** *53* (44), 5974-5977.

155. Ikemoto, H.; Tanaka, R.; Sakata, K.; Kanai, M.; Yoshino, T.; Matsunaga, S., Stereoselective Synthesis of Tetrasubstituted Alkenes via a Cp*CoIII-Catalyzed C−H Alkenylation/Directing Group Migration Sequence. *Angew. Chem. Int. Ed.* **2017,** *56* (25), 7156-7160.

156. Murakami, N.; Yoshida, M.; Yoshino, T.; Matsunaga, S., Synthesis of Fluorine-Containing 6-Arylpurine Derivatives via Cp*Co(III)-Catalyzed C–H Bond Activation. *Chem. Pharm. Bull.* **2018,** *66* (1), 51-54.

157. Kawai, K.; Bunno, Y.; Yoshino, T.; Matsunaga, S., Weinreb Amide Directed Versatile C−H Bond Functionalization under ($\eta^5$-Pentamethylcyclopentadienyl)cobalt(III) Catalysis. *Chem. Eur. J.* **2018,** *24* (40), 10231-10237.

158. Fukagawa, S.; Kato, Y.; Tanaka, R.; Kojima, M.; Yoshino, T.; Matsunaga, S., Enantioselective C($sp^3$)–H Amidation of Thioamides Catalyzed by a CobaltIII/Chiral Carboxylic Acid Hybrid System. *Angew. Chem. Int. Ed.* **2019,** *58* (4), 1153-1157.

159. Yoshino, T.; Matsunaga, S., Cp*CoIII-Catalyzed C–H Functionalization and Asymmetric Reactions Using External Chiral Sources. *Synlett* **2019,** *30* (12), 1384-1400.

160. Tanaka, R.; Kojima, M.; Yoshino, T.; Matsunaga, S., Cobalt-catalyzed Synthesis of Homoallylic Amines from Imines and Terminal Alkenes. *Chem. Lett.* **2019,** *48* (9), 1046-1049.

161. Tanaka, R.; Tanimoto, I.; Kojima, M.; Yoshino, T.; Matsunaga, S., Imidate as the Intact Directing Group for the Cobalt-Catalyzed C–H Allylation. *J. Org. Chem.* **2019,** *84* (20), 13203-13210.

162. Li, J.; Ackermann, L., Cobalt-Catalyzed C-H Cyanation of Arenes and Heteroarenes. *Angew. Chem. Int. Ed.* **2015,** *54*, 3635-3638.

163. Li, J.; Tang, M.; Zang, L.; Zhang, X.; Zhang, Z.; Ackermann, L., Amidines for Versatile Cobalt(III)-Catalyzed Synthesis of Isoquinolines through C-H Functionalization with Diazo Compounds. *Org. Lett.* **2016,** *18*, 2742-2745.

164. Mei, R.; Loup, J.; Ackermann, L., Oxazolinyl-Assisted C-H Amidation by Cobalt(III) Catalysis. *ACS Catal.* **2016,** *6*, 793-797.

165. Moselage, M.; Li, J.; Ackermann, L., Cobalt-Catalyzed C-H Activation. *ACS Catal.* **2016,** *6*, 498-525.

166. Nakanowatari, S.; Mei, R.; Feldt, M.; Ackermann, L., Cobalt(III)-Catalyzed Hydroarylation of Allenes via C-H Activation. *ACS Catal.* **2017,** *7*, 2511-2515.

167. Wang, H.; Lorion, M. M.; Ackermann, L., Domino C-H/N-H Allylations of Imidates by Cobalt Catalysis. *ACS Catal.* **2017,** *7*, 3430-3433.

168. Zell, D.; Bursch, M.; Mueller, V.; Grimme, S.; Ackermann, L., Full Selectivity Control in Cobalt(III)-Catalyzed C-H Alkylations by Switching of the C-H Activation Mechanism. *Angew. Chem. Int. Ed.* **2017,** *56*, 10378-10382.

169. Zell, D.; Mueller, V.; Dhawa, U.; Bursch, M.; Presa, R. R.; Grimme, S.; Ackermann, L., Mild Cobalt(III)-Catalyzed Allylative C-F/C-H Functionalizations at Room Temperature. *Chem. - Eur. J.* **2017,** *23*, 12145-12148.

170. Zhang, Z.; Han, S.; Tang, M.; Ackermann, L.; Li, J., C-H Alkylations of (Hetero)Arenes by Maleimides and Maleate Esters through Cobalt(III) Catalysis. *Org. Lett.* **2017,** *19*, 3315-3318.

171. Detmar, E.; Mueller, V.; Zell, D.; Ackermann, L.; Breugst, M., Cobalt-catalyzed C-H cyanations: insights into the reaction mechanism and the role of London dispersion. *Beilstein J. Org. Chem.* **2018,** *14*, 1537-1545.

172. Pesciaioli, F.; Dhawa, U.; Oliveira, J. C. A.; Yin, R.; John, M.; Ackermann, L., Enantioselective Cobalt(III)-Catalyzed C-H Activation Enabled by Chiral Carboxylic Acid Cooperation. *Angew. Chem. Int. Ed.* **2018,** *57*, 15425-15429.

173. Lorion, M. M.; Kaplaneris, N.; Son, J.; Kuniyil, R.; Ackermann, L., Late-stage peptide diversification through cobalt-catalyzed C-H activation: Sequential multicatalysis for stapled peptides. *Angew. Chem. Int. Ed.* **2019,** *58*, 1684-1688.

174. Luo, C.-Z.; Gandeepan, P.; Jayakumar, J.; Parthasarathy, K.; Chang, Y.-W.; Cheng, C.-H., RhIII-Catalyzed C-H Activation: A Versatile Route towards Various Polycyclic Pyridinium Salts. *Chem. Eur. J.* **2013,** *19* (42), 14181-14186.

175. Zhang, G.; Yang, L.; Wang, Y.; Xie, Y.; Huang, H., An Efficient $Rh/O_2$ Catalytic System for Oxidative C–H Activation/Annulation: Evidence for Rh(I) to Rh(III) Oxidation by Molecular Oxygen. *J. Am. Chem. Soc.* **2013,** *135* (24), 8850-8853.

176. Prakash, S.; Muralirajan, K.; Cheng, C.-H., Cobalt-Catalyzed Oxidative Annulation of Nitrogen-Containing Arenes with Alkynes: An Atom-Economical Route to Heterocyclic Quaternary Ammonium Salts. *Angew. Chem. Int. Ed.* **2016,** *55*, 1844-1848.

177. Yoshino, T.; Matsunaga, S., (Pentamethylcyclopentadienyl)cobalt(III)-Catalyzed C–H Bond Functionalization: From Discovery to Unique Reactivity and Selectivity. *Adv. Synth. Catal.* **2017,** *359* (8), 1245-1262.

178. Gandeepan, P.; Müller, T.; Zell, D.; Cera, G.; Warratz, S.; Ackermann, L., 3d Transition Metals for C–H Activation. *Chem. Rev.* **2019,** *119* (4), 2192-2452.

179. Cornaton, Y.; Djukic, J.-P., A noncovalent interaction insight onto the concerted metallation deprotonation mechanism. *Phys. Chem. Chem. Phys.* **2019,** *21* (36), 20486-20498.

180. Davies, D. L.; Donald, S. M. A.; Macgregor, S. A., Computational Study of the Mechanism of Cyclometalation by Palladium Acetate. *J. Am. Chem. Soc.* **2005,** *127*, 13754-13755.

181. Davies, D. L.; Macgregor, S. A.; McMullin, C. L., Computational Studies of Carboxylate-Assisted C-H Activation and Functionalization at Group 8-10 Transition Metal Centers. *Chem. Rev.* **2017,** *117*, 8649-8709.

182. Davies, D. L.; Donald, S. M. A.; Al-Duaij, O.; Macgregor, S. A.; Poelleth, M., Electrophilic C-H Activation at {Cp*Ir}: Ancillary-Ligand Control of the Mechanism of C-H Activation. *J. Am. Chem. Soc.* **2006,** *128*, 4210-4211.

183. Kuhl, N.; Hopkinson, M. N.; Wencel-Delord, J.; Glorius, F., Beyond Directing Groups: Transition-Metal-Catalyzed C-H Activation of Simple Arenes. *Angew. Chem. Int. Ed.* **2012,** *51* (41), 10236-10254.

184. Sambiagio, C.; Schönbauer, D.; Blieck, R.; Dao-Huy, T.; Pototschnig, G.; Schaaf, P.; Wiesinger, T.; Zia, M. F.; Wencel-Delord, J.; Besset, T.; Maes, B. U. W.; Schnürch, M., A comprehensive overview of directing groups applied in metal-catalysed C–H functionalisation chemistry. *Chem. Soc. Rev.* **2018,** *47* (17), 6603-6743.

185. Sanjose-Orduna, J.; Sarria Toro, J. M.; Perez-Temprano, M. H., HFIP-Assisted C-H Functionalization by $Cp^*Co^{III}$: Access to Key Reactive Cobaltacycles and Implication in Catalysis. *Angew. Chem. Int. Ed.* **2018,** *57*, 11369-11373.

186. Alharis, R. A.; McMullin, C. L.; Davies, D. L.; Singh, K.; Macgregor, S. A., Understanding electronic effects on carboxylate-assisted C–H activation at ruthenium: the importance of kinetic and thermodynamic control. *Faraday Disc.* **2019,** *220* (0), 386-403.

187. Zhou, X.; Luo, Y.; Kong, L.; Xu, Y.; Zheng, G.; Lan, Y.; Li, X., Cp*CoIII-Catalyzed Branch-Selective Hydroarylation of Alkynes via C–H Activation: Efficient Access to α-gem-Vinylindoles. *ACS Catal.* **2017,** *7* (10), 7296-7304.

188. Wang, Q.; Huang, F.; Jiang, L.; Zhang, C.; Sun, C.; Liu, J.; Chen, D., Comprehensive Mechanistic Insight into Cooperative Lewis Acid/Cp*CoIII-Catalyzed C–H/N–H Activation for the Synthesis of Isoquinolin-3-ones. *Inorg. Chem.* **2018,** *57* (5), 2804-2814.

189. Xing, Y.-Y.; Liu, J.-B.; Sun, C.-Z.; Huang, F.; Chen, D.-Z., Mechanistic Exploration of Cp*CoIII/RhIII-Catalyzed Carboamination/Olefination of N-Phenoxyacetamides with Alkenes. *Inorg. Chem.* **2018,** *57* (17), 10726-10735.

190. Qu, S.; Cramer, C. J., Mechanistic Study of $Cp^*Co^{III}/Rh^{III}$-Catalyzed Directed C–H Functionalization with Diazo Compounds. *J. Org. Chem.* **2017,** *82* (2), 1195-1204.

191. Zhang, X.-B.; Yu, B.-B.; Si, S.-M.; Wang, S., Theoretical prediction on the synthesis of 2,3-dihydropyridines through Co(III)-catalysed reaction of unsaturated oximes with alkenes. *Int. J. Quant. Chem.* **2017,** *117* (8), e25353.

192. Kenny, A.; Pisarello, A.; Bird, A.; Chirila, P. G.; Hamilton, A.; Whiteoak*, C. J., A challenging redox neutral Cp*Co(III)-catalysed alkylation of acetanilides with 3-buten-2-one: synthesis and key insights into the mechanism through DFT calculations. *Beilstein J. Org. Chem.* **2018,** *14*, 2366-2374.

193. Chirila, P. G.; Adams, J.; Dirjal, A.; Hamilton, A.; Whiteoak, C. J., Cp*Co(III)-Catalyzed Coupling of Benzamides with a,b-unsaturated Carbonyl Compounds: Preparation of Aliphatic Ketones and Azepinones. *Chem. Eur. J.* **2018,** *24*, 3584-3589.

194. Schmidt, G. F.; Brookhart, M., Implications of Three-Center, Two-Electron M-H-C Bonding for Related Alkyl Migration Reactions: Design and Study of an Ethylene Polymerization Catalyst. *J. Am. Chem. Soc.* **1985,** *107* (5), 1443-1444.

195. Vigalok, A.; Uzan, O.; Shimon, L. J. W.; Ben-David, Y.; Martin, J. M. L.; Milstein, D., Formation of $\eta^2$ C−H Agostic Rhodium Arene Complexes and Their Relevance to Electrophilic Bond Activation. *J. Am. Chem. Soc.* **1998,** *120* (48), 12539-12544.

196. Brookhart, M.; Green, M. L. H.; Parkin, G., Agostic interactions in transition metal compounds. *Proc. Nat. Acad. Sci. USA* **2007,** *104* (17), 6908-6914.

197. Clot, E.; Eisenstein, O., Agostic Interactions from a Computational Perspective: One Name, Many Interpretations. In *Principles and Applications of Density Functional Theory in Inorganic Chemistry II*, Kaltsoyannis, N.; McGrady, J. E., Eds. Springer Berlin Heidelberg: Berlin, Heidelberg, 2004; pp 1-36.

198. Hamdaoui, M.; Djukic, J.-P., Noncovalent Interactions in Key Metal-centred Catalytic Intermediates: Structure–Electronic Relationship. In *Noncovalent Interactions in Catalysis*, Mahmudov, K. T.; Kopylovich, M. N.; Guedes.da.Silva, M. F. C.; Pombeiro, A. J. L., Eds. The Royal Society of Chemistry: 2019; pp 579-607.

199. Klamt, A.; Schüürmann, G., COSMO: a new approach to dielectric screening in solvents with explicit expressions for the screening energy and its gradient. *J. Chem. Soc., Perkin Transactions 2* **1993,** (5), 799-805.

200. Klamt, A., Conductor-like Screening Model for Real Solvents: A New Approach to the Quantitative Calculation of Solvation Phenomena. *J. Phys. Chem.* **1995,** *99* (7), 2224-2235.

201. Klamt, A.; Jonas, V., Treatment of the outlying charge in continuum solvation models. *J. Chem. Phys.* **1996,** *105* (22), 9972-9981.

202. Perdew, J. P.; Burke, K.; Ernzerhof, M., Generalized Gradient Approximation Made Simple. *Phys. Rev. Lett.* **1996,** *77* (18), 3865-3868.

203. Grimme, S.; Hansen, A.; Brandenburg, J. G.; Bannwarth, C., Dispersion-Corrected Mean-Field Electronic Structure Methods. *Chem. Rev.* **2016,** *116* (9), 5105-5154.

204. Grimme, S.; Antony, J.; Ehrlich, S.; Krieg, H., A consistent and accurate ab initio parametrization of density functional dispersion correction (DFT-D) for the 94 elements H-Pu. *J. Chem. Phys.* **2010,** *132*, 154104.

205. Grimme, S.; Ehrlich, S.; Goerigk, L., Effect of the damping function in dispersion corrected density functional theory. *J. Comp. Chem.* **2011,** *32* (7), 1456-1465.

206. Alharis, R. A.; McMullin, C. L.; Davies, D. L.; Singh, K.; Macgregor, S. A., The Importance of Kinetic and Thermodynamic Control when Assessing Mechanisms of Carboxylate-Assisted C–H Activation. *J. Am. Chem. Soc.* **2019,** *141* (22), 8896-8906.

207. Ernzerhof, M.; Scuseria, G. E., Assessment of the Perdew–Burke–Ernzerhof exchange-correlation functional. *J. Chem. Phys.* **1999,** *110* (11), 5029-5036.

208. Steinmann, S. N.; Corminboeuf, C., Comprehensive Benchmarking of a Density-Dependent Dispersion Correction. *J. Chem. Theory Comput.* **2011,** *7* (11), 3567-3577.

209. Neese, F., The ORCA program system. *WIREs Compt. Mol. Sci.* **2012,** *2*, 73-78.

210. Riplinger, C.; Neese, F., An efficient and near linear scaling pair natural orbital based local coupled cluster method. *J. Chem. Phys.* **2013,** *138*, 034106.

211. Riplinger, C.; Sandhoeffer, B.; Hansen, A.; Neese, F., Natural triple excitations in local coupled cluster calculations with pair natural orbitals. *J. Chem. Phys.* **2013,** *139*, 134101.

212. Liakos, D. G.; Sparta, M.; Kesharwani, M. K.; Martin, J. M. L.; Neese, F., Exploring the Accuracy Limits of Local Pair Natural Orbital Coupled-Cluster Theory. *J. Chem. Theory Comput.* **2015,** *11*, 1525-1539.

213. Riplinger, C.; Pinski, P.; Becker, U.; Valeev, E. F.; Neese, F., Sparse maps--A systematic infrastructure for reduced-scaling electronic structure methods. II. Linear scaling domain based pair natural orbital coupled cluster theory. *J. Chem. Phys.* **2016,** *144*, 024109.

214. Schneider, W. B.; Bistoni, G.; Sparta, M.; Saitow, M.; Riplinger, C.; Auer, A. A.; Neese, F., Decomposition of Intermolecular Interaction Energies within the Local Pair Natural Orbital Coupled Cluster Framework. *J. Chem. Theory Comput.* **2016,** *12*, 4778-4792.

215. Stoychev, G. L.; Auer, A. A.; Neese, F., Automatic Generation of Auxiliary Basis Sets. *J. Chem. Theory Comput.* **2017,** *13*, 554-562.

216. Contreras-Garcia, J.; Johnson, E. R.; Keinan, S.; Chaudret, R.; Piquemal, J. P.; Beratan, D. N.; Yang, W., NCIPLOT: a program for plotting non-covalent interaction regions. *J. Chem. Theory Comput.* **2011,** *7*, 625-632.

217. Johnson, E.; Keinan, S.; Mori-Sanchez, P.; Contreras-Garcia, J.; Cohen, A. J.; Yang, W., Revealing noncovalent interactions. *J. Am. Chem. Soc.* **2010,** *132*, 6498-6506.

218. Blanco, M. A.; Martín Pendás, A.; Francisco, E., Interacting Quantum Atoms: A Correlated Energy Decomposition Scheme Based on the Quantum Theory of Atoms in Molecules. *J. Chem. Theory Comput.* **2005,** *1* (6), 1096-1109.

219. Suárez, D.; Díaz, N.; Francisco, E.; Martín Pendás, A., Application of the Interacting Quantum Atoms Approach to the S66 and Ionic-Hydrogen-Bond Datasets for Noncovalent Interactions. *ChemPhysChem* **2018,** *19* (8), 973-987.

220. Francisco, E.; Martín Pendás, A.; Blanco, M. A., A Molecular Energy Decomposition Scheme for Atoms in Molecules. *J. Chem. Theory Comput.* **2006,** *2* (1), 90-102.

221. Bader, R. F. W., *Atoms in Molecules: A Quantum Theory*. Clarendon: Oxford, **1990**.

222. Contreras-García, J.; Yang, W.; Johnson, E. R., Analysis of Hydrogen-Bond Interaction Potentials from the Electron Density: Integration of Noncovalent Interaction Regions. *J. Phys. Chem. A* **2011,** *115* (45), 12983-12990.

223. Boto, R. A.; Peccati, F.; Laplaza, R.; Quan, C.; Carbone, A.; Piquemal, J.-P.; Maday, Y.; Contreras-Garcia, J., NCIPLOT4: A new step towards a fast quantification of noncovalent interactions. **2020**.

224. Jerhaoui, S.; Djukic, J.-P.; Wencel-Delord, J.; Colobert, F., Asymmetric, Nearly Barrierless C($sp^3$)-H Activation Promoted by Easily-Accessible N-protected Aminosulfoxides as New Chiral ligands. *ACS Catal.* **2019,** *9*, 2532-2542.

225. Lu, Q.; Neese, F.; Bistoni, G., Formation of Agostic Structures Driven by London Dispersion. *Angew. Chem. Int. Ed.* **2018,** *57* (17), 4760-4764.

226. Altun, A.; Neese, F.; Bistoni, G., Effect of Electron Correlation on Intermolecular Interactions: A Pair Natural Orbitals Coupled Cluster Based Local Energy Decomposition Study. *J. Chem. Theory Comput.* **2019,** *15*, 215-228.

227. Lu, Q.; Neese, F.; Bistoni, G., London dispersion effects in the coordination and activation of alkanes in σ-complexes: a local energy decomposition study. *Phys. Chem. Chem. Phys.* **2019,** *21*, 11569-11577.

228. Paulechka, E.; Kazakov, A., Efficient DLPNO–CCSD(T)-Based Estimation of Formation Enthalpies for C-, H-, O-, and N-Containing Closed-Shell Compounds Validated Against Critically Evaluated Experimental Data. *J. Phys. Chem. A* **2017,** *121*, 4379-4387.

229. Minenkov, Y.; Chermak, E.; Cavallo, L., Accuracy of DLPNO–CCSD(T) Method for Noncovalent Bond Dissociation Enthalpies from Coinage Metal Cation Complexes. *J. Chem. Theory Comput.* **2015,** *11*, 4664-4676.

230. Scheeren, C.; Maasarani, F.; Hijazi, A.; Djukic, J.-P.; Pfeffer, M.; Zarić, S. D.; Le Goff, X.-F.; Ricard, L., Stereoselective “Electrophilic” Cyclometalation of Planar-Prochiral ($\eta^6$-Arene)tricarbonylchromium Complexes with Asymmetric Metal Centers: pseudo-T-4 $[Cp^*RhCl_2]_2$ and $[Cp^*IrCl_2]_2$. *Organometallics* **2007,** *26* (14), 3336-3345.

231. Duggleby, R. G.; Northrop, D. B., The expression of kinetic isotope effects during the time course of enzyme-catalyzed reactions. *Bioorg. Chem.* **1989,** *17* (2), 177-193.

232. Bigeleisen, J.; Wolfsberg, M., Theoretical and Experimental Aspects of Isotope Effects in Chemical Kinetics. In *Advances in Chemical Physics*, Prigogine, I.; Debye, P., Eds. 1957; Vol. 1, pp 15-76.

233. Gómez-Gallego, M.; Sierra, M. A., Kinetic Isotope Effects in the Study of Organometallic Reaction Mechanisms. *Chem. Rev.* **2011,** *111* (8), 4857-4963.

234. Wesener, J. R.; Moskau, D.; Guenther, H., Intrinsic deuterium/proton NMR isotope effects on carbon-13 chemical shifts: dependence on carbon hybridization and substitution. *J. Am. Chem. Soc.* **1985,** *107* (25), 7307-7311.

235. Aydin, R.; Guenther, H., Secondary deuterium/hydrogen isotope effects on carbon-13 chemical shifts in cycloalkanes. Downfield shifts over three and four bonds. *J. Am. Chem. Soc.* **1981,** *103* (5), 1301-1303.

236. Simmons, E. M.; Hartwig, J. F., On the Interpretation of Deuterium Kinetic Isotope Effects in C-H Bond Functionalizations by Transition-Metal Complexes. *Angew. Chem. Int. Ed.* **2012,** *51* (13), 3066-3072.

237. Bigeleisen, J., The Relative Reaction Velocities of Isotopic Molecules. *J. Chem. Phys.* **1949,** *17*, 675-678.

238. Bigeleisen, J., Statistical mechanics of isotopic systems with small quantum corrections. I. General considerations and the rule of the geometric mean. *J. Chem. Phys.* **1955,** *23*, 2264-2267.

239. Schaad, L. J.; Bytautas, L.; Houk, K. N., Ab initio test of the usefulness of the Redlich-Teller product rule in computing kinetic isotope effects. *Can. J. Chem.* **1999,** *77*, 875-878.

240. Wong, K.-Y.; Richard, J. P.; J., G., Theoretical Analysis of the Kinetic Isotope Effects on Proton Transfer Reactions between Substituted α-Methoxystyrenes and Substituted Acetic Acids. *J. Am. Chem. Soc.* **2009,** *131*, 13963-13971.

241. Wong, K.-Y.; Xu, Y.; Xu, L., Review of computer simulations of isotope effects on biochemmical reactions: From Bigeleisen equation to Feynman’s path integral. *Biochim. Biophys. Acta* **2015,** *1854*, 1782-1794.

242. González-Lafon, À.; Lluch, J. M., Kinetic isotope effects in chemical and biochemical reactions: physical basis and theoretical methods of calculation. *WIREs Comput. Mol. Sci.* **2016,** *6*, 584-603.

243. Buncel, E.; Lee, C. C., *Isotopes in cationic reactions*. Elsevier: Amsterdam, **1980**; Vol. 5, p 234.

244. Schreiner, P. R., Tunneling Control of Chemical Reactions: The Third Reactivity Paradigm. *J. Am. Chem. Soc.* **2017,** *139* (43), 15276-15283.

245. Schreiner, P. R.; Wagner, J. P.; Reisenauer, H. P.; Gerbig, D.; Ley, D.; Sarka, J.; Császár, A. G.; Vaughn, A.; Allen, W. D., Domino Tunneling. *J. Am. Chem. Soc.* **2015,** *137* (24), 7828-7834.

246. Kwart, H., Temperature dependence of the primary kinetic hydrogen isotope effect as a mechanistic criterion. *Acc. Chem. Res.* **1982,** *15* (12), 401-408.

247. Binh, D. H.; Hamdaoui, M.; Fischer-Krauser, D.; Karmazin, L.; Bailly, C.; Djukic, J.-P., Entrapment of THF-Stabilized Iridacyclic IrIII Silylenes from Double H−Si Bond Activation and $H_2$ Elimination. *Chem. Eur. J.* **2018,** *24* (66), 17577-17589.

248. Ossor, H.; Pfeffer, M.; Jastrzebski, J. T. B. H.; Stam, C. H., Reactivity of cycopalladated compounds. 14. Alkyne insertion into the palladium-carbon bond of a metallacycle stabilized by a weak oxygen-palladium bond leading to an unusual ($h^2$-aryl)-palladium interaction molecular structure of $[NC_9H_6CH_2C(CF_3):C(CF_3)]Pd[C(CF_3):C(CF_3)(h^2\text{-}C_{10}H_6)OCH_3]$. *Inorg. Chem.* **1987,** *26* (7), 1169-1171.

249. Pfeffer, M., Reactions of cyclopalladated compounds and alkynes: New pathways for organic synthesis? *Rec. Trav. Chim. Pays-Bas* **1990,** *109* (12), 567-576.

250. Algarra, A. G.; Cross, W. B.; Davies, D. L.; Khamker, Q.; Macgregor, S. A.; McMullin, C. L.; Singh, K., Combined Experimental and Computational Investigations of Rhodium- and Ruthenium-Catalyzed C–H Functionalization of Pyrazoles with Alkynes. *J. Org. Chem.* **2014,** *79* (5), 1954-1970.

251. Han, Y.-F.; Li, H.; Hu, P.; Jin, G.-X., Alkyne Insertion Induced Regiospecific C−H Activation with $[Cp^*MCl_2]_2$ (M = Ir, Rh). *Organometallics* **2011,** *30* (4), 905-911.

252. Omae, I., Intramolecular five-membered ring compounds and their applications. *Coord. Chem. Rev.* **2004,** *248* (11), 995-1023.

253. Yu, X.; Chen, K.; Guo, S.; Shi, P.; Song, C.; Zhu, J., Direct Access to Cobaltacycles via C–H Activation: N-Chloroamide-Enabled Room-Temperature Synthesis of Heterocycles. *Org. Lett.* **2017,** *19* (19), 5348-5351.

254. Zhu, C.; Kuniyil, R.; Jei, B. B.; Ackermann, L., Domino C–H Activation/Directing Group Migration/Alkyne Annulation: Unique Selectivity by $d^6$-Cobalt(III) Catalysts. *ACS Catal.* **2020,** *10* (7), 4444-4450.

255. Liao, G.; Zhou, T.; Yao, Q.-J.; Shi, B.-F., Recent advances in the synthesis of axially chiral biaryls via transition metal-catalysed asymmetric C–H functionalization. *ChemComm.* **2019,** *55* (59), 8514-8523.

256. Luo, J.; Zhang, T.; Wang, L.; Liao, G.; Yao, Q.-J.; Wu, Y.-J.; Zhan, B.-B.; Lan, Y.; Lin, X.-F.; Shi, B.-F., Enantioselective Synthesis of Biaryl Atropisomers by Pd-Catalyzed C−H Olefination using Chiral Spiro Phosphoric Acid Ligands. *Angew. Chem. Int. Ed.* **2019,** *58* (20), 6708-6712.

257. Song, H.; Li, Y.; Yao, Q.-J.; Jin, L.; Liu, L.; Liu, Y.-H.; Shi, B.-F., Synthesis of Axially Chiral Styrenes through Pd-Catalyzed Asymmetric C−H Olefination Enabled by an Amino Amide Transient Directing Group. *Angew. Chem. Int. Ed.* **2020,** *59*, 6576-6580.

258. Han, H.; Zhang, T.; Yang, S.-D.; Lan, Y.; Xia, J.-B., Palladium-Catalyzed Enantioselective C–H Aminocarbonylation: Synthesis of Chiral Isoquinolinones. *Org. Lett.* **2019,** *21* (6), 1749-1754.

259. Jin, L.; Yao, Q.-J.; Xie, P.-P.; Li, Y.; Zhan, B.-B.; Han, Y.-Q.; Hong, X.; Shi, B.-F., Atroposelective Synthesis of Axially Chiral Styrenes via an Asymmetric C–H Functionalization Strategy. *Chem* **2020,** *6* (2), 497-511.

260. Jutzi, P., The Versatility of the Pentamethylcyclopentadienyl Ligand in Main-Group Chemistry. *Comments Inorg. Chem.* **1987,** *6* (3), 123-144.

261. Rottink, M. K.; Angelici, R. J., Ligand and metal effects on the enthalpies of protonation of $Cp'M(PR_3)(PR'_3)X$ complexes (M = ruthenium or osmium). *J. Am. Chem. Soc.* **1993,** *115* (16), 7267-7274.

262. Deeming, A. J., 31.3 - Mononuclear Iron Compounds with $\eta^2$–$\eta^6$ Hydrocarbon Ligands. In *Comprehensive Organometallic Chemistry*, Wilkinson, G.; Stone, F. G. A.; Abel, E. W., Eds. Pergamon: Oxford, **1982**; pp 377-512.

263. Espinet, P.; Albéniz, A. C., 8.06 - Palladium–Carbon π-Bonded Complexes. In *Comprehensive Organometallic Chemistry III*, Mingos, D. M. P.; Crabtree, R. H., Eds. Elsevier: Oxford, **2007**; 315-403.

264. Thiel, I.; Hapke, M., The broad diversity of CpCo(I) complexes. *Rev. Inorg. Chem.* **2014,** *34* (4), 217-245.

265. Piou, T.; Romanov-Michailidis, F.; Romanova-Michaelides, M.; Jackson, K. E.; Semakul, N.; Taggart, T. D.; Newell, B. S.; Rithner, C. D.; Paton, R. S.; Rovis, T., Correction to “Correlating Reactivity and Selectivity to Cyclopentadienyl Ligand Properties in Rh(III)-Catalyzed C–H Activation Reactions: An Experimental and Computational Study”. *J. Am. Chem. Soc.* **2020,** *142* (16), 7709-7709.

266. Piou, T.; Romanov-Michailidis, F.; Romanova-Michaelides, M.; Jackson, K. E.; Semakul, N.; Taggart, T. D.; Newell, B. S.; Rithner, C. D.; Paton, R. S.; Rovis, T., Correlating Reactivity and Selectivity to Cyclopentadienyl Ligand Properties in Rh(III)-Catalyzed C–H Activation Reactions: An Experimental and Computational Study. *J. Am. Chem. Soc.* **2017,** *139* (3), 1296-1310.

267. Piou, T.; Rovis, T., Electronic and Steric Tuning of a Prototypical Piano Stool Complex: Rh(III) Catalysis for C–H Functionalization. *Acc. Chem. Res.* **2018,** *51* (1), 170-180.

268. Yamada, T.; Shibata, Y.; Tanaka, K., Functionalized Cyclopentadienyl Ligands and Their Substituent Effects on a Rhodium(III)-Catalyzed Oxidative [4+2] Annulation of Indole- and Pyrrole-1-Carboxamides with Alkynes. *Asian J. Org. Chem.* **2018,** *7* (7), 1396-1402.

269. Campos, J.; Hintermair, U.; Brewster, T. P.; Takase, M. K.; Crabtree, R. H., Catalyst Activation by Loss of Cyclopentadienyl Ligands in Hydrogen Transfer Catalysis with $Cp^*Ir^{III}$ Complexes. *ACS Catal.* **2014,** *4* (3), 973-985.

270. Jutzi, P.; Reumann, G., Cp* Chemistry of main-group elements *J. Chem. Soc., Dalton Trans.* **2000,** (14), 2237-2244.

271. Park, J.; Chang, S., Comparison of the Reactivities and Selectivities of Group 9 [Cp*MIII] Catalysts in C−H Functionalization Reactions. *Chem. Asian J.* **2018,** *13* (9), 1089-1102.

272. Pitman, C. L.; Finster, O. N. L.; Miller, A. J. M., Cyclopentadiene-mediated hydride transfer from rhodium complexes. *ChemComm..* **2016,** *52* (58), 9105-9108.

273. Quintana, L. M. A.; Johnson, S. I.; Corona, S. L.; Villatoro, W.; Goddard, W. A.; Takase, M. K.; VanderVelde, D. G.; Winkler, J. R.; Gray, H. B.; Blakemore, J. D., Proton–hydride tautomerism in hydrogen evolution catalysis. *Proc. Nat. Acad. Sci.* **2016,** *113* (23), 6409-6414.

274. Peng, Y.; Ramos-Garcés, M. V.; Lionetti, D.; Blakemore, J. D., Structural and Electrochemical Consequences of [Cp*] Ligand Protonation. *Inorg. Chem.* **2017,** *56* (17), 10824-10831.

275. Ma, P.; Chen, H., Ligand-Dependent Multi-State Reactivity in Cobalt(III)-Catalyzed C–H Activations. *ACS Catal.* **2019,** *9* (3), 1962-1972.

276. Ghorai, J.; Anbarasan, P., Developments in the Cp*Co(III) Catalyzed C-H Bond Functionalizaitons. *Asian J. Org. Chem.* **2019,** *8*, 430 -455.

277. Ustynyuk, Y. A.; Barinov, I. V., Nickelocene Interaction with o-halogenated azobenzenes. 4-Phenyl-4H-cyclopenta[*c*]cinnoline, a new pseudo azulene. *J. Organomet. Chem.* **1970,** *23*, 551-557.

278. Hull, J. F.; Balcells, D.; Blakemore, J. D.; Incarvito, C. D.; Eisenstein, O.; Brudvig, G. W.; Crabtree, R. H., Highly Active and Robust Cp* Iridium Complexes for Catalytic Water Oxidation. *J. Am. Chem. Soc.* **2009,** *131* (25), 8730-8731.

279. Patureau F W, Wencel‐Delord J, Glorius F, Cp*Rh-Catalyzed C-H Activations. Versatile Dehydrogenative Cross-Couplings of $Csp^2$ C—H Positions with Olefins, Alkynes, and Arenes. *Aldrichim. Acta* **2012,** *45*, 31-45.

280. Kuhl, N.; Schröder, N.; Glorius, F., Formal SN-Type Reactions in Rhodium(III)-Catalyzed C-H Bond Activation. *Adv. Synth. Catal.* **2014,** *356* (7), 1443-1460.

281. Wu, F.; Deraedt, C.; Cornaton, Y.; Contreras-Garcia, J.; Boucher, M.; Karmazin, L.; Bailly, C.; Djukic, J.-P., Making Base-Assisted C–H Bond Activation by Cp*Co(III) Effective: A Noncovalent Interaction-Inclusive Theoretical Insight and Experimental Validation. *Organometallics* **2020,** *39* (14), 2609-2629.

282. Sanjosé-Orduna, J.; Gallego, D.; Garcia-Roca, A.; Martin, E.; Benet-Buchholz, J.; Pérez-Temprano, M. H., Capturing Elusive Cobaltacycle Intermediates: A Real-Time Snapshot of the Cp*CoIII -Catalyzed Oxidative Alkyne Annulation. *Angew. Chem. Int. Ed.* **2017,** *56*, 1 - 6.

283. Lefebvre, C.; Rubez, G.; Khartabil, H.; Boisson, J.-C.; Contreras-García, J.; Hénon, E., Accurately extracting the signature of intermolecular interactions present in the NCI plot of the reduced density gradient versus electron density. *Phys. Chem. Chem. Phys.* **2017,** *19* (27), 17928-17936.

284. Lefebvre, C.; Khartabil, H.; Boisson, J.-C.; Contreras-García, J.; Piquemal, J.-P.; Hénon, E., The Independent Gradient Model: A New Approach for Probing Strong and Weak Interactions in Molecules from Wave Function Calculations. *ChemPhysChem.* **2018,** *19* (6), 724-735.

285. Klein, J.; Khartabil, H.; Boisson, J.-C.; Contreras-Garcia, J.; Piquemal, J.-P.; Hénon, E., New Way for Probing Bond Strength. *J. Phys. Chem. A* **2020,** *124*, 1850-1860.

286. **2020**. https://echa.europa.eu/substance-information/-/substanceinfo/100.028.325.

287. Payne, L. R., The Hazards of Cobalt. *Occup. Med.* **1977,** *27* (1), 20-25.

288. Leyssens, L.; Vinck, B.; Van Der Straeten, C.; Wuyts, F.; Maes, L., Cobalt toxicity in humans—A review of the potential sources and systemic health effects. *Toxicology* **2017,** *387*, 43-56.

289. Mahey, S.; Kumar, R.; Sharma, M.; Kumar, V.; Bhardwaj, R., A critical review on toxicity of cobalt and its bioremediation strategies. *SN Appl. Sci.* **2020,** *2* (7), 1279.

290. Egorova, K. S.; Ananikov, V. P., Toxicity of Metal Compounds: Knowledge and Myths. *Organometallics* **2017,** *36* (21), 4071-4090.

291. Connelly, N. G.; Geiger, W. E., Chemical Redox Agents for Organometallic Chemistry. *Chem. Rev.* **1996,** *96*, 877−910.

292. Denekamp, C.; Yaniv, M., Benzene Loss from Trityl Cations-A Mechanistic Study. *J. Am. Soc. Mass Spectrom.* **2006,** *17*, 730-736.

293. Schade, C.; Mayr, H., Tritylium ions as initiators and co-initiators in cationic polymerizations. *Makromol. Chem., Rapid Commun.* **1988,** *9*, 477-82.

294. Leleu, J. M.; Bernardo, V.; Polton, A.; Tardi, M.; Sigwalt, P., About the various types of transfer reactions in the cationic polymerization of isobutyl vinyl ether. *Polym. Int.* **1995,** *37*, 219-30.

295. Ofial, A. R., Benzhydrylium and tritylium ions: complementary probes for examining ambident nucleophiles. *Pure Appl. Chem.* **2015,** *87*, 341-351.

296. Huang, Y.; Qiu, C.; Li, Z.; Feng, W.; Gan, H.; Liu, J.; Guo, K., Tritylium Cation as Low Loading Lewis Acidic Organocatalyst in Povarov Reactions. *ACS Sustainable Chem. Eng.* **2016,** *4*, 47-52.

297. Courant, T.; Lombard, M.; Boyarskaya, D. V.; Neuville, L.; Masson, G., Tritylium assisted iodine catalysis for the synthesis of unsymmetrical triarylmethanes. *Org. Biomol. Chem.* **2020,** *18*, 6502-6508.

298. Horn, M.; Schappele, L. H.; Lang-Wittkowski, G.; Mayr, H.; Ofial, A. R., Towards a Comprehensive Hydride Donor Ability Scale. *Chem. - Eur. J.* **2013,** *19*, 249-263.

299. Hayatifar, A.; Borrego, A.; Bosek, D.; Czarnecki, M.; Derocher, G.; Kuplicki, A.; Lytle, E.; Padilla, J.; Paroly, C.; Tubay, G.; Vyletel, J.; Weinert, C. S., Transition metal-free hydrodefluorination of acid fluorides and organofluorines by $Ph_3GeH$ promoted by catalytic $[Ph_3C][B(C_6F_5)_4]$. *ChemComm.* **2019,** *55*, 10852-10855.

300. Bly, R. S.; Bly, R. K.; Hossain, M. M.; Silverman, G. S.; Wallace, E., Reactions of alkyldicarbonyl-$\eta^5$-cyclopentadienyliron compounds with tritylium tetrafluoroborate: a search for hydrogen-atom abstraction following one-electron-transfer. *Tetrahedron* **1986,** *42*, 1093-108.

301. Diversi, P.; Iacoponi, S.; Ingrosso, G.; Laschi, F.; Lucherini, A.; Pinzino, C.; Uccello-Barretta, G.; Zanello, P., Electron Transfer Catalysis in the Activation of C-H Bonds by Iridium Complexes. *Organometallics* **1995,** *14*, 3275-87.

302. Casper, L. A.; Wursthorn, L.; Geppert, M.; Roser, P.; Linseis, M.; Drescher, M.; Winter, R. F., 4-Ferrocenylphenyl-Substituted Tritylium Dyes with Open and Interlinked $C^+Ar_2$ Entities: Redox Behavior, Electrochromism, and a Quantitative Study of the Dimerization of Their Neutral Radicals. *Organometallics* **2020,** *39*, 3275-3289.

303. Uglova, E. V.; Makhaev, V. D.; Reutov, O. A., Mechanism of reduction of trityl perchlorate by symmetric organomercury compounds. *Zh. Org. Khim.* **1970,** *6*, 1337-8.

304. Plesch, P. H.; Stasko, A.; Robson, D., Cathodic reduction of the trityl cation in methylene dichloride. *J. Chem. Soc. B* **1971**, 1634-7.

305. El Murr, N.; Laviron, E., Syntheses using electrochemically generated cobaltocene or cobaltocene anion. *Tetrahedron Lett.* **1975**, 875-8.

306. Baidak, A.; Naumov, S.; Brede, O., Kinetic and Energetic Analysis of the Free Electron Transfer. *J. Phys. Chem. A* **2008,** *112*, 10200-10209.

307. Bank, S.; Ehrlich, C. L.; Zubieta, J. A., Substituent effect on the electrochemical oxidation of trityl anions. *J. Org. Chem.* **1979,** *44* (9), 1454-1458.

308. Azarani, A.; Berinstain, A. B.; Johnston, L. J.; Kazanis, S., Electron transfer reactions between excited diarylmethyl and triarylmethyl carbocations and aromatic donors. *J. Photochem. Photobiol., A* **1991,** *57*, 175-89.

309. Chenneberg, L.; Leveque, C.; Corce, V.; Baralle, A.; Goddard, J.-P.; Ollivier, C.; Fensterbank, L., Single-Electron-Transfer Oxidation of Trifluoroborates and Silicates with Organic Reagents: A Comparative Study. *Synlett* **2016,** *27*, 731-735.

310. Mandon, D.; Toupet, L.; Astruc, D., Electron-transfer pathway in the hydride abstraction by tritylium from exo-substituted cyclohexadiene iron(0) complexes: a key step in the synthesis of heterobifunctional cyclohexadiene from benzene. *J. Am. Chem. Soc.* **1986,** *108*, 1320-2.

311. Robertson, K. N.; Bakshi, P. K.; Lantos, S. D.; Cameron, T. S.; Knop, O., Crystal chemistry of tetraradial species. Part 9. The versatile $BPh_4^-$ anion, or how organoammonium H(N) atoms compete for hydrogen bonding. *Can. J. Chem.* **1998,** *76* (5), 583-611.

312. Nesterov, D. S.; Nesterova, O. V.; Kopylovich, M. N.; Pombeiro, A. J. L., Pronounced retention of stereoconfiguration upon $sp^3$ CH bonds hydroxylation of dimethylcyclohexanes and decahydronaphthalenes with m-CPBA oxidant and a Co-phthalocyanine catalyst. *Mol. Catal.* **2018,** *459*, 8-15.

313. McBride, J. M., The Hexaphenylethane Riddle. *Tetrahedron* **1974,** *30*, 2009-2022.

314. O'Brien, Z. J.; Karlen, S. D.; Khan, S.; Garcia-Garibay, M. A., Solid-State Molecular Rotors with Perdeuterated Stators: Mechanistic Insights from Biphenylene Rotational Dynamics in Ordered and Disordered Crystal Forms. *J. Org. Chem.* **2010,** *75*, 2482-2491.

315. Hinz, A.; Labbow, R.; Reiss, F.; Schulz, A.; Sievert, K.; Villinger, A., Synthesis and structure of tritylium salts. *Struct. Chem.* **2015,** *26*, 1641-1650.

316. Straus, D. A.; Zhang, C.; Tilley, T. D., Trityl tetraphenylborate as a reagent in organometallic chemistry. *J. Organomet. Chem.* **1989,** *369* C13-C17.

317. Dane, L. M.; Janssen, L. J. J.; Hoogland, J. G., The iodine/iodide redox couple at a platinum electrode. *Electrochim. Acta.* **1968,** *13*, 507-518.

318. Popov, A. I.; Geske, D. H., Studies on the Chemistry of Halogen and of Polyhalides. XVI. Voltammetry of Bromine and Interhalogen Species in Acetonitrile. *J. Am. Chem. Soc.* **1958,** *80*, 5346-5349.

319. Baucke, F. G. K.; Bertram, R.; Cruse, K., The iodide-iodine system in acetonitrile: Evaluation of standard thermodynamic data on the association $I^- + I_2 \rightarrow I_3^-$ from potentiometric measurements at 25 and 50°C. *J. Electroanal. Chem.* **1971,** *32*, 247-256.

320. Boschloo, G.; Hagfeldt, A., Characteristics of the Iodide/Triiodide Redox Mediator in Dye-Sensitized Solar Cells. *Acc. Chem. Res.* **2009,** *42*, 1819-1826.

321. El-Hallag, I. S., Electrochemical oxidation of iodide at a glassy carbon electrode in methylene chloride at various temperatures. *J. Chil. Chem. Soc.* **2010,** *55*, 67-73.

322. Huo, Z.; Yang, S.; Zang, D.; Farha, R.; Goldmann, M.; Xu, H.; Antoine, B.; Izzet, G.; Proust, A.; Ruhlmann, L., Photocurrent Generation from Visible Light Irradiation of Covalent Polyoxometalate-Porphyrin Copolymer. *Electrochim. Acta* **2021,** *368*, 137635.

323. Boelsing, F.; Spanuth, E., Triphenylmethyl radicals by inverse Stevens rearrangement. *Z. Naturforsch., B: Anorg. Chem., Org. Chem.* **1976,** *31B*, 531-2.

324. Fukuzumi, S.; Kitano, T.; Ishikawa, M., 10-Methylacridine dimer acting as a unique two-electron donor in the one-electron reduction of triphenylmethyl cation. *J. Am. Chem. Soc.* **1990,** *112*, 5631-2.

325. Janzen, E. G.; Buchheit, M., Detection of the triphenylmethyl radical by electron spin resonance in the thermal decomposition of sodium triphenylacetate. *J. Phys. Chem.* **1972,** *76*, 937-9.

326. Kirste, B.; Harrer, W.; Kurreck, H., ENDOR studies of novel di- and triphenylmethyl radicals generated from galvinols. *J. Am. Chem. Soc.* **1985,** *107*, 20-8.

327. Ponomarchuk, M. P.; Kasukhin, L. F.; Fileleeva, L. I., Triphenylmethane derivatives in single-electron transfer reactions. *Zh. Obshch. Khim.* **1972,** *42*, 2712-15.

328. Schreiner, K.; Berndt, A.; Baer, F., Hyperconjugation in twisted π-radicals. IV. Spin density distribution and stereochemistry of triphenylmethyl radical in solution. Reinvestigation of carbon-13 coupling constants. *Mol. Phys.* **1973,** *26*, 929-39.

329. Trapp, C.; Kulkarni, S. V., Isotope effects in the electron spin resonance spectra of deuterated triphenylmethyl radicals. *J. Phys. Chem.* **1984,** *88*, 2703-8.

330. Van der Hart, W. J., ESR spectra of triarylmethyl radicals. *Mol. Phys.* **1970,** *19*, 75-84.

331. Wang, B.; Lee, Y.-M.; Tcho, W.-Y.; Tussupbayev, S.; Kim, S.-T.; Kim, Y.; Seo, M. S.; Cho, K.-B.; Dede, Y.; Keegan, B. C.; Ogura, T.; Kim, S. H.; Ohta, T.; Baik, M.-H.; Ray, K.; Shearer, J.; Nam, W., Synthesis and reactivity of a mononuclear non-haem cobalt(IV)-oxo complex. *Nat. Commun.* **2017,** *8* (1), 14839.

332. Zanders, D.; Bačić, G.; Leckie, D.; Odegbesan, O.; Rawson, J.; Masuda, J. D.; Devi, A.; Barry, S. T., A Rare Low-Spin CoIV Bis(β-silyldiamide) with High Thermal Stability: Steric Enforcement of a Doublet Configuration. *Angew. Chem. Int. Ed.* **2020,** *59* (33), 14138-14142.

333. Gensch, T.; Klauck, F. J. R.; Glorius, F., Cobalt-Catalyzed C−H Thiolation through Dehydrogenative Cross-Coupling. *Angew. Chem. Int. Ed.* **2016,** *55* (37), 11287-11291.

334. Cornaton, Y.; Djukic, J.-P., A noncovalent interaction insight onto the concerted metallation deprotonation mechanism. *Phys. Chem. Chem. Phys.* **2019,** *21* (36), 20486-20498.

335. Yepes, D.; Munarriz, J.; Daniel, I. A.; Contreras-Garcia, J.; Jaque, P., Real-Space Approach to the Reaction Force: Understanding the Origin of Synchronicity/Nonsynchronicity in Multibond Chemical Reactions. *J. Phys. Chem. A* **2020,** *124* (10), 1959-1972.

336. Contreras-Garcia, J.; Johnson, E. R.; Keinan, S.; Chaudret, R.; Piquemal, J.-P.; Beratan, D. N.; Yang, W., NCIPLOT: A Program for Plotting Noncovalent Interaction Regions. *J. Chem. Theo. Comput.* **2011,** *7*, 625-632.

337. Werlé, C.; Karmazin, L.; Bailly, C.; Ricard, L.; Djukic, J.-P., Stabilization of an Electron-Unsaturated Pd(I)–Pd(I) Unit by Double Hemichelation. *Organometallics* **2015,** *34* (12), 3055-3064.

338. Werlé, C.; Bailly, C.; Karmazin-Brelot, L.; Le Goff, X.-F.; Ricard, L.; Djukic, J.-P., Hemichelation, a Way To Stabilize Electron-Unsaturated Complexes: The Case of T-Shaped Pd and Pt Metallacycles. *J. Am. Chem. Soc.* **2013,** *135* (47), 17839-17852.

339. te Velde, G.; Bickelhaupt, F. M.; Baerends, E. J.; Fonseca Guerra, C.; van Gisbergen, S. J. A.; Snijders, J. G.; Ziegler, T., Chemistry with ADF. *J. Comput. Chem.* **2001,** *22* (9), 931-967.

340. Lenthe, E. v.; Ehlers, A.; Baerends, E.-J., Geometry optimizations in the zero order regular approximation for relativistic effects. *J. Chem. Phys.* **1999,** *110* (18), 8943-8953.

341. Caldeweyher, E.; Ehlert, S.; Hansen, A.; Neugebauer, H.; Spicher, S.; Bannwarth, C.; Grimme, S., A generally applicable atomic-charge dependent London dispersion correction. *J. Chem. Phys.* **2019,** *150* (15), 154122.

342. Pye, C. C.; Ziegler, T., An implementation of the conductor-like screening model of solvation within the Amsterdam density functional package. *Theor. Chem. Acc.* **1999,** *101* (6), 396-408.

343. Khartabil, H.; Doudet, L.; Allart-Simon, I.; Ponce-Vargas, M.; Gérard, S.; Hénon, E., Mechanistic insights into Smiles rearrangement. Focus on π–π stacking interactions along the radical cascade. *Org. Biomol. Chem.* **2020,** *18* (35), 6840-6848.

344. Iwakura, I.; Ikeno, T.; Yamada, T., A DFT Study on Hetero-Diels–Alder Reactions Catalyzed by Cobalt Complexes: Lewis Acidity Enhancement as a Consequence of Spin Transition Caused by Lewis Base Coordination. *Angew. Chem. Int. Ed.* **2005,** *44*, 2524-2527.

345. Sun, J.; Deng, L., Cobalt Complex-Catalyzed Hydrosilylation of Alkenes and Alkynes. *ACS Catal.* **2016,** *6* (1), 290-300.

346. Binh, D. H.; Milovanović, M.; Puertes-Mico, J.; Hamdaoui, M.; Zarić, S. D.; Djukic, J.-P., Is the R3Si Moiety in Metal–Silyl Complexes a Z ligand? An Answer from the Interaction Energy. *Chem. Eur. J.* **2017,** *23* (67), 17058-17069.

347. Harrod, J. F.; Chalk, A. J., Dicobalt Octacarbonyl as a Catalyst for Hydrosilation of Olefins. *J. Am. Chem. Soc.* **1965,** *87* (5), 1133-1133.

348. Chalk, A. J.; Harrod, J. F., Homogeneous Catalysis. IV. Some Reactions of Silicon Hydrides in the Presence of Cobalt Carbonyls. *J. Am. Chem. Soc.* **1967,** *89* (7), 1640-1647.

349. Reichel, C. L.; Wrighton, M. S., Photochemistry of cobalt carbonyl complexes having a cobalt-silicon bond and its importance in activation of catalysis. *Inorg. Chem.* **1980,** *19* (12), 3858-3860.

350. Skrodzki, M.; Patroniak, V.; Pawluć, P., Schiff Base Cobalt(II) Complex-Catalyzed Highly Markovnikov-Selective Hydrosilylation of Alkynes. *Org. Lett.* **2021,** *23* (3), 663-667.

351. Cheng, Z.; Guo, J.; Sun, Y.; Zheng, Y.; Zhou, Z.; Lu, Z., Regio-controllable Cobalt-Catalyzed Sequential Hydrosilylation/Hydroboration of Arylacetylenes. *Angew. Chem. Int. Ed.* **2021,** *60* (41), 22454-22460.

352. Iannetelli, A.; Da Costa, R. C.; Guwy, A. J.; Tizzard, G. J.; Coles, S. J.; Owen, G. R., Transformation of a Norbornadiene Unit to Ethylenylcyclopentene Requiring Cooperation between Boron and Rhodium Centers. *Organometallics* **2020,** *39* (10), 1976-1988.

353. Palmer, W. N.; Diao, T.; Pappas, I.; Chirik, P. J., High-Activity Cobalt Catalysts for Alkene Hydroboration with Electronically Responsive Terpyridine and α-Diimine Ligands. *ACS Catal.* **2014,** *5* (2), 622-626.

354. Ruddy, A. J.; Sydora, O. L.; Small, B. L.; Stradiotto, M.; Turculet, L., (N-phosphinoamidinate)cobalt-catalyzed hydroboration: alkene isomerization affords terminal selectivity. *Chemistry* **2014,** *20* (43), 13918-22.

355. Kikuchi, T.; Nobuta, Y.; Umeda, J.; Yamamoto, Y.; Ishiyama, T.; Miyaura, N., Practical synthesis of pinacolborane for one-pot synthesis of unsymmetrical biaryls via aromatic C–H borylation–cross-coupling sequence. *Tetrahedron* **2008,** *64* (22), 4967-4971.

356. Frith, S. A.; Spencer, J., Inorganic Syntheses: Reagents for Transition Metal Complex and Organometallic Syntheses. In *Inorganic Syntheses*, Angelici, R. J., Ed. **2007**; Vol. 28, pp 273-277.

357. Li, W.; Weng, L.-H.; Jin, G.-X., Hetero-nuclear Co–W complex Cp*CoW(CO)$_2$[Se$_2$C$_2$(B$_{10}$H$_{10}$)]$_2$ from 16-electron half-sandwich complex Cp*Co[Se$_2$C$_2$(B$_{10}$H$_{10}$)]. *Inorg. Chem. Commun.* **2004,** *7* (11), 1174-1177.

358. *M86-EXX229V1 APEX3 User Manual*. Bruker AXS Inc.: Madison, USA, **2016**.

359. Sheldrick, G., SHELXT - Integrated space-group and crystal-structure determination. *Acta Cryst. A* **2015,** *71* (1), 3-8.

360. Sheldrick, G., Crystal structure refinement with SHELXL. *Acta Cryst. C* **2015,** *71* (1), 3-8.

361. Spek, A., Single-crystal structure validation with the program PLATON. *J. Appl. Cryst.* **2003,** *36* (1), 7-13.

362. Sucunza, D.; Cuadro, A. M.; Alvarez-Builla, J.; Vaquero, J. J., Recent Advances in the Synthesis of Azonia Aromatic Heterocycles. *J. Org. Chem.* **2016,** *81* (21), 10126-10135.

363. te Velde, G.; Bickelhaupt, F. M.; Baerends, E. J.; Fonseca Guerra, C.; van Gisbergen, S. J. A.; Snijders, J. G.; Ziegler, T., Chemistry with ADF. *J. Comp. Chem.* **2001,** *22* (9), 931-967.

364. Eisenschitz, R.; London, F., Über das Verhältnis der van der Waalsschen Kräfte zu den homöopolaren Bindungskräften. *Z. Physik* **1930,** *60* (7), 491-527.

365. London, F., The general theory of molecular forces. *Trans. Faraday Soc.* **1937,** *33* (0), 8b-26.

366. van Lenthe, E.; Baerends, E. J.; Snijders, J. G., Relativistic regular two-component Hamiltonians. *J. Chem. Phys.* **1993,** *99* (6), 4597-4610.

367. van Lenthe, E.; Baerends, E. J.; Snijders, J. G., Relativistic total energy using regular approximations. *J. Chem. Phys.* **1994,** *101* (11), 9783-9792.

368. van Lenthe, E.; Ehlers, A.; Baerends, E.-J., Geometry optimizations in the zero order regular approximation for relativistic effects. *J. Chem. Phys.* **1999,** *110* (18), 8943-8953.

369. Macrae, C. F.; Sovago, I.; Cottrell, S. J.; Galek, P. T. A.; McCabe, P.; Pidcock, E.; Platings, M.; Shields, G. P.; Stevens, J. S.; Towler, M.; Wood, P. A., Mercury 4.0: from visualization to analysis, design and prediction. *J. Appl. Cryst.* **2020,** *53* (1), 226-235.

370. Weigend, F.; Ahlrichs, R., Balanced basis sets of split valence, triple zeta valence and quadruple zeta valence quality for H to Rn: Design and assessment of accuracy. *Phys. Chem. Chem. Phys.* **2005,** *7*, 3297-3305.

371. Velde, G. t.; Bickelhaupt, F. M.; Baerends, E. J.; Guerra, C. F.; Gisbergen, S. J. A. v.; Snijders, J. G.; Ziegler, T., Chemistry with ADF. *J. Comput. Chem.* **2001,** *22*, 931-967.

372. Perdew, J. P.; Burke, K.; Ernzerhof, M., Generalized Gradient Approximation Made Simple. *Phys. Rev. Lett.* **1996,** *77*, 3865-3868.

373. Caldeweyher, E.; Ehlert, S.; Hansen, A.; Neugebauer, H.; Spicher, S.; Bannwarth, C.; Grimme, S., A generally applicable atomi-charge dependent London dispersion correction. *J. Chem. Phys* **2019,** *150*, 154122.

374. Lenthe, E. v.; Baerends, E. J.; Snijers, J. G., Relativistic regular two-component Hamiltonians. *J. Chem. Phys.* **1993,** *99*, 4597-4610.

375. Lenthe, E. v.; Baerends, E. J.; Snijders, J. G., Relativistic total energy using regular approximations. *J. Chem. Phys.* **1994,** *101*, 9783-9792.

376. Lenthe, E. v.; Ehlers, A.; Baerends, E. J., Geometry optimizations in the zero order regular approximation for relativistic effects. *J. Chem. Phys.* **1999,** *110*, 8943-8953.

377. Klamt, A.; Schüürmann, G., COSMO: a new approach to dielectric screening in solvent with explicit expressions for the screening energy and its gradient. . *J. Chem. Soc., Perkin Trans.2* **1993**, 799-805.

378. Klamt, A., Conductor-like Screening Model for real solvents: a new approach to the quantitative calculation of solvation phenomena. *J. Phys. Chem.* **1995,** *99*, 2224-2235.

379. Klamt, A.; Jonas, V., Treatment of the outlying charge in continuum solvation models. *J. Chem. Phys.* **1996,** *105*, 9972-9981.

380. Franchini, M.; Philipsen, P. H. T.; Visscher, L., The Becke fuzzy cells integration scheme in the Amsterdam Density Functional program suite. *J. Comput. Chem.* **2013,** *34*, 1819-1827.

381. Henkelmann, G.; Uberuaga, B. P.; Jonsson, H., A climbing image nudged elastic band method for finding saddle points and minimum energy paths. *J. Chem. Phys.* **2000,** *113*, 9901-9904.

382. Deng, L.; Ziegler, T., Reaction path following in mass-weighted internal corrdinates. *Int. J. Quantum Chem.* **1990,** *94*, 5523-5527.

383. Deng, L.; Ziegler, T.; Fan, L., A combined density functional and intrinsic reaction coordinate study on the ground state energy surface of H2CO. *J. Chem. Phys.* **1993,** *99*, 3823.

384. Lefebvre, C.; Rubez, G.; Khartabil, H.; Boisson, J.-C.; Contreras-Garcia, J.; Hénon, E., *Phys. Chem. Chem. Phys.* **2017,** *19*, 17928-17936.

385. Lefebvre, C.; Khartabil, H.; Boisson, J.-C.; Contreras-Garcia, J.; Hénon, E., *ChemPhysChem.* **2018,** *19*, 724-735.

386. Grimme, S.; Antony, J.; Ehrlich, S.; Krieg, H., A consistent and accurate ab initio parametrization of density functional dispersion correction (DFT-D) for the 94 elements H-Pu. *J. Chem. Phys.* **2010,** *132*, 154104.

387. Grimme, S.; Ehrlich, S.; Goerigk, L., Effect of the damping function in dispersion corrected density functional theory. *J. Comput. Chem.* **2011,** *32*, 1456-1465.

388. Barone, V.; Cossi, M., Quantum calculation of molecular energies and energy gradients in solution by a conductor solvent model. *J. Phys. Chem.* **1998,** *102*, 1995-2001.

389. Neese, F., The ORCA program system. *WIREs Comput. Mol. Sci.* **2012,** *2*, 73-78.

390. Bahr, S. R.; Boudjouk, P., Trityl Tetrakis(3,5-Bis(Trifluoromethyl)Phenyl)Borate - a New Hydride Abstraction Reagent. *J. Org. Chem.* **1992,** *57* ( (20)), 5545-5547.

391. O'Brien, Z. J.; Karlen, S. D.; Khan, S.; Garcia-Garibay, M. A., Solid-State Molecular Rotors with Perdeuterated Stators: Mechanistic Insights from Biphenylene Rotational Dynamics in Ordered and Disordered Crystal Forms. *J. Org. Chem.* **2010,** *75* ( (8)), 2482-2491.

392. Moran, M., Reactions of (η-$C_5H_5$)$Co(CO)_2$ and (η-$EtMe_4C_5$)$Co(CO)_2$ with iodine and cyanogen halides, XCN (X = Br or I). *Z. Naturforsch., B: Anorg. Chem., Org. Chem.* **1981,** *36*, 431-3.

393. Roe, D. M.; Maitlis, P. M., Disproportionation of dihalogenocyclopentadienylcobalt complexes to cobaltocenium salts. *J. Chem. Soc. A: Inorg. Phys. Theor.* **1971,** (0), 3173-3175.

394. Knizhnikov, V. A.; Shirokii, V. L.; Sutormin, A. B.; Novikova, M. G.; Maier, N. A.; Ol'dekop, Y. A., Reactions of cyclopentadienyl(cyclopentadiene)cobalt with iodine. *Metalloorg. Khim.* **1989,** *2*, 1160-2.

395. Shirokii, V. L.; Knizhnikov, V. A.; Mosin, A. V.; Novikova, M. G.; Maier, N. A.; Ol'dekop, Y. A., Electrochemical synthesis of ($\eta^5$-cyclopentadienyl)cobalt-$\eta^4$-tetraphenylbutadienes and their interaction with iodine. *Metalloorg. Khim.* **1991,** *4*, 1059-63.

396. Pauson, P. L., Bis(cyclopentadienyl)cobalt. John Wiley & Sons, Ltd.: **2001**; 1-2.

397. Liu, X.-G.; Li, Q.; Wang, H., (Pentamethylcyclopentadienyl)cobalt(III)-Catalyzed Direct Trifluoromethylthiolation of Arenes via C−H Activation. *Adv. Synth. Catal.* **2017,** *359* (11), 1942-1946.

398. Thompson, M. C.; Busch, D. H., Reactions of Coordinated Ligands. VI. Metal Ion Control in the Synthesis of Planar Nickel(II) Complexes of α-Diketo-bis-mercaptoimines. *J. Am. Chem. Soc.* **1964,** *86* (2), 213-217.

399. Costes, J.-P.; Chiboub Fellah, F. Z.; Dahan, F.; Duhayon, C., Role of the kinetic template effect in the syntheses of non symmetric Schiff base complexes. *Polyhedron* **2013,** *52*, 1065-1072.

400. Dötz, K. H.; Stendel, J., Fischer Carbene Complexes in Organic Synthesis: Metal-Assisted and Metal-Templated Reactions. *Chem. Rev.* **2009,** *109* (8), 3227-3274.

401. Dötz, K. H.; Wenzel, B.; Jahr, H. C., Chromium-Templated Benzannulation and Haptotropic Metal Migration. In *Templates in Chemistry I: -/-*, Schalley, C. A.; Vögtle, F.; Dötz, K. H., Eds. Springer Berlin Heidelberg: Berlin, Heidelberg, **2004**; 63-103.

# Annexes I

# Single crystal X-ray diffraction

## X-ray structure of 1a

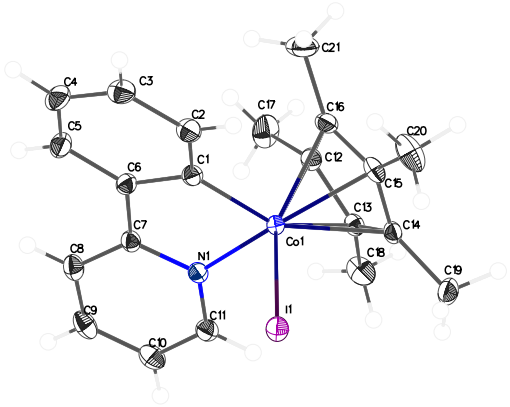


**Table A. 1. Crystal data and structure refinement for 1a.**

| | |
|---|---|
| Identification code | **1a** |
| Empirical formula | $C_{21}H_{23}NCoI$ |
| Formula weight | 475.23 |
| Temperature/K | 120(2) |
| Crystal system | monoclinic |
| Space group | *P2₁/c* |
| a/Å | 13.2639(7) |
| b/Å | 9.0025(5) |
| c/Å | 16.0264(10) |
| α/° | 90 |
| β/° | 103.938(2) |
| γ/° | 90 |
| Volume/Å$^3$ | 1857.34(18) |
| Z | 4 |
| $\rho_{calc}$g/cm$^3$ | 1.700 |
| μ/mm$^{-1}$ | 2.588 |
| F(000) | 944.0 |
| Crystal size/mm$^3$ | 0.2 × 0.18 × 0.15 |
| Radiation | MoKα (λ = 0.71073) |
| 2Θ range for data collection/° | 5.228 to 60.048 |
| Index ranges | -18 ≤ h ≤ 18, -12 ≤ k ≤ 12, -22 ≤ l ≤ 22 |
| Reflections collected | 68361 |
| Independent reflections | 5434 [$R_{int}$ = 0.0255, $R_{sigma}$ = 0.0109] |
| Data/restraints/parameters | 5434/0/222 |
| Goodness-of-fit on F$^2$ | 1.074 |
| Final R indexes [I>=2σ (I)] | $R_1$ = 0.0159, $wR_2$ = 0.0380 |
| Final R indexes [all data] | $R_1$ = 0.0180, $wR_2$ = 0.0393 |
| Largest diff. peak/hole / e Å$^{-3}$ | 0.47/-0.48 |

## X-ray structure of 4a

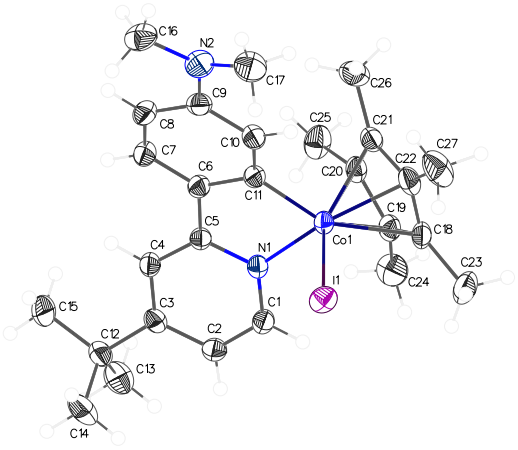


**Table A. 2. Crystal data and structure refinement for 4a.**

| | |
|---|---|
| Identification code | **4a** |
| Empirical formula | $C_{27}H_{36}CoIN_2$ |
| Formula weight | 574.41 |
| Temperature/K | 173(2) |
| Crystal system | triclinic |
| Space group | *P-1* |
| a/Å | 8.6481(3) |
| b/Å | 11.3372(5) |
| c/Å | 13.9563(6) |
| α/° | 78.3310(10) |
| β/° | 75.4490(10) |
| γ/° | 84.3210(10) |
| Volume/Å$^3$ | 1295.41(9) |
| Z | 2 |
| $\rho_{calc}$g/cm$^3$ | 1.473 |
| μ/mm$^{-1}$ | 1.870 |
| F(000) | 584.0 |
| Crystal size/mm$^3$ | 0.16 × 0.1 × 0.08 |
| Radiation | MoKα (λ = 0.71073) |
| 2Θ range for data collection/° | 3.674 to 60.392 |
| Index ranges | -12 ≤ h ≤ 12, -16 ≤ k ≤ 16, -19 ≤ l ≤ 19 |
| Reflections collected | 39425 |
| Independent reflections | 7644 [$R_{int}$ = 0.0342, $R_{sigma}$ = 0.0293] |
| Data/restraints/parameters | 7644/0/290 |
| Goodness-of-fit on $F^2$ | 1.005 |
| Final R indexes [I>=2σ (I)] | $R_1$ = 0.0275, $wR_2$ = 0.0548 |
| Final R indexes [all data] | $R_1$ = 0.0455, $wR_2$ = 0.0600 |
| Largest diff. peak/hole / e Å$^{-3}$ | 0.79/-0.42 |

## X-ray structure of 5a

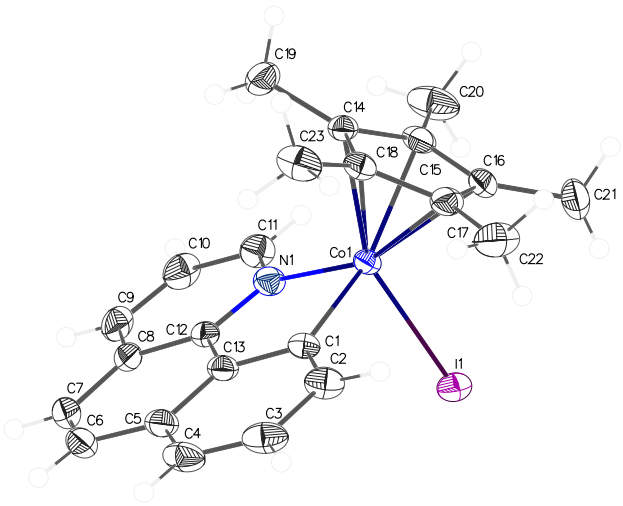


**Table A. 3. Crystal data and structure refinement for 5a.**

| | |
|---|---|
| Identification code | **5a** |
| Empirical formula | $C_{23}H_{23}CoIN$ |
| Formula weight | 499.25 |
| Temperature/K | 173(2) |
| Crystal system | monoclinic |
| Space group | $P2_1/n$ |
| a/Å | 8.2480(5) |
| b/Å | 14.5894(9) |
| c/Å | 16.1813(10) |
| α/° | 90 |
| β/° | 99.481(2) |
| γ/° | 90 |
| Volume/Å$^3$ | 1920.6(2) |
| Z | 4 |
| $\rho_{calc}$g/cm$^3$ | 1.727 |
| μ/mm$^{-1}$ | 2.507 |
| F(000) | 992.0 |
| Crystal size/mm$^3$ | 0.350 × 0.200 × 0.150 |
| Radiation | MoKα (λ = 0.71073) |
| 2Θ range for data collection/° | 3.782 to 60.118 |
| Index ranges | -10 ≤ h ≤ 11, -20 ≤ k ≤ 20, -22 ≤ l ≤ 22 |
| Reflections collected | 49203 |
| Independent reflections | 5625 [$R_{int}$ = 0.0170, $R_{sigma}$ = 0.0085] |
| Data/restraints/parameters | 5625/0/240 |
| Goodness-of-fit on F$^2$ | 1.257 |
| Final R indexes [I>=2σ (I)] | $R_1$ = 0.0238, $wR_2$ = 0.0555 |
| Final R indexes [all data] | $R_1$ = 0.0252, $wR_2$ = 0.0560 |
| Largest diff. peak/hole / e Å$^{-3}$ | 0.54/-0.46 |

## X-ray structure of 7a

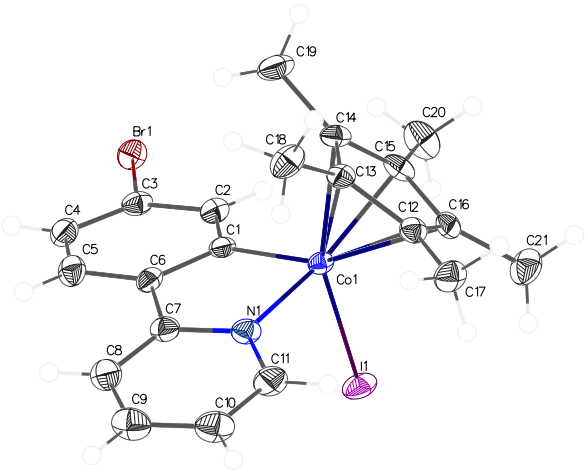


**Table A. 4. Crystal data and structure refinement for 7a.**

| | |
|---|---|
| Identification code | **7a** |
| Empirical formula | $C_{21}H_{22}NBrICo$ |
| Formula weight | 554.13 |
| Temperature/K | 120(2) |
| Crystal system | monoclinic |
| Space group | $P2_1/c$ |
| a/Å | 14.2524(7) |
| b/Å | 8.5837(4) |
| c/Å | 16.6810(8) |
| α/° | 90 |
| β/° | 100.395(2) |
| γ/° | 90 |
| Volume/Å$^3$ | 2007.23(17) |
| Z | 4 |
| $\rho_{calc}$g/cm$^3$ | 1.834 |
| μ/mm$^{-1}$ | 4.387 |
| F(000) | 1080.0 |
| Crystal size/mm$^3$ | 0.160 × 0.120 × 0.100 |
| Radiation | MoKα (λ = 0.71073) |
| 2Θ range for data collection/° | 4.966 to 55.87 |
| Index ranges | -18 ≤ h ≤ 18, -11 ≤ k ≤ 10, -21 ≤ l ≤ 21 |
| Reflections collected | 63902 |
| Independent reflections | 4797 [$R_{int}$ = 0.0672, $R_{sigma}$ = 0.0268] |
| Data/restraints/parameters | 4797/0/231 |
| Goodness-of-fit on F$^2$ | 1.136 |
| Final R indexes [I>=2σ (I)] | $R_1$ = 0.0398, $wR_2$ = 0.0933 |
| Final R indexes [all data] | $R_1$ = 0.0509, $wR_2$ = 0.0983 |
| Largest diff. peak/hole / e Å$^{-3}$ | 0.87/-0.81 |

## X-ray structure of 8a

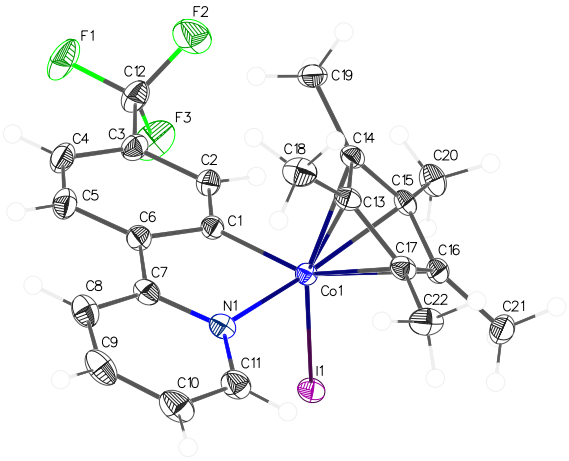


**Table A. 5. Crystal data and structure refinement for 8a.**

| | |
|---|---|
| Identification code | **8a** |
| Empirical formula | $C_{22}H_{22}NF_3CoI$ |
| Formula weight | 543.23 |
| Temperature/K | 120(2) |
| Crystal system | monoclinic |
| Space group | $P2_1/c$ |
| a/Å | 17.0641(6) |
| b/Å | 14.0385(5) |
| c/Å | 8.7326(3) |
| α/° | 90 |
| β/° | 91.7390(10) |
| γ/° | 90 |
| Volume/Å$^3$ | 2090.97(13) |
| Z | 4 |
| $\rho_{calc}$g/cm$^3$ | 1.726 |
| μ/mm$^{-1}$ | 2.330 |
| F(000) | 1072.0 |
| Crystal size/mm$^3$ | 0.220 × 0.140 × 0.120 |
| Radiation | MoKα (λ = 0.71073) |
| 2Θ range for data collection/° | 4.776 to 55.814 |
| Index ranges | -22 ≤ h ≤ 22, -18 ≤ k ≤ 16, -11 ≤ l ≤ 11 |
| Reflections collected | 71245 |
| Independent reflections | 5006 [$R_{int}$ = 0.0350, $R_{sigma}$ = 0.0131] |
| Data/restraints/parameters | 5006/0/258 |
| Goodness-of-fit on F$^2$ | 1.093 |
| Final R indexes [I>=2σ (I)] | $R_1$ = 0.0173, w$R_2$ = 0.0372 |
| Final R indexes [all data] | $R_1$ = 0.0206, w$R_2$ = 0.0389 |
| Largest diff. peak/hole / e Å$^{-3}$ | 0.37/-0.29 |

## X-ray structure of 10a

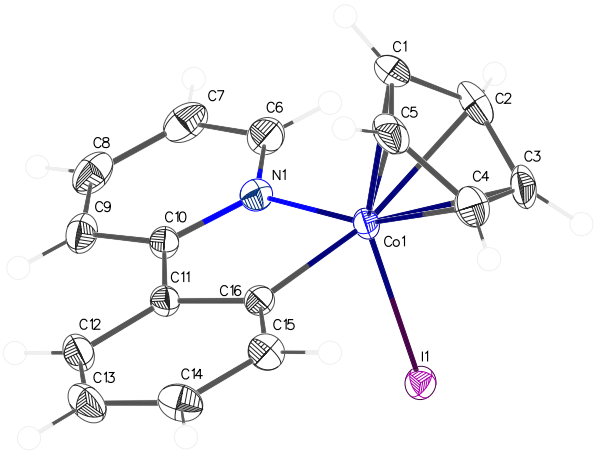


**Table A. 6. Crystal data and structure refinement for 10a.**

| | |
|---|---|
| Identification code | **10a** |
| Empirical formula | $C_{16}H_{13}CoIN$ |
| Formula weight | 405.10 |
| Temperature/K | 120(2) |
| Crystal system | monoclinic |
| Space group | *P2₁/c* |
| a/Å | 10.2517(3) |
| b/Å | 8.4219(3) |
| c/Å | 16.2038(5) |
| α/° | 90 |
| β/° | 97.8910(10) |
| γ/° | 90 |
| Volume/Å$^3$ | 1385.77(8) |
| Z | 4 |
| $\rho_{calc}$g/cm$^3$ | 1.942 |
| μ/mm$^{-1}$ | 3.450 |
| F(000) | 784.0 |
| Crystal size/mm$^3$ | 0.120 × 0.100 × 0.080 |
| Radiation | MoKα (λ = 0.71073) |
| 2Θ range for data collection/° | 4.01 to 58.052 |
| Index ranges | -13 ≤ h ≤ 13, -11 ≤ k ≤ 11, -22 ≤ l ≤ 22 |
| Reflections collected | 42371 |
| Independent reflections | 3676 [$R_{int}$ = 0.0371, $R_{sigma}$ = 0.0164] |
| Data/restraints/parameters | 3676/0/172 |
| Goodness-of-fit on F$^2$ | 1.117 |
| Final R indexes [I>=2σ (I)] | $R_1$ = 0.0214, $wR_2$ = 0.0445 |
| Final R indexes [all data] | $R_1$ = 0.0268, $wR_2$ = 0.0468 |
| Largest diff. peak/hole / e Å$^{-3}$ | 0.84/-0.55 |

## X-ray structure of 1b

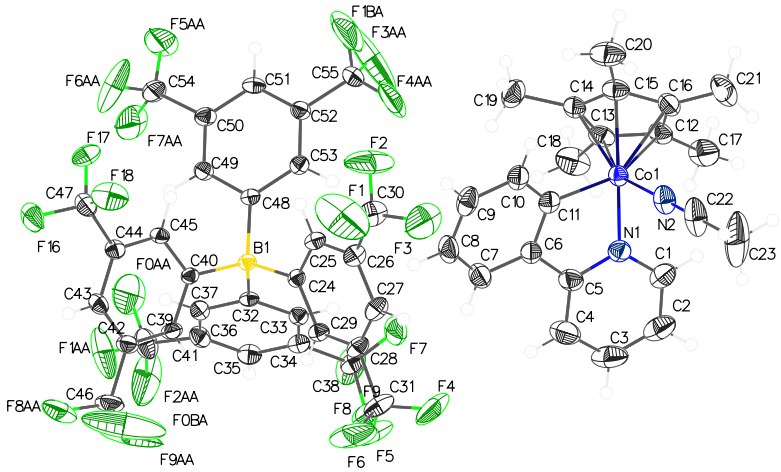


**Table A. 7. Crystal data and structure refinement for 1b.**

| | |
|---|---|
| Identification code | **1b** |
| Empirical formula | $C_{55}H_{38}BCoF_{24}N_2$ |
| Formula weight | 1252.61 |
| Temperature/K | 173(2) |
| Crystal system | triclinic |
| Space group | *P-1* |
| a/Å | 12.5894(6) |
| b/Å | 13.1911(6) |
| c/Å | 17.0725(8) |
| α/° | 91.818(2) |
| β/° | 97.890(2) |
| γ/° | 107.1210(10) |
| Volume/Å$^3$ | 2676.1(2) |
| Z | 2 |
| $\rho_{calc}$g/cm$^3$ | 1.555 |
| μ/mm$^{-1}$ | 0.445 |
| F(000) | 1260.0 |
| Crystal size/mm$^3$ | 0.35 × 0.25 × 0.12 |
| Radiation | MoKα (λ = 0.71073) |
| 2Θ range for data collection/° | 3.24 to 55.968 |
| Index ranges | -16 ≤ h ≤ 16, -17 ≤ k ≤ 17, -22 ≤ l ≤ 22 |
| Reflections collected | 114918 |
| Independent reflections | 12762 [$R_{int}$ = 0.0643, $R_{sigma}$ = 0.0532] |
| Data/restraints/parameters | 12762/0/751 |
| Goodness-of-fit on F$^2$ | 1.017 |
| Final R indexes [I>=2σ (I)] | $R_1$ = 0.0938, w$R_2$ = 0.1985 |
| Final R indexes [all data] | $R_1$ = 0.1313, w$R_2$ = 0.2194 |
| Largest diff. peak/hole / e Å$^{-3}$ | 1.47/-1.05 |

## X-ray structure of 3b

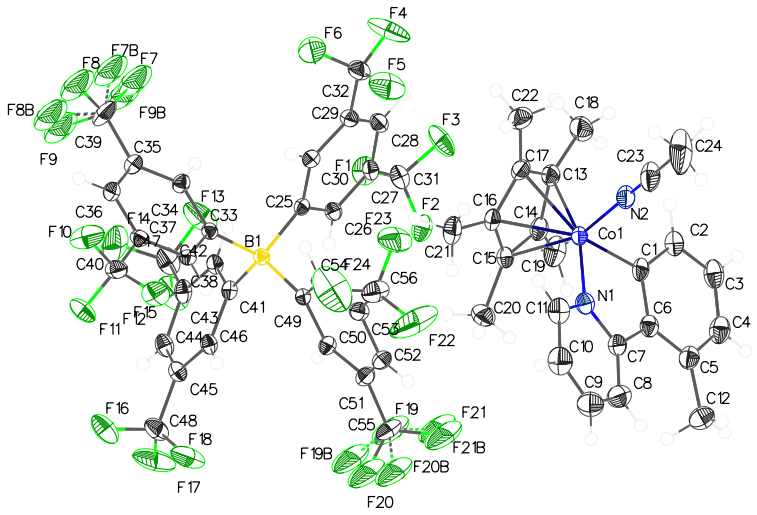


**Table A. 8. Crystal data and structure refinement for 3b.**

| | |
|---|---|
| Identification code | **3b** |
| Empirical formula | $C_{56}H_{40}BCoF_{24}N_2$ |
| Formula weight | 1266.64 |
| Temperature/K | 120(2) |
| Crystal system | triclinic |
| Space group | *P-1* |
| a/Å | 12.5987(5) |
| b/Å | 13.3136(5) |
| c/Å | 17.2460(7) |
| α/° | 93.019(2) |
| β/° | 97.6630(10) |
| γ/° | 106.9780(10) |
| Volume/Å$^3$ | 2729.12(19) |
| Z | 2 |
| $\rho_{calc}$g/cm$^3$ | 1.541 |
| μ/mm$^{-1}$ | 0.437 |
| F(000) | 1276.0 |
| Crystal size/mm$^3$ | 0.200 × 0.150 × 0.100 |
| Radiation | MoKα (λ = 0.71073) |
| 2Θ range for data collection/° | 3.858 to 55.86 |
| Index ranges | -16 ≤ h ≤ 16, -17 ≤ k ≤ 17, -22 ≤ l ≤ 22 |
| Reflections collected | 139336 |
| Independent reflections | 13075 [$R_{int}$ = 0.0385, $R_{sigma}$ = 0.0168] |
| Data/restraints/parameters | 13075/0/758 |
| Goodness-of-fit on F$^2$ | 1.040 |
| Final R indexes [I>=2σ (I)] | $R_1$ = 0.0700, $wR_2$ = 0.1824 |
| Final R indexes [all data] | $R_1$ = 0.0768, $wR_2$ = 0.1894 |
| Largest diff. peak/hole / e Å$^{-3}$ | 2.17/-1.57 |

## X-ray structure of 4b

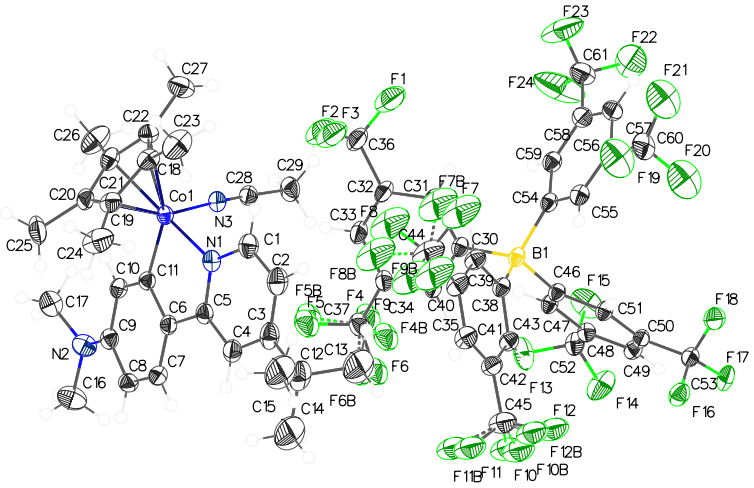


**Table A. 9. Crystal data and structure refinement for 4b.**

| | |
|---|---|
| Identification code | **4b** |
| Empirical formula | $C_{61}H_{51}BCoF_{24}N_3$ |
| Formula weight | 1351.79 |
| Temperature/K | 120(2) |
| Crystal system | triclinic |
| Space group | *P-1* |
| a/Å | 14.6865(7) |
| b/Å | 15.3384(8) |
| c/Å | 16.6795(8) |
| α/° | 99.496(2) |
| β/° | 98.116(2) |
| γ/° | 109.430(2) |
| Volume/Å$^3$ | 3416.3(3) |
| Z | 2 |
| $\rho_{calc}$g/cm$^3$ | 1.314 |
| μ/mm$^{-1}$ | 0.354 |
| F(000) | 1372.0 |
| Crystal size/mm$^3$ | 0.180 × 0.100 × 0.080 |
| Radiation | MoKα (λ = 0.71073) |
| 2Θ range for data collection/° | 4.168 to 64.096 |
| Index ranges | -21 ≤ h ≤ 21, -22 ≤ k ≤ 22, -24 ≤ l ≤ 24 |
| Reflections collected | 143751 |
| Independent reflections | 23751 [$R_{int}$ = 0.0473, $R_{sigma}$ = 0.0363] |
| Data/restraints/parameters | 23751/0/777 |
| Goodness-of-fit on F$^2$ | 1.060 |
| Final R indexes [I>=2σ (I)] | $R_1$ = 0.0823, $wR_2$ = 0.2268 |
| Final R indexes [all data] | $R_1$ = 0.1100, $wR_2$ = 0.2521 |
| Largest diff. peak/hole / e Å$^{-3}$ | 1.71/-1.95 |

## X-ray structure of 5b

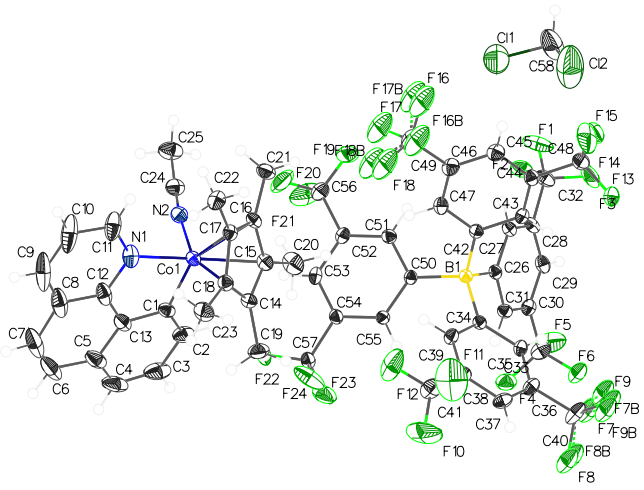


**Table A. 10. Crystal data and structure refinement for 5b.**

| | |
|---|---|
| Identification code | **5b** |
| Empirical formula | $C_{58}H_{40}BCl_2CoF_{24}N_2$ |
| Formula weight | 1361.56 |
| Temperature/K | 120(2) |
| Crystal system | triclinic |
| Space group | *P-1* |
| a/Å | 12.3000(7) |
| b/Å | 12.8438(8) |
| c/Å | 18.7707(11) |
| α/° | 87.846(2) |
| β/° | 81.776(2) |
| γ/° | 74.818(2) |
| Volume/Å$^3$ | 2832.4(3) |
| Z | 2 |
| $\rho_{calc}$g/cm$^3$ | 1.596 |
| μ/mm$^{-1}$ | 0.518 |
| F(000) | 1368.0 |
| Crystal size/mm$^3$ | 0.200 × 0.150 × 0.120 |
| Radiation | MoKα (λ = 0.71073) |
| 2Θ range for data collection/° | 3.836 to 55.856 |
| Index ranges | -16 ≤ h ≤ 16, -16 ≤ k ≤ 16, -24 ≤ l ≤ 24 |
| Reflections collected | 199456 |
| Independent reflections | 13555 [$R_{int}$ = 0.0499, $R_{sigma}$ = 0.0183] |
| Data/restraints/parameters | 13555/0/793 |
| Goodness-of-fit on F$^2$ | 1.044 |
| Final R indexes [I>=2σ (I)] | $R_1$ = 0.0715, $wR_2$ = 0.1967 |
| Final R indexes [all data] | $R_1$ = 0.0798, $wR_2$ = 0.2062 |
| Largest diff. peak/hole / e Å$^{-3}$ | 1.99/-1.88 |

## X-ray structure of 1b'

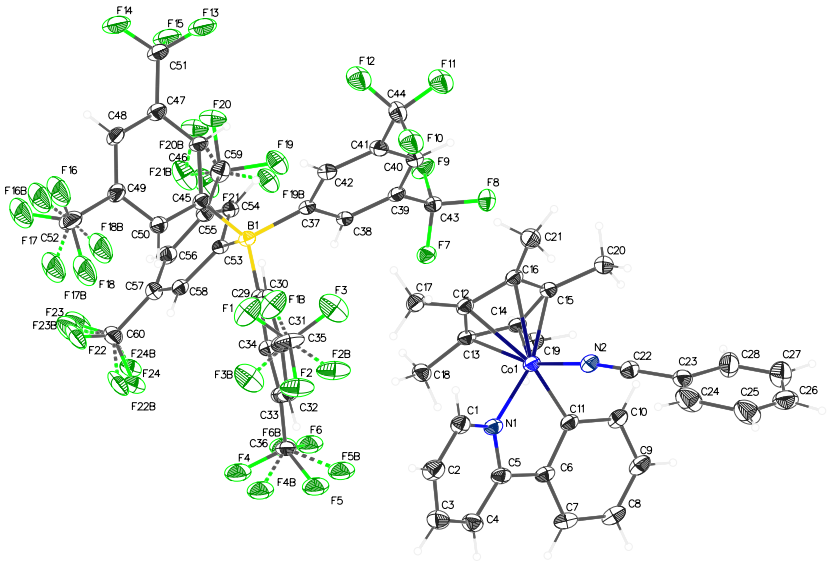

**Table A. 11. Crystal data and structure refinement for 1b'.**

| | |
|---|---|
| Identification code | **1b'** |
| Empirical formula | $C_{60}H_{40}BN_2F_{24}Co$ |
| Formula weight | 1314.68 |
| Temperature/K | 120(2) |
| Crystal system | monoclinic |
| Space group | $P2_1/c$ |
| a/Å | 12.5306(5) |
| b/Å | 29.9654(12) |
| c/Å | 20.1159(8) |
| α/° | 90 |
| β/° | 122.181(3) |
| γ/° | 90 |
| Volume/Å$^3$ | 6392.8(5) |
| Z | 4 |
| $\rho_{calc}$g/cm$^3$ | 1.366 |
| μ/mm$^{-1}$ | 3.076 |
| F(000) | 2648.0 |
| Crystal size/mm$^3$ | 0.14 × 0.1 × 0.06 |
| Radiation | CuKα (λ = 1.54178) |
| 2Θ range for data collection/° | 5.898 to 133.44 |
| Index ranges | -14 ≤ h ≤ 14, -35 ≤ k ≤ 35, -23 ≤ l ≤ 23 |
| Reflections collected | 108746 |
| Independent reflections | 11302 [$R_{int}$ = 0.1136, $R_{sigma}$ = 0.0683] |
| Data/restraints/parameters | 11302/4/789 |
| Goodness-of-fit on F$^2$ | 1.373 |
| Final R indexes [I>=2σ (I)] | $R_1$ = 0.1071, $wR_2$ = 0.3277 |
| Final R indexes [all data] | $R_1$ = 0.1346, $wR_2$ = 0.3569 |
| Largest diff. peak/hole / e Å$^{-3}$ | 1.32/-0.89 |

## X-ray structure of 1f

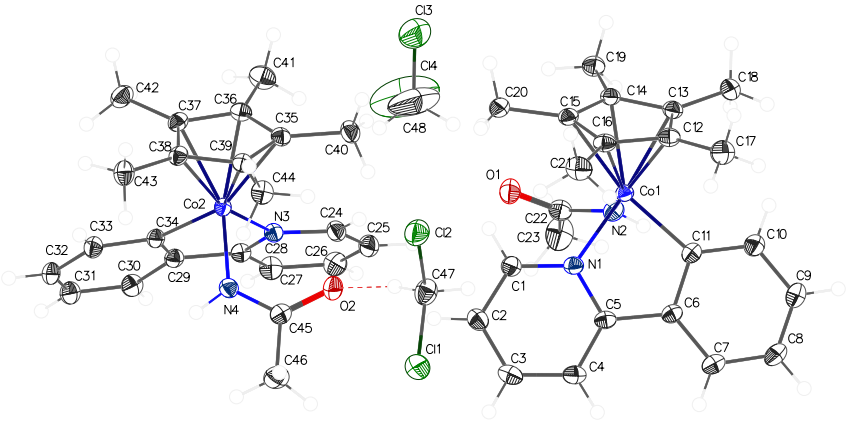


**Table A. 12. Crystal data and structure refinement for 1f.**

| | |
|---|---|
| Identification code | **1f** |
| Empirical formula | $C_{24}H_{29}Cl_2CoN_2O$ |
| Formula weight | 491.32 |
| Temperature/K | 120(2) |
| Crystal system | triclinic |
| Space group | *P-1* |
| a/Å | 13.0238(6) |
| b/Å | 13.1444(6) |
| c/Å | 15.2024(8) |
| α/° | 88.651(2) |
| β/° | 71.961(2) |
| γ/° | 71.357(2) |
| Volume/Å$^3$ | 2336.5(2) |
| Z | 4 |
| $\rho_{calc}$g/cm$^3$ | 1.397 |
| μ/mm$^{-1}$ | 0.981 |
| F(000) | 1024.0 |
| Crystal size/mm$^3$ | 0.220 × 0.180 × 0.150 |
| Radiation | MoKα (λ = 0.71073) |
| 2Θ range for data collection/° | 3.922 to 58.364 |
| Index ranges | -17 ≤ h ≤ 17, -17 ≤ k ≤ 18, -20 ≤ l ≤ 20 |
| Reflections collected | 177479 |
| Independent reflections | 12596 [$R_{int}$ = 0.0378, $R_{sigma}$ = 0.0151] |
| Data/restraints/parameters | 12596/0/561 |
| Goodness-of-fit on F$^2$ | 1.037 |
| Final R indexes [I>=2σ (I)] | $R_1$ = 0.0396, $wR_2$ = 0.0959 |
| Final R indexes [all data] | $R_1$ = 0.0459, $wR_2$ = 0.1016 |
| Largest diff. peak/hole / e Å$^{-3}$ | 1.67/-2.06 |

## X-ray structure of 2b

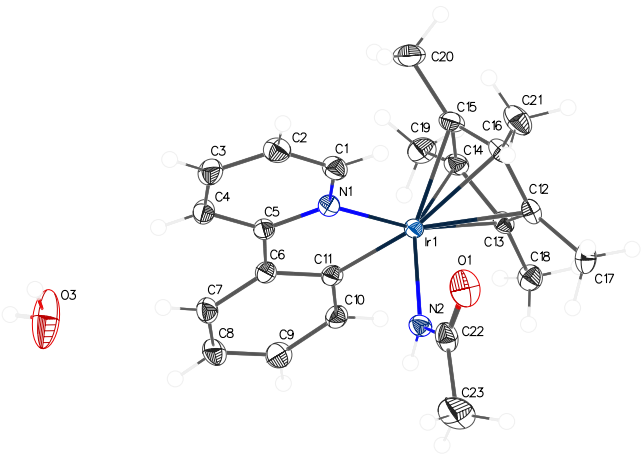


**Table A. 13. Crystal data and structure refinement for 2b.**

| | |
|---|---|
| Identification code | **2b** |
| Empirical formula | $C_{23}H_{29}IrN_2O_2$ |
| Formula weight | 557.68 |
| Temperature/K | 120(2) |
| Crystal system | triclinic |
| Space group | *P-1* |
| a/Å | 10.9189(5) |
| b/Å | 12.9178(5) |
| c/Å | 16.1472(7) |
| α/° | 98.7820(10) |
| β/° | 107.051(2) |
| γ/° | 93.859(2) |
| Volume/Å$^3$ | 2136.70(16) |
| Z | 4 |
| $\rho_{calc}$g/cm$^3$ | 1.734 |
| μ/mm$^{-1}$ | 6.269 |
| F(000) | 1096.0 |
| Crystal size/mm$^3$ | 0.120 × 0.100 × 0.080 |
| Radiation | MoKα (λ = 0.71073) |
| 2Θ range for data collection/° | 4.542 to 60.112 |
| Index ranges | -15 ≤ h ≤ 15, -18 ≤ k ≤ 15, -22 ≤ l ≤ 22 |
| Reflections collected | 81688 |
| Independent reflections | 12491 [$R_{int}$ = 0.0345, $R_{sigma}$ = 0.0220] |
| Data/restraints/parameters | 12491/0/543 |
| Goodness-of-fit on F$^2$ | 1.039 |
| Final R indexes [I>=2σ (I)] | $R_1$ = 0.0197, $wR_2$ = 0.0341 |
| Final R indexes [all data] | $R_1$ = 0.0260, $wR_2$ = 0.0364 |
| Largest diff. peak/hole / e Å$^{-3}$ | 1.51/-1.90 |

## X-ray structure of [1c][$I_3$]

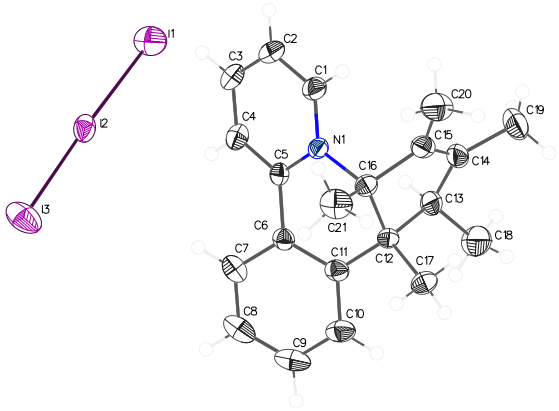


**Table A. 14. Crystal data and structure refinement for [1c][$I_3$].**

| | |
|---|---|
| Identification code | **[1c][$I_3$]** |
| Empirical formula | $C_{21}H_{24}I_3N$ |
| Formula weight | 671.11 |
| Temperature/K | 173(2) |
| Crystal system | monoclinic |
| Space group | *P2₁/c* |
| a/Å | 10.3746(4) |
| b/Å | 13.0748(6) |
| c/Å | 16.9157(7) |
| α/° | 90.00 |
| β/° | 95.694(2) |
| γ/° | 90.00 |
| Volume/Å$^3$ | 2283.22(17) |
| Z | 4 |
| $\rho_{calc}$g/cm$^3$ | 1.952 |
| μ/mm$^{-1}$ | 4.111 |
| F(000) | 1264.0 |
| Crystal size/mm$^3$ | 0.2 × 0.16 × 0.14 |
| Radiation | MoKα (λ = 0.71073) |
| 2Θ range for data collection/° | 3.94 to 60.1 |
| Index ranges | -12 ≤ h ≤ 14, -18 ≤ k ≤ 18, -23 ≤ l ≤ 23 |
| Reflections collected | 42452 |
| Independent reflections | 6692 [$R_{int}$ = 0.0374, $R_{sigma}$ = 0.0231] |
| Data/restraints/parameters | 6692/0/231 |
| Goodness-of-fit on $F^2$ | 1.061 |
| Final R indexes [I>=2σ (I)] | $R_1$ = 0.0435, $wR_2$ = 0.0834 |
| Final R indexes [all data] | $R_1$ = 0.0652, $wR_2$ = 0.0938 |
| Largest diff. peak/hole / e Å$^{-3}$ | 3.06/-2.25 |

## X-ray structure of [1c'][$I_3$]

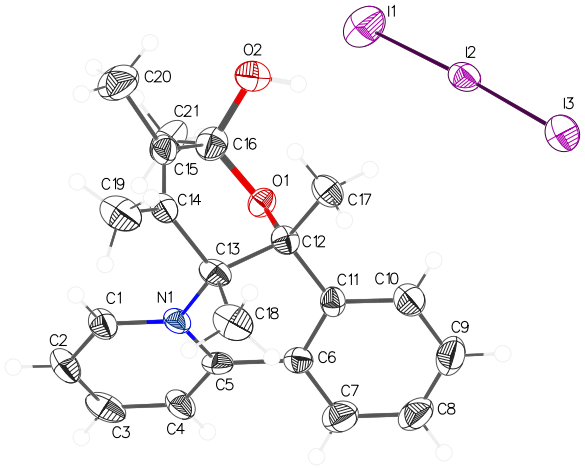


**Table A. 15. Crystal data and structure refinement for [1c'][$I_3$]**

| | |
|---|---|
| Identification code | **[1c'][$I_3$]** |
| Empirical formula | $C_{21}H_{24}I_3NO_2$ |
| Formula weight | 703.11 |
| Temperature/K | 173.15 |
| Crystal system | triclinic |
| Space group | *P-1* |
| a/Å | 11.2989(5) |
| b/Å | 12.8391(5) |
| c/Å | 16.7461(7) |
| α/° | 103.0430(10) |
| β/° | 97.1310(10) |
| γ/° | 90.2630(10) |
| Volume/Å$^3$ | 2347.00(17) |
| Z | 4 |
| $\rho_{calc}$g/cm$^3$ | 1.990 |
| μ/mm$^{-1}$ | 4.010 |
| F(000) | 1328.0 |
| Crystal size/mm$^3$ | 0.2 × 0.1 × 0.08 |
| Radiation | MoKα (λ = 0.71073) |
| 2Θ range for data collection/° | 2.52 to 56.12 |
| Index ranges | -14 ≤ h ≤ 14, -16 ≤ k ≤ 16, -22 ≤ l ≤ 22 |
| Reflections collected | 83359 |
| Independent reflections | 11361 [$R_{int}$ = 0.0906, $R_{sigma}$ = 0.0723] |
| Data/restraints/parameters | 11361/0/497 |
| Goodness-of-fit on $F^2$ | 1.046 |
| Final R indexes [I>=2σ (I)] | $R_1$ = 0.0503, $wR_2$ = 0.0972 |
| Final R indexes [all data] | $R_1$ = 0.1016, $wR_2$ = 0.1090 |
| Largest diff. peak/hole / e Å$^{-3}$ | 2.52/-1.56 |

## X-ray structure of 2c

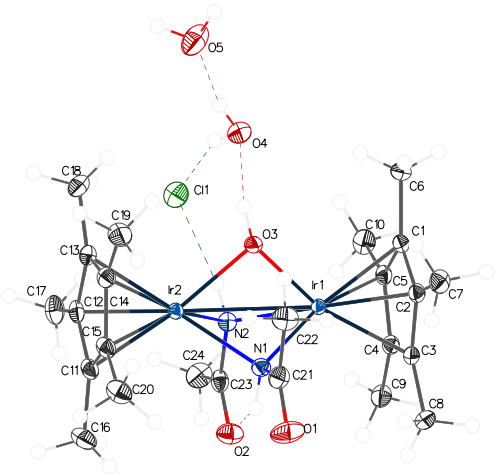


**Table A. 16. Crystal data and structure refinement for 2c.**

| | |
|---|---|
| Identification code | **2c** |
| Empirical formula | $C_{24}H_{43}ClIr_2N_2O_5$ |
| Formula weight | 859.45 |
| Temperature/K | 120(2) |
| Crystal system | triclinic |
| Space group | *P-1* |
| a/Å | 8.4469(4) |
| b/Å | 10.0791(4) |
| c/Å | 17.3569(8) |
| α/° | 93.5250(10) |
| β/° | 95.071(2) |
| γ/° | 111.9100(10) |
| Volume/Å$^3$ | 1358.46(11) |
| Z | 2 |
| $\rho_{calc}$g/cm$^3$ | 2.101 |
| μ/mm$^{-1}$ | 9.920 |
| F(000) | 824.0 |
| Crystal size/mm$^3$ | 0.250 × 0.200 × 0.120 |
| Radiation | MoKα (λ = 0.71073) |
| 2Θ range for data collection/° | 4.378 to 64.142 |
| Index ranges | -12 ≤ h ≤ 12, -14 ≤ k ≤ 15, -25 ≤ l ≤ 25 |
| Reflections collected | 100357 |
| Independent reflections | 9439 [$R_{int}$ = 0.0331, $R_{sigma}$ = 0.0168] |
| Data/restraints/parameters | 9439/0/347 |
| Goodness-of-fit on F$^2$ | 1.118 |
| Final R indexes [I>=2σ (I)] | $R_1$ = 0.0150, $wR_2$ = 0.0379 |
| Final R indexes [all data] | $R_1$ = 0.0158, $wR_2$ = 0.0384 |
| Largest diff. peak/hole / e Å$^{-3}$ | 1.29/-1.46 |

## X-ray structure of {[Cp*Co]$_2$($\mu$-I$_3$)}[I$_3$]

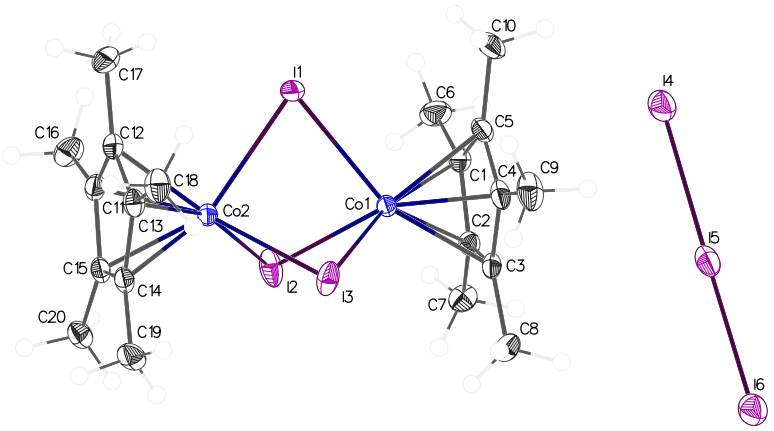


**Table A. 17. Crystal data and structure refinement for {[Cp*Co]$_2$($\mu$-I$_3$)}[I$_3$]**

| | |
|---|---|
| Identification code | **{[Cp*Co]$_2$($\mu$-I$_3$)}[I$_3$]** |
| Empirical formula | $C_{20}H_{30}Co_2I_6$ |
| Formula weight | 1149.70 |
| Temperature/K | 120(2) |
| Crystal system | monoclinic |
| Space group | *P2$_1$/c* |
| a/Å | 12.7403(7) |
| b/Å | 13.8368(7) |
| c/Å | 16.9841(9) |
| α/° | 90 |
| β/° | 101.179(2) |
| γ/° | 90 |
| Volume/Å$^3$ | 2937.2(3) |
| Z | 4 |
| $\rho_{calc}$g/cm$^3$ | 2.600 |
| μ/mm$^{-1}$ | 7.442 |
| F(000) | 2088.0 |
| Crystal size/mm$^3$ | 0.180 × 0.150 × 0.120 |
| Radiation | MoKα (λ = 0.71073) |
| 2Θ range for data collection/° | 3.826 to 58.334 |
| Index ranges | -17 ≤ h ≤ 17, -18 ≤ k ≤ 18, -23 ≤ l ≤ 23 |
| Reflections collected | 106033 |
| Independent reflections | 7912 [$R_{int}$ = 0.0289, $R_{sigma}$ = 0.0118] |
| Data/restraints/parameters | 7912/0/263 |
| Goodness-of-fit on F$^2$ | 1.132 |
| Final R indexes [I>=2σ (I)] | $R_1$ = 0.0221, w$R_2$ = 0.0492 |
| Final R indexes [all data] | $R_1$ = 0.0241, w$R_2$ = 0.0503 |
| Largest diff. peak/hole / e Å$^{-3}$ | 2.44/-2.03 |

## X-ray structure of [1c][BArF$_{24}$]

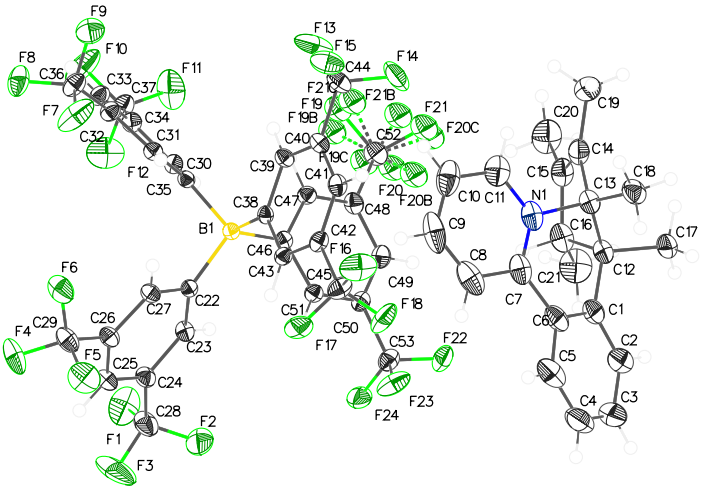


**Table A. 18. Crystal data and structure refinement for [1c][BArF$_{24}$].**

| | |
|---|---|
| Identification code | **[1c][BArF$_{24}$]** |
| Empirical formula | $C_{53}H_{36}BNF_{24}$ |
| Formula weight | 1153.64 |
| Temperature/K | 120(2) |
| Crystal system | triclinic |
| Space group | *P-1* |
| a/Å | 12.1615(5) |
| b/Å | 12.7457(5) |
| c/Å | 17.5248(7) |
| α/° | 78.947(2) |
| β/° | 70.2900(10) |
| γ/° | 72.4030(10) |
| Volume/Å$^3$ | 2425.42(17) |
| Z | 2 |
| $\rho_{calc}$g/cm$^3$ | 1.580 |
| μ/mm$^{-1}$ | 0.156 |
| F(000) | 1164.0 |
| Crystal size/mm$^3$ | 0.300 × 0.200 × 0.150 |
| Radiation | MoKα (λ = 0.71073) |
| 2Θ range for data collection/° | 4.19 to 55.854 |
| Index ranges | -16 ≤ h ≤ 15, -16 ≤ k ≤ 16, -23 ≤ l ≤ 23 |
| Reflections collected | 171592 |
| Independent reflections | 11602 [$R_{int}$ = 0.0286, $R_{sigma}$ = 0.0123] |
| Data/restraints/parameters | 11602/0/723 |
| Goodness-of-fit on F$^2$ | 1.034 |
| Final R indexes [I>=2σ (I)] | $R_1$ = 0.0670, $wR_2$ = 0.1722 |
| Final R indexes [all data] | $R_1$ = 0.0714, $wR_2$ = 0.1761 |
| Largest diff. peak/hole / e Å$^{-3}$ | 1.49/-1.38 |

## X-ray structure of [7c][BArF$_{24}$]

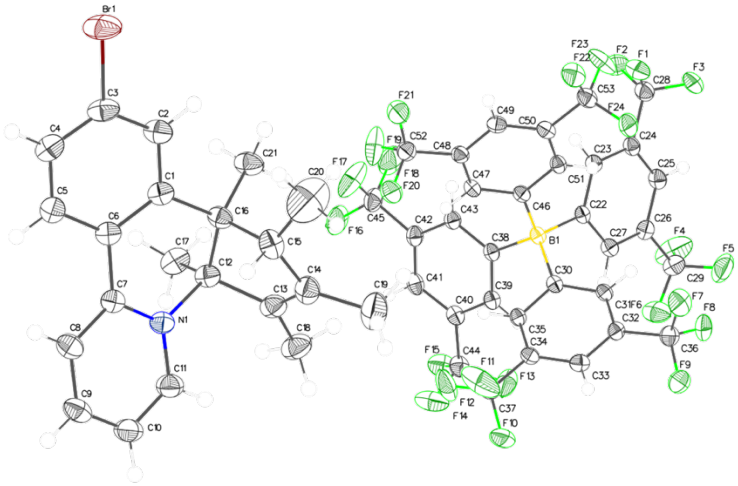

**Table A. 19. Crystal data and structure refinement for [7c][BArF$_{24}$].**

| | |
|---|---|
| Identification code | **[7c][BArF$_{24}$]** |
| Empirical formula | $C_{53}H_{35}NBF_{24}Br$ |
| Formula weight | 1232.54 |
| Temperature/K | 120(2) |
| Crystal system | triclinic |
| Space group | *P-1* |
| a/Å | 12.5126(7) |
| b/Å | 12.9558(9) |
| c/Å | 17.5115(12) |
| α/° | 77.264(2) |
| β/° | 69.227(2) |
| γ/° | 69.990(2) |
| Volume/Å$^3$ | 2478.1(3) |
| Z | 2 |
| $\rho_{calc}$g/cm$^3$ | 1.652 |
| μ/mm$^{-1}$ | 0.960 |
| F(000) | 1232.0 |
| Crystal size/mm$^3$ | 0.180 × 0.150 × 0.120 |
| Radiation | MoKα (λ = 0.71073) |
| 2Θ range for data collection/° | 3.962 to 55.94 |
| Index ranges | -15 ≤ h ≤ 16, -17 ≤ k ≤ 17, -23 ≤ l ≤ 23 |
| Reflections collected | 169912 |
| Independent reflections | 11905 [$R_{int}$ = 0.0662, $R_{sigma}$ = 0.0249] |
| Data/restraints/parameters | 11905/0/726 |
| Goodness-of-fit on F$^2$ | 1.024 |
| Final R indexes [I>=2σ (I)] | $R_1$ = 0.0532, $wR_2$ = 0.1357 |
| Final R indexes [all data] | $R_1$ = 0.0679, $wR_2$ = 0.1484 |
| Largest diff. peak/hole / e Å$^{-3}$ | 1.80/-1.36 |

## X-ray structure of [8c][BArF$_{24}$]

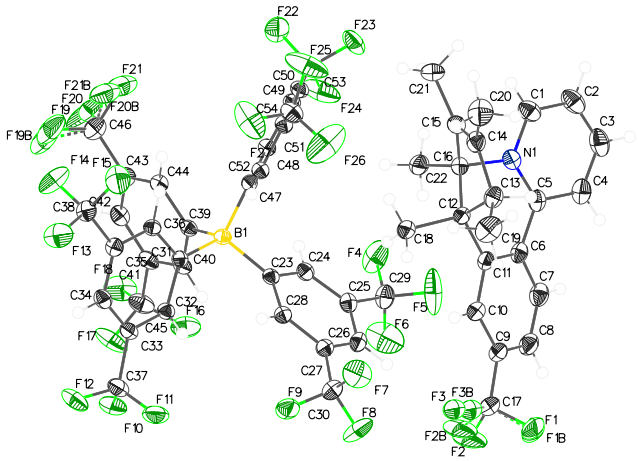


**Table A. 20. Crystal data and structure refinement for [8c][BArF$_{24}$].**

| | |
|---|---|
| Identification code | [**8c**][BArF$_{24}$] |
| Empirical formula | $C_{54}H_{35}NBF_{27}$ |
| Formula weight | 1221.64 |
| Temperature/K | 120(2) |
| Crystal system | triclinic |
| Space group | *P-1* |
| a/Å | 12.8233(6) |
| b/Å | 12.8600(6) |
| c/Å | 17.6228(8) |
| α/° | 77.166(2) |
| β/° | 69.467(2) |
| γ/° | 69.564(2) |
| Volume/Å$^3$ | 2533.7(2) |
| Z | 2 |
| $\rho_{calc}$g/cm$^3$ | 1.601 |
| μ/mm$^{-1}$ | 0.163 |
| F(000) | 1228.0 |
| Crystal size/mm$^3$ | 0.220 × 0.180 × 0.120 |
| Radiation | MoKα (λ = 0.71073) |
| 2Θ range for data collection/° | 3.978 to 58.12 |
| Index ranges | -17 ≤ h ≤ 17, -17 ≤ k ≤ 17, -24 ≤ l ≤ 24 |
| Reflections collected | 130182 |
| Independent reflections | 13524 [$R_{int}$ = 0.0436, $R_{sigma}$ = 0.0218] |
| Data/restraints/parameters | 13524/0/777 |
| Goodness-of-fit on F$^2$ | 1.028 |
| Final R indexes [I>=2σ (I)] | $R_1$ = 0.0543, w$R_2$ = 0.1270 |
| Final R indexes [all data] | $R_1$ = 0.0730, w$R_2$ = 0.1416 |
| Largest diff. peak/hole / e Å$^{-3}$ | 0.87/-0.66 |

## X-ray structure of [7d][BArF$_{24}$]

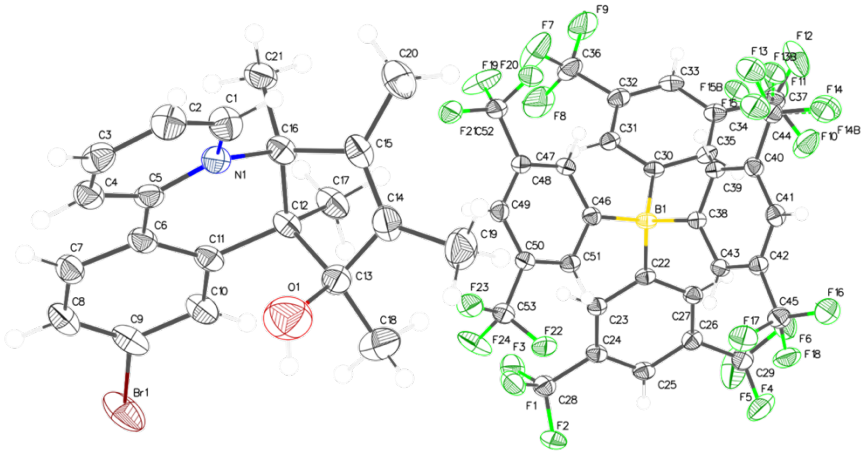


**Table A. 21. Crystal data and structure refinement for [7d][BArF$_{24}$].**

| | |
|---|---|
| Identification code | [**7d**][BArF$_{24}$] |
| Empirical formula | $C_{53}H_{35}NOBF_{24}Br$ |
| Formula weight | 1248.54 |
| Temperature/K | 120(2) |
| Crystal system | triclinic |
| Space group | *P-1* |
| a/Å | 12.5105(5) |
| b/Å | 13.0148(5) |
| c/Å | 17.4366(7) |
| α/° | 76.7020(10) |
| β/° | 69.7650(10) |
| γ/° | 70.3110(10) |
| Volume/Å$^3$ | 2487.31(17) |
| Z | 2 |
| $\rho_{calc}$g/cm$^3$ | 1.667 |
| μ/mm$^{-1}$ | 0.959 |
| F(000) | 1248.0 |
| Crystal size/mm$^3$ | 0.120 × 0.100 × 0.080 |
| Radiation | MoKα (λ = 0.71073) |
| 2Θ range for data collection/° | 3.92 to 56.116 |
| Index ranges | -16 ≤ h ≤ 14, -17 ≤ k ≤ 17, -23 ≤ l ≤ 23 |
| Reflections collected | 117077 |
| Independent reflections | 12054 [$R_{int}$ = 0.0839, $R_{sigma}$ = 0.0424] |
| Data/restraints/parameters | 12054/0/739 |
| Goodness-of-fit on F$^2$ | 1.044 |
| Final R indexes [I>=2σ (I)] | $R_1$ = 0.0703, $wR_2$ = 0.1729 |
| Final R indexes [all data] | $R_1$ = 0.1021, $wR_2$ = 0.1961 |
| Largest diff. peak/hole / e Å$^{-3}$ | 2.05/-1.31 |

## X-ray structure of [8d][BArF$_{24}$]

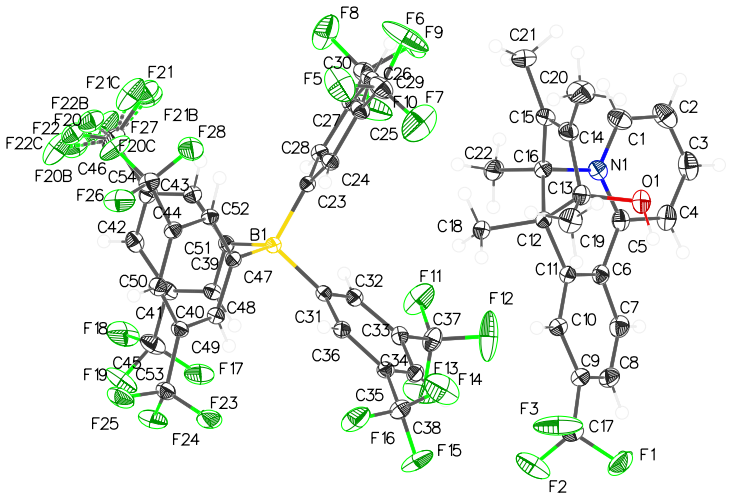


**Table A. 22. Crystal data and structure refinement for [8d][BArF$_{24}$].**

| | |
|---|---|
| Identification code | [**8d**][BArF$_{24}$] |
| Empirical formula | $C_{54}H_{35}NBF_{27}O$ |
| Formula weight | 1237.64 |
| Temperature/K | 120(2) |
| Crystal system | triclinic |
| Space group | *P-1* |
| a/Å | 12.7809(5) |
| b/Å | 12.9782(6) |
| c/Å | 17.3787(8) |
| α/° | 76.563(2) |
| β/° | 70.971(2) |
| γ/° | 70.330(2) |
| Volume/Å$^3$ | 2541.6(2) |
| Z | 2 |
| $\rho_{calc}$g/cm$^3$ | 1.617 |
| μ/mm$^{-1}$ | 0.165 |
| F(000) | 1244.0 |
| Crystal size/mm$^3$ | 0.200 × 0.140 × 0.120 |
| Radiation | MoKα (λ = 0.71073) |
| 2Θ range for data collection/° | 3.908 to 58.12 |
| Index ranges | -17 ≤ h ≤ 17, -17 ≤ k ≤ 17, -23 ≤ l ≤ 23 |
| Reflections collected | 192638 |
| Independent reflections | 13577 [$R_{int}$ = 0.0340, $R_{sigma}$ = 0.0140] |
| Data/restraints/parameters | 13577/0/784 |
| Goodness-of-fit on F$^2$ | 1.047 |
| Final R indexes [I>=2σ (I)] | $R_1$ = 0.0490, $wR_2$ = 0.1194 |
| Final R indexes [all data] | $R_1$ = 0.0560, $wR_2$ = 0.1258 |
| Largest diff. peak/hole / e Å$^{-3}$ | 0.77/-0.75 |

## X-ray structure of [10c][BArF$_{24}$]

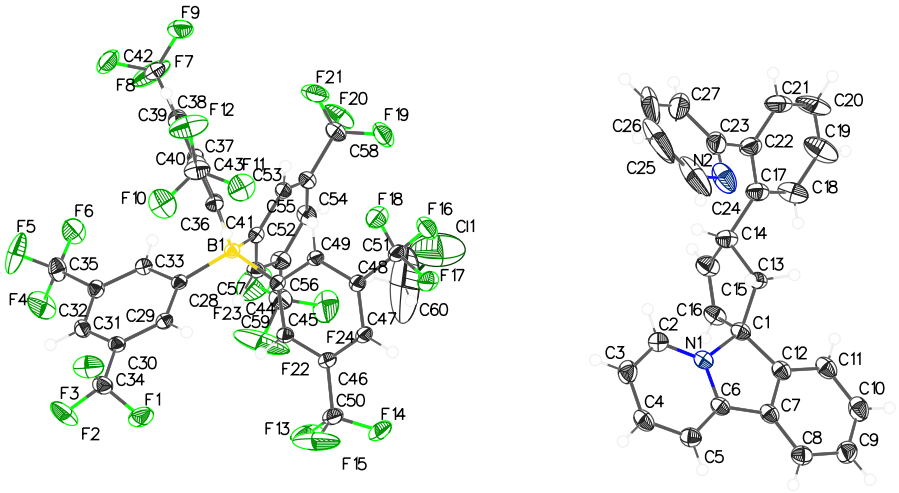


**Table A. 23. Crystal data and structure refinement for [10c][BArF$_{24}$].**

| | |
|---|---|
| Identification code | [**10c**][BArF$_{24}$] |
| Empirical formula | $C_{119}H_{68}B_2F_{48}N_4Cl_2$ |
| Formula weight | 2558.29 |
| Temperature/K | 120(2) |
| Crystal system | triclinic |
| Space group | *P-1* |
| a/Å | 12.6465(4) |
| b/Å | 14.4270(4) |
| c/Å | 16.3560(5) |
| α/° | 79.6400(10) |
| β/° | 70.3980(10) |
| γ/° | 77.4660(10) |
| Volume/Å$^3$ | 2725.58(14) |
| Z | 1 |
| $\rho_{calc}$g/cm$^3$ | 1.559 |
| μ/mm$^{-1}$ | 0.196 |
| F(000) | 1286.0 |
| Crystal size/mm$^3$ | 0.120 × 0.100 × 0.090 |
| Radiation | MoKα (λ = 0.71073) |
| 2Θ range for data collection/° | 4.084 to 55.834 |
| Index ranges | -16 ≤ h ≤ 16, -18 ≤ k ≤ 18, -21 ≤ l ≤ 21 |
| Reflections collected | 57228 |
| Independent reflections | 12991 [$R_{int}$ = 0.0307, $R_{sigma}$ = 0.0259] |
| Data/restraints/parameters | 12991/0/781 |
| Goodness-of-fit on F$^2$ | 1.022 |
| Final R indexes [I>=2σ (I)] | $R_1$ = 0.0711, $wR_2$ = 0.1943 |
| Final R indexes [all data] | $R_1$ = 0.0811, $wR_2$ = 0.2054 |
| Largest diff. peak/hole / e Å$^{-3}$ | 1.17/-1.24 |

## X-ray structure of [5a'][BArF$_{24}$]

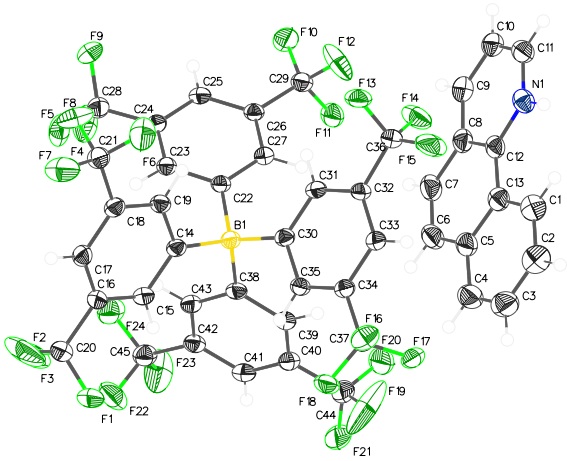


**Table A. 24. Crystal data and structure refinement for [5a'][BArF$_{24}$].**

| | |
|---|---|
| Identification code | **[5a'][BArF$_{24}$]** |
| Empirical formula | $C_{45}H_{22}BNF_{24}$ |
| Formula weight | 1043.44 |
| Temperature/K | 120(2) |
| Crystal system | monoclinic |
| Space group | *C2/c* |
| a/Å | 38.276(2) |
| b/Å | 12.9570(8) |
| c/Å | 17.4202(11) |
| α/° | 90 |
| β/° | 105.898(2) |
| γ/° | 90 |
| Volume/Å$^3$ | 8309.0(9) |
| Z | 8 |
| $\rho_{calc}$g/cm$^3$ | 1.668 |
| μ/mm$^{-1}$ | 0.173 |
| F(000) | 4160.0 |
| Crystal size/mm$^3$ | 0.15 × 0.12 × 0.1 |
| Radiation | MoKα (λ = 0.71073) |
| 2Θ range for data collection/° | 3.942 to 55.858 |
| Index ranges | -50 ≤ h ≤ 48, -17 ≤ k ≤ 17, -22 ≤ l ≤ 22 |
| Reflections collected | 111016 |
| Independent reflections | 9950 [$R_{int}$ = 0.0641, $R_{sigma}$ = 0.0279] |
| Data/restraints/parameters | 9950/0/640 |
| Goodness-of-fit on F$^2$ | 1.021 |
| Final R indexes [I>=2σ (I)] | $R_1$ = 0.0523, $wR_2$ = 0.1191 |
| Final R indexes [all data] | $R_1$ = 0.0772, $wR_2$ = 0.1353 |
| Largest diff. peak/hole / e Å$^{-3}$ | 0.74/-0.62 |

## X-ray structure of [1e][$I_3$]

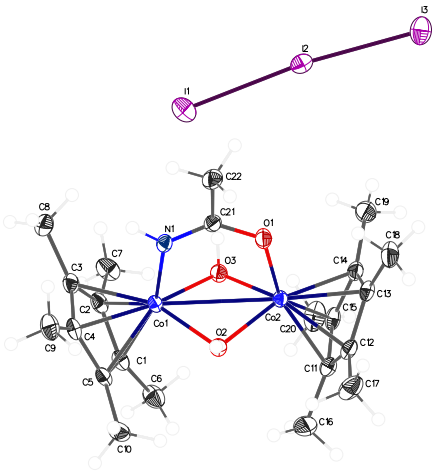


**Table A. 25. Crystal data and structure refinement for [1e][$I_3$].**

| | |
|---|---|
| Identification code | **[1e][$I_3$]** |
| Empirical formula | $C_{22}H_{36}Co_2I_3NO_3$ |
| Formula weight | 861.08 |
| Temperature/K | 120(2) |
| Crystal system | triclinic |
| Space group | *P-1* |
| a/Å | 8.5835(6) |
| b/Å | 9.9507(7) |
| c/Å | 17.0139(12) |
| α/° | 93.269(3) |
| β/° | 100.004(3) |
| γ/° | 93.577(3) |
| Volume/Å$^3$ | 1424.90(17) |
| Z | 2 |
| $\rho_{calc}$g/cm$^3$ | 2.007 |
| μ/mm$^{-1}$ | 4.436 |
| F(000) | 824.0 |
| Crystal size/mm$^3$ | 0.350 × 0.150 × 0.120 |
| Radiation | MoKα (λ = 0.71073) |
| 2Θ range for data collection/° | 4.112 to 60.254 |
| Index ranges | -12 ≤ h ≤ 12, -14 ≤ k ≤ 14, -23 ≤ l ≤ 23 |
| Reflections collected | 81284 |
| Independent reflections | 8340 [$R_{int}$ = 0.0382, $R_{sigma}$ = 0.0195] |
| Data/restraints/parameters | 8340/0/299 |
| Goodness-of-fit on $F^2$ | 1.073 |
| Final R indexes [I>=2σ (I)] | $R_1$ = 0.0259, $wR_2$ = 0.0526 |
| Final R indexes [all data] | $R_1$ = 0.0338, $wR_2$ = 0.0567 |
| Largest diff. peak/hole / e Å$^{-3}$ | 1.31/-1.53 |

## X-ray structure of [1e'][$I_3$]

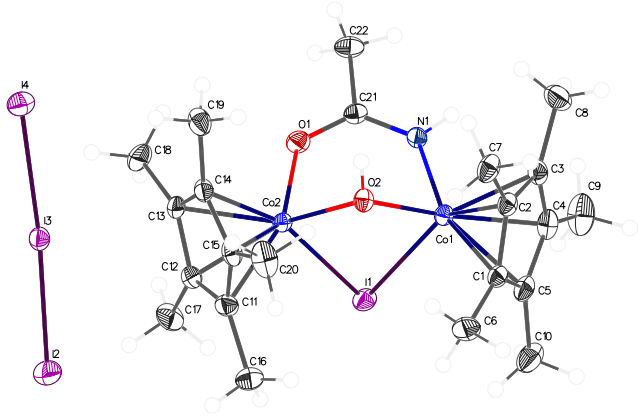


**Table A. 26. Crystal data and structure refinement for [1e'][$I_3$].**

| | |
|---|---|
| Identification code | **[1e'][$I_3$]** |
| Empirical formula | $C_{22}H_{35}NO_2Co_2I_4$ |
| Formula weight | 970.97 |
| Temperature/K | 120(2) |
| Crystal system | triclinic |
| Space group | *P-1* |
| a/Å | 7.5349(4) |
| b/Å | 12.6023(7) |
| c/Å | 15.8053(9) |
| α/° | 100.869(2) |
| β/° | 92.059(2) |
| γ/° | 90.909(2) |
| Volume/Å$^3$ | 1472.56(14) |
| Z | 2 |
| $\rho_{calc}$g/cm$^3$ | 2.190 |
| μ/mm$^{-1}$ | 5.338 |
| F(000) | 912.0 |
| Crystal size/mm$^3$ | 0.2 × 0.18 × 0.15 |
| Radiation | MoKα (λ = 0.71073) |
| 2Θ range for data collection/° | 3.802 to 64.198 |
| Index ranges | -11 ≤ h ≤ 11, -18 ≤ k ≤ 18, -23 ≤ l ≤ 23 |
| Reflections collected | 132549 |
| Independent reflections | 10273 [$R_{int}$ = 0.0298, $R_{sigma}$ = 0.0129] |
| Data/restraints/parameters | 10273/0/295 |
| Goodness-of-fit on $F^2$ | 1.301 |
| Final R indexes [I>=2σ (I)] | $R_1$ = 0.0275, $wR_2$ = 0.0591 |
| Final R indexes [all data] | $R_1$ = 0.0300, $wR_2$ = 0.0600 |
| Largest diff. peak/hole / e Å$^{-3}$ | 1.10/-1.36 |

# NMR Spectra

## 1a

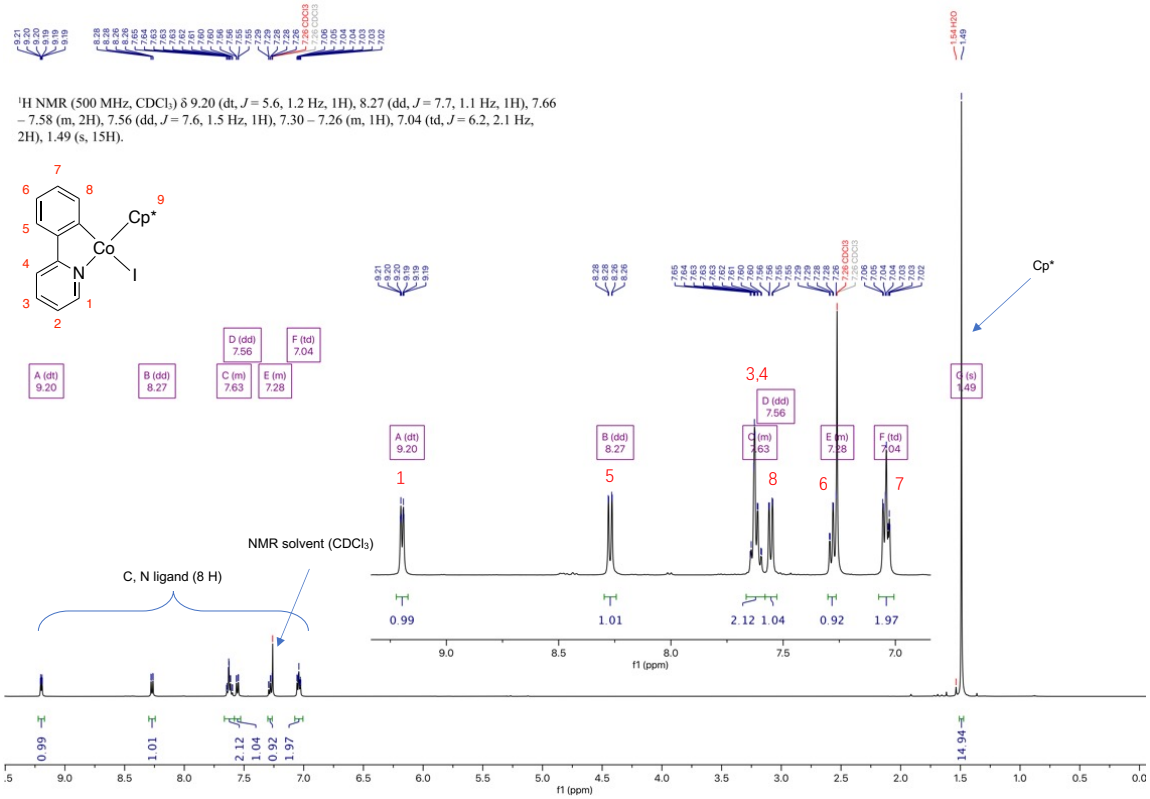


**Figure A. 1**. $^{1}$H NMR spectrum (500 MHz, $CDCl_3$) of **1a**

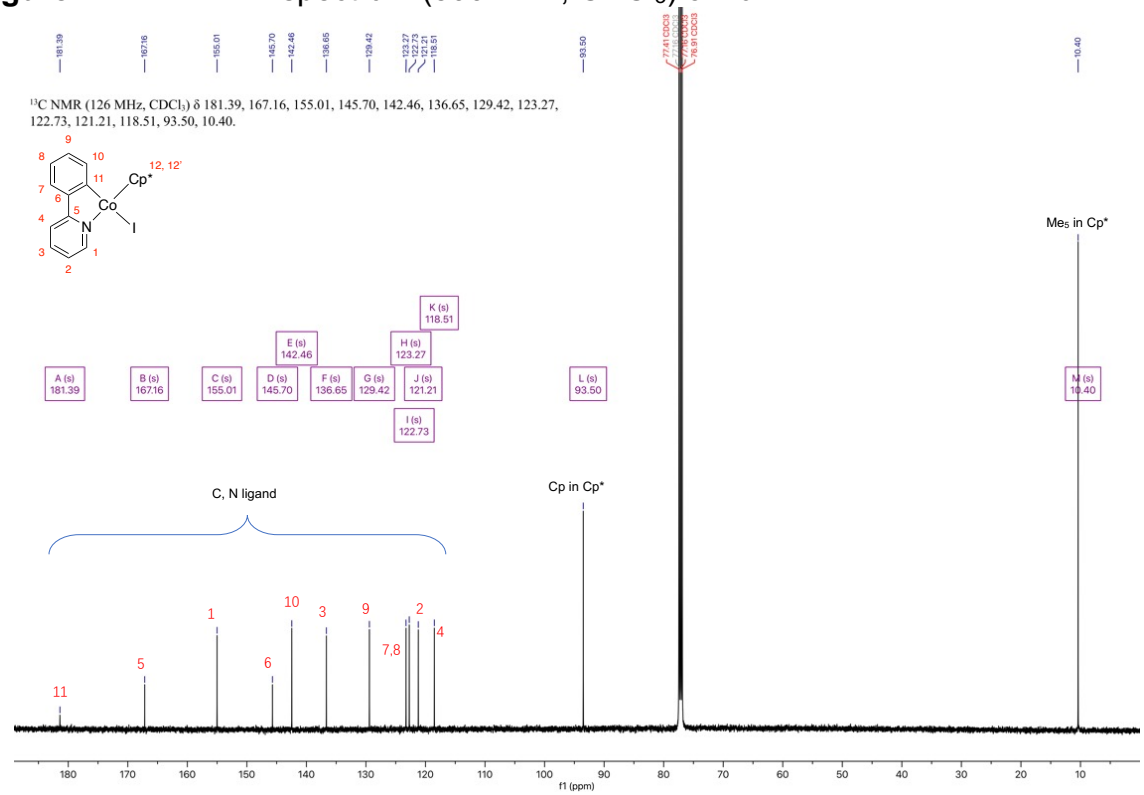


**Figure A. 2.** $^{13}$C NMR spectrum (126 MHz, $CDCl_3$) of **1a**

**3a**

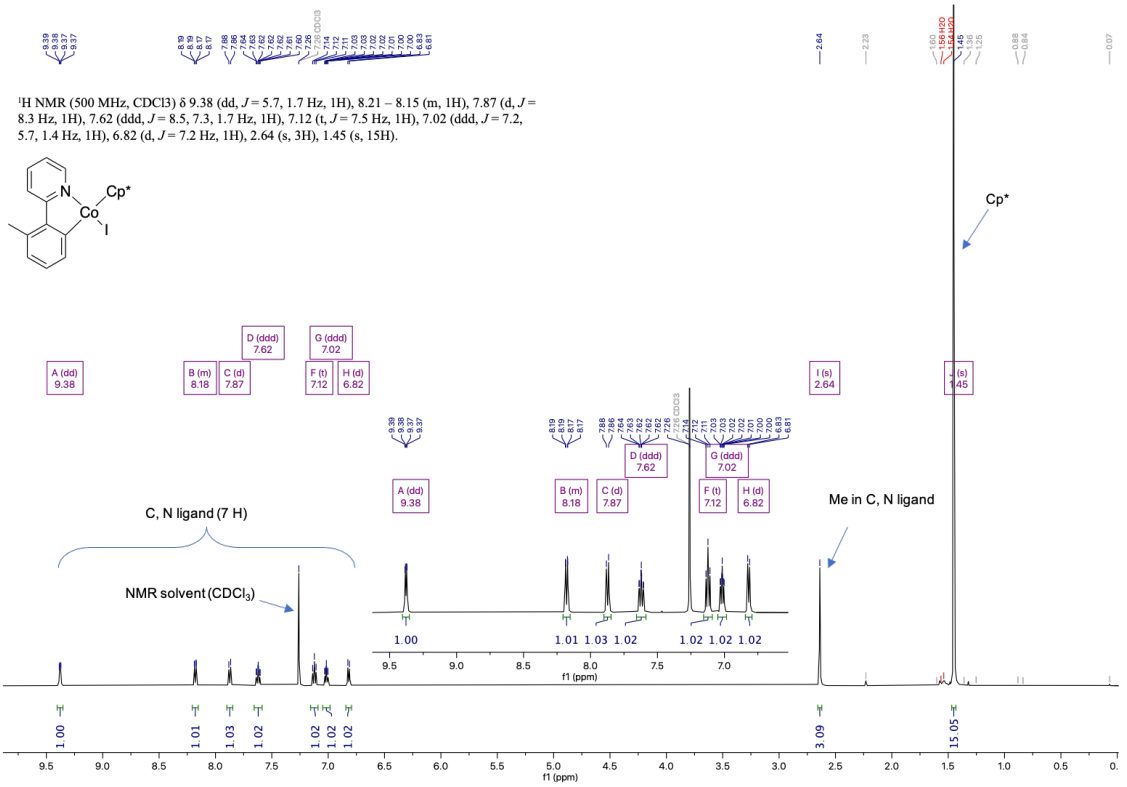


**Figure A. 3.** $^{1}$H NMR spectrum (500 MHz, $CDCl_3$) of **3a**

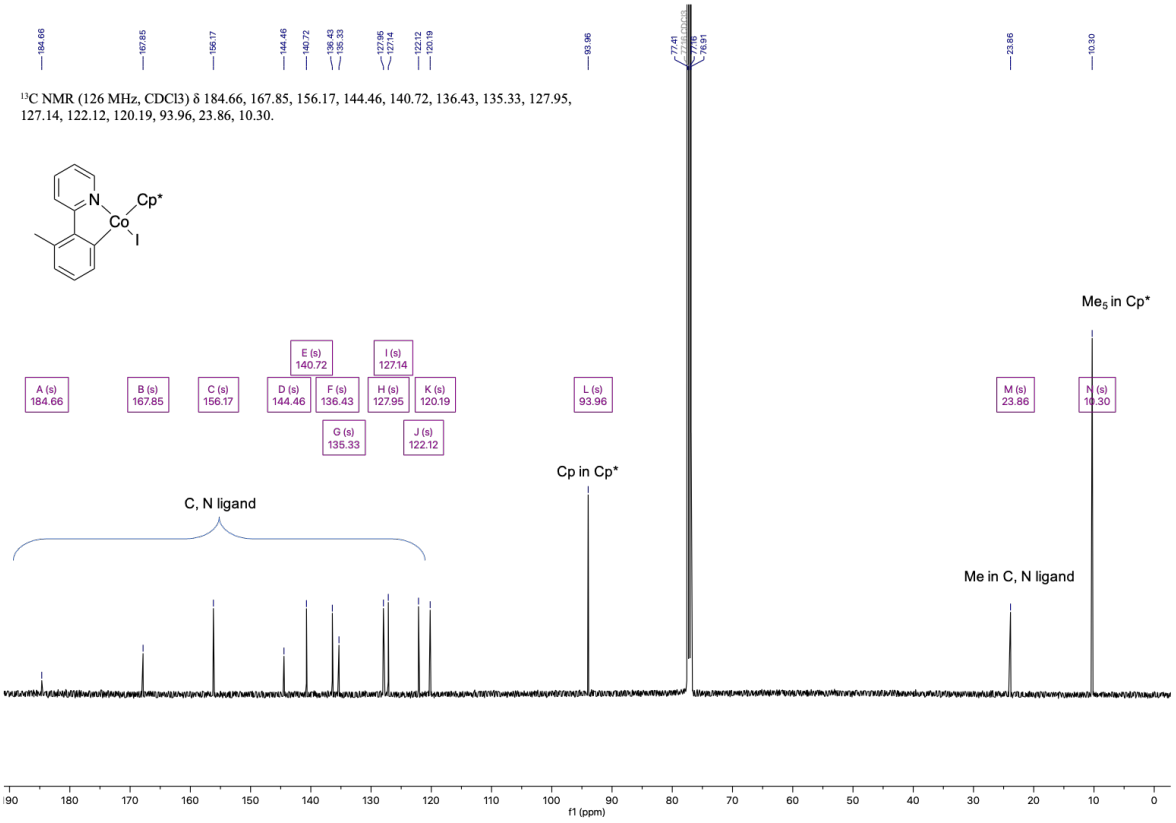


**Figure A. 4.** $^{13}$C NMR spectrum (126 MHz, $CDCl_3$) of **3a**

**4a**

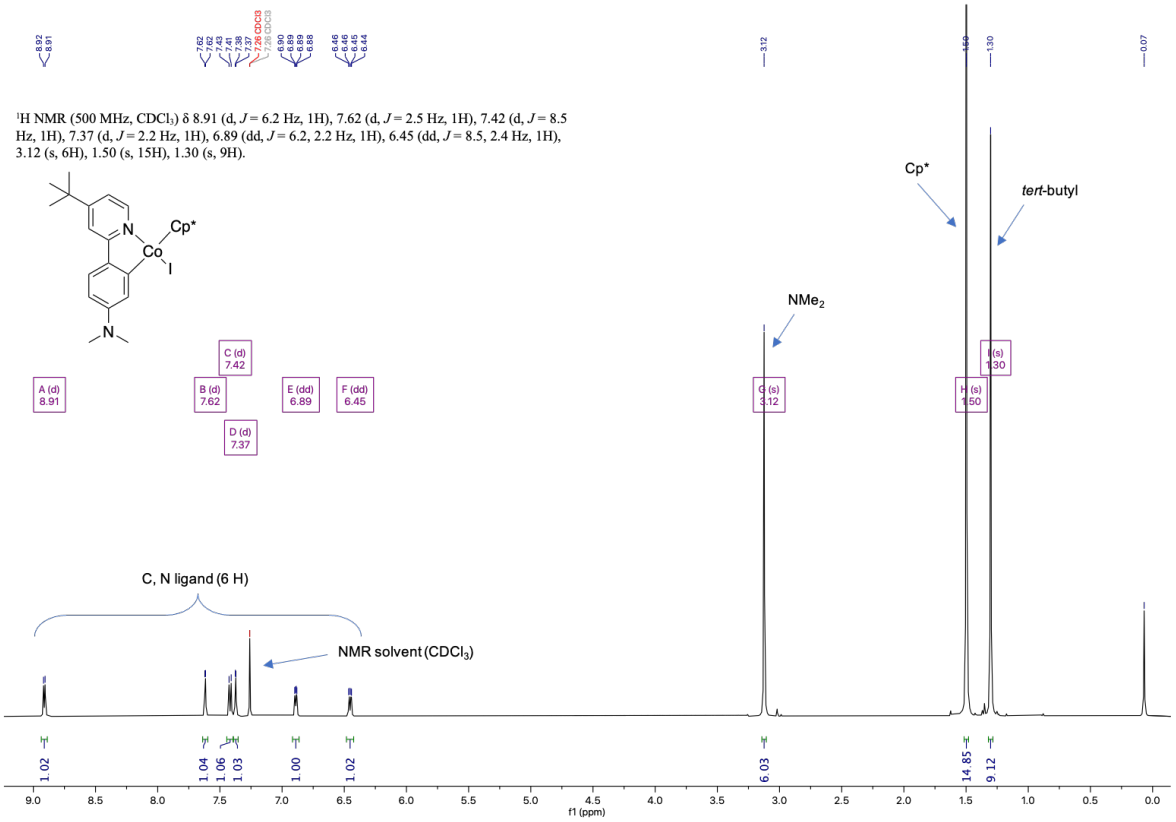


**Figure A. 5.** $^{1}$H NMR spectrum (500 MHz, $CDCl_3$) of **4a**

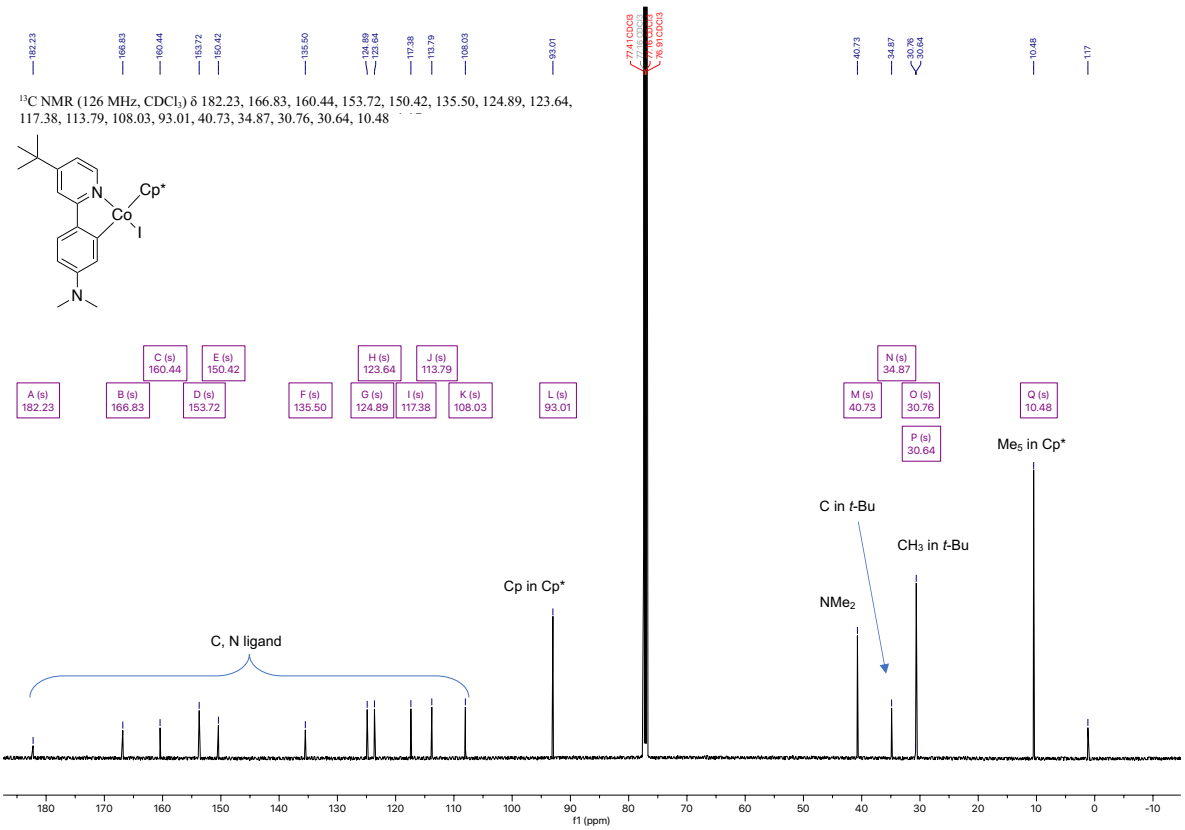


**Figure A. 6.** $^{13}$C NMR spectrum (126 MHz, $CDCl_3$) of **1a**

**5a**

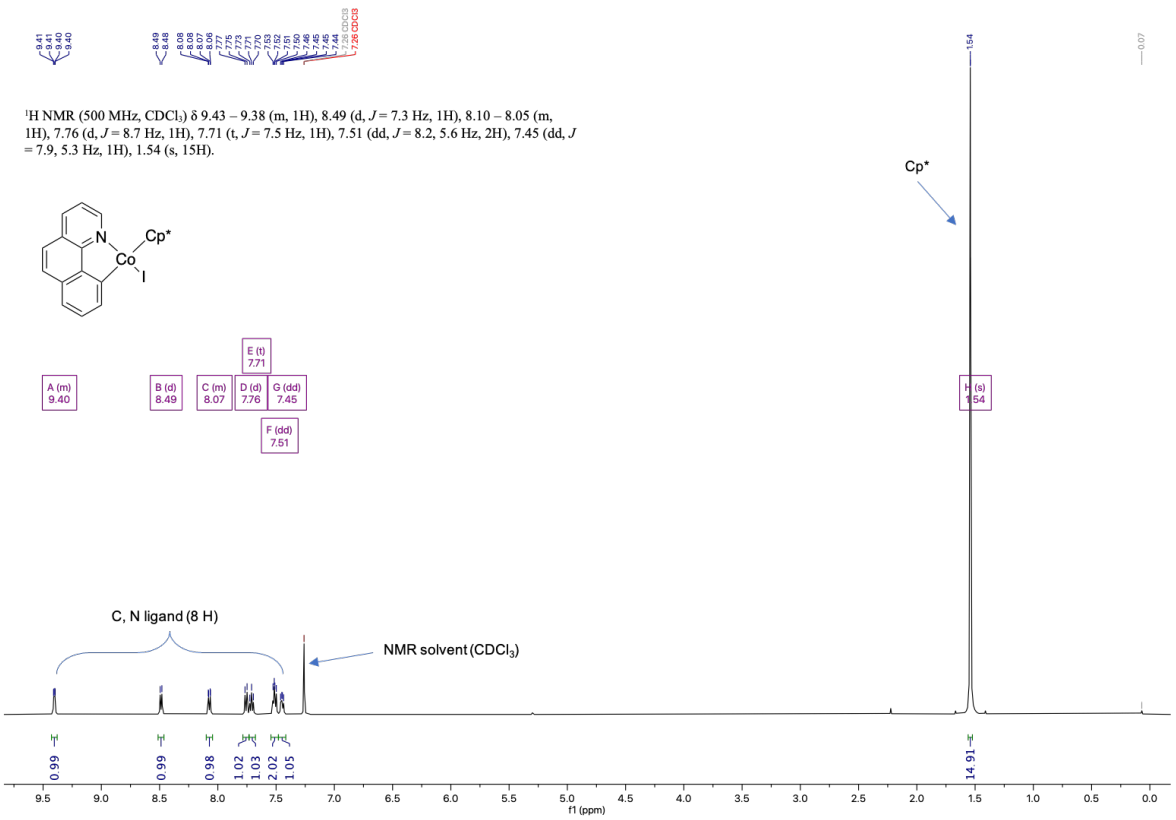


**Figure A. 7**. $^1$H NMR spectrum (500 MHz, $CDCl_3$) of **5a**

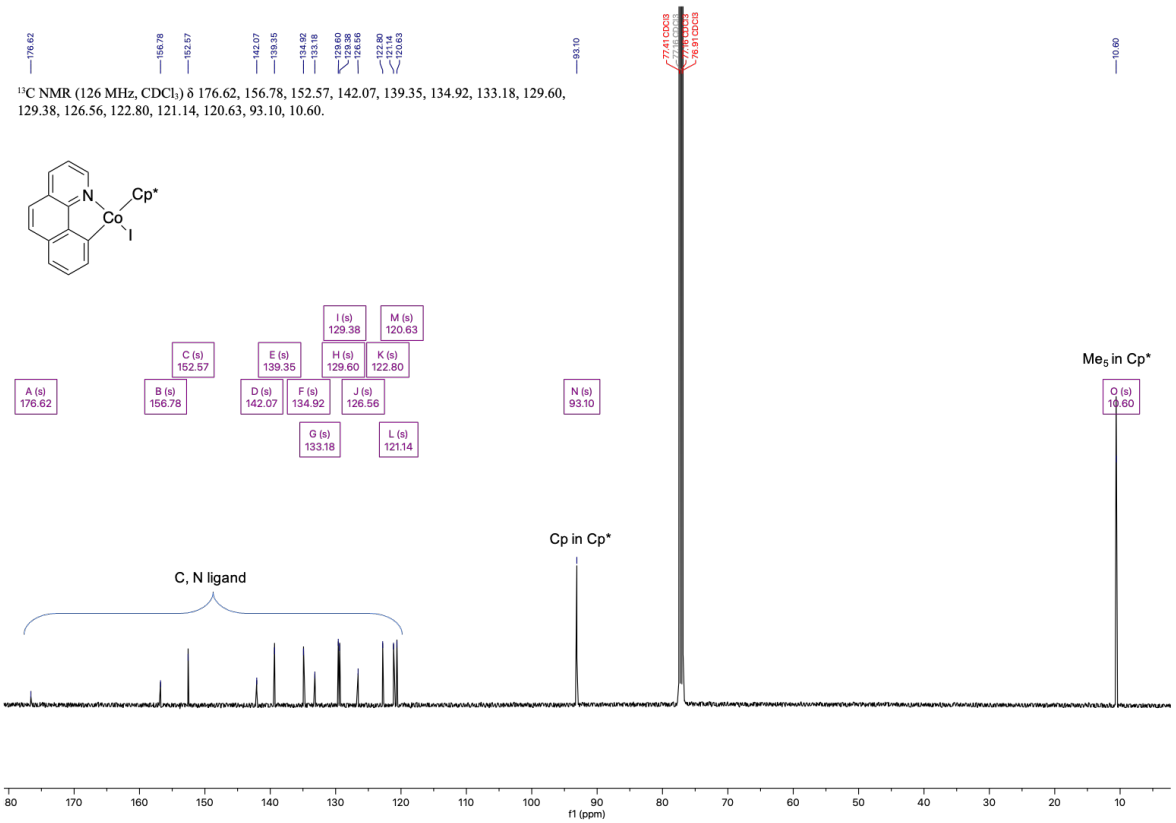


**Figure A. 8.** $^{13}$C NMR spectrum (126 MHz, $CDCl_3$) of **5a**

**6a**

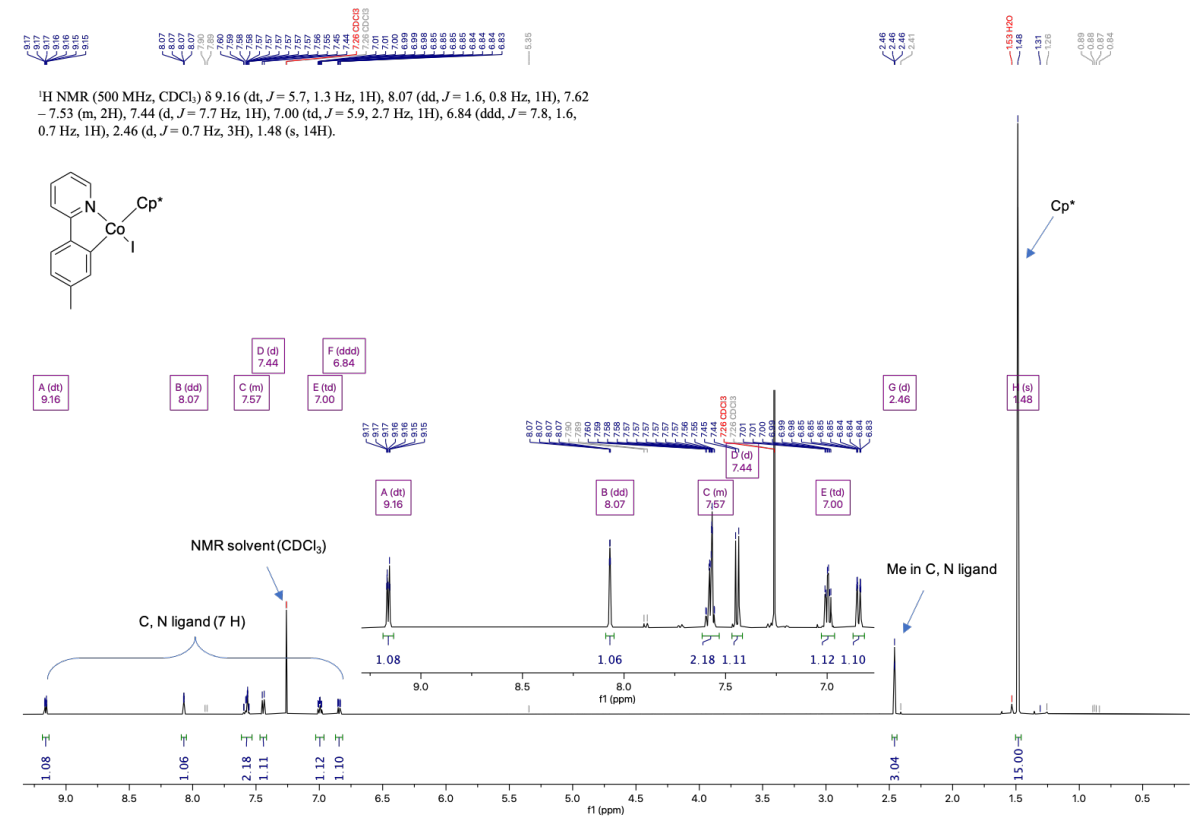


**Figure A. 9.** $^{1}$H NMR spectrum (500 MHz, $CDCl_3$) of **6a**

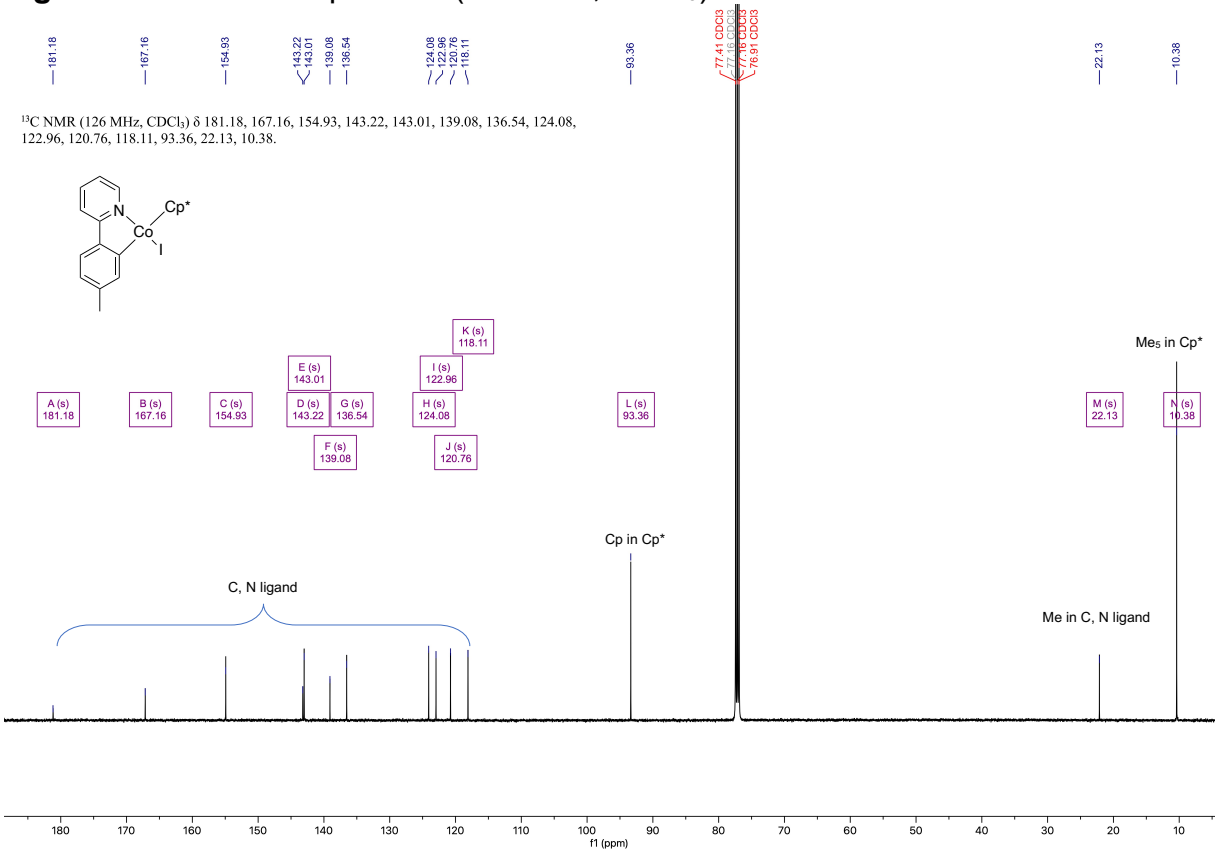


**Figure A. 10.** $^{13}$C NMR spectrum (126 MHz, $CDCl_3$) of **6a**

**7a**

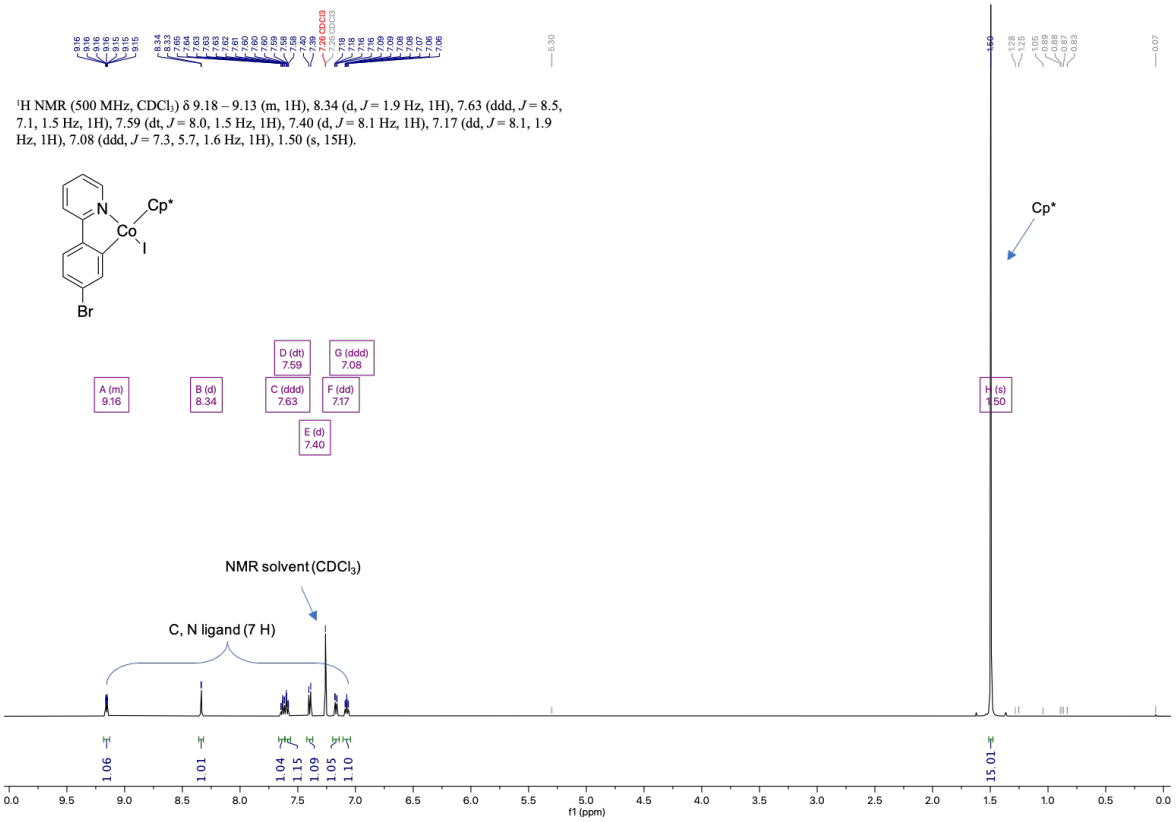


**Figure A. 11.** $^{1}$H NMR spectrum (500 MHz, $CDCl_3$) of **7a**

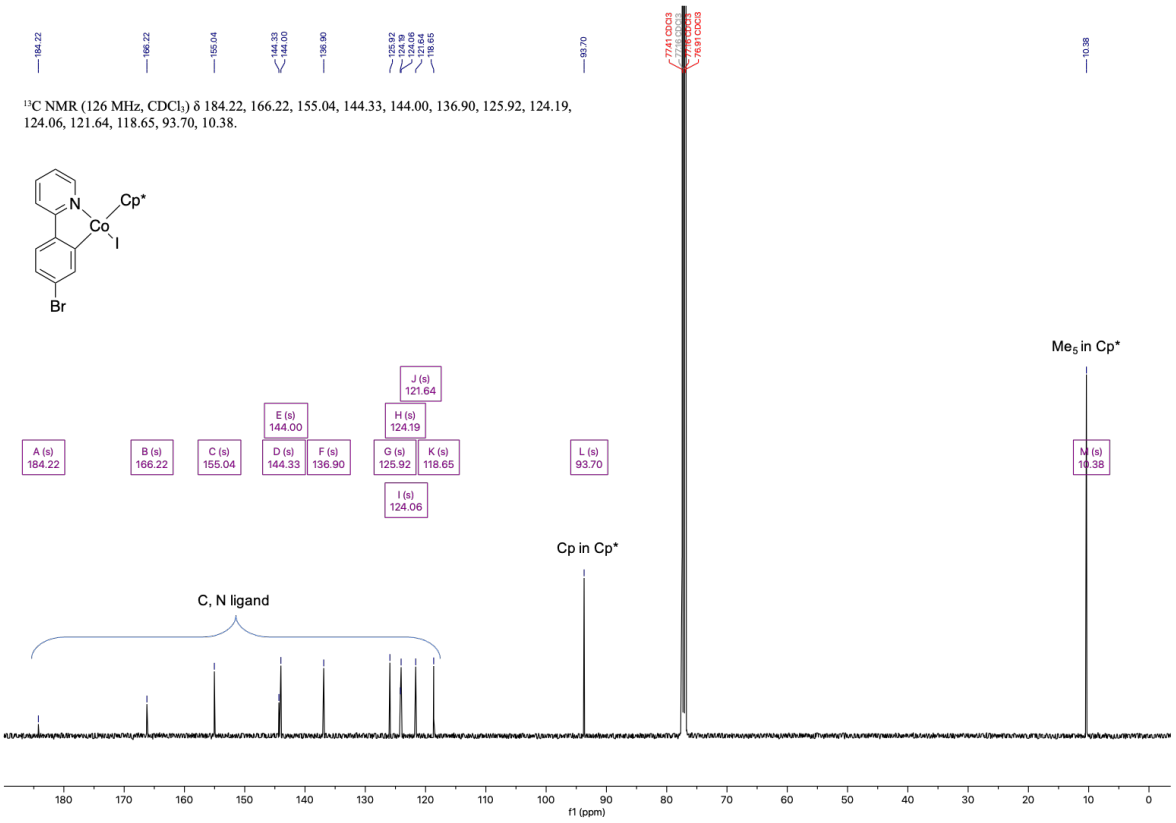


**Figure A. 12.** $^{13}$C NMR spectrum (126 MHz, $CDCl_3$) of **7a**

**8a**

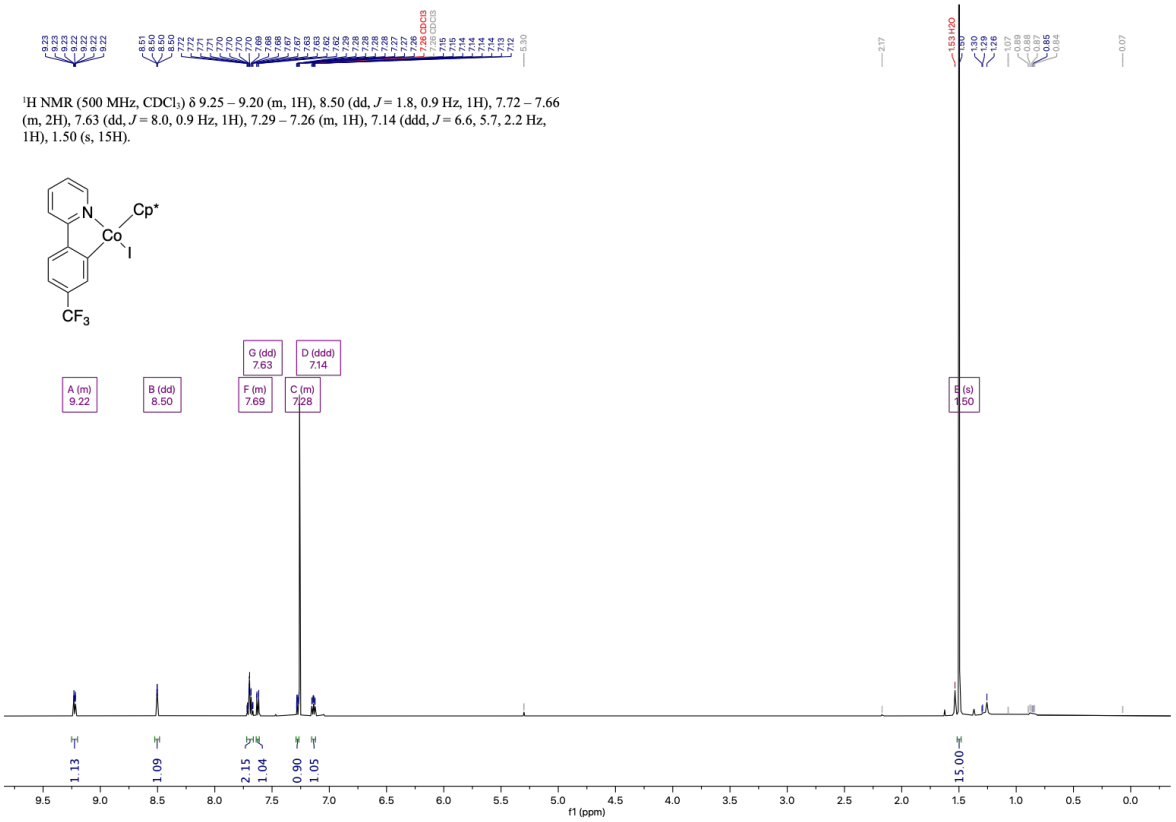


**Figure A. 13.** $^1$H NMR spectrum (500 MHz, $CDCl_3$) of **8a**

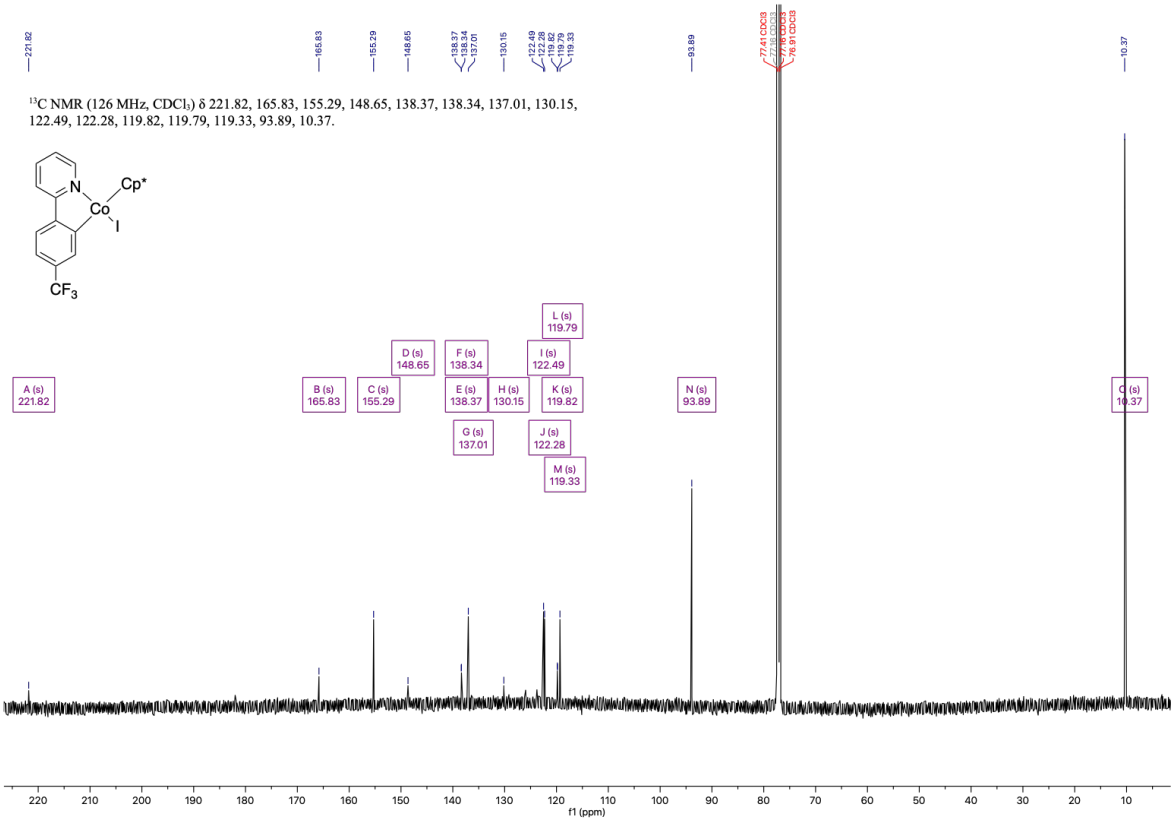


**Figure A. 14.** $^{13}$C NMR spectrum (126 MHz, $CDCl_3$) of **8a**

**9a**

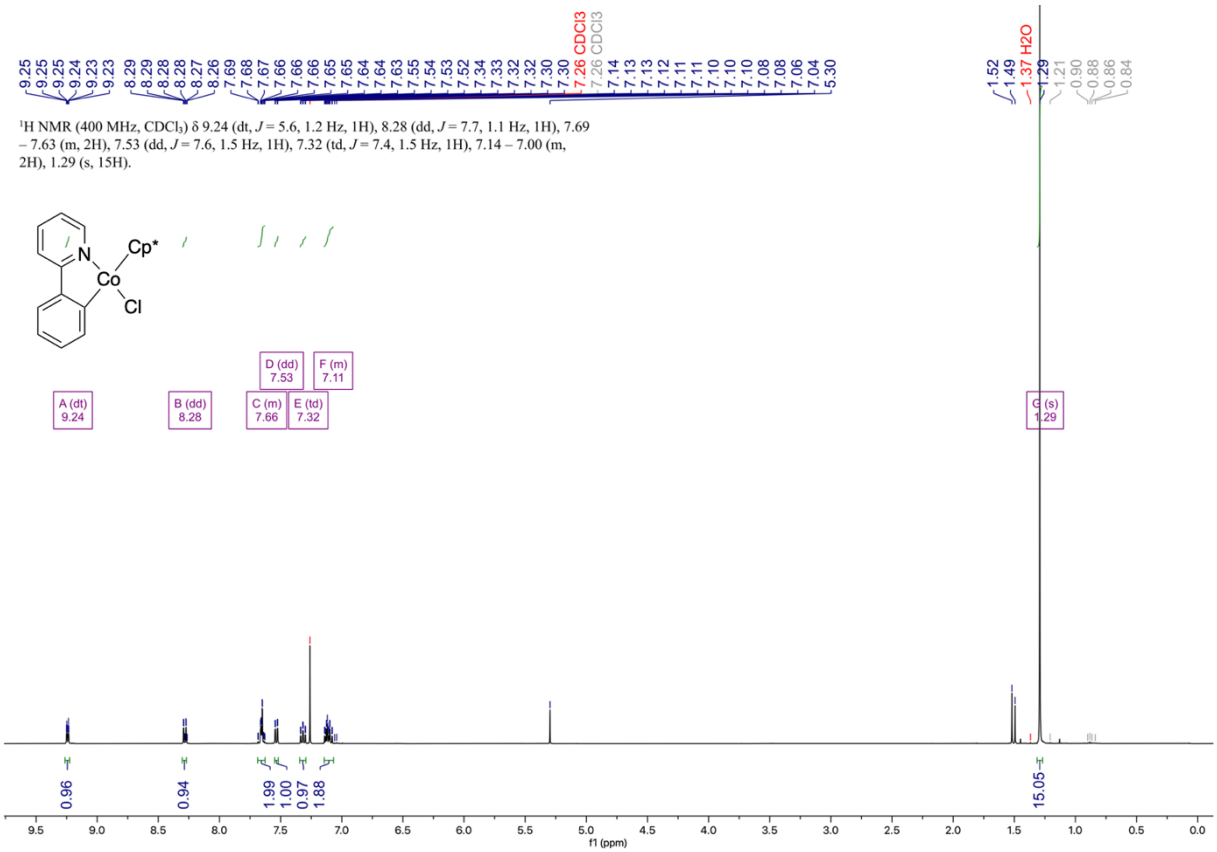


**Figure A. 15.** $^{1}H$ NMR spectrum (400 MHz, $CDCl_3$) of **9a**

**10a**

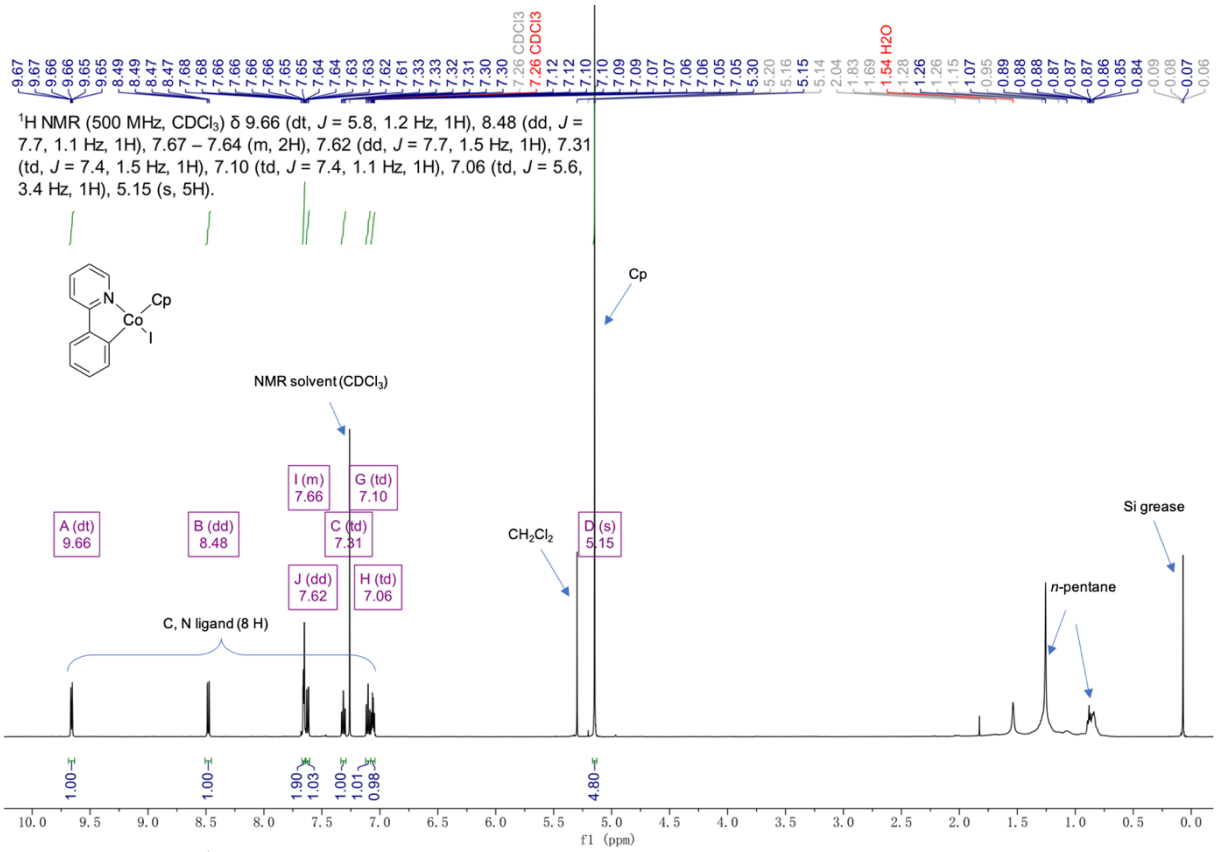


**Figure A. 16.** $^1$H NMR spectrum (500 MHz, $CDCl_3$) of **10a**

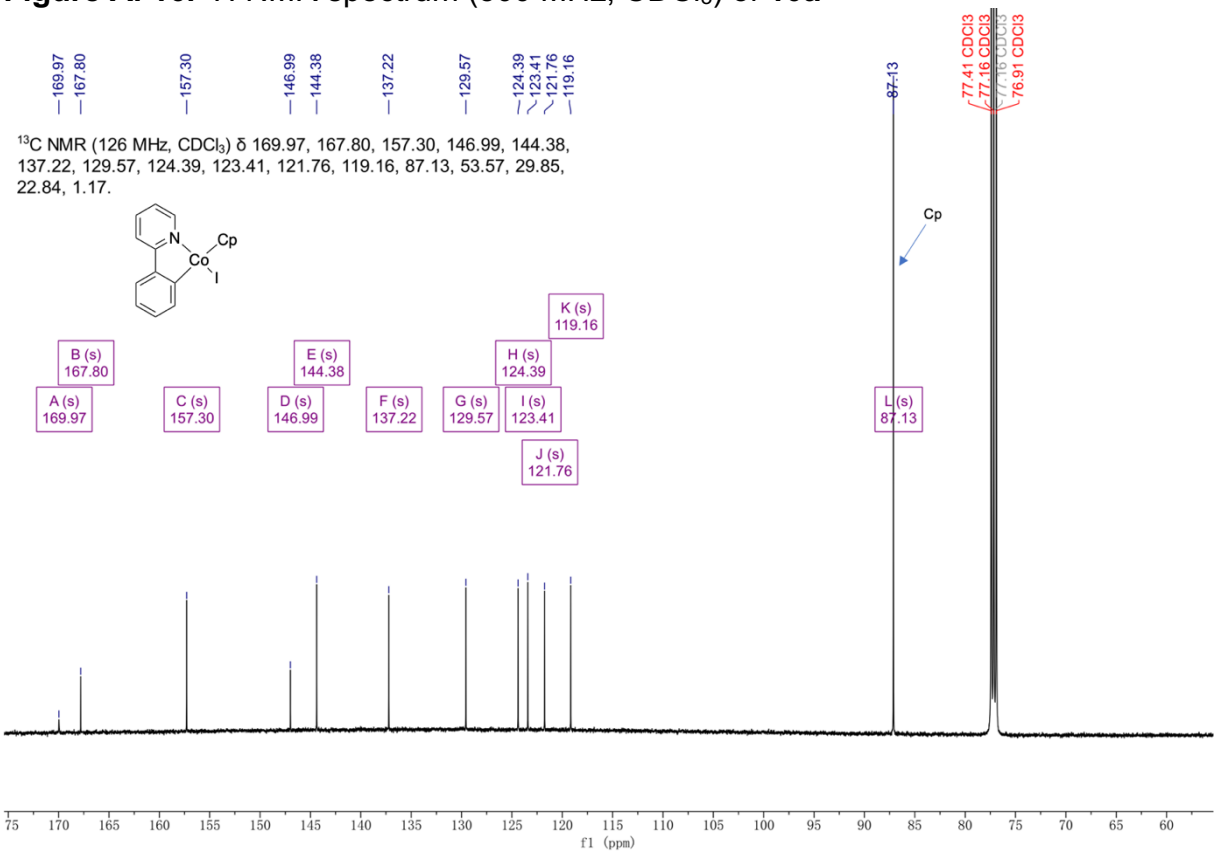


**Figure A. 17.** $^{13}$C NMR spectrum (126 MHz, $CDCl_3$) of **10a**

**1b**

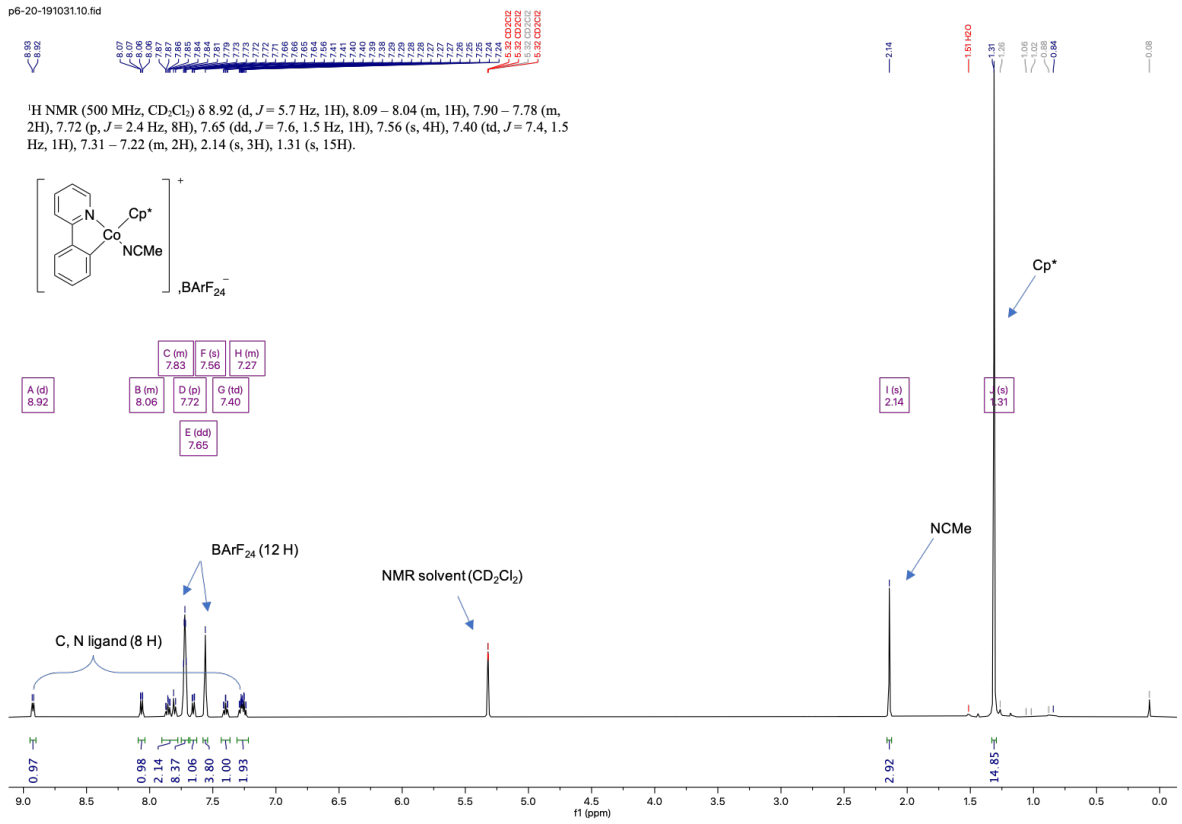


**Figure A. 18**. $^1$H NMR spectrum (500 MHz, $CD_2Cl_2$) of **1b**

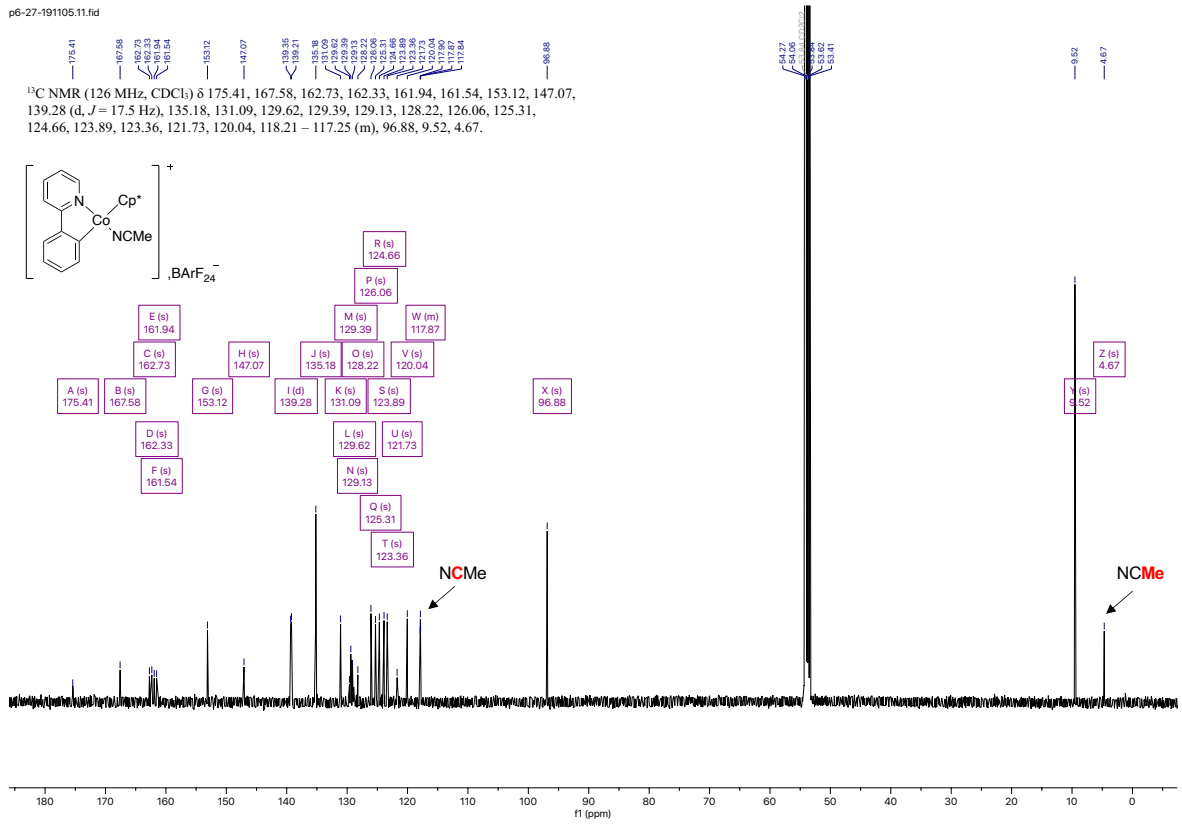


**Figure A. 19**. $^{13}$C NMR spectrum (126 MHz, $CD_2Cl_2$) of **1b**

**1b'**

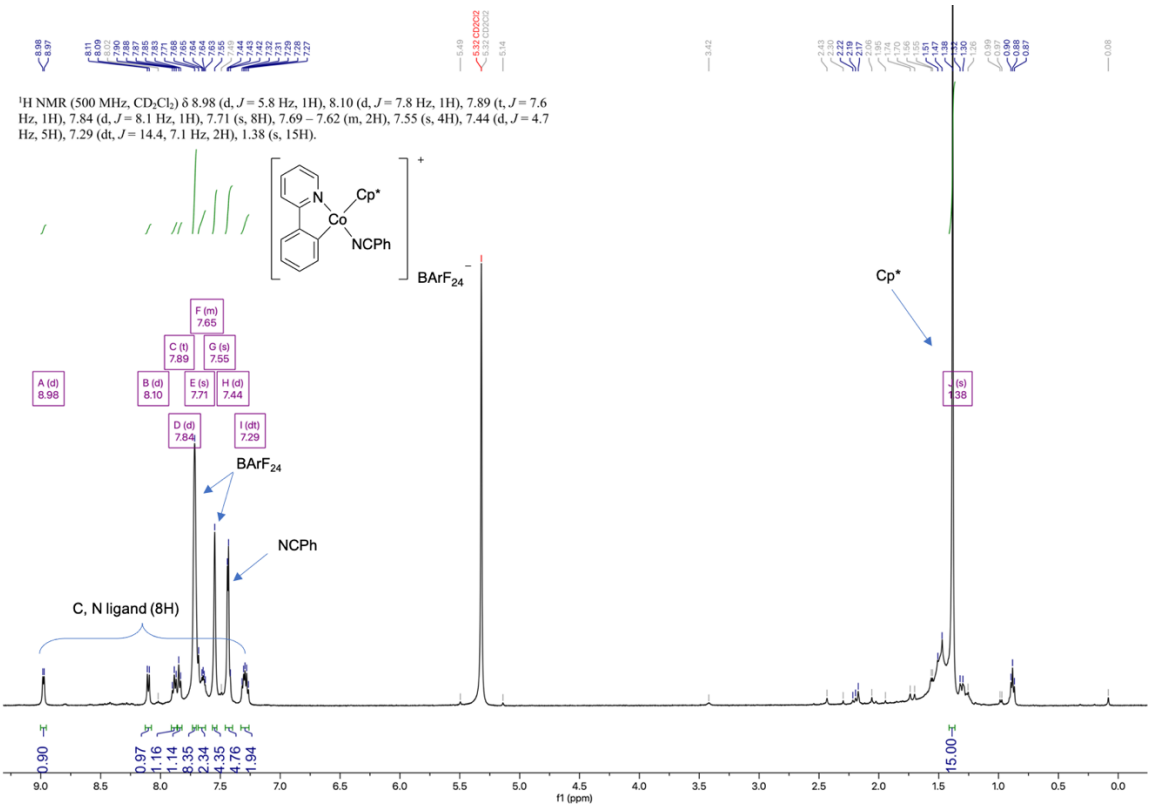


**Figure A. 20**. $^{1}H$ NMR spectrum (500 MHz, $CD_2Cl_2$) of **1b'**

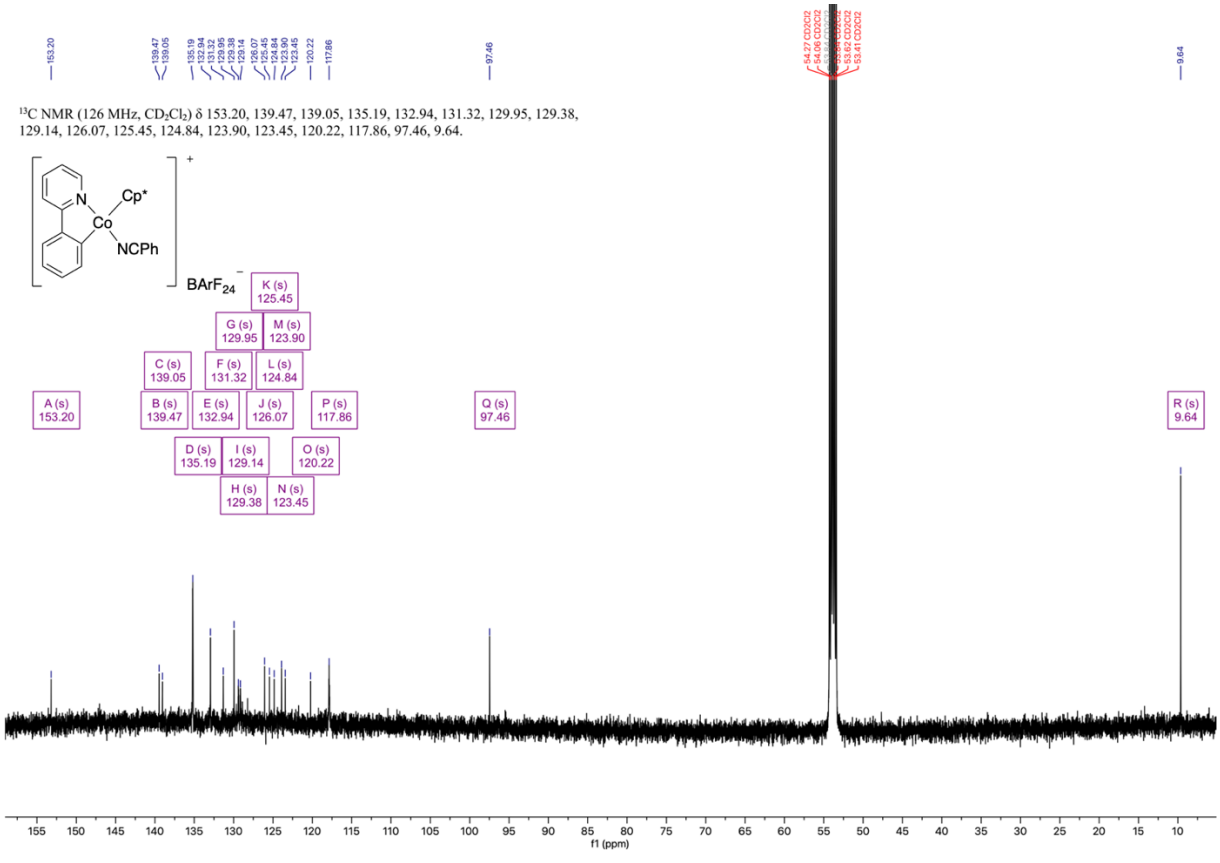


**Figure A. 21**. $^{13}C$ NMR spectrum (126 MHz, $CD_2Cl_2$) of **1b'**

**3b**

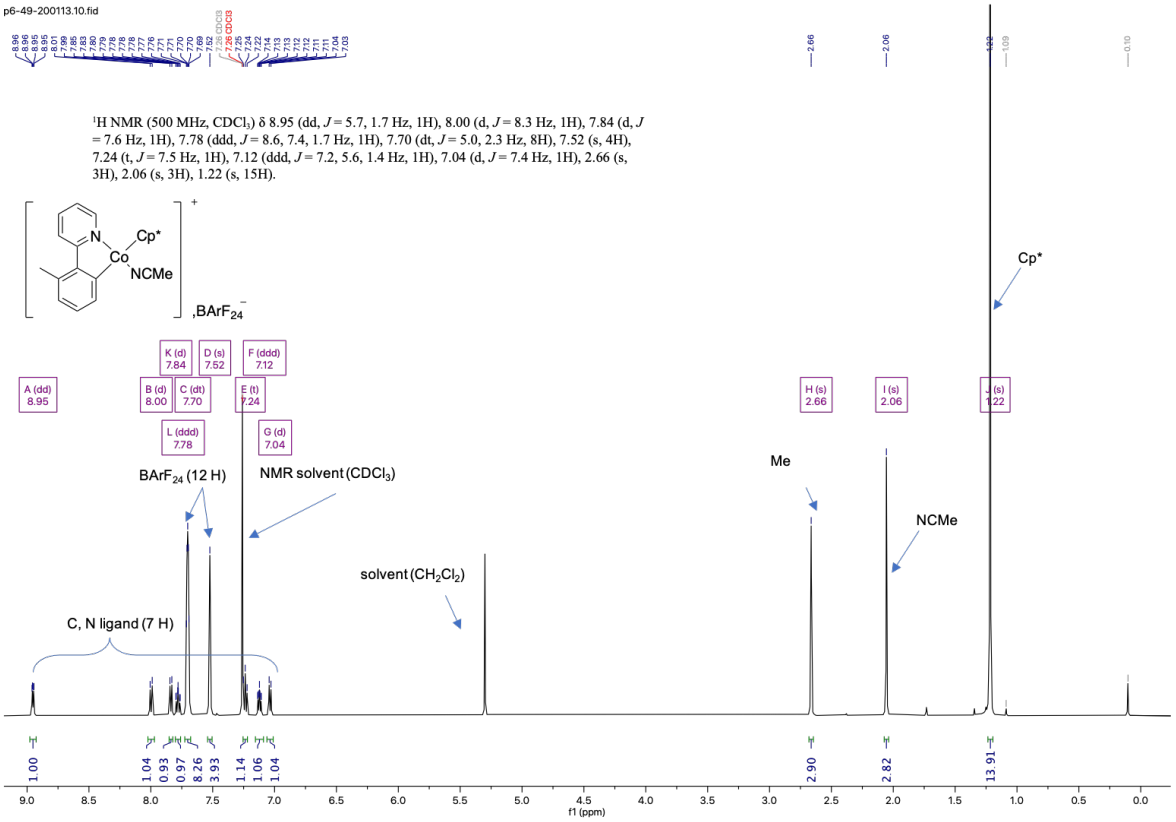


**Figure A. 22.** $^{1}$H NMR spectrum (500 MHz, $CDCl_3$) of **3b**

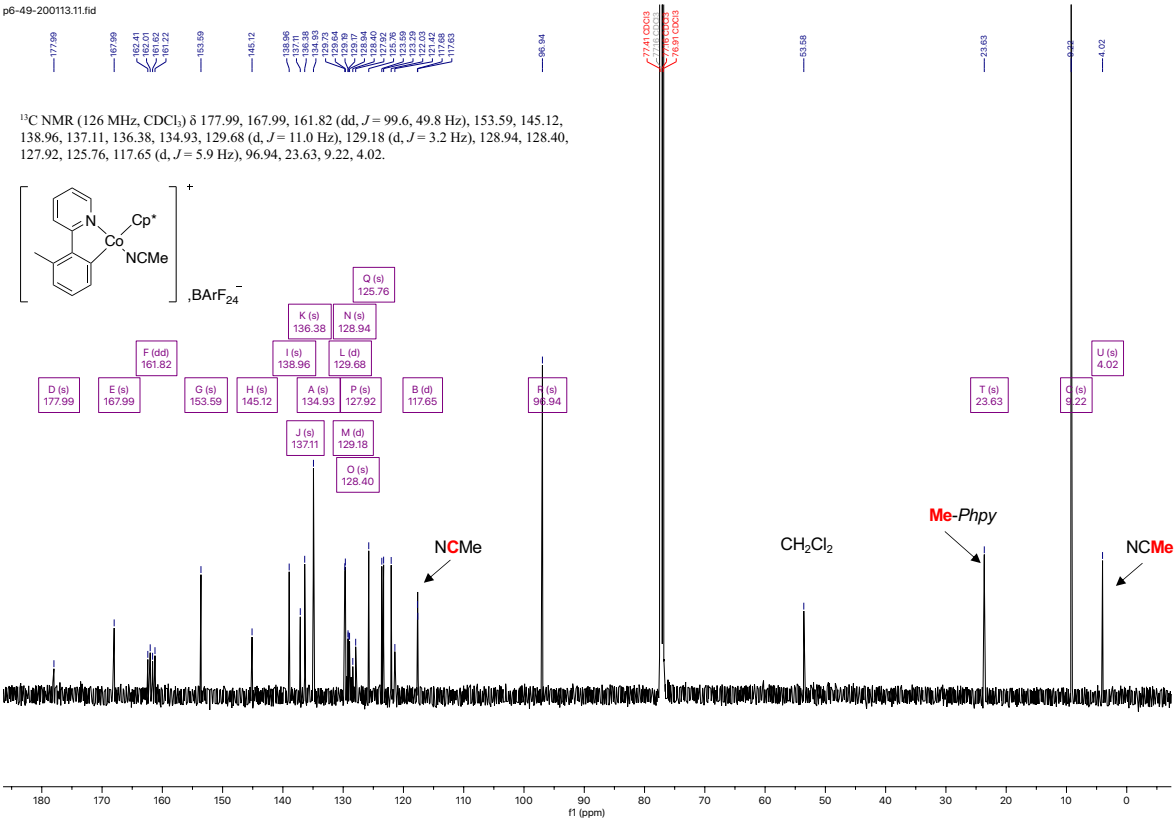


**Figure A. 23.** $^{13}$C NMR spectrum (126 MHz, $CDCl_3$) of **3b**

**4b**

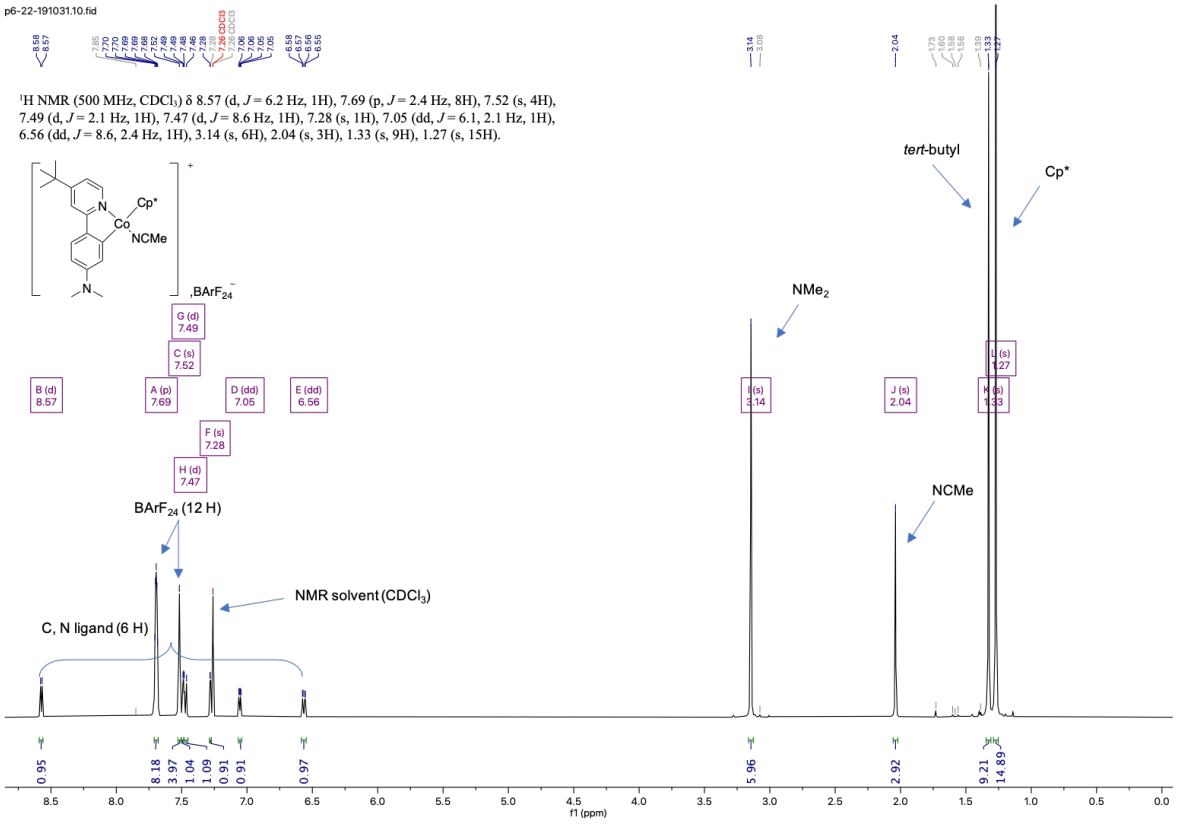


**Figure A. 24**. $^{1}$H NMR spectrum (500 MHz, $CDCl_3$) of **4b**

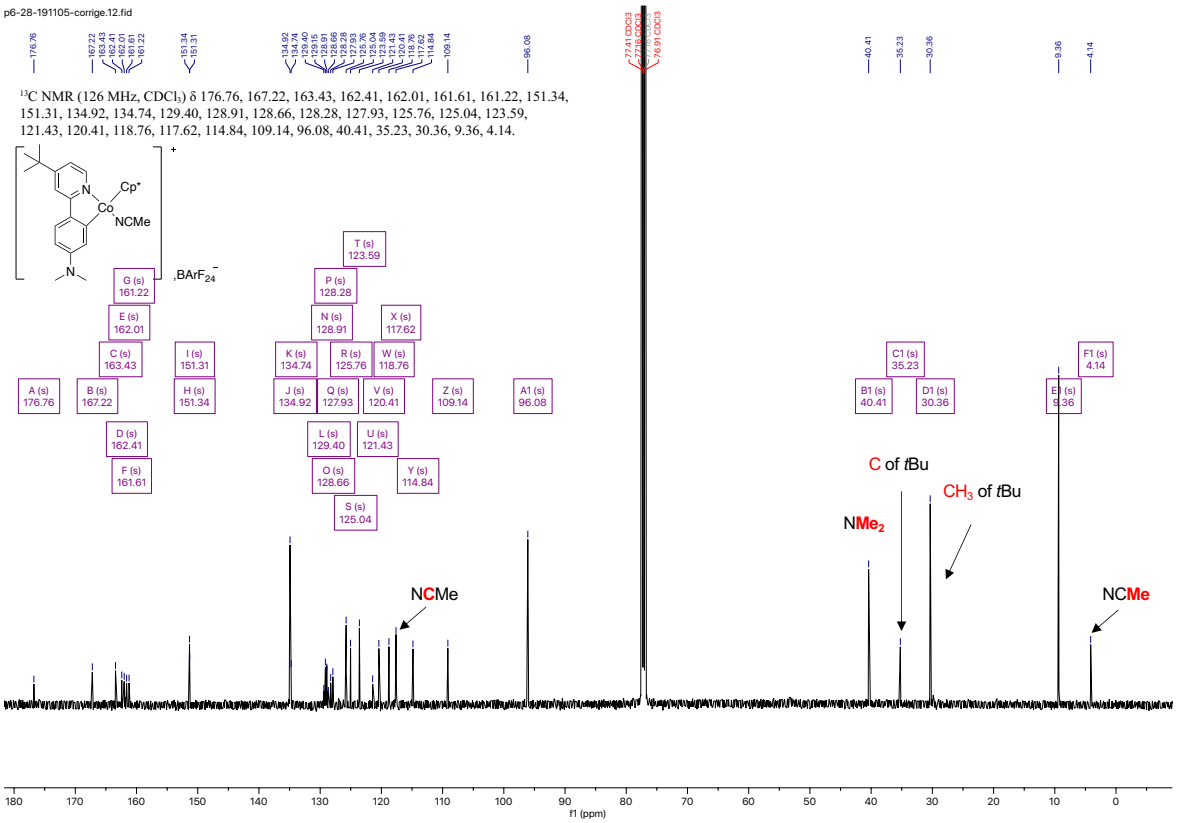


**Figure A. 25**. $^{13}$C NMR spectrum (126 MHz, $CDCl_3$) of **4b**

**5b**

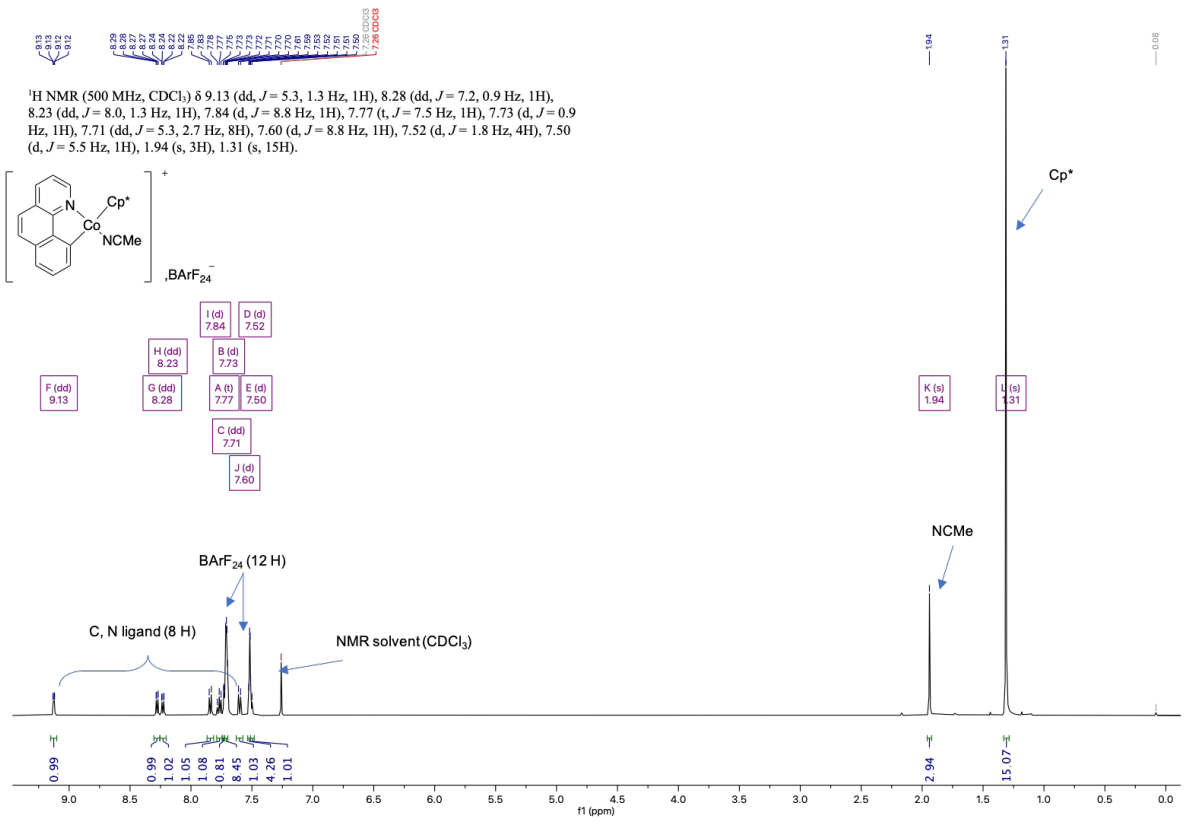


**Figure A. 26.** $^1$H NMR spectrum (500 MHz, $CDCl_3$) of **5b**

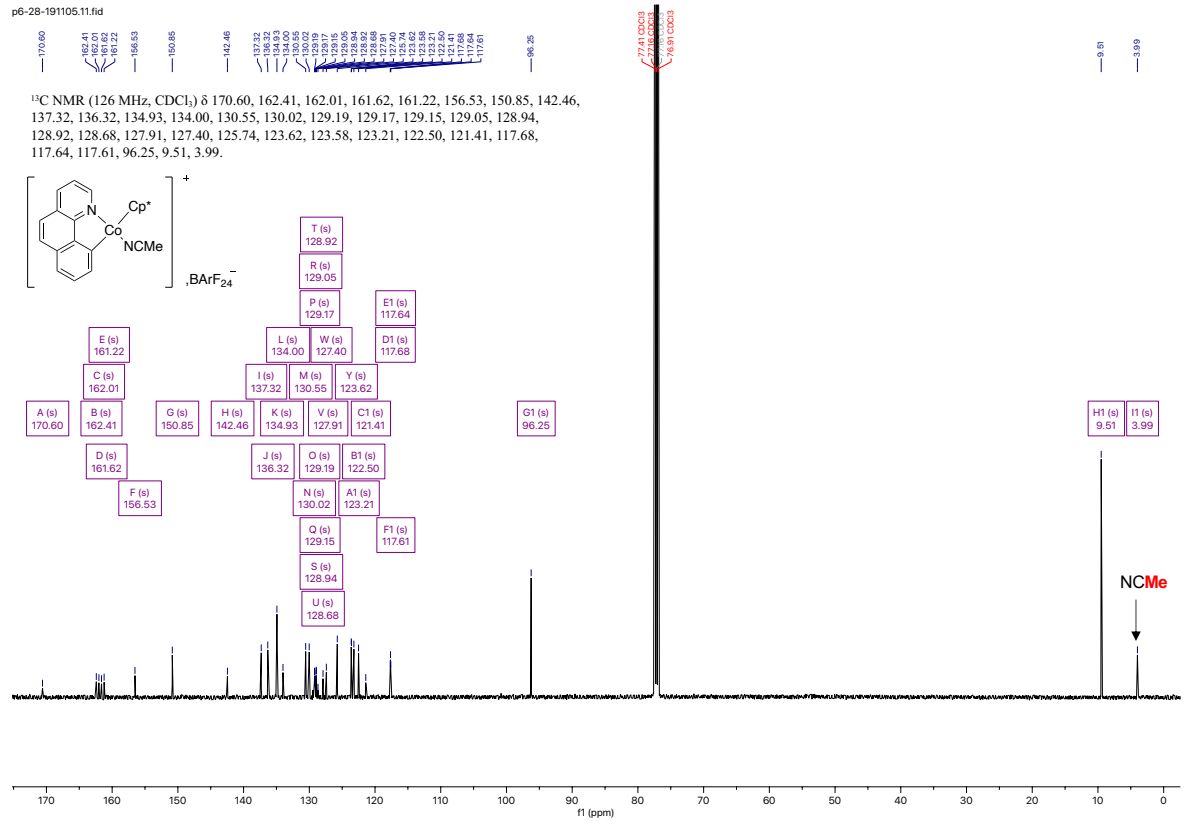


**Figure A. 27.** $^{13}$C NMR spectrum (126 MHz, $CDCl_3$) of **5b**

## 2b

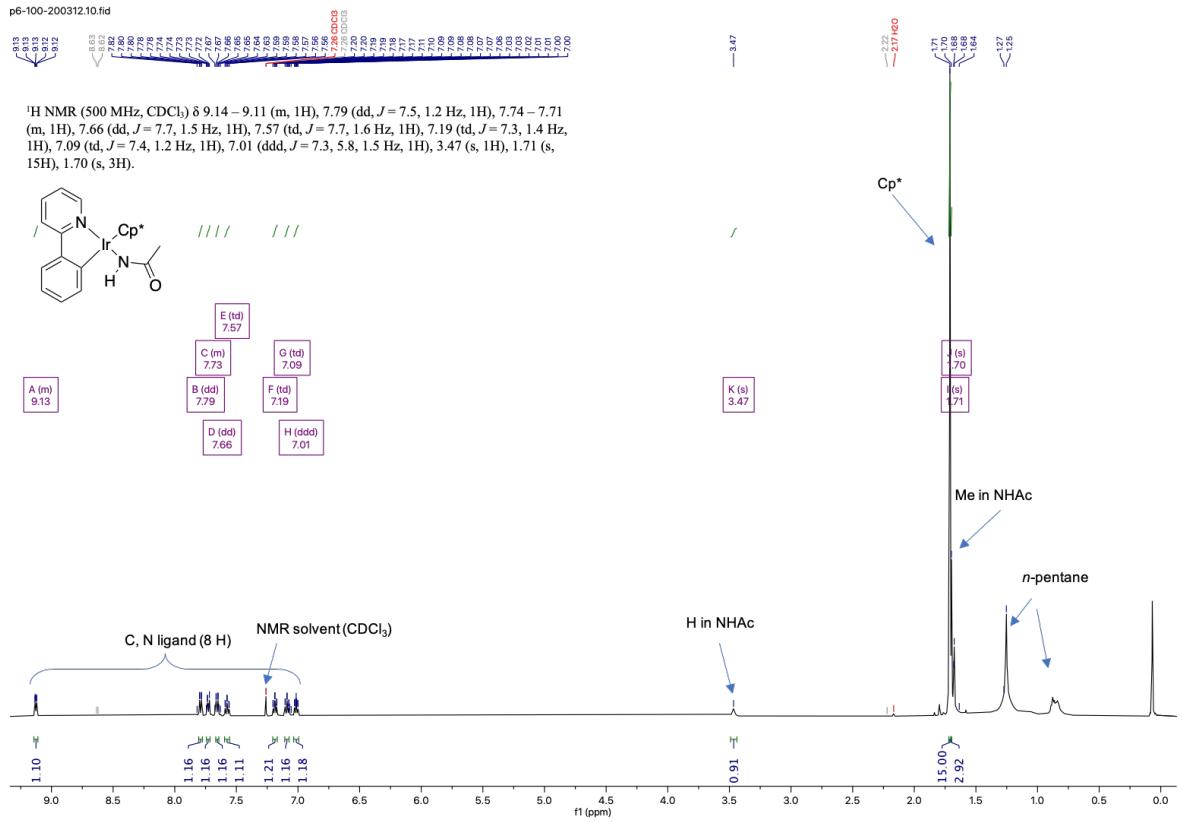


**Figure A. 28.** $^{1}$H NMR spectrum (500 MHz, $CDCl_3$) of **2b**

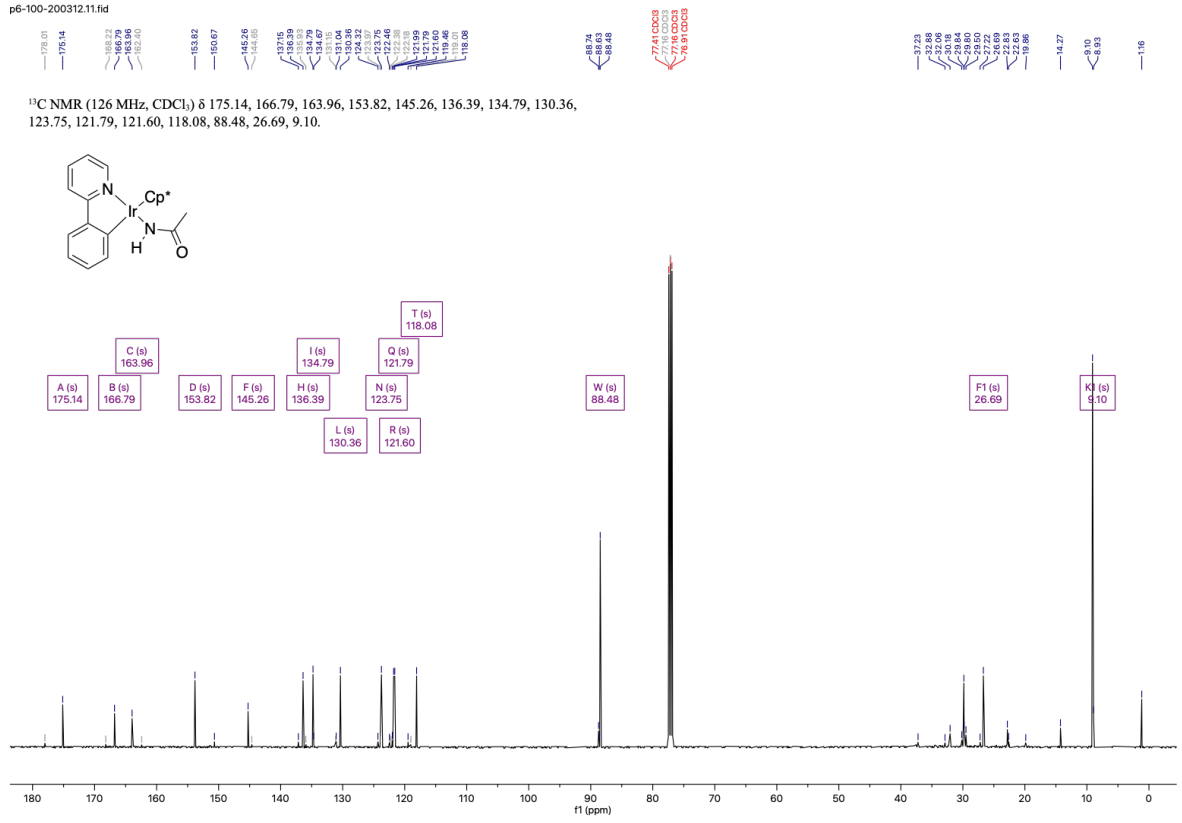


**Figure A. 29.** $^{13}$C NMR spectrum (126 MHz, $CDCl_3$) of **2b**

**1f**

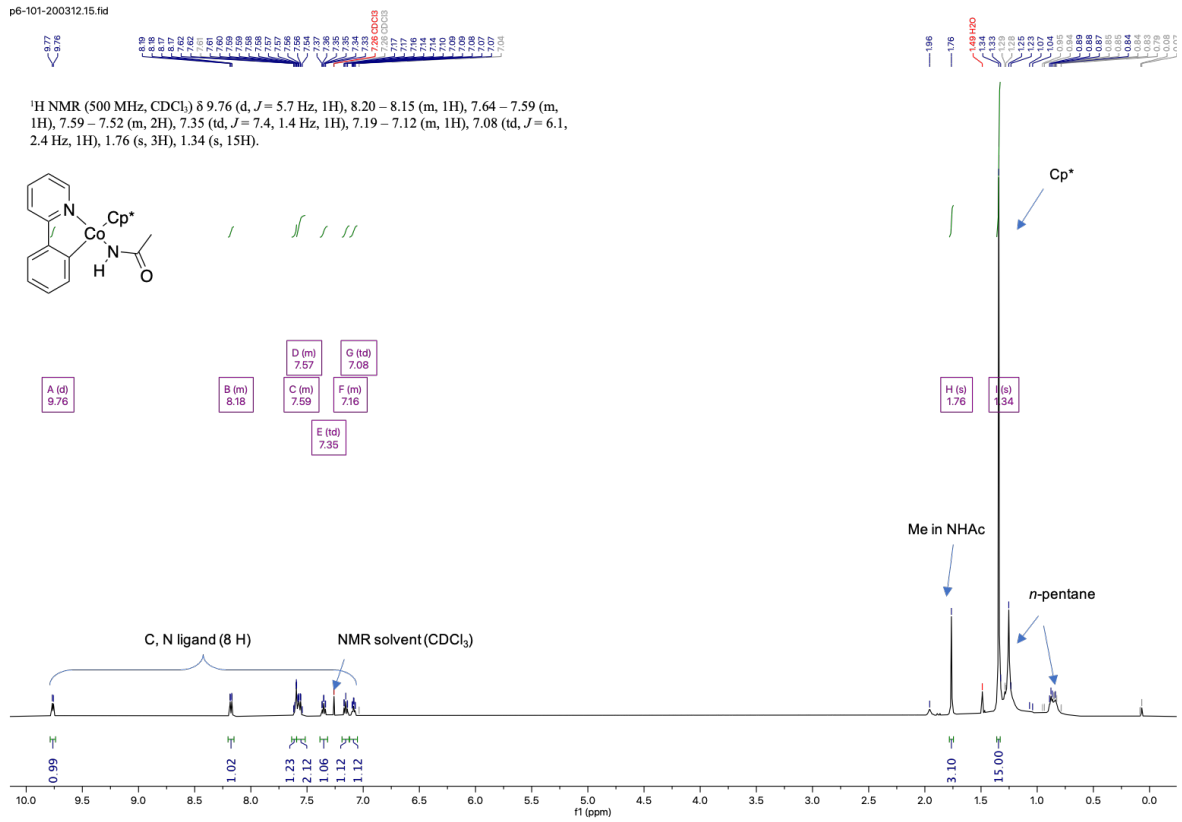


**Figure A. 30.** $^{1}$H NMR spectrum (500 MHz, $CDCl_3$) of **1f**

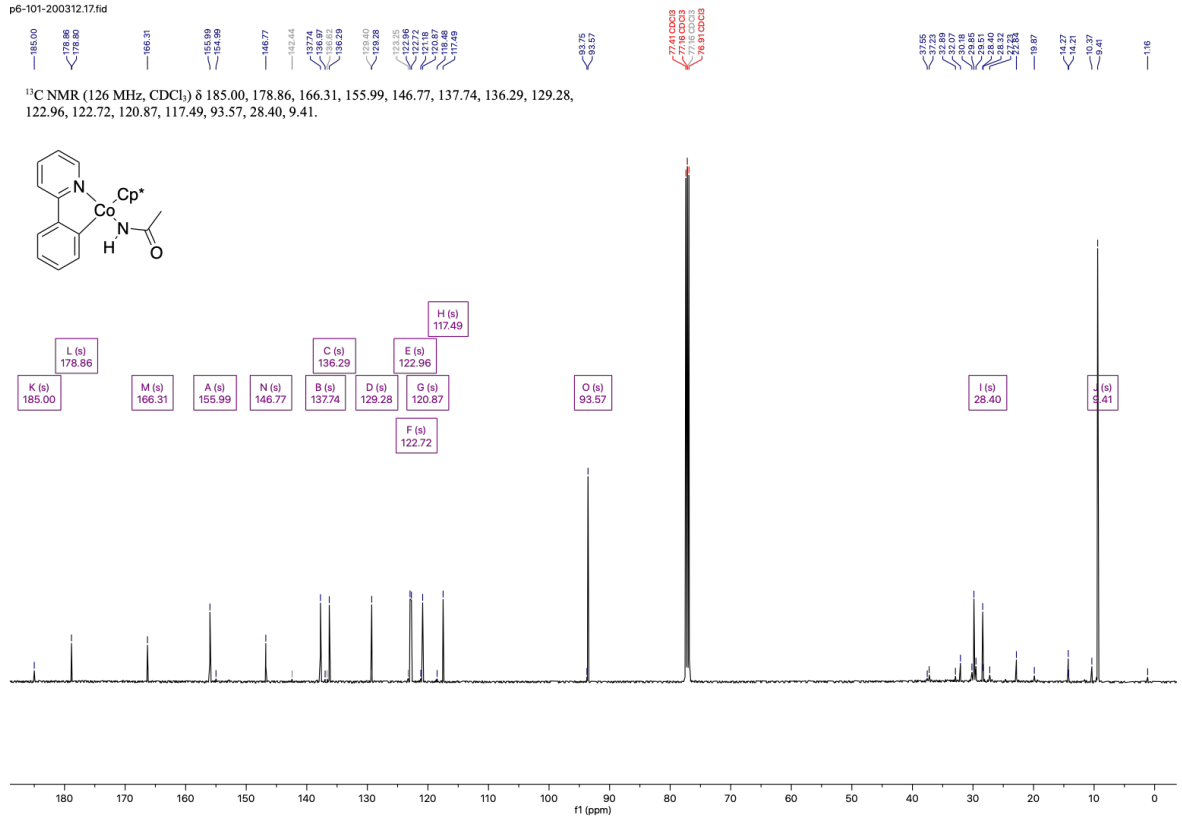


**Figure A. 31.** $^{13}$C NMR spectrum (126 MHz, $CDCl_3$) of **1f**

## NMR Spectra [1c][BArF$_{24}$]

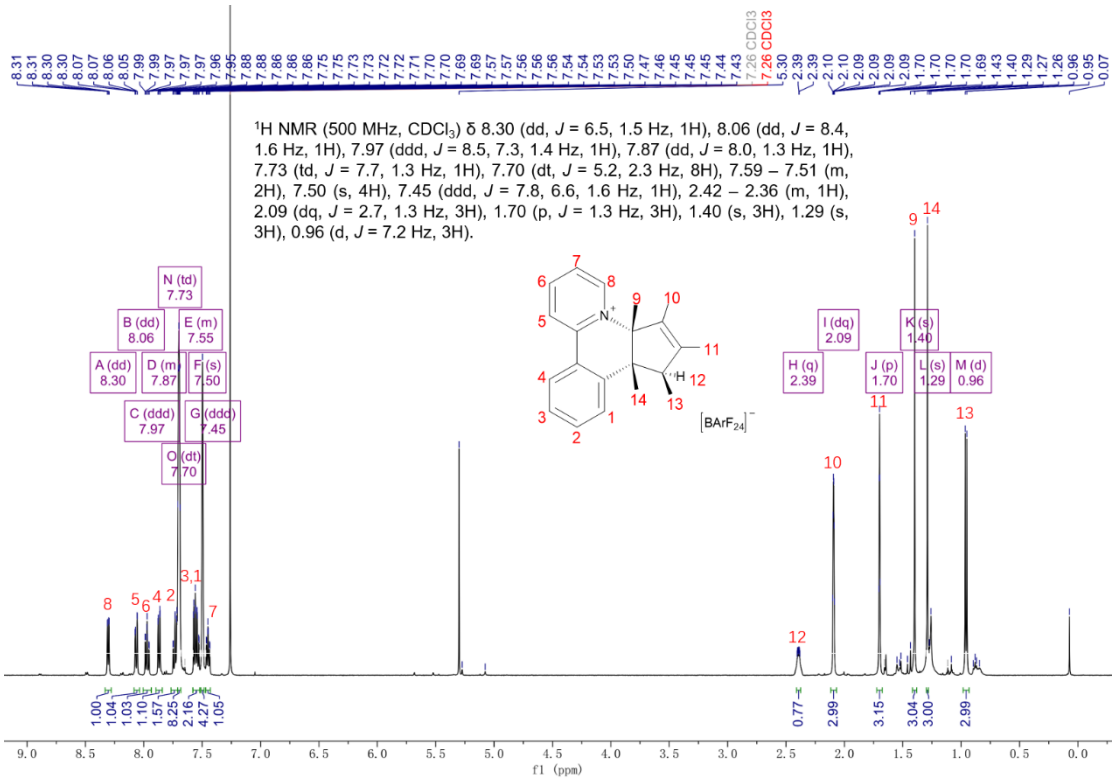


**Figure A. 32.** $^1$H NMR spectrum (500 MHz, CDCl$_3$) of [**1c**][BArF$_{24}$]

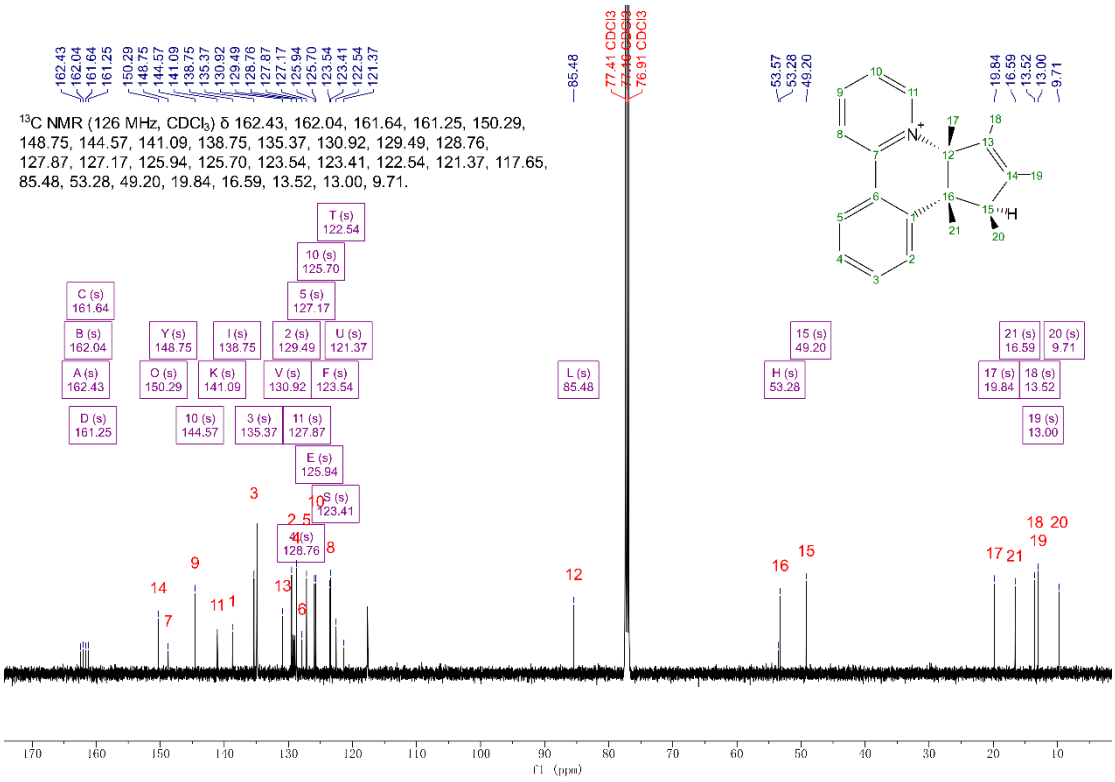


**Figure A. 33.** $^{13}$C NMR spectrum (126 MHz, CDCl$_3$) of [**1c**][BArF$_{24}$]

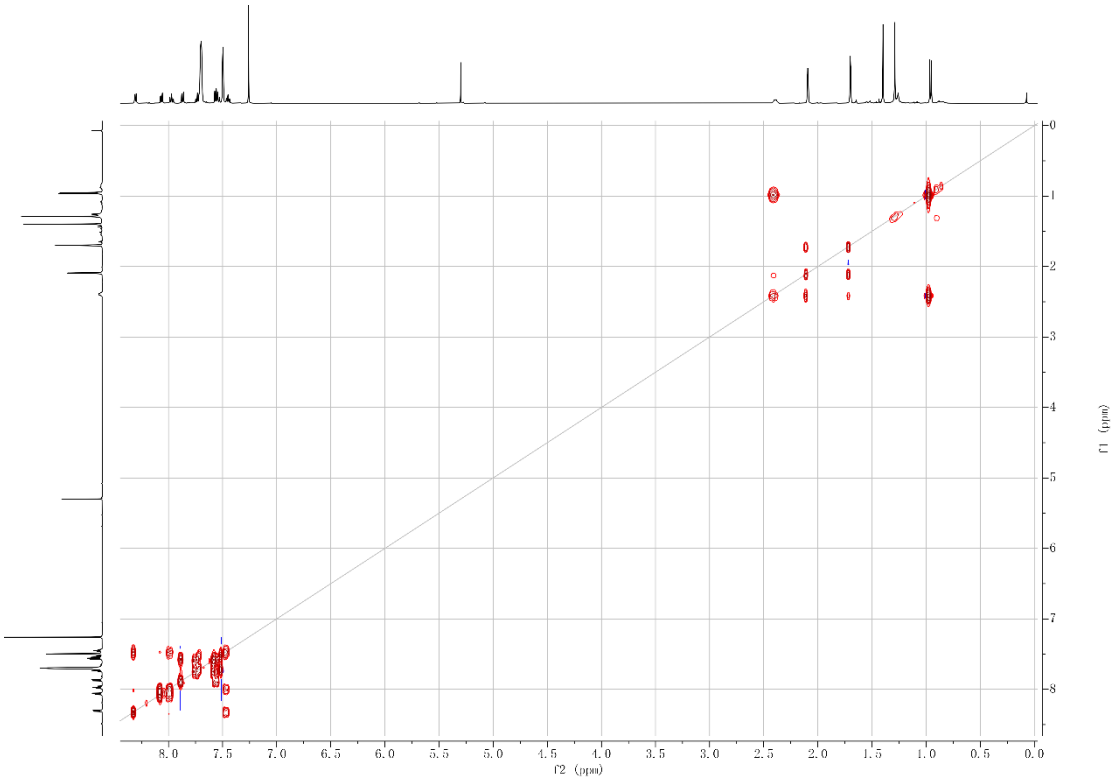


**Figure A. 34.** $^{1}$H-$^{1}$H COSY spectrum of **[1c]**[$BArF_{24}$]

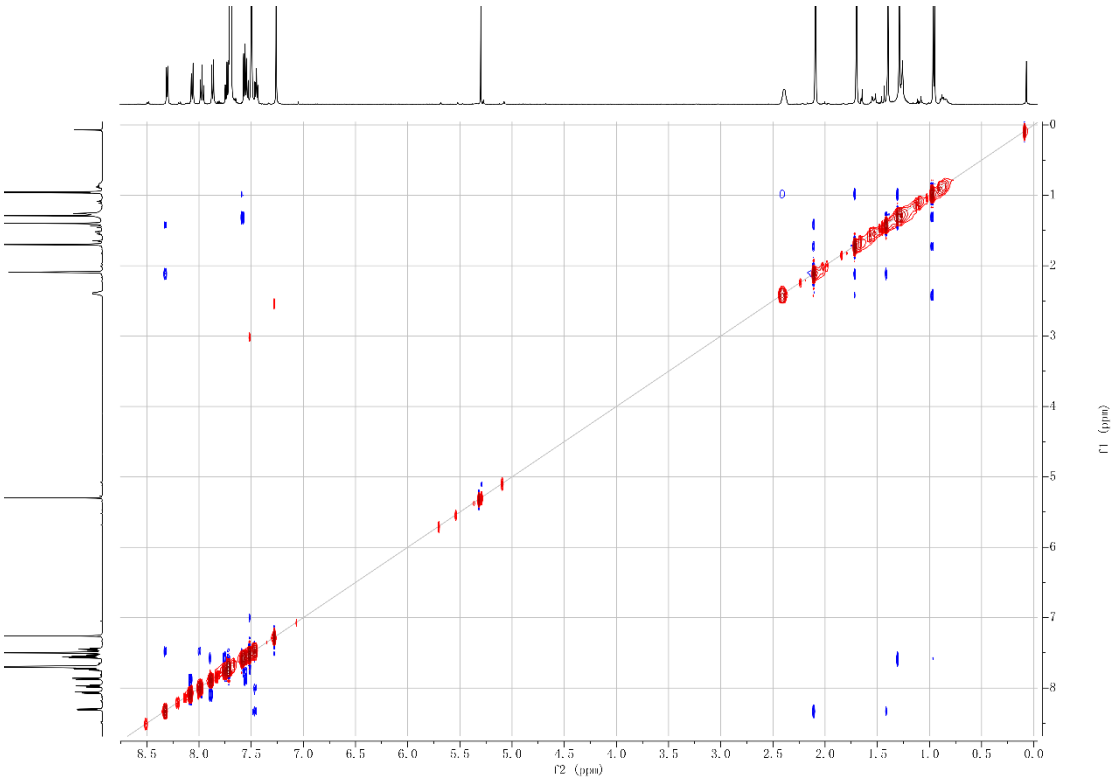


**Figure A. 35.** $^{1}$H-$^{1}$H NOESY spectrum of **[1c]**[$BArF_{24}$]

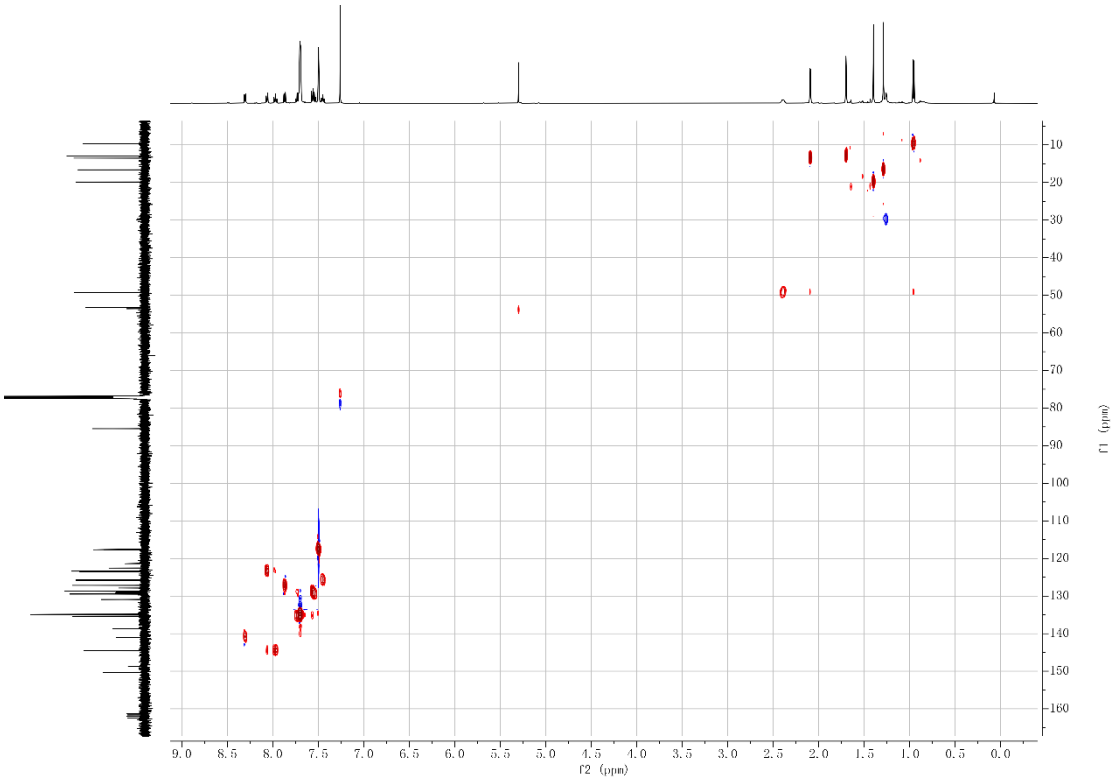

**Figure A. 36.** $^{1}H$-$^{13}C$ HSQC spectrum of [**1c**][$BArF_{24}$]

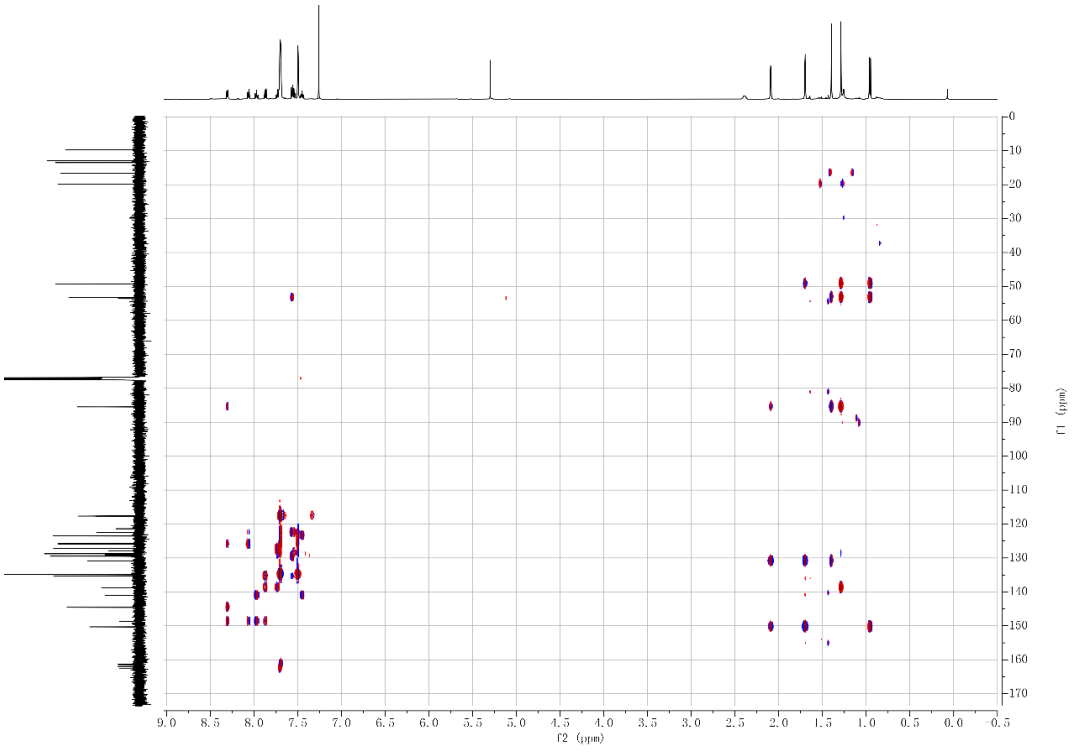

**Figure A. 37.** $^{1}H$-$^{13}C$ HMBC spectrum of [**1c**][$BArF_{24}$]

## NMR Spectra of [7c][BArF$_{24}$]

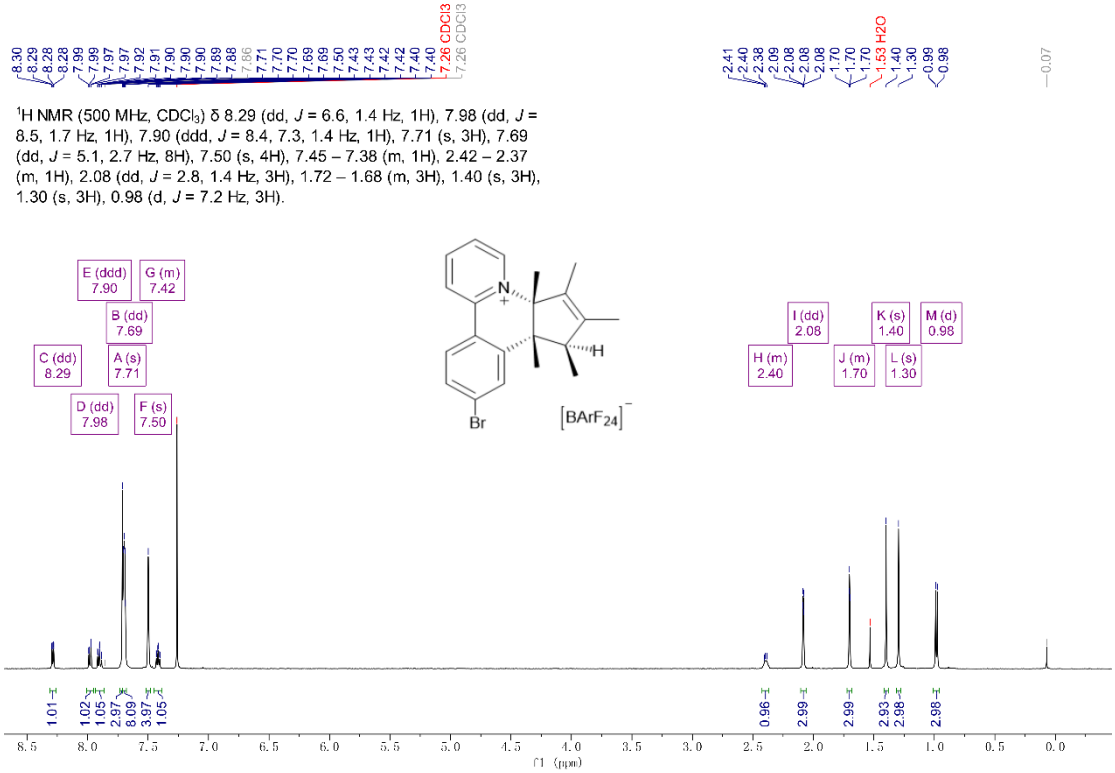


**Figure A. 38**. $^1$H NMR spectrum (500 MHz, CDCl$_3$) of [**7c**][BArF$_{24}$]

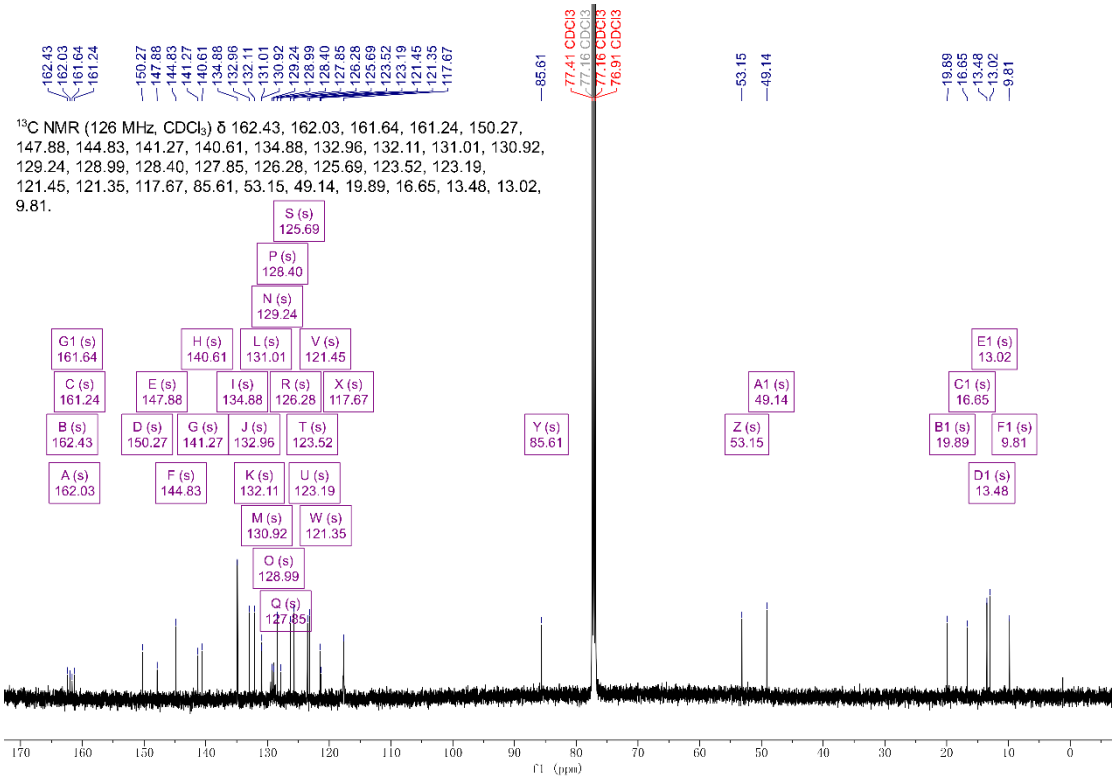


**Figure A. 39.** $^{13}$C NMR spectrum (126 MHz, CDCl$_3$) of [**7c**][BArF$_{24}$]

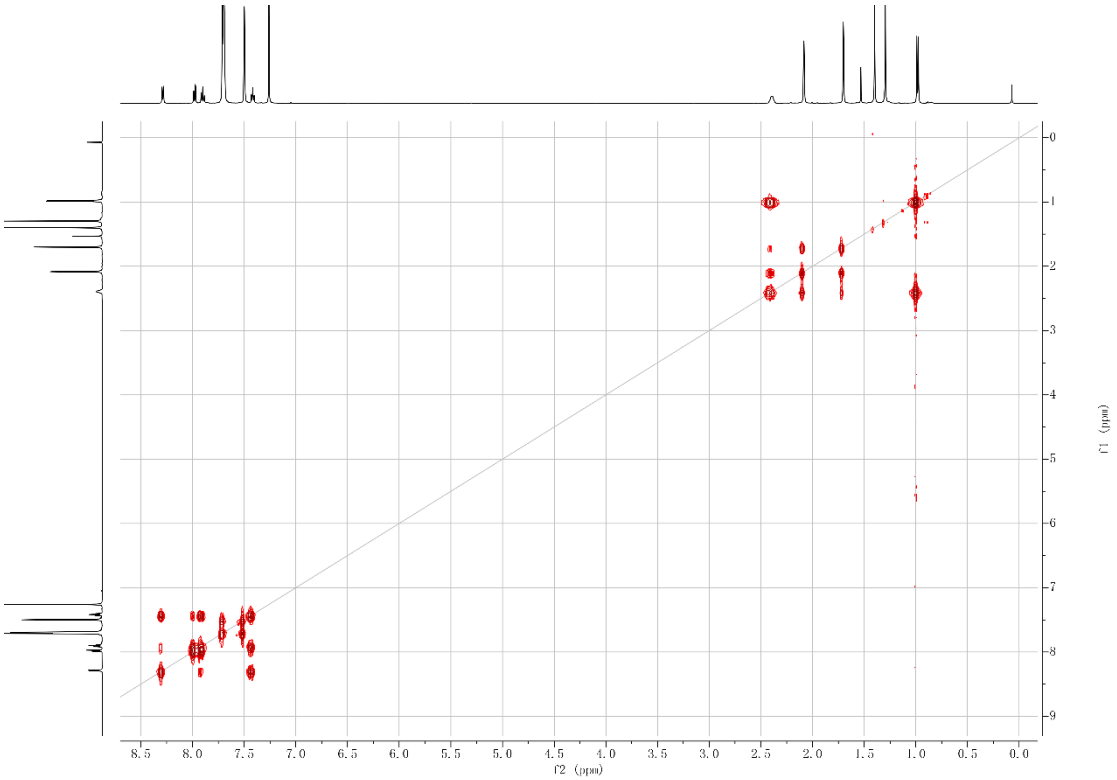


**Figure A. 40.** $^{1}$H-$^{1}$H COSY spectrum of [**7c**][BArF$_{24}$]

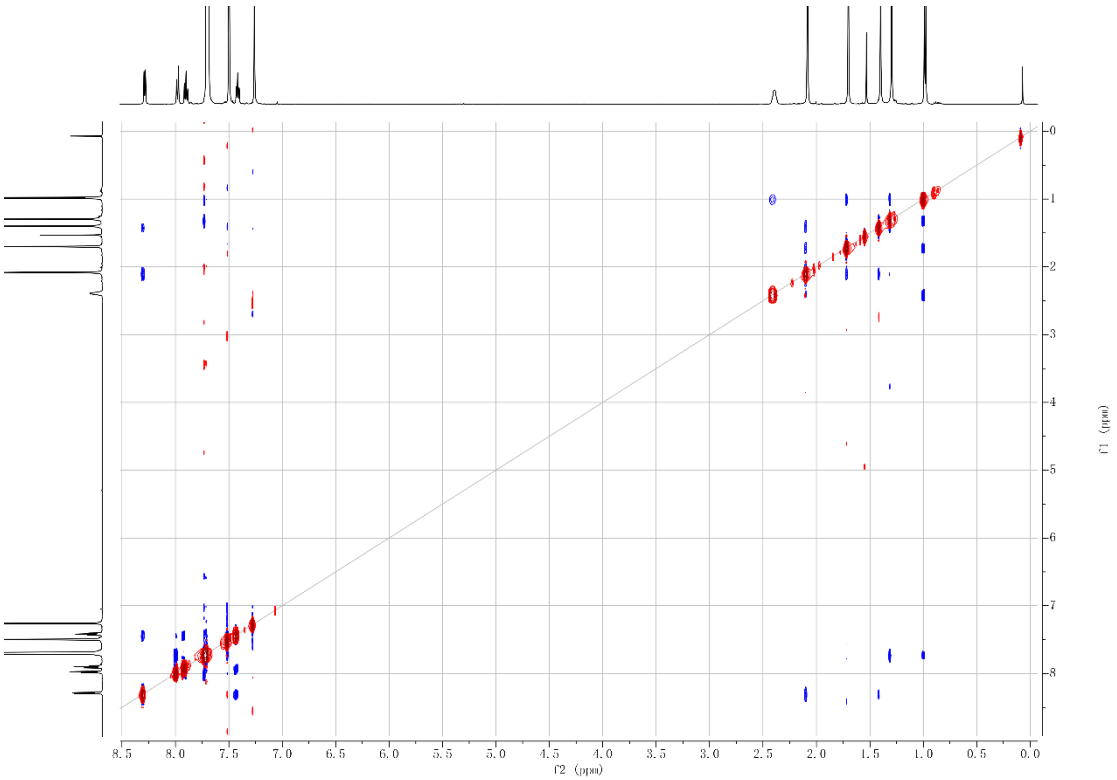


**Figure A. 41.** $^{1}$H-$^{1}$H NOESY spectrum of [**7c**][BArF$_{24}$]

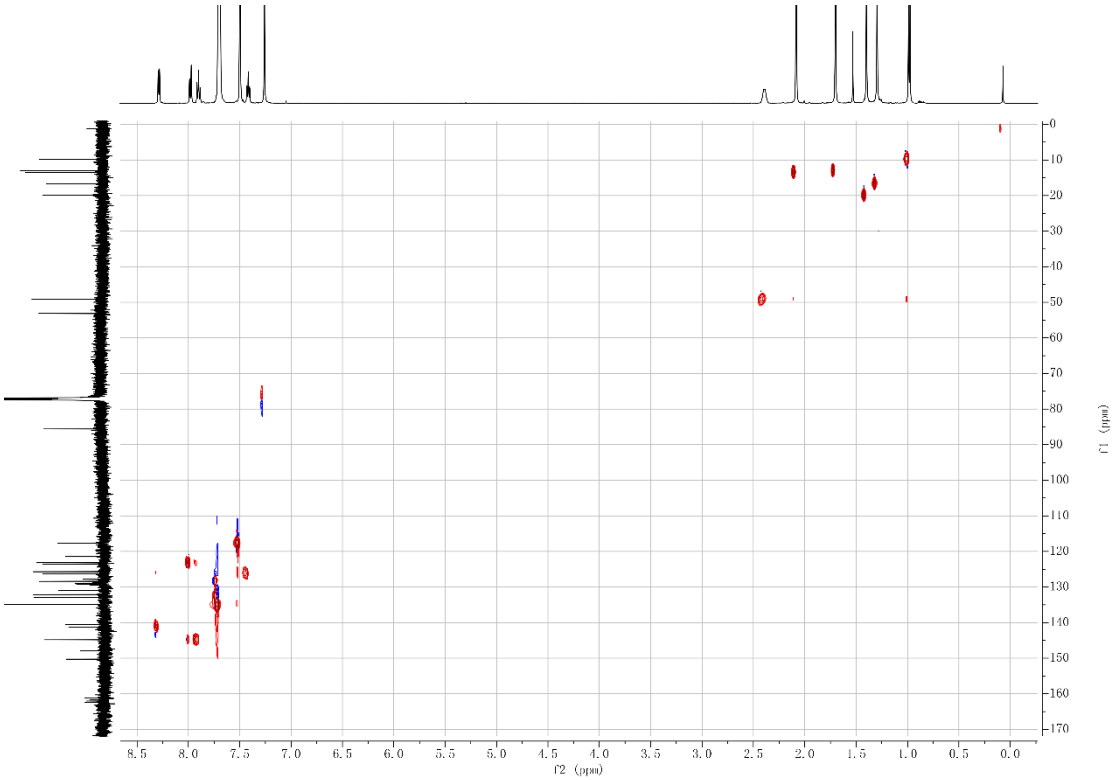

**Figure A. 42.** $^{1}H$-$^{13}C$ HSQC spectrum of [**7c**][$BArF_{24}$]

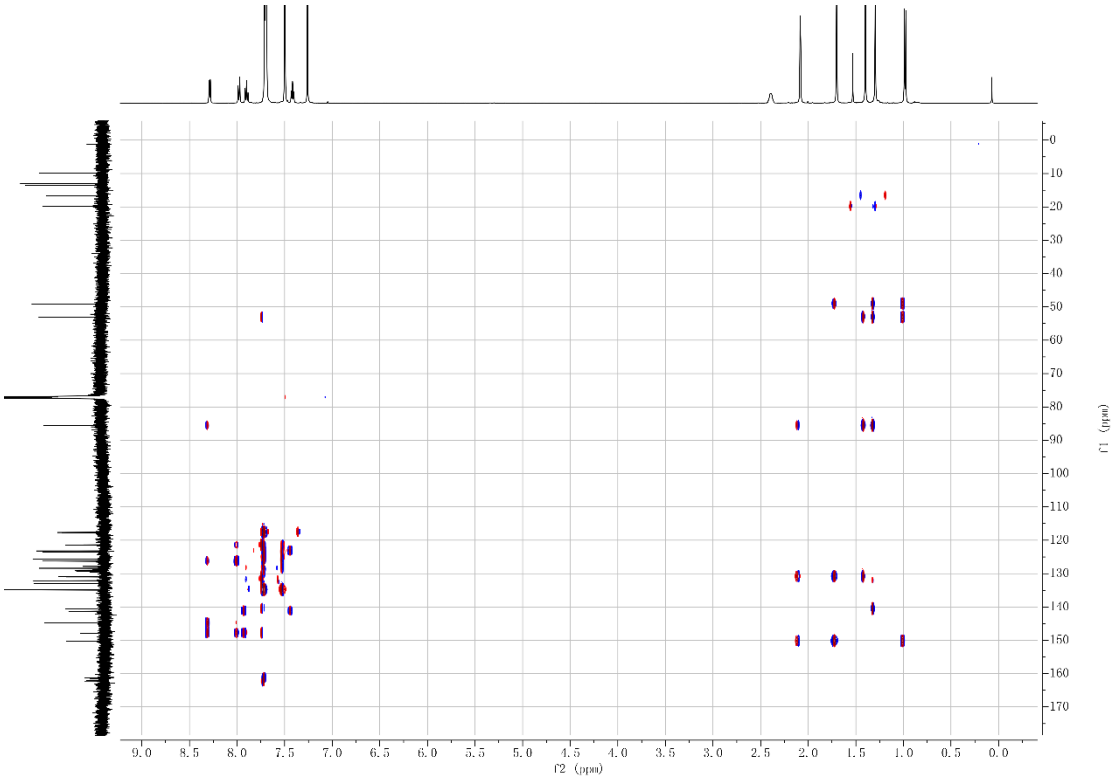

**Figure A. 43.** $^{1}H$-$^{13}C$ HMBC spectrum of [**7c**][$BArF_{24}$]

## NMR Spectra of [8c][BArF$_{24}$]

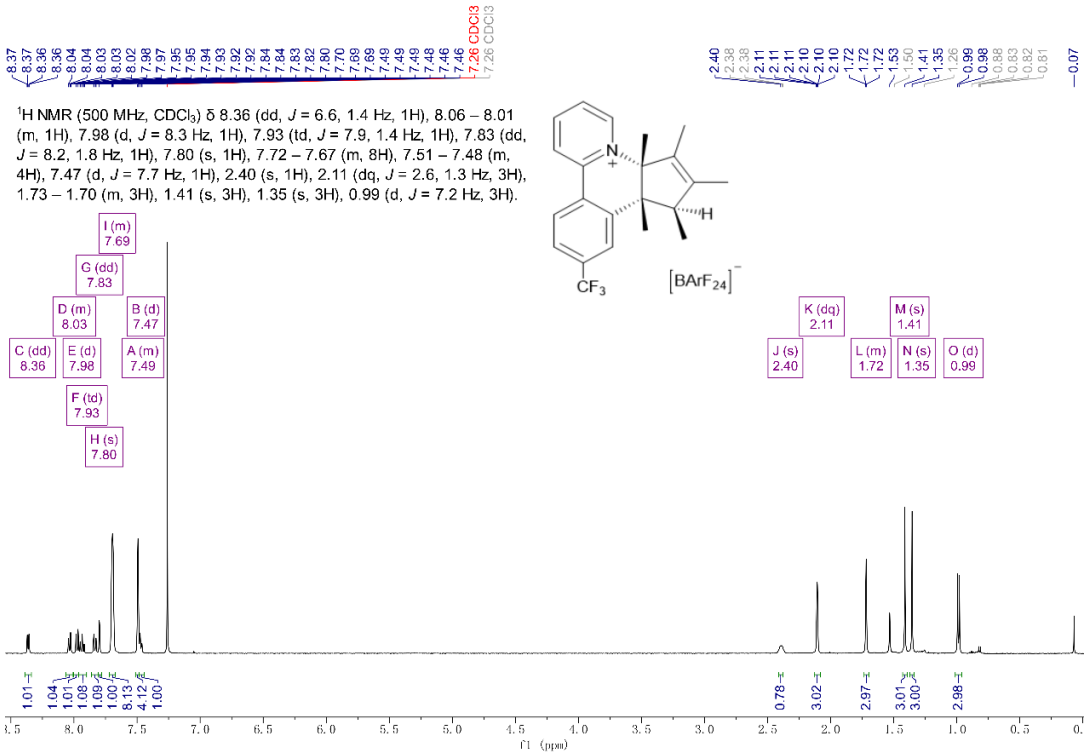


**Figure A. 44.** $^1$H NMR spectrum (500 MHz, CDCl$_3$) of [**8c**][BArF$_{24}$]

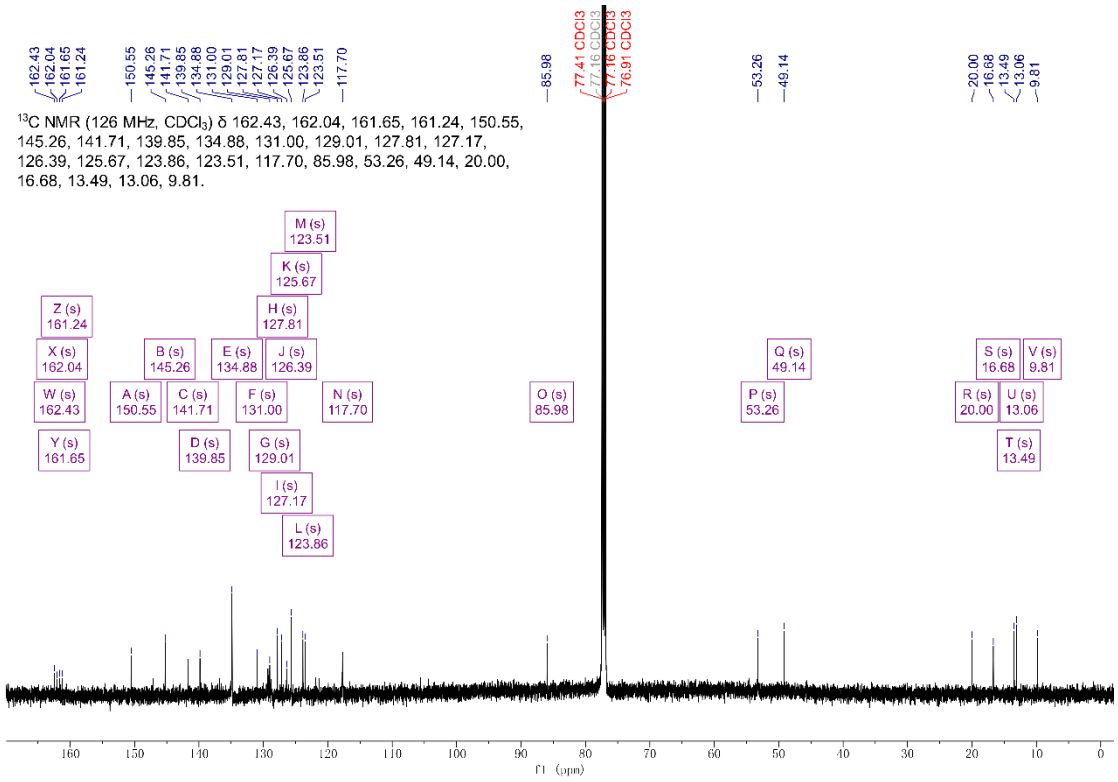


**Figure A. 45.** $^{13}$C NMR spectrum (126 MHz, CDCl$_3$) of [**8c**][BArF$_{24}$]

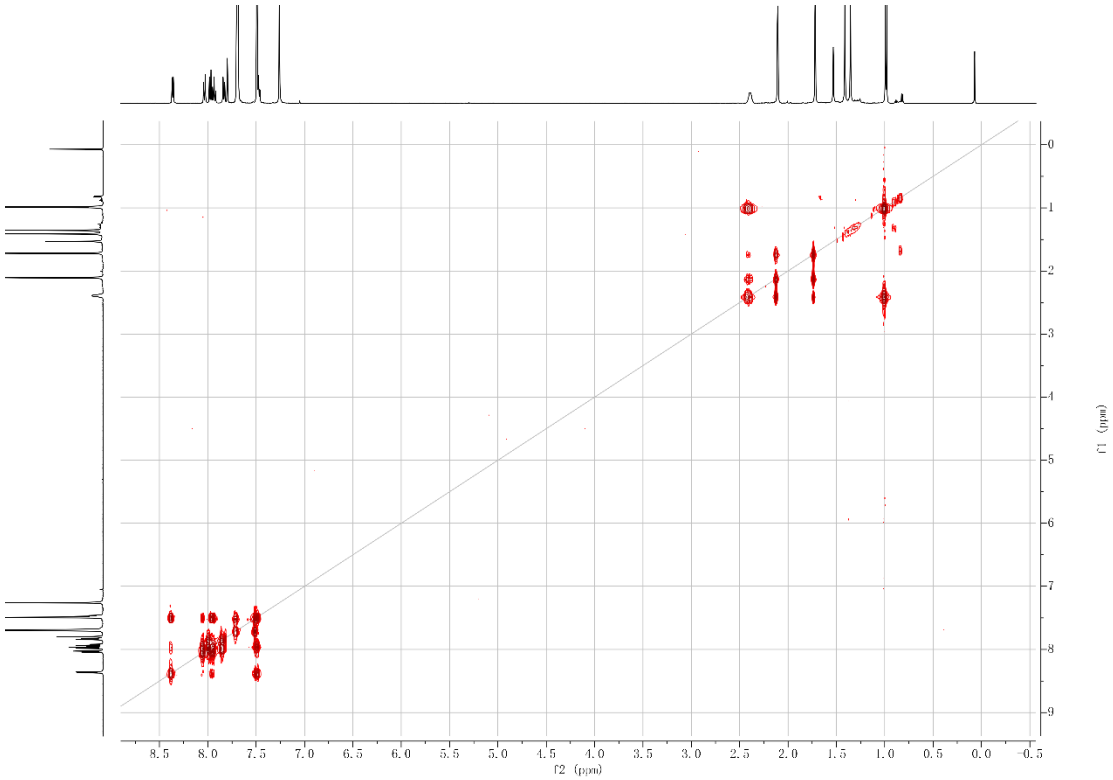


**Figure A. 46.** $^{1}H$-$^{1}H$ COSY spectrum of [**8c**][$BArF_{24}$]

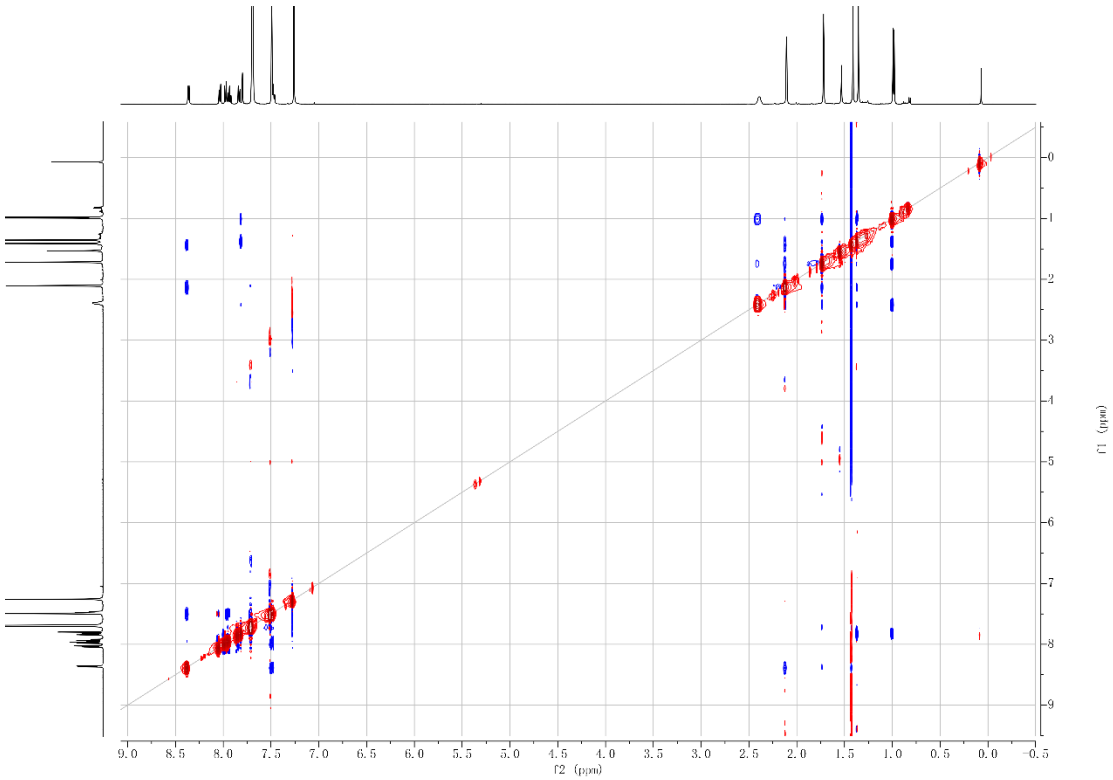


**Figure A. 47.** $^{1}H$-$^{1}H$ NOESY spectrum of [**8c**][$BArF_{24}$]

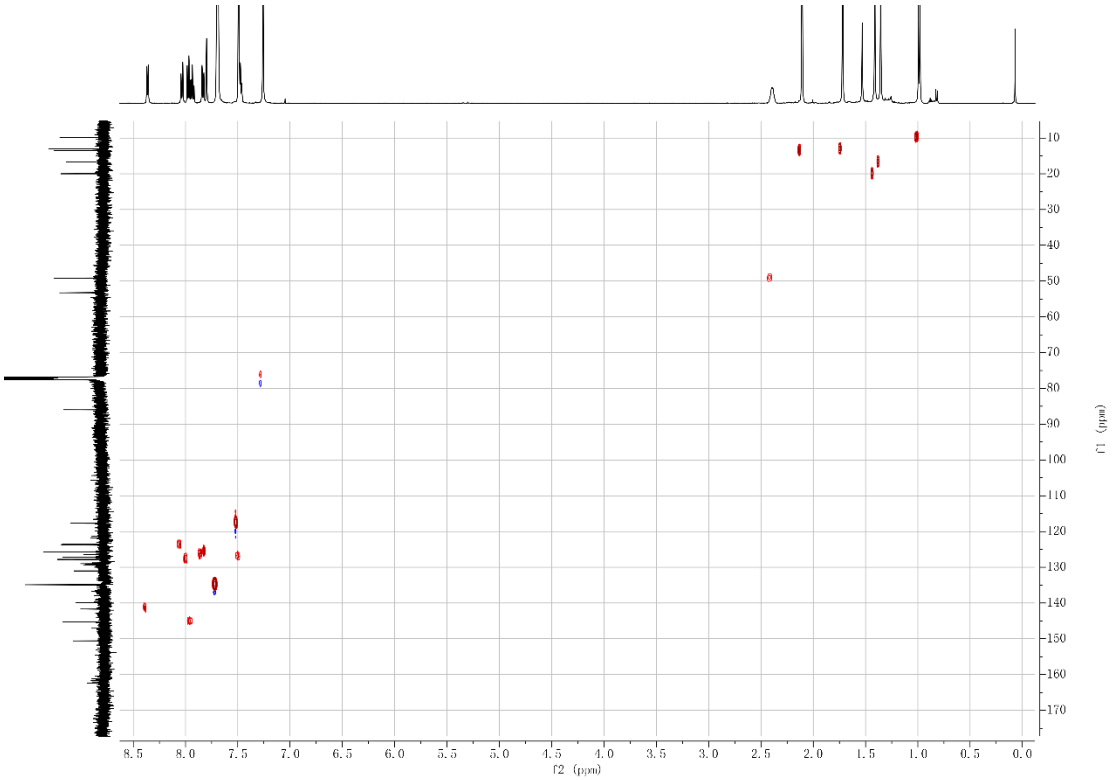

**Figure A. 48.** $^{1}H$-$^{13}C$ HSQC spectrum of [**8c**][$BArF_{24}$]

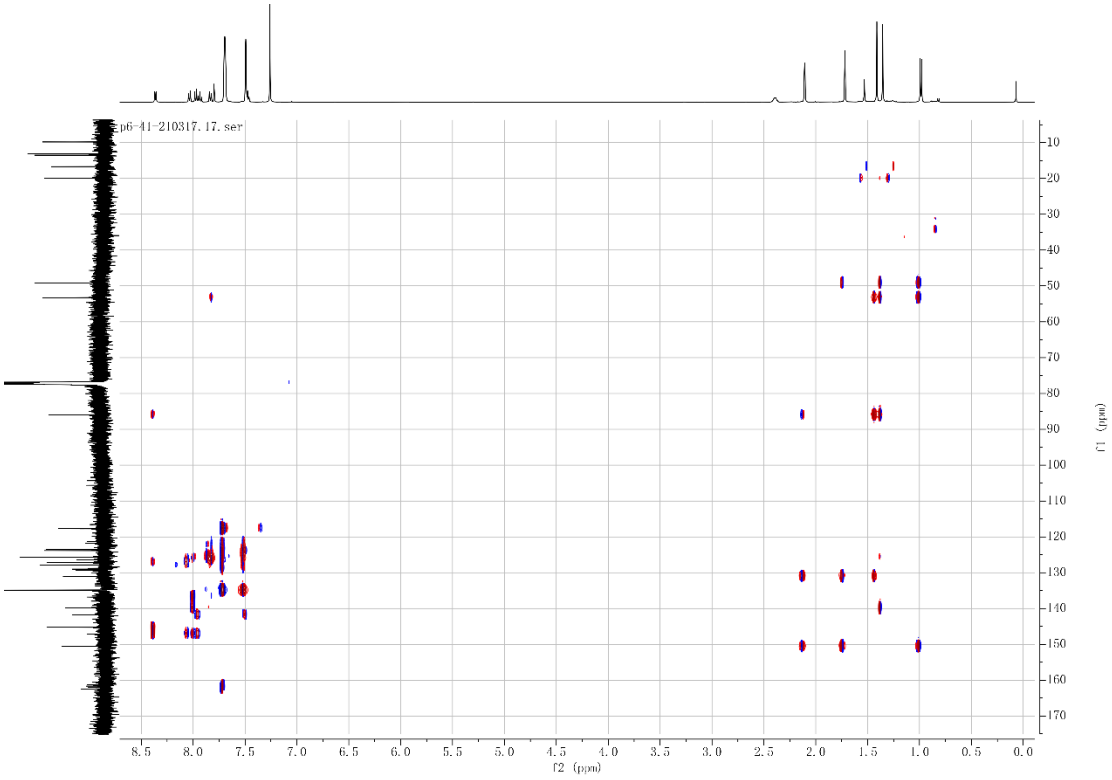

**Figure A. 49.** $^{1}H$-$^{13}C$ HMBC spectrum of [**8c**][$BArF_{24}$]

## NMR Spectra of [7d][BArF$_2$4]

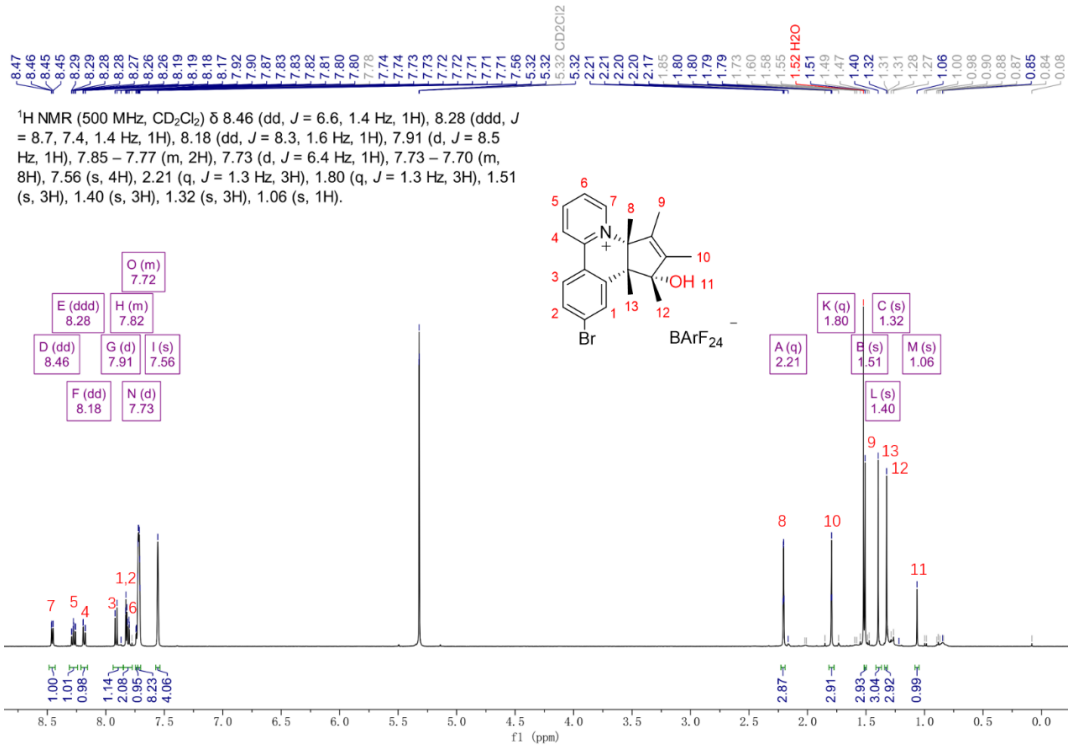


**Figure A. 50.** $^1$H NMR spectrum (500 MHz, $CD_2Cl_2$) of [**7d**][BArF$_{24}$]

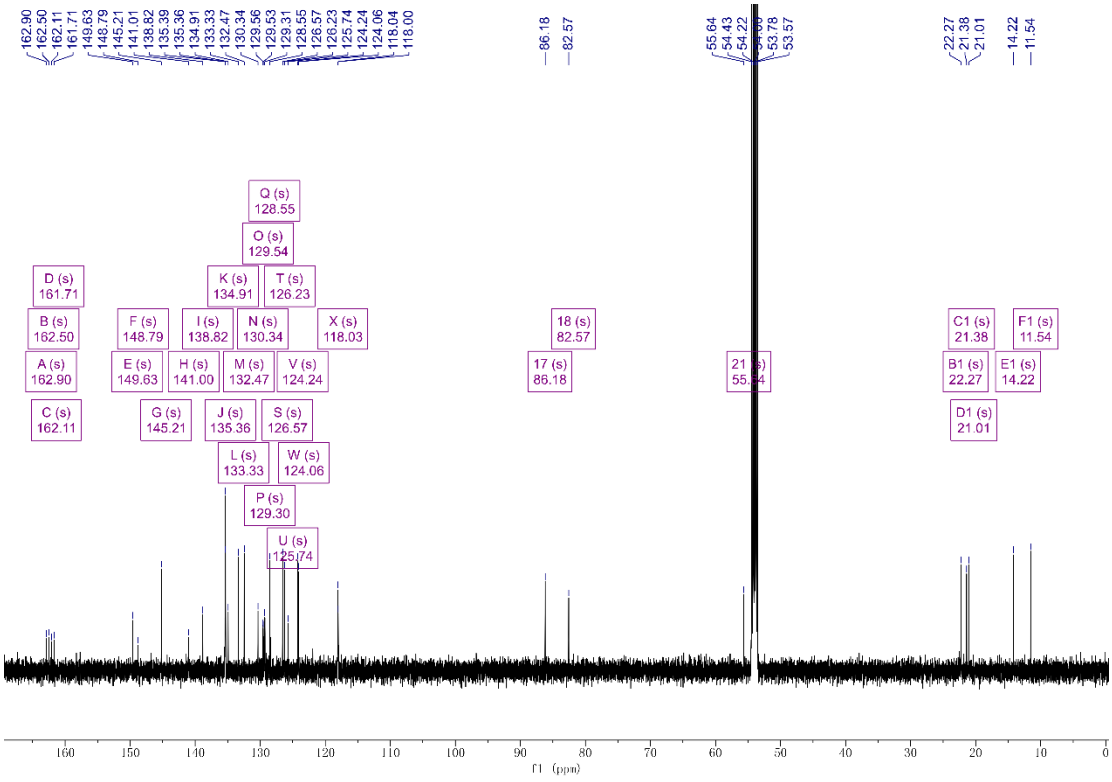


**Figure A. 51.** $^{13}$C NMR spectrum (126 MHz, $CD_2Cl_2$) of [**7d**][BArF$_{24}$]

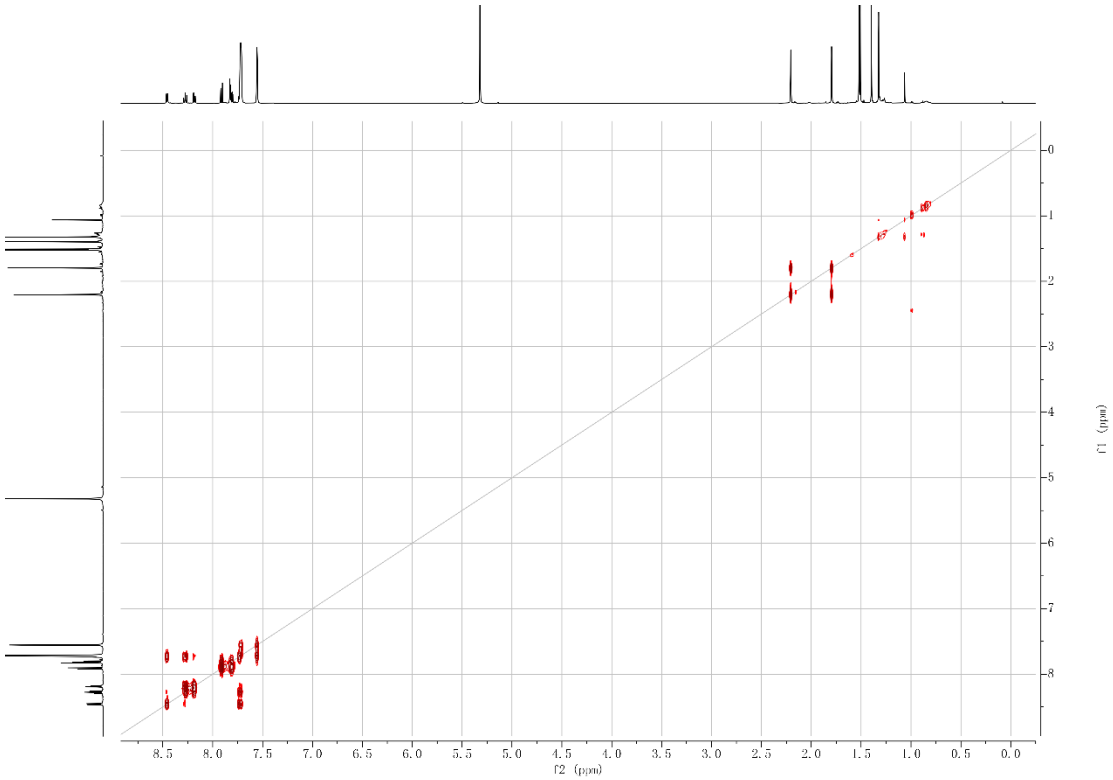


**Figure A. 52.** $^{1}$H-$^{1}$H COSY spectrum of [**7d**][BArF$_{24}$]

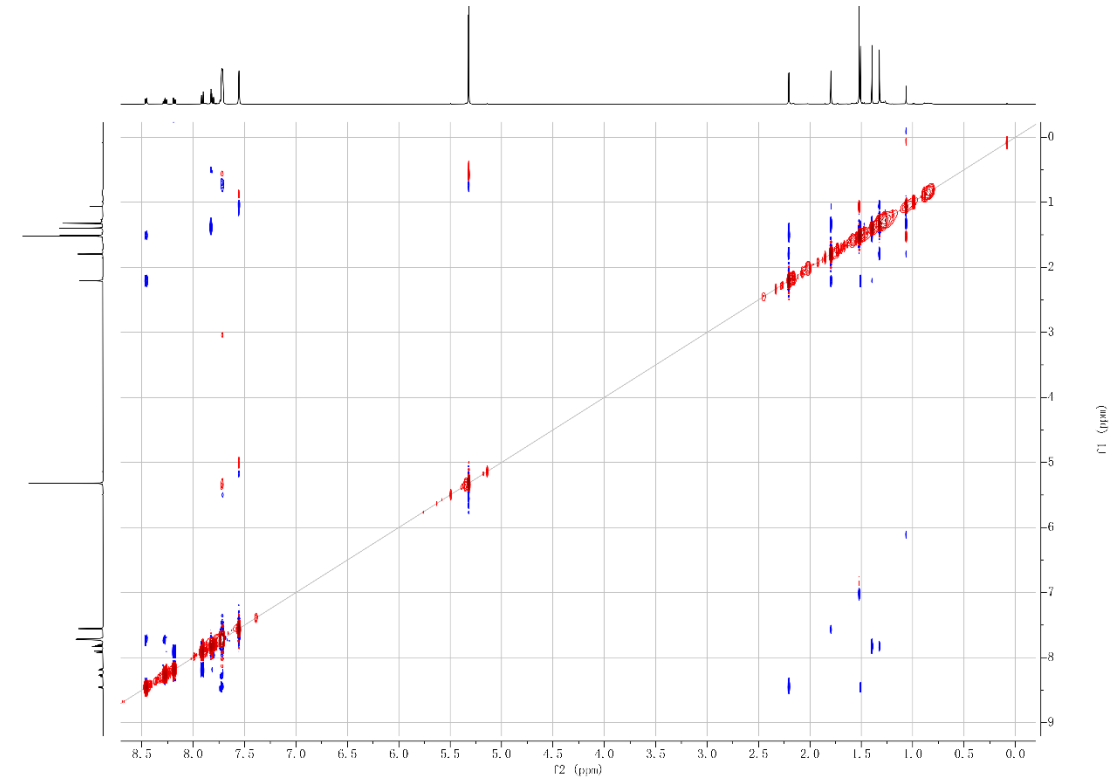


**Figure A. 53.** $^{1}$H-$^{1}$H NOESY spectrum of [**7d**][BArF$_{24}$]

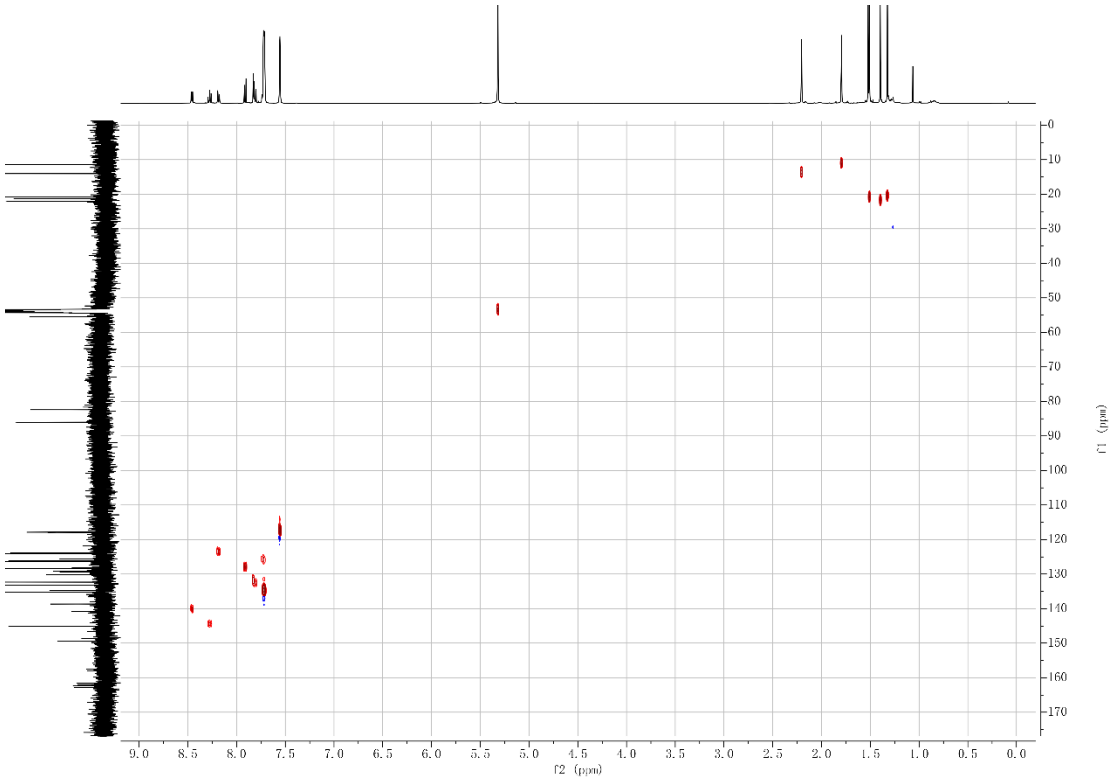

**Figure A. 54.** $^{1}H$-$^{13}C$ HMBC spectrum of [**7d**][$BArF_{24}$]

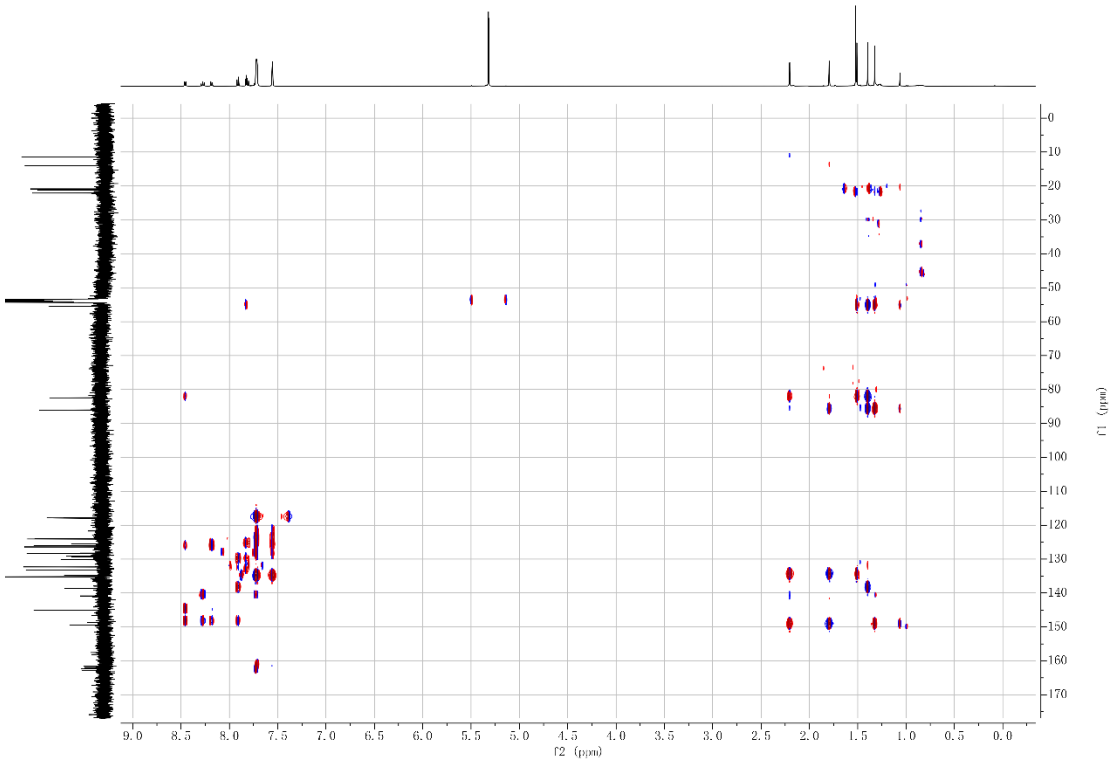

**Figure A. 55.** $^{1}H$-$^{13}C$ HMBC spectrum of [**7d**][$BArF_{24}$]

## NMR Spectra of [8d][BArF$_{24}$]

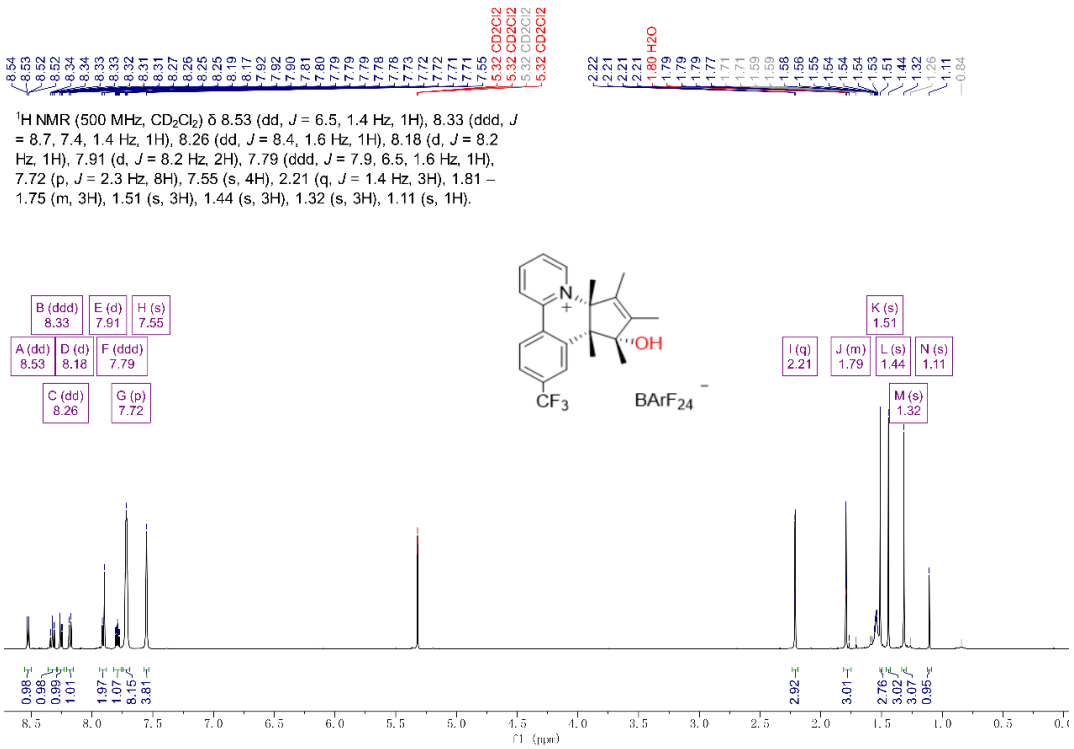


**Figure A. 56.** $^1$H NMR spectrum (500 MHz, $CD_2Cl_2$) of [**8d**][BArF$_{24}$]

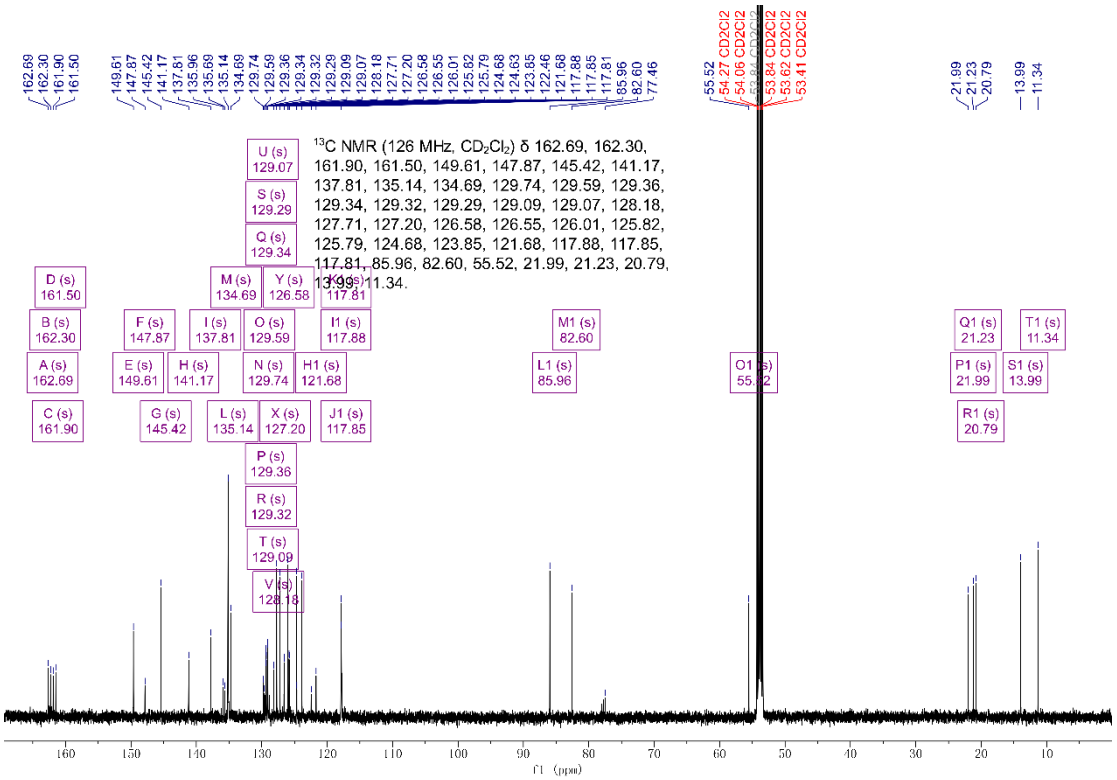


**Figure A. 57.** $^{13}$C NMR spectrum (126 MHz, $CD_2Cl_2$) of [**8d**][BArF$_{24}$]

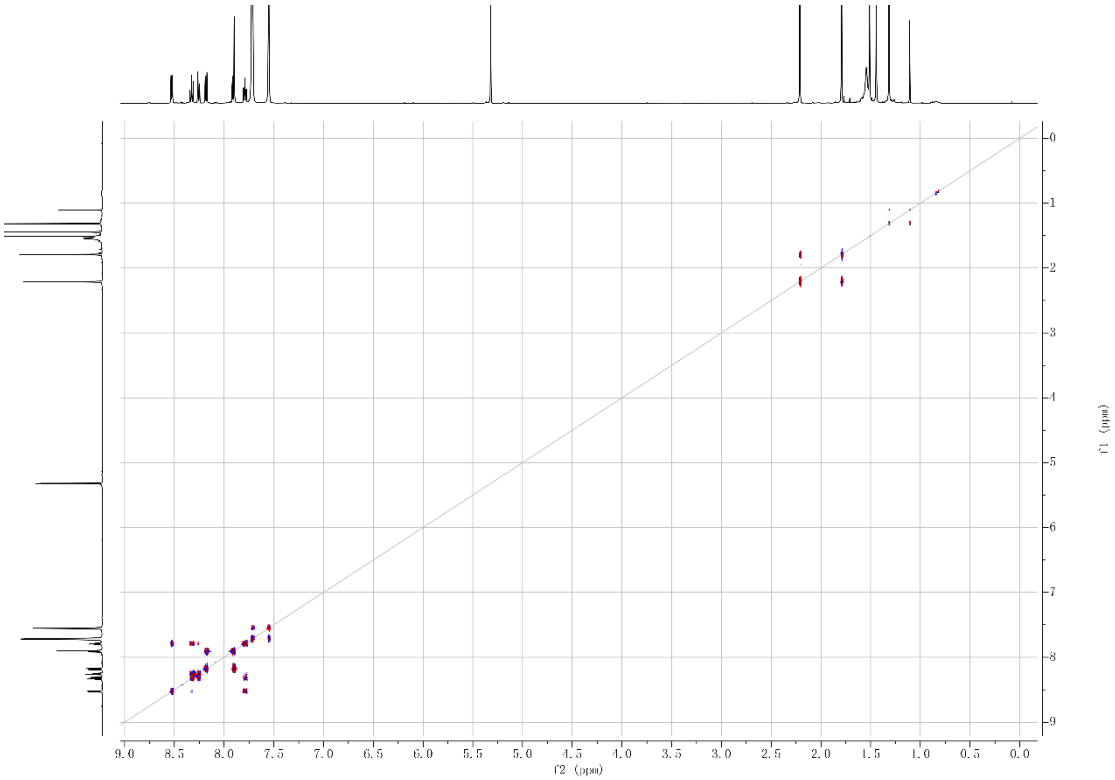

**Figure A. 58.** $^{1}$H-$^{1}$H COSY spectrum of [**8d**][BArF$_{24}$]

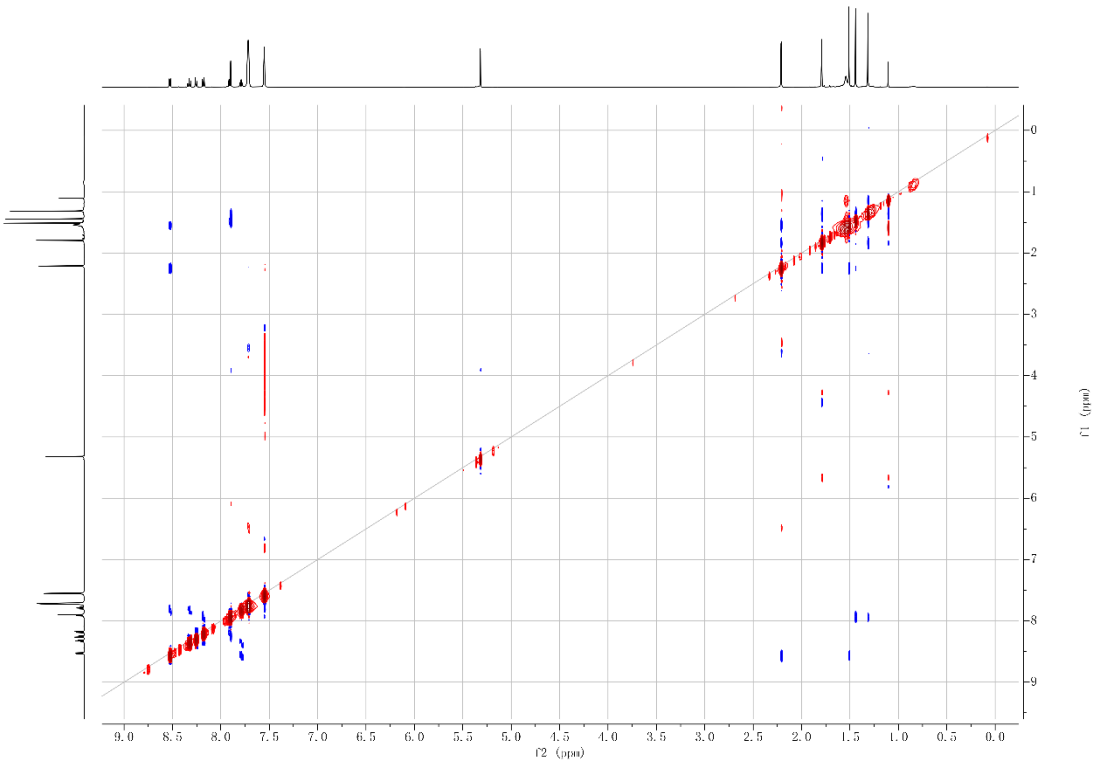

**Figure A. 59.** $^{1}$H-$^{1}$H NOESY spectrum of [**8d**][BArF$_{24}$]

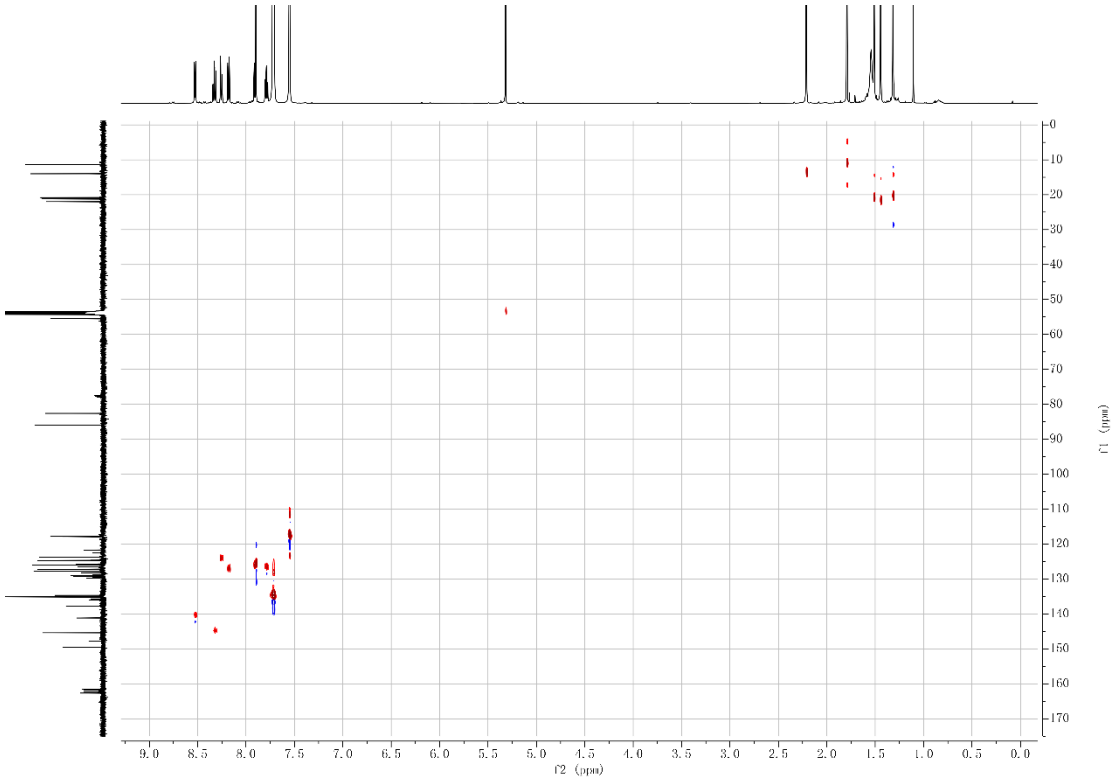

**Figure A. 60.** $^{1}H$-$^{13}C$ HMBC spectrum of [**8d**][$BArF_{24}$]

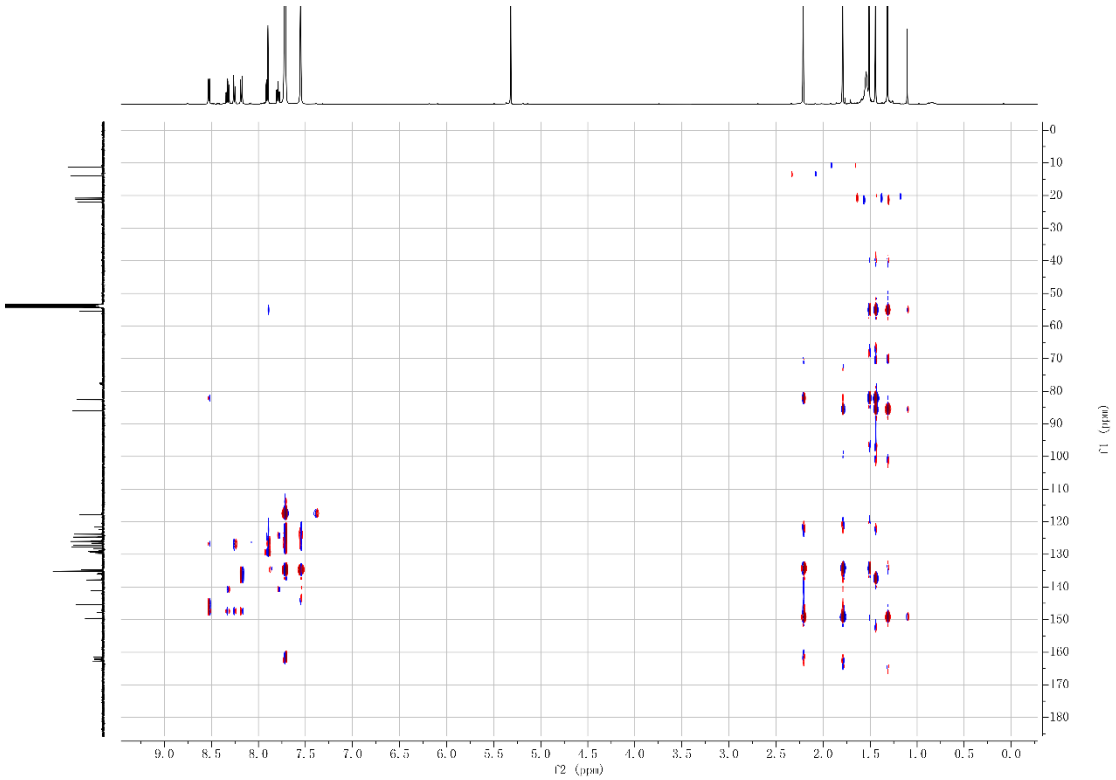

**Figure A. 61.** $^{1}H$-$^{13}C$ HMBC spectrum of [**8d**][$BArF_{24}$]

## NMR Spectra of [10c][$BArF_{24}$]

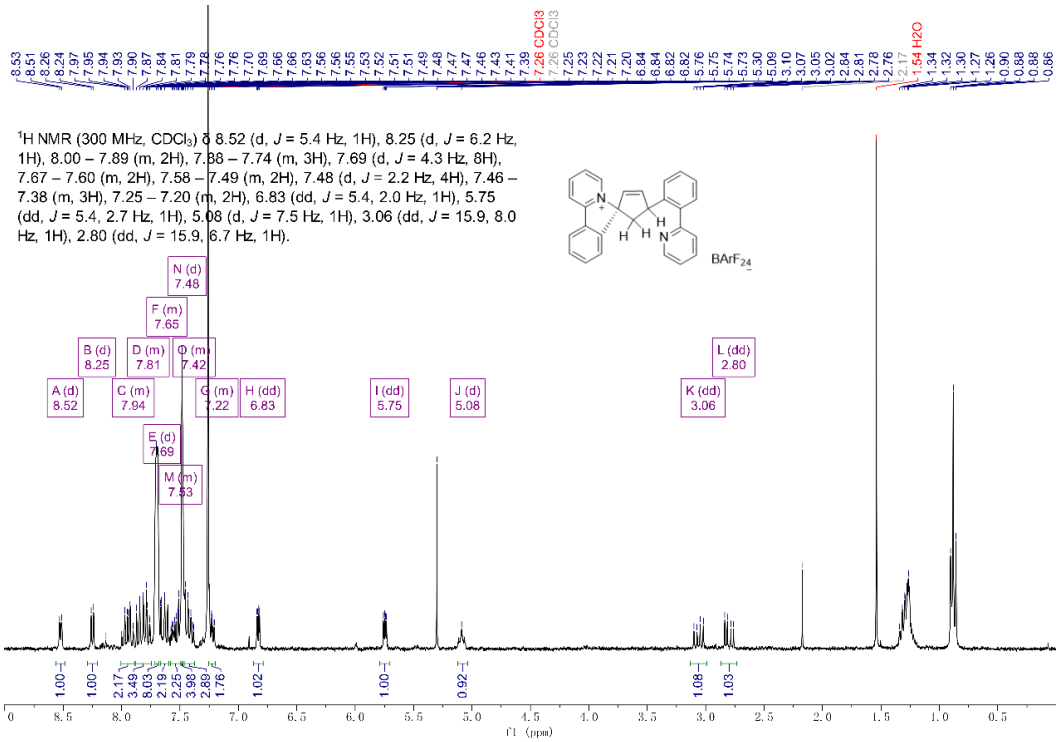


**Figure A. 62.** $^{1}H$ NMR spectrum (300 MHz, $CD_2Cl_2$) of [**10c**][$BArF_{24}$]

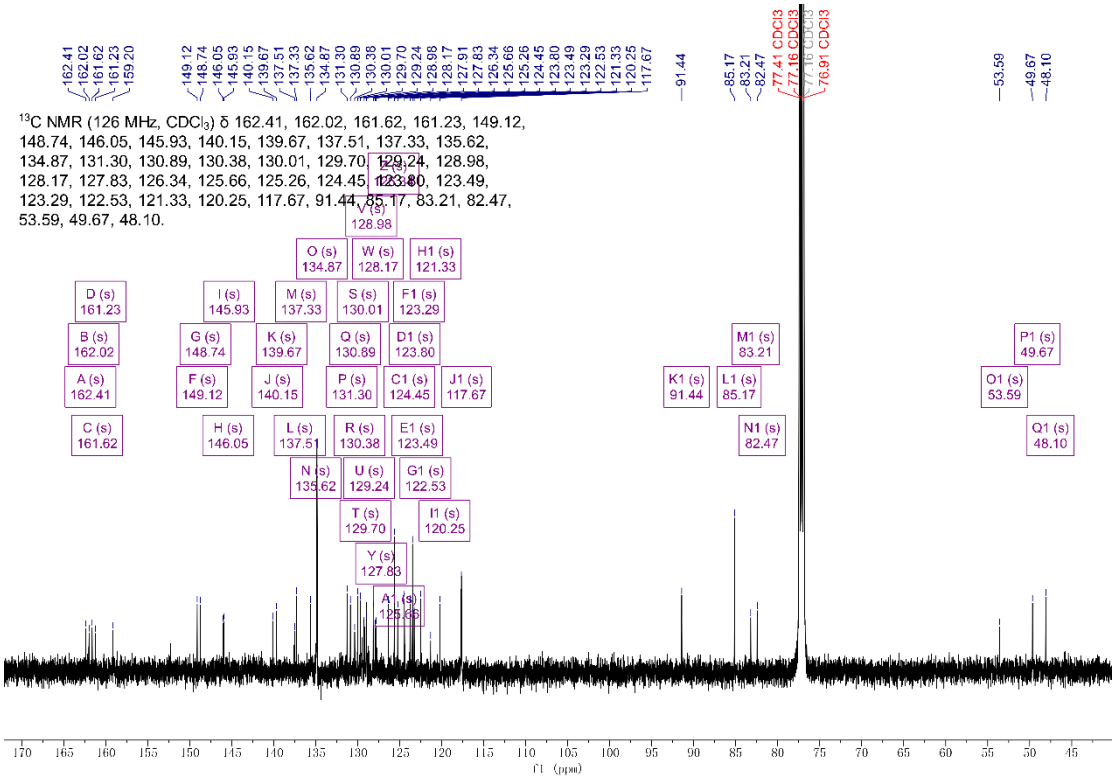


**Figure A. 63.** $^{13}C$ NMR spectrum (126 MHz, $CD_2Cl_2$) of [**10c**][$BArF_{24}$]

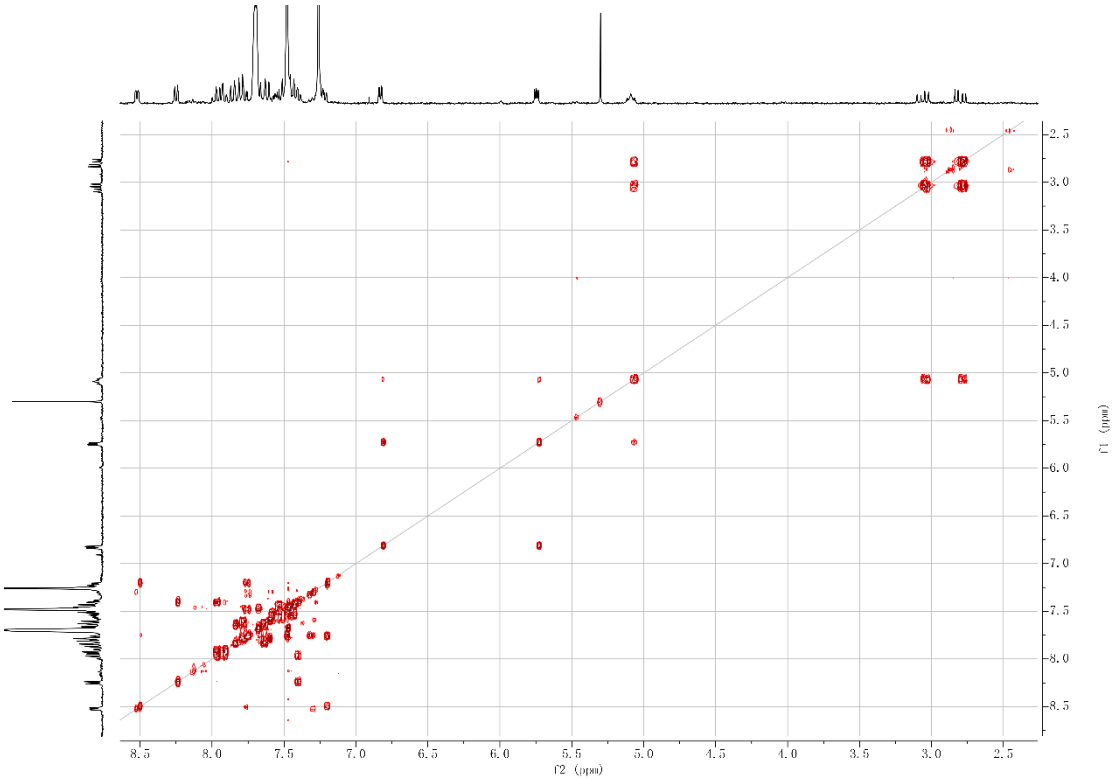

**Figure A. 64.** $^{1}$H-$^{1}$H COSY spectrum of [**10c**][BArF$_{24}$]

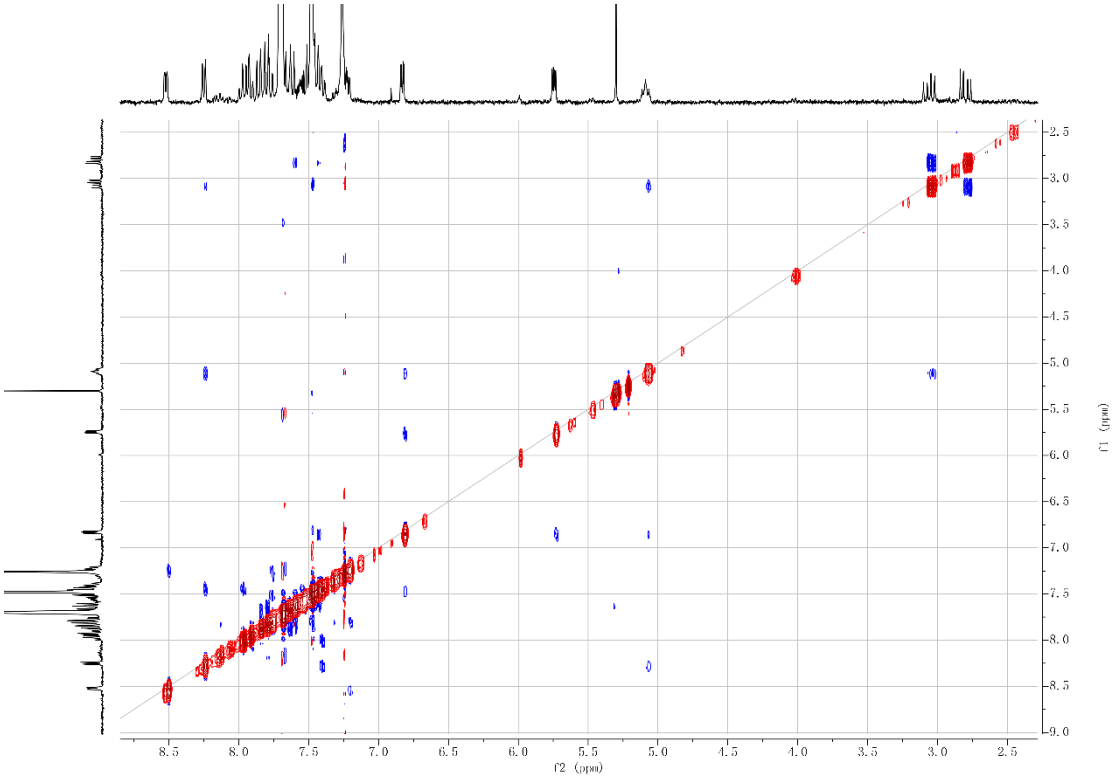

**Figure A. 65.** $^{1}$H-$^{1}$H NOESY spectrum of [**10c**][BArF$_{24}$]

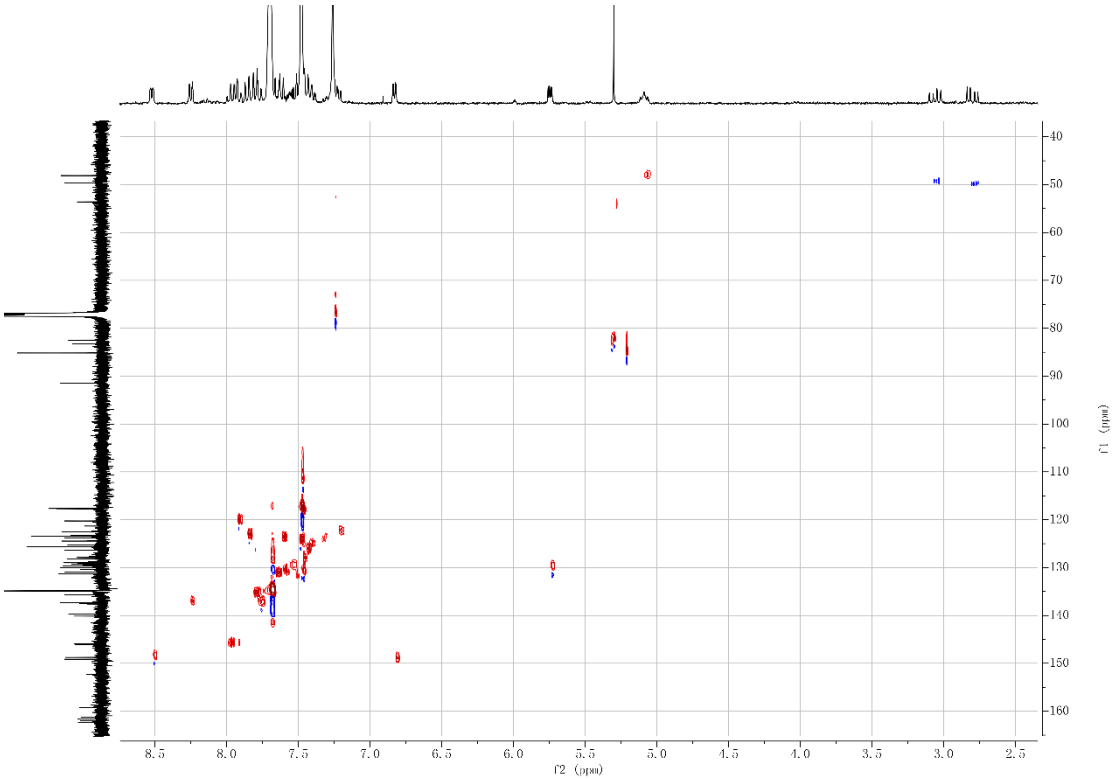


**Figure A. 66.** $^{1}H$-$^{13}C$ HSQC spectrum of [**10c**][$BArF_{24}$]

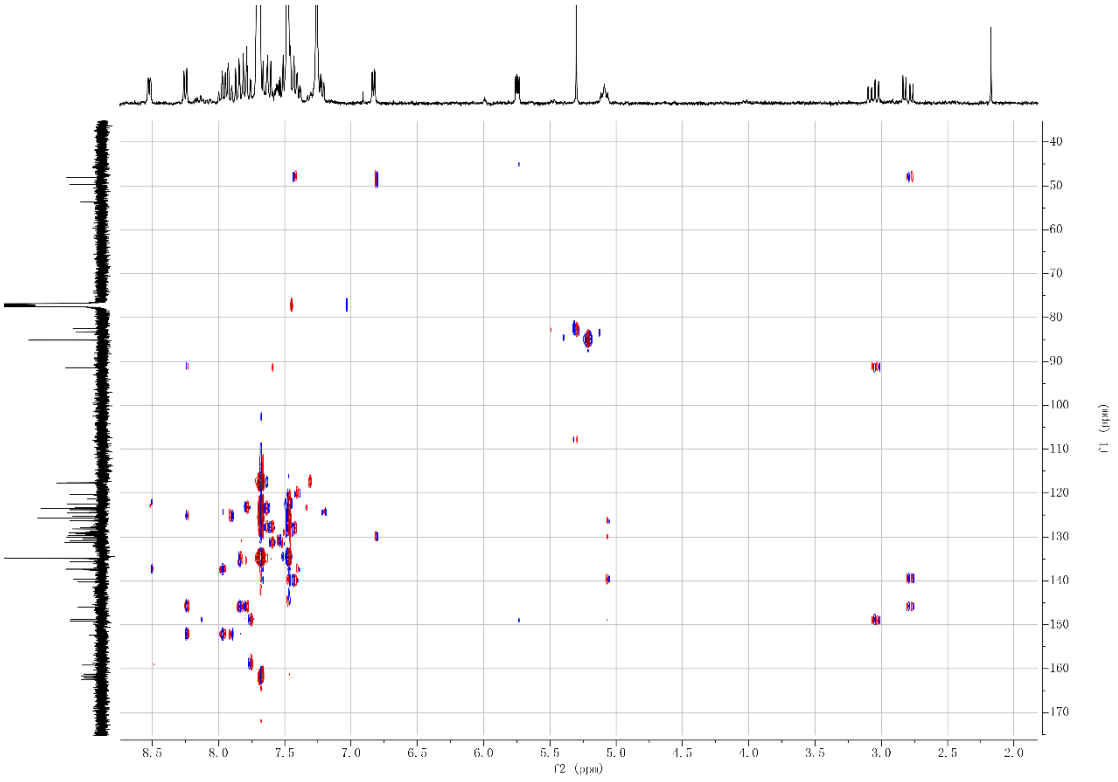


**Figure A. 67.** $^{1}H$-$^{13}C$ HMBC spectrum of [**10c**][$BArF_{24}$]

## Mass spectra of the crude mixture of the reaction of 1a with $I_2$

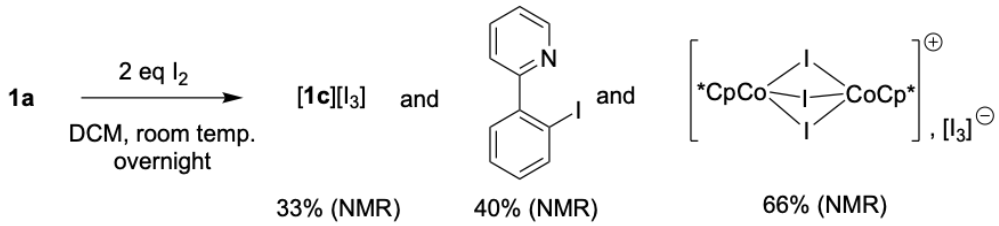


**Service de Spectrometrie de Masse - Federation de Chimie Le Bel - FR 2010 - CNRS / UDS**

**Analysis Info**

| | | | |
|---|---|---|---|
| Analysis Name | F08004SK.d | Acquisition Date | 2/9/2021 11:20:21 AM |
| Method | Tune_neg_Standard.m | Operator | BDAL@DE |
| Sample Name | Cp*Co+I2 NEG | Instrument | micrOTOF II |

**Acquisition Parameter**

| | | | | | | | |
|---|---|---|---|---|---|---|---|
| Source Type | ESI | Capillary | 3000 V | Nebulizer | 0.3 Bar | Set Hexapole RF | 70.0 Vpp |
| Ion Polarity | Negative | Dry Heater | 200 °C | Dry Gas | 3.0 l/min | Set Capillary Exit | -70.0 V |

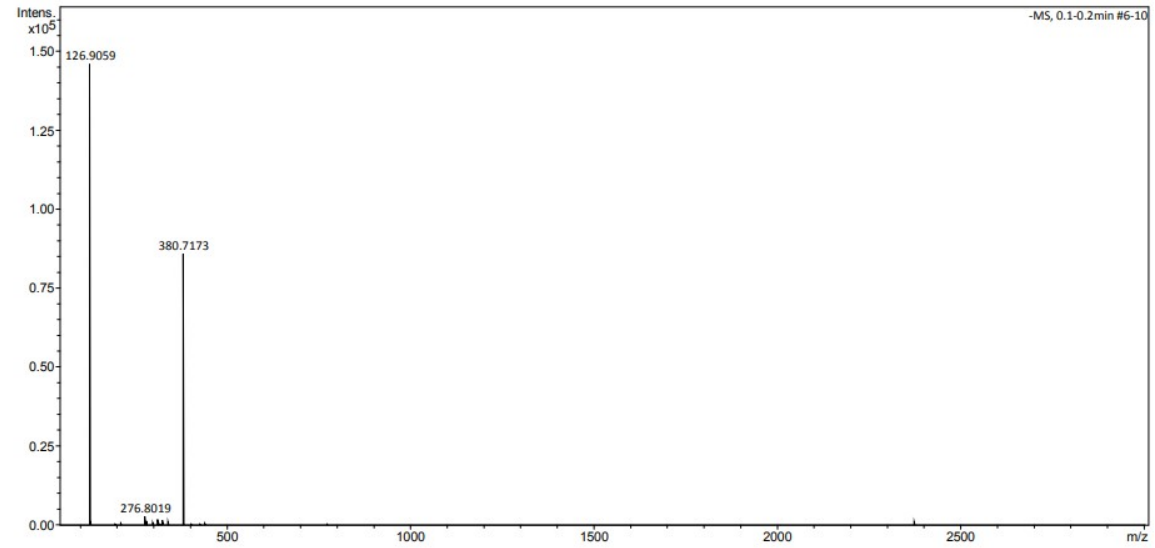


**Figure A. 68.** Mass spectrum (ESI, negative mode) of the crude reaction mixture in negative mode. $I_3^-$ (m/z 380.7) and $I^-$ (m/z 126.9) were observed.

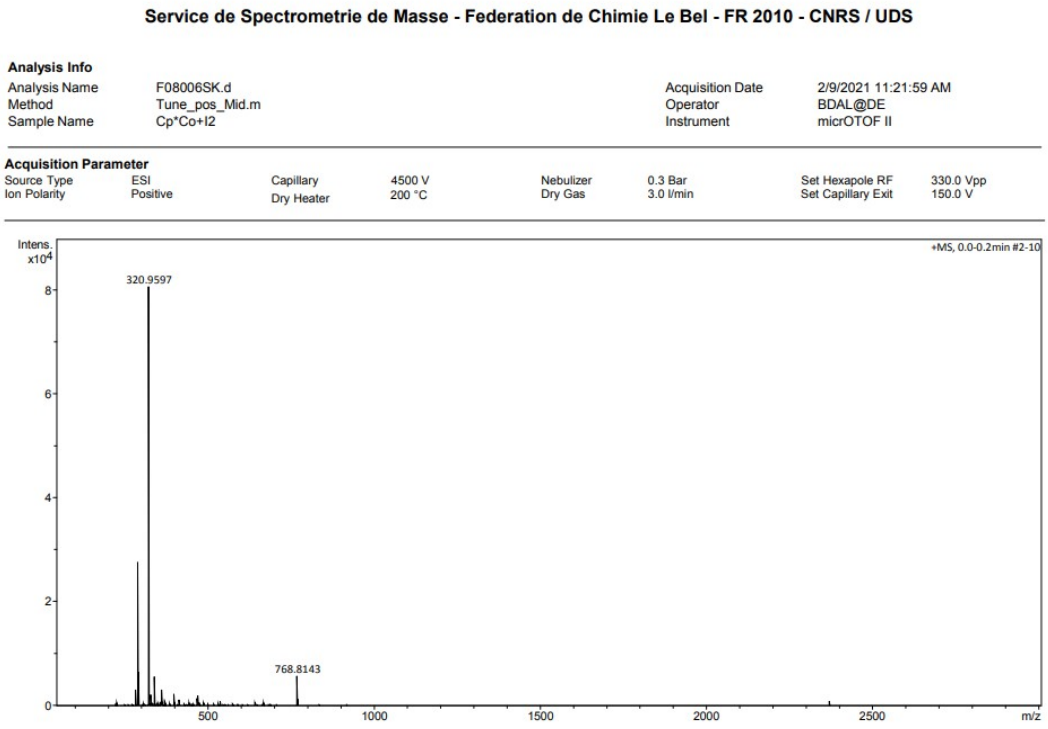


**Figure A. 69.** Mass spectrum (ESI) overview of the crude mixture in positive mode.

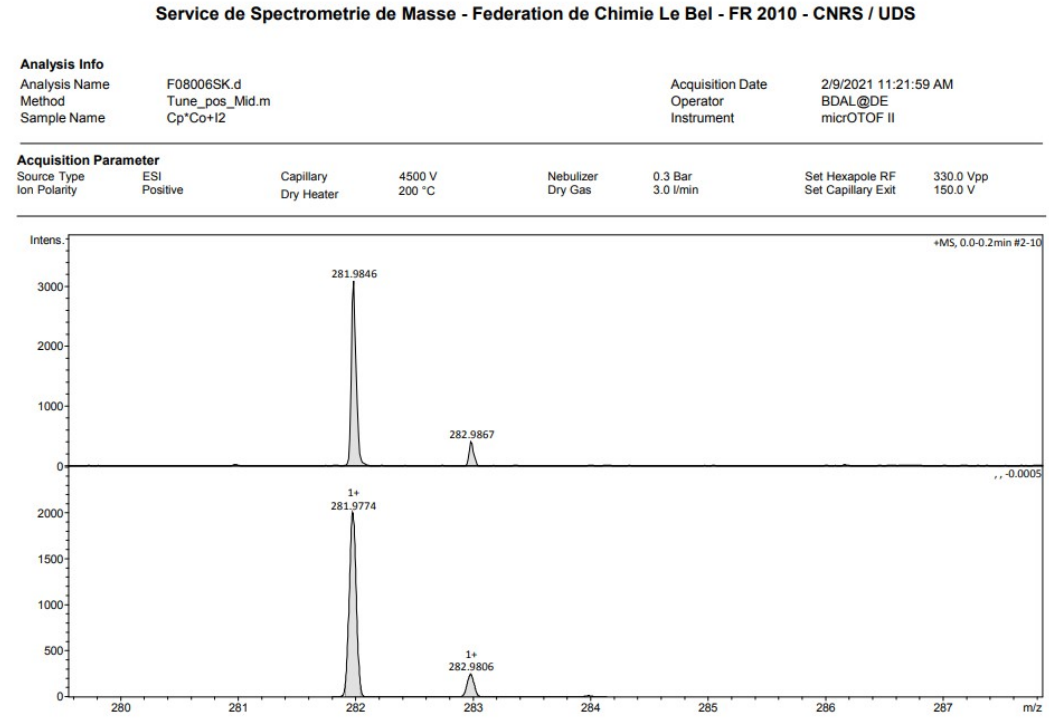


**Figure A. 70.** Zoomed mass spectrum of the crude residue, and simulation of protonated iodo-phenylpyridine. The protonated iodo 2-phenylpyridine and was observed at m/z 281.

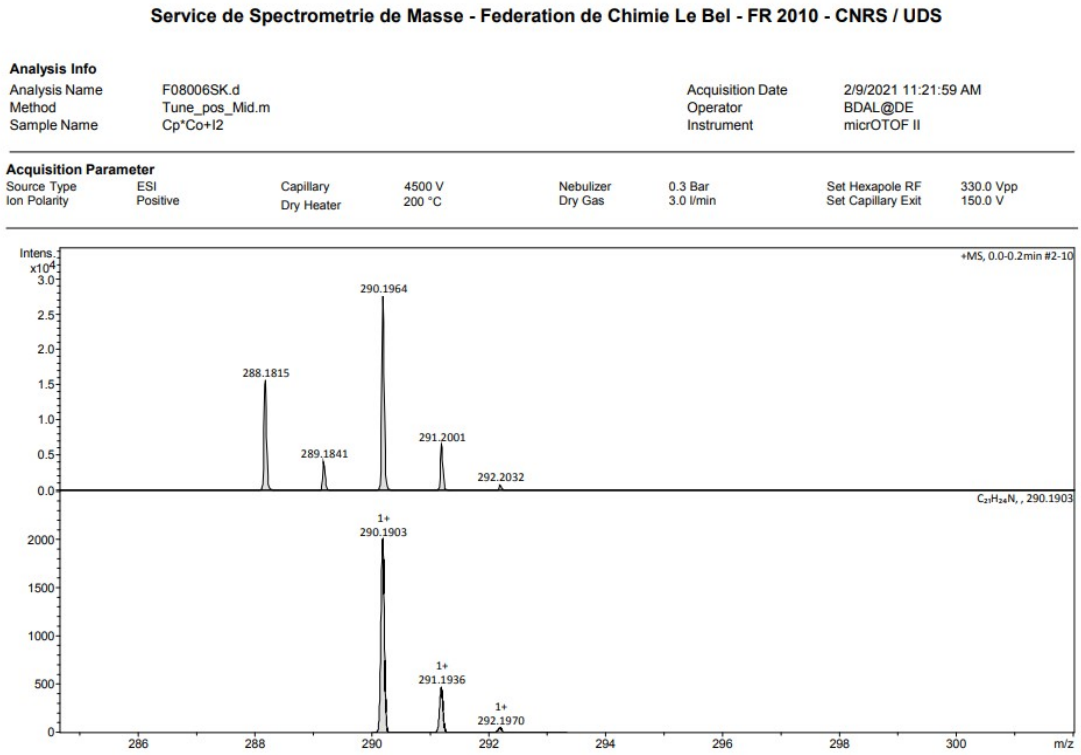


**Figure A. 71.** Zoomed mass spectrum of the crude mixture, and simulation of [**1c**]$^+$. [**1c**]$^+$ was observed at m/z 290.19 as expected.

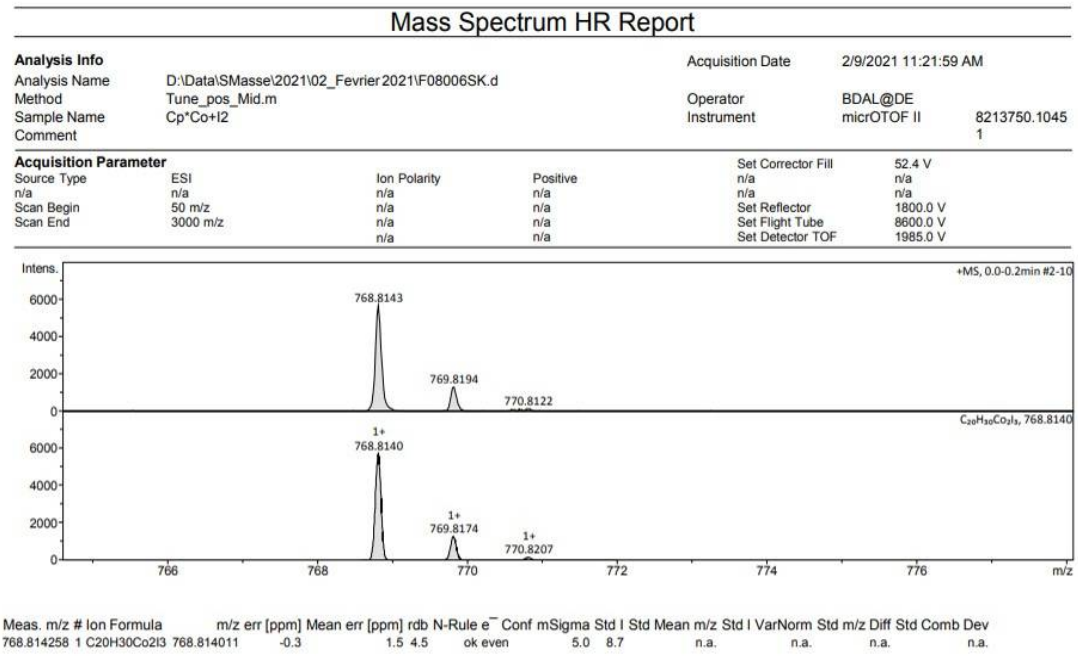


**Figure A. 72.** Zoomed mass spectrum of the crude mixture, and simulation of {[Cp*Co]$_2$($\mu$-I$_3$)}$^+$. {[Cp*Co]$_2$($\mu$-I$_3$)}$^+$ was observed at m/z 768.8 as well as Cp*CoI ("half" of this dimer) at m/z 320.

# Mass spectra of the crude mixture resulting of the reaction of 1a with $[Ph_3C][BArF_{24}]$

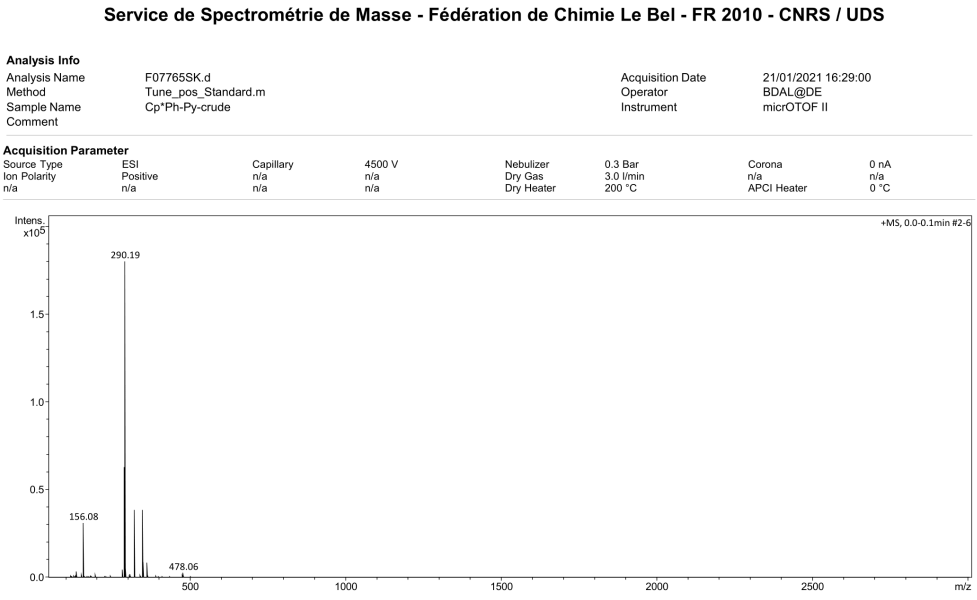


**Figure A. 73.** Mass spectrum (ESI) overview of the crude compound in positive mode.

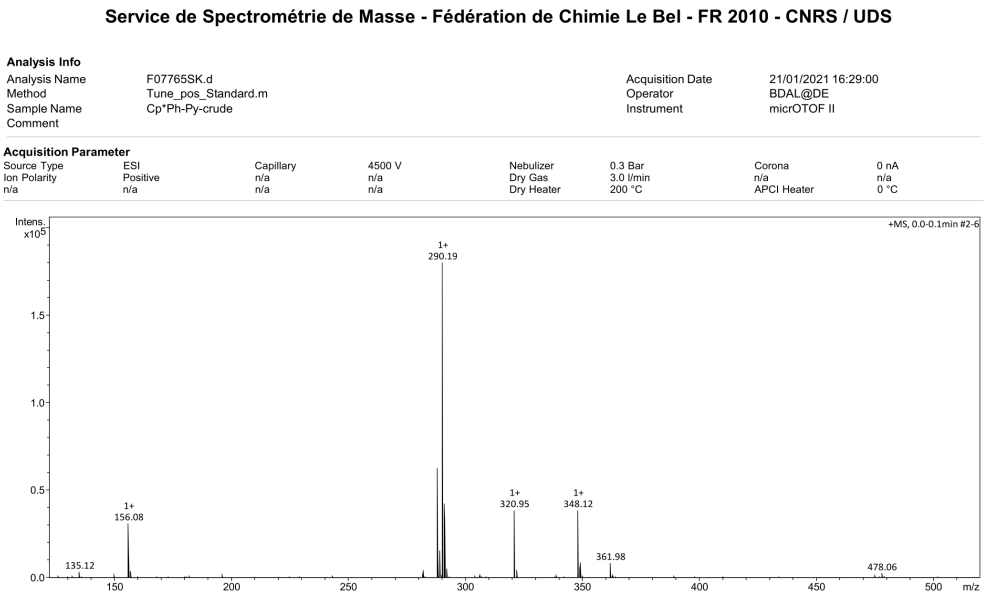


**Figure A. 74.** Zoomed mass spectrum (ESI) of the crude compound in positive mode. Phpy-Cp* was observed at m/z 290.19.

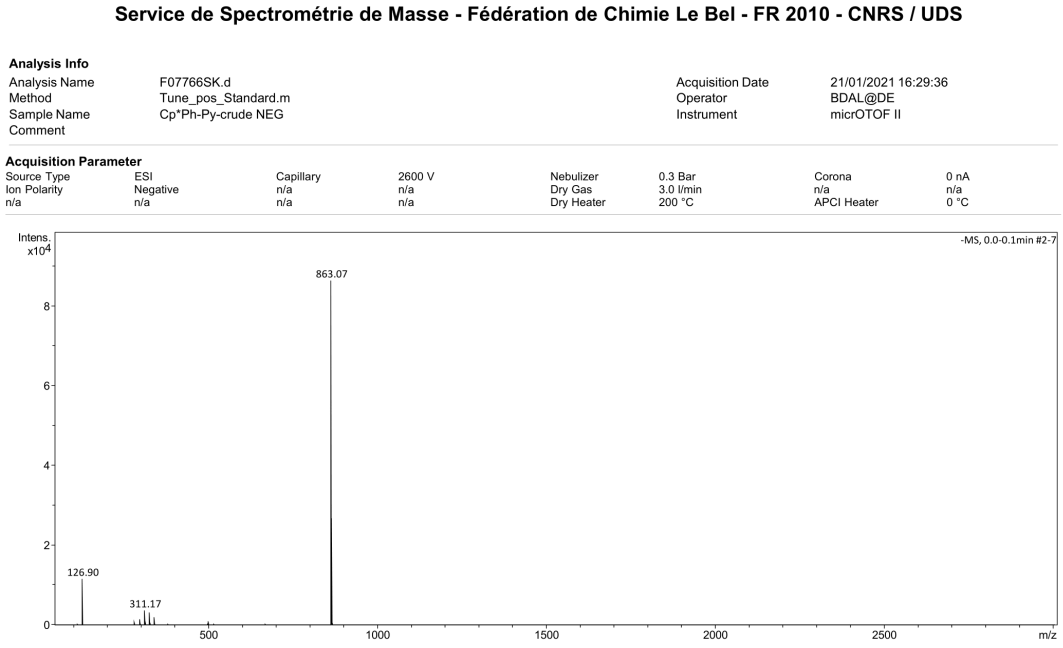


**Figure A. 75.** Mass spectrum (ESI) overview of the crude compound in negative mode. $BArF_{24}^-$ was observed at m/z 863.07, $I^-$ was observed at m/z 126.90

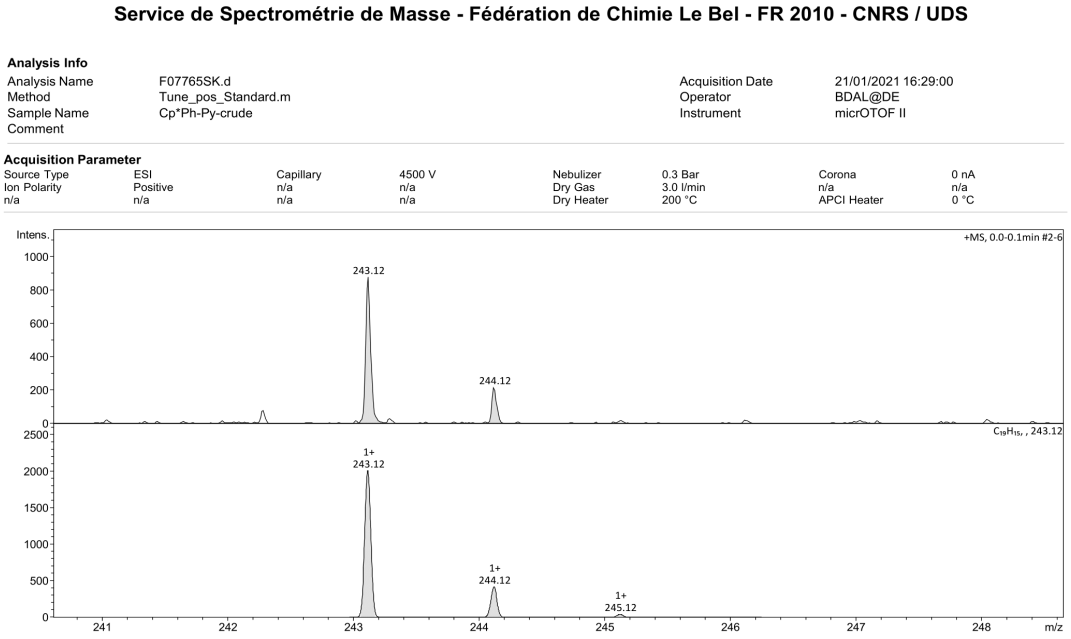


**Figure A. 76.** Zoomed mass spectrum of the crude compound. $Ph_3C^+$ was observed at m/z 243.12.

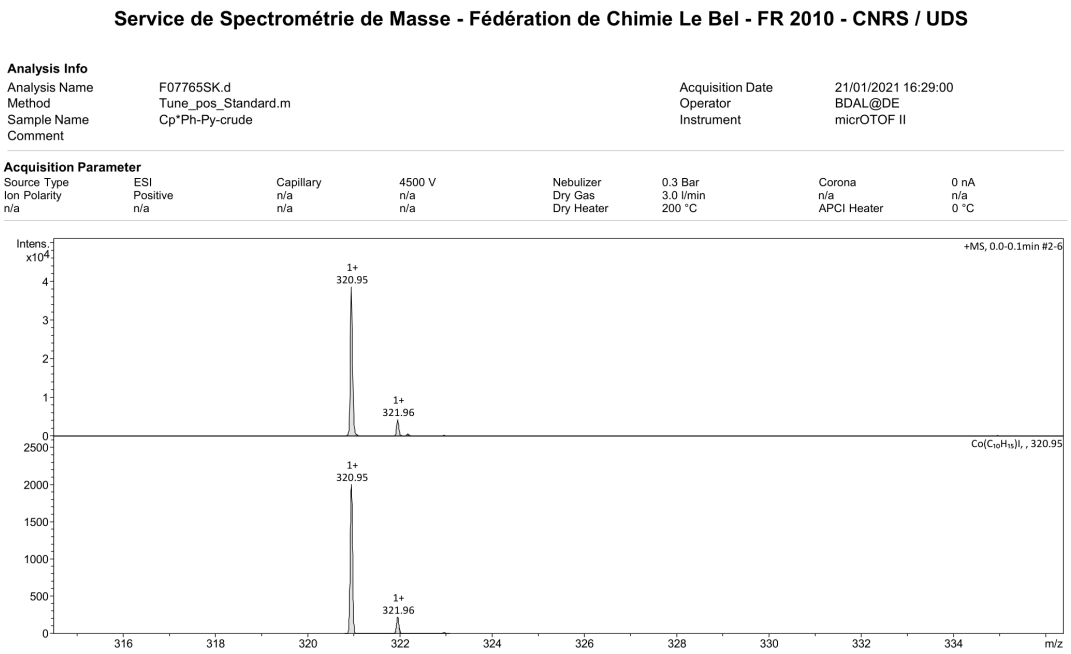


**Figure A. 77.** Zoomed mass spectrum of the crude mixture. The Cp*Co-I fragment was observed at m/z 320.95.

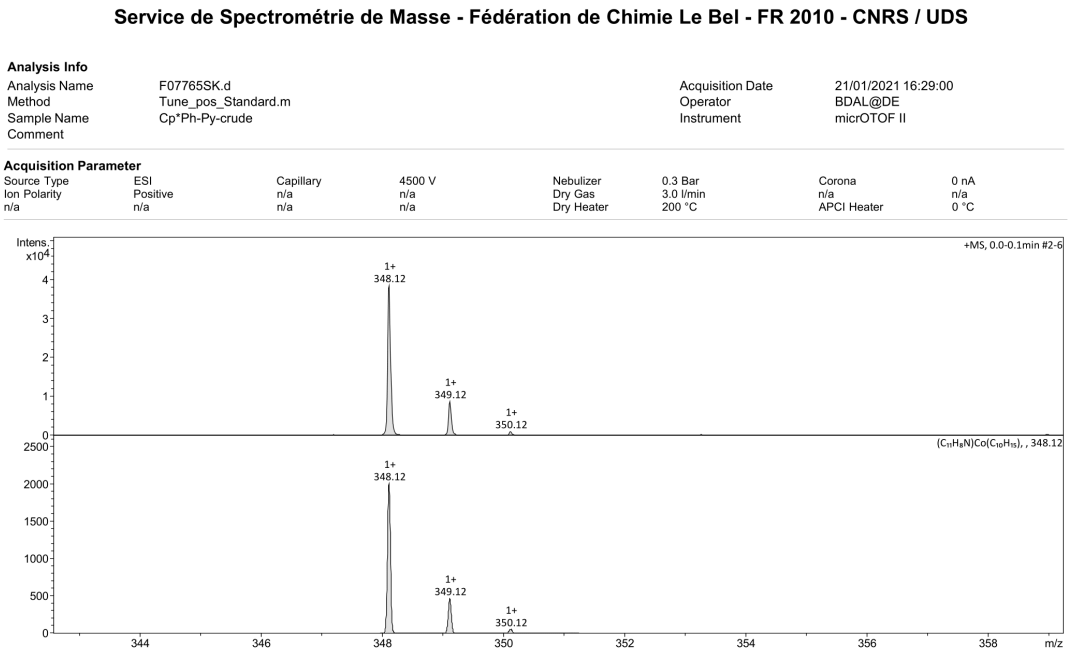


**Figure A. 78.** Zoomed mass spectrum of the crude compound. The Cp*Co(phpy) fragment was observed at m/z 348.12.

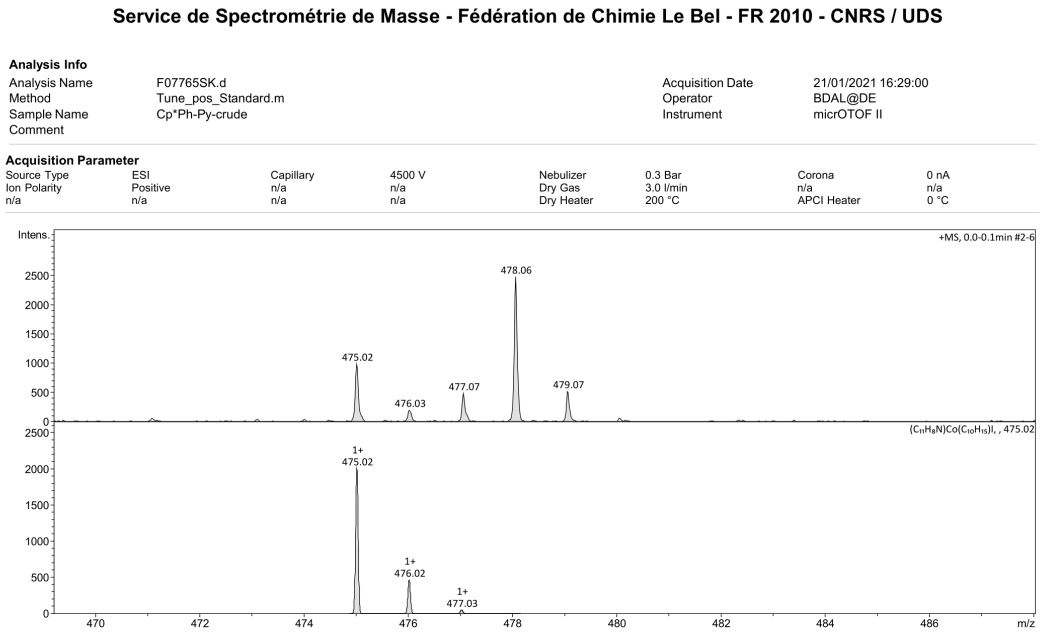


**Figure A. 79.** Zoomed mass spectrum of the crude reaction mixture.

## Mass spectra of the crude compound of the reaction of 1a with $AgPF_6$

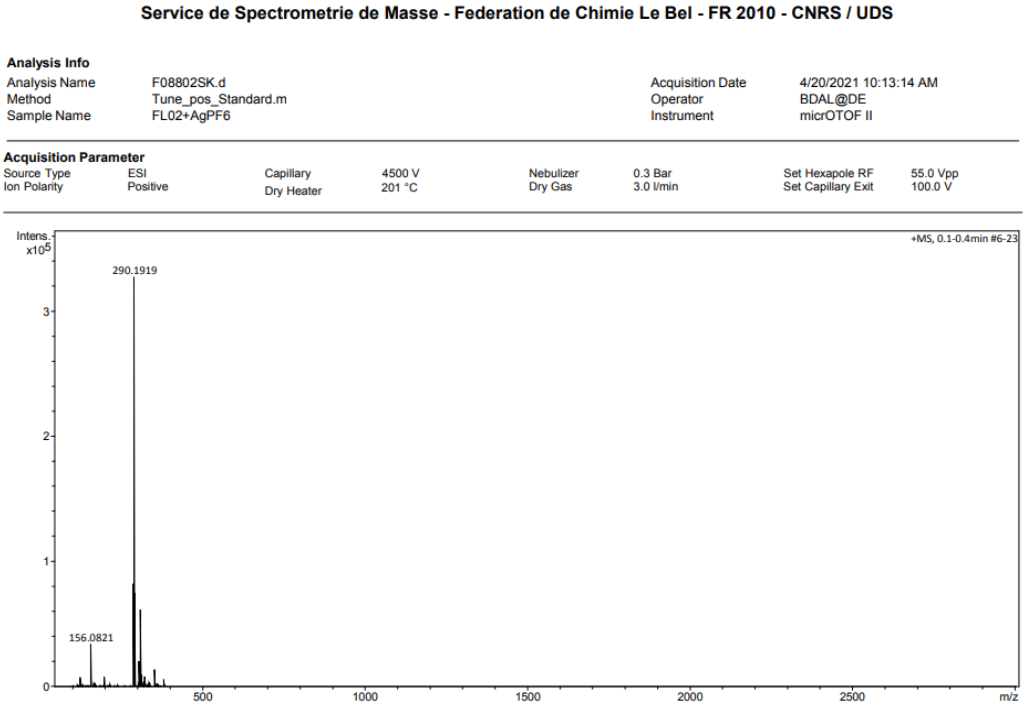


**Figure A. 80.** Mass spectrum overview of the crude mixture of the reaction between **1a** and $AgPF_6$ (positive mode). Protonated 2-phenylpyridine at m/z 156.08 was observed along [**1c**]$^+$.

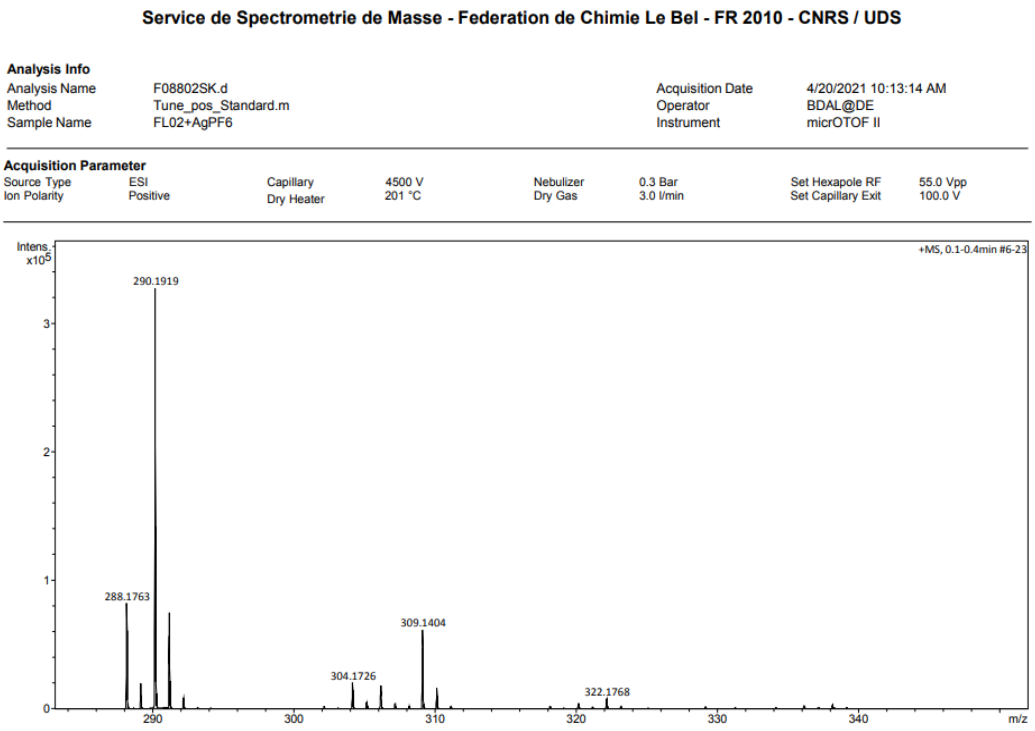


**Figure A. 81.** Zoomed mass spectrum of the crude mixture of the reaction between **1a** and $AgPF_6$ (positive mode). $[\mathbf{1c}]^+$ at m/z 290.19 was observed. A dimer of protonated 2-phenylpyridine resulting from an homocoupling is observed at m/z 309.14.

# Annexes II

# Theoretical material for chapter 2

## DFT Calculations: Energies of Stationary points (COSMO($CH_2Cl_2$)-ZORA-PBE-D3(BJ)/all electron TZP)

### Co-OAc

### anag

| Temp | | Transl | Rotat | Vibrat | Total |
|---|---|---|---|---|---|
| 298.15 | Entropy (cal/mole-K): | 43.910 | 34.952 | 104.651 | 183.514 |
| | Internal Energy (Kcal/mole): | 0.889 | 0.889 | 288.003 | 289.781 |
| | Constant Volume Heat Capacity (cal/mole-K): | 2.981 | 2.981 | 103.700 | 109.662 |

Summary of energy terms

| | hartree | eV | kcal/mol | kJ/mol |
|---|---|---|---|---|
| Bond Energy: | -12.271991518394209 | -333.9379 | -7700.79 | -32220.11 |
| Internal Energy: | 0.461794652277326 | 12.5661 | 289.78 | 1212.44 |
| pV/n = RT: | 0.000944186013486 | 0.0257 | 0.59 | 2.48 |
| Enthalpy H: | -11.809252680103397 | -321.3461 | -7410.42 | -31005.19 |
| -T*S: | -0.087193311636014 | -2.3727 | -54.71 | -228.93 |
| Gibbs free energy: | -11.896445991739411 | -323.7188 | -7465.13 | -31234.11 |

### TS-ag

| Temp | | Transl | Rotat | Vibrat | Total |
|---|---|---|---|---|---|
| 298.15 | Entropy (cal/mole-K): | 43.910 | 34.910 | 94.150 | 172.970 |
| | Internal Energy (Kcal/mole): | 0.889 | 0.889 | 286.065 | 287.842 |
| | Constant Volume Heat Capacity (cal/mole-K): | 2.981 | 2.981 | 98.287 | 104.248 |

Contributions from frequencies below 20 1/cm

| | |
|---|---|
| Frequency (1/cm): | 16.358 |
| Entropy (cal/mole-K): | 7.033 |
| Internal Energy (Kcal/mole): | 0.593 |
| Constant Volume Heat Capacity (cal/mole-K): | 1.986 |

Summary of energy terms

| | hartree | eV | kcal/mol | kJ/mol |
|---|---|---|---|---|
| Bond Energy: | -12.252814575632121 | -333.4160 | -7688.76 | -32169.76 |
| Internal Energy: | 0.458706109496748 | 12.4820 | 287.84 | 1204.33 |
| pV/n = RT: | 0.000944186013486 | 0.0257 | 0.59 | 2.48 |
| Enthalpy H: | -11.793164280121886 | -320.9083 | -7400.32 | -30962.95 |
| -T*S: | -0.082183500545028 | -2.2363 | -51.57 | -215.77 |
| Gibbs free energy: | -11.875347780666914 | -323.1447 | -7451.89 | -31178.72 |

### ag

| Temp | | Transl | Rotat | Vibrat | Total |
|---|---|---|---|---|---|
| 298.15 | Entropy (cal/mole-K): | 43.910 | 34.874 | 105.392 | 184.176 |
| | Internal Energy (Kcal/mole): | 0.889 | 0.889 | 287.370 | 289.147 |
| | Constant Volume Heat Capacity (cal/mole-K): | 2.981 | 2.981 | 103.909 | 109.871 |

Summary of energy terms

| | hartree | eV | kcal/mol | kJ/mol |
|---|---|---|---|---|
| Bond Energy: | -12.260285986099655 | -333.6194 | -7693.45 | -32189.38 |
| Internal Energy: | 0.460785123862548 | 12.5386 | 289.15 | 1209.79 |
| pV/n = RT: | 0.000944186013486 | 0.0257 | 0.59 | 2.48 |
| Enthalpy H: | -11.798556676223621 | -321.0551 | -7403.71 | -30977.11 |
| -T*S: | -0.087507897391291 | -2.3812 | -54.91 | -229.75 |

## TS-CH

| Temp | | Transl | Rotat | Vibrat | Total |
|---|---|---|---|---|---|
| 298.15 | Entropy (cal/mole-K): | 43.910 | 34.816 | 95.474 | 174.200 |
| | Internal Energy (Kcal/mole): | 0.889 | 0.889 | 284.068 | 285.846 |
| | Constant Volume Heat Capacity (cal/mole-K): | 2.981 | 2.981 | 100.599 | 106.560 |

Contributions from frequencies below 20 1/cm

| | |
|---|---|
| Frequency (1/cm): | 19.107 |
| Entropy (cal/mole-K): | 6.725 |
| Internal Energy (Kcal/mole): | 0.593 |
| Constant Volume Heat Capacity (cal/mole-K): | 1.986 |

Summary of energy terms

| | hartree | eV | kcal/mol | kJ/mol |
|---|---|---|---|---|
| Bond Energy: | -12.251200923488641 | -333.3721 | -7687.75 | -32165.52 |
| Internal Energy: | 0.455524386533448 | 12.3954 | 285.85 | 1195.98 |
| pV/n = RT: | 0.000944186013486 | 0.0257 | 0.59 | 2.48 |
| Enthalpy H: | -11.794732350941707 | -320.9510 | -7401.31 | -30967.07 |
| -T*S: | -0.082767880663257 | -2.2522 | -51.94 | -217.31 |
| Gibbs free energy: | -11.877500231604964 | -323.2032 | -7453.24 | -31184.37 |

## MCH

| Temp | | Transl | Rotat | Vibrat | Total |
|---|---|---|---|---|---|
| 298.15 | Entropy (cal/mole-K): | 43.910 | 34.854 | 104.695 | 183.460 |
| | Internal Energy (Kcal/mole): | 0.889 | 0.889 | 287.574 | 289.352 |
| | Constant Volume Heat Capacity (cal/mole-K): | 2.981 | 2.981 | 103.762 | 109.724 |

Summary of energy terms

| | hartree | eV | kcal/mol | kJ/mol |
|---|---|---|---|---|
| Bond Energy: | -12.267019303421160 | -333.8026 | -7697.67 | -32207.05 |
| Internal Energy: | 0.461111169430714 | 12.5475 | 289.35 | 1210.65 |
| pV/n = RT: | 0.000944186013486 | 0.0257 | 0.59 | 2.48 |
| Enthalpy H: | -11.804963947976960 | -321.2294 | -7407.73 | -30993.93 |
| -T*S: | -0.087167647900566 | -2.3720 | -54.70 | -228.86 |
| Gibbs free energy: | -11.892131595877526 | -323.6014 | -7462.43 | -31222.79 |

# Co-NHAc

## anag

| Temp | | Transl | Rotat | Vibrat | Total |
|---|---|---|---|---|---|
| 298.15 | Entropy (cal/mole-K): | 43.903 | 34.968 | 98.913 | 177.785 |
| | Internal Energy (Kcal/mole): | 0.889 | 0.889 | 294.883 | 296.660 |
| | Constant Volume Heat Capacity (cal/mole-K): | 2.981 | 2.981 | 103.229 | 109.191 |

Contributions from frequencies below 20 1/cm

| | |
|---|---|
| Frequency (1/cm): | 18.519 |
| Entropy (cal/mole-K): | 6.787 |
| Internal Energy (Kcal/mole): | 0.593 |
| Constant Volume Heat Capacity (cal/mole-K): | 1.986 |

Summary of energy terms

| | hartree | eV | kcal/mol | kJ/mol |
|---|---|---|---|---|
| Bond Energy: | -12.454835339909538 | -338.9133 | -7815.53 | -32700.17 |
| Internal Energy: | 0.472758137644034 | 12.8644 | 296.66 | 1241.23 |
| pV/n = RT: | 0.000944186013486 | 0.0257 | 0.59 | 2.48 |
| Enthalpy H: | -11.981133016252018 | -326.0232 | -7518.28 | -31456.46 |
| -T*S: | -0.084471227633381 | -2.2986 | -53.01 | -221.78 |
| Gibbs free energy: | -12.065604243885399 | -328.3218 | -7571.28 | -31678.24 |

## TS-ag

| Temp | | Transl | Rotat | Vibrat | Total |
|---|---|---|---|---|---|
| 298.15 | Entropy (cal/mole-K): | 43.903 | 34.946 | 98.760 | 177.609 |
| | Internal Energy (Kcal/mole): | 0.889 | 0.889 | 294.110 | 295.887 |
| | Constant Volume Heat Capacity (cal/mole-K): | 2.981 | 2.981 | 101.765 | 107.727 |

Contributions from frequencies below 20 1/cm

| | |
|---|---|
| Frequency (1/cm): | 19.309 |
| Entropy (cal/mole-K): | 6.704 |
| Internal Energy (Kcal/mole): | 0.593 |
| Constant Volume Heat Capacity (cal/mole-K): | 1.986 |

Summary of energy terms

| | hartree | eV | kcal/mol | kJ/mol |
|---|---|---|---|---|
| Bond Energy: | -12.442851033285256 | -338.5872 | -7808.01 | -32668.70 |
| Internal Energy: | 0.471526326835612 | 12.8309 | 295.89 | 1237.99 |
| pV/n = RT: | 0.000944186013486 | 0.0257 | 0.59 | 2.48 |
| Enthalpy H: | -11.970380520436159 | -325.7306 | -7511.53 | -31428.23 |
| -T*S: | -0.084387920613332 | -2.2963 | -52.95 | -221.56 |
| Gibbs free energy: | -12.054768441049491 | -328.0269 | -7564.48 | -31649.79 |

## ag

| Temp | | Transl | Rotat | Vibrat | Total |
|---|---|---|---|---|---|
| 298.15 | Entropy (cal/mole-K): | 43.903 | 34.904 | 104.010 | 182.818 |
| | Internal Energy (Kcal/mole): | 0.889 | 0.889 | 295.072 | 296.849 |
| | Constant Volume Heat Capacity (cal/mole-K): | 2.981 | 2.981 | 105.199 | 111.160 |

Summary of energy terms

| | hartree | eV | kcal/mol | kJ/mol |
|---|---|---|---|---|
| Bond Energy: | -12.448415727849707 | -338.7386 | -7811.50 | -32683.31 |
| Internal Energy: | 0.473059626211084 | 12.8726 | 296.85 | 1242.02 |
| pV/n = RT: | 0.000944186013486 | 0.0257 | 0.59 | 2.48 |
| Enthalpy H: | -11.974411915625137 | -325.8403 | -7514.06 | -31438.81 |
| -T*S: | -0.086862576230690 | -2.3637 | -54.51 | -228.06 |
| Gibbs free energy: | -12.061274491855826 | -328.2040 | -7568.56 | -31666.87 |

## TS-CH

| Temp | | Transl | Rotat | Vibrat | Total |
|---|---|---|---|---|---|
| 298.15 | Entropy (cal/mole-K): | 43.903 | 34.829 | 93.850 | 172.582 |
| | Internal Energy (Kcal/mole): | 0.889 | 0.889 | 292.153 | 293.931 |
| | Constant Volume Heat Capacity (cal/mole-K): | 2.981 | 2.981 | 101.450 | 107.412 |

Summary of energy terms

| | hartree | eV | kcal/mol | kJ/mol |
|---|---|---|---|---|
| Bond Energy: | -12.448519930733772 | -338.7415 | -7811.57 | -32683.58 |
| Internal Energy: | 0.468408489464901 | 12.7460 | 293.93 | 1229.81 |
| pV/n = RT: | 0.000944186013486 | 0.0257 | 0.59 | 2.48 |
| Enthalpy H: | -11.979167255255385 | -325.9697 | -7517.04 | -31451.30 |
| -T*S: | -0.081999408451539 | -2.2313 | -51.46 | -215.29 |
| Gibbs free energy: | -12.061166663706924 | -328.2010 | -7568.50 | -31666.59 |

## MCH

| Temp | | Transl | Rotat | Vibrat | Total |
|---|---|---|---|---|---|
| 298.15 | Entropy (cal/mole-K): | 43.903 | 34.861 | 102.055 | 180.819 |
| | Internal Energy (Kcal/mole): | 0.889 | 0.889 | 295.678 | 297.455 |
| | Constant Volume Heat Capacity (cal/mole-K): | 2.981 | 2.981 | 104.530 | 110.492 |

Summary of energy terms

| | hartree | eV | kcal/mol | kJ/mol |
|---|---|---|---|---|
| Bond Energy: | -12.465924197660872 | -339.2151 | -7822.49 | -32729.28 |
| Internal Energy: | 0.474024981342458 | 12.8989 | 297.46 | 1244.55 |
| pV/n = RT: | 0.000944186013486 | 0.0257 | 0.59 | 2.48 |
| Enthalpy H: | -11.990955030304928 | -326.2905 | -7524.44 | -31482.25 |
| -T*S: | -0.085912767688622 | -2.3378 | -53.91 | -225.56 |
| Gibbs free energy: | -12.076867797993550 | -328.6283 | -7578.35 | -31707.81 |

# Ir-OAc

## anag

| Temp | | Transl | Rotat | Vibrat | Total |
|---|---|---|---|---|---|
| 298.15 | Entropy (cal/mole-K): | 44.757 | 35.170 | 96.338 | 176.264 |
| | Internal Energy (Kcal/mole): | 0.889 | 0.889 | 286.637 | 288.414 |
| | Constant Volume Heat Capacity (cal/mole-K): | 2.981 | 2.981 | 100.322 | 106.284 |

Contributions from frequencies below 20 1/cm

| | |
|---|---|
| Frequency (1/cm): | 17.773 |
| Entropy (cal/mole-K): | 6.869 |
| Internal Energy (Kcal/mole): | 0.593 |
| Constant Volume Heat Capacity (cal/mole-K): | 1.986 |

Summary of energy terms

| | hartree | eV | kcal/mol | kJ/mol |
|---|---|---|---|---|
| Bond Energy: | -12.272063483265541 | -333.9398 | -7700.84 | -32220.30 |
| Internal Energy: | 0.459617324747465 | 12.5068 | 288.41 | 1206.73 |
| pV/n = RT: | 0.000944186013486 | 0.0257 | 0.59 | 2.48 |
| Enthalpy H: | -11.811501972504590 | -321.4073 | -7411.83 | -31011.09 |
| -T*S: | -0.083748891613994 | -2.2789 | -52.55 | -219.88 |
| Gibbs free energy: | -11.895250864118584 | -323.6862 | -7464.38 | -31230.98 |

## TS-ag

| Temp | | Transl | Rotat | Vibrat | Total |
|---|---|---|---|---|---|
| 298.15 | Entropy (cal/mole-K): | 44.757 | 35.066 | 111.648 | 191.470 |
| | Internal Energy (Kcal/mole): | 0.889 | 0.889 | 287.238 | 289.015 |
| | Constant Volume Heat Capacity (cal/mole-K): | 2.981 | 2.981 | 104.796 | 110.757 |

Summary of energy terms

| | hartree | eV | kcal/mol | kJ/mol |
|---|---|---|---|---|
| Bond Energy: | -12.261529612357618 | -333.6532 | -7694.23 | -32192.64 |
| Internal Energy: | 0.460574723809572 | 12.5329 | 289.02 | 1209.24 |
| pV/n = RT: | 0.000944186013486 | 0.0257 | 0.59 | 2.48 |
| Enthalpy H: | -11.800010702534561 | -321.0946 | -7404.62 | -30980.92 |
| -T*S: | -0.090973753245572 | -2.4755 | -57.09 | -238.85 |
| Gibbs free energy: | -11.890984455780133 | -323.5702 | -7461.71 | -31219.78 |

## ag

| Temp | | Transl | Rotat | Vibrat | Total |
|---|---|---|---|---|---|
| 298.15 | Entropy (cal/mole-K): | 44.757 | 35.109 | 97.917 | 177.783 |
| | Internal Energy (Kcal/mole): | 0.889 | 0.889 | 285.859 | 287.636 |
| | Constant Volume Heat Capacity (cal/mole-K): | 2.981 | 2.981 | 98.800 | 104.762 |

Contributions from frequencies below 20 1/cm

| | |
|---|---|
| Frequency (1/cm): | 13.659 |
| Entropy (cal/mole-K): | 7.392 |
| Internal Energy (Kcal/mole): | 0.593 |
| Constant Volume Heat Capacity (cal/mole-K): | 1.986 |

Summary of energy terms

| | hartree | eV | kcal/mol | kJ/mol |
|---|---|---|---|---|
| Bond Energy: | -12.254329787130294 | -333.4573 | -7689.71 | -32173.74 |
| Internal Energy: | 0.458377563718904 | 12.4731 | 287.64 | 1203.47 |
| pV/n = RT: | 0.000944186013486 | 0.0257 | 0.59 | 2.48 |
| Enthalpy H: | -11.795008037397904 | -320.9585 | -7401.48 | -30967.79 |
| -T*S: | -0.084470250189199 | -2.2986 | -53.01 | -221.78 |
| Gibbs free energy: | -11.879478287587103 | -323.2571 | -7454.49 | -31189.57 |

## TS-CH

| Temp | | Transl | Rotat | Vibrat | Total |
|---|---|---|---|---|---|
| 298.15 | Entropy (cal/mole-K): | 44.757 | 35.040 | 93.471 | 173.267 |
| | Internal Energy (Kcal/mole): | 0.889 | 0.889 | 283.069 | 284.847 |
| | Constant Volume Heat Capacity (cal/mole-K): | 2.981 | 2.981 | 99.164 | 105.126 |

Contributions from frequencies below 20 1/cm

| | |
|---|---|
| Frequency (1/cm): | 15.980 |
| Entropy (cal/mole-K): | 7.080 |
| Internal Energy (Kcal/mole): | 0.593 |
| Constant Volume Heat Capacity (cal/mole-K): | 1.986 |

Summary of energy terms

| | hartree | eV | kcal/mol | kJ/mol |
|---|---|---|---|---|
| Bond Energy: | -12.261525728176252 | -333.6531 | -7694.22 | -32192.63 |
| Internal Energy: | 0.453932088844508 | 12.3521 | 284.85 | 1191.80 |
| pV/n = RT: | 0.000944186013486 | 0.0257 | 0.59 | 2.48 |
| Enthalpy H: | -11.806649453318260 | -321.2753 | -7408.79 | -30998.35 |
| -T*S: | -0.082324772165576 | -2.2402 | -51.66 | -216.14 |
| Gibbs free energy: | -11.888974225483835 | -323.5154 | -7460.44 | -31214.50 |

## MCH

| Temp | | Transl | Rotat | Vibrat | Total |
|---|---|---|---|---|---|
| 298.15 | Entropy (cal/mole-K): | 44.757 | 35.106 | 100.665 | 180.527 |
| | Internal Energy (Kcal/mole): | 0.889 | 0.889 | 286.844 | 288.622 |
| | Constant Volume Heat Capacity (cal/mole-K): | 2.981 | 2.981 | 102.384 | 108.346 |

Contributions from frequencies below 20 1/cm

| | |
|---|---|
| Frequency (1/cm): | 8.616 |
| Entropy (cal/mole-K): | 8.307 |
| Internal Energy (Kcal/mole): | 0.593 |
| Constant Volume Heat Capacity (cal/mole-K): | 1.987 |

Summary of energy terms

| | hartree | eV | kcal/mol | kJ/mol |
|---|---|---|---|---|
| Bond Energy: | -12.276810490819294 | -334.0690 | -7703.82 | -32232.76 |
| Internal Energy: | 0.459947897582999 | 12.5158 | 288.62 | 1207.59 |
| pV/n = RT: | 0.000944186013486 | 0.0257 | 0.59 | 2.48 |
| Enthalpy H: | -11.815918407222808 | -321.5275 | -7414.60 | -31022.69 |
| -T*S: | -0.085774414904061 | -2.3340 | -53.82 | -225.20 |
| Gibbs free energy: | -11.901692822126870 | -323.8615 | -7468.43 | -31247.89 |

# Ir-NHAc

## anag

| Temp | | Transl | Rotat | Vibrat | Total |
|---|---|---|---|---|---|
| 298.15 | Entropy (cal/mole-K): | 44.751 | 35.181 | 100.160 | 180.092 |
| | Internal Energy (Kcal/mole): | 0.889 | 0.889 | 294.790 | 296.567 |
| | Constant Volume Heat Capacity (cal/mole-K): | 2.981 | 2.981 | 103.655 | 109.617 |

Contributions from frequencies below 20 1/cm

| | |
|---|---|
| Frequency (1/cm): | 17.927 |
| Entropy (cal/mole-K): | 6.851 |
| Internal Energy (Kcal/mole): | 0.593 |
| Constant Volume Heat Capacity (cal/mole-K): | 1.986 |

Summary of energy terms

| | hartree | eV | kcal/mol | kJ/mol |
|---|---|---|---|---|
| Bond Energy: | -12.459391046387385 | -339.0373 | -7818.39 | -32712.13 |
| Internal Energy: | 0.472610024719462 | 12.8604 | 296.57 | 1240.84 |
| pV/n = RT: | 0.000944186013486 | 0.0257 | 0.59 | 2.48 |
| Enthalpy H: | -11.985836835654437 | -326.1512 | -7521.23 | -31468.81 |
| -T*S: | -0.085567641407969 | -2.3284 | -53.69 | -224.66 |
| Gibbs free energy: | -12.071404477062407 | -328.4796 | -7574.92 | -31693.47 |

## TS-ag

| Temp | | Transl | Rotat | Vibrat | Total |
|---|---|---|---|---|---|
| 298.15 | Entropy (cal/mole-K): | 44.751 | 35.204 | 99.792 | 179.747 |
| | Internal Energy (Kcal/mole): | 0.889 | 0.889 | 294.205 | 295.982 |
| | Constant Volume Heat Capacity (cal/mole-K): | 2.981 | 2.981 | 101.859 | 107.821 |

Contributions from frequencies below 20 1/cm

| | |
|---|---|
| Frequency (1/cm): | 16.155 |
| Entropy (cal/mole-K): | 7.058 |
| Internal Energy (Kcal/mole): | 0.593 |
| Constant Volume Heat Capacity (cal/mole-K): | 1.986 |

Summary of energy terms

| | hartree | eV | kcal/mol | kJ/mol |
|---|---|---|---|---|
| Bond Energy: | -12.450385564392356 | -338.7922 | -7812.74 | -32688.48 |
| Internal Energy: | 0.471677461860631 | 12.8350 | 295.98 | 1238.39 |
| pV/n = RT: | 0.000944186013486 | 0.0257 | 0.59 | 2.48 |
| Enthalpy H: | -11.977763916518239 | -325.9315 | -7516.16 | -31447.61 |
| -T*S: | -0.085403588367597 | -2.3239 | -53.59 | -224.23 |
| Gibbs free energy: | -12.063167504885836 | -328.2555 | -7569.75 | -31671.84 |

## ag

| Temp | | Transl | Rotat | Vibrat | Total |
|---|---|---|---|---|---|
| 298.15 | Entropy (cal/mole-K): | 44.751 | 35.275 | 104.344 | 184.370 |
| | Internal Energy (Kcal/mole): | 0.889 | 0.889 | 294.816 | 296.593 |
| | Constant Volume Heat Capacity (cal/mole-K): | 2.981 | 2.981 | 103.510 | 109.472 |

Summary of energy terms

| | hartree | eV | kcal/mol | kJ/mol |
|---|---|---|---|---|
| Bond Energy: | -12.460736208900574 | -339.0739 | -7819.23 | -32715.66 |
| Internal Energy: | 0.472650937403440 | 12.8615 | 296.59 | 1240.94 |
| pV/n = RT: | 0.000944186013486 | 0.0257 | 0.59 | 2.48 |
| Enthalpy H: | -11.987141085483648 | -326.1867 | -7522.05 | -31472.23 |
| -T*S: | -0.087600065012271 | -2.3837 | -54.97 | -229.99 |
| Gibbs free energy: | -12.074741150495919 | -328.5704 | -7577.02 | -31702.23 |

## ag-col

| Temp | | Transl | Rotat | Vibrat | Total |
|---|---|---|---|---|---|
| 298.15 | Entropy (cal/mole-K): | 44.751 | 35.056 | 99.940 | 179.748 |
| | Internal Energy (Kcal/mole): | 0.889 | 0.889 | 293.773 | 295.551 |
| | Constant Volume Heat Capacity (cal/mole-K): | 2.981 | 2.981 | 103.495 | 109.456 |

Contributions from frequencies below 20 1/cm

| | |
|---|---|
| Frequency (1/cm): | 17.312 |
| Entropy (cal/mole-K): | 6.921 |
| Internal Energy (Kcal/mole): | 0.593 |
| Constant Volume Heat Capacity (cal/mole-K): | 1.986 |

Summary of energy terms

| | hartree | eV | kcal/mol | kJ/mol |
|---|---|---|---|---|
| Bond Energy: | -12.458727508376384 | -339.0192 | -7817.97 | -32710.38 |
| Internal Energy: | 0.470990251892357 | 12.8163 | 295.55 | 1236.58 |
| pV/n = RT: | 0.000944186013486 | 0.0257 | 0.59 | 2.48 |
| Enthalpy H: | -11.986793070470542 | -326.1772 | -7521.83 | -31471.32 |
| -T*S: | -0.085404080454200 | -2.3240 | -53.59 | -224.23 |
| Gibbs free energy: | -12.072197150924742 | -328.5012 | -7575.42 | -31695.55 |

## TS-CH

| Temp | | Transl | Rotat | Vibrat | Total |
|---|---|---|---|---|---|
| 298.15 | Entropy (cal/mole-K): | 44.751 | 35.047 | 96.900 | 176.699 |
| | Internal Energy (Kcal/mole): | 0.889 | 0.889 | 292.478 | 294.256 |
| | Constant Volume Heat Capacity (cal/mole-K): | 2.981 | 2.981 | 101.609 | 107.571 |

Contributions from frequencies below 20 1/cm

| | |
|---|---|
| Frequency (1/cm): | 10.991 |
| Entropy (cal/mole-K): | 7.823 |
| Internal Energy (Kcal/mole): | 0.593 |
| Constant Volume Heat Capacity (cal/mole-K): | 1.987 |

Summary of energy terms

| | hartree | eV | kcal/mol | kJ/mol |
|---|---|---|---|---|
| Bond Energy: | -12.453523203496044 | -338.8776 | -7814.70 | -32696.72 |
| Internal Energy: | 0.468925979823461 | 12.7601 | 294.26 | 1231.16 |
| pV/n = RT: | 0.000944186013486 | 0.0257 | 0.59 | 2.48 |
| Enthalpy H: | -11.983653037659098 | -326.0918 | -7519.86 | -31463.08 |
| -T*S: | -0.083955222176349 | -2.2845 | -52.68 | -220.42 |
| Gibbs free energy: | -12.067608259835445 | -328.3763 | -7572.54 | -31683.50 |

## MCH

| Temp | | Transl | Rotat | Vibrat | Total |
|---|---|---|---|---|---|
| 298.15 | Entropy (cal/mole-K): | 44.751 | 35.105 | 100.025 | 179.882 |
| | Internal Energy (Kcal/mole): | 0.889 | 0.889 | 294.912 | 296.689 |
| | Constant Volume Heat Capacity (cal/mole-K): | 2.981 | 2.981 | 103.159 | 109.120 |

Contributions from frequencies below 20 1/cm

| | |
|---|---|
| Frequency (1/cm): | 17.666 |
| Entropy (cal/mole-K): | 6.881 |
| Internal Energy (Kcal/mole): | 0.593 |
| Constant Volume Heat Capacity (cal/mole-K): | 1.986 |

Summary of energy terms

| | hartree | eV | kcal/mol | kJ/mol |
|---|---|---|---|---|
| Bond Energy: | -12.480775538673159 | -339.6192 | -7831.81 | -32768.27 |
| Internal Energy: | 0.472804221259592 | 12.8657 | 296.69 | 1241.35 |
| pV/n = RT: | 0.000944186013486 | 0.0257 | 0.59 | 2.48 |
| Enthalpy H: | -12.007027131400081 | -326.7278 | -7534.52 | -31524.45 |
| -T*S: | -0.085467684508398 | -2.3257 | -53.63 | -224.40 |
| Gibbs free energy: | -12.092494815908479 | -329.0535 | -7588.16 | -31748.84 |

## DFT Calculations: QTAIM-IQA data

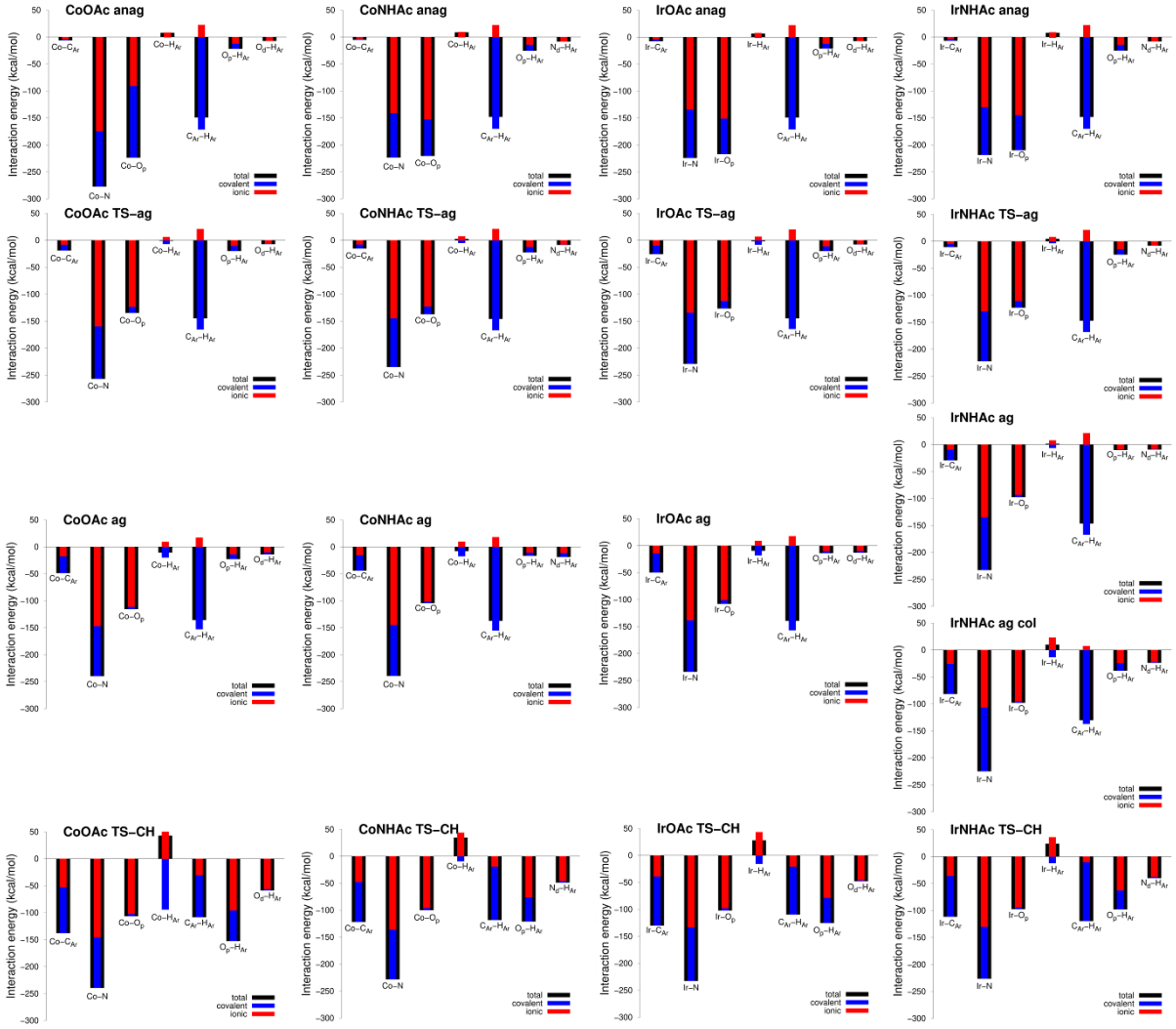


**Figure A. 82.** IQA analysis of anag, TS-ag, ag and TS-CH in CoOAc, CoNHAc, IrOAc and IrNHAc systems (and ag-col in IrNHAc). Histograms of atom-pair interaction energies within the reactive site (black coloured, total $E_{int}$ in kcal/mol) are decomposed into their covalent component (blue colored bars) and ionic component (red colored bars).

## LED analysis of the DLPNO-CCS(D)T computations

**Table A. 27.** DLPNO-CCSD(T)/LED results for Co-OAc (All energies in kcal/mol)

| | anag | TS-ag | ag | TS-CH | MCH |
|---|---|---|---|---|---|
| Etot | -1554789 | -1554777 | -1554776 | -1554766 | -1554780 |
| $E_{2-1}$ | 334 | 438 | 527 | 482 | 377 |
| $E_{3-1}$ | -1346 | -1103 | -1077 | -988 | -792 |
| $E_{4-1}$ | -1015 | -1272 | -1589 | -2096 | -2731 |
| $E_{5-1}$ | -4296 | -4575 | -4373 | -3901 | -3511 |
| $E_{3-2}$ | -140 | -157 | -176 | -343 | -555 |
| $E_{4-2}$ | -701 | -726 | -741 | -499 | -214 |
| $E_{5-2}$ | -120 | -160 | -187 | -164 | -124 |
| $E_{4-3}$ | 143 | 162 | 184 | 137 | 162 |
| $E_{5-3}$ | 220 | 194 | 184 | 179 | 157 |
| $E_{5-4}$ | 163 | 218 | 255 | 247 | 250 |

**Table A. 28.** DLPNO-CCSD(T)/LED results for Co-NHAc (All energies in kcal/mol)

| | anag | TS-ag | ag | TS-CH | MCH |
|---|---|---|---|---|---|
| Etot | -1542315 | -1542303 | -1542304 | -1542296 | -1542315 |
| $E_{2-1}$ | 334 | 418 | 520 | 481 | 366 |
| $E_{3-1}$ | -1616 | -1383 | -1357 | -1315 | -1041 |
| $E_{4-1}$ | -981 | -1201 | -1542 | -1922 | -2761 |
| $E_{5-1}$ | -4063 | -4356 | -4203 | -3749 | -3287 |
| $E_{3-2}$ | -154 | -167 | -185 | -296 | -573 |
| $E_{4-2}$ | -695 | -715 | -739 | -573 | -202 |
| $E_{5-2}$ | -118 | -149 | -180 | -160 | -119 |
| $E_{4-3}$ | -159 | -177 | -201 | -166 | -179 |
| $E_{5-3}$ | 237 | 210 | 192 | 195 | 161 |
| $E_{5-4}$ | 153 | 199 | 242 | 230 | 237 |

**Table A. 29.** DLPNO-CCSD(T)/LED results for Ir-OAc (All energies in kcal/mol)

| | **anag** | **TS-ag** | **ag** | **TS-CH** | **MCH** |
|---|---|---|---|---|---|
| Etot | -752850 | -752829 | -752839 | -752833 | -7528551 |
| $E_{2-1}$ | 333 | 426 | 487 | 481 | 365 |
| $E_{3-1}$ | -1036 | -880 | -868 | -838 | -661 |
| $E_{4-1}$ | -849 | -1051 | -12552 | -1631 | -2011 |
| $E_{5-1}$ | -3347 | -3512 | -3341 | -3001 | -27883 |
| $E_{3-2}$ | -139 | -153 | -159 | -296 | -557 |
| $E_{4-2}$ | -699 | -717 | -731 | --540 | -198 |
| $E_{5-2}$ | -126 | -165 | 184 | -175 | -131 |
| $E_{4-3}$ | 141 | 159 | 177 | 145 | 153 |
| $E_{5-3}$ | 206 | 196 | 180 | 177 | 154 |
| $E_{5-4}$ | 169 | 221 | 248 | 251 | 261 |

**Table A. 30.** DLPNO-CCSD(T)/LED results for Ir-NHAc (All energies in kcal/mol)

| | **anag** | **TS-ag** | **ag** | **ag-col** | **TS-CH** | **MCH** |
|---|---|---|---|---|---|---|
| Etot | -740380 | -740369 | -740378 | -740371 | -740369 | -740390 |
| $E_{2-1}$ | 333 | 362 | 341 | 473 | 472 | 354 |
| $E_{3-1}$ | -1242 | -1113 | -1195 | -1074 | -1060 | -867 |
| $E_{4-1}$ | -830 | -908 | -885 | -1355 | -1492 | -2021 |
| $E_{5-1}$ | -3167 | -3440 | -3443 | -3062 | -2938 | -2575 |
| $E_{3-2}$ | -153 | -156 | -115 | -211 | -260 | -571 |
| $E_{4-2}$ | -693 | -696 | -713 | -673 | -603 | -191 |
| $E_{5-2}$ | -123 | -140 | -130 | -171 | -168 | -122 |
| $E_{4-3}$ | 156 | 152 | 143 | 184 | 172 | 171 |
| $E_{5-3}$ | 227 | 226 | 201 | 203 | 197 | 161 |
| $E_{5-4}$ | 157 | 183 | 181 | 228 | 231 | 242 |

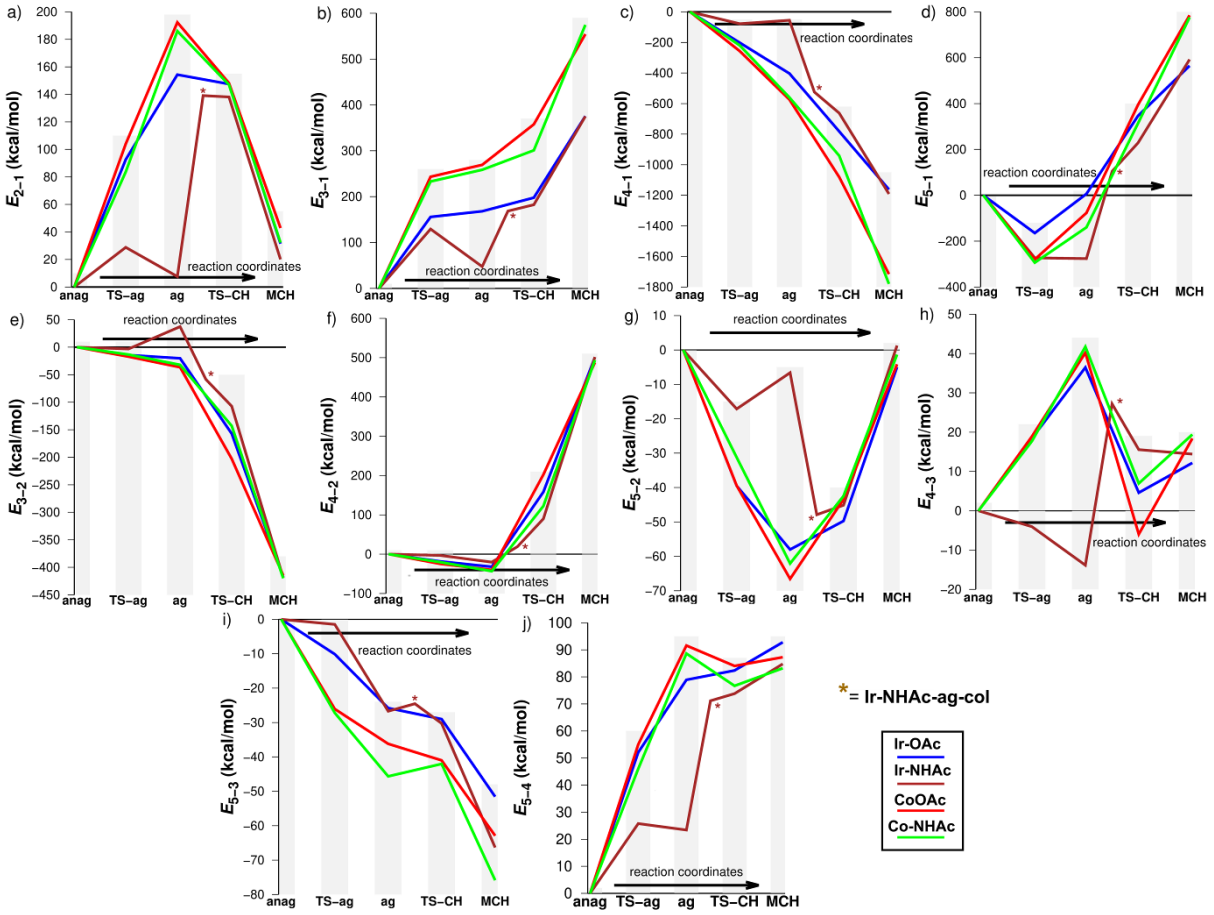


**Figure A. 83.** LED analysis for Co-OAc (red lines), Co-NHAc (green lines), Ir-OAc (blue lines) and Ir-NHAc (brown lines) systems along the reaction coordinates of the CMD mechanism with plots of inter-fragment interaction energies $E_{i-j}$, where *i* and *j* are the considered molecular fragment numbers : a) interaction energy between fragments 2 ($H^+$) and 1 (metal), b) interaction energy between fragments 3 (auxiliary basis) and 1 (metal), c) interaction energy between fragments 4 (2-*phpy*$^-$) and 1 (metal), d) interation energy between fragments 5 (Cp* ligand) and 1 (metal), e) interaction energy between fragments 3 (auxiliary basis) and 2 ($H^+$), f) interaction energy between fragments 4 (2-*phpy*$^-$) and 2 ($H^+$), g) interaction energy between fragments 5 (Cp* ligand) and 2 ($H^+$), h) interaction energy between fragments 4 (2-*phpy*$^-$) and 3 (auxiliary basis), i) interaction energy between fragments 5 (Cp* ligand) and 3 (auxiliary basis), j) interaction energy between fragments 5 (Cp* ligand) and 4 (2-*phpy*$^-$).

## Electrophilic C-H activation profile, energies (COSMO ($CH_2Cl_2$) - ZORA - PBE-D3(BJ) / all electron TZP)

### $[Cp^*Co]^{2+}$

Summary of energy terms

| | hartree | eV | kcal/mol | kJ/mol |
|---|---|---|---|---|
| Bond Energy: | -5.193480509846736 | -141.3218 | -3258.96 | -13635.48 |
| Internal Energy: | 0.226576047255176 | 6.1654 | 142.18 | 594.88 |
| pV/n = RT: | 0.000944186013486 | 0.0257 | 0.59 | 2.48 |
| Enthalpy H: | -4.965960276578073 | -135.1307 | -3116.19 | -13038.13 |
| -T*S: | -0.054711611543022 | -1.4888 | -34.33 | -143.65 |
| Gibbs free energy: | -5.020671888121095 | -136.6194 | -3150.52 | -13181.77 |

### 2-*phpyH*

Summary of energy terms

| | hartree | eV | kcal/mol | kJ/mol |
|---|---|---|---|---|
| Bond Energy: | -5.148539652192721 | -140.0989 | -3230.76 | -13517.49 |
| Internal Energy: | 0.173169979936746 | 4.7122 | 108.67 | 454.66 |
| pV/n = RT: | 0.000944186013486 | 0.0257 | 0.59 | 2.48 |
| Enthalpy H: | -4.974425486242488 | -135.3610 | -3121.50 | -13060.35 |
| -T*S: | -0.044859292856173 | -1.2207 | -28.15 | -117.78 |
| Gibbs free energy: | -5.019284779098661 | -136.5817 | -3149.65 | -13178.13 |

### EA-π (2+)

Summary of energy terms

| | hartree | eV | kcal/mol | kJ/mol |
|---|---|---|---|---|
| Bond Energy: | -10.462359766787859 | -284.6953 | -6565.23 | -27468.92 |
| Internal Energy: | 0.404317609803391 | 11.0020 | 253.71 | 1061.54 |
| pV/n = RT: | 0.000944186013486 | 0.0257 | 0.59 | 2.48 |
| Enthalpy H: | -10.057097970970982 | -273.6676 | -6310.92 | -26404.91 |
| -T*S: | -0.074224259503733 | -2.0197 | -46.58 | -194.88 |
| Gibbs free energy: | -10.131322230474716 | -275.6873 | -6357.50 | -26599.78 |

### EA-pre-TS (2+)

Summary of energy terms

| | hartree | eV | kcal/mol | kJ/mol |
|---|---|---|---|---|
| Bond Energy: | -15.634413983919819 | -425.4341 | -9810.74 | -41048.15 |
| Internal Energy: | 0.580363622440300 | 15.7925 | 364.18 | 1523.74 |
| pV/n = RT: | 0.000944186013486 | 0.0257 | 0.59 | 2.48 |
| Enthalpy H: | -15.053106175466032 | -409.6159 | -9445.97 | -39521.92 |
| -T*S: | -0.099572324699498 | -2.7095 | -62.48 | -261.43 |
| Gibbs free energy: | -15.152678500165530 | -412.3254 | -9508.45 | -39783.35 |

### EA-TS-CH (2+)

Summary of energy terms

| | hartree | eV | kcal/mol | kJ/mol |
|---|---|---|---|---|
| Bond Energy: | -15.628210571346047 | -425.2652 | -9806.85 | -41031.86 |
| Internal Energy: | 0.575121170229745 | 15.6498 | 360.89 | 1509.98 |
| pV/n = RT: | 0.000944186013486 | 0.0257 | 0.59 | 2.48 |
| Enthalpy H: | -15.052145215102817 | -409.5897 | -9445.36 | -39519.40 |
| -T*S: | -0.094260050190373 | -2.5649 | -59.15 | -247.48 |
| Gibbs free energy: | -15.146405265293190 | -412.1547 | -9504.51 | -39766.88 |

### EA-MCH (2+)

Summary of energy terms

| | hartree | eV | kcal/mol | kJ/mol |
|---|---|---|---|---|
| Bond Energy: | -15.649161782477812 | -425.8354 | -9820.00 | -41086.87 |
| Internal Energy: | 0.581024366988613 | 15.8105 | 364.60 | 1525.48 |
| pV/n = RT: | 0.000944186013486 | 0.0257 | 0.59 | 2.48 |
| Enthalpy H: | -15.067193229475713 | -409.9992 | -9454.81 | -39558.91 |
| -T*S: | -0.093412647094798 | -2.5419 | -58.62 | -245.25 |
| Gibbs free energy: | -15.160605876570511 | -412.5411 | -9513.42 | -39804.17 |

## Theoretical material for chapter 3

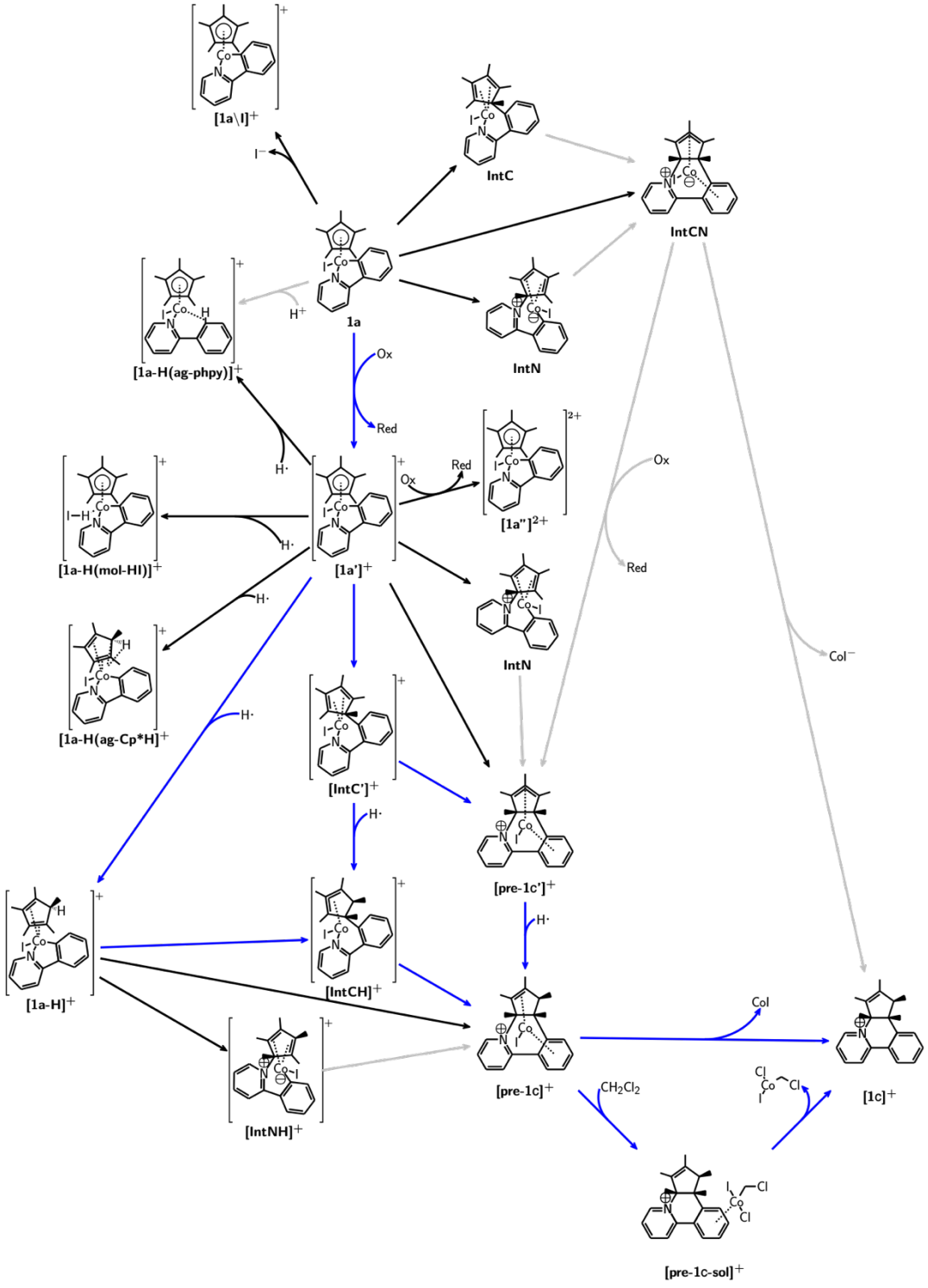


**Scheme A. 1.** Theoretically considered structures and pathways for the formation of [**1c**]$^+$ from **1a**. (black arrows) considered pathways, (blue arrows) proposed pathways, (gray arrow) pathways not explored in this study.

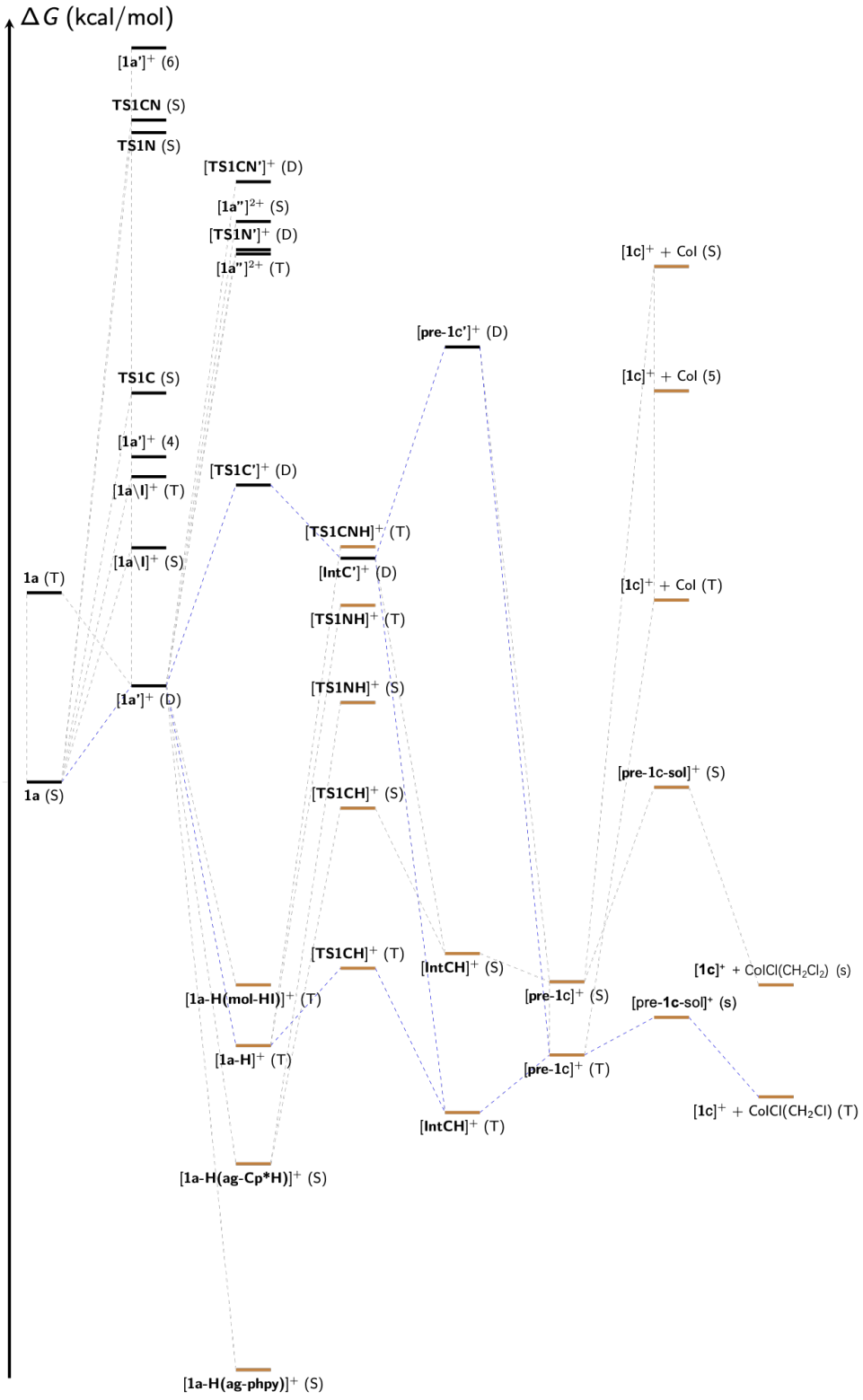


**Figure A. 84.** Gibbs free energy (ZORA-PBE-D4(EEQ)/all electron TZP/COSMO($CH_2Cl_2$) level) diagram of the considered pathways for the formation of [**1c**]$^+$ from 1a, considering the presence of a fictitious H• in the reactive medium. The energy of the abstraction of H• (*e.g.* +71.4 kcal/mol if H• originates from

triphenylmethane) should be added to the energies represented by brown lines. (grey dotted lines) considered pathways, (blue dotted lines) proposed pathways.

**Table A. 31.** Energies of optimized geometries at the ZORA-PBE-D4(EEQ)/all electron TZP/COSMO($CH_2Cl_2$) level

| System | Spin multiplicity | Bond energy (kcal/mol) | Enthalpy (kcal/mol) | Gibbs free energy (kcal/mol) |
|---|---|---|---|---|
| **1a** | 1 | -6761.02 | -6511.23 | -6561.07 |
| **1a** | 3 | -6740.24 | -6491.08 | -6542.94 |
| [**1a'**]$^+$ | 2 | -6648.17 | -6398.68 | -6446.90 |
| [**1a'**]$^+$ | 4 | -6622.39 | -6373.07 | -6424.96 |
| [**1a'**]$^+$ | 6 | -6589.88 | -6341.46 | -6395.15 |
| [**1a''**]$^{2+}$ | 1 | -6498.37 | -6250.16 | -6297.51 |
| [**1a''**]$^{2+}$ | 3 | -6499.24 | -6249.81 | -6300.59 |
| **TS1C (1a→IntC)** | 1 | -6723.95 | -6475.43 | -6523.92 |
| **TS1N (1a→IntN)** | 1 | -6699.06 | -6450.54 | -6498.94 |
| **TS1CN (1a→IntCN)** | 1 | -6697.13 | -6448.92 | -6497.75 |
| [**1a-H**(**ag-phpy**)]$^+$ | 1 | -6744.68 | -6487.52 | -6537.97 |
| [**1a-H(ag-Cp*H)**]$^+$ | 1 | -6723.99 | -6467.95 | -6518.30 |
| [**1a-H**]$^+$ | 3 | -6713.74 | -6457.55 | -6506.93 |
| [**1a-H**(**mol-HI**)]$^+$ | 3 | -6702.37 | -6449.72 | -6501.20 |
| [**TS1C**]$^+$ **(1a-H→IntCH)** | 1 | -6690.21 | -6435.26 | -6484.30 |
| [**TS1N**]$^+$ **(1a-H→IntNH)** | 1 | -6679.96 | -6425.54 | -6474.22 |
| [**TS1C**]$^+$ **(1a-H→IntCH)** | 3 | -6706.83 | -6450.51 | -6499.50 |
| [**TS1N**]$^+$ **(1a-H→IntNH)** | 3 | -6671.68 | -6415.37 | -6464.80 |
| [**TS1CN**]$^+$ **(1a-H→pre-1c)** | 3 | -6665.12 | -6409.12 | -6459.25 |
| **IntCH** | 1 | -6703.47 | -6448.47 | -6498.14 |
| **IntCH** | 3 | -6721.61 | -6463.62 | -6513.33 |
| [**pre-1c**]$^+$ | 3 | -6718.70 | -6460.47 | -6507.79 |
| [**pre-1c**]$^+$ | 1 | -6712.51 | -6453.91 | -6500.75 |
| [**TS1C'**]$^+$ **(1'a→IntC')** | 2 | -6628.50 | -6379.10 | -6427.70 |
| [**TS1N'**]$^+$ **(1'a→IntN')** | 2 | -6605.77 | -6356.55 | -6405.19 |
| [**TS1CN'**]$^+$ **(1'a→pre-1c')** | 2 | -6598.55 | -6349.50 | -6398.70 |
| [**IntC'**]$^+$ | 2 | -6635.55 | -6385.12 | -6434.69 |
| [**pre-1c'**]$^+$ | 2 | -6617.88 | -6367.16 | -6414.52 |
| [**pre-1c-sol**]$^+$ | 3 | -7203.70 | -6924.30 | -6980.18 |

| | | | | |
|---|---|---|---|---|
| [**pre-1c-sol**]$^+$ | 1 | -7183.08 | -6902.94 | -6958.23 |
| CoICl($CH_2Cl$) | 1 | -670.58 | -647.20 | -675.11 |
| CoICl(CH2Cl) | 3 | -680.42 | -656.96 | -685.75 |
| [**1a\\I**]$^+$ | 1 | -6594.29 | -6346.77 | -6391.91 |
| [**1a\\I**]$^+$ | 3 | -6585.38 | -6337.51 | -6385.13 |
| **Ir-1a** | 1 | -6774.30 | -6525.30 | -6574.50 |
| **Ir-1a** | 3 | -6730.28 | -6482.34 | -6534.50 |
| [**Ir-1a'**]$^+$ | 2 | -6660.12 | -6410.77 | -6460.16 |
| CoI | 1 | -114.89 | -112.14 | -130.32 |
| CoI | 3 | -146.69 | -143.96 | -162.22 |
| CoI | 5 | -126.44 | -123.73 | -142.16 |
| [**1c**]$^+$ | 1 | -6513.55 | -6258.70 | -6302.05 |
| $Ph_3C^+$ | 1 | -5094.07 | -4913.77 | -4950.42 |
| $Ph_3C^\cdot$ | 2 | -5197.87 | -5018.72 | -5055.40 |
| $Ph_3CH$ | 1 | -5301.71 | -5114.75 | -5152.48 |
| $Ph_3CI$ | 1 | -5238.08 | -5056.74 | -5097.19 |
| 4-$(Ph_3C)(CPh_2)C_6H_5$ | 1 | -10405.07 | -10044.71 | -10102.20 |
| 4-$(Ph_3C)(CPh_2)C_6H_4^\cdot$ | 2 | -10326.64 | -9973.70 | -10030.99 |
| $I_2$ | 1 | -54.95 | -52.24 | -70.89 |
| $I^-$ | 1 | -130.96 | | |
| $H^\cdot$ | 2 | -25.68 | | |
| $CH_2Cl_2$ | 1 | -476.90 | -456.31 | -476.07 |

Université de Strasbourg

EDSC École Doctorale des Sciences Chimiques

# Fule WU

# Cobaltacycles du Cp*Co(III): Synthèse rationnelle et implication en catalyse homogène


## Résumé en français

Les catalyseurs Cp*Co(III) ont attiré beaucoup d'attention en tant qu'alternative attrayante aux métaux de transition nobles, par exemple Cp*Rh(III) et Cp*Ir(III), pour l'activation de liaison C-H. Jusqu'à présent, la compréhension mécanistique fondamentale concernant le fonctionnement des protocoles catalysés par le Cp*Co(III) est considérablement peu développée. Dans ce manuscrit, nous présentons la synthèse et la caractérisation de complexes Cp*Co(III) cyclométallisés via le mécanisme CMD assisté par une base, et nous élucidons le mécanisme de fonctionnement du clivage des liaisons C-H médié par Cp*Co(III). Leur application en catalyse homogène a également été étudiée de manière préliminaire. En outre, la décomposition irréversible des métallacycles Cp*Co(III) dans des cas spécifiques et la formation d'alcaloïdes ont été étudiés de manière approfondie, tant sur le plan expérimental que théorique. Le métallacyclique Cp*Co(III) est un intermédiaire clé en catalyse, qui peut subir des réactions de fonctionnalisation C-H ultérieures. Cependant, comme nous l'avons montré dans notre travail, il peut également réagir rapidement en solution avec des oxydants à un électron pour donner de nouveaux alcaloïdes cationiques tridimensionnels par la cyclocondensation de la 2-aryl pyridine et du Cp* via un intermédiaire Co(IV), où un atome H migre vers un atome de carbone du Cp*, mais l'origine des atomes H capturés n'a pas encore été entièrement déterminée. Globalement, ce résultat inattendu jette une nouvelle lumière sur les systèmes catalytiques largement acceptés, remettant ainsi en question leur robustesse.



**Mots clés :** Cobaltacycles, mécanisme CMD assisté par acétamidate, catalyse homogène, effondrement, oxydatif, alcaloïdes cationiques.



## Résumé en anglais

The Cp*Co(III)-catalysts have attracted significant attention as an attractive alternative for noble transition metals, e,g., Cp*Rh(III) and Cp*Ir(III) in C-H activation. Until now, the fundamental mechanistic understanding concerning how Cp*Co(III)-catalyzed protocols operate is significantly overlooked. In this manuscript are presented the synthesis and characterization of cyclometalated Cp*Co(III)-complexes via base-assisted CMD mechanism, and to elucidate the operating mechanism in the Cp*Co(III)-mediated cleavage of C-H bonds. Their application in homogeneous catalysis was also preliminarily investigated. Moreover, the irreversible collapse of Cp*Co(III) metallacycles in specific cases and the formation of alkaloids were comprehensively investigated both experimentally and theoretically. The Cp*Co(III) metallacycle, is a key intermediate in catalysis, which can undergo subsequent C-H functionalization reactions. However, as shown in our work, it can also react swiftly in solution with one-electron oxidants to afford new three-dimensional cationic alkaloids by the cyclocondensation of the 2-aryl pyridine and Cp* via a Co(IV) intermediate, where an H atom migrates to a carbon atom of the Cp*, but the origin of the H atoms captured has not yet been fully settled. Overall, this unexpected result draws new lights on the widely accepted catalytic systems, thus questioning their robustness.



**Key word :** Cobaltacycles, acetamidate-assisted CMD mechanism, homogeneous catalysis, collapse, oxidative, cationic alkaloids.